APPLIED COMPUTATIONAL ELECTROMAGNETICS SOCIETY JOURNAL

THE APPLIED COMPUTATIONAL ELECTROMAGNETICS SOCIETY

JOURNAL

TABLE OF CONTENTS

A Review of Recent Advances in Designing True-Time-Delay Microwave Lenses Exploiting Metamaterials with Non-Resonant Constituting Unit Cells

Nader Behdad

Department of Electrical and Computer Engineering
University of Wisconsin, Madison, WI 53706, USA
behdad@wisc.edu

Abstract ─ This paper presents a review of recent developments in the design of planar microwave lenses capable of operating over broad bandwidths in a true-time-delay fashion. The lenses discussed in this paper consist of planar apertures populated with miniature, sub-wavelength time-delay units. Each time delay unit is the unit cell of an appropriately-designed Frequency Selective Surface (FSS) with non-resonant, sub-wavelength constituting unit cells and is designed to provide a constant time-delay unit over the frequency range at which the lens operates. Designs that exploit both band-pass and low-pass FSSs are presented and discussed. Because of the non-resonant nature of their constituting unit cells and their small dimensions, such lenses can operate over broad bandwidths with wide fields of views. When used in conjunction with appropriately designed feed antennas, these lenses can be used in multi-beam, high-gain, broadband antenna apertures.

Index Terms ─ Frequency selective surfaces, microwave lenses, multi-beam antennas, phased-array antennas.

I. INTRODUCTION

Microwave lenses have been used in a variety of applications ranging from imaging and radar systems [1]-[2], to high-gain phased arrays [3]. A microwave lens generally acts as a transformer converting a spherical wave front generated by a feed antenna located on its focal point to a planar wave front at the output aperture of the lens. This transformation, however, is frequency dependent and generally works perfectly fine at only one frequency in most microwave lenses reported in the literature. In broadband, pulsed applications, a microwave lens must preserve the temporal characteristics of the transmitted pulse and pass it through with minimal distortion. Alternatively, in the receiving mode, all the frequency components of a broadband pulse incident on the aperture of the lens must be focused to the same focal point and chromatic aberrations must be minimized. In such applications, microwave lenses that act in a True Time Delay (TTD) fashion and satisfy Fermat's principle at every point on the aperture are highly desired.

Over the past several decades, numerous different types of microwave lenses and collimating structures have been reported. Examples include dielectric lenses [4]-[5], planar microwave lenses consisting of an array of transmitting and receiving antennas coupled together using a phase shifting or a time-delay mechanism [6]-[9], and Frequency Selective Surface (FSS) based microwave lenses [10]. Planar microwave lenses that use antenna arrays tend to suffer from poor scanning performance. This is primarily due to the relatively large spacing between the different phase shifting (or time delay) units that occupy the aperture of such lenses [6]-[9]. This behavior is also observed in FSS-based microwave lenses that exploit traditional frequency selective surfaces. Such FSSs are essentially identical to antenna arrays where the elements of the array are terminated with reactive elements. They too tend to suffer from poor scanning performances [10]. Additionally, the great majority of the planar microwave lenses reported in the literature are designed based on the phase

matching condition, where the lens aperture is designed to collimate a spherical incident wave into a planar output wave only at a single frequency. Therefore, such lenses are not well-suited for broadband operation where pulses with wide instantaneous bandwidths are used.

In recent years, several new classes of frequency selective surfaces that consist of sub-wavelength periodic structures with primarily non-resonant constituting unit cells were reported [11]-[13]. Since these FSSs do not use antenna elements as their constituting unit cells, their unit cells can be made extremely small. This feature leads to very stable responses for a wide range of incidence angles and polarizations of the incident wave. These FSSs, referred to as Miniaturized-Element FSSs (MEFSSs), have also been used to design planar microwave lenses [14]-[16]. In [14], the unit cells of appropriately-designed MEFSSs with band-pass frequency responses were used as spatial phase shifters to design a broadband planar lens. This lens demonstrated a wide field of view with a good scanning performance in the ±60° range. However, the lens reported in [14] satisfied Fermat's principle only at one single frequency and suffered from chromatic aberrations. Subsequently, the same types of unit cells were used in [15] to design Time-Delay Units (TDUs) capable of operating over a broad frequency band with minimal frequency dispersion. Using these TDUs, an MEFSS-based true-time-delay lens was reported in [15]. It was demonstrated that such MEFSS-based lenses can operate over very wide bandwidths without introducing any significant distortion in the temporal content of the incident pulse. Planar microwave lenses based on low-pass MEFSS were introduced in [16]. Such lenses tend to operate over an even wider frequency band than those based on band-pass MEFSSs, and they are particularly well suited for applications that work at lower microwave frequencies. The primary aim of this article is to provide a concise review of MEFSS-based true-time-delay microwave lenses and discuss their design procedures and methods for fabrication and characterization. This article reviews the recent developments in this area and it is based on the materials presented at the 2013 Harbin Engineering University Computational Electromagnetics and Applications Workshop.

II. MEFSS-BASED MICROWAVE LENSES

Figure 1 shows the topology of an MEFSS-based microwave lens. The lens is illuminated with a feed antenna located at its focal point. The spherical wave front generated by the feed antenna is converted to a planar wave front at the output aperture of the lens. The lens' aperture is populated with a number of pixels. Each pixel has sub-wavelength dimensions and acts as a time-delay unit providing a desired, constant time-delay value across the entire frequency of operation of the lens. This way, if a broadband pulse is radiated by the feed antenna, all of the frequency components of the broadband pulse will arrive at the output aperture of the lens at the same time, ensuring that no temporal distortion is introduced in the radiated pulse. Alternatively, if a plane wave arrives at the input aperture of the lens, all of the components of the incident pulse are focused at the same focal point and chromatic aberrations in the lens are minimized.
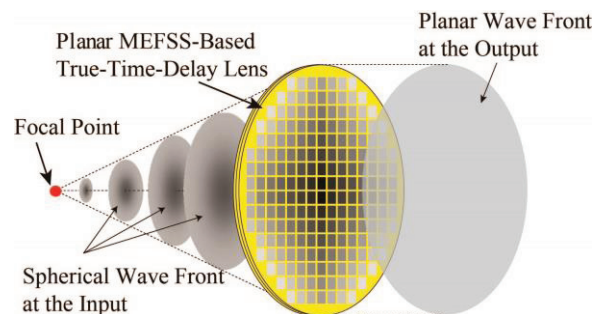
Fig. 1. Topology of a miniaturized-element frequency selective surface based microwave lens illuminated with an antenna located at its focal point.

Figure 2 (a) shows the side view of a typical MEFSS-based TTD lens. In this case, a point source is assumed to be located at the focal point of the lens generating a perfect spherical wave. The lens is conceptually illustrated with multiple metallic layers separated from each other by thin dielectric slabs. To work in a true-time-delay fashion, all the rays that leave the point source in different directions and are intercepted by the input aperture of the lens, must arrive at the output aperture of the lens at *the same time*. Let us assume that the

aperture of the lens is divided into a number of circular concentric zones with different inner and outer radii. Let us further assume that each zone of the lens is populated with identical time-delay units. In this case, the mathematical condition that needs to be satisfied to ensure that all of the rays departing the feed point arrive at the output aperture of the lens at the same time is given by the following:

$$T_1 + TD_1 = T_2 + TD_2 = \cdots = T_M + TD_M, \quad (1)$$

where T_i is the time that it takes an electromagnetic wave to travel the distance between the feed point and the center of the ith zone, and TD_i is the time-delay provided by the pixels occupying the ith zone of the lens. Since the value of T_i increases as we move away from the center of the lens towards its outer periphery, TD_i should decrease to ensure the output aperture of the lens remains and equal-time surface. Assuming that the TD_i values are constant over the desired frequency band of the lens, the phase response of each pixel will be a linear function of frequency. The higher the TD_i value is, the steeper the slope of the phase versus frequency function will be. This behavior is illustrated in Fig. 2 (b), where the ideal phase responses of TDUs occupying different zones of a typical MEFSS-based planar lens are shown. As can be seen, as the zone number increases, the slope of the phase response increases as well, which indicates a larger time delay value.

(a)   (b)
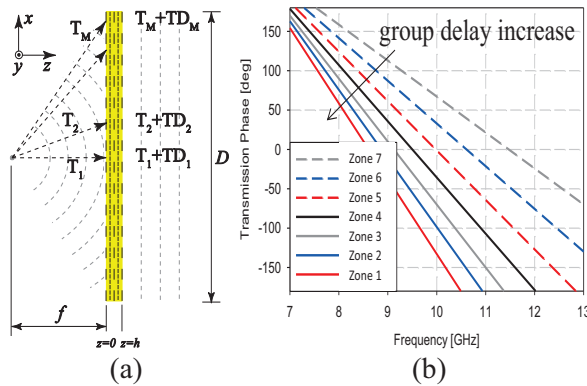
Fig. 2. (a) Side view of an MEFSS-based true-time-delay microwave lens and (b) the phase response of the different spatial time delay units occupying the aperture of the lens.

The time-delay units of an MEFSS-based microwave lens are unit cells of appropriately-designed miniaturized element frequency selective surfaces. Since these MEFSSs are designed to be impedance matched, the microwave lenses are also impedance matched. The response of an MEFSS is identified by its transfer function. In the design of MEFSS-based lenses, all pixels of the lens operate within the pass band of the MEFSSs that constitute them. Under this operational condition, each pixel introduces a minimal insertion loss and the magnitude of the transmission coefficient of the MEFSS that constitutes the pixel becomes irrelevant. In other words, only the phase response of the MEFSS and the variations of its phase response with frequency become relevant in the design of MEFSS-based microwave lenses. The design process of these lenses is based on designing MEFSSs with linear phase responses within the desired frequency band of operation. Such an MEFSS will have a constant group delay (time delay) across the frequency range where its phase response remains linear. The group delay of the MEFSS is a function of the order of its response function and the bandwidth of the FSS. For a given fixed FSS bandwidth, the group delay can be increased by increasing the order of the filter response. For a fixed filter response order, the group delay can be increased by decreasing the bandwidth of the filter. These two mechanisms can be used to design the pixels that go into the different zones of an MEFSS-based microwave lens. In the next section, we will discuss doing this in practice using MEFSSs with band-pass and low-pass responses.

III. DESIGN OF TRUE-TIME-DELAY LENSES USING BAND-PASS MEFSSs

A. Design and simulation

Figure 3 shows the unit cell topology of a band-pass MEFSS with a fourth-order response. Band-pass MEFSSs of this type are composed of a number of sub-wavelength capacitive patches and sub-wavelength inductive wires separated from one another by thin dielectric substrates. Using the design procedure presented in [12], MEFSSs of arbitrarily high orders can be designed to demonstrate a wide range of different response types, including filter responses with maximally flat group delays or linear phase types. Such MEFSSs with N^{th} order band-pass responses are composed of N capacitive layers and N-1 inductive layers. The detailed design process for MEFSSs of

this type is presented in [12] and will not be repeated here for brevity.
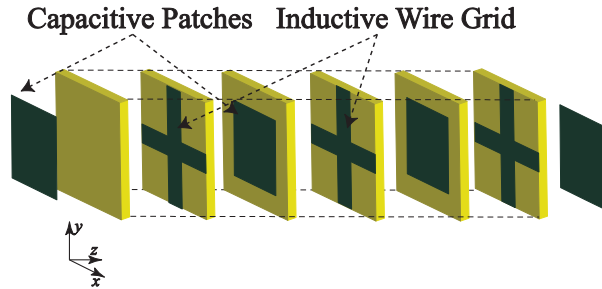
Fig. 3. Topology of a unit cell of a band-pass MEFSS of the type reported in [12]. This MEFSS has a fourth-order bandpass response and is composed of 7 metal layers and six dielectric layers.

An MEFSS-based microwave lens using band-pass MEFSSs of the type shown in Fig. 3 was presented in [15]. This lens has a circular aperture with a diameter of D=18.6 cm and a focal length of f=19 cm. This corresponds to an $f/D \approx 1$. With such aperture dimensions and f/D ratio, the maximum time delay variation over the aperture of the lens is limited to approximately 63 ns. Such a time-delay range can be achieved with an MEFSS with a fourth-order bandpass response similar to the one shown in Fig. 3. In this case, the different pixels of the lens can provide linear phase responses over the frequency band of 8.5-10.5 GHz. Figure 4 shows the simulated frequency responses of the different MEFSSs that constitute the pixels of this lens. For clarity, only a subset of the responses is shown. Figure 4 (a) shows the phase responses of the different pixels that occupy different zones of the lens. The desired phase responses that will result in an ideal true-time-delay lens are also shown for each of the 16 zones of this lens. As can be observed, the pixels provide an excellent approximation of these ideal phase responses over the highlighted frequency range. Within this frequency range, the pixels act as equivalent time-delay units.

In this lens, all of the different pixels that occupy the different zones of the lens are implemented with MEFSSs with fourth-order band-pass responses. To achieve different group delays, the bandwidth of the response of each of the MEFSSs is changed. This scenario is shown in Fig.

4 (b), where the magnitudes of the transmission and reflection coefficients of the MEFSSs that were used to design the pixels occupying each of the 16 different zones of the lens are shown. As can be seen, these MEFSSs have different transmission coefficients. However, over the highlighted frequency range in Fig. 4 (b), all of their transmission coefficients overlap with one another. Within that range, each of the MEFSSs act simply as a spatial time-delay unit providing a time-delay characterized by the negative of the derivative of the phase response of the device shown in Fig. 4 (a), with respect to the frequency.

(a)

(b)
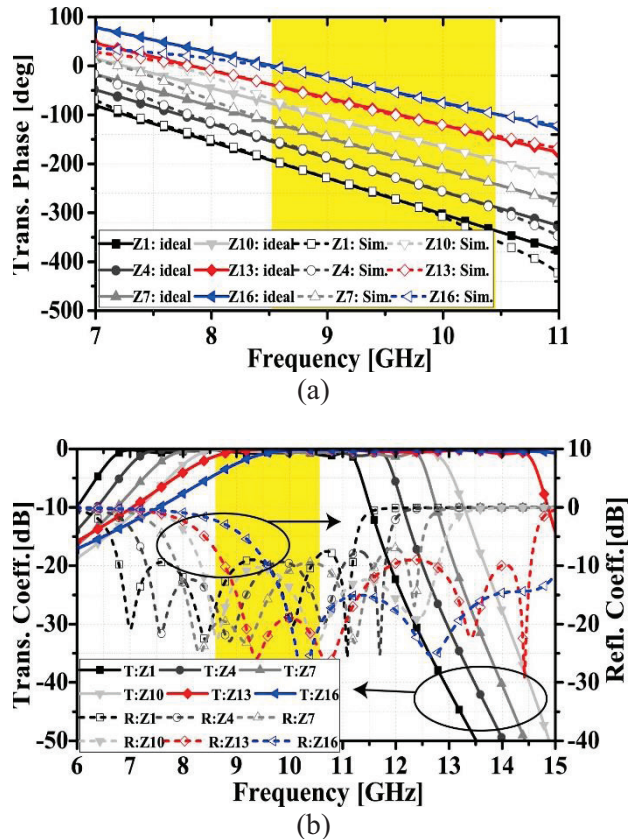
Fig. 4. (a) The simulated phase responses of the time delay units occupying the different zones of the MEFSS-based microwave lens discussed in Section III and (b) the magnitudes of the transmission and reflection coefficients of the different pixels of the lens.

B. Fabrication and measurement

The lens discussed in Section III-A is fabricated using standard Printed-Circuit-Board (PCB) fabrication and substrate bonding techniques [15].

Figure 5 shows a photograph of the fabricated prototype. The performance of the lens is characterized using a number of different measurements. First, the lens is illuminated with a plane wave from the normal direction, and the focal point of the lens is determined after the received power intensity is measured in the near field region of the lens and the location of the maximum field intensity is determined. This procedure is performed at different frequencies to experimentally determine the focal length of the antenna as a function of frequency. One of the characteristics of lenses with chromatic aberration is that their focal lengths change with frequency. Figure 6 shows the measured focal length of this lens versus frequency. As can be observed, the focal length of the lens does not change significantly with frequency, indicating minimal chromatic aberrations. For comparison, the measured focal lengths of two other MEFSS-based microwave lenses, which are not true-time-delay lenses, are also presented in Fig. 6 (these lenses are reported in [14]). Both of these lenses were designed to operate at 10.0 GHz and have bandwidths exceeding 20%. As can be observed, in both cases, the focal lengths of the lenses varies significantly with frequency, indicating that a considerable amount of chromatic aberration is present in each of them.
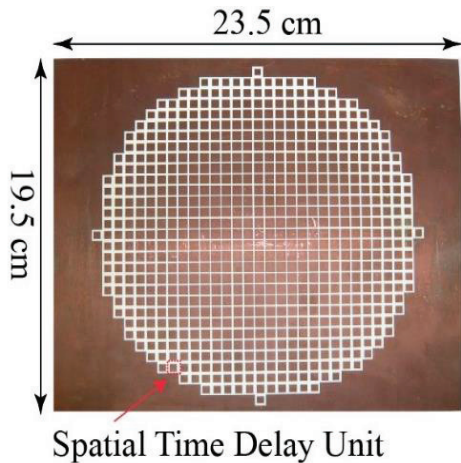
Fig. 5. Photograph of the fabricated prototype of an MEFSS-based planar microwave lens using band-pass MEFSSs (after [15]).
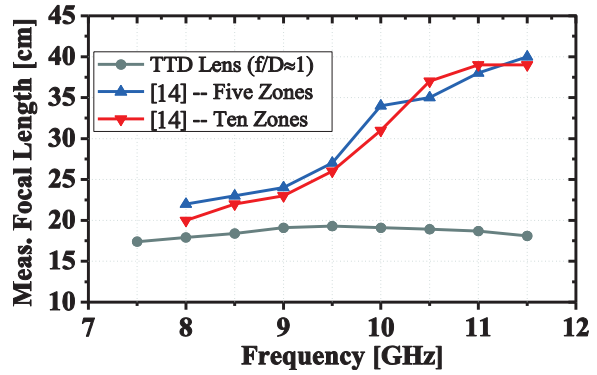
Fig. 6. Measured focal length of the lens discussed in Section III vs. frequency. For comparison the measured focal lengths of two non-TTD lenses reported in [14] are also presented.

The scanning performance of this lens is characterized using the system shown in Fig. 7. In this case, the lens is illuminated with a transmitting antenna at various incidence angles to generate plane waves arriving at the aperture of the lens from different directions. The received power pattern is then measured on the focal arc of the antenna. Because of reciprocity, if a feed antenna is placed at the location of maximum field intensity on the focal arc, a far field beam in the direction of the incoming plane wave would be excited. The measured power patterns on the focal arc of the lens are shown in Fig. 8 for three different frequencies and incidence angles in the 0°-60° range. These measured results suggest that this lens is expected to be able to operate with fields of views in the range of ±60°.
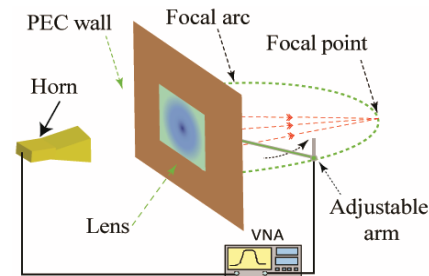
Fig. 7. The measurement setup used to measure the scanning performance of the lens under receiving conditions.
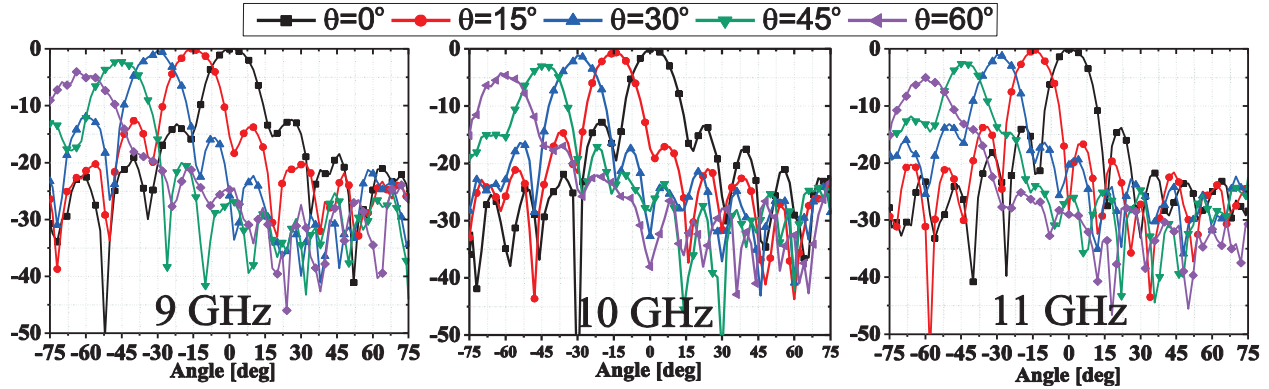
Fig. 8. Measured power patterns on the focal arc of the lens at different frequencies across its entire band of operation for different incidence angles in the 0°-60° range.

To examine the time-domain performance of the lens, its fidelity factor was measured when the lens was excited with broadband Gaussian pulses. The fidelity factor is a measure to quantify the correlation between the signal incident on the surface of the lens and the transmitted one. The procedure for calculating the fidelity factor is described in [15]. A fidelity factor of 1 means that the transmitted signal is a perfect copy of the incident signal and no temporal distortion is introduced in the signal by the lens. Fidelity factors lower than 1 indicate the level of distortion caused by the variations of the response of the lens from a perfect true time delay one. For the lens discussed in this section, the fidelity factor was measured when the Gaussian incident pulse had a center frequency of 9.5 GHz with fractional bandwidths of 10%, 20%, and 30%, and was found to be respectively equal to 0.985, 0.972, and 0.96. The fact that the fidelity factor is very close to 1.0 further confirms the true-time-delay nature of this lens. As the bandwidth of the incident pulse increases, however, the fidelity factor decreases. This can be explained by examining the phase responses shown in Fig. 4 (a). As can be observed, the responses of the spatial TDUs of this lens start to deviate from those of ideal TDUs as we approach the edge of the band. This cases the fidelity factor to deteriorate as the bandwidth of the incident pulse increases.

IV. DESIGN OF TRUE-TIME-DELAY LENSES USING LOW-PASS MEFSSs

A. Design and simulation

The TTD lens shown in Fig. 1 can also be designed if low-pass MEFSSs are used. The unit cell of such a low-pass MEFSS is shown in Fig. 9. This structure is composed of a number of sub-wavelength non-resonant capacitive patches separated from one another by thin dielectric substrates. If the dielectric substrates have small thicknesses and relatively low dielectric constants, they act as series inductors in the path of the propagating EM wave. Therefore, this structure can act as a classical low-pass filter of order $2N$-1, where N is the number of capacitive patches used. Similar to the design methodology described in Section III, the phase responses of these low-pass MEFSSs can be fitted to those of ideal true-time-delay units to synthesize the TDUs needed to populate the aperture of an MEFSS-based of the type depicted in Fig. 1.
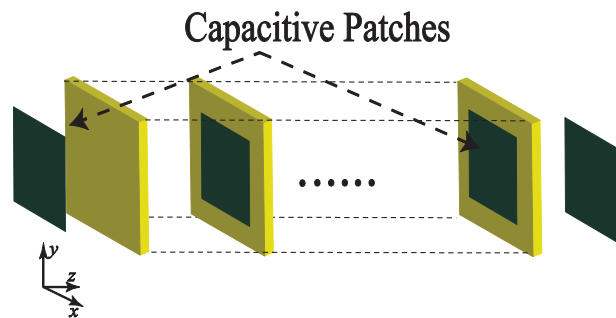
Fig. 9. Topology of a unit cell of a low-pass MEFSS. The structure is composed of a number of non-resonant metallic patches separated from each other by thin dielectric substrates.

To illustrate this in practice, let us consider an MEFSS-based lens with an aperture diameter of 19

cm and a focal length of 19 cm (i.e., *f/D*=1). The aperture of this lens is divided into 17 concentric zones and each zone is populated with identical low-pass type TDUs. Similar to the previous case, the maximum time delay variation over the lens aperture is 63 ns. This time-delay variation over the aperture of the lens can be compensated using a seventh-order low-pass MEFSS composed of four metallic layers separated from one another with three dielectric substrates. Figure 10 (a) shows the simulated phase responses of the TDUs occupying several different zones of this lens. To allow for easy comparison, the desired phase responses needed from TDUs occupying the aperture of an ideal TTD lens are also plotted in that figure. As can be seen, over the frequency range of 6.5-8.5 GHz, the TDUs provide linear phase responses and approximate the desired ideal response very well. Figure 10 (b) shows the magnitudes of the transmission and reflection coefficients of the different TDUs occupying the different zones of the lens. Similar to the previous case, the operational frequency band of the lens (6.5-8.5 GHz) falls within the pass bands of all low-pass MEFSSs used in this design. Therefore, within this operational band, the lens is expected to be completely impedance matched with no significant reflection and low insertion loss.

(b)
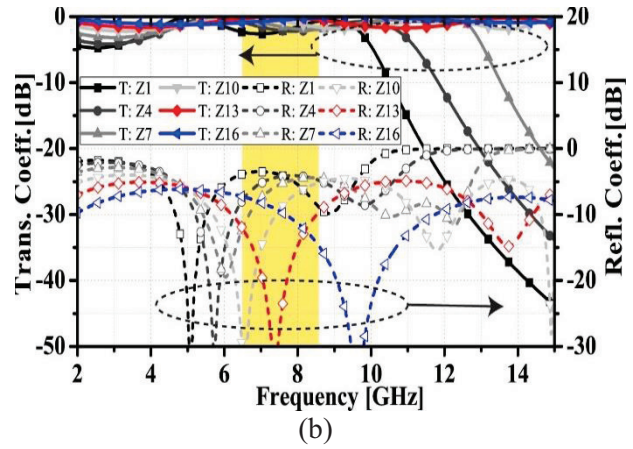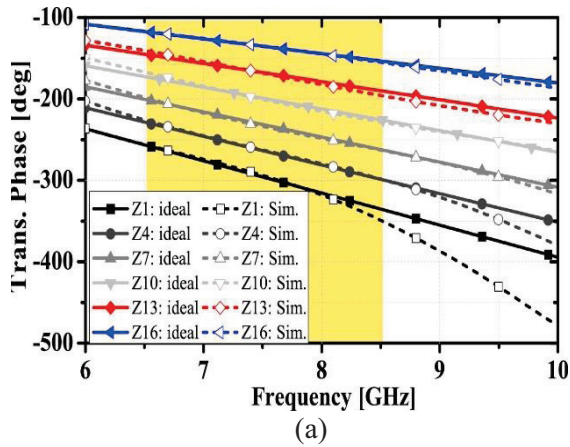
Fig. 10. (a) The simulated phase responses of the time delay units occupying the different zones of the MEFSS-based microwave lens discussed in Section IV and (b) the magnitudes of the transmission and reflection coefficients of the different pixels of the lens.

B. Fabrication and measurement

A prototype of this lens is also fabricated using the standard PCB lithography and substrate bonding techniques. Figure 11 shows the photograph of the fabricated prototype. The lens' response is characterized experimentally using the procedures discussed in Section III-B. Figure 12 shows the measured focal length of the lens as a function of frequency. As can be observed, the focal length of the antenna remains constant in the 7.0-9.0 GHz frequency range, which indicates that over this band, the lens does not suffer from chromatic aberrations. This frequency band is slightly different from the 6.5-8.5 GHz frequency range predicted by the simulations (see Fig. 10). This can be primarily attributed to the fact that the simulations shown in Fig. 10 are conducted when the unit cells are placed in periodic structures with infinite dimensions; whereas, the unit cells of the low-pass MEFSSs are actually used in a non-periodic environment (the lens). Nevertheless, the

(a)

lens does operate over the expected bandwidth of 2.0 GHz. The fidelity factor of this lens is also measured using the procedure described in the previous section. In this case, the lens was excited with a Gaussian pulse with a center frequency that coincides with that of the lens and bandwidths of 10%, 20%, and 30%, and the fidelity factors were measured to be respectively 0.974, 0.96, and 0.95. This further confirms the true-time-delay nature of the lens.

Fig. 12. Measured focal length of the low-pass-MEFSS-based planar lens described in Section IV. Over the frequency range of 7-9 GHz, the focal length of the lens remains the same, indicating very small levels of chromatic aberrations in this band.

The scanning properties of this MEFSS-based lens were measured using the setup shown in Fig. 7, and the results are presented in Fig. 13. As can be seen, over its entire band of operation, the lens can perform well when illuminated with incidence angles in the range of ±60°. Based on these results, it is expected that when lenses of this type are used in scanning antennas or multiple-beam antennas, fields of views in the ±60° range can be easily obtained.

Fig. 11. Photograph of the fabricated prototype of an MEFSS-based planar microwave lens using low-pass MEFSSs (after [16]).
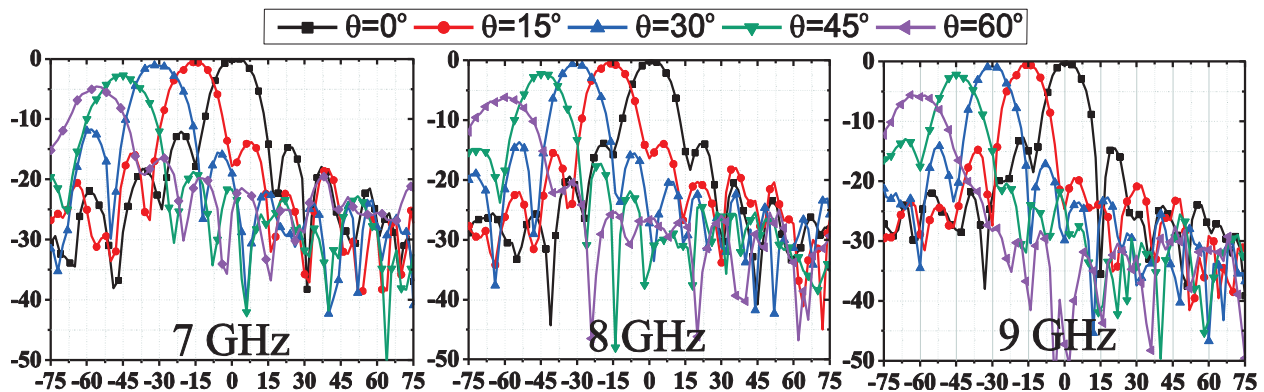
Fig. 13. Measured power patterns on the focal arc of the lens at different frequencies across its entire band of operation for different incidence angles in the 0°-60° range.

V. CONCLUSIONS

A review of the recent developments in the design of planar, true-time-delay microwave lenses exploiting the concept of miniaturized-element frequency selective surfaces was presented. TTD planar microwave lenses can be designed using either band-pass MEFSS of the type reported in [12], or using low-pass MEFSSs as described in [16]. In both cases, lenses with relatively broad bandwidths and minimal or no chromatic aberrations can be obtained. The use of low-pass MEFSSs in designing TTD lenses has the certain advantages in terms of the simplicity of the design process and its amenability to the operation at lower

frequency bands. Nevertheless, both techniques can conveniently be used at microwave frequencies to design low-profile, broadband, TTD microwave lenses. The small sub wavelength dimensions of the spatial time-delay units used in these planar lenses enhances their responses when they are illuminated with oblique incidence angles. These planar microwave lenses can be useful in broadband, multi-beam, true-time-delay scanning antenna arrays.

ACKNOWLEDGMENT

REFERENCES

[1] J. T. Shen and P. M. Platzma, "Near field imaging with negative dielectric constant lenses," *Appl. Phys. Lett.*, vol. 80, pp. 3286-3288, May 2002.

[2] B. Schoenlinner, X. Wu, J. P. Ebling, G. V. Eleftheriades, and G. M. Rebeiz, "Wide-scan spherical-lens antennas for automotive radars," *IEEE Trans. Microw. Theory Tech.*, vol. 50, no. 9, pp. 2166-2175, September 2002.

[3] I. Aghanejad, H. Abiri, and A. Yahaghi, "Design of high-gain lens antenna by gradient-index metamaterials using transformation optics," *IEEE Trans. Antennas Propag.*, vol. 60, no. 9, pp. 4074-4081, September 2012.

[4] G. Bekefi and G. W. Farnell, "A homogeneous dielectric sphere as a microwave lens," *Can. J. Phys.*, vol. 34, pp. 790-803, 1956.

[5] S. Lee, M. S. Sheshadri, V. Jamnejad, and R. Mittra, "Refraction at a curved dielectric interface: geometrical optics solution," *IEEE Trans. Microw. Theory Tech.*, vol. MTT-30, no. 1, pp. 12-19, January 1982.

[6] A. Abbaspour-Tamijani, K. Sarabandi, and G. M. Rebeiz, "A millimeter-wave bandpass filter lens array," *Microw. Antennas Propag.*, vol. 1, no. 2, pp. 388-395, 2007.

[7] M. Barba, E. Carrasco, and J. A. Encinar, "Suitable planar transmit-arrays in x-band," *in Proc. Eur. Conf. Antennas Propag.*, Nice, France, p. 533.1, November 6-10, 2006.

[8] P. Padilla and M. Sierra-Castañer, "Design and prototype of a 12 GHz transmit-array," *Microw. Opt. Technol. Lett.*, vol. 49, no. 12, pp. 3020-3026, December 2007.

[9] D. M. Pozar, "Flat lens antenna concept using aperture coupled microstrip patches," *Electron. Lett.*, vol. 32, no. 23, pp. 2109-2111, November 1996.

[10] Y. Fan, B. Ooi, H. D. Hristov, and M. Leong, "Compound diffractive lens consisting of Fresnel zone plate and frequency selective screen," *IEEE Trans. Antennas Propag.*, vol. 58, no. 6, pp. 1842-1847, June 2010.

[11] M. Al-Joumayly and N. Behdad, "Low-profile, highly-selective, dual-band frequency selective surfaces with closely spaced bands of operation," *IEEE Transactions on Antennas and Propagation*, vol. 58, no. 12, pp. 4042-4050, December 2010.

[12] M. Al-Joumayly and N. Behdad, "A generalized method for synthesizing low-profile, band-pass frequency selective surfaces with non-resonant constituting elements," *IEEE Trans. Antennas Propag.*, vol. 58, no. 12, pp. 4033-4041, December 2010.

[13] N. Behdad and M. Al-Joumayly, "A generalized synthesis procedure for low-profile frequency selective surfaces with odd-order band-pass responses," *IEEE Trans. Antennas Propag.*, vol. 58, no. 7, pp. 2460-2464, July 2010.

[14] M. Al-Joumayly and N. Behdad, "Wideband planar microwave lenses using sub-wavelength spatial phase shifters," *IEEE Trans. Antennas Propag.*, vol. 59, no. 12, pp. 4542-4552, December 2011.

[15] M. Li, M. A. Al-Joumayly, and N. Behdad, "Broadband true-time-delay microwave lenses based on miniaturized-element frequency selective surfaces," *IEEE Trans. Antennas Propag.*, vol. 61, no. 3, pp. 1166-1179, March 2013.

[16] M. Li and N. Behdad, "Wideband true-time-delay microwave lenses based on metallo-dielectric and all-dielectric lowpass frequency selective surfaces," *IEEE Trans. Antennas Propag.*, vol. 61, no. 8, pp. 4109-4119, August 2013.

Nader Behdad received his B.S. degree in Electrical Engineering from Sharif University of Technology in 2000 and his M.S. and Ph.D. degrees in Electrical Engineering from the University of Michigan - Ann Arbor in 2003 and 2006, respectively. Currently he is an Associate Professor in the Electrical and Computer Engineering Department at the University of Wisconsin - Madison. His research expertise is in the area of applied electromagnetics. In particular, his research interests

include electrically-small antennas, antenna arrays, antennas for biomedical applications, biomedical applications of RF/microwaves, periodic structures, frequency selective surfaces, passive high-power microwave devices, metamaterials, and biomimetics and biologically inspired systems in electromagnetics. He is currently serving as an Associate Editor for IEEE Antennas and Wireless Propagation Letters and served as the Co-Chair of the technical program committee of the 2012 IEEE International Symposium on Antennas and Propagation and USNC/URSI National Radio Science Meeting.

Behdad received the 2012 R. W. P. King and the 2012 Piergiorgio L. E. Uslenghi Letter Prize Paper Awards of the IEEE Antennas and Propagation Society. He is also the recipient of the 2011 CAREER award from the National Science Foundation, the 2011 Young Investigator Award from Air Force Office of Scientific Research, and the 2011 Young Investigator Award from the Office of Naval Research. He received the Office of Naval Research Senior Faculty Fellowship in 2009, the Young Scientist Award from the International Union of Radio Science (URSI) in 2008, the Horace H. Rackham Predoctoral Fellowship from the University of Michigan in 2005-2006, the Best Paper Awards in the Antenna Applications Symposium in September 2003, and the second prize in the paper competition of the USNC/URSI National Radio Science Meeting, Boulder, CO, in January 2004. His graduate students were the recipients of ten different awards/recognitions at the IEEE Pulsed Power & Plasma Science (2013), IEEE AP-S/URSI Symposium (2010, 2012, 2013), and the Antenna Applications Symposium (2008, 2010, 2011).

Active Metamaterial Incorporating Gain Device/Medium: A Review

Qi Tang [1] and Hao Xin [1,2]

[1] Department of Electrical Engineering
[2] Department of Physics
University of Arizona, Tucson, AZ 85721, USA
tangqi@email.arizona.edu, hxin@ece.arizona.edu

Abstract ─ Metamaterials intrigue many exciting applications in the broad electromagnetic spectrum ranging from microwave to optics. However, many of the envisaged applications still remain in theory, largely because of the intrinsic loss and dispersion associated with passive metamaterials. Incorporating active devices or media into conventional passive metamaterial structures for loss compensation, as well as dispersion control, is very attractive and may finally enable many desired applications. In addition, because of the added design degree of freedom in active metamaterials, new and rich physical phenomena and insights can be discovered. In this paper, we review the recent progress in the realm of active, gain-assisted metamaterials. Physical limitations on loss and bandwidth of metamaterials are firstly discussed. Recent experimental efforts in transmission-line and volumetric metamaterials with net gain in the microwave and optical regime are then examined. The idea of utilizing non-Foster active devices to reduce the dispersion and achieve broad bandwidth is also presented. Finally, one of the important issues of active metamaterial design, stability, is briefly discussed.

Index Terms ─ Active metamaterials, gain, negative index.

I. BACKGROUND ON METAMATERIALS AND APPLICATIONS

Metamaterials are artificial composite materials that often involve periodic structures to achieve unconventional and advantageous material properties. The earliest study of artificial materials for manipulating electromagnetic waves dates back more than 100 years [1]. In 1967, Veselago theoretically studied materials with simultaneous negative permittivity (-ε) and permeability (-μ) [2], and predicted some unique properties such as the negative refractive index, opposite directions of the phase velocity and Poynting vector (the left-handedness of the wave propagation), the reversed Snell's law, and the reversed Doppler effects.

The first experimental demonstration of Negative Index Metamaterial (NIM) with simultaneous -ε and -μ (sometimes referred to as DNG, double negative) is conducted at microwave frequency (10.5 GHz). The designed NIM comprises a 2-D array of wires and Split Ring Resonators (SRRs) (see Fig. 1 (a)) [3]. Thereafter, various metamaterials including single negative (ε-negative, ENG and μ-negative, MNG) [4], near-zero index [5] and gradient index [6] materials have been studied. Another type of realization of metamaterials is based on the microwave transmission line theory [7-9], as shown in Fig. 1 (b). A simple analogy between the circuit model and the effective permittivity and permeability is described in [10,11].

(a)   (b)
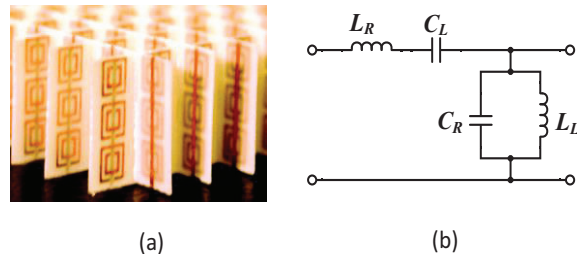
Fig. 1. Two most commonly studied metamaterial examples: (a) a wire (provides -ε) and SRR (provides -μ) array (figure adapted from [3]), and (b) a unit cell of composite Left-Hand/Right-Hand Transmission Line (CLRH-TL).

The unique properties of NIMs and other metamaterials lead to many exciting applications; for example, "invisible cloaking" [12-14], "perfect lens" [15,16], nanoplasmonics [17,18], electrically small antennas [19], highly directional antennas [20,21], leaky wave antennas [22], coupled-line couplers [10], phase shifting lines, broadband balun [11], etc. Despite of the large variety of intriguing applications, intrinsic loss and narrow bandwidth associated with existing metamaterials significantly hamper the wide implementation of metamaterials in practice.

Many theoretical studies assume lossless or low-loss scenario, which is hardly to achieve in reality. For example, at optical frequencies, all the demonstrated passive NIMs have large loss accompanying the negative refractive index. Even at microwave frequencies, especially for some typical resonant-type metamaterials, loss is still a problem and severely degrades or even completely eliminates the advantages of metamaterial based components and applications such as "cloaking" devices and electrically small antennas. Another example is the "perfect lens" [15], a slab with a refractive index $n = -1$ which overcomes the diffraction limit; however, the predicted "perfect image" cannot be realized unless the NIM slab is completely lossless [23].

Another bottleneck is the limited bandwidth. Metamaterials are intrinsically dispersive because of the causality requirement, thus only present interesting effective medium properties within a narrow bandwidth. Take the "cloaking" for example. It would be much less useful that the object inside the metamaterial layers would only be invisible for a single frequency, compared to a true broadband "cloaking" device. Also, for data communication or sensor applications, wide bandwidth is also desirable for high data rate and resolution.

Loss and dispersion are inherent in the constitutive parameters of natural materials [24,25] and even more so for NIMs, due to causality requirement. Some theoretical studies attempt to prove whether a lossless and dispersionless NIM violates any fundamental physics, and if it did not, what the optimal bandwidth with low loss one can achieve given a target constant material property, such as $n = -1$ for the 'perfect lens' application [26]. The loss generation in NIM can be divided into the dissipative loss due to the constitutive

material properties [27,28], and the radiation loss [29] due to the shape and geometry of the unit cell structure. Various practical approaches to "passively" reduce the loss, for example, advances in fabrication, tailoring the shape and geometry [30,31], and the use of a stack of alternating negative and positive index layers [32], have been investigated but complete loss elimination remains elusive.

II. ACTIVE METAMATERIALS

The idea of incorporating gain device or medium into metamaterial structure to compensate the loss is quite natural and attractive [33,34]. First, losses associated with conductors, dielectrics and radiation can be compensated by the availability of gain. Second, with the additional gain as a design tradeoff, more bandwidth may be realized [35]. With consistent efforts on theoretical studies, fabrications and experimental validations, significant progress in active metamaterials has been made in recent years. Active metamaterials, recognized as the next stage of the technological revolution in metamaterials, also enables some new applications to appear on the horizon of possibilities, such as optical data processing and quantum information applications [36].

The term "active metamaterial", from an engineering point of view, is used to distinguish it from conventional passive metamaterial, such as SRR, fishnet structure, and CLRH-TL constructed from only passive constituents; i.e., metals and dielectrics. The word "active" can be either noted as embedding an energy source in the structure to ameliorate some undesirable properties, such as loss and dispersion, or adding an external control to realize tunable or other special functionalities. Some examples of the latter category include semiconducting varactors controlled impedance surfaces for antenna applications [37,38], electronically reconfigured magnetic-resonant metamaterial for phase modulator [39-42] and transistor-based nonreciprocal metamaterial for isolating functionality [43]. In this review, we will focus on the first category of active metamaterials for loss compensation and dispersion management only.

In the microwave regime, negative resistance elements can be implemented into the passive unit cell structure of a metamaterial to achieve loss compensation and even amplification [44-48]. Such

negative resistance elements can be realized by active devices, such as resonant tunneling diodes, Gunn diodes, lambda diodes, negatron and transistor-based circuits [49,50], which have been widely applied in oscillator, amplifier, and mixer designs. A detailed review on a resonant tunneling diode based active CLRH-TL metamaterials will be given in Section IV.

In the optical regime, active gain media are well-established in lasers and optical amplifiers [51]. Loss compensation, steady-state net amplification, and nanoscopic lasing in optical frequencies become possible via the incorporation of gain materials adjacent to or within NIM structures [52-56]. We will also present a brief review on state of the art in optical active metamaterials in Section IV, although the main focus of this paper is on microwave active metamaterials. A more detailed review on active optical metamaterials can be found in [57] and [58].

Recently there have been increasing interests in designing non-dispersive metamaterials using "non-Foster" elements [59-64]. A non-Foster element is a negative inductance or negative capacitance realized by active electronic circuits [65,66]. Such circuits have been widely investigated in the designs of voltage controlled oscillators, active filters, amplifiers, and more recently electrically small antennas [67-69].

In the following sections, we begin by concisely reviewing some theoretical constraints on the properties of passive metamaterials, explaining why a dispersionless negative index metamaterial with negligible loss is not achievable and how to estimate the bounds of loss and bandwidth for metamaterials. We then give an overview of proof-of-concept realizations of gain-assisted active metamaterials. In the interest of brevity, we focus on the microwave regime, and briefly introduce the development of active optical metamaterials. The novel direction of non-dispersive active metamaterials by implementing active negative impedance circuits is reviewed next. We then present a brief discussion on stability issues of active metamaterials as all active circuits and materials are prone to instability. Finally, we conclude by an outlook of the important challenges that remain to be addressed in the future.

III. LOSS AND DISPERSION OF METAMATERIALS

A. Inevitable loss or dispersion

A straightforward method to prove a linear passive NIM with negligible loss has to be dispersive is by using a simplified Poynting's theorem [70]. Assuming a low-loss system with ε and μ such that $\varepsilon'' << |\varepsilon'|$ and $\mu'' << |\mu'|$, and consider a wave of a relatively narrow bandwidth in comparison to the bandwidth over which $\varepsilon(\omega)$ and $\mu(\omega)$ changes appreciably, the time-averaged internal stored energy can be calculated by [24,25]:

$$\overline{U} = \frac{1}{2}\text{Re}[\frac{d(\omega\varepsilon)}{d\omega}]\Big|_{\omega=\omega_0}\left\langle E^2\right\rangle + \frac{1}{2}\text{Re}[\frac{d(\omega\mu)}{d\omega}]\Big|_{\omega=\omega_0}\left\langle H^2\right\rangle, \quad (1)$$

where ω_0 is the central frequency of the narrow band signal. If ε and μ are not frequency dependent, i.e., dispersionless, the above Eq. (1) becomes to:

$$\overline{U} = \frac{1}{2}\varepsilon\left\langle E^2\right\rangle + \frac{1}{2}\mu\left\langle H^2\right\rangle. \quad (2)$$

By the law of the increase of entropy, we must have $\overline{U} > 0$ for a passive medium. Therefore, the values of ε and μ in Eq. (2) cannot be both negative, which seems to contradict to the existence of NIMs. This leads to an important conclusion that dispersion cannot be neglected for a passive NIM. In other words, for a passive NIM with negligible loss, dispersion is unavoidable.

The second important question is whether a lossless NIM is achievable in principle. Reference [71] is one attempt to study the lower bound on the loss of NIM by imposing Kramers-Kronig relations on $\varepsilon(\omega)\mu(\omega)$, in which it asserts that "any loss compensation or significant reduction at and near the observation frequency will lead to the disappearance of the negative refraction itself due to the dispersion relation dictated by the causality." This statement caused a number of objections and later has been proved to be inaccurate [72-78]. A consensus is reached that negative refractive index is achievable at a single frequency with arbitrarily low loss. This point has been confirmed by a number of experimental results [46-48,52-56], which we will review in detail in Section IV. Reference [73] has further pointed out that a passive low loss NIM is achievable only if there is large loss or large dispersion immediately below the observation frequency, or, there are singularities at

real frequencies.

B. Bounds for loss and dispersion of passive metamaterials

The derivation of bounds on dispersion and loss of passive NIMs is a nontrivial problem. For an analytical function at the upper half plane, the Hilbert transform gives the relationship between the real part and imaginary part of the function; i.e., Kramers-Kronig relations, yielding:

$$\varepsilon''(\omega) = \frac{2\omega}{\pi} P \int_0^\infty \frac{\varepsilon'(\omega')-1}{\omega^2 - \omega'^2} d\omega',$$

$$\varepsilon'(\omega) - 1 = \frac{2\omega}{\pi} P \int_0^\infty \frac{\varepsilon''(\omega')\omega'}{\omega'^2 - \omega^2} d\omega', \tag{3}$$

where P denotes the Cauchy principal value. Causality in a linear dispersive medium implies that, $\varepsilon(t)$ and $\mu(t)$ have to be zero for $t < 0$ and real values for $t \geq 0$. Therefore, in the frequency domain, for permittivity, it yields:

$$\varepsilon(-\omega^*) = \varepsilon^*(\omega). \tag{4}$$

Furthermore, at very high frequency, the electrons behave like they are free, yielding the constraint of high-frequency asymptote:

$$|\varepsilon(\omega) - 1| \sim \frac{1}{\omega^2}, \omega \to \infty. \tag{5}$$

Permeability also follows the same causality arguments as the permittivity in Eqs. (3)-(5). In addition, assuming a passive system, we have:

$$\int_{-\infty}^T \mathbf{E}(t) \cdot \frac{\partial \mathbf{D}(t)}{\partial t} dt \geq 0,$$

$$\int_{-\infty}^T \mathbf{H}(t) \cdot \frac{\partial \mathbf{B}(t)}{\partial t} dt \geq 0. \tag{6}$$

Using the above physical constraints, [75] derives the limitation of the bandwidth of passive NIMs by constructing and bounding Herglotz functions. Equation (7) gives a lower bound of loss within a finite bandwidth or an upper bound of bandwidth with a fixed loss for a passive medium.

$$\max_{\omega_1 < \omega < \omega_2} |\varepsilon(\omega) - \varepsilon_m|$$

$$\geq \frac{B}{1 + B/2}(\varepsilon_\infty - \varepsilon_m) \begin{cases} 1/2, & \text{lossy case,} \\ 1, & \text{lossless case,} \end{cases} \tag{7}$$

where ε_m is the targeted permittivity, ε_∞ is the high-frequency asymptote which equals to 1, and $B = (\omega_2 - \omega_1)/\omega_0$ is the relative bandwidth with ω_0 as the center frequency. Take a medium with targeted $\varepsilon_m = -1$ as an example. For a deviation between the realized and targeted permittivity of

1%, the calculated maximum relative bandwidth is 1% for the lossy case, and approximates 0.5% for the lossless case.

For the case of an insulating medium, i.e., without static conductivity, the constraint can be further restricted to be:

$$\max_{\omega_1 < \omega < \omega_2} \frac{|\varepsilon(\omega) - \varepsilon_m|}{|\varepsilon(\omega) - \varepsilon_\infty|}$$

$$\geq \frac{B}{1 + B/2} \frac{|\varepsilon_m - \varepsilon_s|}{(\varepsilon_s - \varepsilon_\infty)} \begin{cases} 1/2, & \text{lossy case,} \\ 1, & \text{lossless case,} \end{cases} \tag{8}$$

where ε_s is the static permittivity (the low-frequency asymptote).

C. Active metamaterial for loss compensation/gain and dispersion control

The consideration and analysis in III.A and III.B have led to the conclusion that a passive metamaterial cannot be simultaneously lossless and non-dispersive, and lower bound of loss and upper bound of bandwidth exist. However, with the incorporation of gain device/medium (or effectively, external energy source) in a metamaterial structure, the limits derived previously for passive metamaterials are no longer valid. Although, there have been controversies on the causality of an effective medium simultaneously with a negative refractive index and a net gain [71-78], many theoretical and experimental studies have been reported with the goal to achieve complete or even over compensation (i.e., gain) of loss for NIM over a wide frequency spectrum from microwave to optics [46-48,52-56]. In fact, based on the causality inherently described by the energy conservation, the condition for achieving a NIM with zero loss or gain from Poynting's theorem can be derived [79,80]. In the following sections, some of the interesting loss compensated metamaterials and broadband metamaterials utilizing active device/medium are reviewed.

IV. GAIN-ASSISTED METAMATERIALS

Incorporating active constituents with gain into metamaterials has been recognized as a promising technique for compensating losses. There have been sustained theoretical and experimental efforts to reduce or eliminate the loss associated with metamaterials. In this section, we review a number of these works with a focus on experimental

validations [45-47,56,81-83].

A. Active transmission line metamaterials loaded with resonant tunneling diodes

Conventional microwave transmission line can be regarded as a 1-D homogeneous medium and modeled by cascading a number of unit cells with dimension much smaller than the wavelength. The equivalent circuit of the unit cell of a conventional transmission line can be expressed as a set of a series distributed inductance and a shunt distributed capacitance, which always leads to a positive phase velocity in the direction of energy flow. This characteristic can be classified as the Right-Handed Transmission Line (RH-TL). On the contrary, a unit cell of a Left-Handed Transmission Line (LH-TL) consists of a series distributed capacitance and a shunt distributed inductance, leading to a negative phase velocity. A pure LH-TL does not exist due to the unavoidable parasitics at high frequencies. Instead, a more realistic design of CLRH-TL is usually studied that exhibits negative phase velocity (LH) at low frequency range and positive phase velocity (RH) at high frequency range [84-86]. A bandgap generally exists between the LH and RH frequency region which is named as unbalanced. The gap would disappear, if the cutoff frequencies of LH and RH coincide (balanced). Such unique properties of CLRH-TLs are utilized in a number of applications, including leaky-wave antennas, compact coupled-line coupler, phase shifters, sub-wavelength resonators, distributed mixer/ amplifiers [10,11,22,87-91], etc. Because of the non-resonant nature of both permittivity and permeability, similar to a Drude medium, a CLRH-TL metamaterial exhibits larger frequency range of effective negative refractive index and lower loss compared to the resonant volumetric metamaterial [89]. Nevertheless, when frequency increases, losses in conductor and dielectric and due to radiation will inevitably increase. Moreover, lumped elements are essential components for this kind of transmission lines. At higher frequencies (i.e., higher than a few GHz), high quality lumped elements (especially inductors) are rare and limited in their achievable values.

Consider a unit cell of a CLRH-TL as shown in Fig. 2 (a), in which the series resistance R and the shunt conductance G representing the distributed losses. If a negative resistance and/or a negative

conductance can be incorporated in the unit cell (i.e., $R<0$ and/or $G<0$), a CLRH-TL with loss compensation and even amplification could be realized. Figures 2 (b) and 2 (c) plot the calculated real part (α) and imaginary part (β) of the propagation constant ($\gamma=\alpha+j\beta$) of a CLRH-TL design with the following parameters: $L_R=1$ nH, $C_L=1$ pF, $L_L=1$ nH, $C_R=1$ pF, $G=0$ S, and R from -100 to 100 Ω.

(a)

(b)

(c)
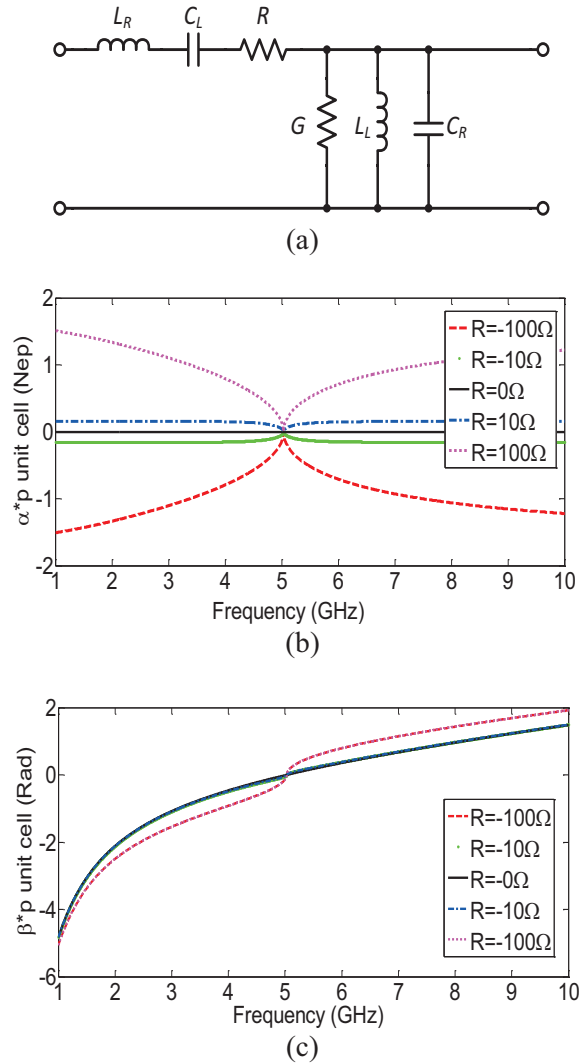
Fig. 2. (a) Equivalent circuit model of a unit cell of a CLRH-TL metamaterial, (b) calculated attenuation constant α ($\alpha>0$-loss, $\alpha=0$-lossless, $\alpha<0$-gain), and (c) phase constant β ($\beta>0$-RH, $\beta<0$-LH) (figure adapted from [45]).

It can be observed in Figs. 2 (b) and 2 (c), that

positive R leads to loss while negative R provides gain while the phase propagation constant β is not impacted much by the value of R. Thus, for this simple example, negative index of refraction and gain are achieved simultaneously by incorporating an ideal negative resistance in the unit cell.

This above concept has been confirmed experimentally. In [46], a CLRH-TL at microwave frequency with net gain by incorporating a Germanium tunneling diode (General Electric TD261) at the unit cell level is implemented and tested. This tunneling diode has a pronounced Negative Differential Resistance (NDR) region, as can be observed in its I-V curve plotted in Fig. 3 (a). As the schematic of the unit cell in Fig. 3 (b) shows, a series interdigited capacitance (C_L), a shunt narrow line with a shorting via (L_L), and the tunneling diode device connected in series are used to implement the active CLRH-TL. It is demonstrated that the addition of the DC pumped diode not only maintains the left handedness, but also provides gain. In the design procedure, a passive CLRH-TL is first realized with appropriate equivalent circuit parameters to guarantee left-handedness in the interested frequency band. Then the tunneling diode with NDR behavior is added into the unit cell design to compensate for loss and provide gain while maintaining left-handedness of the transmission line. Three prototypes of one, two and three unit cells are studied experimentally.

A photo of the fabricated one unit-cell active CLRH-TL is shown in Fig. 3 (c). Two-port S-parameters of the fabricated samples are measured using a vector network analyzer. The complex propagation constant γ can be extracted from the measured S-parameters by Eq. (9), where p is the unit cell length and N is the number of unit cells of the CLRH-TL under consideration. The sign in Eq. (9) is determined according to [90]. An alternative method for extracting the propagation constant γ involving finding the Nth root of the ABCD matrix of the CLRH-TL [87] is also applied and the same propagation constant γ for all three cases (1, 2, and 3 unit cells) are obtained (note that the time dependence convention $e^{j\omega t-\gamma z}$ is used here).

$$\gamma = \pm \frac{1}{Np} \cosh^{-1}\left(\frac{1+S_{12}S_{21}-S_{11}S_{22}}{2S_{21}} \right). \quad (9)$$
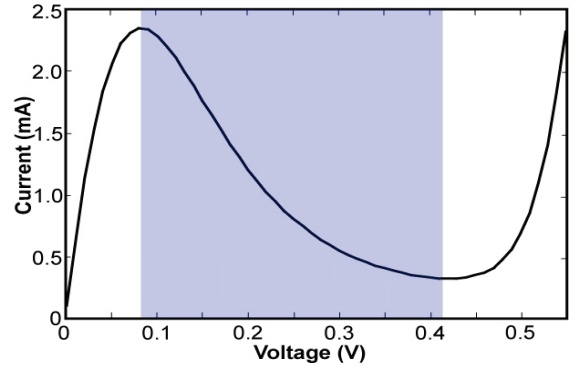
(a)
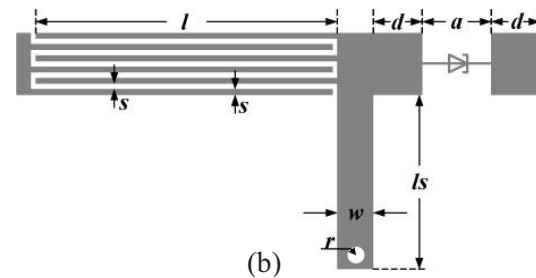
(b)
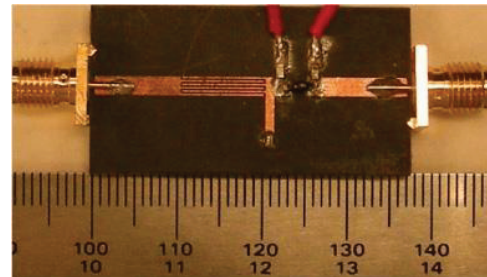
(c)

Fig. 3. (a) Current voltage relation (I-V curve) of the Germanium tunneling diode. The differential negative resistance appears at 0.15-0.3 V. (b) Schematic of a designed active CLRH-TL unit cell in microstrip configuration incorporating the resonant tunneling diode. The dimensions are: a=2.5 mm, d=1.5 mm, l=9.7 mm, w=1 mm, s=0.2 mm, l_s=5.9 mm, r=0.3 mm. (c) Photo of a fabricated single unit cell of the active CLRH-TL (figure adapted from [46]).

Figure 4 shows the simulated (Fig. 4 (a)) and measured (Fig. 4 (b)) propagation attenuation constant α and phase constant β, and the extracted material effective index of refraction (Fig. 4 (c)). The simulated results are obtained from the

combination of full-wave electromagnetic models of the passive parts of the CLRH-TL and the equivalent circuit model of the tunneling diode. It can be observed from Fig. 4 (a) that for all three cases of one, two and three unit cells, the simulated propagation constants are identical with simultaneous negative β (negative index) and negative α (gain) from 1.75 GHz to 2.75 GHz.

Compared to the passive CLRH-TL without the tunneling diode in [46], this active CLRH-TL is unbalanced with a lower transition frequency due to the extra parasitics of the tunneling diode. It is also observed from Fig. 4 (b), that for the single unit cell case, the measured β is negative from 1.75 GHz to 2.75 GHz while the measured α is also negative, indicating left-handedness with gain in that frequency range. The corresponding effective index of refraction n is calculated and plotted in Fig. 4 (c). From 1.75 GHz to 2.75 GHz, the real and imaginary part of n is negative and positive correspondingly, indicating negative index with gain. For the two- and three-unit cell cases, negative β are observed from 1.75 GHz to 2.75 GHz as well, quite similar to the single unit cell case. Most importantly, simultaneous negative β and negative α are also experimentally confirmed, although in narrower frequency ranges, from 1.75 GHz to 2.2 GHz and from 1.75 GHz to 2.1 GHz for the two- and three-unit cell cases, respectively. The similar behavior of the propagation constants for the one-, two- and three-unit cell cases confirm that this active CLRH-TL can be considered as an effective negative index material with gain. The differences in the measured propagation constants (especially for the attenuation constant α which is due to the negative resistance associated with the tunneling diode [45]) for the three cases are likely due to the non-uniformity of the diodes in each unit cell.

(a)

(b)

(c)
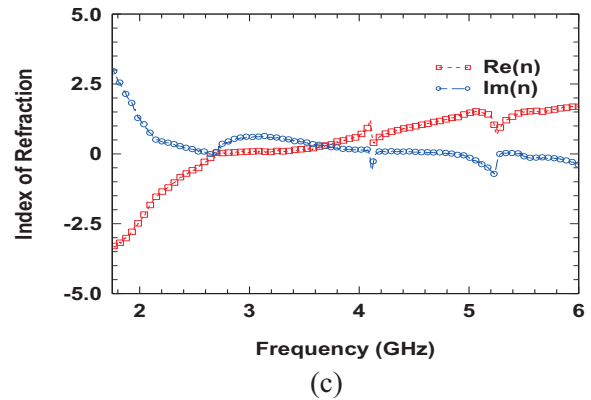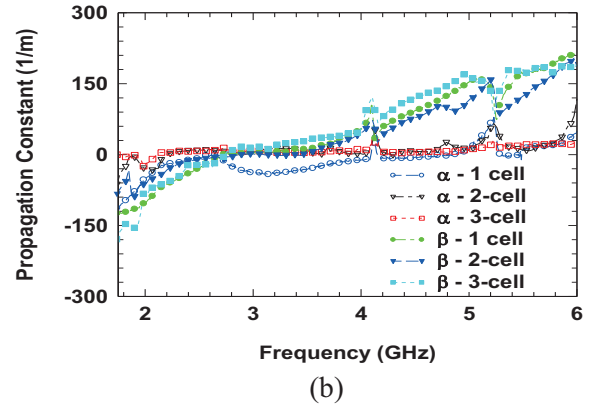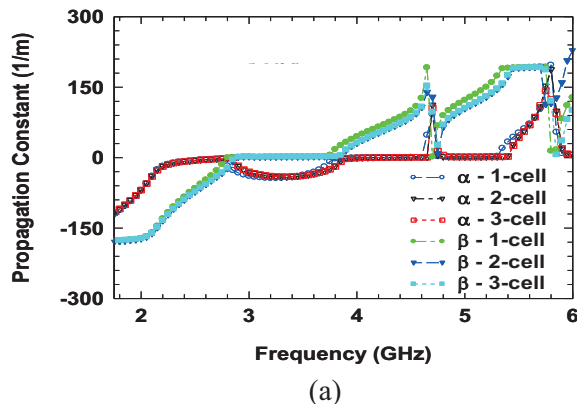
Fig. 4. (a) Simulated and (b) measured propagation constants of the active CLRH-TL incorporating tunneling diodes with one, two and three unit cells; (c) extracted refractive index from the measured one unit cell results with a time dependence convention $e^{j\omega t - \gamma z}$ (figure adapted from [46]).

Another interesting aspect of this active metamaterial transmission line is that the negative resistance value can be controlled by the bias voltage. Figure 5 plots the measured S_{21} of the one-unit cell structure under different bias voltages from 0.21 to 0.25 V. It is observed that with different bias voltage (thus different $-R$ values), the level of loss compensation/gain can be controlled. Besides demonstrating the existence of NIM with gain in a finite bandwidth, the nonlinear power dependence and harmonics generation of the active CLRH-TL is also measured. It is observed that at low input power level (i.e., $P_{in} \leq -35$ dBm) the active CLRH-TL behaves linearly without significant harmonics generation. However, at higher input power, nonlinearity clearly sets in that leads to gain compression and harmonics generation. More detailed results can be found in [46].

It is very important to point out that since all active devices and gain media are inherently nonlinear, it is crucial to consider the nonlinearity and power handling capability in active metamaterial design and associated applications. Furthermore, similar to any other active components design, especially power amplifiers, stability issues of active metamaterials are of critical importance and can be challenging. References [92-94] study the wave propagation in nonlinear composite medium, and experimentally demonstrate the spatiotemporal dynamics of active metamaterials, including the generation and propagation of solitons for the backward-wave regime.
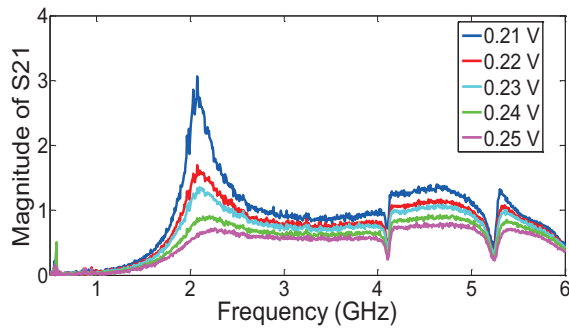
Fig. 5. Measured transmission S_{21} of the one-unit cell active CLRH-TL with the tunneling diode biased from 0.21 to 0.25 V. The level of loss compensation/gain can be controlled by the bias voltage.

B. A balanced active CLRH-TL metamaterial

As discussed previously, the first active CLRH-TL incorporating tunneling diode is unbalanced due to the parasitics of the diode. In [47], an active CLRH-TL is designed to achieve the following goals which are of practical importance for many applications: balanced response with the diode parasitics taking into account; symmetric unit cell structure (i.e., $S_{11}=S_{22}$); and to evaluate the effect of number of unit cells on the CLRH-TL properties.

Figure 6 (a) shows the schematic layout of the improved design. Instead of using a series inter-digital capacitor as in [46], two lumped-element capacitors are placed symmetrically in the unit cell. The shunt inductor is also split into two symmetrically while the tunnel diode is placed at the center of the unit cell to maintain symmetry. The values of the equivalent circuit model elements

and the associated dimensions are determined to obtain balanced response. According to the equivalent circuit model parameters, the estimated transition frequency is about 3.87 GHz.

Figures 6 (b) and 6 (c) plot the extracted phase constant β and attenuation constant α from simulated S-parameters for different number of unit cells, respectively. It is observed that left-handedness (or NRI) with gain is achieved from 2 to 3.83 GHz, with the transition frequency at 3.83 GHz, consistent with the equivalent circuit model estimation. The propagation properties of the CLRH-TL with different number of unit cells are mostly identical, demonstrating the validity of treating them as uniform transmission lines, or, effective media.

As a potential application, the performance of passive and active versions of a single unit-cell zeroth order resonator antenna based on the CLRH-TL is also compared. The benefit of the active CLRH-TL unit cell is demonstrated in terms of radiated power [47].

(a)

(b)

(c)
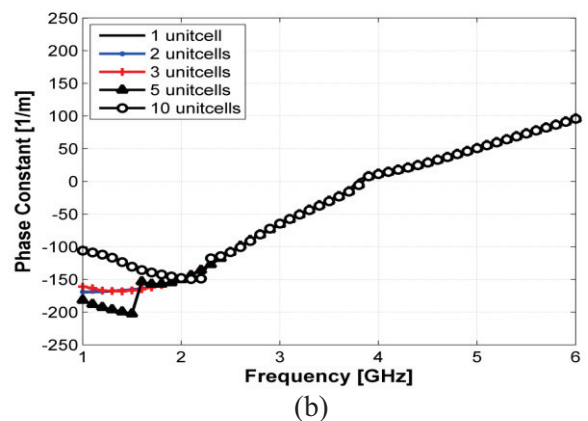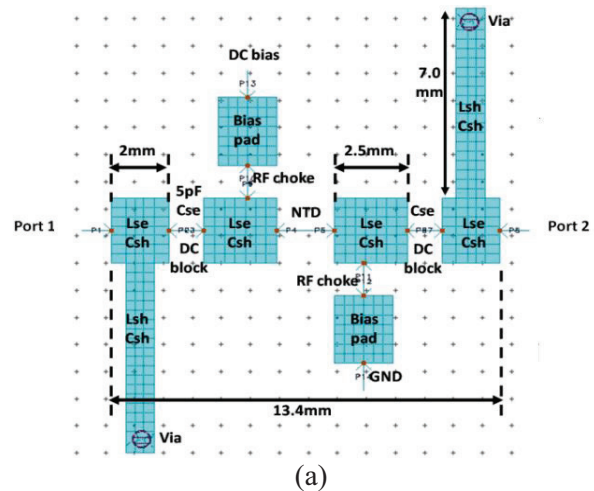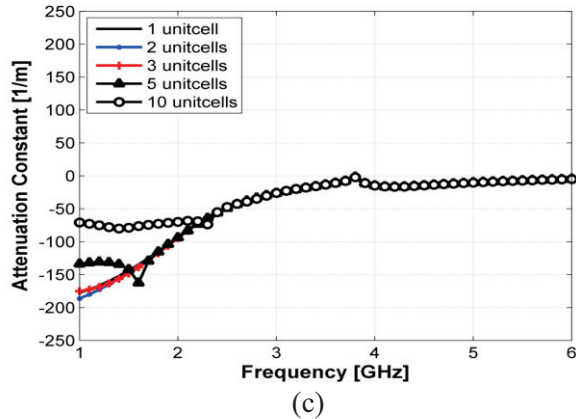
Fig. 6. (a) Schematic layout of a balanced and symmetric active CLRH-TL unit-cell design; simulated (b) phase constants β and (c) attenuation constants α of 1, 2, 3, 5 and 10 unit cells of the balanced active CLRH-TL (figure adapted from [47]).

C. Active volumetric metamaterials

The merit of a volumetric metamaterial is its convenience of frequency scaling. For example, SRR structures have been demonstrated from microwave to optical frequencies. In microwave frequency, loss compensation can still be achieved by embedding active devices such as tunneling diodes into the conventional sub-wavelength metamaterial unit cells. An active metamaterial with embedded microwave tunnel diodes exhibits a band-limited Lorentzian dispersion with an over-compensated loss (gain) and a negative refractive index is demonstrated in Fig. 7 [79]. It shows examples of sub-wavelength wire and SRR cells with embedded tunneling diode. This kind of active metamaterial design is very interesting because of its versatility. For example, by incorporating the NDR diode in the wire (permittivity)/SRR (permeability) part of the unit cell, activeness associated with the permittivity/permeability can be selected independently. Therefore, various model systems can be realized to investigate the rich physics related to active metamaterials.

Besides NIMs, other types of metamaterials incorporating active devices have also been studied. Reference [44] experimentally demonstrates an active SRR metamaterial unit cell with a control of different combinations of the real part and imaginary part of the permeability, which is achieved by embedding surface mount amplifiers,

voltage controlled phase shifters, and a pair of sensing and driven loops. Despite of the "bulky" and complicated active loads, the unit length is still much smaller ($\sim \lambda/10$) than the wavelength, taking advantages of the integrated circuit technology. The results show that $\mu' < 1$ is achieved near 590 MHz, and μ'' can be tuned from positive to negative values including zero by controlling the bias voltage of the phase shifter.
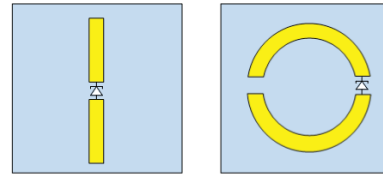
Fig. 7. A schematic example of a NDR diode-loaded metamaterial unit cell to compensate loss or provide gain while maintaining its negative permittivity (left) or negative permeability (right).

D. Optical gain-assisted metamaterials

At optical frequencies, NIMs are usually built from noble metal such as silver or gold. The material loss is severe, which plagues their potential applications in optics. Other known sources of loss in optical metamaterials stem from surface roughness, size effect, quantum effect and chemical interface effects. There are a number of reported theoretical studies with various gain models which predicts drastic improvement on loss compensation [95-97]. Reference [58] uses the Maxwell-Bloch methodology and transformed Poynting's theorem to predict that a steady-state net gain can be achieved when the pumped gain is bigger than the dissipation loss and smaller than the sum of dissipation and radiation loss. If there was no radiation loss, the two thresholds coincide, hence, suggesting only lasing light but not amplification would be possible. Techniques investigated experimentally include optically pumped gain media such as organic dyes, quantum wells and quantum dots, and nonlinear optical parametric amplification [52-58,81-83].

Reference [56] demonstrates an extremely low-loss optical NIM using organic dye molecules pumped by a laser pulse. A delicate "double-fishnet" structure is fabricated from two layers of silver with air or solvent as the spacer and alumina pillars as support. Epoxy doped with Rhodamine 800 dye

material is coated on the structure afterwards. The sample is at first characterized by transmission and reflection measurements in the far field. The negative refractive index is obtained from 720 nm to 760 nm. A pump-probe experiment is then conducted to show a progressively increased transmission of the sample with pumped laser compared to the case without the pump, which proves that the loss compensation is provided by the dye material. The associated Figure-of-Merit (FOM = Re$\{n\}$/Im$\{n\}$) is increased from 1 to 26 with the pump wavelength of 737 nm, and to the order of 10^6 with the pump wavelength of 738 nm (Re$\{n\}$=-1.26 and Im$\{n\}$=1×10^{-6}), but the whole system still remains in lossy state.

Another useful technique to compensate the loss is to employ semiconductor gain materials, such as quantum dots and quantum wells, into the passive structures [80-82]. The advantage of using semiconductor gain materials is the long life time and stable performance compared to the dye materials. Reference [81] reports a gain-assisted magnetic metamaterial based on an array of SRRs fabricated on an InGaAs quantum well layer, pumped with 810 nm laser pulse. The transmission of the quantum well with SRRs changes substantially larger than the case of the quantum well alone, which indicates a strong local-field coupling between SRRs and the quantum well.

Although there have been many reports on optical active metamaterials for loss compensation, it is worth to point out that, to our knowledge, there has not been experimental demonstration of NIM with steady state net gain so far. This can probably be attributed to the challenges in fabrication requirements at optical wavelengths.

V. ACTIVE METAMATERIALS FOR DISPERSION CONTROL

Non-dispersive metamaterials (or more precisely, metamaterials with broadband response) have received increasing attentions in microwave regime in recent years [59-64]. Reference [35] firstly predicts the existence of non-dispersive metamaterials with active inclusions in 2001. The active inclusions involve the use of negative capacitance or inductance based on active feedback devices, which does not obey the Foster's reactance theorem (Fig. 8), therefore, named as non-Foster elements. Non-Foster elements can be realized by transistors, operational amplifiers, as well as

negative resistance devices [65,66]. Although there are many different circuit configurations, the underlying mechanism is likely the same. That is all of them are using some positive feedback systems, therefore, the circuit is easily unstable. One common non-Foster configuration is based on Linvill's circuit, which is a pair of cross-coupled transistors, as shown in Fig. 9. The circuit has the same configuration as a typical oscillator; however, the only difference is non-Foster element is operating at its stable region.
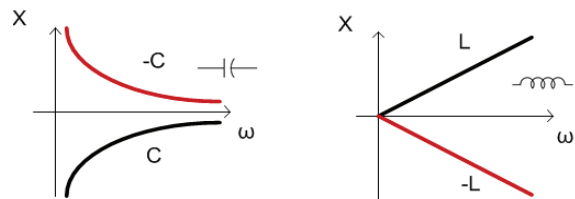
Fig. 8. The reactance behavior of negative capacitance and negative inductance compared with normal positive capacitance and inductance obeying Foster's reactance theorem.
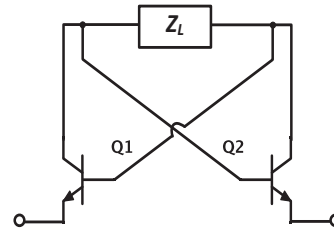
Fig. 9. A schematic of a negative impedance circuit example based on Linvill's configuration. The output impedance approximates to be Z_{in}=-Z_L.

Reference [60] experimentally demonstrates a transmission line type of a one-dimensional epsilon-near-zero metamaterial with negative capacitance, as shown in Fig. 10 (a). The measurement results verify the broadband behavior of the relative permittivity (from 0.27 to 0.37) within the frequency range of 2 to 40 MHz, spanning a bandwidth of 20:1.

A typical transmission line type of one-dimensional epsilon-near-zero metamaterial comprises a transmission line periodically loaded with shunt inductances, of which the effective permittivity can be expressed as:

$$\varepsilon_r(\omega) = \frac{1}{\varepsilon_0}(C_p - \frac{1}{\omega^2 L_p \Delta z}), \qquad (10)$$

where C_p is the distributed shunt capacitance per unit length and L_p is the shunt inductance per unit length. A broadband epsilon-near-zero material is designed by paralleling negative capacitance $-C_N$, so that:

$$\varepsilon_r(\omega) = \frac{1}{\varepsilon_0}(C_p - \frac{C_N}{\Delta z}) . \qquad (11)$$

Therefore, the dispersion in the effective permittivity can be cancelled within a broad bandwidth.

Figure 10 (b) shows a schematic of another type of non-Foster metamaterials SRR with a negative inductance load. An approximated expression of effective permeability of the split-ring resonator without the negative inductance load is given as [90]:

$$\mu_{\text{eff}} = 1 - \frac{F}{1 - 1/\omega^2 LC + i(R/\omega L)}, \qquad (12)$$

where F is a factor related to the dimensions of the unit cell structure. If the gap reactance $-1/\omega C$ is replaced by a negative inductance $-\omega L_N$, the frequency dependency of the effective permeability would be cancelled (assuming negligible resistance and parasitics), yielding a broadband negative permeability medium,

$$\mu_{\text{eff}} = 1 - \frac{F}{1 - L_N/L + i(R/\omega L)} \overset{R \to 0}{\approx} 1 - \frac{F}{1 - L_N/L} . \qquad (13)$$

a)

b)
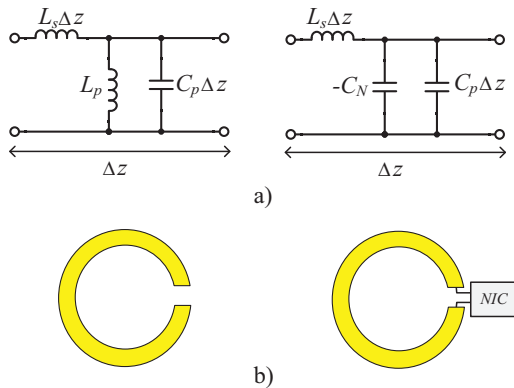
Fig. 10. (a) (left) An equivalent circuit model of a unit cell of a conventional epsilon-near-zero metamaterial transmission line, and (right) a broadband epsilon-near-zero metamaterial transmission line by replacing the periodic loaded inductance with a parallel negative capacitance [60]; (b) (left) a prototype of a SRR metamaterial with negative permeability, and (right) a scheme of a broadband SRR by embedding a negative impedance circuit at the gap.

VI. STABILITY ISSUE

Stability is one of the most challenging aspects in the design of active NIM incorporating devices or media with gain. For simplification, we consider an ideal infinite large system without boundary conditions. Two types of instability may exist in such an active system, namely absolute instability and convective instability. Absolute instability means that the EM fields blow up with time at each point of the space, while in the case of convective instability the fields at each point do not blow up with time but field grows along the propagation in space [98]. If the analytical function of the constitutive material properties are given, the medium is considered to be absolutely instable if $\varepsilon(\omega)\mu(\omega)$ contains poles or odd-order zeros in the upper half side of the complex plane. If an accurate equivalent circuit model of an active metamaterial was given, circuit stability analysis methods, for example, the normalized determinant function method [99] can be implemented. For "non-Foster" metamaterials, the internal stability of the active load (e.g., negative capacitance and inductance) as well as the overall stability of the whole system needs to be examined [100,101]. For example, a Linvill's negative impedance circuit may be internally unstable due to the feedback loop of the circuit configuration, and it highly depends on the load impedance. The parasitics of the non-Foster elements also have a severe impact on the stability and the performance. Therefore, a thoughtful design must include the consideration of the operating frequency, the cutoff frequency of the active devices, bias conditions and many others.

VII. SUMMARY AND OUTLOOK

There has been significant progress on the research of active metamaterial recently, including the understanding of fundamental limitations, fabrication and experiment techniques. Active metamaterials will not only pave the way for realizing low loss and broadband metamaterials and enabling many proposed electromagnetic applications such as "perfect" lens, "cloaking", and electrically small antennas, but also may lead to new and exciting physical insights and phenomena beyond the realm of passive metamaterials. Various challenges such as stability and nonlinearity are still currently being addressed. Further development of active metamaterials greatly depends on the advances in fabrication as well as the application

demands.

REFERENCES

[1] R. W. Ziolkowski and N. Engheta, "Metamaterial special issue introduction," *IEEE Trans. Antennas and Propag.*, 51, pp. 2546, October 2003.

[2] V. G. Veselago, "The electrodynamics of substances with simultaneously negative values of ε and μ," *Soviet Physics Uspekhi*, 10, 4, pp. 509-514, 1968.

[3] R. A. Shelby, D. R. Smith, and S. Schultz "Experimental verification of a negative index of refraction," *Science*, 292, pp. 77, April 2001.

[4] A. Alu, et al., "Single-negative, double-negative, and low-index metamaterials and their electromagnetic applications," *IEEE Antennas Propag. Mag.*, 49, pp. 23, 2007.

[5] S. Enoch, "A metamaterial for direct emission," *Phys. Rev. Lett.*, 76, pp. 213902, November 2002.

[6] D. Schurig, et al., "Metamaterial electromagnetic cloak at microwave frequencies," *Science*, 314, pp. 977, November 2006.

[7] A. K. Iyer and G. V. Eleftheriades, "Negative refractive index metamaterials supporting 2-D waves," *IEEE MTT-S IMS Digest*, 2, pp. 412, 2002.

[8] C. Caloz and T. Itoh, "Application of the transmission line theory of left-handed (LH) materials to the realization of a microstrip LH transmission line," *IEEE Antenna and Propagation Symp.*, vol. 2, pp. 415, 2002.

[9] A. A. Oliner, "A periodic-structure negative-refractive-index medium without resonant elements," *IEEE Antenna and Propagation Symp.*, pp. 41, 2002.

[10] C. Caloz and T. Itoh, "Metamaterials for high-frequency electronics," *Proceedings of IEEE*, 93, pp. 1744, October 2005.

[11] G. V. Eleftheriades, "Enabling RF/microwave devices using negative-refractive-index transmission line (NRI-TL) metamaterials," *IEEE Antennas Prop. Mag.*, 49, pp. 34, April 2007.

[12] A. Alù and N. Engheta, "Achieving transparency with plasmonic and metamaterial coatings," *Phys. Rev. E*, vol. 72, no. 1, p. 016623, July 2005.

[13] J. B. Pendry, D. Schurig, and D. R. Smith, "Controlling electromagnetic fields," *Science*, vol. 312, no. 5781, pp. 1780-2, June 2006.

[14] D. Schurig, J. J. Mock, B. J. Justice, S. A. Cummer, J. B. Pendry, A. F. Starr, and D. R. Smith, "Metamaterial electromagnetic cloak at microwave frequencies," *Science*, vol. 314, no. 5801, pp. 977-80, November 2006.

[15] J. B. Pendry, "Negative refraction makes a perfect lens," *Phys. Rev. Lett.*, vol. 85, no. 18, pp. 3966-3969, October 2000.

[16] N. Fang, H. Lee, C. Sun, and X. Zhang, "Sub-diffraction-limited optical imaging with a silver superlens," *Science*, vol. 308, no. 5721, pp. 534-7, April 2005.

[17] A. V Kabashin, P. Evans, S. Pastkovsky, W. Hendren, G. A. Wurtz, R. Atkinson, R. Pollard, V. A. Podolskiy, and A. V Zayats, "Plasmonic nanorod metamaterials for biosensing," *Nat. Mater.*, vol. 8, no. 11, pp. 867-71, November 2009.

[18] N. Liu, T. Weiss, M. Mesch, L. Langguth, U. Eigenthaler, M. Hirscher, C. Sönnichsen, and H. Giessen, "Planar metamaterial analogue of electromagnetically induced transparency for plasmonic sensing," *Nano Lett.*, vol. 10, no. 4, pp. 1103-7, April 2010.

[19] R. W. Ziolkowski and A. D. Kipple, "Application of double negative materials to increase the power radiated by electrically small antennas," *IEEE Trans. Antennas Propag.*, vol. 51, no. 10, pp. 2626-2640, October 2003.

[20] S. Enoch, "A metamaterial for direct emission," *Phys. Rev. Lett.*, 76, pp. 213902, November 2002.

[21] G. Lovat, et al., "Analysis of directive radiation from a line source in a metamaterial slab with low permittivity," *IEEE Trans. Antennas Propag.*, 54, pp. 1017, 2006.

[22] A. Grbic and G. V. Eleftheriades, "Experimental verification of backward-wave radiation from a negative refractive index metamaterial," *J. Appl. Phys.*, vol. 92, no. 10, p. 5930, October 2002.

[23] J. B. Pendry and S. A. Ramakrishna, "Refining the perfect lens," *Physica B: Condensed Matter*, vol. 338, pp. 329-332, 2003.

[24] L. D. Landau, L. P. Pitaevskii, and E. M. Lifshitz, "Electrodynamics of continuous media," *Butterworth-Heinemann*, 1979.

[25] J. D. Jackson, "*Classical electrodynamics third edition*," *Wiley*, 1998.

[26] J. Skaar and K. Seip, "Bounds for the refractive indices of metamaterials," *J. Phys. D. Appl. Phys.*, vol. 39, no. 6, pp. 1226-1229, March 2006.

[27] V. P. Drachev, U. K. Chettiar, A. V. Kildishev, H. K. Yuan, W. Cai, and V. M. Shalaev, "The ag dielectric function in plasmonic metamaterials," *Opt. Express*, vol. 16, no. 2, p. 1186, 2008.

[28] P. Tassin, T. Koschny, M. Kafesaki, and C. M. Soukoulis, "A comparison of graphene, superconductors and metals as conductors for metamaterials and plasmonics," *Nat. Photonics*, vol. 6, no. 4, pp. 259-264, March 2012.

[29] K. L. Tsakmakidis, M. S. Wartak, J. J. H. Cook, J. M. Hamm, and O. Hess, "Negative-permeability electromagnetically induced transparent and magnetically active metamaterials," *Phys. Rev. B*, vol. 81, no. 19, p. 195128, May 2010.

[30] D. Güney, T. Koschny, and C. Soukoulis, "Reducing ohmic losses in metamaterials by geometric tailoring," *Phys. Rev. B*, vol. 80, no. 12, p. 125129, September 2009.

[31] L. Zhu, F. Y. Meng, L. Dong, J. H. Fu, and Q. Wu, "Low-loss magnetic metamaterial at THz frequencies by suppressing radiation losses," *IEEE Trans. Terahertz Sci. Technol.*, vol. 3, no. 6, pp. 805-811, November 2013.

[32] J. A. Bossard, S. Yun, D. H. Werner, and T. S. Mayer, "Synthesizing low loss negative index metamaterial stacks for the mid-infrared using genetic algorithms," *Opt. Express*, vol. 17, no. 17, p. 14771, August 2009.

[33] D. J. Bergman and M. I. Stockman, "Surface plasmon amplification by stimulated emission of radiation: quantum generation of coherent surface plasmons in nanosystems," *Phys. Rev. Lett.*, vol. 90, p. 027402, 2003.

[34] S. A. Ramakrishna and J. B. Pendry, "Removal of absorption and increase in resolution in a near-field lens via optical gain," *Phys. Rev. B*, vol. 67, no. 20, p. 201101, May 2003.

[35] S. A. Tretyakov, "Meta-materials with wideband negative permittivity and permeability," *Microw. Opt. Technol. Lett.*, vol. 31, no. 3, pp. 163-165, November 2001.

[36] N. I. Zheludev, "Applied physics: the road ahead for metamaterials," *Science*, vol. 328, no. 5978, pp. 582-3, April 2010.

[37] D. F. Sievenpiper, J. H. Schaffner, H. J. Song, R. Y. Loo, and G. Tangonan, "Two-dimensional beam steering using an electrically tunable impedance surface," *IEEE Trans. Antennas Propag.*, vol. 51, no. 10, pp. 2713-2722, October 2003.

[38] H. Xin, J. B. West, J. C. Mather, J. P. Doane, J. A. Higgins, H. Kazemi, and M. J. Rosker, "A two-dimensional millimeter wave phase scanned lens utilizing analog electromagnetic crystal (EMXT) waveguide phase shifters," *IEEE Trans. Antennas Propag.*, vol. 53, no. 1, pp. 151-159, January 2005.

[39] H. T. Chen, W. J. Padilla, J. M. O. Zide, A. C. Gossard, A. J. Taylor, and R. D. Averitt, "Active terahertz metamaterial devices," *Nature*, vol. 444, no. 7119, pp. 597-600, November 2006.

[40] I. V. Shadrivov, S. K. Morrison, and Y. S. Kivshar, "Tunable split-ring resonators for nonlinear negative-index metamaterials," *Opt. Express*, vol. 14, no. 20, p. 9344, 2006.

[41] H. T. Chen, W. J. Padilla, M. J. Cich, A. K. Azad, R. D. Averitt, and A. J. Taylor, "A metamaterial solid-state terahertz phase modulator," *Nature Photonics*, vol. 3. pp. 148-151, 2009.

[42] Y. S. Kivshar, "Tunable and nonlinear metamaterials: toward functional metadevices," *Adv. Nat. Sci. Nanosci. Nanotechnol.*, vol. 5, no. 1,

p. 013001, November 2013.

[43] B. I. Popa and S. A. Cummer, "Nonreciprocal active metamaterials," *Phys. Rev. B*, vol. 85, no. 20, p. 205101, May 2012.

[44] Y. Yuan, B. I. Popa, and S. A. Cummer, "Zero loss magnetic metamaterials using powered active unit cells," *Opt. Express*, vol. 17, no. 18, pp. 16135-43, August 2009.

[45] L. M. Si, T. Jiang, K. Chang, T. C. Chen, X. Lv, L. Ran, and H. Xin, "Active microwave metamaterials incorporating ideal gain devices," *Materials*, vol. 4, no. 1, pp. 73-83, December. 2010.

[46] T. Jiang, K. Chang, L. M. Si, L. Ran, and H. Xin, "Active microwave negative-index metamaterial transmission line with gain," *Phys. Rev. Lett.*, vol. 107, no. 20, p. 205503, November 2011.

[47] K. Chang, T. Jiang, L. Ran, and H. Xin, "Investigation of microwave negative refractive index (NRI) transmission lines incorporating tunnel diodes," *IEEE Antennas Wirel. Propag. Lett.*, vol. 11, pp. 671-674, 2012.

[48] W. Xu, W. J. Padilla, and S. Sonkusale, "Loss compensation in metamaterials through embedding of active transistor based negative differential resistance circuits," *Opt. Express*, vol. 20, no. 20, pp. 22406-11, September 2012.

[49] E. W. Herold, "Negative resistance and devices for obtaining it," *Proc. IRE*, vol. 23, no. 10, pp. 1201-1223, October 1935.

[50] A. Cidronali, V. Nair, G. Collodi, J. H. Lewis, M. Camprini, G. Manes, and H. Goronkin, "MMIC applications of heterostructure interband tunnel devices," *IEEE Trans. Microw. Theory Tech.*, vol. 51, no. 4, pp. 1351-1367, April 2003.

[51] M. Premaratne and G. P. Agrawal, "Light propagation in gain media," *Cambridge University Press New York*, 2011.

[52] A. K. Popov and V. M. Shalaev, "Compensating losses in negative-index metamaterials by optical parametric amplification," *Opt. Lett.*, vol. 31, no. 14, p. 2169, 2006.

[53] M. A. Noginov, G. Zhu, M. Bahoura, J. Adegoke, C. E. Small, B. A. Ritzo, V. P. Drachev, and V. M. Shalaev, "Enhancement of surface plasmons in an ag aggregate by optical gain in a dielectric medium," *Opt. Lett.*, vol. 31, no. 20, p. 3022, 2006.

[54] M. Noginov, G. Zhu, M. Mayy, B. Ritzo, N. Noginova, and V. Podolskiy, "Stimulated emission of surface plasmon polaritons," *Phys. Rev. Lett.*, vol. 101, no. 22, p. 226806, November 2008.

[55] N. I. Zheludev, S. L. Prosvirnin, N. Papasimakis, and V. A. Fedotov, "Lasing spaser," *Nat. Photonics*, vol. 2, no. 6, pp. 351-354, May 2008.

[56] S. Xiao, V. P. Drachev, A. V Kildishev, X. Ni, U. K. Chettiar, H. K. Yuan, and V. M. Shalaev, "Loss-free and active optical negative-index

metamaterials," *Nature*, vol. 466, no. 7307, pp. 735-8, August 2010.

[57] A. D. Boardman, V. V. Grimalsky, Y. S. Kivshar, S. V. Koshevaya, M. Lapine, N. M. Litchinitser, V. N. Malnev, M. Noginov, Y. G. Rapoport, and V. M. Shalaev, "Active and tunable metamaterials," *Laser Photon. Rev*., vol. 5, no. 2, pp. 287-307, March 2011.

[58] O. Hess, J. B. Pendry, S. A. Maier, R. F. Oulton, J. M. Hamm, and K. L. Tsakmakidis, "Active nanoplasmonic metamaterials," *Nat. Mater*., vol. 11, no. 7, pp. 573-84, July 2012.

[59] S. Hrabar, I. Krois, I. Bonic, and A. Kiricenko, "Negative capacitor paves the way to ultra-broadband metamaterials," *Appl. Phys. Lett*., vol. 99, no. 25, p. 254103, 2011.

[60] S. Hrabar, I. Krois, I. Bonic, and A. Kiricenko, "Ultra-broadband simultaneous superluminal phase and group velocities in non-foster epsilon-near-zero metamaterial," *Appl. Phys. Lett*., vol. 102, no. 5, p. 054108, 2013.

[61] S. Saadat, M. Adnan, H. Mosallaei, and E. Afshari, "Composite metamaterial and metasurface integrated with non-foster active circuit elements: a bandwidth-enhancement investigation," *IEEE Trans. Antennas Propag*., vol. 61, no. 3, pp. 1210-1218, March 2013.

[62] M. Barbuto, A. Monti, F. Bilotti, and A. Toscano, "Design of a non-foster actively loaded SRR and application in metamaterial-inspired components," *IEEE Trans. Antennas Propag*., vol. 61, no. 3, pp. 1219-1227, March 2013.

[63] Y. Fan, K. Z. Rajab, and Y. Hao, "Noise analysis of broadband active metamaterials with non-foster loads," *J. Appl. Phys*., vol. 113, no. 23, p. 233905, June 2013.

[64] P. Y. Chen, C. Argyropoulos, A. Alu, and A. Alù, "Broadening the cloaking bandwidth with non-foster metasurfaces," *Phys. Rev. Lett*., vol. 111, no. 23, p. 233001, December 2013.

[65] L. C. Verman, "Negative circuit constants," *Proc. IRE*, vol. 19, no. 4, pp. 676-681, April 1931.

[66] J. G. Linvill, "Transistor negative-impedance converters," *Proc. IRE*, vol. 41, no. 6, pp. 725-729, June 1953.

[67] S. E. Sussman-Fort and R. M. Rudish, "Non-foster impedance matching of electrically-small antennas," *IEEE Trans. Antennas Propag*., vol. 57, no. 8, pp. 2230-2241, August 2009.

[68] R. W. Ziolkowski, "Broad-bandwidth, electrically small antenna augmented with an internal non-foster element," *IEEE Antennas Wirel. Propag. Lett*., vol. 11, pp. 1116-1120, 2012.

[69] C. R. White, J. S. Colburn, and R. G. Nagele, "A non-foster VHF monopole antenna," *IEEE Antennas Wirel. Propag. Lett*., vol. 11, pp. 584-

587, 2012.

[70] S. Tretyakov and S. Maslovski, "Veselago materials: what is possible and impossible about the dispersion of the constitutive parameters," *IEEE Antennas Propag. Mag*., vol. 49, no. 1, pp. 37-43, February 2007.

[71] M. Stockman, "Criterion for negative refraction with low optical losses from a fundamental principle of causality," *Phys. Rev. Lett*., vol. 98, no. 17, p. 177404, April 2007.

[72] T. Mackay and A. Lakhtakia, "Comment on 'criterion for negative refraction with low optical losses from a fundamental principle of causality'," *Phys. Rev. Lett.*, vol. 99, no. 18, p. 189701, November 2007.

[73] J. Skaar, "Causality and its implications for passive and active media," *URSI International Symp. Electromag. Theory, EMTS*, Berlin, 2010.

[74] P. Kinsler and M. McCall, "Causality-based criteria for a negative refractive index must be used with care," *Phys. Rev. Lett*., vol. 101, no. 16, p. 167401, October 2008.

[75] M. Gustafsson and D. Sjöberg, "Sum rules and physical bounds on passive metamaterials," *New J. Phys*., vol. 12, no. 4, p. 043046, April 2010.

[76] M. I. Stockman, "Spaser action, loss compensation, and stability in plasmonic systems with gain," *Phys. Rev. Lett*., vol. 106, no. 15, p. 156802, April 2011.

[77] S. Wuestner, A. Pusch, K. L. Tsakmakidis, J. M. Hamm, and O. Hess, "Comment on 'spaser action, loss compensation, and stability in plasmonic systems with gain'," *Phys. Rev. Lett*., vol. 107, no. 25, p. 259701, December 2011.

[78] J. B. Pendry and S. A. Maier, "Comment on 'spaser action, loss compensation, and stability in plasmonic systems with gain'," *Phys. Rev. Lett*., vol. 107, no. 25, p. 259703, December 2011.

[79] D. Ye, K. Chang, L. Ran, and H. Xin "Volumetric microwave gain medium with negative refractive index," *under review*.

[80] V. V. Varadan and R. Ro, "Analyticity, causality, energy conservation and the sign of the imaginary part of the permittivity and permeability," *In 2006 IEEE Antennas Propag. Society Intern. Symp*., pp. 499-502, 2006.

[81] N. Meinzer, M. Ruther, S. Linden, C. M. Soukoulis, G. Khitrova, J. Hendrickson, J. D. Olitzky, H. M. Gibbs, and M. Wegener, "Arrays of ag split-ring resonators coupled to InGaAs single-quantum-well gain," *Opt. Express*, vol. 18, no. 23, pp. 24140-51, November 2010.

[82] K. Tanaka, E. Plum, J. Y. Ou, T. Uchino, and N. I. Zheludev, "Multifold enhancement of quantum dot luminescence in plasmonic metamaterials," *Phys. Rev. Lett*., vol. 105, no. 22, p. 227403, November

2010.

[83] E. Plum, V. A. Fedotov, P. Kuo, D. P. Tsai, and N. I. Zheludev, "Towards the lasing spaser: controlling metamaterial optical response with semiconductor quantum dots," *Opt. Express*, vol. 17, no. 10, p. 8548, May 2009.

[84] G. V. Eleftheriades, A. K. Iyer, and P. C. Kremer, "Planar negative refractive index media using periodically L-C loaded transmission lines," *IEEE Trans. Microw. Theory Tech.*, vol. 50, no. 12, pp. 2702-2712, December 2002.

[85] A. Lai, C. Caloz, and T. Itoh, "Composite right/left-handed transmission line metamaterials," *IEEE Microw. Mag.*, vol. 5, no. 3, pp. 34-50, September 2004.

[86] N. Engheta, "Circuits with light at nanoscales: optical nanocircuits inspired by metamaterials," *Science*, vol. 317, no. 5845, pp. 1698-702, September 2007.

[87] S. Paulotto, P. Baccarelli, F. Frezza, and D. R. Jackson, "Full-wave modal dispersion analysis and broadside optimization for a class of microstrip CLRH leaky-wave antennas," *IEEE Trans. Microw. Theory Tech.*, vol. 56, no. 12, pp. 2826-2837, December 2008.

[88] Q. Tang, F. Y. Meng, Q. Wu, and J. C. Lee, "A balanced composite backward and forward compact waveguide based on resonant metamaterials," *J. Appl. Phys.*, vol. 109, no. 7, p. 07A319, April 2011.

[89] C. Caloz, "Perspectives on EM metamaterials," *Mater. Today*, vol. 12, no. 3, pp. 12-20, 2009.

[90] H. Chen, L. Ran, J. Huangfu, T. M. Grzegorczyk, and J. A. Kong, "Equivalent circuit model for left-handed metamaterials," *J. Appl. Phys.*, vol. 100, no. 2, p. 024915, July 2006.

[91] F. P. Casares-Miranda, C. Camacho-Penalosa, and C. Caloz, "High-gain active composite right/left-handed leaky-wave antenna," *IEEE Trans. Antennas Propag.*, vol. 54, no. 8, pp. 2292-2300, August 2006.

[92] A. B. Kozyrev, I. V. Shadrivov, and Y. S. Kivshar, "Soliton generation in active nonlinear metamaterials," *Appl. Phys. Lett.*, vol. 104, 084105, 2014.

[93] N. L. Tsitsas, A. Lakhtakia, and D. J. Frantzeskakis, "Solitons in a homogenized two-phase, isotropic, nonlinear, particulate composite medium," *J. Opt. Soc. Am. B*, vol. 29, no. 9, pp. 2610-2616, September 2012.

[94] N. L. Tsitsas, "Analysis of electromagnetic wave propagation in frequency bands of nonlinear metamaterials," *Applied Computational Electromagnetics Society Journal*, vol. 27, no. 2, pp. 169-180, February 2012.

[95] M. Wegener, J. L. García-Pomar, C. M. Soukoulis, N. Meinzer, M. Ruther, and S. Linden, "Toy model for plasmonic metamaterial resonances coupled to two-level system gain," *Opt. Express*, vol. 16, pp. 19785-19798, 2008.

[96] A. Fang, T. Koschny, and C. M. Soukoulis, "Self-consistent calculations of loss-compensated fishnet metamaterials," *Phys. Rev. B*, vol. 82, no. 12, p. 121102, September 2010.

[97] Y. Sivan, S. Xiao, U. K. Chettiar, A. V Kildishev, and V. M. Shalaev, "Frequency-domain simulations of a negative-index material with embedded gain," *Opt. Express*, vol. 17, pp. 24060-24074, 2009.

[98] A. D. Boardman, Y. G. Rapoport, N. King, and V. N. Malnev, "Creating stable gain in active metamaterials," *J. Opt. Soc. Am. B*, vol. 24, no. 10, p. A53, 2007.

[99] A. P. A. Platzker, W. S. W. Struble, and K. T. H. K. T. Hetzler, "Instabilities diagnosis and the role of K in microwave circuits," *1993 IEEE MTT-S Int. Microw. Symp. Dig.*, 1993.

[100] K. Z. Rajab, Y. Hao, D. Bao, C. G. Parini, J. Vazquez, and M. Philippakis, "Stability of active magnetoinductive metamaterials," *J. Appl. Phys.*, vol. 108, no. 5, p. 054904, 2010.

[101] K. Z. Rajab, Y. F. Fan, and Y. Hao, "Characterization of active metamaterials based on negative impedance converters," *J. Opt.*, vol. 14, no. 11, p. 114004, November 2012.

Qi Tang received his B.S. degree in Communication Engineering, in 2009, and his M.S. degree in Microwave Engineering, in 2011, from Harbin Institute of Technology, Harbin, China. He is currently working towards his Ph.D. degree with the Electrical and Computer Engineering department, University of Arizona, Tucson, AZ, USA. His doctoral research focuses on metamaterials, microwave circuits, antennas, THz technologies, and millimeter wave wireless communication systems.

Hao Xin Professor of Electrical and Computer Engineering at the University of Arizona. He was named an Arizona Engineering fellow in Aug. 2013. He received his Ph.D in Physics from Massachusetts Institute of Technology in February 2001.

From 2000 to 2003, he was a Research Scientist with the Rockwell Scientific Company. He was a Sr. Principal Multidisciplinary Engineer with Raytheon Company from 2003 to 2005.

His primary research interests are in the area of microwave/millimeter wave/THz devices, circuits, antennas and their applications in wireless communication and sensing systems. His recent research activities have covered a broad range of high frequency technologies, including applications of new technologies and materials in microwave and millimeter wave circuits such as electromagnetic band gap crystals and other mea-materials, carbon nano-tubes devices, solid state devices and circuits, active or semi-active antennas, and passive circuits. He has authored over 200 referred publications and 14 patents (12 issued and 2 pending) in the areas of microwave and millimeter-wave technologies, random power harvesting based on ferro-fluidic nano-particles and carbon nanotube based devices. He is a senior member of IEEE and Chair of the joint chapter of IEEE AP/MTT/EMC/COMM in Tucson AZ. He is a General Co-Chair of the 8th International Workshop on Antenna Technology. He also serves as an Associate Editor for IEEE Antennas and Wireless Propagation Letters.

An Overview of Equivalent Circuit Modeling Techniques of Frequency Selective Surfaces and Metasurfaces

Filippo Costa, Agostino Monorchio, and Giuliano Manara

Dipartimento di Ingegneria dell'Informazione
University of Pisa, Pisa, 56122, Italy
filippo.costa@iet.unipi.it, a.monorchio@iet.unipi.it, g.manara@iet.unipi.it

Abstract ─ Circuit analysis of frequency selective surfaces is reviewed with the aim to underline range of validity of different models and their advantages in terms of simplicity and physical insight. The circuit approach is based on an equivalent representation of the FSSs with series or shunt connections of inductances and capacitances. Dense non-resonant periodic surfaces (i.e.: grid or patch arrays) can be analyzed analytically by computing the values of inductors or capacitors via the homogenization theory. As the lattice period increases with respect to the operating wavelength or the element shape becomes resonant, a fully analytical circuital approach fails, in particular, in the presence of thin substrates. However, simple circuit approaches can still be employed by deriving lumped parameters values via a quick pre-processing and then generalizing them. The results are accurate up to the resonant frequency region of the element. By including an additional lumped element it is possible, taking into account the effect of the first high order Floquet harmonic. The multi-mode formulation is also able to catch the highly non-linear response of FSS screens in the grating lobe region provided that the current profile of the element does not change significantly.

Index Terms ─ Equivalent circuit model, frequency selective surfaces, periodic gratings.

I. INTRODUCTION

The fact that non-continuous surfaces can diffract electromagnetic waves, was proved for the first time by the American physicist David Rittenhouse in 1786 [1]. He found explanation to the curious phenomenon observed by Mr. Hopkinson, that is, the presence of multiple images when he tried to observe a distant street lamp through a silk handkerchief. Rittenhouse reproduced a grating by using 50 hairs between two finely threaded screws. In 1821, Fraunhofer built a similar diffraction grating which used to measure wavelength of specific colors and dark lines in the solar spectrum [2]. In 1902 and 1904, Wood [3] and Rayleigh [4] debated on the popular Wood's anomalies of periodic gratings. Rayleigh formulated a theory that was able to predict diffraction angles of the grating [5], but a comprehensive understanding of resonance effects observed by Wood was achieved with the papers of Fano in 1941 [5], and Hessel and Oliner in 1965 [7]. Probably, the first microwave application of gratings at microwaves by Marconi and Franklin who designed in 1919 a parabolic reflector built of wire sections instead of a continuous surface [8]. Although, the concept of frequency selective surface is known at microwaves since the beginning of 20th century, the filtering capability of these periodic surfaces were scarcely exploited. Some applicative works have been done in the fifties: in 1956, Trentini proposed the use of gratings for enhancing the gain of antennas [9]. In the same period, Marcuvitz, Oliner and other scientists studied the properties of waveguides loaded with periodic structures [10]-[12] and proposed waveguide antennas based on leaky-waves [13]-[16]. Besides the aforementioned seminal research findings, early practical applications of selective surfaces were mainly focused in Cassegainian subreflectors in parabolic dish antennas. The satellite Voyager 77 exploited a frequency selective surface for implementing a double-frequency reflector [17]. The principle was

extended to four frequency bands in the satellite Cassini in 1996 [18]. Nowadays, FSSs [19], [20] are employed at microwave frequencies for designing frequency selective radomes [21], leaky wave/Fabry-Perot, low-profile and low-RCS antennas [22]-[24], reflectarays, trasmittarrays and lenses [25], [26], polarization converting surfaces [27], waveguide filters [28], electromagnetic shielding [29], radar absorbing materials [30], and more in general, to synthesize the bidimensional version of metamaterials, that is, metasurfaces [31]. In the THz domain, Frequency Selective Surfaces are frequently addressed as metasurfaces and are massively employed for designing sensors, spatial filters, absorbers, THz modulators and imaging devices [32]-[34]. In optical domain, FSSs have been recently proposed to improve the efficiency of photovoltaic cells [35], [36], but more frequently they are employed to achieve light diffraction (diffraction gratings). In the latter case, the lattice period is several wavelengths for achieving light diffraction towards different directions. Diffraction gratings are used in several optical commercial devices such as monochromators, spectrometers, lasers, wavelength division multiplexing devices, optical pulse compressing devices, optical microscopes and many others [2].

Classical numerical methods for the analysis of frequency selective surfaces are based on the Finite Difference Time Domain (FDTD) or Finite Element Method (FEM) techniques. These methodologies can be applied to arbitrary FSS configurations (single-layer, multi-layer, finite, and curved frequency-selective surfaces), but they are computationally onerous. Conversely, other dedicated highly efficient methods have been proposed since the seventies. The most famous is the Integral Equation Method (IEM), used in conjunction with the Method of Moments (MoM) [37]-[40].

A helpful way to understand the FSS behavior is to establish an analogy between lumped filters and the periodic surfaces. A circuital analysis, unlike full-wave simulations, provides immediate results and a good physical insight into the design properties of the structure.

This paper is organized as follows. In the next section a comprehensive review of the literature is presented. The third section is dedicated to the description of three efficient methods to represent the FSS response in different operating regimes. In the fourth section it describes a simple procedure for calculating the transmission and reflection coefficient of the FSS within a multi-layer. Lastly, the fifth section describes the results obtained with the equivalent circuit models on various meaningful examples of FSS elements.

II. LITERATURE REVIEW OF FSS MODELLING

In the beginning of 20th century, MacFarlane [41], Wessel [42], and Hornejäger [43] showed that the scattering problem of a parallel wire grid can be solved using a transmission line model, where the wire grid is modeled as a shunt impedance and the homogeneous surrounding medium is modeled as infinite transmission lines. Initially, only simple elements comprising wire grids or patches were considered. Later, Trentini [44] included the periodical loading of the wire grid with lumped circuit elements, and Wait developed the MacFarlane model to analyze the reflection properties in the vicinity of a dielectric interface [45], [46]. In the sixties, Ulrich [47] improved the equivalent circuits for inductive and capacitive grids with an additional capacitor or inductor, respectively, to take into account resonant effects of these structures as the periodicity of the mesh becomes approximately equal to λ. The value of these extra circuit elements was evaluated from the measurements by matching the resonance at in the circuit model with measurements. Lee and Zarrillo [48] compared the accuracy of different models for inductive or capacitive grids.

An alternative way to derive the impedance of the metallic grids was proposed by Kontorovich and Astrakhan in [49], [50] by averaging the currents flowing on the periodic structure. The expression of the surface impedance for array of patches can be obtained by using the Babinet principle [51]. The averaged model works properly in the quasi-static regime where grids or patches have respectively a pure inductive and capacitive behavior. When the frequency increases up to the first resonance, this model clearly fails because it does not take into account any resonance phenomenon. The accuracy of the averaged capacitances/inductances can be improved further by taking into account terms of higher orders [52]. The main limitations of these

models are:
- *only simple FSS configurations are considered;*
- *the effect of a thin nearby material interface is not adequately modeled.*

Attempts to derive formulas for more complex FSS shapes (e.g., loops, crosses, Jerusalem crosses) have been made in the eighties [53]-[57], but the derived formulas often contain empirical derived correction factors turning out to lose the intuitive understanding on which a model is based.

The effect of substrates is generally taken into account by multiplying the FSS capacitance through the averaged permittivity of the dielectrics enclosing the FSS [51]. This approximation is acceptable only for thick dielectric substrates (thicker than an half of the cell periodicity) or when the FSS periodicity is much lower than the operating wavelength [58], [59]. In practical cases, the supporting dielectrics are usually much thinner than the wavelength, and the dielectric thickness also has to be taken into account in computing the averaged permittivity. In order to achieve more accurate results, valid also for thin substrates, a corrected single mode circuit [58] or a multi-mode formulation may be adopted [60]-[62].

III. FSS MODELING

An important parameter in the FSS analysis is the wavelength at which the grating lobes or trapped modes onset [1], [63]. For freestanding FSS, the wavelength of the first high order Floquet harmonic reads:

$$\lambda_g^{\varepsilon_r} = D\left(\sqrt{\varepsilon_r} + \sin(\vartheta)\right), \qquad (1)$$

where D represents the inter-element spacing, c is the speed of light and θ is the incident angle, and ε_r is the dielectric permittivity of the media where the FSS is embedded. For wavelengths longer that λ_g (or frequencies smaller that c/λ_g) the only propagating Floquet harmonic is the fundamental one. Higher modes are evanescent and decay exponentially away from the mesh. At normal incidence, the grating lobes wavelength is equal to the FSS periodicity. However, it has to be pointed out that when the FSS is embedded with dielectric media, the first high-order phenomenon is represented by the onset of trapped dielectric modes [19] (or trapped surface waves) that occurs well below the propagation of the first grating lobe.

In the analysis of periodic structures, three different fundamental regions can be individuated [63]. At long wavelengths, when the FSS periodicity D is much larger than the operating wavelength λ, quasi-static regime, the periodic surface can be efficiently analyzed by using homogenized theory. The intermediate frequency range, where the FSS periodicity is smaller but comparable with the operating wavelength, the periodic surface element can be resonant. In this region the FSS can still be modeled by using the circuit theory, but the values of the lumped parameters need to be retrieved by using full-wave simulations followed by an inversion procedure. The last region, where the operating wavelength becomes shorter than guided wavelength λg, is highly non-linear because more than one Floquet harmonic is in propagation and FSS elements (also single resonant ones) need to be represented by using a multi-mode network. The three regions are summarized in Fig. 1. In the following paragraphs we briefly summarize three efficient approaches for analyzing FSSs in the three described frequency regions.

Fig. 1. Three characteristic regions of periodic structures.

A. Averaged approach

For simple non-resonant elements as wire grids or patch arrays, the impedance is mainly inductive or capacitive, respectively [65] (Fig. 2). The calculation of the inductance or the capacitance value can be accomplished by averaging the currents flowing on the periodic structure. The derived FSS impedance is of the second order since it is angle dependent and it has a different expression for the TE and the TM polarization. In the case of a patch array, the impedance $Z_{patch}^{TE/TM} = 1/\left(j\omega C_{patch}\right)$, is just a capacitor [51]:

$$C_{patch}^{TE} = \frac{D\varepsilon_0\left(\varepsilon_{r1}+\varepsilon_{r2}\right)}{\pi}\ln\left(\frac{1}{\sin\left(\frac{\pi w}{2D}\right)}\right)\left(1-\frac{k_0^2}{k_{eff}^2}\frac{\sin^2(\vartheta)}{2}\right)$$

$$C_{patch}^{TM} = \frac{D\varepsilon_0\left(\varepsilon_{r1}+\varepsilon_{r2}\right)}{\pi}\ln\left(\frac{1}{\sin\left(\frac{\pi w}{2D}\right)}\right), \qquad (2)$$

while for grids, the impedance $Z_{grid}^{TE/TM} = j\omega L_{grid}$, is an inductor:

$$L_{grid}^{TE} = \frac{D\mu_0}{2\pi}\ln\left(\frac{1}{\sin\left(\frac{\pi w}{2D}\right)}\right)$$

$$L_{grid}^{TM} = \frac{D\mu_0}{2\pi}\ln\left(\frac{1}{\sin\left(\frac{\pi w}{2D}\right)}\right)\left(1-\frac{k_0^2}{k_{eff}^2}\frac{\sin^2(\vartheta)}{2}\right), \qquad (3)$$

where D represents the periodicity of the FSS, w is the gap between the squares patches and k_0 is the wave number in free space, $k_{eff} = k_0\sqrt{\left(\varepsilon_{r1}+\varepsilon_{r2}\right)/2}$ is the wave number of the incident wave vector in the effective host medium, θ is the incident angle. ε_{r1} and ε_{r2} are the relative dielectric permittivity of the dielectric slabs surrounding the periodic surface (typically the upper dielectric is air).
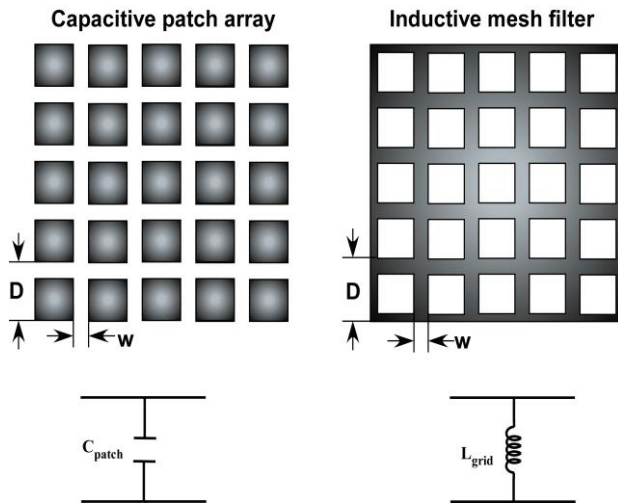
Fig. 2. Bi-dimensional sketch of non-resonant capacitive and inductive FSS filters with their lumped model.

The agreement between the approximated and full-wave results are good if the FSS periodicity is smaller than an half-wavelength. In [66], [67] the formulas for an array of Jerusalem crosses are also proposed, but they are sufficiently accurate only up to the first resonance of the Jcross.

B. First order retrieving method

The simple circuit model presented in the previous section can be improved by adding additional lumped components which allow to follow the FSS response even in the second zone; i.e., the resonant one. A simple LC circuit can fit the frequency response of a capacitive frequency selective surface, whereas, a shunt LC connection replaces the LC series for an inductive FSS. In absence of losses, the FSS impedance is purely imaginary and it is represented by two lumped parameters. Losses can be introduced by adding a series resistance in the equivalent circuit [68]-[70].

In order to compute FSS reactance, the knowledge of the current density on the FSS element is necessary even for the zero order approximation. Alternatively, a retrieving approach which starts from on the determination of the complex reflection coefficient through a preliminary full-wave simulation can be employed [58], [71]-[73]. Then, according to classical transmission line theory, it is possible to obtain the impedance of the freestanding FSS as follows:

$$Z_{FSS} = -\frac{Z_0^2\left(1+\Gamma_{in}\right)}{2Z_0\Gamma_{in}}, \qquad (4)$$

where Γ_{in} is the reflection coefficient of the periodic structure calculated at the FSS position and Z_0 is the free space impedance. Once computed the FSS impedance at two frequency points, it is possible to calculate the values of the capacitance and the inductance approximating the actual impedance by solving a two equations system [58]. Even if the inversion procedure is quick, it is unstable with respect to the chosen inversion frequency points ω_1 and ω_2, leading to some inaccuracies in the calculation of L and C values. A more reliable procedure starts from the calculation of the null of the FSS impedance and then computes the inductance by an iterative procedure which minimizes the Euclidean distance between the MoM and the LC series impedance, while imposing $C = 1/\omega_{zero}^2 L$. If the frequency selective surface is embedded within dielectric layers, additional transmission lines representing the dielectric layers need to be considered in retrieving L and C parameters. Figure 3 reports, for instance, the model of an FSS embedded within two dielectric layers. The reflection coefficient Γ_{in} used in (4) is determined from the

reflection coefficient Γ_d obtained with a full-wave simulation. The additional quantities are defined in Fig. 1. After the calculation of the load impedance Z_L by using classical transmission line formulas, it is sufficient to solve a simple parallel circuit to extract the FSS impedance as shown above.
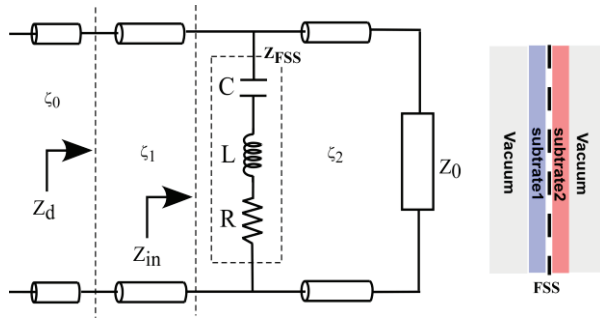

Fig. 3. Transmission line model for the analysis of an embedded FSS.

The equivalent circuit parameters are obtained for a particular FSS configuration but several degrees of freedom; e.g., repetition period of the unit cell, the angle of incidence of the incoming wave, influence the values of the equivalent inductance and capacitance. If these corrections are understood and modeled, the capacitances and inductances, preemptively obtained at normal incidence and stored in a database of shapes, can be used for computing the response of generic FSS configurations with no additional computation effort. Let us now briefly analyze separately the effect of these degree of freedom.

Cell periodicity
If all FSS element geometrical dimensions are simply rescaled with a certain scaling factor, a shift of the resonance frequencies is obtained. Starting from a given periodicity (e.g.: 10 mm), the frequency behavior of the scaled FSS can be obtained by rescaling all the inductance and capacitance values. Clearly, this stretch of the unit cell leads to the modification of the elements

lengths as well. For this reason it is more convenient to think FSS element dimensions not as an absolute value but referred to the element periodicity.

Dielectric effects
The resonant frequency of an FSS in presence of a thick dielectric substrates on both sides is reduced by a factor equal to $\sqrt{\varepsilon_r}$, and by a factor $\sqrt{(\varepsilon_r+1)/2}$ when the dielectric is present only on one side of the FSS [51]. However, fixing the relative permittivity of the substrate, the decrease of its thickness leads to a gradual shift of the FSS resonance towards higher frequencies.

The presence of thin dielectric substrates involves a relevant number of Floquet modes [62], and given the complexity of the problem, a closed formula which relates the capacitance to the dielectric thickness and permittivity is hard to find. A good solution can be the derivation of a simple interpolating formula which exactly matches the variation of the effective permittivity as a function of the dielectric thickness. To this aim, the variation of capacitance as a function of thickness and dielectric constant of the substrate is analyzed for a patch array embedded within two dielectric substrates. The optimal capacitance values obtained with the retrieving procedure are normalized to the freestanding values to obtain a thickness dependent effective permittivity. An expression that fits very well, the effective permittivity reads [58]:

$$\varepsilon_{eff} = \varepsilon_r^{av} + \left(\varepsilon_r^{av} - 1\right)\left[\frac{-1}{\exp^N(x)}\right], \qquad (5)$$

where $x = 10*d/D$, $\varepsilon_r^{av} = \left(d_1\varepsilon_{r1} + d_2\varepsilon_{r2}\right)/\left(d_1 + d_2\right)$ and N is an exponential factor that takes into account the slope of the curve. This parameter can vary for different cell shapes depending on the unit cell filling factor [58]. The effective permittivity as a function of the dielectric thickness obtained by using MoM simulations and the interpolating relation is shown in Fig. 4.
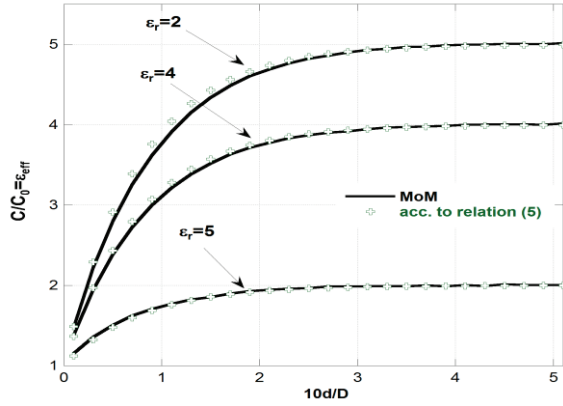
Fig. 4. Effective permittivity as a function of substrate thickness computed by iterative MoM simulations. Parameters are: D=10 mm, w=2.5 mm. The fitting of numerical values has been obtained by means of the formula (5).

Incidence angle

When an oblique electromagnetic wave strikes the FSS, the impedance of the periodic structure should be expressed in a matrix form. The mutual terms due to the coupling between the modes and the dependence on azimuthal angle φ, can be considered negligible for symmetric unit cells. In this case, the expression of the FSS impedance for oblique incidence becomes a two terms matrix valid for TE and TM polarizations. In order to get some insight in the angular variation of the FSS impedance, the expressions derived for patch arrays by using the averaged approach [62] can help. These expressions include the first order tangential derivative, and therefore are valid for normal and oblique incidence when the grid is reasonably homogeneous (D<λ/2). According to this formulation, the patch array capacitance for TE polarization is angle dependent [51]. The same expression can be used as an interpolating function for all elements by just replacing the number *2* with a parameter α, which in our case, would depend from the chosen element:

$$C_{TE}^{\vartheta} = C_{TE}^{0}\left(1 - \frac{k_0^2}{k_{eff}^2}\frac{\sin^2(\vartheta)}{\alpha}\right), \qquad (6)$$

where C_{TE}^{0} is the capacitance computed at normal incidence, and the other quantities have been already defined.

The dependence of the FSS capacitance on the incident angle is analyzed by the MoM iterative procedure for different elements (Fig. 5). The variations of patch and ring capacitance are in agreement with the relation (6) when the parameter α is suitably chosen. The angular dependence of the TE capacitance is weak in the case of a cross element. The angular dependence of the TM capacitance can be neglected for capacitive elements.
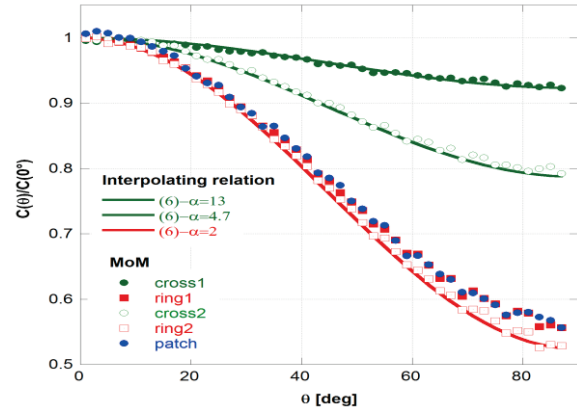
Fig. 5. Dependence of lumped capacitance on the incidence angle for different shapes.

C. Multi-mode approach

The generalized analysis presented in Section III is valid in the resonance region of the FSS, since frequency response of FSSs above the visible range involve non-linear behaviors due to the onset of higher order Floquet modes. In this region, the energy is not reflected or transmitted only in the direction stated by the Snell law, but also in other directions according to Rayleigh theory [5].

In order to describe the behavior of frequency selective surfaces in the frequency region between resonant zone and the grating lobe propagation zone as well as after the propagation of the grating lobes, a number of additional elements are necessary in the circuit model. To this purpose, two additional impedances can be connected in series with the lumped circuit comprising inductances and capacitances to take into account resonant phenomena due to the lattice [63]. The improved circuit model is reported in Fig. 6. The two impedances, which take into account the TE and TM high-order Floquet modes, read [63]:

$$Z_L(\omega) = \sum_{h=1}^{N_{TE}} A_h^{TE} Z_{TE,h}^{in}(\omega), \qquad (7)$$

$$Z_C(\omega) = \sum_{g=1}^{N_{TM}} A_g^{TM} Z_{TM,g}^{in}(\omega), \qquad (8)$$

where A_h and A_g account the degree of excitation of the harmonics, the indices h and g are referred to a particular couple of *(m,n)* pair. The excitation factors, in general, depend on the frequency, but if the current on the FSS element does not significantly vary, they can be reasonably hypothesized frequency independent [63]. This hypothesis is verified when the element does not resonate in the second FSS region of Fig. 1, that is, the size of the element is much smaller than FSS periodicity. Z_{TE}^{in} and Z_{TM}^{in} represent the shunt connection between the impedances seen from the left and from the right of the FSS [74]:

$$Z_{TE,h}^{in}(\omega) = \left(\frac{1}{Z_{v,TE,h}^{left}} + \frac{1}{Z_{v,TE,h}^{right}} \right), \qquad (9)$$

$$Z_{TM,g}^{in}(\omega) = \left(\frac{1}{Z_{v,TM,g}^{left}} + \frac{1}{Z_{v,TM,g}^{right}} \right). \qquad (10)$$

Left and right impedances are derived, for any considered mode *(m,n)*, by using the conventional transmission line relation recursively for every substrate:

$$Z_{v,c}^{TE/TM,right/left,h/g} = Z_c^{TE,TM} \frac{\left[Z_{v,c-1}^{TE,TM} + Z_c^{TE,TM} \tan(k_{z,c}d_c) \right]}{\left[Z_c^{TE,TM} + Z_{v,c-1}^{TE,TM} \tan(k_{z,c}d_c) \right]}. (11)$$

In (11) c stands for the cth dielectric layer. $Z_c^{TE,TM}$ represents the modal characteristic impedance of every dielectric slab and is calculated as follows:

$$Z_{c,mn}^{TE}(\omega) = \frac{\omega\mu_0}{k_{z,mn}}, \qquad (12)$$

$$Z_{c,mn}^{TM}(\omega) = \frac{k_{z,mn}}{\omega\varepsilon_0\varepsilon_r}, \qquad (13)$$

where $k_{z,mn} = \sqrt{\varepsilon_r k_0^2 - k_x^2 - k_y^2}$ is the normal component of the wavenumber. The transverse wavenumbers are:

TE polarization

$$k_{x,m} = k_0 \sin(\vartheta) + 2m\pi/D_x \, ; \, k_{y,n} = 2n\pi/D_y$$

TM polarization

$$k_{x,m} = 2m\pi/D_x \, ; \, k_{y,n} = k_0 \sin(\vartheta) + 2n\pi/D_y \, . \, (14)$$

The values of the excitation coefficients and the L and C parameters can be calculated after a run of a full-wave simulation in a sufficient number of frequency points. In [63], it is suggested to choose a couple of frequency points in the low frequency range and one frequency point just before the onset of every considered high-order mode, but when the number of harmonic increases the procedure is not always stable. The introduction of many high-order modes allows to describe a highly non-linear frequency response of FSSs within the grating lobe zone provided that the element does not resonate. As the element becomes resonant within the zero-order harmonic frequency range, the current distribution cannot be anymore assumed as frequency independent. As a consequence, the harmonic excitation coefficients A in (7) and (8), may become frequency dependent leading to a reduction of accuracy of the method within the grating lobe zone. As remarked in [63], the multi-mode approach is a matching procedure mainly aimed to understand the physical mechanisms which lead to nonlinearities in the frequency response of FSSs.

It has been finally pointed out, that the described multi-mode approach is also helpful to improve the accuracy of the first order retrieving method between the resonant zone up to the propagation of the first grating lobe. To this aim, it is sufficient to include the first high order mode (TE$_{-1,0}$ for TE excitation, and TM$_{0,-1}$ for TM excitation) by computing its excitation coefficient.
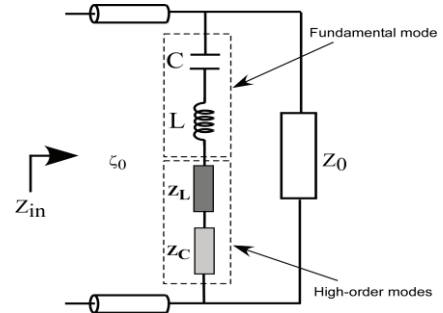

Fig. 6. Equivalent circuit of a single resonant FSS with high-order impedances.

IV. CALCULATION OF THE FREQUENCY RESPONSE OF A GENERIC FSS SYSTEM

Once derived the equivalent circuit parameters, the approximate reflection and transmission coefficients (s_{11}, s_{21}) of the FSS are

computed by using conventional transmission line theory [76]:

$$s_{11} = \frac{AZ_0 + B - CZ_0^2 - DZ_0}{AZ_0 + B + CZ_0^2 + DZ_0}, \qquad (15)$$

$$s_{21} = \frac{2Z_0}{AZ_0 + B + CZ_0^2 + DZ_0}, \qquad (16)$$

where A, B, C, D represents the terms of the ABCD matrix of the system comprising the FSS and a generic number N of dielectrics:

$$\begin{bmatrix} A & B \\ C & D \end{bmatrix} = [M_1] \cdot \ldots \cdot [M_n] \cdot [M_{FSS}] \cdot [M_{n+1}] \cdot \ldots \cdot [M_N]. \ (17)$$

In equation (17), the subscript n stands for the nth dielectric substrate and M represents the scattering matrix of every layer:

$$[M_n] = \begin{bmatrix} \cos(k_{zn}d_n) & jZ_n \sin(k_{zn}d_n) \\ j\dfrac{\sin(k_{zn}d_n)}{Z_n} & \cos(k_{zn}d_n) \end{bmatrix} \qquad (18)$$

$$[M_{FSS}] = \begin{bmatrix} 1 & 0 \\ 1/Z_{FSS} & 1 \end{bmatrix},$$

where Z_{FSS} is the approximate FSS impedance computed with the retrieved LC parameters, $Z_n^{TE} = (\omega\mu_r\mu_0)/k_{zn}$ and $Z_n^{TM} = k_{zn}/(\omega\varepsilon_r\varepsilon_0)$ are the characteristic impedances of the slab for TE and TM polarization, $k_{zn} = \sqrt{\varepsilon_r k_0^2 - k_t^2}$ is the normal component of the wavenumber, $k_t = k_0 \sin(\vartheta)$ is the transverse component of the wavenumber with ϑ representing the incidence angle of the incoming wave with respect to the normal and k_0 the free space propagation constant. The quantities ε_0, ε_r, μ_0, μ_r represent the free space and the relative dielectric permittivity and magnetic permeability. Since the FSS is a passive reciprocal system, the transmission coefficient of the structure is identical independently of the incidence side. If the analyzed configuration is symmetrical (same dielectrics on both side of the FSS) also, the reflection coefficients computed on the two sides of the FSS coincide (symmetric scattering matrix).

V. FSS ELEMENTS AND RESULTS

The choice of the suitable element is of outmost importance in the design of a frequency selective surface. An almost infinite set of geometries can be adopted as unit cell of a periodic screen. Some of these geometries are more popular than others and are also simple to control. We propose in Table 1 a classification of the most popular geometries on the basis of resonant properties and equivalent circuits. The number of lumped elements is directly proportional to the number of resonances. It can be demonstrated that the expression of the FSS reactance satisfies the Foster theorem [75], that is, it possesses the same pole-zero analytical properties as a passive LC network.

Table 1: Classification of FSS elements on the basis of resonant properties (symbol // means shunt connection and multiplication means series connection)

Element Type	Element Shape	Equivalent Circuit
Non-resonant elements	Strip, patch, wire grid	C
Single-resonant	Loop, dipole, cross, tripole, dogbone	(LC)
Double-resonant	Double cross, double loop, Jerusalem cross, etc.	(LC)//(LC) or (LC)(L//C)
Multi-resonant (geometrical)	Concentric loops, fractal elements	(LC)//(LC)//(LC)….
Multi-resonant (current distribution)	Quadrifilar spiral, meandered dipole or loop, genetically optimized	Not physical

In the following paragraphs some numerical results about some popular FSS elements are shown with the aim to demonstrate the validity regions of the presented equivalent circuits.

Non-resonant elements-patch arrays

The first analyzed configuration is a simple patch array. For this element, it is possible to compare the first-order retrieving model with the analytical averaged model. Even if a purely analytical approach should not be compared with a semi-analytical one, this comparison serves to show that the inclusion of the inductance in the equivalent circuit allows going beyond the limits

of effective grid parameters. The patch is characterized by a periodicity of 10 mm, which leads to the onset of grating lobes for normal incidence at 30 GHz. Figure 7 reports the reflection coefficients obtained by employing approximate impedances for two different values of the patch gap. For large gaps, the retrieving method agrees very well with the MoM code up to the propagation of the grating lobes, while the averaged model loses its validity when the cell repetition period exceeds an half wavelength. For small gaps, the averaged model is instead applicable closer to the frequency where grating lobes emerge. The capacitances obtained by using averaged relations and by using the retrieving approach are summarized in Table 2. The values computed by the retrieving approach are systematically lower than those computed by using averaged relations, since the employed circuit model considers also the inductive component of the impedance.
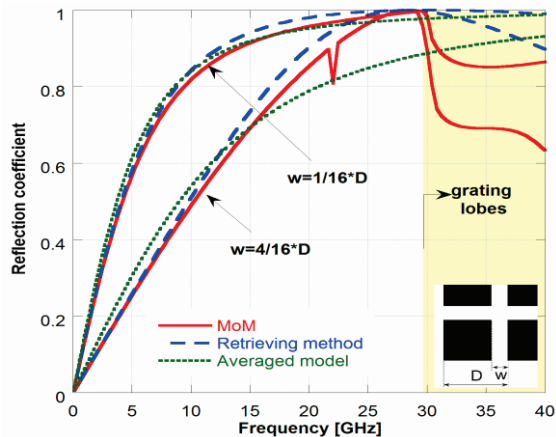
Fig. 7. Reflection coefficients obtained with different models. Parameters: D=10 mm and different w.

Table 2: Capacitance and inductance values computed by using averaged relations and by using the retrieving method (patch array with periodicity, D=10 mm)

	C_0 Averaged [fF]	C_0 Retrieved [fF]	L_0 Retrieved [nH]
w=12/16*D	54.12	43.76	0.729
w=14/16*D	90.28	81.04	0.352
w=15/16*D	130.9	117.35	0.24

Single-resonant elements

A couple of popular resonant FSS elements are the loop and the cross type. The resonance of the loop occurs when the length approaches to one wavelength while the cross element resonates when its length equals half wavelength. Figures 8 and 9 report the impedance and the reflection coefficient for a cross shaped FSS. The approximated responses are computed both by using the retrieving method and the multimode approach. The multimode approach includes just the first high-order mode in order to limit the complexity of the equivalent circuit.

It is evident that the resonant behavior of the element is caught by the LC circuit while the effects due to the lattice (Wood's anomaly) are well approximated only by including at least one high order mode. The geometrical parameters of the simulated cross are reported in Table 3 together to the values of the lumped elements employed in the transmission line model to retrieve the FSS response. In Fig. 10, the reflection coefficient for a loop shaped FSS is also reported. Also in this case, the introduction of the first HO harmonic allows to correctly match the reflection behavior up to the onset of the grating lobes. Table 4 reports the geometrical parameter of the simulated loop element together to the values of the lumped elements employed in the circuit model to retrieve the FSS response.
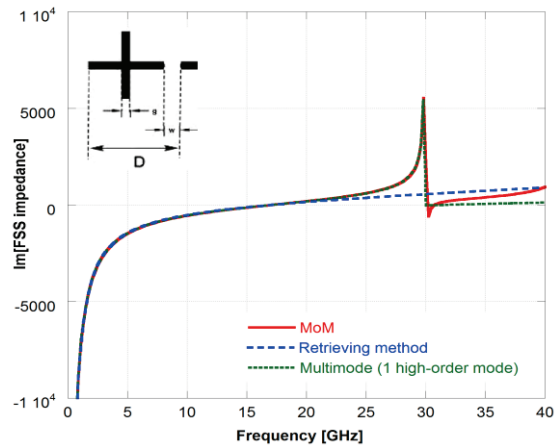
Fig. 8. Impedance of a freestanding cross FSS obtained through MoM approach, the retrieving method and the multi-mode approach with one high-order mode (TE01). Geometrical parameters: D=10 mm, w=2/16*D, g=2/16*D.
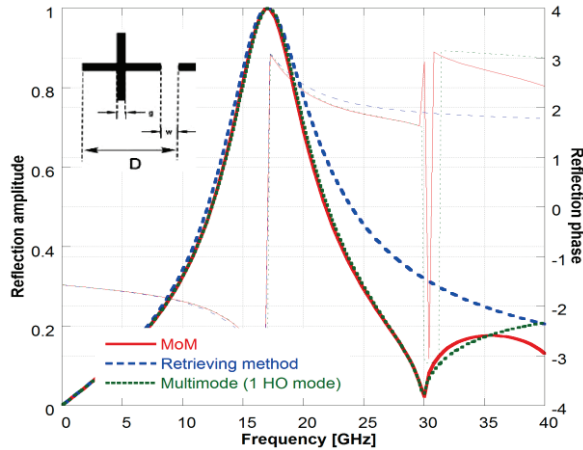
Fig. 9. Reflection coefficient of a freestanding cross FSS obtained by using MoM code, the retrieving method and the multi-mode approach including only 1 high-order mode (TE01). Geometrical parameters: D=10 mm, w=2/16*D, g=2/16*D.

Table 3: Geometrical parameters and values of the electrical parameters in the lumped circuits of the simulated cross element

Physical Parameters		Retrieving Method		Multi-mode Circuit (1 HO mode)	
D	10 mm	C_s	20.00 fF	C_s	19.91 fF
G	2/16*D	L_s	4.37 nH	L_s	1.29 nH
W	2/16*D			A_{1TE}	2.49
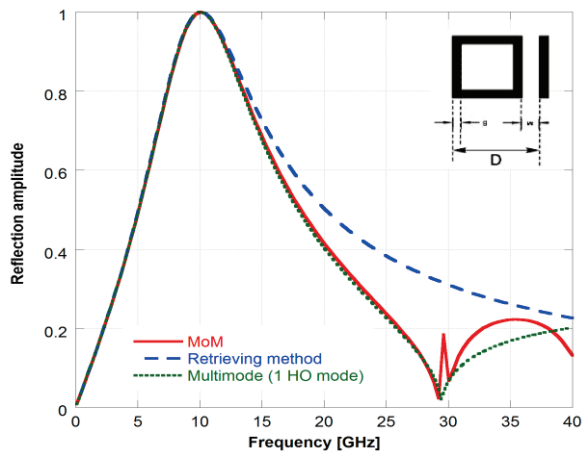
Fig. 10. Reflection coefficient of a freestanding loop shaped FSS obtained by using MoM code, the retrieving method and the multi-mode approach including only 1 high-order mode. Geometrical parameters: D=10 mm, w=2/16*D, g=1/16*D.

Table 4: Geometrical parameters and values of the electrical parameters in the lumped circuits of the simulated loop element

Physical Parameters		Retrieving Method		Multi-mode Circuit (1 HO mode)	
D	10 mm	C_s	72.34 fF	C_s	72.39 fF
g	1/16*D	L_s	3.45 nH	L_s	0.61 nH
w	2/16*D			A_{1TE}	2.67

Multi-resonant elements

There is often the necessity of employing more complex FSS elements in the design of narrow band, multi-band filters or even in multi-resonant High-Impedance Surfaces (HIS) [77], [78]. Some FSS elements can generate a double resonant, or more in general, a multi-resonant behavior in the zero-order Floquet propagating zone. These structures can be analyzed by introducing additional lumped elements in the resonant circuit. A common FSS shape is the so called Jerusalem Cross. This element is basically a cross with loading ends which enhance the capacitance value. An additional series LC circuit in parallel with the original one in the equivalent circuit is needed, since the electric field couples also with the two end-loading dipoles. A layout of the geometry of the double resonant unit cell and its corresponding equivalent circuit is shown in Fig. 11.

(a)   (b)
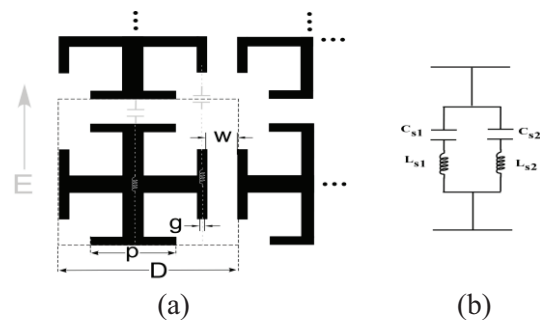
Fig. 11. Jerusalem cross element: (a) with its equivalent circuit and cross-frame element and (b) with its equivalent circuit.

The impedance of the circuit reads:

$$Z_{LC//LC} = \frac{\left(1-\omega^2 L_{s1} C_{s1}\right)\left(1-\omega^2 L_{s2} C_{s2}\right)}{j\omega\left[C_{s1} + C_{s2} - \omega^2 C_{s1} C_{s2}\left(L_{s1} + L_{s2}\right)\right]}. \quad (19)$$

The values of the unknown capacitance and inductances can be computed by solving by running an iterative matching procedure. The

procedure starts from the computation of the three resonance frequencies ω_{z1}, ω_{z2} and ω_{p2}, by detecting the nulls of the derivative function of the actual FSS impedance. The following relations between the lumped components of the LC//LC circuit hold:

$$C_{s1} = \frac{1}{L_{s1}\omega_{z_1}^2} ; \; C_{s2} = \frac{1}{L_{s2}\omega_{z_1}^2} ;$$

$$L_{s2} = \frac{\left(\frac{\omega_{p_2}^2}{\omega_{z_2}^2}\right)L_{s1}C_{s1} - \left(\frac{1}{\omega_{z_2}^2}\right)}{C_{s1}\left(1 - \frac{\omega_{p_2}^2}{\omega_{z_2}^2}\right)}. \quad (20)$$

The value of the inductance L_{s1} is obtained by an iterative procedure that minimizes the Euclidean distance between the impedance computed by the MoM approach and the one obtained by the equivalent circuit model. The first pole ω_{p1} falls at $\omega=0$ since the FSS is capacitive. Figure 12 shows the comparison between the reflection coefficients obtained by a MoM analysis and by the circuital approach for the two analyzed FSS configuration. The lumped components are summarized in Table 5, where the values of the geometrical parameters are also specified. The value of the capacitance C_{s1} is higher than that of the simple cross, since the end loading improves the capacitive coupling between the neighboring crosses. The additional capacitor, due to the capacitive effect introduced by the two end loading strips aligned with the electric field is lower than the main effect, due to the central cross as expected.
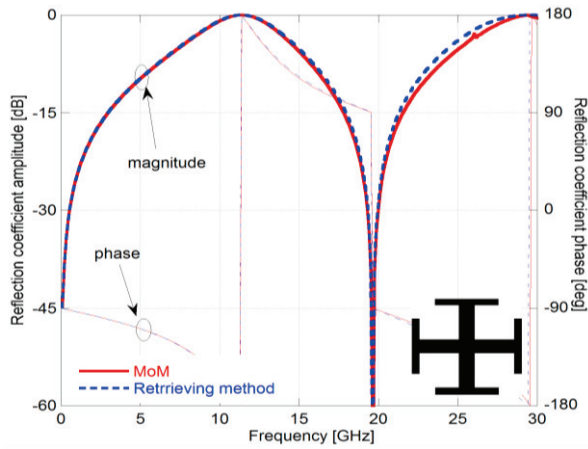
Fig. 12. Reflection coefficient of a freestanding Jerusalem cross array obtained by a periodic MoM approach and by the retrieving method.

Table 5: Lumped parameters of the simulated Jcross (the geometrical parameters are: D=10 mm, w=D/8, g=D/16, p=3/8D)

Jerusalem Cross Array			
C_{s1}	37.93 fF	C_{s2}	10.70 fF
L_{s1}	5.15 nH	L_{s2}	2.71 nH

The surface current on the Jerusalem cross and the electric field distribution on the same plane are reported at the two resonances with unitary reflection (i.e.: 11 GHz and 29 GHz) in Fig. 13. As it is evident from the color plot, the central cross is mostly excited in correspondence of the former resonance, while the end loading dipole represented by the second LC series circuit determines the position of the latter resonance (its length is equal to an half wavelength in correspondence of the second unitary reflection resonance). FSS elements characterized by a higher number of resonances within the fundamental Floquet harmonic zone can still be modeled by extending the aforementioned equivalent circuits to n^{th} order resonant circuits [78].
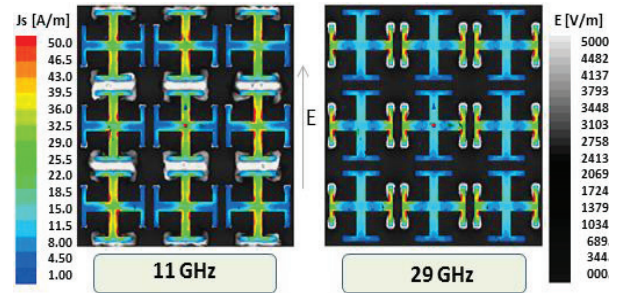
Fig. 13. Surface current and electric field distribution on the plane of the Jerusalem cross array at the two reflection resonances.

A multi-resonant element useful for understanding the limitations of the equivalent circuit approach is the spiral cross array. The matching of the reflection coefficient of the investigated spiral structure can be obtained by using the same equivalent circuit of Jcross as reported in Fig. 14. However, in this case the equivalent circuit does not catch the physical behavior of the structure. Indeed, differently from the previous multi-resonant element, where the resonances were due to the element geometry, this

element resonates because of the high-order modes of the current distribution. As it is evident from Fig. 15, the fundamental resonance occurs when the length of the spiral approaches at half wavelength, while the second resonance occurs when the length of the arms is equal to $3/2\lambda$. Other more complex and more compact element configurations are also possible [79], [80] and their behavior can still be matched by using a pole-zero matching procedure [75].
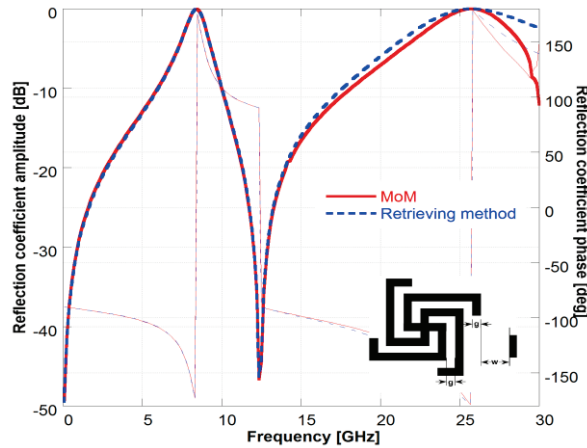

Fig. 14. Reflection coefficient of a freestanding spiral cross array obtained by MoM approach and by the retrieving method. The geometrical parameters are: D=10 mm, w=3/16D, g=D/16.
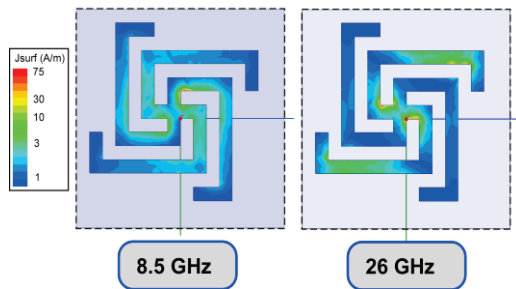
Fig. 15. Surface current on the plane of the spiral cross array at the two reflection resonances.

VI. DISCUSSION ON LUMPED ELEMENTS VALUES

Simple electrostatic relationships can be exploited to qualitatively understand the reason why certain shapes determine specific values of capacitance and inductance. As it is well known, the static capacitance of an ideal parallel plate capacitor is directly proportional to the plate area

A and inversely proportional to the plate separation d ($C = \varepsilon_0\varepsilon_r A/d$). The capacitance value of the cross element is the lowest one, since the parallel plate capacitor formed by the two adjacent crosses has a small area. For the same reason, the patch capacitance is comparable than the loop one.

In Fig. 16, the capacitance values for different unit cell elements are reported as a function of the element over periodicity. It is clear the capacitive coupling increases exponentially by reducing the gap between adjacent elements. The inductance values can be explained by resorting to the expression of the inductance of two parallel wires with length l, radius a and distance d ($L = l/\pi \ln(d/a)$). As the distance between the parallel wires decreases, the inductance decreases as well. In the case of the patch element, we can infer that the inductance value is very low because the plate is very large and in the previous formula corresponds, unwrapping the wire, to enhance the value of the wire radius. Cross and loop elements are characterized by higher inductances because of the narrow strips composing the single element. By observing the calculated optimal values of the inductances in Tables 3 and 4, it is evident the inductance values drop as the first TE high order mode is included in the multi-mode model. This is due to the fact that the impedance of the first TE harmonic is inductive. As a consequence, the inductive component of the element is now shared between the inductor and the first TE harmonic.
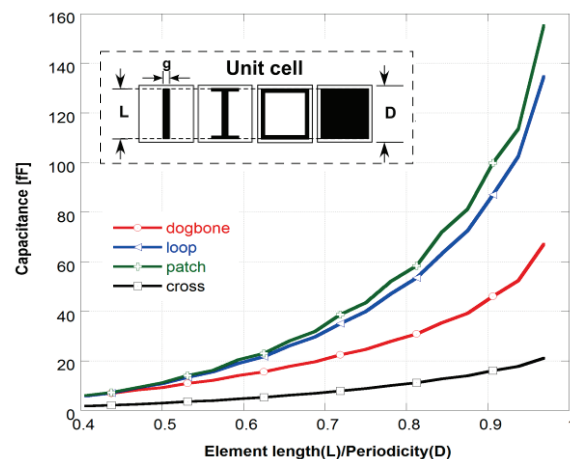
Fig. 16. Capacitance values of 4 different elements as a function of the element size with respect to the lattice periodicity. The element width (g) is fixed to D/16.

VII. CONCLUSION

A comprehensive overview of FSS circuit modeling has been presented. Different models based on fully analytical or semi-analytical formulations are described with the aim to clarify their range of validity and their accuracy. Fully analytical models based on averaged expressions are accurate for dense periodic arrays (quasi-static region), while a simple semi-analytical approach can be employed also in the resonant region of FSSs. The latter approach can be applied to generic FSS elements and it can be generalized with simple relations. Finally, an efficient multi-mode approach which allows to match the complex response of the FSS screens within non-linear grating lobes region has also been discussed.

REFERENCES

[1] D. Rittenhouse, "An optical problem, proposed by mr. hopkinson, and solved by mr. Rittenhouse," *Trans. Amer. Phil. SOC.*, vol. 2, pp. 201-206, 1786.

[2] E. G. Loewen and E. Popov, "Diffraction gratings and applications," *CRC Press*, 1997.

[3] R. W. Wood, "On a remarkable case of uneven distribution of light in a diffraction grating spectrum," *Philos. Mag.*, vol. 4, pp. 396-402, 1902.

[4] L. Rayleigh, "Note on the remarkable case of diffraction spectra described by prof. wood," *Philos. Mag.*, vol. 14, pp. 60-65, 1907.

[5] L. Rayleigh, "On the dynamical theory of gratings," *Proceedings of the Royal Society of London. Series A, Containing Papers of a Mathematical and Physical Character*, 79 (532), pp. 399-416, 1907.

[6] U. Fano, "The theory of anomalous diffraction gratings and of quasi-stationary waves on metallic surfaces (sommerfeld's waves)," *J. Opt. Soc. Am.*, vol. 31, pp. 213-222, March 1941.

[7] A. Hessel and A. A. Oliner, "A new theory of wood's anomalies on optical gratings," *Applied Optics*, 4.10, 1275-1297, 1965.

[8] G. Marconi and C. S. Franklin, "Reflector for use in wireless telegraphy and telephony," *US Patent 1,301,473*, April 1919.

[9] G. von Trentini, "Partially reflecting sheet arrays," *IRE Trans. Antennas Propagation*, vol. AP-4, pp. 666-671, 1956.

[10] N. Marcuvitz (ed.), "Waveguide handbook," IEE Electromagnetic Waves Series 21, *McGraw-Hill*, New York, 1951.

[11] W. Rotman and A. A. Oliner, "Periodic structures in trough waveguide," *IRE Trans. on Microwave Theory and Tech.*, vol. 7, no. 1, pp. 134,142, January 1959.

[12] L. Goldstone and A. A. Oliner, "Leaky-wave antennas I: rectangular waveguides," *IRE Trans. on Antennas and Propag.*, vol. 7, no. 4, pp. 307,319, October 1959.

[13] D. R. Jackson and N. G. Alexópoulos, "Gain enhancement methods for printed circuit antennas," *IEEE Trans. Antennas Propag.*, vol. 33, pp. 976-987, September 1985.

[14] D. R. Jackson and A. A. Oliner, "A leaky-wave analysis of the high gain printed antenna configuration," *IEEE Trans. Antennas Propag.*, vol. 36, no. 7, pp. 905-910, 1988.

[15] T. Zhao, D. R. Jackson, J. T. Williams, H. D. Yang, and A. A. Oliner, "2-D periodic leaky-wave antennas-part I: metal patch design," *IEEE Trans. Antennas Propag.*, vol. 53, no. 11, pp. 3505-3514, 2005.

[16] G. Lovat, P. Burghignoli, and D. R. Jackson, "Fundamental properties and optimization of broadside radiation from uniform leaky-wave antennas," *IEEE Trans. Antennas Propag.*, vol. 54, pp. 1442-1452, 2006.

[17] V. Agrawal and W. Imbriale, "Design of a dichroic cassegrain subreflector," *IEEE Trans. on Antennas and Propag.*, vol. 27, no. 4, pp. 466-473, July 1979.

[18] T. K. Wu, "Four-band frequency selective surface with double-square-loop patch elements," *IEEE Trans. on Antennas and Propag.*, vol. 42, no. 12, 1994.

[19] B. A. Munk, "Frequency selective surfaces-theory and design," *John Wiley & Sons*, New York, 2000.

[20] T. K. Wu, "Frequency selective surface and grid array," New York, *John Wiley & Sons, Inc.*, 1995.

[21] F. Costa and A. Monorchio, "A frequency selective radome with wideband absorbing properties," *IEEE Trans. on Antennas and Propag.*, vol. 60, no. 6, pp. 2740-2747, 2012.

[22] D. R. Jackson, P. Burghignoli, G. Lovat, F. Capolino, J. Chen, D. R. Wilton, and A. A. Oliner, "The fundamental physics of directive beaming at microwave and optical frequencies and the role of leaky waves," *Proc. of the IEEE*, vol. 99, no. 10, pp. 1780-1805, 2011.

[23] F. Costa, O. Luukkonen, C. R. Simovski, A. Monorchio, S. A. Tretyakov, and P. De Maagt, "TE surface wave resonances on high-impedance surface based antennas: analysis and modeling," *IEEE Trans. on Antennas and Propag.*, vol. 59, no. 10, pp. 3588-3596, October 2011.

[24] S. Genovesi, F. Costa, A. Monorchio, "Wideband Radar Cross Section Reduction of Slot Antennas Arrays" *IEEE Trans. on Antennas and Propag.*, vol. 62, no. 1, pp. 163-173, January 2014.

[25] N. Gagnon, A. Petosa, and D. A. McNamara, "Research and development on phase-shifting

surfaces (PSSs)," *IEEE Antennas and Propagation Magazine*, vol. 55, no. 2, pp. 29-48, April 2013.

[26] J. Huang, "Reflectarray antenna," *John Wiley & Sons, Inc.*, 2007.

[27] R. Lech, M. Mazur, and J. Mazur, "Analysis and design of a polarizer rotator system," *IEEE Trans. on Antennas and Propag.*, vol. 56, no. 3, pp. 844-847, March 2008.

[28] F. Costa, C. Amabile, A. Monorchio, and E. Prati, "Waveguide dielectric permittivity measurement technique based on resonant FSS filters," *IEEE Microwave and Wireless Comp. Letters*, vol. 21, no. 5, pp. 273-275, May 2011.

[29] M. Philippakis, et al., "Application of FSS structures to selectively control the propagation of signals into and out of buildings," *Ofcom Ref. AY4464A*, 2004.

[30] F. Costa, A. Monorchio, and G. Manara, "Analysis and design of ultra thin electromagnetic absorbers comprising resistively loaded high impedance surfaces," *IEEE Trans. on Antennas and Propag.*, vol. 58, no. 5, pp. 1551-1558, 2010.

[31] J. B. Pendry and D. R. Smith, "The quest for the superlens," *Sci. Amer.*, vol. 295, no. 1, pp. 60-67, July 2006.

[32] T. Maier and H. Bruckl, "Wavelength-tunable microbolometers with metamaterial absorbers," *Optics Letters*, vol. 34 (19), p. 3012, 2009.

[33] S. A. Kuznetsov, A. G. Paulish, A. V. Gelfand, P. A. Lazorskiy, and V. N. Fedorinin, "Bolometric THz-to-IR converter for terahertz imaging," *Appl. Phys. Lett.*, vol. 99, 023501, 2011.

[34] H. T. Chen, W. J. Padilla, M. J. Cich, A. K. Azad, R. D. Averitt, and A. J. Taylor, "A metamaterial solid state terahertz phase modulator," *Nature Photonics*, vol. 3, 148-151, 2009.

[35] E. Rephaeli and S. Fan, "Absorber and emitter for solar thermophotovoltaic systems to achieve efficiency exceeding the shockley-queisser limit," *Opt. Express*, 17, 15, 145-159, 2009.

[36] Liu, T. Tyler, T. Starr, A. F. Starr, N. M. Jokerst, and W. J. Padilla, "Taming the blackbody with infrared metamaterials as selective thermal emitters," *Phys. Rev. Lett.*, 107(4), p. 045901, 2011.

[37] C. C. Chen, "Transmission through a conductive screen perforated periodically with apertures," *IEEE Trans. Microwave Theory & Tech.*, vol. 18, no. 9, pp. 627-632, 1970.

[38] R. Mittra, C. H. Chan, and T. Cwik, "Techniques for analyzing frequency selective surfaces, a review," *Proc. of the IEEE*, vol. 76, no. 12, pp. 1593-1615, 1988.

[39] R. Orta, R. Tascone, and R. Zich, "A unified formulation for the analysis of general frequency selective surfaces," *Electromagnetics*, vol. 5, no. 4, pp. 307-329, 1985.

[40] M. Bozzi and L. Perregrini, "Efficient analysis of thin conductive screens perforated periodically with arbitrarily shaped apertures," *Electronics Letters*, vol. 35, no. 13, pp. 1085-1087, June 1999.

[41] G. G. MacFarlane, "Surface impedance of an infinite wire grid, at oblique angles of incidence," *J. IEE*, vol. 93 (III E), pp. 1523-1527, December 1946.

[42] W. Wessel, "On the passage of electromagnetic waves through a wire grid," *Hochfrequenztechnik*, vol. 54, pp. 62-69, January 1939.

[43] R. Hornejäger, "Electromagnetic properties of wire grids," *Ann. der Phys*ik, vol. 4, pp. 25-35, January 1948.

[44] G. von Trentini, "Gratings as circuit elements of electric waves in space," *Zeit. angew. Phys.*, vol. 5, pp. 221-231, June 1953.

[45] J. R. Wait, "The impedance of wire grid parallel to a dielectric interface," *IRE Trans. Microwave Theory Tech.*, vol. MTT-5, no. 2, pp. 99-102, April 1957.

[46] J. Young and J. R. Wait, "Note on the impedance of a wire grid parallel to a homogeneous interface," *IEEE Trans. Microwave Theory Tech.*, vol. 37, no. 7, pp. 1136-1138, July 1989.

[47] R. Ulrich, K. F. Renk, and L. Genzel, "Tunable submillimeter interferometers of the fabry-perot type," *IEEE Trans. Microwave Theory Tech.*, vol. 11, no. 5, pp. 363-371, 1963.

[48] S. W. Lee, G. Zarrillo, and C. L. Law, "Simple formulas for transmission through periodic metal grids or plates," *IEEE Trans. Antennas Propag.*, vol. AP-30, no. 5, pp. 904-909, 1982.

[49] M. I. Kontorovich, V. Y. Petrunkin, N. A. Yesepkina, and M. I. Astrakhan, "The coefficient of reflection of a plane electromagnetic wave from a plane wire mesh," *Radio Eng. Electron Phys.*, no. 7, pp. 222-231, 1962.

[50] M. I. Astrakhan, "Averaged boundary conditions on the surface of a lattice with rectangular cells," *Radio Eng. Electron Phys.*, no. 9, pp. 1239-1241, 1964.

[51] O. Luukkonen, C. Simovski, G. Granet, G. Goussetis, D. Lioubtchenko, A. V. Räisänen, and S. A. Tretyakov, "Simple and accurate analytical model of planar grids and high-impedance surfaces comprising metal strips or patches," *IEEE Trans. on Antennas and Propag.*, vol. 56, no. 6, pp. 1624-1632, 2008.

[52] V. V. Yatsenko, S. A. Tretyakov, S. I. Maslovski, and A. A. Sochava, "Higher order impedance boundary conditions for sparse wire grids," *IEEE Trans. Antennas Propag.*, vol. 48, no. 5, pp. 720-

727, 2000.

[53] R. J. Langley and A. J. Drinkwater, "An improved empirical model for the Jerusalem cross," *IEE Proc. H, Microw. Optics and Antennas*, vol. 129, no. 1, pp. 1-6, 1982.

[54] R. J. Langley and E. A. Parker, "Equivalent circuit model for arrays of square loops," *Electronics Letters*, vol. 18, no. 7, pp. 294-296, April 1982.

[55] R. J. Langley and E. A. Parker, "Double square frequency selective surfaces and their equivalent circuit," *Electronics Letters*, vol. 19, no. 17, pp. 675-677, August 1983.

[56] C. K. Lee and R. J. Langley, "Equivalent-circuit models for frequency selective surfaces at oblique angles of incidence," *IEE Proc. H, Microwaves, Antennas and Propagation*, vol. 132, no. 6, pp. 395-399, October 1985.

[57] S. B. Savia and E. A. Parker, "Equivalent circuit model for superdense linear dipole FSS," *IEE Proc. H, Microwaves, Antennas and Propagation*, vol. 150, no. 1, pp. 37-42, February 2003.

[58] F. Costa, A. Monorchio, and G. Manara, "Efficient analysis of frequency selective surfaces by a simple equivalent circuit model," *IEEE Antennas and Propagation Magazine*, vol. 54, no. 4, pp. 35-48, 2012.

[59] P. Callaghan, E. A. Parker, and R. J. Langley, "Influence of supporting dielectric layers on the transmission properties of frequency selective surfaces," *IEE Proc. H, Microwaves, Antennas and Propagation*, vol. 138, no. 5, pp. 448-454, 1991.

[60] R. Dubrovka, J. Vazquez, C. Parini, and D. Moore, "Equivalent circuit method for analysis and synthesis of frequency selective surfaces," *IEE Proc. Microwaves, Antennas and Propag.*, vol. 153, no. 3, pp. 213-220, June 2006.

[61] S. Monni, G. Gerini, A. Neto, and A. G. Tijhuis, "Multi-mode equivalent networks for the design and analysis of frequency selective surfaces," *IEEE Trans. Antennas Propag.*, vol. 55, pp. 2824-2835, 2007.

[62] R. Rodriguez-Berral, F. Medina, F. Mesa, and M. Garcia-Vigueras, "Quasi-analytical modeling of transmission/reflection in strip/slit gratings loaded with dielectric slabs," *IEEE Trans. on Microwave Theory and Tech.*, vol. 60, no. 3, pp. 405-418, March 2012.

[63] M. Garcia-Vigueras, F. Mesa, F. Medina, R. Rodriguez-Berral, and J. L. Gomez-Tornero, "Simplified circuit model for arrays of metallic dipoles sandwiched between dielectric slabs under arbitrary incidence," *IEEE Trans. Antennas Propag.*, vol. 60, no. 10, pp. 4637,4649, October 2012.

[64] C. L. Holloway, E. F. Kuester, J. A. Gordon, J. O'Hara, J. Booth, and D. R. Smith, "An overview of the theory and applications of metasurfaces: the two-dimensional equivalents of metamaterials," *IEEE Antennas and Propagation Magazine*, vol. 54, no. 2, pp. 10,35, April 2012.

[65] S. Tretyakov, "Analytical modelling in applied electromagnetics," *Artech House*, Boston, 2003.

[66] A. B. Yakovlev, O. Luukkonen, C. R. Simovski, S. A. Tretyakov, S. Paulotto, P. Baccarelli, and G. W. Hanson, "Analytical modeling of surface waves on high impedance surfaces," *Metamaterials and Plasmonics: Fundamentals, Modelling, Applications NATO Science for Peace and Security Series B*, pp. 239-254, 2009.

[67] I. Andersson, "On the theory of self-resonant grids," *The Bell System Technical Journal*, vol. 55, pp. 1725-1731, 1975.

[68] J. E. Raynolds, B. A. Munk, J. B. Pryor, and R. J. Marhefka, "Ohmic loss in frequency-selective surfaces," *Journal of Applied Physics*, vol. 93, no. 9, pp. 5346-5358, May 2003.

[69] F. Costa, S. Genovesi, A. Monorchio, and G. Manara, "A circuit-based model for the interpretation of perfect metamaterial absorbers," *IEEE Trans. Antennas Propag.*, vol. 61, no. 3, pp. 1201-1209, March 2013.

[70] F. Costa and A. Monorchio, "Closed-form analysis of reflection losses of microstrip reflectarray antennas," *IEEE Trans. Antennas Propag.*, vol. 60, no. 10, pp. 4650-4660, October 2012.

[71] Y. E. Erdemli, K. Sertel, R. A. Gilbert, D. E. Wright, and J. L. Volakis, "Frequency selective surface to enhance performance of broad-band reconfigurable arrays," *IEEE Trans. Antennas Propag.*, vol. 40, no. 12, pp. 1716-1724, 2002.

[72] C. Mias, C. Tsokonas, and C. Oswald, "An investigation into the feasibility of designing frequency selective windows employing periodic structures," *Technical Report AY3922, The Nottingham Trent University*, Burton Street, Nottingham, NG1 4BU, U.K., 2002.

[73] M. Ohira, H. Deguchi, M. Tsuji, and H. Shigesawa, "Analysis of frequency-selective surfaces with arbitrarily shaped element by equivalent circuit model," *Electronics and Communications in Japan (Part II: Electronics)*, vol. 88, no. 6, pp. 9-17, June 2005.

[74] C. C. Chen, "Scattering by a two-dimensional periodic array of conducting plates," *IEEE Trans. Antennas Propag.*, AP-18, 660-665, 1970.

[75] S. Maci, M. Caiazzo, A. Cucini, and M. Casaletti, "A pole-zero mathcing method for EBG surfaces composed of a dipole FSS printed on a grounded dielectirc slab," *IEEE Trans. Antennas Propag.*, vol. 53, no. 1, pp. 70-81, January 2005.

[76] D. M. Pozar, "Microwave engineering," 2nd ed., *Toronto: John Wiley &Sons*, 1998.

[77] D. J. Kern, D. H. Werner, A. Monorchio, L. Lanuzza, and M. J. Wilhelm, "The design synthesis of multi-band artificial magnetic conductors using high impedance frequency selective surfaces," *IEEE Trans. Antennas Propag.*, vol. 53, no. 1, pp. 8-17, 2005.

[78] F. Costa, S. Genovesi, and A. Monorchio, "A chipless RFID based on multi-resonant high-impedance surfaces," *IEEE Trans. on Microwave Theory and Tech.*, vol. 61, no. 1, pp. 146-153, 2013.

[79] S. Genovesi, F. Costa, B. Cioni, V. Miceli, G. Annino, G. Gallone, G. Levita, A. Lazzeri, A. Monorchio, and G. Manara, "Miniaturized high impedance surfaces with angular stability by using zirconium tin titanate (ZST) substrates and convoluted FSS elements," *Microwave and Optical Technology Letters*, vol. 51, no. 11, pp. 2753-2758, August 2009.

[80] A. Vallecchi and A. G. Schuchinsky, "Entwined planar spirals for artificial surfaces," *IEEE Antennas and Wireless Propagation Letters*, vol. 9, pp. 994-997, 2010.

Filippo Costa was born in Pisa, Italy, on October 31, 1980. He received his M.Sc. degree in Telecommunication Engineering and his Ph.D. degree in Applied Electromagnetism from the University of Pisa, Pisa, Italy, in 2006 and 2010, respectively. From March to August 2009, he was a Visiting Researcher in the Department of Radio Science and Engineering, Helsinki University of Technology, TKK (now Aalto University), Finland. Since January 2010, he's been a Postdoctoral Researcher at the University of Pisa.

His research is focused on the analysis and modelling of Frequency Selective Surfaces and Artificial Impedance Surfaces with emphasis to their application in electromagnetic absorbing materials, leaky antennas, radomes, Radio Frequency Identification, waveguide filters and techniques for retrieving dielectric permittivity of materials. He was recipient of the Young Scientist Award of the URSI International Symposium on Electromagnetic Theory and URSI General Assembly in 2013 and 2014, respectively.

Agostino Monorchio received the Laurea degree in Electronics Engineering and his Ph.D. degree in Methods and Technologies for Environmental Monitoring from the University of Pisa, Pisa, Italy, in 1991 and 1994, respectively. He is currently an Associate Professor at the School of Engineering, University of Pisa, and Adjunct Professor at the Italian Naval Academy of Livorno. He is also an Adjunct Professor in the Department of Electrical Engineering, Penn State. He is on the Teaching Board of the Ph.D. course in "Remote Sensing" and on the council of the Ph.D. School of Engineering "Leonardo da Vinci" at the University of Pisa.

His research interests include the development of novel numerical and asymptotic methods in applied electromagnetics, both in frequency and time domains, with applications to the design of antennas, microwave systems and RCS calculation, the analysis and design of frequency-selective surfaces and novel materials, and the definition of electromagnetic scattering models from complex objects and random surfaces for remote sensing applications. He has been a reviewer for many scientific journals and he has been supervising various research projects related to Applied Electromagnetic, commissioned and supported by national companies and public institutions. Monorchio is IEEE Fellow. He has served as Associate Editor of the IEEE Antennas and Wireless Propagation Letters. He received a Summa Foundation Fellowship and a NATO Senior Fellowship.

Giuliano Manara received the Laurea (Doctor) degree in Electronics Engineering (summa cum laude) from the University of Florence, Italy, in 1979. Currently, he is a Professor at the School of Engineering of the University of Pisa, Italy. Since 1980, he has been collaborating with the Department of Electrical Engineering of the Ohio State University, Columbus, Ohio, where, in the summer and fall of 1987, he was involved in research at the ElectroScience Laboratory.

His research interests have centered mainly on the asymptotic solution of radiation and scattering problems to improve and extend the uniform geometrical theory of diffraction. In this framework, he has analyzed electromagnetic wave scattering from material bodies, with emphasis on the scattering from both isotropic and anisotropic impedance wedges. He has also been engaged in research on numerical, analytical and hybrid techniques (both in frequency and time domain), scattering from rough surfaces,

Frequency Selective Surfaces (FSS), and electromagnetic compatibility. More recently, his research has also been focused on the design of microwave antennas with application to broadband wireless networks, and on the development and testing of new microwave materials (metamaterials). Manara was elected an IEEE Fellow in 2004 for "contributions to the uniform geometrical theory of diffraction and its applications." In August 2011, he was elected Chair of the International Commission B of URSI.

Manipulation of Electromagnetic Waves Based on New Unique Metamaterials: Theory & Applications

Q. Wu, K. Zhang, and G. H. Yang

Department of Microwave Engineering
Harbin Institute of Technology, Harbin, 150001, China
qwu@hit.edu.cn, zhangkuang@hit.edu.cn, gh.yang@hit.edu.cn

Abstract ─ Metamaterials are typically engineered by arranging a set of unit cells in a regular array throughout a region of space, thus, obtaining some desirable macroscopic electromagnetic behavior. The desired property is often one that is not normally found naturally (negative refractive index, near-zero index, etc.). Over the past few years, the flexibilities of the metamaterials in choosing the numerical value of the effective permittivity or permeability have led to kinds of novel theoretical and practical possibilities for different applications, ranging from microwave to optical regime. In this paper, the theoretical mechanism for constructing metamaterials is described, and the unique feature of electromagnetic waves can be manipulated is verified by their applicability to construct various devices or components Some typical application is given, including: (1) novel RF devices realized by optical transformation principle, such as energy concentrators and universal waveguide connectors; (2) metamaterial-based wave absorbers; (3) gain enhancement approach of aperture antennas by planar metamaterial lenses loaded; (4) ultra-thin lenses with dual-polarization filtering features; and (5) beam tunable antennas by metamaterial device. Undoubtely, the reported results suggest promising applications in the next-generation communication system.

Index Terms ─ Absorbers, antennas, lenses, metamaterials.

I. INTRODUCTION

Recently, metamaterials have been attracting growing attentions. Responding to the incident electric and/or magnetic fields, metamaterials could exhibit specific effective permittivity ε and/or permeability μ, including the Double Negative (DNG for short, the real part of both ε and μ is negative, which was first proposed by Veselago theoretically in 1968 [1]), Single Negative (ENG [2] or MNG [3] for short, the real part of ε or μ is negative), and the Zero-Index Metamaterials [4] (ZIM, the real part of ε and/or μ is near zero). Due to the exotic electromagnetic characteristics, metamaterials have shown great potentials in kinds of applications, such as invisibility cloak [5], perfect lens [6], and many other kinds of novel applications in microwave [7-9], terahertz [10] and optical regime [11], etc.

Manipulation of electromagnetic waves as desired has been a hot topic in the field of electromagnetism for a long time. The emerge of metamaterials provides great opportunity for the control of the transmissions and distributions of electromagnetic waves and energy. In this paper, the applications of metamaterials in the manipulation of electromagnetic waves are discussed. In Section II, the theory of transform optics is introduced. Then based on the form invariance's properties, electromagnetic energy concentrator and waveguide connector are proposed and simulated. After simplification processing of constitution parameters, the proof-of-principle experiment is completed to verify the theoretical work. In Section III, metamaterials are applied to build a novel broadband absorber. In Section IV, zero index metamaterials with matched impedance are constructed and applied to enhance the gain of horn antenna. Measurements of gain and far-field pattern verify the theoretical design. In Section V, ultra-thin lens is proposed based on the phase discontinuities. Due to the

different response to the helicity of the incidence, dual-polarization ultra-thin lens is proposed and simulated. Simulations show good agreement with theoretical results. In Section VI, a novel method of building electronically beam steerable antenna system using Active Frequency Selective Surfaces (AFSS) is proposed. The design methods and special principals of the active frequency selective surfaces built for flexible antenna beam scanning are studied. The antenna system is fabricated and experimentally investigated. The front-to-back ratio is more than 30 dB with the null point of -59 dB. The gain can be promoted to be 7.0 dBi. Furthermore, multi-beam functionality is achieved and the amplitudes of the beams can be controlled. It is believed, that all these studies suggest potential applications in the communication system or subsystems.

II. THEORY OF TRANSFORM OPTICS AND APPLICATIONS

The transform optics was first proposed based on the remarkable fact that Maxwell's equations are form-invariant under any coordinate transformation. Maxwell's equations still preserve their form inside the transformed space, but the material transforms into an anisotropic material to convey the effect of the coordinate transformation to the electromagnetic fields. This feature provides an intuitive way of designing material tuning the electromagnetic fields in a desired manner, which has led to numerous useful and beautiful applications. The transform optics has also started a new era for design and application of metamaterials in the manipulation of electromagnetic waves.

A. Transform optics description

Suppose a general transformation f transform the original space α to the transformed space α', which also map each point P in the original space into P' in the transformed space. In order to preserve the form invariance of Maxwell's equations, the general transformation yields an inhomogeneous and anisotropic material. The constitutive parameters can be then derived as:

$$\overline{\overline{\varepsilon}}' = \frac{JJ^T}{\det(J)} \overline{\overline{\varepsilon}} , \qquad (1a)$$

$$\overline{\overline{\mu}}' = \frac{JJ^T}{\det(J)} \overline{\overline{\mu}} , \qquad (1b)$$

where J is the jacobian transform matrix defined as:

$$J = \begin{bmatrix} \dfrac{\partial x'}{\partial x} & \dfrac{\partial x'}{\partial y} & \dfrac{\partial x'}{\partial z} \\[2mm] \dfrac{\partial y'}{\partial x} & \dfrac{\partial y'}{\partial y} & \dfrac{\partial y'}{\partial z} \\[2mm] \dfrac{\partial z'}{\partial x} & \dfrac{\partial z'}{\partial y} & \dfrac{\partial z'}{\partial z} \end{bmatrix} , \qquad (2)$$

in the Cartesian coordinates. Then according to equation (1)-(2), the constitutive parameters of the transformed material can be calculated according to certain function of transformation. Here, below we will use the transform optics to achieve the polygonal cloak, electromagnetic energy concentrator and the waveguide connector.

B. Realization of the transform optics

First, the cylindrical EM concentrator is taken into consideration. The optical transformation for the concentrator can be expressed that the region $r' \in [0, R_2]$ is compressed into the region $r \in [0, R_1]$, and the region $r' \in [R_2, R_3]$ is stressed into the region $r \in [R_1, R_3]$, as shown in Fig. 1. Here, r and r' represents the radius of the physical space and the virtual space, respectively. For the transformation between $r' \in [0, R_2]$ and $r \in [0, R_1]$, namely the core region, the transformation function can be easily expressed as the linear function. For the circular region, the numerical value of ε_r and ε_θ is reciprocal, if one of them is set as a constant, the other can be also fixed as constant. Based on this relationship we can establish the ordinary differential equation, and the solution is the constitutive tensor for the circular region, which can be expressed as:

$$\varepsilon_\theta = \frac{1}{\varepsilon_r} = m_0 , \qquad (3a)$$

$$\varepsilon_z = m_0 \left(\frac{r}{R_3} \right)^{2(m_0 - 1)} , \qquad (3b)$$

where $m_0 = \log_{\frac{R_3}{R_1}} \frac{R_3}{R_2}$. Hence, we have obtained all the constitutive parameters of the cylindrical EM concentrator. It could be seen that the relative permittivity ε_r and ε_θ are obtained as constants, and only ε_z is the function of radius, which could also be homogenized through layered structure.

Furthermore, it can be observed in equation (3) that the constitutive tensor is nonsingular and positive, which improves the flexibilities for 2D EM concentrator design. Moreover, the impedance of the concentrator at the outer boundary can be expressed as $Z|_{r=R_3} = \sqrt{\mu_\theta / \varepsilon_z} = 1$. The EM concentrator is always impedance matched with the free space, which indicates minimized scattering fields of the concentrator.

Fig. 2. (a) Electric field distributions of the cylindrical EM concentrator, and (b) normalized power flow distribution of the concentrator.


Fig. 1 Sketch of the cylindrical EM concentrator.

Then lossless cases are studied based on the simulation results of the commercial software based on Finite-Element Method (FEM). Here, the geometry parameters are selected that $R_3=2R_2=4R_1=0.4$ m, and the frequency is selected at 2 GHz. Based on all the geometry parameters, the constitutive parameters of the circular region can be calculated through equation (3). Figure 2 (a) shows the electric fields distributions of the concentrator. It can be seen that the electric fields are concentrated into the inner core region smoothly, and the fields outside are rarely disturbed. Furthermore, the power flow of the EM fields are also calculated and shown in Fig. 2 (b). It can be seen that power flow is enhanced obviously in the inner core region. Through the transformation function of equation, it can be observed that the enhancing ratio can be expressed as the ratio of R_2 and R_1, and enhancement theoretically diverges to infinity as R_1 goes to zero [11]. It should be noted that in our design, all components but one in the constitutive tensor are constants. Compared with the former results [5], our design provides greatly facility for the practical constructions.

Second, we focus our concentration on the waveguide connector shown in Fig. 3 (a). Here, finite embedded optical transformation is applied to the design of waveguide connector. Considering a Two-Dimensional (2D) structure in the Cartesian coordinate system, the optical transformation that transfers the original space ABCD into the transformed space ABC'D', can be simply defined as the linear function. Then, the constitutive parameters can be derived according to equation (1) and (2). For the facility of the construction of the connector, here, we just consider the Transverse Magnetic (TM) polarization, for which only ε_{xx}, $\varepsilon_{xy}(\varepsilon_{yx})$, ε_{yy} and μ_{zz} components of the constitutive tensor are relevant. Furthermore, the nonmagnetic material parameters can be transformed into the diagonal matrix through rotating its optical axis by a certain angle with the z-axis, as shown in Fig. 3 (b). Moreover, the anisotropic metamaterial with diagonal constitutive tensor can be expressed by the two alternating mediums based on the effective medium theory.
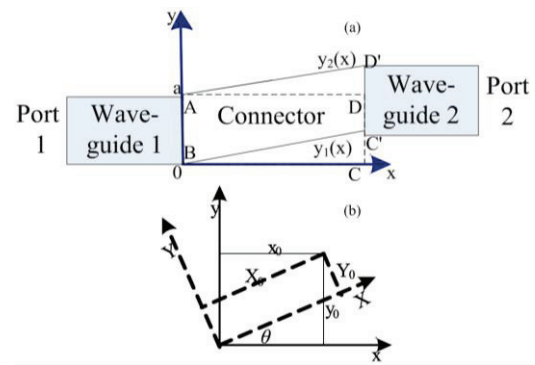
Fig. 3. (a) Sketch of the waveguide connector, and (b) sketch of the rotated coordinate.

In order to support the theoretical results, a proof-of-concept experiment is conducted in the microwave frequency. The system above is designed and fabricated, including the following parts: two square waveguides (40mm*40mm*100mm, as shown in Fig. 4 (a)), two coaxial-to-waveguide adapters (inner radius of the cylindrical cavity is 3.25 mm and 17 mm respectively, and the length of each cavity is 12.5 mm, as shown in Fig. 4 (b)) and the connector (40mm*40mm*50mm, as shown in Fig. 4 (c)) with the slope of 16.7°. For the alternating dielectric materials filled in the connector, the microwave composite-dielectric substrate and air are selected, whose relative permittivity is 5.5 and 1, respectively. To satisfy the effective medium theory, the thickness of the microwave composite substrate and the air spacing is set as 1.5 mm and 3 mm (about 0.03λ and 0.06λ with respect to the central working frequency, as shown in Fig. 4 (d), respectively.
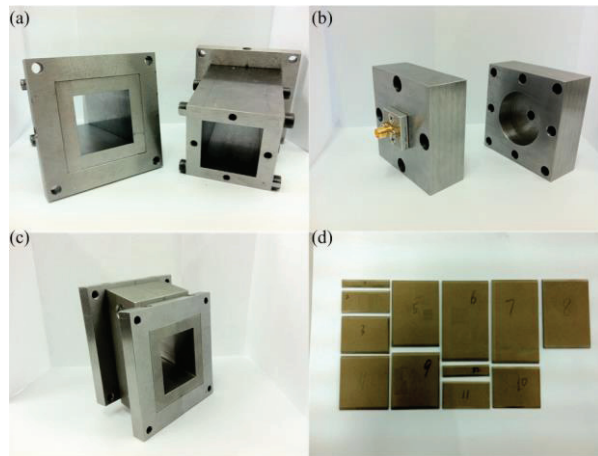

Fig. 4. The photos of the fabricated proof-of-concept experimental system, including: (a) the square waveguides, (b) the coaxial-to-waveguide adapters, (c) the connector, and (d) the dielectric slabs.

Then, the transmission parameters (S_{21}) of three cases are tested around 6 GHz through the vector network analyzer (Agilent E8363B): (I) the single square waveguide; (II) the connector filled with only air; and (III) the connector filled with alternating dielectric slabs. Here, all the other experimental data are normalized by the experimental result of the S_{21} of the single square waveguide (case (I)), and the experimental results are shown in Fig. 5. It could be seen that when filled with the material with designed constitutive parameters and geometrical parameters, the connector can achieve the relative high transmission parameters around the central working frequency, compared to the connector filled just with air. So the design principles and the constitutive parameters proposed are verified [7].
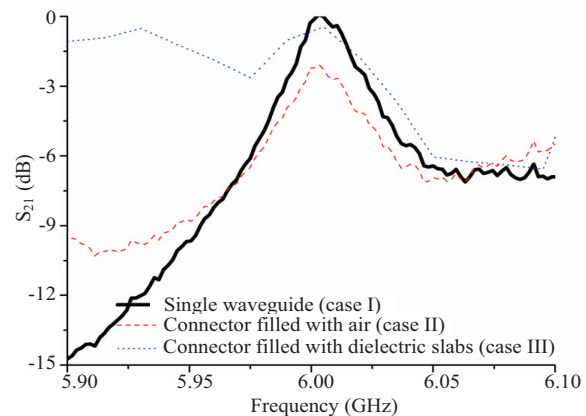
Fig. 5. The experimental results of the transmission parameters (S_{21}).

III. BROADBAND POLARIZATION-INSENSITIVE ABSORBER BASED ON METAMATERIALS

A. Gradient structure absorber

A gradient structure absorber is presented in this section. The unit cell geometry of the proposed Metamaterial Absorber (MA) is illustrated in Fig. 6. The top layer consists of gradient Split Resonant Rings (SRRs), Square Metallic Patches (SMPs) and resistors mounted crosswire. The lossy dielectric board and the bottom layer is same as the single SRR absorber. Side length of dielectric substrate unit cell is A=29.6 mm, while thickness is D=1.6 mm. Length of crosswire is c=7 mm. The split width of SRRs and separation distance between adjacent crosswire is g=0.4 mm. Width of all copper wire is w=0.6 mm. Resistance value is R=50 Ω. The side length of gradient SRRs and SMPs are a_{ij} and b_{ij} respectively, which is given in Table 1.

(a) The plan view   (b) The stereogram
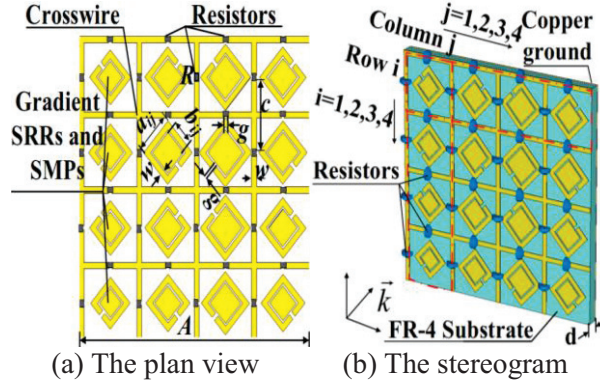
Fig. 6. The structure of the unit cell of the proposed MA.

Table 1: The sizes of gradient of SRRs and SMPs

a_{ij}, b_{ij}/mm	j=1	j=2	j=3	j=4
i=1	3.8, 2.2	4.2, 2.6	4.6, 3.0	4.2, 2.6
i=2	4.0, 2.4	4.4, 2.8	4.8, 3.2	4.4, 2.8
i=3	3.8, 2.2	4.2, 2.6	4.6, 3.0	4.2, 2.6
i□□	3.6, 2.0	4.0, 2.4□	4.4, 2.8	4.0, 2.4

Every four SRRs and SMPs are put obliquely around the central crosswire. There are 16 pairs of SRRs and SMPs in each unit cell, which are designed with gradient length parameters to make the 16 pairs resonator resonant at adjacent frequencies to increase the operating frequency band. In addition, the resistors mounted crosswire is leaded in this structure which is able to draw into a new resonant frequency to further increase the bandwidth. Moreover, resistors could transfer EM energy to heat and fulfill resistive loss through which the quality factor of the MA is decreased and the bandwidth is increased. Through simulation and optimization, resistance R=50 Ω is selected. It is worth mentioning that the structures of the unit cell are all almost symmetry so that the MA will have similar absorption effect on both TE and TM wave; namely, the MA should be polarization-insensitive.

The unit cell is simulated in CST MWS 2012 with PBC. In order to illustrate the absorbing mechanism of the proposed MA, two cases at 16.48 GHz and 24.64 GHz are selected as examples. The magnetic field distribution and

surface currents at the two frequencies for TE wave are illustrated in Fig. 7. It can be summarized from Fig. 7, that the strong absorption of broadband EM wave is based on the two following points: firstly, it can be observed that a strong magnetic field is generated around the SRR and SMP which form the "magnetic loop trap" structure. The EM energy is stored around this structure, which effectively blocks the EM wave to spread outwards. Thus, current is excited on the top of the unit cell. In this way, EM wave could be consumed in the FR-4 dielectric substrates and the chip resistors. Secondly, comparing with the surface current distribution at two different frequencies, it can be seen clearly that different SRRs of the unit cell resonate at corresponding frequencies. Since the presence of the gradient structure, the unit cell contains resonators at adjacent frequencies which make the absorber function in a broadband frequency.

(a) 16.48 GHz   (b) 24.64 GHz
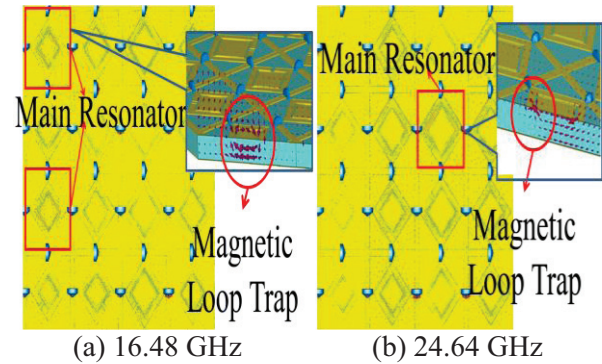
Fig. 7. The simulated surface current and magnetic field distribution.

It can be observed from Fig. 8, that S_{11} is quite small in a wide band and S_{21}=0 as expect. From Fig. 9, it can be obtained that for both TE and TM waves, the absorption rate of the absorber are both larger than 60% from 12.38 GHz to 22.28 GHz, whose relative bandwidth is 57.13%. The maximum absorption rate of the MA is 98.37% in this frequency band. In addition, it is worth noting that the substrate used in this paper is ordinary FR-4 with a loss tangent of only 0.025. MA in use of higher-loss-tangent materials is expected to obtain a better absorption property.
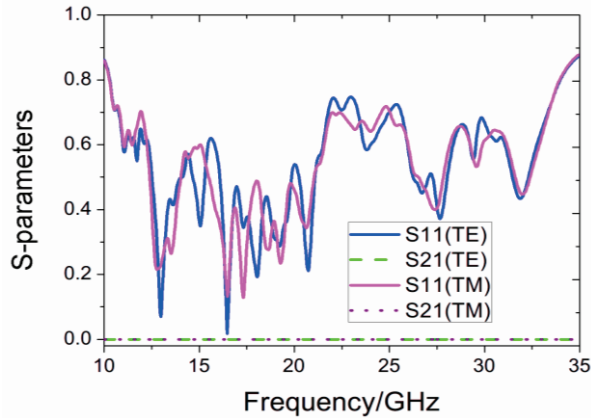
Fig. 8. The simulated S-parameters for TE wave and TM wave.
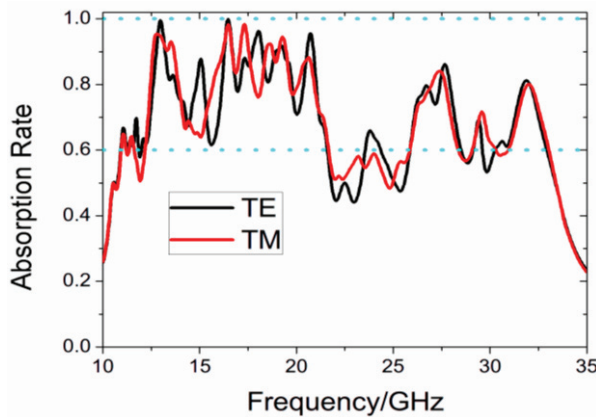
Fig. 9. The calculated absorption rate for both TE and TM wave.

IV. METAMATERIAL LENS-ELECTRIC AND MAGNETIC RESONANCE STRUCTURE

Zero Index Metamaterial (ZIM) has been investigated comprehensively for directive emission since 2002 [4]. Varieties of designs of ZIM have been presented to enhance antenna directivity and gain. However, the impedance match between ZIM and free space is always hard to achieve. The antenna and ZIM should be designed together and ZIM is not universal for different kinds of antennas. In this section, a Metamaterial Lens (ML) is presented for antenna directivity and gain enhancement.

A. The construction of the ZIM unit cell

The structure and the corresponding parameters are illustrated in Fig. 10. The magnetic resonant structure is Modified Split Ring Resonator (MSRR), which is composed of two square rings with two slot at the opposite sides. MSRR is introduced for its larger bandwidth. The metal patch in Fig. 10 is the electric resonant structure of the ZIM unit cell. The unit cell is simulated in CST MWS. Its S-parameters are depicted in Fig. 11 and a large passband centered at 9.9 GHz with high S_{21} is observed.

The constitutive parameter extracted from the S-parameters are calculated and depicted in Fig. 12, which is based on the algorithm of [12]. It can be seen that μ_{eff} and ε_{eff} in turn approach zero at 9.4 GHz and 9.7 GHz, respectively, which will make the corresponding effective refractive index n to be near zero in a band as broad as possible [13]. Particularly, at 9.0 GH and 9.9 GHz, one finds that the effective permittivity and permeability has the same value of 0.8 and 0.3, respectively, which leads the ZIM to have both near-zero refractive index for directive emission and perfectly wave impedance matching with free space.
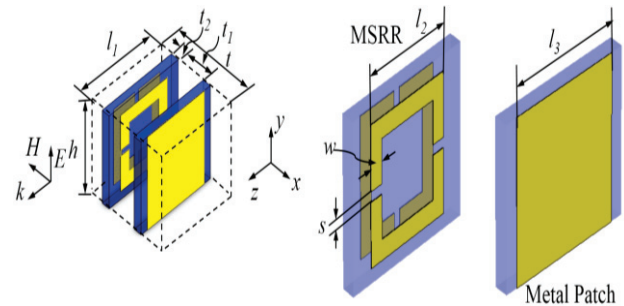

Fig. 10. The structure and parameters of the unit cell, in which l_1=8 mm, l_2=5.4 mm, l_3=h=6.6 mm, t=8.2 mm, t_1=2.9 mm, t_2=0.8 mm, w=0.8 mm and s=0.4 mm.
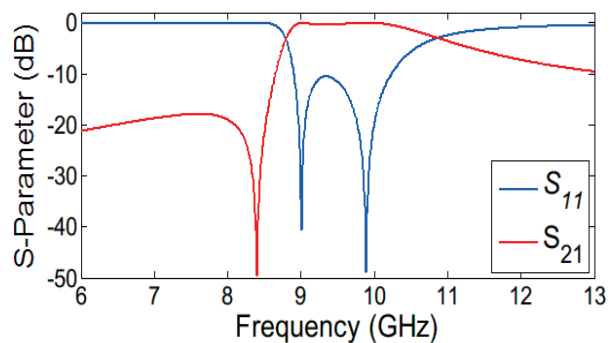
Fig. 11. The S-Parameters of the unit cell.
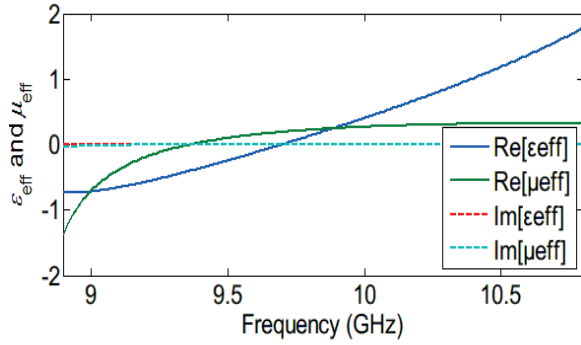
Fig. 12. The effective constitutive parameters of the unit cell.

B. Fabricated and tested planar metamaterial lens

The Metamaterial Lens (ML) is formed by arranging the unit cell in one plane. It is fabricated and measured with an H-plane horn antenna with center frequency of 9.9 GHz, as shown in Fig. 13.
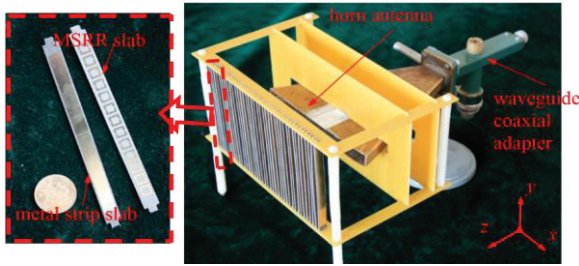
Fig. 13. The phototype of ML and the H-plane horn antenna.

For the H-plane horn antenna, the size of the ML is 19×13 unit cells. The measured return loss of the horn antenna is depicted in Fig. 14. The return loss of the H-plane horn antenna is also slightly affected by the ML. The measured E-plane radiation patterns of the H-plane horn antenna with and without ML are illustrated and contrasted in Fig. 15. The main lobe of the E-plane radiation pattern of the antenna at 9.9 GHz is obviously sharpened. The main lobe width is reduced from 91.4° to 14.8°. The directivity of the H-plane horn antenna is greatly enhanced. The antenna gain of the H-plane horn antenna is also enhanced by 4.43 dB, which is a significant improvement. The gain enhancement of the ML with different distance between the lens and antenna is also depicted in Fig. 16. The ML proposed in this section is capable of enhancing antenna gain in a wideband from 9.5 GHz to 10.6 GHz. Additionally, the gain

enhancement barely varies with the distance thanks to good impedance match between lens and free space, which is an advantage over lens based on Fabry-Perot resonance [14].
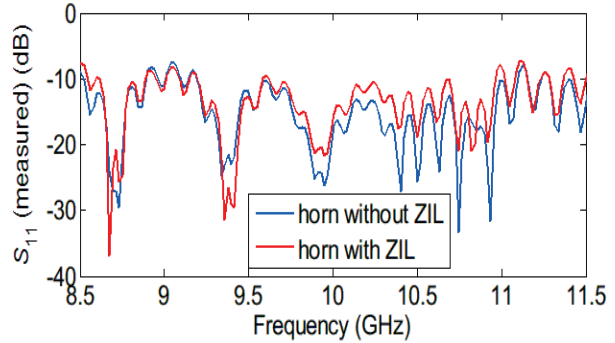
Fig. 14. The measured return loss of the H-plane horn antenna with and without the ML, here ZIL in the legend is short for zero-index lens.
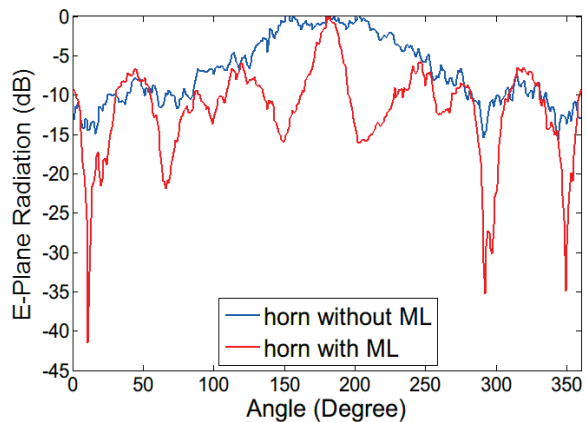
Fig. 15. The E-plane radiation pattern of the H-plane horn antenna with and without the ML.
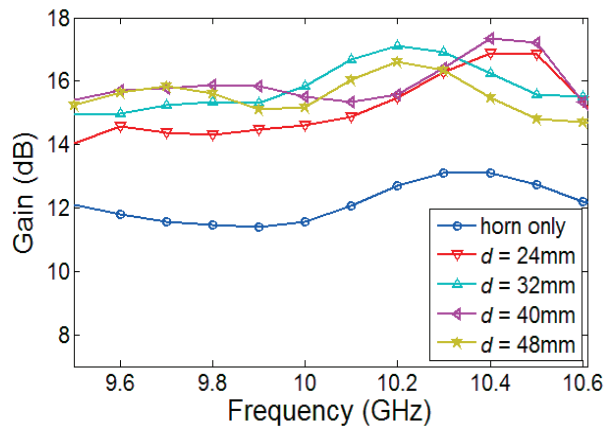
Fig. 16. The gain enhancement of the H-plane horn antenna loading ML with different distance.

V. ULTRA-THIN PLANAR METALENS WITH PHASE DISCONTINUITY

The metalens with phase discontinuity provides the abrupt phase change at the interface. By introducing abrupt phase changes with sub-wavelength unit cells, phase accumulation in the traditional lens can be substituted by the phase discontinuities on the interface, which provides possibilities of constructing the ultra-thin metalens. However, the conversion efficiency, defined as the ratio of the energy of transmitted cross-polarized wave to that of the total incident wave, is relatively low for the published designs operating under cross-polarized fields [15,16], and the maximum efficiency achieved was only a few percent. It was predicted theoretically, that the maximum attainable cross-coupling is 25%, based on the S-parameters of the four ports network [17].

A. Unit cell structure

The proposed metalens and the unit cell are schematically shown in Fig. 17 (a) and (b), respectively. The unit cell has a miniaturized structure, which is beneficial for more compact design. For the normal incident plane wave linearly polarized along x- or y-axis, the transmission coefficients are shown in Fig. 17 (c), while Fig. 17 (d) illustrates the transmission coefficients for the transmitted Left-Circularly Polarized (LCP) and Right-Circularly Polarized (RCP) components under LCP incident wave. Simulation results also show that the transmission coefficients are independent of θ, which depicts the orientation angle of the optical axes of the individual unit cell in clockwise direction with respect to y-axis, as shown in Fig. 17 (b).

To achieve the desired phase changes in microwave band, the P-B phase is adopted here. A Phase Factor (PF) is achieved when the polarization changes from the initial state to the final state. The two poles on the Poincaré sphere indicate the RCP and LCP states. The PF is equal to half of the area, which is encompassed by the loop on the sphere, and the absolute value can be calculated as $2|\theta_1 - \theta_0|$. Using Jones calculus, the transmitted field of the P-B elements can be given by Eq. (4) as:

$$\left| \vec{E}_{out} \right\rangle = \sqrt{\eta_E} \left| \vec{E}_{in} \right\rangle + \left(\sqrt{\eta_R} e^{\pm i2\theta} \left| \vec{R} \right\rangle + \sqrt{\eta_L} e^{\mp i2\theta} \left| \vec{L} \right\rangle \right), \quad (4)$$

where $\eta_E = \left| \frac{1}{2}(t_x + t_y e^{i\phi}) \right|^2$, $\eta_R = \left| \frac{1}{2}(t_x - t_y e^{i\phi}) \left\langle \vec{E}_{in} | \vec{L} \right\rangle \right|^2$,

$\eta_L = \left| \frac{1}{2}(t_x - t_y e^{i\phi}) \left\langle \vec{E}_{in} | \vec{R} \right\rangle \right|^2$ and η_E, η_R, η_L are the polarization order coupling efficiencies, <|> denotes inner product, $\left| \vec{R} \right\rangle$ ($\left| \vec{L} \right\rangle$) represents the RCP (LCP) component, t_x and t_y are the amplitudes of the transmission coefficients for two linear polarizations which are perpendicular and parallel to the optical axes, and φ is the phase difference between the transmission coefficients.

When RCP (or LCP) is the incident wave, η_R (or η_L) equals to zero, and Eq. (4) illustrates that the transmitted field from a P-B element comprises two polarization orders. One maintains the phase and original polarization state of the incident wave, while the other one exhibits opposite helicity and a phase modification of ±2θ, where ±1 corresponds to both the rotating direction of the unit cells and the helicity of the incidence. Therefore, by arranging the unit cell with different orientations an ultra-thin metalens with the phase discontinuity can be achieved, and EM waves can be manipulated with great latitude subsequently.
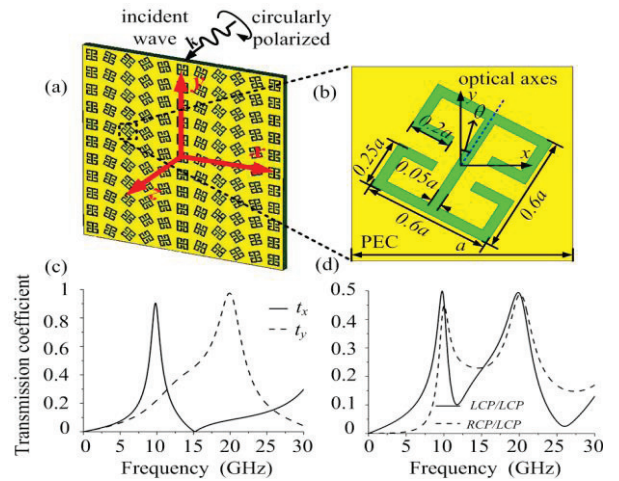

Fig. 17. Illustration of the transmission of EM waves through the unit cell: (a) sketch of the metalens, (b) geometric parameters of the unit cell, (c) transmission coefficients under linear-polarized incident wave when θ=0, and (d) transmission coefficients under LCP incident wave when θ=0.

In this research, we find that at the first resonant frequency of 9.8 GHz, the incident wave with linear polarization along x-axis can pass through the lens completely, while transmission is suppressed for y-polarized incidence, as shown in Fig. 17 (c). As a result, when the incident wave is circularly polarized, half of the incident energy can transmit. Figure 17 (d) shows that the cross-polarized and co-polarized fields both exist in the transmitted field under LCP incident wave. The transmission coefficients for the transmitted LCP and RCP components are the same with value 0.5 at the first resonance, which means that our design has reached the theoretical limit on the maximum coupling efficiency of 25% for cross-polarized component.

B. Bi-functional ultra-thin metalens design

As demonstrated above, the unit cell of metalens responds differently to the LCP and RCP incident wave. Thus, we can utilize this phenomenon to construct bi-functional metalens. For a given focal length f, Eq. (5) gives the relationship between the rotation angle θ and the position of the unit cells:

$$\theta = \pm 0.5 \frac{2\pi}{\lambda}(\sqrt{f^2 + x^2} - |f|), \qquad (5)$$

where x=na (n=0, ±1, ±52, …), and ±1 represents the clockwise or anti-clockwise rotation respectively. In this letter, a metalens with focal length f of 300 mm is proposed. The working frequency is around 10 GHz, thus, it can be considered to be operating in the far-field region (f ≈10λ). Figures 18 and 19 show the results of the electric field distribution. It can be seen that for the normal RCP incident wave, the design operates as an ultra-thin converging lens (Fig. 18 (a)). When the polarization of the incident plane wave changes into LCP, the metalens exhibits a diverging effect (Fig. 19 (a)). According to Eq. (4), the transmitted cross-polarized component is affected by the lens, and the transmitted co-polarized component keeps original state. Although, not as perfect as the pure cross-polarized transmission, the total fields still perform the same converging or diverging effects after superimposed with the transmitting co-polarized wave. This makes our metalenses competitive for practical applications. In general, our design can be tailored to be working as

converging or diverging lens only depending on the helicity of the incident plane wave.
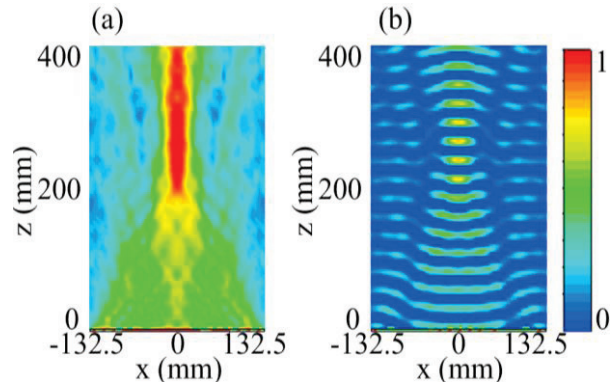
Fig. 18. (a) Simulation result of the distribution of the transmitted electric fields amplitude of pure cross-pol component for the converging lens, and (b) simulation result of the distribution of the transmitted E_y component.
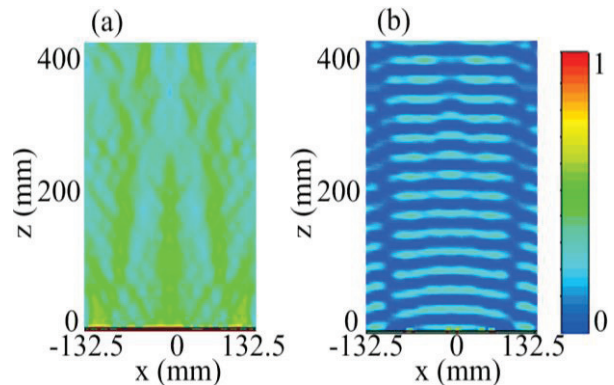
Fig. 19. (a) Simulation result of the distribution of the transmitted electric fields amplitude of pure cross-pol component for the diverging lens, and (b) simulation result of the distribution of the transmitted E_y component.

VI. ELECTRONICALLY RADIATION PATTERN STEERABLE ANTENNAS USING ACTIVE FREQUENCEY SELECTIVE SURFACES

With the expansion of wireless communication industry, the demand for electronically steerable antenna solutions is increasing such as point-to-multi-point links for base stations.

In this work, a new method to build 360° steerable antenna is proposed. The control

methods and design requirements for both single- and multi-beam modes are presented and discussed. The working mechanism is to modify the path of EM wave emitted from the inner antenna using AFSS mounted with varactor diodes. Another advantage of using varactor diodes is the low power consumption. Unlike the PIN diodes, when varactor diodes are reversely biased, the leakage current is low. In this work, the total power consumption is less than 1.02 mW.

A. Configuration and beam scanning

As shown in Fig. 20, ten columns of AFSS unit cells are employed to construct a cylinder array with a radius of 50 mm. Figure 21 shows three methods to configure the antenna in each sector for single-beam mode. Multi-beam ability is also studied in this work. With the help of continuously tuning capability, the amplitudes of the beams can be also controlled. Figure 22 illustrates two cases for introduction, there are many other combinations.
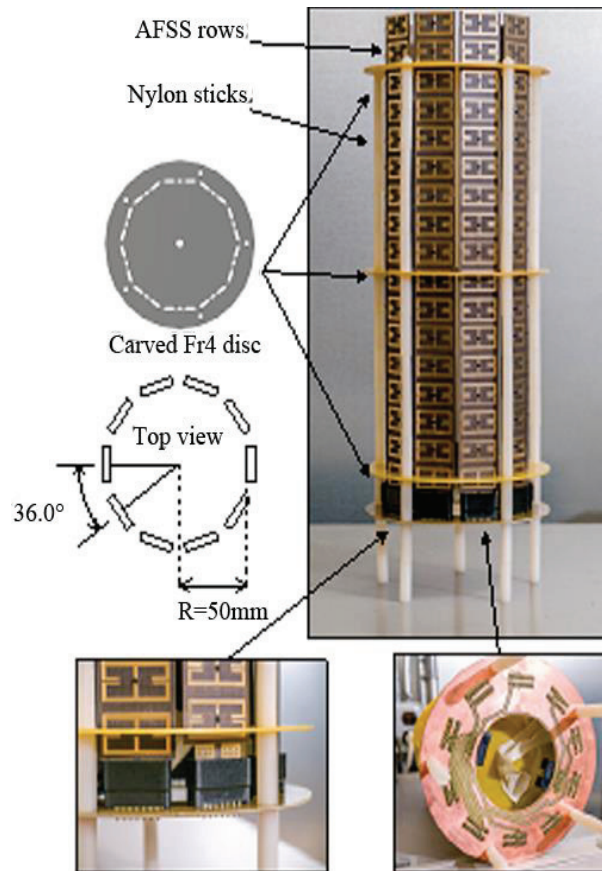
Fig. 20. Antenna structure and installation.
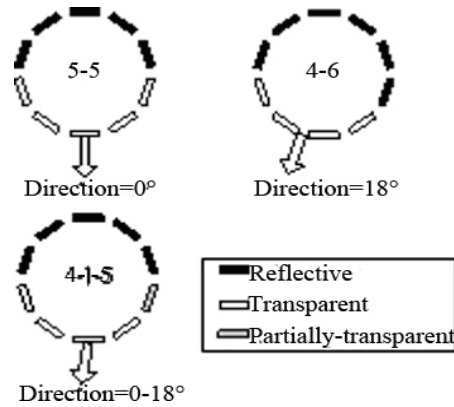
Fig. 21. Single-beam control methods.
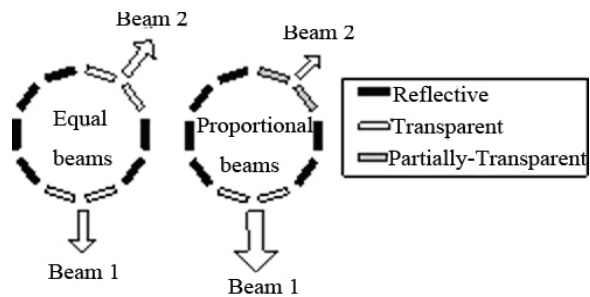
Fig. 22. Multi-beam control methods.

B. AFSS array

The structure of AFSS unit is shown in Fig. 23. The top side of the unit cell consists of a pair of vertical-symmetric anchor-shaped metal strips and a varactor mounted in the middle. The bottom side includes the DC biasing network, as shown in the bottom view in Fig. 23.
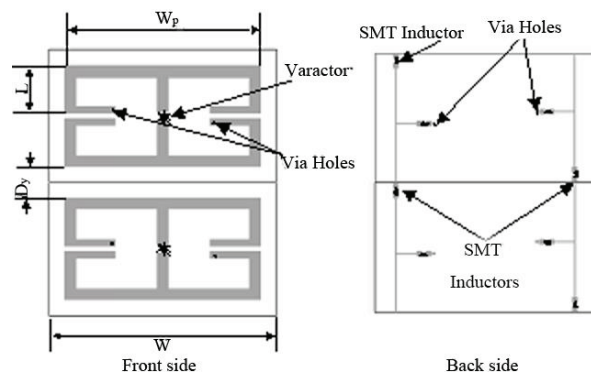
Fig. 23. Layout of the unit cell.

C. Fabrication and measurement

To validate the proposed theory, an antenna prototype was fabricated and assembled. A multi-

channel programmable 0-30 V voltage controller based on Atmega128 processor and high voltage DACs is also designed and fabricated.

The radiation patterns for both vertically and horizontally polarization are measured and shown in Fig. 24. For 5-5 mode, the main lobe direction is 178°, 3 dB width is 77°. The gain of the COCO antenna is 3.6 dBi. The designed AFSS antenna is 7.0 dBi for 5-5 mode, 6.9 dBi for 4-6 mode and 6.6 dBi for 4-5-1 mode.

The configuration is shown in Fig. 25, and the measured results are shown in Fig. 26. The gains are directly shown in the figure for the reader to evaluate the energy distribution. Obviously, if there are more columns of the AFSS, it should be more flexible to control radiation, as well as with higher resolution.
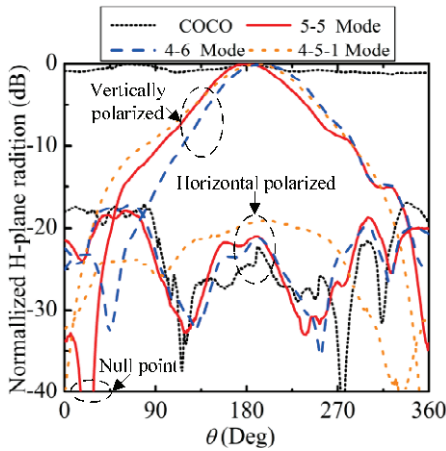
Fig. 26. Tested radiation patterns of the dual-beam modes in H-plane.

VII. CONCLUSION

The theory, design, simulation, measurement and application of metamaterials in the manipulations of electromagnetic waves have been discussed. First, the theory of transform optics is introduced briefly. Then electromagnetic concentrator and waveguide connector are proposed based on the transform optics. Both simulation and measurements results verify the theoretical results. Second, broadband polarization-insensitive absorber based on gradient structure metamaterial is designed and simulated. The metamaterial absorber has an excellent broadband property for its gradient structure. Simulation results verify that the designed sample has a good absorption effect on both TE wave and TM wave in a wide band. Third, a zero-index metamaterial is proposed for antenna gain enhancement. Both simulated and measured results show that the proposed metamaterial is able to achieve antenna gain enhancement in a broad frequency range from 8.9 GHz to 10.8 GHz and the greatest gain enhancement reaches up to 4.02 dB. Fourth, dual-polarity ultra-thin lens are proposed. The efficiency of cross-pol conversion approaches to the theoretical limit. The property of converging and diverging EM wave only depends on the helicity of the incident wave. Finally, a new AFSS structure mounted with varactor diodes has been proposed and designed. Then a radiation-pattern steerable antenna has been fabricated and tested based on the AFSS. By controlling the bias voltage, the radiation pattern sweeps in the whole

Fig. 24. Radiation patterns of single-beam modes and COCO antenna in H-plane.

Fig. 25. Configuration methods of dual-beam modes.

azimuth plane for both the single-beam modes and the dual-beam modes. In addition, the amplitudes of the two beams for dual-beam modes are also controllable. With sub-wavelength control of phase and amplitude of electromagnetic waves, we believe metamaterials will be a promising technology for the communication system of the next generation.

ACKNOWLEDGMENT

REFERENCES

[1] V. G. Veselago, "The electrodynamics of substances with simultaneously negative values of ε and μ," *Sov. Phys. Uspekhi*, 10, pp. 509-514, 1968.

[2] J. B. Pendry, A. J. Holden, W. J. Stewart, and I. Youngs, "Extremely low frequency plasmons in metallic mesostructures," *Phys. Rev. Lett.*, 76, pp. 4773-4776, 1996.

[3] J. B. Pendry, A. J. Holden, D. J. Robbins, and W. J. Stewart, "Magnetism from conductors and enhanced nonlinear phenomena," *IEEE Trans. Microwave Theory Tech.*, 47, pp. 2075-2084, 1999.

[4] S. Enoch, G. Tayeb, P. Sabouroux, N. Guérin, and P. Vincent, "A metamaterial for directive emission," *Phys. Rev. Lett.*, 89, pp. 213902-4, 2002.

[5] D. Schurig, J. J. Mock, B. J. Justice, S. A. Cummer, and J. B. Pendry, "Metamaterial electromagnetic cloak at microwave frequencies," *Science*, 314, 977-980, 2006.

[6] J. B. Pendry, "Negative refraction makes a perfect lens," *Phys. Rev. Lett.*, 85, pp. 3966-3969, 2000.

[7] K. Zhang, F. Meng, Q. Wu, J. H. Fu, and L. W Li, "Waveguide connector constructed by normal layered dielectric materials based on embedded optical transformation," *EPL*, 99, pp. 47008-5, 2012.

[8] H. F. Ma and T. J. Cui, "Three-dimensional broadband and broad-angle transformation-optics lens," *Nat. Commun.*, 1, pp. 124, 2010.

[9] T. Driscoll, G. Lipworth, J. Hunt, N. Landy, N. Kundtz, D. N. Basov, and D. R. Smith, "Performance of a three dimensional transformation-optical-flattened Lüneburg lens," *Opt. Express*, 20, pp. 13262-13273, 2012.

[10] L. Cong, W. Cao, Z. Tian1, J. Gu, J. Han, and W. Zhang, "Manipulating polarization states of terahertz radiation using metamaterials," *New J. Phys.*, 14, pp. 115013, 2012.

[11] K. Zhang, Q. Wu, J. Fu, and L. W. Li. "Cylindrical electromagnetic concentrator with only axial constitutive parameter spatially variant," *J. Opt. Soc. Am. B*, 28, pp. 1573-1577, 2011.

[12] R. W. Ziolkowski, "Extraction of effective metamaterial parameters by parameter fitting of dispersive models," *IEEE Trans. Antennas Propag.*, 51, pp. 1516-1529, 2003.

[13] E. Ekmekci and G. Turhan-Sayan, "Comparative investigation of resonance characteristics and electrical size of the double-sided SRR, BC-SRR and conventional SRR type metamaterials for varying substrate parameters," *PIER B*, 12, pp. 35-62, 2009.

[14] F. Y. Meng, Y. L. Li, K. Zhang, Q. Wu, and J. L. W. Li, "A detached zero index metamaterial lens for antenna gain enhancement," *PIER*, 132, pp. 463-478, 2012

[15] N. Yu, P. Genevet, M. A. Kats, F. Aieta, J. P. Tetienne, F. Capasso, and Z. Gaburro, "Light propagation with phase discontinuities: generalized laws of reflection and refraction," *Science*, 334, pp. 333-337, 2011.

[16] X. J. Ni, N. K. Emani, A. V. Kildishev, A. Boltasseva, and V. M. Shalaev, "Broadband light bending with plasmonic nanoantennas," *Science*, 335, pp. 427, 2012.

[17] F. Monticone, N. M. Estakhri, and A. Alù, "Full control of nanoscale optical transmission with a composite metascreen," *Phys. Rev. Lett.*, 110, pp. 203903-5, 2013.

Qun Wu received his B.Sc. in Radio Engineering, his M. Eng. in Electromagnetic Fields and Microwaves, and his Ph.D. in Communication and Information Systems, all at Harbin Institute of Technology (HIT), Harbin, China in 1977, 1988, and 1999, respectively. He worked as a Visiting Professor at Seoul National University (SNU) in Korea, from 1998 to 1999, and Pohang University of Science and Technology, from 1999 to 2000, and a two-month short period of Visiting Professor at National University of Singapore from 2003 to 2010 and Nanyang Technological University in 2011, respectively. Since 1990, he has been with the School of Electronics and Information Engineering at HIT, China, where he is currently a Professor and a Director of Center for Microwaves and EMC.

Wu has published over 100 international and regional refereed journal papers. He is a Member of Microwave Society of the Chinese Institute of Electronics, and Senior Member of the IEEE. He is a Technical Reviewer for several international journals. His recent research interests are mainly in electromagnetic compatibility, metamaterals, RF microwave active and passive circuits, and millimeter wave MEMS devices. He is also a Vice Chair for IEEE Harbin Section, and Chair of IEEE Harbin EMC/AP/MTT Joint Society Chapter. He worked as a Chair or Member in the TPC of international conferences for many times. He also is invited to give a keynote report or invited papers in some international conferences for many times.

Kuang Zhang received the B.Eng. degree in Communication Engineering, the M.Eng. degree in Electronic Engineering and Ph.D. degree in Information and Communication Engineering, all from Harbin Institute of Technology, Harbin, China, in 2005, 2007 and 2011, respectively. Now he is the Assistant Professor with the School of Electronics and Information Engineering, HIT. His recent research interests are mainly in transform optics and ultra-thin metasurface.
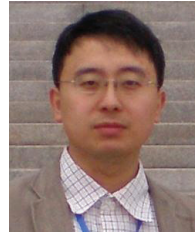
Guohui Yang received the B.Eng. degree in Communication Engineering, the M.Eng. degree in Instrument Science and Engineering and Ph.D. degree in Microelectronics and Solid State Electronics, all from Harbin Institute of Technology, Harbin, China, in 2003, 2006 and 2009, respectively. Now he is the Assistant Professor and the Postdoctoral Fellow with the School of Electronics and Information Engineering, HIT. His recent research interests are mainly in frequency selective surface, tunable antenna; frequency selective surfaces; electromagnetic wave absorber.

Finite-Element Domain Decomposition Methods for Analysis of Large-Scale Electromagnetic Problems

Ming-Feng Xue and Jian-Ming Jin

Department of Electrical and Computer Engineering
University of Illinois at Urbana-Champaign, Urbana, Illinois 61801, USA
xue6@illinois.edu, j-jin1@illinois.edu

Abstract ─ This paper presents an overview of our recent development of domain decomposition methods for finite element analysis of large-scale electromagnetic problems. More specifically, it presents several domain decomposition algorithms based on the Dual-Primal Finite Element Tearing Interconnecting (FETI-DP) method for solving vector wave equations. These algorithms expand the capability and improve the performance of the FETI-DP method by: (1) lifting the requirement of conformal meshes on subdomain interfaces, (2) speeding up the convergence of the iterative solution of the global interface problem, and (3) incorporating appropriate truncation boundaries for more accurate simulation. Numerical results are presented to demonstrate the application, accuracy, efficiency, and capability of these algorithms.

Index Terms ─ Domain Decomposition Method (DDM), Dual-Primal Finite Element Tearing and Interconnecting (FETI-DP), Finite Element Method (FEM), higher-order transmission condition.

I. INTRODUCTION

Full-wave electromagnetic simulation has been widely used for analysis, design, and optimization in modern electrical and electronic engineering. Several Computational Electromagnetics (CEM) techniques, such as the Finite Element Method (FEM), the Method of Moments (MoM), and the Finite-Difference Time-Domain (FDTD) method, have made great progress during the past few decades [1]. Nevertheless, the scope and application of these rigorous numerical tools are still limited by the problem size and complexity, for which computation time and computer memory requirements become excessive. A popular solution is to develop a Domain Decomposition Method (DDM), which is a numerical approach that decomposes a large-scale simulation problem into many small subdomain problems that can be computed simultaneously with parallel processors [2-4]. The combination of the DDM and the FEM is much more efficient than that of the DDM and the MoM because the FEM involves only local interaction. With the use of unstructured meshes and curvilinear elements, the FEM is much better at modeling curved surfaces, fine structures, and composite materials than does the FDTD. As a result, the FEM-based DDMs have attracted the most attention among all the DDMs.

The FEM-based DDMs can be categorized into two groups: one based on the Schwarz method and the other based on the Schur complement method. Among a variety of Schur complement DDMs [2], the Dual-Primal Finite Element Tearing and Interconnecting (FETI-DP) method, developed by Farhat, et al. [5-9], shows excellent numerical scalability and parallel efficiency. When first introduced to CEM, the FETI-DP method assumed an unknown Neumann boundary condition on a subdomain interface with the aid of one Lagrange multiplier [10]. It was a typical nonoverlapping iterative substructuring DDM. Later, an unknown Robin boundary condition was introduced on the subdomain interface with the aid of two Lagrange multipliers to improve the convergence of the global interface iterative solution for high-frequency applications [11,12]. Both FETI-DP versions construct a global corner system that relates the fields at the crosspoints

between the subdomains through a Dirichlet continuity condition. This corner system provides a coarse grid correction to speed up the convergence of the global interface iterative solution by propagating residual errors over the entire computational domain in each iteration.

The FETI-DP algorithms developed in [10,11] require a conformal interface mesh, which means that two neighboring subdomains must have the same surface mesh at their interface. Although this requirement is naturally satisfied in applications where a global mesh is generated first for the entire domain and then decomposed into many subdomain meshes, it is hard to achieve when the entire domain is very large so that one has to first break it into small subdomains and then mesh each subdomain individually. In such a case, two neighboring subdomains usually have different surface meshes at their interface. To handle such nonconformal interface meshes, one has to introduce two sets of unknown variables and develop special DDMs to couple the solution in the adjacent subdomains [13-18].

As another important DDM, the Optimized Schwarz Method (OSM) optimizes transmission conditions on subdomain interfaces to speed up the iterative convergence for solving the global interface problem [19-21]. To derive optimized higher-order transmission conditions for vector electromagnetic fields, one surface curl-curl term related to the interface electric field and another gradient that corresponds to the interface surface charge density were proposed to ensure the convergence of both Transverse-Electric (TE) and Transverse-Magnetic (TM) evanescent modes, respectively [22-28]. Similar ideas can be found in the development of higher-order Absorbing Boundary Conditions (ABCs) in early publications [29-31]. As can be expected, this idea of using a higher-order transmission condition can also benefit the FETI-DP method formulated with two Lagrange multipliers.

For some real-life engineering problems, it is neither necessary nor desirable to mesh a computational domain together. For example, in the Computer Aided Design (CAD) of electronic devices, it is often the case that only a portion of the entire device has to be redesigned repeatedly to achieve an optimal performance [32]. Therefore, this portion has to be re-meshed multiple times, whereas the mesh for the remaining portion can be kept the same. Therefore, there is an engineering need for a DDM that can allow the user to generate meshes for different regions separately based on geometrical features and then decompose each mesh independently using an automatic mesh decomposer. With such a process, the entire computational domain may contain conformal interfaces (generated by a mesh decomposer) and nonconformal interfaces between different regions partitioned before mesh generation. For such an application, it is necessary to develop an effective DDM to deal with mixed conformal/nonconformal multi-region meshes [33,34].

This paper presents a brief overview of our recent development of FETI-DP methods for FEM analysis of large-scale electromagnetic problems. The rest of this paper is organized as follows. In Sections II.A and II.B, we first extend the conformal Lagrange Multiplier (LM)-based FETI-DP method to the case with nonconformal interface and corner meshes. Then, we consider the TE Second-Order Transmission Condition (SOTC-TE) to significantly improve the iterative convergence of the interface solution in Section II.C. Afterwards, we discuss a hybrid method and a general crosspoint correction technique in Section II.D for an efficient modeling of multi-region problems. Finally, we present several antenna radiation and wave propagation examples to demonstrate the accuracy and efficiency of the proposed solvers in Section III.

II. FORMULATION

In this section, we first review the formulation of the nonconformal LM-based FETI-DP method, then incorporate the SOTC-TE into the dual-primal framework, and finally discuss the hybrid FETI/FETI-DP scheme.

A. FETI-DP for nonconformal interface and conformal corner meshes

Assume that the entire computational domain V is first divided into N_s nonoverlapping subdomains. The problem for the sth subdomain is defined by the second-order curl-curl equation:

$$\nabla \times (\mu_r^{-1} \nabla \times \mathbf{E}^s) - k_0^2 \varepsilon_r \mathbf{E}^s = -jk_0 Z_0 \mathbf{J}_{\text{imp}}^s \text{ in } V_s, \quad (1)$$

and the Robin boundary condition:

$$\hat{n}^s \times (\mu_r^{-1} \nabla \times \mathbf{E}^s) + \alpha^s \hat{n}^s \times (\hat{n}^s \times \mathbf{E}^s) = \mathbf{\Lambda}^s \text{ on } S_s, \quad (2)$$

where k_0 and Z_0 are the free-space wavenumber and intrinsic impedance, respectively, $\mathbf{J}_{\text{imp}}^s$ is an

impressed current, $\hat{n}^s$ is the outward normal unit vector of the sth subdomain, α^s is a complex parameter chosen to make the subdomain problem well posed, and $\mathbf{\Lambda}^s$ is an unknown variable defined on the subdomain interface. For the portion of the subdomain boundary S_s coinciding with the exterior surface of the computational domain S_0, we can either apply an ABC, a Perfectly Matched Layer (PML), or a Boundary Integral (BI) equation to the field.

To formulate the boundary-value problem defined in (1) and (2) using the FEM, the subdomain is discretized into finite elements such as tetrahedra. The vector electric field within each subdomain can then be expanded with hierarchical vector basis functions such that $\mathbf{E}^s = \{\mathbf{N}^s\}^T\{E^s\}$ [35]. By applying Galerkin's method, the FEM equation for the sth subdomain can be derived as:

$$\begin{bmatrix} K_{ii}^s & K_{ib}^s & K_{ic}^s \\ K_{bi}^s & K_{bb}^s+M_{bb}^s & K_{bc}^s \\ K_{ci}^s & K_{cb}^s & K_{cc}^s \end{bmatrix}\begin{Bmatrix} E_i^s \\ E_b^s \\ E_c^s \end{Bmatrix}=\begin{Bmatrix} f_i^s \\ f_b^s \\ f_c^s \end{Bmatrix}-\begin{Bmatrix} 0 \\ B_{bb}^s\lambda_b^s+L_{bc}^sE_c^s \\ \lambda_c^s \end{Bmatrix}, \quad (3)$$

where

$$[K_{uv}^s]=\iiint_{V_s}[\mu_r^{-1}(\nabla\times\mathbf{N}_u^s)(\nabla\times\mathbf{N}_v^s)$$
$$-k_0^2\varepsilon_r\mathbf{N}_u^s\mathbf{N}_v^s]dV \quad (u,v=i,b,c),$$

$$\{f_u^s\}=-jk_0Z_0\iiint_{V_s}\mathbf{N}_u^s\mathbf{J}_{\mathrm{imp}}^sdV \quad (u=i,b,c),$$

$$[M_{bb}^s]=\iint_{S_s}\alpha^s(\hat{n}^s\times\mathbf{N}_b^s)(\hat{n}^s\times\mathbf{N}_b^s)dS,$$

$$[B_{bb}^s]=\iint_{S_s}\mathbf{N}_b^s\mathbf{N}_b^sdS,$$

$$[L_{bc}^s]=\iint_{S_s}\alpha^s(\hat{n}^s\times\mathbf{N}_b^s)(\hat{n}^s\times\mathbf{N}_c^s)dS,$$

$$\{\lambda_c^s\}=-jk_0Z_0\iint_{S_s}\mathbf{N}_c^s(\hat{n}^s\times\mathbf{H})dS.$$

Different from the conformal FETI-DP method [10,11], the dual unknown $\mathbf{\Lambda}^s$ here is explicitly expanded in terms of a set of curl-conforming vector basis functions defined on S_s such that $\mathbf{\Lambda}^s = \{\mathbf{N}_b^s\}^T\{\lambda^s\}$. Therefore, $[B_{bb}^s]$ is no longer a Boolean matrix. By using the subscripts i, b, and c, each vector is partitioned into three parts, which are associated with the interior, interface, and corners of the subdomain, respectively. The separation of the corner unknowns is one of the most important features of the dual-primal idea. Equation (3) can be written in a compact form as:

$$\begin{bmatrix} K_{rr}^s & K_{rc}^s \\ K_{cr}^s & K_{cc}^s \end{bmatrix}\begin{Bmatrix} E_r^s \\ E_c^s \end{Bmatrix}=\begin{Bmatrix} f_r^s \\ f_c^s \end{Bmatrix}-\begin{Bmatrix} [R_{br}^s]^T(B_{bb}^s\lambda_b^s+L_{bc}^sE_c^s) \\ 0 \end{Bmatrix}, \quad (4)$$

where

$$[K_{rr}^s]=\begin{bmatrix} K_{ii}^s & K_{ib}^s \\ K_{bi}^s & K_{bb}^s+M_{bb}^s \end{bmatrix}, \quad [K_{rc}^s]=\begin{bmatrix} K_{ic}^s \\ K_{bc}^s \end{bmatrix},$$

$$[K_{cr}^s]=[K_{ci}^s\ K_{cb}^s]=[K_{rc}^s]^T,$$

$$\{E_r^s\}=\begin{Bmatrix} E_i^s \\ E_b^s \end{Bmatrix}, \text{ and } \{f_r^s\}=\begin{Bmatrix} f_i^s \\ f_b^s \end{Bmatrix}.$$

With the aid of a Boolean matrix $[R_{br}^s]$, which extracts the interface electric field $\{E_b^s\}$ out of $\{E_r^s\}$, we obtain the system equation for the dual unknowns from the first equation of (4) as:

$$\{E_b^s\}=[R_{br}^s]\{E_r^s\}=[R_{br}^s][K_{rr}^s]^{-1}\big(\{f_r^s\}$$
$$-[R_{br}^s]^T[B_{bb}^s]\{\lambda_b^s\}-([K_{rc}^s]+[R_{br}^s]^T[L_{bc}^s])\{E_c^s\}\big). \quad (5)$$

From the second equation of (4), another system equation can be derived for the primal unknowns, which is:

$$\big([K_{cc}^s]-[K_{cr}^s][K_{rr}^s]^{-1}([K_{rc}^s]+[R_{br}^s]^T[L_{bc}^s])\big)[B_c^s]\{E_c\}$$
$$=\{f_c^s\}-\{\lambda_c^s\}-[K_{cr}^s][K_{rr}^s]^{-1}\{f_r^s\}$$
$$+[K_{cr}^s][K_{rr}^s]^{-1}[R_{br}^s]^T[B_{bb}^s]\{\lambda_b^s\}, \quad (6)$$

where the Boolean matrix $[B_c^s]$ is introduced to extract the local corner unknowns from the global corner unknowns, which can be expressed mathematically as $[B_c^s]\{E_c\}=\{E_c^s\}$. Assembling (6) through all subdomains yields a global corner-related finite element system, which will be discussed later. It is important to note that $\{\lambda_c^s\}$ of all subdomains are cancelled out after the global assembly due to the Neumann continuity condition.

Next, we introduce the global boundary unknown vector $\{\lambda_b\}$ and the Boolean projection matrix $[Q^s]$ to extract $\{\lambda_b^s\}$ from $\{\lambda_b\}$ such that $\{\lambda_b^s\}=[Q^s]\{\lambda_b\}$, as defined in [11]. In order to obtain the global interface equation, we make use of the First-Order Transmission Condition (FOTC) on the subdomain interfaces:

$$\begin{cases} \mathbf{\Lambda}_b^s+\mathbf{\Lambda}_b^q=(\alpha^s+\alpha^q)\hat{n}^q\times(\hat{n}^q\times\mathbf{E}_b^q) \\ \mathbf{\Lambda}_b^q+\mathbf{\Lambda}_b^s=(\alpha^s+\alpha^q)\hat{n}^s\times(\hat{n}^s\times\mathbf{E}_b^s) \end{cases} \text{on } \Gamma_{sq}. \quad (7)$$

The choice of α has to satisfy the condition that $\alpha^s+\alpha^q \neq 0$. Note, that by enforcing (7), the tangential electric and magnetic fields are guaranteed to be continuous across the interface Γ_{sq}. Taking the sth subdomain as reference, we can discretize the first equation of (7) to obtain:

$$[N_{bb}^s]_q \{\lambda_b^s\}_q + [L_{bc}^s]_q \{E_c^s\}_q = -[N_{bb}^{sq}]\{\lambda_b^q\}_s$$
$$-[L_{bc}^{sq}]\{E_c^q\}_s - [M_{bb}^{sq}]\{E_b^q\}_s, \qquad (8)$$

where

$$[N_{bb}^s]_q = \iint_{\Gamma_{sq}} \mathbf{N}_b^s \mathbf{N}_b^s dS,$$

$$[L_{bc}^s]_q = \iint_{\Gamma_{sq}} \alpha^s (\hat{n}^s \times \mathbf{N}_b^s)(\hat{n}^s \times \mathbf{N}_c^s) dS,$$

$$[N_{bb}^{sq}] = \iint_{\Gamma_{sq}} \mathbf{N}_b^s \mathbf{N}_b^q dS,$$

$$[L_{bc}^{sq}] = \iint_{\Gamma_{sq}} \alpha^q (\hat{n}^q \times \mathbf{N}_b^s)(\hat{n}^q \times \mathbf{N}_c^q) dS,$$

$$[M_{bb}^{sq}] = \iint_{\Gamma_{sq}} (\alpha^s + \alpha^q)(\hat{n}^q \times \mathbf{N}_b^s)(\hat{n}^q \times \mathbf{N}_b^q) dS.$$

Note, that $[N_{bb}^s]_q$ is always diagonally dominant as long as the same set of basis function is used to expand the auxiliary variable $\mathbf{\Lambda}$ defined on both sides of the shared interface. Therefore, we can take the inversion of $[N_{bb}^s]_q$ to write the transmission condition (8) as:

$$\{\lambda_b^s\}_q + [N_{bb}^s]_q^{-1}[L_{bc}^s]_q[S_q^s]\{E_c^s\}$$
$$= -[N_{bb}^s]_q^{-1}[N_{bb}^{sq}][T_s^q]\{\lambda_b^q\} - [N_{bb}^s]_q^{-1}[L_{bc}^{sq}][S_s^q]\{E_c^q\}$$
$$-[N_{bb}^s]_q^{-1}[M_{bb}^{sq}][T_s^q]\{E_b^q\}, \qquad (9)$$

where we introduced another two Boolean matrices $[T_q^s]$ and $[S_q^s]$ to extract the unknowns associated with interface Γ_{sq} from those on S_s, such that $\{E_b^s\}_q = [T_q^s]\{E_b^s\}$, $\{\lambda_b^s\}_q = [T_q^s]\{\lambda_b^s\}$, and $\{E_c^s\}_q = [S_q^s]\{E_c^s\}$. Equation (9) can further be simplified by eliminating $\{E_b^q\}$ and the result is:

$$\{\lambda_b^s\}_q + [N_{bb}^s]_q^{-1}([N_{bb}^{sq}][T_s^q] - [M_{bb}^{sq}][T_s^q][F_{bb}^q])\{\lambda_b^q\}$$
$$+[N_{bb}^s]_q^{-1}[L_{bc}^s]_q[S_q^s][B_c^s]\{E_c\}$$
$$+[N_{bb}^s]_q^{-1}([L_{bc}^{sq}][S_s^q][B_c^q] - [M_{bb}^{sq}][T_s^q][F_{bc}^q])\{E_c\}$$
$$= -[N_{bb}^s]_q^{-1}[M_{bb}^{sq}][T_s^q]\{d_r^q\}, \qquad (10)$$

where

$$[F_{bb}^q] = [R_{br}^q][K_{rr}^q]^{-1}[R_{br}^q]^T[B_{bb}^q],$$
$$[F_{bc}^q] = [R_{br}^q][K_{rr}^q]^{-1}([K_{rc}^q] + [R_{br}^q]^T[L_{bc}^q])[B_c^q],$$
$$\{d_r^q\} = [R_{br}^q][K_{rr}^q]^{-1}\{f_r^q\}.$$

On one hand, we can assemble (10) over all s and q to obtain an interface system for all subdomains as:

$$F(\{E_c\}, \{\lambda_b\}, \{f\}) = 0. \qquad (11)$$

On the other hand, we can assemble the contribution from the primal unknowns (defined on corners) in (6) as:

$$\{E_c\} = G(\{\lambda_b\}, \{f\}). \qquad (12)$$

By combining (11) and (12) and eliminating $\{E_c\}$, we obtain the nonconformal FETI-DP interface equation for the dual unknowns $\{\lambda_b\}$, which can be solved using a Krylov subspace method. After $\{\lambda_b\}$ is solved, $\{E_c\}$ can be obtained from (12) and the electric field inside each subdomain can be obtained by solving (5).

B. Extension to nonconfomal interface and corner meshes

To further enhance the capability of the LM-based FETI-DP scheme to deal with arbitrary meshes, we now focus on the extension to nonconformal corner cases in this section. Assume that four subdomains share one global corner edge. We denote the number of unknowns defined on each local corner edge as N_c, then call the corner with most unknowns as "master" corner and the others as "slave" corners so that $N_c^{\text{slave}} \le N_c^{\text{master}}$. Note, that subdomains with more than one crosspoint could contain both master and slave corners. We impose the Dirichlet continuity condition at the corner as:

$$\mathbf{E}_t^{\text{master}} = \mathbf{E}_t^{\text{slave}}, \qquad (13)$$

in a weak sense, where the subscript t specifies the tangential electric field along the corner edge.

The tangential electric field for the master and slave subdomains (taking one slave subdomain for example) can be expanded by two independent sets of basis functions $\{\mathbf{N}_c^{\text{master}}\}$ and $\{\mathbf{N}_c^{\text{slave}}\}$ as:

$$\begin{cases} \mathbf{E}_t^{\text{slave}} = \sum_{n=1}^{N_c^{\text{slave}}} E_{c,n}^{\text{slave}} \mathbf{N}_{c,n}^{\text{slave}} \\ \mathbf{E}_t^{\text{master}} = \sum_{n=1}^{N_c^{\text{master}}} E_{c,n}^{\text{master}} \mathbf{N}_{c,n}^{\text{master}} \end{cases}. \qquad (14)$$

By substituting (14) into (13) and testing both sides using $\{\mathbf{N}_c^{\text{slave}}\}$, we obtain:

$$[G_{cc}^{\text{slv-slv}}]\{E_c^{\text{slave}}\} = [H_{cc}^{\text{slv-mst}}]\{E_c^{\text{master}}\}, \qquad (15)$$

where

$$G_{cc,mn}^{\text{slv-slv}} = \int_{\Gamma_c} \mathbf{N}_{c,m}^{\text{slave}} \cdot \mathbf{N}_{c,n}^{\text{slave}} dl,$$

$$H_{cc,mn}^{\text{slv-mst}} = \int_{\Gamma_c} \mathbf{N}_{c,m}^{\text{slave}} \cdot \mathbf{N}_{c,n}^{\text{master}} dl.$$

Because $[G_{cc}^{\text{slv-slv}}]$ is always diagonal, we have:

$$\{E_c^{\text{slave}}\} = [G_{cc}^{\text{slv-slv}}]^{-1}[H_{cc}^{\text{slv-mst}}]\{E_c^{\text{master}}\}, \qquad (16)$$

which means that the corner unknowns defined on the slave corners can be represented by those on the

master corners. Therefore, one can construct a global coarse problem by using only the corner unknowns on all the master corners.

C. Second-order transmission condition

The FOTC employed in Section II.A can be replaced by a higher-order transmission condition to speed up the convergence of the iterative solution of the global interface problem [25-27]. Among them, the SOTC-TE is of particular interest because it can be implemented without introducing any extra auxiliary variables on subdomain interfaces. When incorporated into the dual-primal framework, it does not change the sparsity pattern of the subdomain matrices compared to that in the FOTC case. The subdomain matrix symmetry is also preserved, which is highly desirable for the storage and factorization by a direct sparse solver [34].

For the sth subdomain, the SOTC-TE can be written as:

$$\hat{n}^s \times (\mu_r^{-1} \nabla \times \mathbf{E}^s) + \alpha^s \hat{n}^s \times (\hat{n}^s \times \mathbf{E}^s)$$
$$- \beta^s \nabla \times [\hat{n}^s (\nabla \times \mathbf{E}^s)_n] = \mathbf{\Lambda}^s \text{ on } S_s, \quad (17)$$

where $(\nabla \times \mathbf{E}^s)_n = \hat{n}^s (\nabla \times \mathbf{E}^s)$ and β^s can be determined based on the smallest mesh size and the order of basis functions on the subdomain interface to account for all the evanescent modes supported by the interface mesh [25,26]. More specifically, $\beta^s = -j / (k_0 + \tilde{k})$, with $\tilde{k} = -j(k_{max}^2 - k_0^2)^{1/2}$, and $k_{max} = \pi / h_{min}$, where h_{min} denotes the smallest mesh size on the subdomain interface.

Adding the transmission conditions from two neighboring subdomains and eliminating the tangential magnetic field, we have:

$$\begin{cases} \mathbf{\Lambda}_b^s + \mathbf{\Lambda}_b^q = (\alpha^s + \alpha^q)\hat{n}^q \times (\hat{n}^q \times \mathbf{E}_b^q) \\ \qquad - (\beta^s + \beta^q)\nabla \times [\hat{n}^q (\nabla \times \mathbf{E}_b^q)_n], \\ \mathbf{\Lambda}_b^q + \mathbf{\Lambda}_b^s = (\alpha^s + \alpha^q)\hat{n}^s \times (\hat{n}^s \times \mathbf{E}_b^s) \\ \qquad - (\beta^s + \beta^q)\nabla \times [\hat{n}^s (\nabla \times \mathbf{E}_b^s)_n] \end{cases} \quad (18)$$

on Γ_{sq}. It can be seen that in addition to the Dirichlet and Neumann continuity conditions, the SOTC-TE also enforces the continuity of $\nabla \times [\hat{n}(\nabla \times \mathbf{E})_n]$, which is related to the tangential variation of the normal magnetic flux density. Due to the use of the SOTC-TE, the computation of some matrices in Section II.A has to be modified as follows:

$$[M_{bb}^s] = \iint_{S_s} [\alpha^s (\hat{n}^s \times \mathbf{N}_b^s)(\hat{n}^s \times \mathbf{N}_b^s)$$

$$+ \beta^s (\nabla \times \mathbf{N}_b^s)_n (\nabla \times \mathbf{N}_b^s)_n] dS,$$

$$[L_{bc}^s] = \iint_{S_s} [\alpha^s (\hat{n}^s \times \mathbf{N}_b^s)(\hat{n}^s \times \mathbf{N}_c^s)$$

$$+ \beta^s (\nabla \times \mathbf{N}_b^s)_n (\nabla \times \mathbf{N}_c^s)_n] dS,$$

$$[L_{bc}^s]_q = \iint_{\Gamma_{sq}} [\alpha^s (\hat{n}^s \times \mathbf{N}_b^s)(\hat{n}^s \times \mathbf{N}_c^s)$$

$$+ \beta^s (\nabla \times \mathbf{N}_b^s)_n (\nabla \times \mathbf{N}_c^s)_n] dS,$$

$$[L_{bc}^{sq}] = \iint_{\Gamma_{sq}} [\alpha^q (\hat{n}^q \times \mathbf{N}_b^s)(\hat{n}^q \times \mathbf{N}_c^q)$$

$$+ \beta^q (\nabla \times \mathbf{N}_b^s)_n (\nabla \times \mathbf{N}_c^q)_n] dS,$$

$$[M_{bb}^{sq}] = \iint_{\Gamma_{sq}} (\alpha^s + \alpha^q)(\hat{n}^q \times \mathbf{N}_b^s)(\hat{n}^q \times \mathbf{N}_b^q)$$

$$+ (\beta^s + \beta^q)(\nabla \times \mathbf{N}_b^s)_n (\nabla \times \mathbf{N}_b^q)_n] dS.$$

D. Hybrid nonconformal FETI/conformal FETI-DP

For the multi-region domain decomposition, when a subdomain interface resides within one region, it must be mesh-conformal and geometry-conformal. In this case, $[B_{bb}^s]$ in Section II.A is reduced to a projection Boolean matrix, $[N_{bb}^s]_q$ and $[N_{bb}^{sq}]$ become identity matrices, and one does not have to deal with projections on the geometrical crosspoints as described in Section II.B. Thus, it is necessary to design an efficient hybrid algorithm to take advantage of the partially conformal meshes.

For this, we propose a general crosspoint correction technique to ensure good accuracy, fast convergence, and a nonsingular global interface matrix [33,34]. The basic idea includes the following guidelines: (1) the Lagrange multipliers need to be split into two when they are defined on the edges connecting an inter-region interface and an interior interface within one region. (2) By automatic domain decomposition, it is possible to have geometry crosspoints sitting on an inter-region interface. If this is the case, convert the original corner unknowns into non-corner interface unknowns, define Lagrange multipliers on these crosspoints and split each Lagrange multiplier into two. (3) In geometry-nonconformal cases, one Lagrange multiplier may be shared by more than two neighboring subdomains. In this case, split such a Lagrange multiplier according to the number of overlapped neighboring subdomains and let each Lagrange multiplier after splitting take care of the communication from the reference subdomain to each neighboring subdomain.

Actually, Guidelines 1 and 2 are two special cases described by Guideline 3. It should be noted that splitting Lagrange multiplier introduces extra boundary unknowns into the original global interface problem, which may lead to a singular global interface matrix equation. For this, a corner penalty term technique is employed to remove the singularity or near singularity due to the redundancy [27].

III. NUMERICAL EXAMPLES

The algorithms described in Section II have been implemented on different serial and parallel computing platforms. In this section, we present several numerical examples to demonstrate their accuracy and convergence performance. For antenna array simulations, the repetition of the array structure is fully exploited in order to save time for generating the mesh and factorizing repeated subdomain matrices.

A. Vivaldi antenna array

The first example is designed to explore the capability of the LM-based FETI-DP method to analyze large-scale antenna arrays, and compare its performance to that of the FETI-DPEM2 [11] and the Cement-Element (CE)-based FETI-DP method [18]. The size of the simulated Vivaldi antenna array increases from 3×3 to 100×100. To truncate the computational domain, the first-order ABC is placed at one extra unit cell surrounding the array in the xy-plane. The distance between two adjacent elements in both the x- and y-directions is set to be 36 mm. Figure 1 (a) shows the Vivaldi antenna element, where the height, width, and thickness of the substrate are d=33.3 mm, w=34.0 mm, and h=1.27 mm, respectively. The lossless substrate has a relative permittivity of 6.0. The radius of the hollow circle is chosen to be R=2.5 mm. The half-width of the slot line varies with z according to an exponential function given by $w(z)$=0.25exp(0.123z) mm. This function gives a half-width of 15 mm at the open mouth. The antenna is fed by a coaxial line with an inner radius r_{in}=0.375 mm and an outer radius r_{out}=0.875 mm from under the ground. A 5-mm coaxial line is modeled and then terminated with a waveguide port boundary condition with only the TEM mode assumed at the end of the coax.

The convergence history of the iterative solution of the global interface problem for the 100×100 array simulated by the conformal, LM-based, and CE-based FETI-DP methods is plotted in Fig. 1 (a), and the computed radiation patterns are compared in Figs. 1 (b) and 1 (c). The BiCGStab iterative solver is employed with a stopping criterion of 10^{-3}. For this array, the LM- and CE-based FETI-DP methods have a similar convergence behavior and yield nearly identical results to that of the conformal FETI-DP method.


(a)

(b)

(c)
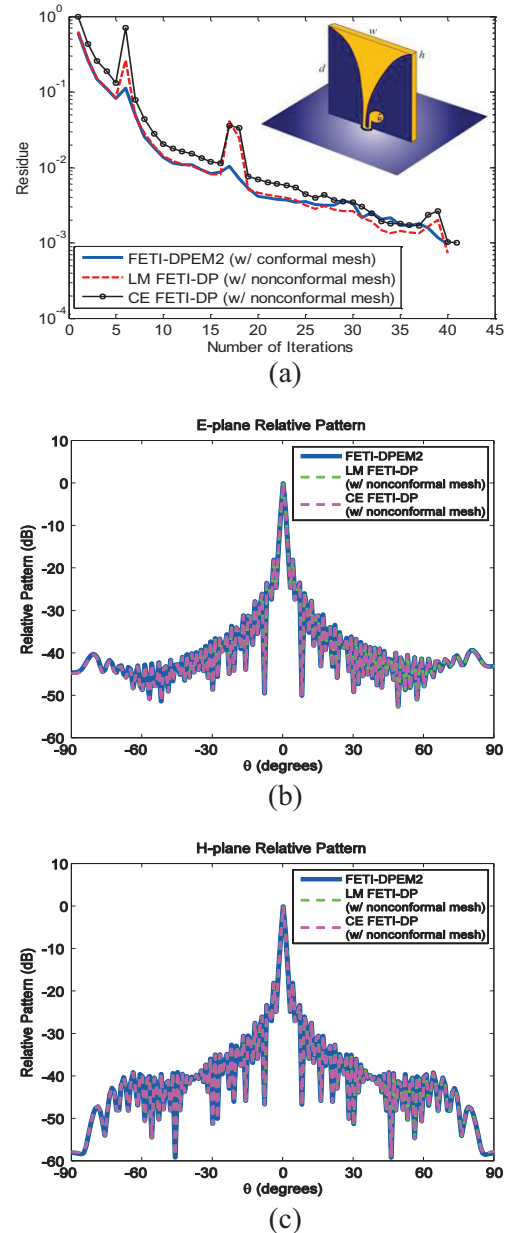
Fig. 1. Simulation of the 100×100 Vivaldi antenna array at 3 GHz. (a) Convergence history, (b) broadside scan E-plane relative pattern, and (c) broadside scan H-plane relative pattern.

In Table 1, we list the computation resources used to simulate Vivaldi antenna arrays of different sizes by the LM-based FETI-DP method. All examples are run on an HP workstation, equipped with a 2.66-GHz Intel Xeon processor and 12 GB memory. To plot the scalability curve as shown in Fig. 2, we record the computation time for solving the global interface dual unknowns as well as the total computation time. It is observed that the computation time increases linearly with the total number of unknowns in this case.

Table 1: Computational information of the nonconformal FETI-DP method for simulating various Vivaldi antenna arrays. The computation time is in the hour:minute:second format

Array Size	# of Unknowns	Interface Time (# of Iterations)	Total Time
3×3	209,792	00:00:21 (28)	00:02:20
10×10	1,908,552	00:04:54 (44)	00:13:43
31×31	17,410,080	00:49:27 (51)	02:01:21
100×100	178,235,832	07:19:58 (40)	19:32:20
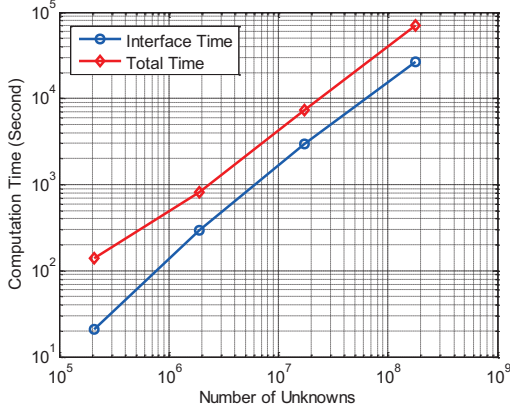
Fig. 2. Computation time as a function of the total number of unknowns for various Vivaldi antenna arrays.

Antenna array is a typical case where the outgoing wave may propagate towards the truncation boundary at an oblique direction. If this is the case, no matter how far away the ABC is placed, its absorption is limited and the artificial reflection may not be reduced to a desired level. To effectively reduce the artificial reflection, we can employ an oblique ABC as [36]:

$$\hat{n} \times (\nabla \times \mathbf{E}) = -jk_0 \cos\theta_s \hat{n} \times (\hat{n} \times \mathbf{E})$$
$$+ (jk_0 / \cos\theta_s)\hat{t}(\hat{t}\mathbf{E}), \qquad (19)$$

where $\hat{t} = (\hat{\phi}_s \times \hat{n})\sin\theta_s \cos\phi_s + \hat{\phi}_s \sin\theta_s \sin\phi_s$ and $\hat{n}$ denotes the outward unit normal vector of the planar truncation surface. The angle for perfect absorption of this ABC can be tuned by parameters θ_s and ϕ_s. Obviously, (19) is reduced to the conventional ABC if $\theta_s = 0^\circ$. Therefore, we can always tune this ABC to minimize the reflection error for the analysis of large finite phased arrays as long as the direction of the main beam of the radiated wave is specified.

To investigate the performance of the oblique ABC, a 20×20 Vivaldi antenna array is considered. For the mesh truncation of the upper half space, we have two setups. One is a hemispherical surface with a base radius of 7λ, whereas the other is a rectangular surface placed 1λ away from both the top and the side of the antenna array. The size of the rectangular box is $8.8\lambda \times 9.2\lambda \times 1.33\lambda$. Apparently, the second setup is computationally more efficient than the first one because its computational domain is much smaller. However, in the second setup, the radiated field will be incident on the top truncation surface at a much larger angle than in the first one if the antenna array is set to radiate away from broadside. In this case, the oblique ABC can provide a good absorption performance while minimizing the size of the computational domain. The 20×20 Vivaldi antenna array is simulated at 3.0 GHz using: (1) the conventional ABC with the hemispherical truncation surface, (2) the conventional ABC with the rectangular truncation surface, and (3) the oblique ABC with the rectangular truncation surface for the main beam (θ_s, ϕ_s) steered to $(60^\circ, 0^\circ)$. The near-zone field distributions in the yz-plane are plotted in Fig. 3. We take the result of Case 1 shown in Fig. 3 (a) as the reference solution and enlarge the portion close to the antenna array in Fig. 3 (b) for a better comparison between the results of Cases 2 and 3, which are shown in Figs. 3 (c) and 3 (d). For the case of $(\theta_s, \phi_s) = (60^\circ, 0^\circ)$, Case 3 yields a visually much better result than does Case 2, as shown in Figs. 3 (c) and 3 (d). The far-field radiation patterns calculated in the three cases above are compared in Fig. 4, which shows that the result of

Case 2 deviates from the reference solution by 3 dB, whereas the result of Case 3 has a much smaller derivation. For Cases 2 and 3, it takes 9.2 minutes to finish the simulation of one frequency point on one computational node which contains 16 Intel Xeon 2.70-GHz processors. The result of the reference case (Case 1) is obtained using the hybrid conformal/nonconformal domain decomposition solver described in Section II.D with 43.5 minutes for one frequency on the same node.

Fig. 4. Co-polarized radiation patterns for the 20×20 Vivaldi antenna array in the xz-plane at 3.0 GHz when the main beam is steered to $(\theta_s, \phi_s) = (60^\circ, 0^\circ)$.

B. NRL Vivaldi antenna array with a radome

In this example, we consider the near-field interaction between a phased-array antenna and its surrounding environment. The antenna array adopted was designed by the Naval Research Lab (NRL) [37]. A radome is placed on the top of the array for mechanical protection. The hybrid nonconformal FETI/conformal FETI-DP method is employed to solve this multi-region problem.

In the 11×11 dual-polarized array, each Vivaldi antenna element consists of three layers of metal printed on a dielectric substrate with a height of 246.253 mm, a width of 35.56 mm, and a thickness of 3.3274 mm. The relative permittivity of the dielectric slab is $\varepsilon_r = 2.2 - j0.0009$. The metallic layers are equally spaced and are connected by vias with a radius of 0.79 mm. All antenna elements are connected to each other by solid metal posts and mounted vertically on a finite ground whose size is 528 mm × 528 mm. For more geometrical details, the reader is referred to [37].

At 3.02 GHz, the hemispherical radome has a base radius of 5.5λ. The thickness and the relative permittivity of the radome are 0.1λ and $\varepsilon_r = 2.0 - j1.0$, respectively. The conventional first-order ABC is used on a hemispherical surface placed 1λ away from the exterior boundary of the hemispherical radome. In this case, the first-order ABC is a better choice because the truncation

Fig. 3. $|\mathrm{Re}(E)|$ for the 20×20 Vivaldi antenna array in the xz-plane at 3.0 GHz with steering angle set at $(\theta_s, \phi_s) = (60^\circ, 0^\circ)$. (a) Computed using the conventional ABC with a hemispherical truncation surface, (b) same as (a) but plotted in a limited region for the purpose of comparison, (c) computed using the conventional ABC with a rectangular truncation surface, and (d) computed using the oblique ABC with a rectangular truncation surface.

surface can be made conformal to the radome to reduce the size of the computational domain. In addition, it provides good absorption for waves radiating along any direction. Figure 5 shows the radiation patterns of the array with and without the radome. All radiation patterns are normalized by the value in the maximum radiation direction of the array without the radome. It can be seen that due to the loss of the radome, the emitted power in the main beam direction is reduced by around 3 dB. The result using conformal meshes on the inter-region interfaces is also plotted for comparison. Apparently, using nonconformal inter-region interface meshes does not sacrifice the accuracy of the solution since two sets of data are on the top of each other. The field distribution is also plotted in Fig. 6 for the cases with and without the radome. Finally, the convergence history the iterative solution of the global interface problem for the array with the radome is given in Fig. 7. It should be noted that for large-scale problems, the nonconformal meshes on the interfaces between different regions may introduce some numerical resonance and yield slower convergence than a conformal mesh does.
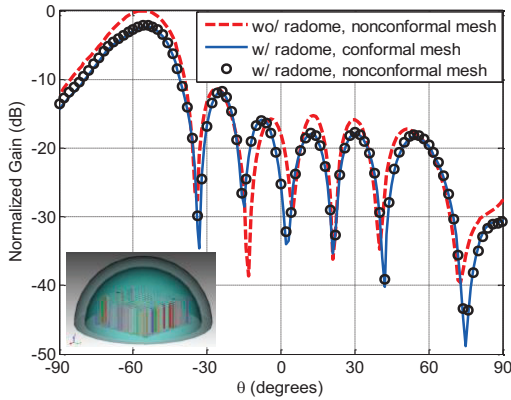
Fig. 5. Comparison between the radiation patterns for the array with and without the radome at 3.02 GHz and steering angle $\theta_s = -60^\circ$ and $\phi_s = 0^\circ$.

(a)

(b)
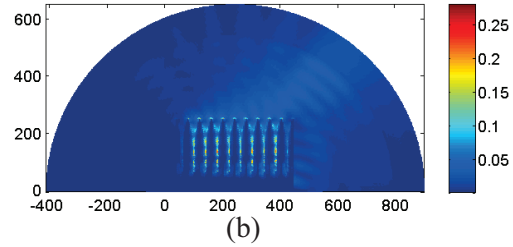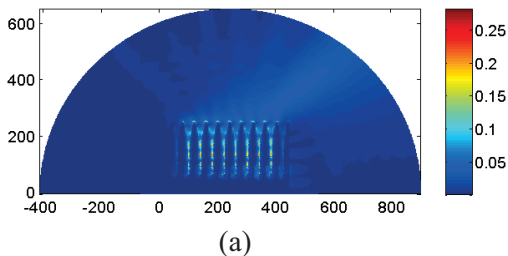
Fig. 6. $|E|$ in the $\phi = 0^\circ$ plane for H-pol excitation at 3.02 GHz and steering angle $\theta_s = 60^\circ$ and $\phi_s = 0^\circ$. (a) The NRL array itself, and (b) the NRL array with a radome.
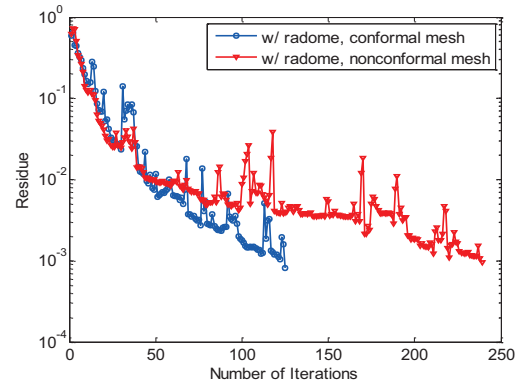
Fig. 7. Convergence history of the iterative solution of the global interface problem for the NRL array with the radome.

C. Subwavlength wave guiding and focusing

As the last example, we simulate a taper transition device which can guide waves from a wavelength-scale transmission line to a subwavelength-scale one. The basic structure is a periodic arrangement of metallic bricks standing on a metallic surface, as shown in Fig. 8 (a). The period of each brick-groove pair is $d = \lambda / 8 = 0.2$ mm, the length and height of each metallic brick are $l = 0.5d$ and $h = 1.5d$, and the width shrinks from $w_{\text{in}} = 16d$ to $w_{\text{out}} = 0.5d$ linearly through an 18-period transition. The input and output ports of the entire device are connected to the taper structure by 12- and 18-period uniform waveguides, respectively. The entire structure is made of aluminum, which has $\varepsilon_r = -3.39 \times 10^4 - j3.5 \times 10^6$ at $\lambda = 1.6$ mm . At this frequency, the aluminum can also be modeled as a Perfect Electric Conductor (PEC), because the modal effective index as a function of w for a PEC

is almost the same as that for the aluminum [38]. In the simulation, the grating lies on an infinitely large ground plane, which is also modeled as a PEC. To excite the fundamental TM-like mode whose magnetic field is parallel to the groove orientation, a current sheet is placed perpendicularly to the wave propagation direction at the input port. The ABC or PML truncation is placed one wavelength away from the top and four sides of the device. In this paper, we implement the PML as a diagonally anisotropic artificial medium, with $\ddot{\mu}_r = \mu_r[D]$ and $\ddot{\varepsilon}_r = \varepsilon_r[D]$, where:

$$[D] = \begin{bmatrix} a & 0 & 0 \\ 0 & b & 0 \\ 0 & 0 & c \end{bmatrix}. \qquad (20)$$

The diagonal entries of $[D]$ can be further written as $a = s_y s_z / s_x$, $b = s_z s_x / s_y$, and $c = s_x s_y / s_z$, where s_x, s_y, and s_z are functions of spatial variables x, y, and z, respectively. In the PML region, s_x, s_y, and s_z can be expressed as $s_a = s' - js''$, where a could be x, y, or z, and s' and s'' are real numbers with $s' \geq 1$ and $s'' \geq 0$, which are used to control the attenuation of the evanescent and propagating waves in the PML [1].

To compare the convergence performance of the FETI-DP method with the SOTC-TE when the computational domain is truncated using either the ABC or the PEC-back PML, we discretize the entire computational domain with the same mesh, reset the material properties of the tetrahedral elements in the PML region, and change the boundary condition at the exterior boundary. With this, the number of unknowns using two different truncations remains roughly the same. When the entire computational domain is divided into 512 subdomains, there are 3,342,990 primal unknowns, 724,544 dual unknowns, and 22,933 corner unknowns for the ABC truncation, whereas those for the PML truncation are 3,302,780, 719,112, and 22,932, respectively. Figure 8 (b) shows the simulated electric field intensity distribution in the plane $30\,\mu\text{m}$ above the waveguide. As can be seen, when propagating in the taper, the mode size becomes smaller and smaller with a gradually increased intensity, which demonstrates the wave squeezing and focusing phenomenon observed in the experiment [38]. The convergence history of the iterative solution of the

global interface problem using the FETI-DP method with the SOTC-TE and the cement element method with the SOTC-FULL [26] is given in Fig. 9 for both the ABC and PML truncations. In both cases, the FETI-DP method outperforms the cement element method in terms of iteration steps. Also, the convergence does not slow down too much when the ABC is replaced with the PML.

(a)

(b)
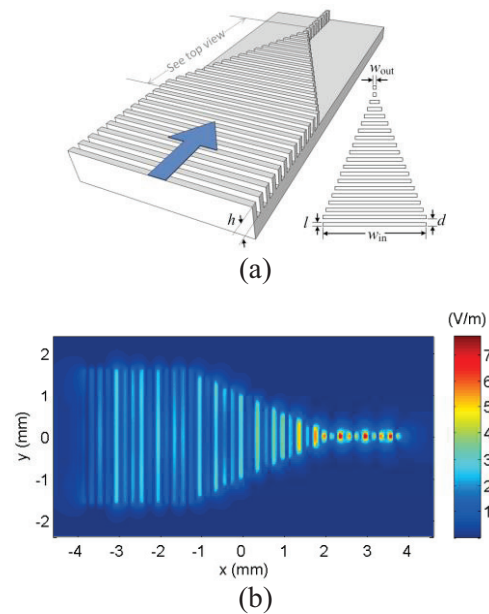
Fig. 8. Subwavelength waveguiding and focusing device. (a) Geometry; the waveguide width transits from $L_{in} = 16d$ to $L_{out} = 0.5d$ after 18 periods, and (b) electric field in the plane $30\,\mu\text{m}$ above the waveguide.
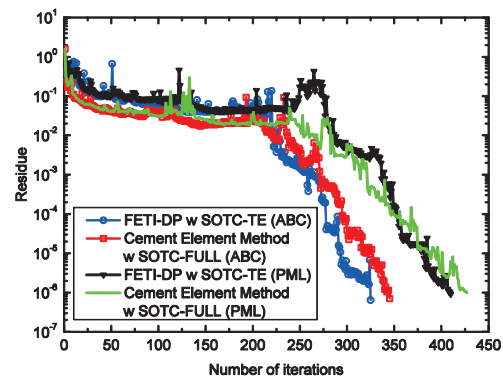

Fig. 9. Convergence history of the iterative solution of the global interface problem when the computational domain is truncated by ABC and PEC-backed PML.

IV. CONCLUSION

In this paper, we presented an overview of our recent effort on the domain decomposition finite element analysis of large-scale electromagnetic problems. First, we described the formulation of the LM-based FETI-DP method to deal with nonconformal interface and corner meshes. Then we discussed an approach to employ a higher-order transmission condition to improve the convergence performance of the interface iterative solution. Afterwards, we introduced a hybrid nonconformal FETI/conformal FETI-DP scheme to model multi-region electromagnetic problems, which relies on a general corner correction technique to handle mesh-nonconformal and geometry-nonconformal meshes on the inter-region interface. Finally, we gave a few numerical examples to demonstrate the finite element analysis of various antenna arrays, where we employed an oblique ABC designed for absorbing waves radiating from an array. In addition, we validated the PML mesh truncation through the simulation of a wave-guiding and focusing device. The application examples demonstrated that the finite element-based DDM is a powerful numerical simulation technique for the analysis of large-scale electromagnetic problems.

REFERENCES

[1] J. M. Jin, "The finite element method in electromagnetics," 2nd edition, *Wiley*, New York, 2002.

[2] A. Toselli and O. Widlund, "Domain decomposition methods-algorithms and theory," *Springer-Verlag*, Berlin, 2005.

[3] B. Després, P. Joly, and J. E. Roberts, "A domain decomposition method for the harmonic maxwell equations," *In Iterative Methods In Linear Algebra*, North-Holland, Amsterdam, pp. 475-484, 1992.

[4] B. Stupfel and M. Mognot, "A domain decomposition method for the vector wave equation," *IEEE Trans. Antennas Propag.*, vol. 48, no. 5, pp. 653-660, May 2000.

[5] C. Farhat and F. Roux, "A method of finite element tearing and interconnecting and its parallel solution algorithm," *Int. J. Numer. Meth. Eng.*, vol. 32, no. 6, pp. 1205-1227, October 1991.

[6] C. Farhat, A. Macedo, M. Lesoinne, F. X. Roux, and F. Magoulès, "Two-level domain decomposition methods with lagrange multipliers for the fast iterative solution of acoustic scattering problems," *Comput. Methods Appl. Mech. Eng.*, vol. 184, no. 2-4, pp. 213-239, April 2000.

[7] C. Farhat, M. Lesoinne, P. LeTallec, K. Pierson, and D. Rixen, "FETI-DP: a dual-primal unified FETI method-part I: a faster alternative to the two-level FETI method," *Int. J. Numer. Meth. Eng.*, vol. 50, no. 7, pp. 1523-1544, March 2001.

[8] C. Farhat, J. Li, and P. Avery, "A FETI-DP method for the parallel iterative solution of indefinite and complex-valued solid and shell vibration problems," *Int. J. Numer. Meth. Eng.*, vol. 63, no. 3, pp. 398-427, May 2005.

[9] C. Farhat, P. Avery, R. Tezaur, and J. Li, "FETI-DPH: a dual-primal domain decomposition method for acoustic scattering," *J. Comput. Acoust.*, vol. 13, no. 3, pp. 499-524, March 2005.

[10] Y. J. Li and J. M. Jin, "A vector dual-primal finite element tearing and interconnecting method for solving 3D large-scale electromagnetic problems," *IEEE Trans. Antennas Propag.*, vol. 54, no. 10, pp. 3000-3009, October 2006.

[11] Y. J. Li and J. M. Jin, "A new dual-primal domain decomposition approach for finite element simulation of 3D large-scale electromagnetic problems," *IEEE Trans. Antennas Propag.*, vol. 55, no. 10, pp. 2803-2810, October 2007.

[12] Y. J. Li and J. M. Jin, "Implementation of the second-order ABC in the FETI-DPEM method for 3D EM problems," *IEEE Trans. Antennas Propag.*, vol. 56, no. 8, pp. 2765-2769, August 2008.

[13] S. C. Lee, M. N. Vouvakis, and J. F. Lee, "A non-overlapping domain decomposition method with non-matching grids for modeling large finite antenna arrays," *J. Comput. Phys.*, vol. 203, no. 1, pp. 1-21, February 2005.

[14] M. N. Vouvakis, Z. Cendes, and J. F. Lee, "A FEM domain decomposition method for photonic and electromagnetic band gap structures," *IEEE Trans. Antennas Propag.*, vol. 54, pp. 721-733, February 2006.

[15] K. Zhao, V. Rawat, S. C. Lee, and J. F. Lee, "A domain decomposition method with nonconformal meshes for finite periodic and semi-periodic structures," *IEEE Trans. Antennas Propag.*, vol. 55, no. 9, pp. 2559-2570, September 2007.

[16] Z. Q. Lu, X. An, and W. Hong, "A fast domain decomposition method for solving three-dimensional large-scale electromagnetic problems," *IEEE Trans. Antennas Propag.*, vol. 56, no. 8, pp. 2200-2210, August 2008.

[17] M. F. Xue and J. M. Jin, "Application of a nonconformal FETI-DP method in antenna array simulations," *In IEEE APS Int. Symp. Dig.*, pp. 1-2, July 2012.

[18] M. F. Xue and J. M. Jin, "Nonconformal FETI-DP methods for large-scale electromagnetic simulation," *IEEE Trans. Antennas Propag.*, vol. 60, no. 9, pp. 4291-4305, September 2012.

[19] M. J. Gander, F. Magoulès, and F. Nataf, "Optimized schwarz methods without overlap for the helmholtz equation," *SIAM J. Sci. Comput*., vol. 24, no. 1, pp. 38-60, 2003.

[20] M. J. Gander, L. Halpern, and F. Magoulès, "An optimized schwarz method with two-sided robin transmission conditions for the helmholtz equation," *Int. J. Numer. Meth. Fluids*, vol. 55, no. 2, pp. 163-175, September 2007.

[21] M. J. Gander and F. Kwok, "Best robin parameters for optimized schwarz methods at cross points," *SIAM J. Sci. Comput*., vol. 34, no. 4, pp. 1849-1879, 2010.

[22] P. Collino, G. Delbue, P. Joly, and A. Piacentini, "A new interface condition in the non-overlapping domain decomposition for the maxwell equations," *Comput. Methods Appl. Mech. Eng*., vol. 148, no. 1-2, pp. 195-207, August 1997.

[23] A. Alonso-Rodriguez and L. Gerardo-Giorda, "New nonoverlapping domain decomposition methods for the harmonic maxwell system," *SIAM J. Sci. Comput*., vol. 28, no. 1, pp. 102-122, 2006.

[24] V. Dolean, M. J. Gander, and L. Gerardo-Giorda, "Optimized schwarz methods for maxwell's equations," *SIAM J. Sci. Comput*., vol. 31, no. 3, pp. 2193-2213, 2009.

[25] Z. Peng, V. Rawat, and J. F. Lee, "One way domain decomposition method with second order transmission conditions for solving electromagnetic wave problems," *J. Comput. Phys*., vol. 229, no. 4, pp. 1181-1197, February 2010.

[26] Z. Peng and J. F. Lee, "Non-conformal domain decomposition method with second-order transmission conditions for time-harmonic electromagnetics," *J. Comput. Phys*., vol. 229, no. 8, pp. 5615-5629, August 2010.

[27] Z. Peng and J. F. Lee, "Non-conformal domain decomposition method with mixed true second order transmission condition for solving large finite antenna arrays," *IEEE Trans. Antennas Propag*., vol. 59, no. 5, pp. 1638-1651, May 2011.

[28] J. Ma, J. M. Jin, and Z. Nie, "A nonconformal FEM-DDM with tree-cotree splitting and improved transmission condition for modeling subsurface detection problems," *IEEE Trans. Geosci. Remote Sens*., vol. 52, no. 1, pp. 355-364, January 2014.

[29] A. F. Peterson, "Absorbing boundary conditions for the vector wave equation," *Microwave Opt. Technol. Lett*., vol. 1, no. 2, pp. 62-64, April 1988.

[30] J. P. Webb and V. N. Kanellopoulos, "Absorbing boundary conditions for the finite element solution of the vector wave equation," *Microwave Opt. Technol. Lett*., vol. 2, no. 10, pp. 370-372, October 1989.

[31] B. Stupfel, "Numerical implementation of second- and third-order conformal absorbing boundary conditions for the vector-wave equation," *IEEE Trans. Antennas Propag*., vol. 45, no. 3, pp. 487-492, March 1997.

[32] Q. He and D. Jiao, "A rigorous divide-and-conquer algorithm for fast DC-mode extraction," in *IEEE APS Int. Symp. Dig*., pp. 1630-1631, July 2013.

[33] M. F. Xue and J. M. Jin, "A hybrid nonconformal FETI/conformal FETI-DP method for arbitrary nonoverlapping domain decomposition modeling," *In IEEE APS Int. Symp. Dig*., pp. 1628-1629, July 2013.

[34] M. F. Xue and J. M. Jin, "A hybrid conformal/ nonconformal domain decomposition method for multi-region electromagnetic modeling," *IEEE Trans. Antennas Propag*., in press.

[35] J. P. Webb, "Hierarchical vector basis functions of arbitrary order for triangular and tetrahedral elements," *IEEE Trans. Antennas Propag*., vol. 47, no. 8, pp. 1244-1253, August 1999.

[36] M. F. Xue and J. M. Jin, "Application of an oblique absorbing boundary condition in the finite element simulation of phased-array antennas," *Microwave Opt. Technol. Lett*., vol. 56, no. 1, pp. 178-184, January 2014.

[37] M. F. Xue, J. M. Jin, S. Wong, C. Macon, and M. Kragalott, "Experimental validation of the FETI-DPEM algorithm for simulating phased-array antennas," *In IEEE APS Int. Symp. Dig*., pp. 2495-2498, July 2011.

[38] W. Zhao, O. M. Eldaiki, R. Yang, and Z. Lu, "Deep subwavelength waveguiding and focusing based on designer surface plasmons," *Opt. Express*, vol. 18, no. 20, pp. 21498-21503, September 2010.

Ming-Feng Xue received the B.S. degree in Electronic Information Engineering from Anhui University, Hefei, China, in 2005, and the M.S. degree in Electromagnetic Field and Microwave Technology from Shanghai Jiao Tong University, Shanghai, China, in 2008, respectively. He is currently working towards the Ph.D. degree in Electrical and Computer Engineering at the University of Illinois at Urbana-Champaign.

Since 2008, he has been a Research Assistant with the Center for Computational Electromagnetics at the University of Illinois at Urbana-Champaign. His research interests include finite element boundary integral methods, domain decomposition methods, and parallel electromagnetics simulation.

Jian-Ming Jin joined the University of Illinois at Urbana-Champaign in 1993 and is currently the Y. T. Lo Chair Professor of Electrical and Computer Engineering, and Director of the Electromagnetics Laboratory and Center for Computational Electromagnetics. He has authored and co-authored over 200 papers in refereed journals and 20 book chapters. He has also authored The Finite Element Method in Electromagnetics (Wiley, 1st edition 1993, 2nd edition 2002), Electromagnetic Analysis and Design in Magnetic Resonance Imaging (CRC, 1998), Theory and Computation of Electromagnetic Fields (Wiley, 2010), and co-authored Computation of Special Functions (Wiley, 1996), Fast and Efficient Algorithms in Computational Electromagnetics (Artech, 2001), and Finite Element Analysis of Antennas and Arrays (Wiley, 2008). His current research interests include computational electromagnetics, scattering and antenna analysis, electromagnetic compatibility, high-frequency circuit modeling and analysis, bioelectromagnetics, and magnetic resonance imaging. He was elected by ISI as one of the world's most cited authors in 2002.

Recent Advances in FDTD Modeling of Electromagnetic Wave Propagation in the Ionosphere

Bach T. Nguyen, Alireza Samimi, and Jamesina J. Simpson

Department of Electrical and Computer Engineering
University of Utah, Salt Lake City, UT 84112, USA
bach.nguyen@utah.edu, ar.samimi@utah.edu, jamesina.simpson@utah.edu

Abstract ─ Finite-Difference Time-Domain (FDTD) modeling of electromagnetic wave propagation in the Earth-ionosphere waveguide has gained significant interest over the past two decades. Initially, FDTD modeling capabilities were largely limited to two-dimensional models assuming a plasma ionosphere (but incapable of accounting for Faraday rotation), or to three-dimensional global models assuming a simple, isotropic conductivity profile ionosphere. Two algorithm developments have recently advanced the state-of-the-art in electromagnetic wave calculation capabilities in the ionosphere:

(1) A new, three-dimensional efficient FDTD magnetized plasma model.
(2) A Stochastic FDTD (S-FDTD) model of magnetized ionospheric plasma.

The first capability permits longer-distance, higher frequency and higher altitude propagation studies by greatly reducing the memory requirements and simulation time relative to previous plasma models. The second capability introduces for the first time a way of solving for not only mean electromagnetic field values, but also their variance. This paper provides an overview of these two recent advances.

Index Terms ─ Earth, electromagnetic wave propagation, Finite-Difference Time-Domain (FDTD), global propagation, ionosphere, magnetized plasma, plasma, stochastic processes.

I. INTRODUCTION

Many communications, radar, and geophysical studies and applications rely on accurate knowledge of both the state of the ionosphere and the characteristics of Electromagnetic (EM) signal propagation through or reflected by the ionosphere. Satellite communications, the Global Positioning System (GPS), over-the-horizon radar, target direction finding, and ionospheric remote sensing are some example applications. The success of these applications would be greatly improved with the availability of accurate modeling capabilities. Three major challenges, however, must be overcome in order to perform realistic calculations of EM propagation through the ionosphere:

(1) For most applications, the EM wave frequency is high enough such that complex magnetized plasma physics must be accommodated.
(2) The ionosphere exhibits high variability and uncertainty in both time and space.
(3) The ionosphere is comprised of both large and small-scale structures that often need to be accommodated.

Several approximate methods involving ray tracing have been proposed to calculate trans-ionospheric EM wave propagation (e.g., [1-4]); however, these methods are incapable of taking into account the full ionospheric variability and/or terrain between the transmitters and receivers. Further, as the frequency of the EM wave is reduced, their calculated results diverge from the true solution as the physical reality departs from the short-wavelength asymptotic assumptions underlying geometrical optics and ray tracing. Finally, for techniques such as phase screen or Rytov approximations, the calculated results are only valid for weak fluctuations of the ionosphere.

The Finite-Difference Time-Domain (FDTD) method [5,6] is a robust computational EM technique that has been applied to problems across the EM spectrum, from low-frequency geophysical problems below 1 Hz and up into the optical frequency range [6]. The advantages of FDTD for

Earth-ionosphere wave propagation problems include [7,8]:

- As a grid-based method, the 3-D spatial material variations of the ionosphere composition, topography/bathymetry, lithosphere composition, geomagnetic field, targets, and antennas, etc., may be accommodated. Figure 1 for example, shows FDTD-calculated global EM propagation in the Earth-ionosphere waveguide below 1 kHz that includes details of the Earth's topography, bathymetry, oceans, and an (isotropic) conductivity layering in the ionosphere, which is sufficient for propagation below 1 kHz.
- The complex shielding, scattering and diffraction of EM wave may be calculated in a straightforward manner.
- Any number of simultaneous sources may be accommodated (antennas, plane waves, lightning, ionospheric currents, etc.).
- Any number of observation points may be accommodated, and movies may be created of the time-marching propagating waves.
- As a time-domain method, FDTD can model arbitrary time-varying source waveforms, movement of objects, and time variations in the ionosphere.
- Results may be obtained over a large spectral bandwidth via a discrete Fourier transform.
- A fully 3-D magnetized ionospheric plasma FDTD algorithm may be used to calculate all important ionospheric effects on signals, including absorption, refraction, phase and group delay, frequency shift, polarization, and Faraday rotation.

The downside of being able to accommodate all of the above details and physics, is that the FDTD model may quickly become very memory- and time-intensive, and thus, require significant supercomputing resources. This makes real-time calculations difficult or sometimes even impossible to obtain. Further, if the EM frequency is high enough (and the required grid resolution low enough), the required grid size may become computational infeasible, especially for long propagation paths.
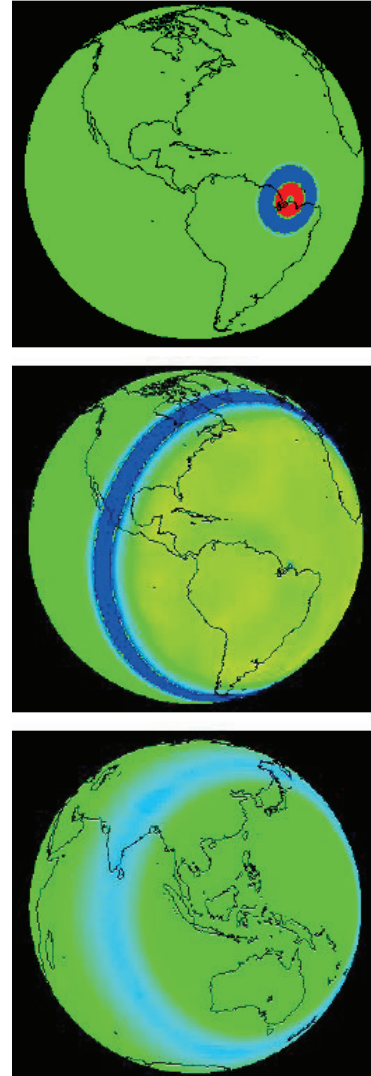
Fig. 1. Snapshot visualizations of round-the-world EM propagation below 1 kHz as calculated by a 3-D FDTD model, including details of the Earth's topography, oceans, and isotropic ionosphere (figure courtesy of [7]).

Although supercomputing capabilities continue to improve, efficient FDTD algorithms are needed to make EM wave propagation modeling in the ionosphere feasible and manageable. Section II provides an overview of the current state of the art for trans-ionospheric EM wave propagation. Section III then describes a new, efficient, 3-D

FDTD magnetized ionospheric plasma model [9] that may be used to greatly advance the current state of the art. Next, Section IV describes a new capability: Stochastic FDTD (S-FDTD) [10,11] magnetized ionospheric plasma modeling [12], which can yield both average as well as variance electric and magnetic fields due to variances and uncertainties in the ionosphere composition. Section V gives an overview of the input parameters that may be used to populate the Earth-ionosphere models. The paper then concludes with a discussion of application possibilities of these models.

II. CURRENT STATE OF THE ART

In 1837, W. R. Hamilton introduced a system of differential equations describing ray paths through general anisotropic media [13]. In 1954, J. Haselgrove proposed that Hamilton's equations were suitable for numerical integration on electronic computers and could provide a means of calculating ray paths in the ionosphere [14]. In 1960, Haselgrove and Haselgrove implemented such a ray-tracing program to calculate "twisted ray paths" through a model ionosphere using Cartesian coordinates [15,1].

In 1975, M. Jones and J. J. Stephenson generated "an accurate, versatile FORTRAN computer program for tracing rays through an anisotropic medium whose index of refraction varies continuously in three dimensions" [16]. This model and variations of it are still in use today, and have been applied to such applications as over-the-horizon radar [1]. Additionally, many other related techniques have now been generated especially for higher frequency scintillation studies, including the phase screen [3] or Rytov approximation, parabolic equation method [2], and even hybrid methods, such as combining the complex phase method and the technique of a random screen [4].

These techniques, however, are only valid under certain conditions. The complex phase method, for example, is only valid for EM wave propagation above 1 GHz. The phase screen or Rytov approximation is only valid for weak fluctuations of the ionosphere. And for all of these methods involving ray tracing, as the frequency of the EM wave is reduced and its wavelength increases, the calculated results diverge from the

true solution as the physical reality departs from the short-wavelength asymptotic assumptions underlying geometrical optics and ray tracing [17].

Ray tracing has been traditionally employed for ionospheric propagation because it is computationally inexpensive; however, it is:

- Incapable of taking into account the variable terrain and structural material properties of and between the transmitters and receivers.

- Restrictive, in that particular methodologies of implementing the ray tracing are limited to certain frequency ranges, and its accuracy depends on the plasma properties.

- It provides solutions at only individual frequencies (steady-state solutions may be obtained; pulses cannot be studied).

An alternative to ray tracing is full-vector Maxwell's equations FDTD modeling, which is not limited by the above issues.

FDTD plasma models have been developed by a number of groups [e.g., 18-20]. However, all of these models require large amounts of computer memory, require very small time steps linked to the plasma parameters rather than the Courant limit, or produce nonphysically spurious electrostatic waves (of numerical origin) due to the spatially non-collocated status of electric fields and current densities, resulting in late-time instabilities [17]. Section III describes an FDTD plasma method [12] that does not suffer from these drawbacks.

To study the performance capability of an example FDTD plasma algorithm, FDTD plasma model results have previously been compared to ray-tracing results for the application of reducing the radar cross-section of targets [21]. Although Chaudhury and Chaturvedi limited their study to unmagnetized, collisional cold plasmas, they conclude that FDTD is more accurate and less restrictive than ray tracing, at the cost of being more computationally demanding. For example, they determine that ray tracing only yields accurate results in their study when both the density scale length is long compared to the free-space wavelength of the incident wave, and when the conduction current is small as compared to the displacement current in the medium. Additionally, ray tracing provides solutions at only individual frequencies (i.e., for sinusoidal steady-state signals, not for pulses).

III. MAGNETIZED IONOSPHERIC PLASMA ALGORITHM

The new FDTD plasma modeling methodology is analogous for each of the electrons, positive ions, and negative ions, so due to space constraints, only electrons will be considered here. In the new formulation [12], the coupled Maxwell's equations-Lorentz equation of motion plasma model may be solved using an algorithm originally used by Borris [22] to calculate the velocity of particles in Particle-In-Cell (PIC) plasma models [23]. PIC codes track trajectories of particles or groups of particles ("super-particles") and solve for electrodynamic fields. By using the Borris approach, the resulting FDTD plasma model is stable while also reducing the memory requirements and the execution time compared to all previous FDTD plasma formulations [12,17].

A. Collisional plasma algorithm

The plasma may be considered collisionless or collisional. This section will consider the more general collisional cases. Under the cold plasma condition and by assuming a known electron density, the momentum equation can be simplified as follows [18]:

$$\frac{\partial \vec{J_e}}{\partial t} + v\vec{J_e} = \epsilon_0 \omega_{pe}^2 \vec{E} + \overrightarrow{\omega_{ce}} \times \vec{J_e}, \qquad (1)$$

where $\vec{J_e}$ is electric current due to electrons, v is the collision frequency, ϵ_0 is the electric permittivity, ω_{pe} is the electron plasma frequency, and $\overrightarrow{\omega_{ce}}$ is the electron gyro-frequency.

The difficulty in solving equation (1) in the collisional regime is that the current density vector is needed at time step $n + \frac{1}{2}$, which is not yet known. In order to solve this issue, a two-step method known as the predictor-corrector method is employed. In the first (predictor) step, the current vector at $n - \frac{1}{2}$ is used to predict the current density at $n + \frac{1}{2}$. In the second (corrector) step, the predicted current density vector from the first step is used and all the equations are solved again. A second, new current density vector is found at $n + \frac{1}{2}$, that is known as the corrector current density vector. The average of the predicted current density vector and the corrector current density vector at $n + \frac{1}{2}$ is used for current density vector at $n + \frac{1}{2}$. The predictor-corrector method is second order

accurate [24,25].

Equation (1) in discrete form in the predictor step [12,22] is as follows:

$$\frac{\vec{J}_{e,p}^{n+\frac{1}{2}} - \vec{J}_e^{n-\frac{1}{2}}}{\Delta t} + v\vec{J}_e^{n-\frac{1}{2}}$$
$$= +\epsilon_0 \omega_{pe}^2 \vec{E}^n 0 - \omega_{C_e}^2$$
$$\times \left(\frac{\vec{J}_{e,p}^{n+\frac{1}{2}} + \vec{J}_e^{n-\frac{1}{2}}}{2} \right). \qquad (2)$$

In equation (2), it appears that the current density components should be collocated with the electric field component. However, in the time domain, the current densities are solved out of sync with the electric fields, which are solved at each integer time step; i.e., (n). Instead, the current densities are solved at the same time step as the H-fields (or at each half time step); i.e., $(n + \frac{1}{2})$. In order to simplify equation (2), the E-field should be incorporated into the current vector term. We define two auxiliary current density components [12,22] as follows:

$$\vec{J}^+ = \vec{J}_{e,p}^{n+\frac{1}{2}} - \frac{\Delta t\epsilon_0 \omega_{pe}^2 \vec{E}^n}{2} + \frac{\Delta t v \vec{J}_e^{n-\frac{1}{2}}}{2}, \qquad (3)$$

$$\vec{J}^- = \vec{J}_e^{n-\frac{1}{2}} + \frac{\Delta t\epsilon_0 \omega_{pe}^2 \vec{E}^n}{2} - \frac{\Delta t v \vec{J}_e^{n-\frac{1}{2}}}{2}. \qquad (4)$$

The cross product does not change the energy; therefore, $|J^+| = |J^-|$. However, the direction of the vector is changed. Figure 2 demonstrates the rotation of the current density vector around $\overrightarrow{\omega_{C_e}}$ that is for simplicity (only for the figure) assumed to be perpendicular to the current density components. The direction of the $\overrightarrow{\omega_{C_e}}$ and the B-field is out of the paper.
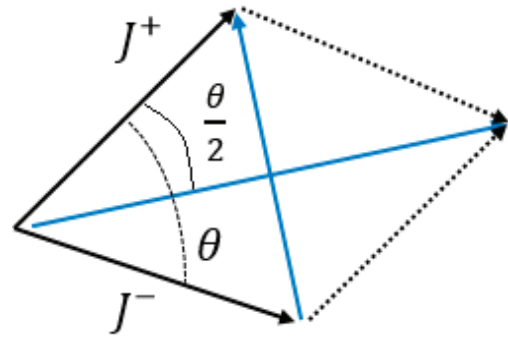

Fig. 2. Rotation of the current vector around $\overrightarrow{\omega_{C_e}}$. Figure adapted from [23].

From Fig. 2, the angle of rotation is:

$$\frac{\theta}{2} = \tan^{-1}\frac{\vec{J}^+ - \vec{J}^-}{\vec{J}^+ + \vec{J}^-} = \tan^{-1}\frac{|\overrightarrow{\omega_{Ce}}|\Delta t}{2}. \qquad (5)$$

The sampling frequency should be twice the electron gyro-frequency to accurately model it. Therefore, $\Delta t < \frac{\pi}{\omega_{ce}}$, which means $\theta \leq 115°$. For smaller angles the results are more precise. The $\vec{J}^+$ can be found in four steps as follows [12,22,23]:

$$\vec{J}_0 = \vec{J}^- \times \vec{t}, \qquad (6.1)$$
$$J_1 = \vec{J}^- + \vec{J}_0, \qquad (6.2)$$
$$\vec{J}_2 = \vec{J}_1 \times \vec{s}, \qquad (6.3)$$
$$\vec{J}^+ = \vec{J}^- + \vec{J}_2, \qquad (6.4)$$

where $\vec{t} = -\frac{\overrightarrow{\omega_{Ce}}}{|\overrightarrow{\omega_{Ce}}|}\tan(\frac{\theta}{2})$, and $\vec{s} = \frac{\overrightarrow{\omega_{Ce}}}{|\overrightarrow{\omega_{Ce}}|}\sin(\theta)$.

As part of the predictor-corrector method, equation (1) is discretized in the corrector step as follows [12,22]:

$$\frac{\vec{J}_{e,c}^{n+\frac{1}{2}} - \vec{J}_e^{n-\frac{1}{2}}}{\Delta t} + \nu\vec{J}_{e,p}^{n+\frac{1}{2}}$$
$$= +\epsilon_0\omega_{pe}^2\vec{E}^n - \omega_{Ce}^2$$
$$\times \left(\frac{\vec{J}_{e,c}^{n+\frac{1}{2}} + \vec{J}_e^{n-\frac{1}{2}}}{2}\right). \qquad (7)$$

The auxiliary current density vectors are then defined as [12,22]:

$$\vec{J}^+ = \vec{J}_{e,c}^{n+\frac{1}{2}} - \frac{\Delta t\epsilon_0\omega_{pe}^2\vec{E}^n}{2} + \frac{\Delta t\nu\vec{J}_{e,p}^{n+\frac{1}{2}}}{2}, \qquad (8)$$

$$\vec{J}^- = \vec{J}_e^{n-\frac{1}{2}} + \frac{\Delta t\epsilon_0\omega_{pe}^2\vec{E}^n}{2} - \frac{\Delta t\nu\vec{J}_{e,p}^{n+\frac{1}{2}}}{2}. \qquad (9)$$

The final current vector is [12,22]:

$$\vec{J}_e^{n+\frac{1}{2}} = \frac{\vec{J}_{e,p}^{n+\frac{1}{2}} + \vec{J}_{e,c}^{n+\frac{1}{2}}}{2}. \qquad (10)$$

The maximum allowed time step that may be used depends on the electron gyro frequency; i.e., $\Delta t < \frac{\pi}{\omega_{ce}}$.

Several validation tests are performed in [Samimi and Simpson, submitted] to demonstrate the accuracy and capability of the newly developed FDTD plasma model. Section III (B) below provides an example validation, and Section III (C) summarizes the performance of this new model.

B. Example validation

As an example validation, the propagation of an electromagnetic wave inside a small plasma spherical waveguide is investigated. This simulation case is chosen so that propagation over a short distance may be modeled and compared to theory. It serves as a high-resolution validation of the global FDTD plasma model of [26,12]. Additional validation cases are provided in [12].

The spherical waveguide has an internal radius 2.673 m and external radius 3.6978 m. A magnetic field is considered in the south-north direction and its strength is $B_0 = 0.06\ T$. The electron density is $n_e = 10^{18}\ 1/m^3$. The source of the electromagnetic wave is located at $30°\ S$ and propagation toward the equator is examined. The source creates a linearly polarized electromagnetic plane wave polarized in the radial (r)-direction and having a Gaussian time-waveform according to:

$$E_{source} = \exp\left(-\frac{(t-50\Delta t)^2}{2(7\Delta t)^2}\right). \qquad (11)$$

This pulse is expected to excite the R-wave and L-wave as well as low frequency whistler mode. The whistler mode is part of the R-wave dispersion relation that can propagate at frequencies less than the electron gyro-frequency.

Figure 3 shows the time domain electric field in the r-direction; i.e., $E_r(t)$, 40 cells (approximately 40 mm) from the source. The low frequency whistler mode arrives at the observation point at around 1.2 ps. Figure 4 shows the power spectrum of the electric field corresponding to the time-waveform of Fig. 3. The L-wave cutoff frequency, ω_L, the R-wave cutoff frequency, ω_R, and the whistler mode with frequency band less than the electron cyclotron frequency ($< \omega_{ce}$) are apparent in the figure. These results are also in very good agreement with plasma theory and the simulation results of the previous anisotropic model [26].

Note, that in this validation test, the time step value for solving Maxwell's equations is chosen according to the Courant stability condition and is $\Delta t = 1.5$ ps. This time step value corresponds to a rotation angle $\theta = 0.9°$ that yields a numerical electron gyro-frequency error of less than 0.5%. Therefore, there is no need to use a different time step for solving the current equation compared to

Maxwell's equations.
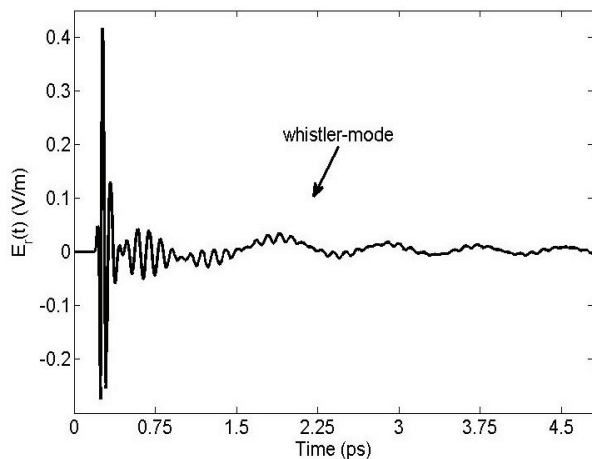
Fig. 3. Time-domain electric-field waveform in the r-direction recorded ~40 mm from the source along the magnetic field (figure courtesy of [12]).
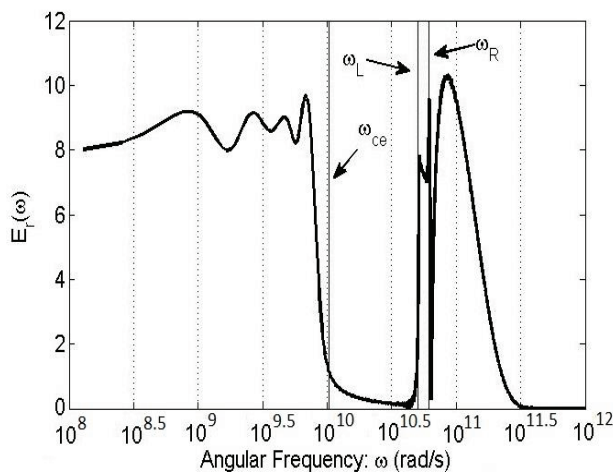
Fig. 4. Power spectrum of the electric field in the r-direction recorded ~40 mm from the source along the magnetic field line (figure courtesy of [12]).

C. Summary of performance

The advantages of the new FDTD plasma model [12] over the previous formulation of [17] are as follows:

- It permits the use of two different time steps for solving the current equation vs. the Maxwell's equations. The previous anisotropic model did include this capability, and so for some cases the time-step requirements of the current density solutions could drastically slow down the solutions to the Maxwell's equations. As

such, obtaining solutions for cases involving high collision frequencies was nearly impossible due to the necessary long computational time.

- It is faster than the previous model. Depending upon the size of the time step needed to solve the current equation, the new algorithm is more than 50 percent faster than the previous version.
- Implementation of the algorithm is much simpler and no matrix equation must be solved.
- The memory requirements are drastically less than for the previous formulation (3 additional real numbers are stored per cell relative to traditional FDTD compared to 9 additional real numbers stored per cell as for the previous plasma formulation; also, it does not require storage or re-calculation of a coefficient matrices of size at least 6x6 at every grid cell).

The only disadvantage of the new algorithm is that for simulating wave propagation in dense plasma, the stability condition can be smaller than Courant limit. The plasma frequency puts an additional restriction on the maximum allowable time step value. Therefore, either the Courant condition or a $dt < \frac{0.87}{\omega_{pe}}$, whichever is smaller, should be chosen for the time step for Maxwell's equations.

IV. STOCHASTIC FDTD

A second recent development that has advanced time-domain modeling of ionospheric propagation is a new stochastic FDTD plasma model that solves for mean as well as variance electromagnetic fields due to uncertainties or variances in the ionosphere composition. The variability of the ionosphere renders many propagation problems too complex to be solved using a deterministic formulation. The structure of the ionosphere can depend not only on the altitude, time of day, and season, but also on the latitude, longitude, sun spot cycle, and occurrence of space weather events. A useful approach to such a highly complex problem is to consider it as a random medium problem.

Numerical EM techniques, however, typically use only average (mean) values of the constitutive parameters of the materials and then solve for expected (mean) electric and magnetic fields. The Monte Carlo method is a well-established and widely-used brute force technique for evaluating random medium problems via multiple realizations

[10]. Depending on the nature of the statistical correlation, a random medium problem may require tens or hundreds of thousands of realizations. This yields an extremely inefficient brute force approach, particularly for 2-D and 3-D problems, and therefore is rarely used in EM modeling.

Stochastic FDTD (S-FDTD) is an efficient formulation that runs the ensemble averages in a single realization scheme [10,11]. S-FDTD was recently extended to EM wave propagation in the ionosphere by extending the stochastic variables to both Maxwell's equations and the Lorentz equation of motion [9]. The electric fields, magnetic fields, current densities, electron/ion densities and collision frequencies all are treated as random variables with their own statistical variation. The resulting mean and variance calculations of the EM fields and current densities provides new capabilities; for example, the ability to determine the confidence level that a communications/remote sensing/radar system will operate as expected under abnormal ionospheric conditions. It may also be useful in a wide variety of geophysical studies.

The advantage of S-FDTD is that it requires only about twice as much computer simulation time and memory as a traditional FDTD simulation regardless of the number of random variables. On the other hand, its limitation is that it can only bound the field variances according to a best estimate approximation for the cross correlation coefficients.

In [9], an S-FDTD method is developed for the previous (less efficient) magnetized plasma algorithm of [17]. Recently, a more efficient magnetized plasma model was developed [12] as presented in Section III of this paper. In the remainder of this section, general guidelines are provided for extending the S-FDTD approach to the more efficient magnetized plasma model of Section III and [12]. The general approach is analogous to that of [9].

A. Mean field equations

Using the Delta method [27], the average (or expected) EM fields and current density values may be found by solving Maxwell's equations and the current equation while using mean (average) values of the variables [10]. For the S-FDTD magnetized cold plasma model, the equations for the mean values of the EM fields and current densities are of the same form as for those of the regular 3-D FDTD magnetized cold plasma model. Thus, the mean EM field and current density values are found by using the mean plasma frequency of ω_{Pe}, or equivalently, the mean of electron density n_e.

B. Variance field equations

The variance fields may also be derived by using the delta method and the statistical values. When solving only Maxwell's equations, the variance field equations may be solved separately from the mean field equations no matter the dimensionality of the problem [10]. However, in the 3-D magnetized cold plasma model, the momentum equation (1) is coupled to Maxwell equations, which leads to a complicated but linear system. As a result, the electric field and current density variances must be computed simultaneously. When variance equations are derived, covariances are needed for the E, H fields and current density J_e in both time and space. Equation (1) also relates the current density to the collision frequency and the electric field to the plasma frequency of the ionosphere, resulting in additional covariance terms of between the current density and collision frequency, and the electric field and plasma frequency. For S-FDTD method, a critical step is to approximate these correlation coefficients, which controls the accuracy of the algorithm.

Figure 5 shows a diagram of the iteration process for each time step of the S-FDTD method. What is changed from regular FDTD updating is the addition of the calculation of the variances after the mean values are obtained. Therefore, the running time as well as the memory required for S-FDTD is roughly double that needed for traditional FDTD (and double that for the regular FDTD plasma model). Also, since both the mean fields and their variances behave like waves, both require boundary conditions. Thus, an absorbing boundary condition is needed for the E, H, and J_e mean values as well as for their variances. In [9], Mur's boundary conditions are used because that boundary condition was found to provide good absorption regardless of the magnetic field direction [28].
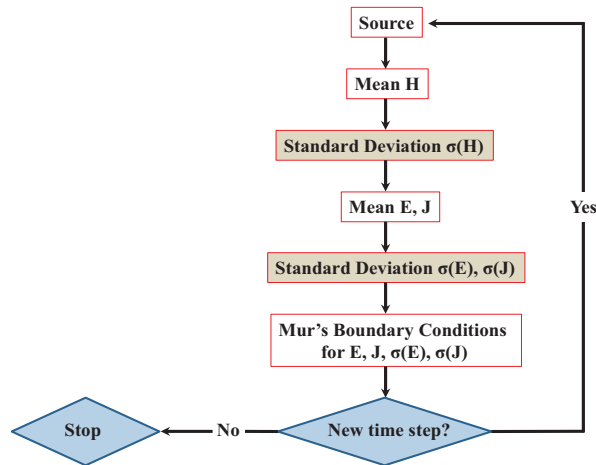
Fig. 5. S-FDTD flow chart (figure adapted from [10]).

V. INPUT TO THE FDTD MODELS

Since the FDTD model may account for highly detailed structures and materials, it is useful to populate the FDTD grid with realistic data. The Earth's topography and bathymetry data may be obtained; for example, from the National Oceanic and Atmospheric Administration (NOAA) National Geophysical Data Center (NGDC). The Earth's magnetic field data and its direction and amplitude variation with position may be obtained from the International Geomagnetic Reference Field (IGRF).

For an isotropic conductivity profile ionosphere to be used in lower frequency EM propagation models, relatively simple profiles based on measurements and analytical calculations may be used, such as an exponential conductivity profile [29] or a knee profile [30]. To model an anisotropic magnetized plasma ionosphere to be used in higher frequency EM propagation models, electron and ion densities and collision frequencies and their variation with time and position may be obtained from the International Reference Ionosphere (IRI) and other sources. IRI has recently been expanded to include stochastic information about the ionosphere composition (e.g., [31]).

VI. CONCLUSION

This paper provided an overview of two recent advances in FDTD EM wave propagation modeling in the ionosphere:
(1) A new, efficient 3-D magnetized ionospheric plasma model.

(2) A stochastic FDTD model of ionospheric plasma.
The combination of these models provides the capability to model high frequency EM wave propagation over longer distances than previously possible, while also solving for not only mean but also variance electric and magnetic fields due to uncertainties or variances in the ionosphere. Applications of these models range from remote sensing to communications and space weather.

ACKNOWLEDGMENTS

REFERENCES

[1] S. C. Aune, "Comparison of ray tracing through ionospheric models," *Master's Thesis, Department of the Air Force, Air Force Institute of Technology, Wright-Patterson Air Force Base*, Ohio, March 2006.

[2] K. C. Yeh and C. Liu, "Radio wave scintillations in the ionosphere," *Proc. of the IEEE*, vol. 70, no. 4, 1982.

[3] C. L. Rino, "A power law phase screen model for ionospheric scintillation: 1. weak scatter," *Radio Science*, vol. 14, no. 6, pp. 1135-1145, 1979.

[4] V. E. Gherm, N. N. Zernov, and H. J. Strangeways, "Propagation model for transionoshperic fluctuating paths of propagation: simulator of the transionospheric channel," *Radio Science*, vol. 40, RS1003, doi:10.1029/2004RS003097, 2005.

[5] K. S. Yee, "Numerical solution of initial boundary value problems involving maxwell's equations in isotropic media," *IEEE Trans. Antennas Propagat.*, vol. AP-14, pp. 302-307, 1966.

[6] A. Taflove and S. C. Hagness, "Computational electromagnetics: the finite-difference time-domain (FDTD) method," *Artech House*, 3rd ed., 2005.

[7] J. J. Simpson and A. Taflove, "A review of progress in FDTD maxwell's equations modeling of impulsive sub-ionospheric propagation below 300 kHz," *IEEE Trans. Antennas & Propagation*, vol. 55, no. 6, pp. 1582-1590, 2007.

[8] J. J. Simpson, "Current and future applications of 3-D global earth-ionosphere models based on the full-vector maxwell's equations FDTD method," *Surveys in Geophysics*, vol. 30, no. 2, pp. 105-130, 2009.

[9] B. Nguyen, C. Furse, and J. J. Simpson, "A 3-D stochastic FDTD model of electromagnetic wave

propagation in magnetized ionosphere plasma," *IEEE Trans. Antenna Propagat.*, (submitted).

[10] S. M. Smith and C. Furse, "Stochastic FDTD for analysis of statistical variation in electromagnetic fields," *IEEE Trans. Antennas Propagat.*, vol. 60, no. 7, pp. 3343-3350, July 2012.

[11] T. Tan, A. Taflove, and V. Backman, "Single realization stochastic FDTD for weak scattering waves in biological random media," *IEEE Trans. Antennas Propagat.*, vol. 61, pp. 818-828, 2013.

[12] A. Samimi and J. J. Simpson, "An efficient 3-D FDTD model of electromagnetic wave propagation in magnetized plasma," *Trans. Antenna Propagat.*, (submitted).

[13] W. R. Hamilton, "Third supplement to treatise on geometrical optics," 1931.

[14] J. Haselgrove, "Ray theory and a new method for ray tracing," *Report of Conference on the Physics of the Ionosphere, London: London Physical Society*, pp. 355-364, 1954.

[15] C. B. Haselgrove and J. Haselgrove, "Twisted ray paths in the ionosphere," *Proc. Phys. Soc. London*, vol. 75, 357-361, 1960.

[16] R. M. Jones and J. J. Stephenson, "A versatile three-dimensional ray tracing computer program for radio waves in the ionosphere," *Institute for Telecommunication Sciences, Office of Telecommunications, US Dept. of Commerce, Springfield: National Technical Information Service*, 1975.

[17] Y. Yu and J. J. Simpson "An E-J collocated 3-D FDTD model of electromagnetic wave propagation in magnetized cold plasma," *IEEE Trans. Antenna Propagat.*, vol. 58, no. 2, pp. 469-478, 2010.

[18] W. Hu and S. A. Cummer, "An FDTD model for low and high altitude lightning-generated EM fields," *IEEE Trans. Antennas Propag.*, vol. 54, pp. 1513-1522, May 2006.

[19] J. H. Lee and D. K. Kalluri, "Three dimensional FDTD simulation of electromagnetic wave transformation in a dynamic inhomogeneous magnetized plasma," *IEEE Trans. Antennas Propag.*, vol. 47, pp. 1148-1151, 1999.

[20] M. Thèvenot, J. P. Bérenger, T. Monedière, and F. Jecko, "A FDTD scheme for the computation of VLF-LF propagation in the anisotropic earth-ionosphere waveguide," *Ann. Télécommun.*, vol. 54, pp. 297-310, 1999.

[21] B. Chaudhury and S. Chaturvedi, "Comparison of wave propagation studies in plasmas using three-dimensional finite-difference time-domain and ray tracing methods," *Physics of Plasmas*, vol. 13, 123-302, 2006.

[22] J. P. Boris, "The acceleration calculation from a scalar potential," *Plasma Physics Laboratory, Princeton University*, MATT-152, March 1970.

[23] C. K. Birdsall and A. B. Langdon, "Plasma physics via computer simulation," *Institute of Physics*, New York, 1991.

[24] G. A. Sod, "A survey of several finite difference methods for systems of nonlinear hyperbolic conservation laws," *Journal of Computational Physics*, vol. 27, no. 1, pp. 1-31, 1978.

[25] R. Garcia and R. A. Kahawita, "Numerical solution of the st. venant equations with the maccormack finite-difference scheme," *Int. J. Numer. Meth. Fluids*, vol. 6, pp. 259-274, 1986.

[26] Y. Yu, J. Niu, and J. J. Simpson, "A 3-D global earth-ionosphere FDTD model including an anisotropic magnetized plasma ionosphere," *IEEE Antennas and Propagation*, vol. 60, no. 7, pp. 3246-3256, 2012.

[27] G. Casella and R. L. Berger, "Statistical inference," 2nd ed., *Thompson Learning*, 2002.

[28] Y. Yu and J. J. Simpson, "A magnetic field-independent absorbing boundary condition for the FDTD E-J collocated magnetized cold plasma algorithm," *IEEE Antenn. Wireless Propagat. Letters*, vol. 10, pp. 294-297, 2011.

[29] P. Bannister, "ELF propagation update," *IEEE J. Ocean. Eng.*, vol. 0E-9, no. 3, pp. 179-188, 1984.

[30] H. Yang and V. P. Pasko, "Three-dimensional finite-difference time-domain modeling of the earth-ionosphere cavity resonances," *Geophys. Res. Lett.*, vol. 32, no. L03114, 2005.

[31] O. Oladipo, J. Adeniyi, S. Radicella, and I. Adimula, "Variability of the ionospheric electron density at fixed heights and validation of IRI-2007 profiles prediction at ilorin," *Advances in Space Research*, vol. 47, no. 3, pp. 496-505, February 2011.

Bach T. Nguyen was born in Hanoi, Vietnam. He received his B.Eng. and M.Eng. degrees in Electrical Engineering from National Defense Academy of Japan, Yokosuka, Kanagawa, Japan, in 2007 and 2009, respectively. From 2010 to 2012, he was with the Vietnam Military Academy of Science and Technology, Hanoi, Vietnam. Currently, he is pursuing his Ph.D. degree in the Electrical and Computer Engineering Department, University of Utah, Salt Lake City, UT. His research interests include computational electromagnetics, RF/Microwave technology, RF-IC, and liquid crystal. His current research focuses on stochastic FDTD simulation of electromagnetic wave propagation in the ionosphere.

Alireza Samimi received his B.S. degree in Electrical Engineering from Shiraz University, Shiraz, Iran in 2005, his M.S. degree in Electrical Engineering from University of Tabriz, Tabriz, Iran, in 2008, and his Ph.D. degree in Electrical Engineering from Virginia Tech in 2013.His research interests include physics of the upper atmosphere, Finite-Difference Time-Domain (FDTD) solution of Maxwell's equations and its applications in simulating wave propagation in the Earth-Ionosphere-Magnetosphere system, active modification of the ionosphere and particle-in-cell computational modeling of plasma instabilities.

He is currently working as a Postdoctoral Fellow in the Department of Electrical and Computer Engineering, University of Utah, Salt Lake City. He participated in two experimental research campaigns at High Frequency Active Auroral Research Program (HAARP) facilities to study generation mechanism of the narrow-band stimulated electromagnetic emission spectral features excited during ionospheric heating near second electron gyro-harmonic. Samimi has been a member of American Geophysical Union (AGU) since 2010 and IEEE since 2011.

Jamesina J. Simpson received her B.S. and Ph.D. degrees in Electrical Engineering from Northwestern University, Evanston, IL, in 2003 and 2007, respectively. In 2007, she joined the Electrical and Computer Engineering Department, University of New Mexico, Albuquerque, as a tenure-track Assistant Professor. As of July 2012, she is an Associate Professor in the Electrical and Computer Engineering Department, University of Utah, Salt Lake City. Her research lab encompasses the application of the full-vector Maxwell's equations Finite-Difference Time-Domain (FDTD) method to a wide variety of scientific and engineering applications across the electromagnetic spectrum.

Simpson is a recipient of the National Science Foundation (NSF) Graduate Research Fellowship and the IEEE AP-S and MTT-S Graduate Research Awards. In 2010, she received an NSF CAREER award, and in 2012 she received the Donald G. Dudley, Jr. Undergraduate Teaching Award of the IEEE AP-S. From 2010-2014, Simpson was an Associate Editor of IEEE Transactions on Antennas and Propagation.

Phi Coprocessor Acceleration Techniques for Computational Electromagnetics Methods

Xiaoling Yang and Wenhua Yu

2COMU, Inc.
4031 University Dr., Suite 100, Fairfax, VA 22030, USA
ybob@2comu.com, wenyu@2comu.com

Abstract — In this paper, we introduce the architecture of Intel Xeon Phi coprocessor, programming and acceleration techniques in the computational electromagnetic methods. This paper describes how to develop the acceleration codes based on the Intel Xeon® Phi coprocessors in the parallel format for general computational electromagnetics methods. We also present management of the cores and threads in the Intel Xeon Phi coprocessors to accelerate computational electromagnetics simulations. The Intel Phi coprocessor can be used as a regular CPU and shares the same source codes for Intel Xeon E3 and E5 CPUs with a different compilation option. The examples shown here are for acceleration of the parallel FDTD methods. The Intel Xeon Phi coprocessor is not a GPU and is a general hardware acceleration simulation platform.

I. INTRODUCTION

Intel Xeon Phi coprocessor is a general numerical acceleration platform, which can be used to accelerate the computational electromagnetics methods such as FDTD [1-4], FEM [5], MoM [6], and so on. The Intel Xeon Phi coprocessor (price from $1,600 to $4,500) includes 60 compute cores, four hardware threads per core, two pipelines, 512-bit SIMD instructions, 32 512-bit wide vector registers which hold 16 singles or 8 doubles, up to 16 GB 16-channel GDDR5 RAM, and 320 GB/s memory bandwidth. One motherboard can hold maximum four Intel Xeon Phi coprocessors, as shown in Fig. 1.

A Phi coprocessor card can be handled as a Linux node, and each one has an on-board flash device that loads the coprocessor OS (Operating System) on boot and can be monitored by an optional cluster monitoring software Ganglia (http://ganglia.info/) [7,8], as shown in Fig. 2. The Phi coprocessor programming uses the Intel MIC (Many Integrated Core) instructions. One code can be executed on the host CPU, on both the host CPU and Phi coprocessor at the same time, or on the Phi coprocessor only that is totally different from GPU, as shown in Fig. 3.
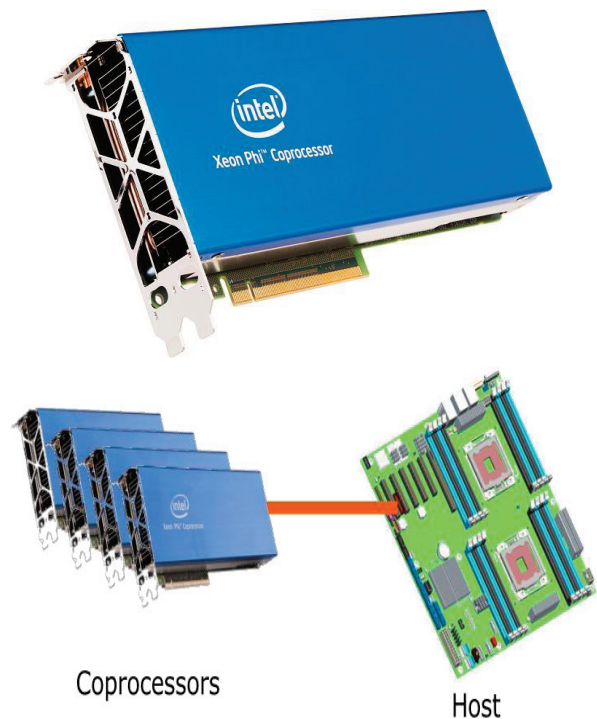
Fig. 1. Intel Xeon Phi coprocessor and cluster artwork (www.intel.com) Copyright©Intel.
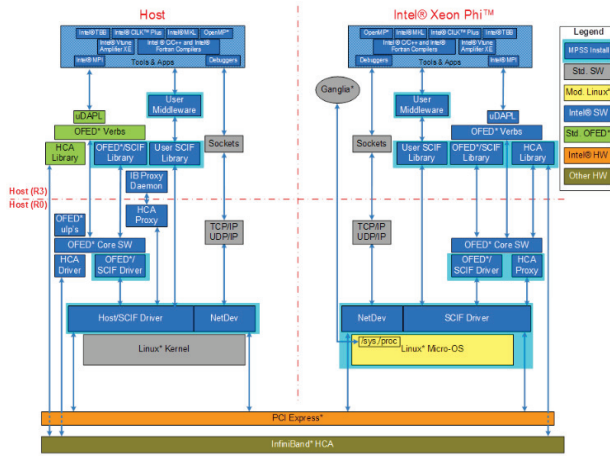
Fig. 2. Intel Xeon Phi coprocessor architecture (www.intel.com) Copyright©Intel.
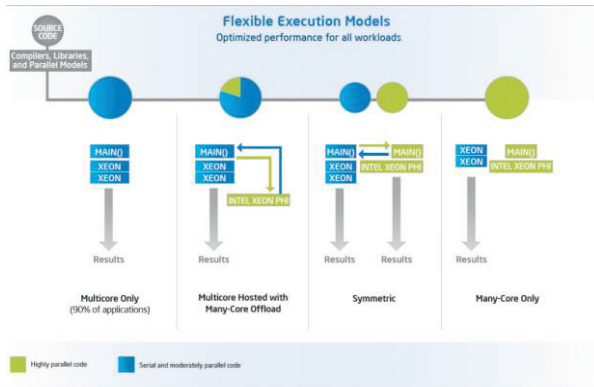
Fig. 3. Code processing with the host CPU and Phi coprocessor (www.intel.com) Copyright©Intel.

II. CODE DEVELOPMENT TECHNIQUES

The code processing on the Phi coprocessor has four levels; namely, card level, core level, thread level and vector unit level. The code excitation can be assigned to different cards, cores, threads and vector units, as shown in Fig. 4. We use the parallel FDTD method to demonstrate how to develop the parallel code on the Phi coprocessor. If the storage of a 3-D array in the memory is continuous along the z-direction, we divide the data into 60 blocks in the x-y plane, which is equal to the number of cores in the Phi coprocessor. Select one column in an individual block and assign it to two threads, all cores will be coalesced and each thread will work on one-half column of the selected data. The vector unit will work on 16 adjacent data at the same time

and generate 16 results in each cycle. The job assignment procedure is shown in Fig. 5.

Fig. 4. A sample core processing on the Intel Xeon Phi coprocessor.
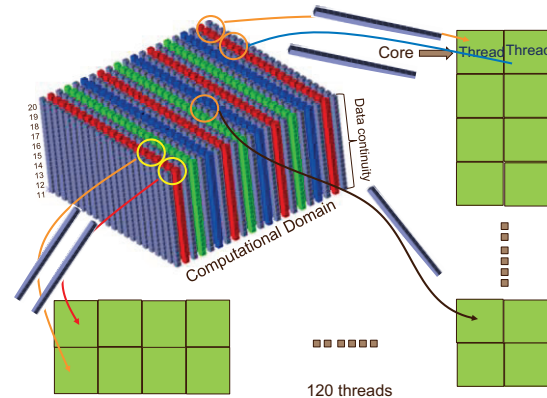
(a) Job assignment for threads on Phi coprocessor
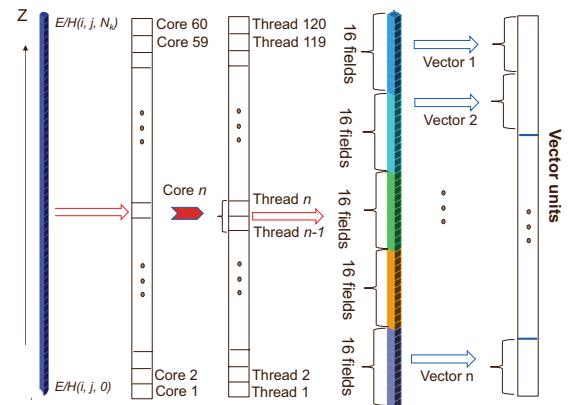
(b) Job assignment strategy on Phi coprocessor

Fig. 5. Job assignment method for the parallel FDTD method.

In both the Finite Element Method (FEM) and the Method of Moments (MoM), solving matrix equations is most time consuming. Now, we investigate how to use the Phi coprocessor to calculate the multiplication of two matrixes. We begin with the following equation:

$$C_{nl} = A_{nm}B_{ml}, \qquad (1)$$

where C_{nl}, A_{nm} and B_{ml} are matrixes and the subscripts indicate the number of rows and columns of the corresponding matrixes. If we define a 1-D array and map the 1-D array to a 2-D array that is used to allocate memory for the matrixes in (1), one matrix with 5×3 elements can be mapped from a 1-D array with 15 elements, as shown in Fig. 6. It is obvious from Fig. 6, that the data of the matrix C is continuous along its row index m.

If we follow the idea described above to allocate the matrixes A and B, the column of matrix B will not be continuous, in turn, the multiplication operation of the matrixes A and B is very low efficient. It is a well-known fact that we need to make a transpose of B to speed up the matrix multiplication. If we calculate the matrix multiplication on the Phi coprocessor, it is observed that the calculation for the smaller A and B is much faster than the larger A and B. This happens because the elements of smaller A and B can be held in the cache to increase the cache hit rate. The cache hit rate becomes lower when the matrixes A and B become larger.
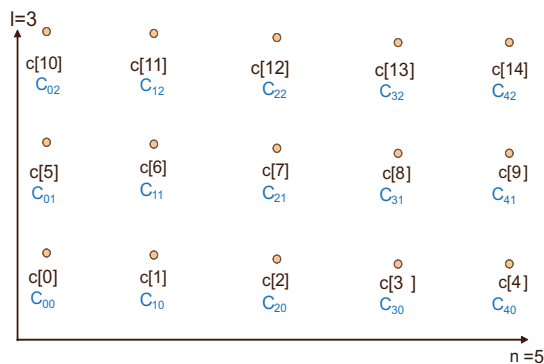
Fig. 6. Mapping relationship from a 1-D array to a 2-D array.

Now we use the following pseudo-code to explain the programming techniques on the Phi coprocessor. A 5110P Phi coprocessor includes 60 cores and 240 hardware threads. We need to use OpenMp to split the task to smaller pieces based on the number of threads (nThreads=240 for 5110P Phi model). We split the matrix A to be the $nn\times mm$ blocks and the matrix B to be the $mm\times ll$ blocks so that the matrix C to be the $nn\times ll$ blocks. The block size of the matrix C is 16×16; the block size of the matrix A is 16×64 and the block size of matrix B is 64×16. It ensures that the data is continuous in memory. The index k (the column of matrix A and row of matrix B) is normalized by 16 based on the 512-bit SIMD instruction and the constant nBlockSizeBySIMD is 4 in this case for the better code performance.

Code segment; use the standalone format and run the code on Phi:

```
#pragma omp parallel for
//Use OpenMP on Phi coprocessor
for (iThread=0; iThread<nThreads;
iThread ++) {
//240 hardware threads
for (t=iThread; t<nn * ll; t+=nThreads)
{
//t is block index
for (k=0; k<mm * nBlockSizeBySIMD;
k+=nBlockSizeBySIMD) {
//k is the column index of matrix A and the row index of
//matrix B counted by SIMD width
for (i=i0; i<i1; i ++) {
//i0(t) and i1(t) are index in matrix  for the tth block
for (j=j0; j<j1; j ++) {
//j0(t) and j1(t) are index in matrix  for the tth block
v=_mm512_set1_ps(0.0);
//initialize the variable v
v=_mm512_fmadd_ps(vA[i][k],vB[j][k],v);
//calculate A(i,k)*B(j,k) + v
v=_mm512_fmadd_ps(vA[i][k+1],
vB[j][k+1], v);
//calculate A(i,k+1)*B(j,k+1) + v
v=_mm512_fmadd_ps(vA[i][k+2],
vB[j][k+2], v);
//calculate A(i,k+2)*B(j,k+2) + v
v=_mm512_fmadd_ps(vA[i][k+3],
vB[j][k+3], v);
//calculate A(i,k+3)*B(j,k+3) + v
C[i][j] +=_mm512_reduce_add_ps(v);
// Summate elements of the vector v and add to C[i][j]
    }
   }
  }
 }
}
```

For two matrixes A and B with 2048×2048 elements, the perfromance of the solving matrix without the domain decomposition technique on an Intel Xeon E5 2640 v2 Ivy-Bridge CPU is 0.63 seconds, but the perfromance with the domain

decomposition technique on the same CPU is 0.4 seconds. The perfromance of the solving matrix with the domain decomposition technique on the Intel Xeon Phi Coprocessor 5100P is 0.15 seconds.

III. NUMERICAL RESULTS

In this section, we use the parallel FDTD code based on the Phi coprocessor to demonstrate the performance of the Phi coprocessor. The host computer incudes two Intel Xeon E5-2640 v2 CPUs with 32 GB DDR3 RAM and one 5110P Phi coprocessor is mounted on the host through a PCI-16 slot. The Phi coprocessor is installed with 8 GB GDDR5 RAM. We use a typical example, an empty box truncated by the PEC boundary, to demonstrate the performance of the Phi coprocessor. The problem size we first test is 1.29 GB and the performance is 1,200 million cells per second. The performance on a single Phi card can be easily achieved to 1,200 million cells per second and the performance increases to 1,350 million cells per second when the problem size increases to 7.2 GB, as shown in Fig. 7.
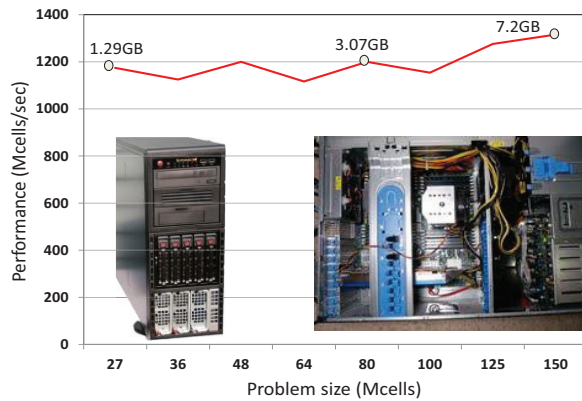
Fig. 7. Performance of the 5110P Phi coprocessor for the parallel FDTD code with the regular size of problems.

In the MIC instruction set, a single instruction allows us to perform a multiplication and one addition; for example, we have three variables A, B and C, the result of multiplication A and B and then addition with C can be reached by on operation in the MIC instruction:

$$D = A \times B + C. \tag{2}$$

The feature in (2) is called FMA (Fused Multiply-Add) in the MIC instruction. We demonstrate the performance of Phi coprocessor for the small problems such as 0.2 million cells and check the performance of the FMA feature on the FDTD code. The result is plotted in Fig. 8, and we cannot observe the performance down significantly for the small problems and the performance improvement from the FMA feature neither from Fig. 8.
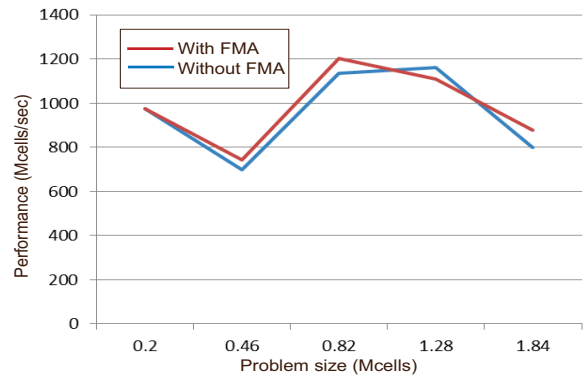
Fig. 8. Performance of the 5110P Phi coprocessor for the parallel FDTD code with the small size of problems.

IV. CONCLUSIONS

Intel Xeon Phi coprocessor is used to accelerate the electromagnetic simulations using its many core architecture and 512-bit vector units. Unlike the GPU acceleration, the Intel Xeon Phi coprocessor acceleration is more general and supports OpenMp. If a source code is compiled on an Intel Xeon E3 or E5 CPU, it can be run directly on a Phi coprocessor with a compilation option "-mmic".

REFERENCES

[1] A. Taflove and S. Hagness, "Computational electromagnetics: the finite-difference time-domain method," 3rd ed., *Artech House*, Norwood, MA, 2005.

[2] W. Yu, X. Yang, Y. Liu, et al., "Parallel finite-difference time-domain method," *Artech House*, Norwood, MA, 2006.

[3] W. Yu, X. Yang, and W. Li, "VALU, AVX, GPU acceleration techniques for parallel finite difference time domain methods," *SciTech Publisher Inc.*, Raleigh, NC, 2013.

[4] A. Elsherbeni and V. Demir, "The finite difference time domain method for electromagnetics: with MATLAB simulations," *SciTech Publisher Inc.*, Raleigh, NC, 2009.

[5] J. M. Jin, "The finite element method in electromagnetics," (2nd edition), *New York: John Wiley & Sons*, 2002.

[6] A. Peterson and R. Mittra, "Computational methods for electromagnetics," *Wiley-IEEE Press*, 1997.

[7] "Intel® Xeon Phi™ coprocessor: system software developers guide," http://www.intel.com/content/www/us/en/processors/xeon/xeon-phi-coprocessor-system-software-developers-guide.html.

[8] "Intel® Manycore platform software stack," http://registrationcenter.intel.com/irc_nas/3988/MPSS_Users_Guide.pdf.

Xiaoling Yang graduated from Tianjin University, China with B.S. in Applied Mathematics and B.E. in Electric Engineering in 2001 and M.S. in Applied Mathematics in 2004. After that, he joined the Electromagnetic Communication Lab of Pennsylvania State University for several years as Research Associate. He has published over twenty conference and journal papers and co-authored four books in computational electromagnetics field. He also served as Reviewer for multiple conferences and journals. He was elevated as IEEE senior member in 2010. His research interests includes FDTD and FEM methods, parallel computing, hardware acceleration (GPU and Phi), 3-D modeling and visualization.

Wenhua Yu is Tepin Professor of Jiangsu Normal University, the President of 2COMU, Inc. and a Visiting Professor of Harbin Engineering University. He is the Director of Big-Data Analysis and Processing Key Lab of Jiangsu Province. He was a Visiting Professor/Research Associate of Pennsylvania State University from 1996 to 2010. He has worked on the topics related to FDTD methods, software development techniques, high performance computing techniques, and engineering applications for many years, first time applied the vector units and Phi coprocessors to solve electromagnetic problems, and has published more than 150 technical papers on the parallel FDTD methods and simulation techniques. He also authored Conformal Finite Difference Time Domain Maxwell's Equations Solver Software and User's Guide (Artech House, 2003), Parallel Finite Difference Time Domain Methods (Artech House, 2006), Electromagnetic Simulation Techniques Based FDTD Methods (John Wiley & Sons, 2009), Advanced FDTD Method: Acceleration, Parallelization, and Engineering Applications (Artech House, 2011), and VALU Acceleration Techniques for Parallel FDTD Methods (IET/SciTech Publisher, 2013), Advanced Computational Electromagnetics Methods and Applications (Editor, Artech House, 2014), and three books in Chinese (2005, 2010, 2012). He also translated one book (from English to Chinese) Understanding the Finite Difference Time Domain Method (John B. Schneider, Washington State University) (Tsinghua University Press, 2014). He is the General Co-Chair of several international conferences on the topic of computational electromagnetics, antennas and microwave circuits. He is a Lead Guest Editor of the Journal of International Antennas and Propagation on special issue "Small Antennas: Miniaturization Techniques and Applications." He is the member of technical committee of several international journals and a Guest Editor of special issue of Harbin University Workshop of Journal of Applied Computational Electromagnetics Society. He is a TPC Co-Chair of 2014 International Conference on Wireless Communications and Signal Processing. He is a senior member of IEEE and a primary developer of the GEMS software package. He is also the founder of Global Chinese Electromagnetic Network (www.globalchineseEM.org).

A Simple GPU Implementation of FDTD/PBC Algorithm for Analysis of Periodic Structures

Veysel Demir

Department of Electrical Engineering
Northern Illinois University, DeKalb, IL 60115, USA
vdemir@niu.edu

Abstract ─ Constant horizontal wavenumber approach is a simple method to model Periodic Boundary Conditions (PBC) in the Finite-Difference Time-Domain (FDTD) method proposed for efficient analysis of periodic structures; however, it requires execution of the FDTD simulations many times, each time for a different value of horizontal wavenumber to achieve useful results. Therefore, although each simulation may take a short time to complete, a sweep of simulations still takes a long time and there is a need to employ methods to speed-up the simulations. In this contribution we present an implementation of the FDTD/PBC algorithm using the Compute Unified Device Architecture (CUDA) to run the simulations on Graphics Processor Unit (GPU) devices to speed-up the the FDTD/PBC simulations. We also present a method in which a problem space is extended by one padded cell on each of the four periodic sides. As a consequence, programming is simplified, especially for the GPU code for the field update process at the boundaries, the problem space and efficiency of calculations as well is improved.

Index Terms ─ Finite-Difference Time-Domain (FDTD) method, Graphics Processor Unit (GPU), Periodic Boundary Conditions (PBC).

I. INTRODUCTION

Many electromagnetic applications require the use of periodic structures such as Frequency Selective Surfaces (FSS), Electromagnetic Band Gap (EBG) structures, corrugated surfaces, phased antenna arrays, periodic absorbers or negative index materials. These structures extend to several wavelengths in size; therefore, their analyses are time-consuming and memory-extensive using the conventional Finite-Difference Time-Domain (FDTD) [1]-[2] method. To overcome the limitation of the conventional FDTD method, a class of techniques, referred to as Periodic Boundary Conditions (PBC), have been developed. These techniques consider a periodic structure as infinitely periodic and then utilizes the infinite periodicity to analyze only one unit cell of the periodicity instead of the entire structure and obtains the results for the entire infinite size structure.

The PBC algorithms are generally divided into two main categories: field transformation methods and direct field methods [3]. The field transformation methods introduce auxiliary fields to eliminate the need for time-advanced data. The transformed field equations are then discretized and solved using FDTD techniques. The split-field method [4] and multi-spatial grid method [5] are two approaches in this category. The direct field category methods work directly with Maxwell's equations, and hence, there is no need for any field transformation. The sine-cosine method [6] is an example of this category. It should be noted that this method is a single frequency method and does not maintain the wide-band capability of FDTD.

A direct field method, referred to as constant horizontal wavenumber approach, is introduced in [7]-[10]. In this approach, the FDTD simulation is performed by setting a Constant Horizontal Wavenumber (CHW) instead of a specific angle of incidence. With this approach, one can achieve wideband results; however, the results will be valid for a different angle for each frequency. Therefore, the results from a single simulation usually are not meaningful. In order to obtain

useful results, one can sweep the horizontal wavenumber; i.e., run the simulation for a number of different horizontal wavenumbers, and construct a two-dimensional image of reflection or transmission coefficient distribution on the horizontal wavenumber-frequency plane. Although, running the simulation in a single unit cell makes the problem space much smaller than what it would be, a sweep of simulations takes a long time to achieve useful results. Therefore, still there is a need to employ methods to speed up the simulations. In this context, we consider to speed up the simulations using Graphic Processor Units (GPUs).

In this contribution, we present a GPU implementation of the CHW approach using Compute Unified Device Architecture (CUDA) to improve the computation speed. We also present a method in which a problem space is extended by one padded cell on each of the four periodic sides. Though this treatment increases the size of a problem space, it allows a simpler field update process at the boundaries. As a consequence, programming is simplified, especially for the GPU code, and efficiency of calculations as well is improved.

We present a summary of the CHW algorithm in Section II, and then we discuss the GPU implementation of the algorithm using CUDA in Section III. In Section IV, we illustrate speed up factors achieved using the presented implementation.

II. HORIZONTAL WAVENUMBER METHOD

Consider an infinitely periodic structure with periodicity in the xy plane. The periodic structure is illuminated by an obliquely incident plane wave. Figure 1 shows the computational domain of a unit cell of a periodic structure. The unit cell is terminated by PBC boundaries on four sides and Convolutional Perfectly Matched Layer (CPML) [11] absorbing boundaries on top and bottom sides. The incident plane wave is injected into this domain on a source plane.

Figure 2 shows the field components on the xy plane-cut of the grid of a unit cell problem space. The size of the problem space is $P_x = N_x \Delta x$ in the x direction and $P_y = N_y \Delta y$ in the y direction, where

N_x and N_y are number of cells, and Δx and Δy are the cell sizes in respective directions. At steady state, a field component on the right boundary of the grid is a time delayed equivalent of a field on the left boundary. For instance, one can write:

$$E_y(x = P_x, y, z, t) = E_y(x = 0, y, z, t - \frac{P_x}{c}\sin\theta_{inc}), \quad (1)$$

where c is the speed of the wave propagating in free space and θ_{inc} is the incident angle. Similarly, a field component on the back boundary of the grid is a time delayed equivalent of a field on the front boundary. When transformed from time-domain to frequency-domain, (1) can be written as:

$$E_y(x = P_x, y, z) = E_y(x = 0, y, z)e^{-jk_x P_x}, \quad (2)$$

which implies that the field component on the right boundary of the grid is a phase delayed equivalent of a field on the left boundary. Here, k_x is x component of the wavenumber.

The phase relation between the fields that have a periodic distance of P_x or P_y is utilized to develop an FDTD algorithm that simulates the infinite periodic structure. For instance, in order to calculate an electric field component on the front boundary in Fig. 2, that is indexed as $E_x^{n+1}(i,1,k)$, one needs the value of the magnetic field component below it that could be indexed as $H_z^{n+0.5}(i,0,k)$. While $H_z^{n+0.5}(i,0,k)$ is not in the computational space of the unit cell in consideration, thus, its value is not known; a phase shifted equivalent of it, $H_z^{n+0.5}(i,N_y,k)$, can be used instead following the Floquet theory as $H_z^{n+0.5}(i,0,k) = H_z^{n+0.5}(i,N_y,k)e^{jk_y P_y}$. Then, the electric field updating equation can be written for $E_x^{n+1}(i,1,k)$ as:

$$E_x^{n+1}(i,1,k) = C_{exe}(i,1,k) \times E_x^n(i,1,k)$$
$$+ C_{exhz}(i,1,k) \times [H_z^{n+0.5}(i,1,k) - H_z^{n+0.5}(i,N_y,k)e^{jk_y P_y}]$$
$$+ C_{exhy}(i,1,k) \times [H_y^{n+0.5}(i,1,k) - H_y^{n+0.5}(i,1,k-1)], \quad (3)$$

where C_{exe}, C_{exhz}, and C_{exhy} are the updating coefficients. All other fields on the four side boundaries are treated in the same manner and their updates are completed using the phase shifted equivalents of their periodic components.
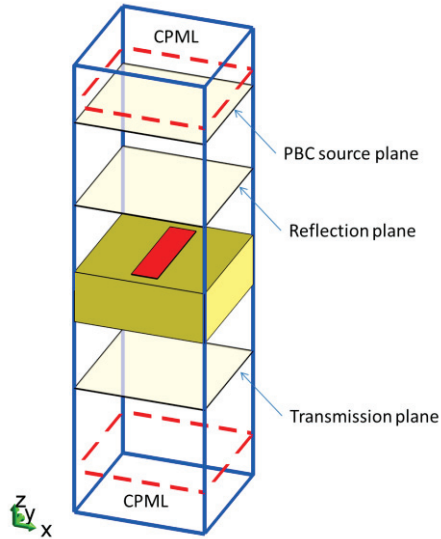
Fig. 1. Problem space of a unit cell of a periodic structure.
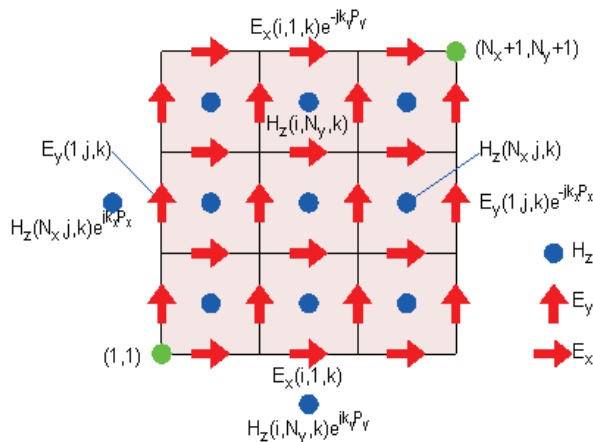
Fig. 2. Field components on the *xy* plane-cut of a unit cell in a three-dimensional domain.

III. IMPLEMENTATION OF PBC

A. General considerations

An existing FDTD code can be modified to accommodate PBC calculations as well. Some PBC specific considerations are discussed in this section.

One main consideration in PBC programming is that, as equation (3) includes the complex exponential phase term, the fields are evaluated in complex time domain rather than real time domain. Therefore, it should be noted that the time domain simulation results are not meaningful, while the frequency domain results such as

reflection and transmission coefficients are still valid. Since all fields are complex valued, their respective three dimensional arrays need to be defined as complex data types instead of real data types in the code. To minimize the modification to an existing code, additional three dimensional field arrays with real data type can be used to store the imaginary parts of the complex field values instead of changing the data types of existing arrays. Then field updates can be performed first for the real parts and then for the imaginary parts of the fields in separate subroutines since the updating coefficients are the same as the regular FDTD coefficients.

Other additional steps to the time-marching loop of an existing FDTD program are calculation and addition of incident fields to the fields on the source plane, and capturing the averaged fields after phase corrections.

B. Programming for GPU using CUDA

Recent developments in the design of graphics processing units, introduced a new generation of graphical computation cards which can be programmed to run scientific codes orders of magnitudes faster than Central Processor Units (CPUs). Especially, the introduction of the Compute Unified Device Architecture (CUDA) development environment from NVIDIA made GPU computing much easier and widespread. CUDA has been reported as the programming environment for implementation of FDTD in several articles, which include [12]-[13] as some of the earlier implementations. We also have presented an implementation of an FDTD code in [14]. In this contribution, we discuss the implementation of PBC as an extension to that of [14], therefore we refer the reader to [14] for further details.

As discussed in the previous subsection, one needs to use additional three dimensional arrays for the imaginary part of field values to have the existing code accommodate the PBC calculations. Hence, three dimensional arrays for the imaginary parts of the fields are defined. For a minimum modification to the existing code, the field update functions are executed for a second time, after they are executed to update the real parts of the fields to update the imaginary parts of the fields. For instance, the code section in Listing 3 of [14] is called a second time as shown in Listing 1

below.

```
update_magnetic_fields_on_kernel
<<<grid, threads, shared_memory_size>>>
(nxx, nyy, nx, ny, nz,
Ex_im, Ey_im, Ez_im, Hx_im, Hy_im, Hz_im,
Chxh,Chyh,Chzh,Chxey,
Chxez,Chyez,Chyex,Chzex,Chzey);
```

Listing 1. CUDA code to call kernel function for imaginary part of magnetic field updates.

In the CHW method, calculation of incident field on the source plane requires multiplication of each field at each field point with a phase shift term. Since the phase shift term is a constant value for each point on the source plane, a two dimensional array that carries the phase shift value for each respective field point is constructed before the time-marching loop starts. Then, these arrays are used to adjust the phases of the incident field components during each time step and these incident field components are added to the respective field components on the source plane to excite the problem space. Similar phase shift terms are needed while capturing the fields on reflection and transmission planes. These phase shift terms as well are stored in two dimensional arrays and they are used during the time marching loop to adjust the phases of the fields on the reflection and transmission planes before they are averaged to obtain a single value for reflection and transmission at each time step.

PBC formulation requires the special update of electric field components on the side boundaries, such as shown in (3). For instance, as presented in [10], first, all electric fields in the problem space except for the ones on the side boundaries are updated following the usual updating equations. Then, the electric fields on the left, right, top, and bottom boundaries, except for the corner components, are updated using the phase shifted periodic magnetic field components. Then, as the last step, each of the four corner field components are updated, however, this time using two of the phase shifted periodic magnetic field components for each corner. The steps of this procedure are illustrated in Fig. 3. One can notice that there are many steps as well as exceptions in this flow chart. This kind of granular treatment of fields makes it difficult to write the code for both the CPU and GPU. It may also detriment the

efficiency on a GPU since efficiency of computations on GPU mainly relies on the data parallelism of the algorithm.
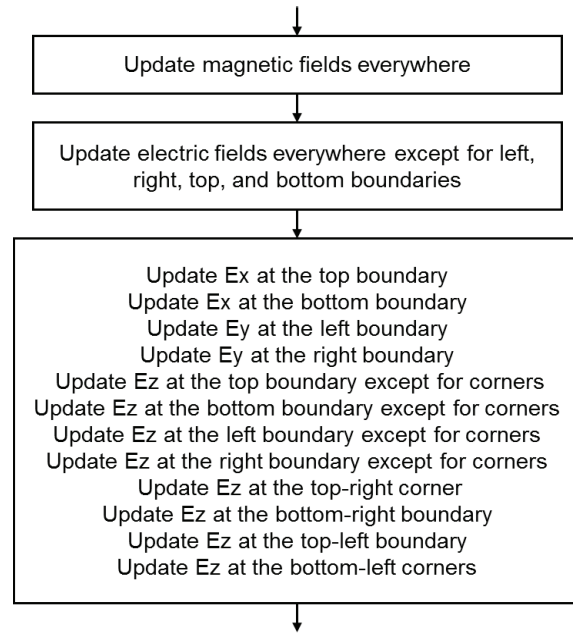
Fig. 3. Conventional field update process for treatment of periodic boundary conditions.

We employed a different approach to avoid the granular treatment of electric field components on the boundaries; we extended the problem space by one padded cell on each of the four sides as illustrated in Fig. 4. Here, the shaded region is the original problem space which is the same as the one in Fig. 2. The extended problem space is terminated by PEC boundaries on four sides; thus, it does not require any special boundary treatment. In each time step, all of the magnetic field components in the extended problem space are updated as usual. Then, the magnetic field components in row 1 are multiplied by the phase shift term $e^{-jk_y P_y}$ and copied to row $N_y + 1$. The magnetic field components in row N_y are multiplied by the phase shift term $e^{jk_y P_y}$ and copied to row 0. Similarly, the magnetic field components in column 1 are multiplied by the phase shift term $e^{-jk_x P_x}$ and copied to column $N_x + 1$. The magnetic field components in column N_x are multiplied by the phase shift term $e^{jk_x P_x}$ and copied to column 0. This operation is a simple product and copy and it

is more efficient to perform on GPU compared with the procedure described in [10]. Then, there is no need for treatment of electric field components on the boundary; all electric field components are updated in the entire problem space using the usual updating equations, where the particular field components on the periodic boundary will find the required phase shifted magnetic fields available in the extended cells. The steps of this procedure are illustrated in Fig. 5. Comparing the flow charts in Figs. 3 and 5, reveals the simplicity of the presented approach.
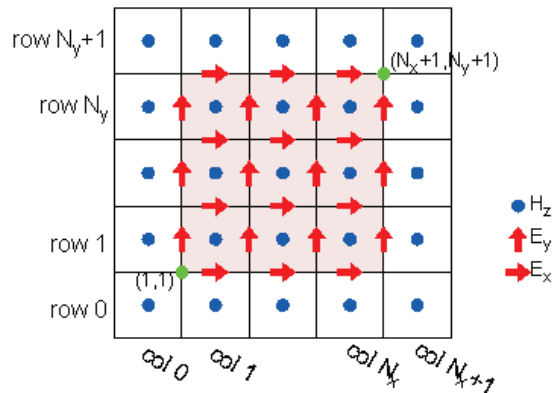
Fig. 4. Field components on the *xy* plane-cut of an extended unit cell.
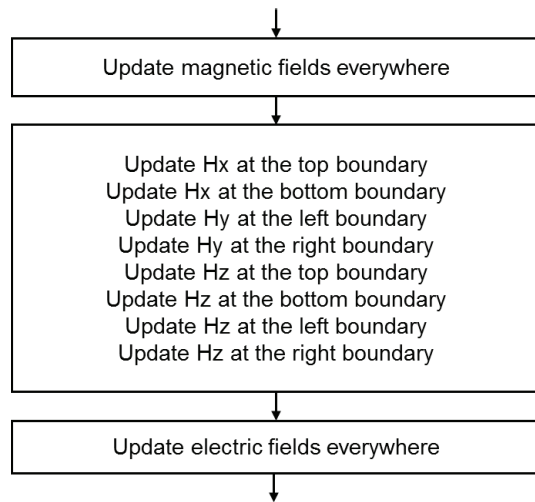
Fig. 5. Proposed field update process for treatment of periodic boundary conditions.

IV. RESULTS

The periodic structure in Fig. 1 is used as a test case to demonstrate the speed up obtained by the GPU implementation. This structure is referred to as a dipole Frequency Selective Surface (FSS) [15]. The metal patch of rectangular shape is placed on a dielectric substrate. The PEC patch has a length of 12 mm and a width of 3 mm. The substrate has a thickness of 6 mm and relative permittivity of 2.2. The periodicity is 15 mm in both *x* and *y* directions. The reflection plane is placed 16 mm above the substrate, while the transmission plane is at 3 mm below the substrate. The source plane is 18 mm above the substrate. The simulations are performed using cubic Yee cells of 0.5 mm on a side. The problem space is composed of $32 \times 32 \times 82 = 83,968$ cells. The structure is illuminated by incident plane wave of TE mode. Simulations are repeated for a sweep of horizontal wavenumber k_x by varying it from 21 to 100 for 80 distinct values. In all these simulations the horizontal wavenumber k_y is kept as a constant value of 7.8.

The code that runs on CPU is developed using FORTRAN, while the code for GPU is developed using CUDA for C. Simulations are performed on a computer with a CPU of Intel® Core™2 Quad Processor Q9550 at 2.83 GHz, and an NVIDIA GTX480 graphics card. Results are obtained for reflection and transmission coefficients to construct distribution of these coefficients on the horizontal wavenumber-frequency plane. Figure 6 shows the result for magnitude of reflection coefficient; whereas, Fig. 7 shows the result for magnitude of transmission coefficient for a frequency range between 3 GHz to 13 GHz. It should be noted that the results are the same for both the GPU and CPU computations. Simulations are repeated 80 times, each time for a different k_x value. Each simulation is run for 10,000 time steps. Total simulation time is recorded as 59 minutes using the CPU, while it is recorded as 7.8 minutes using the GPU. The GPU/CPU speed-up factor is obtained as 7.5. It should be noted that problem size is rather small in terms of number of cells in this example. As discussed in [16], it is more efficient to solve larger FDTD domains than smaller domains on GPU. In order to demonstrate the performance improvement for a larger problem, the dipole FSS simulations are repeated using cubic Yee cell of 0.25 mm on a side. The problem space is composed of $62 \times 62 \times 144 = 553,536$ cells. Total simulation

time is recorded as 490 minutes using the CPU, while it is recorded as 18 minutes using the GPU. The GPU/CPU speed-up factor is obtained as 27.
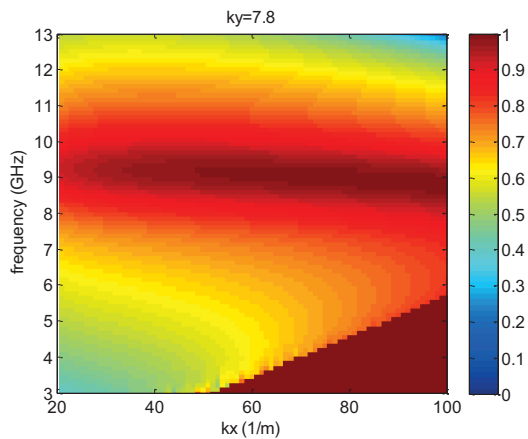

Fig. 6. Magnitude of reflection coefficient in the horizontal wavenumber-frequency plane.
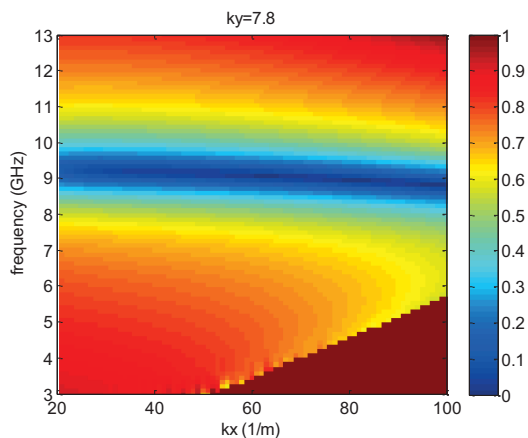

Fig. 7. Magnitude of transmission coefficient in the horizontal wavenumber-frequency plane.

V. CONCLUSION

In this contribution we presented implementation of constant horizontal wavenumber periodic boundary condition as an extension to an existing FDTD implementation using CUDA to speed up the periodic boundary analyses utilizing the computational power of GPU devices. Presented implementation is programmed with the goal of minimum modification to the existing code. It has been shown that results can be achieved in a much shorter time using a GPU card for computations. It

should be noted that efficiency can be further improved by an implementation which uses three dimensional arrays of complex data type to store the fields and optimize the kernel functions that run in GPU for these arrays. Moreover, as the simulations run more efficiently on GPU devices when the problem spaces are larger, as illustrated in [16], an algorithm can be developed to stack multiple PBC problem spaces and run them in a single simulation to further speed up the PBC analyses.

REFERENCES

[1] A. Taflove and S. C. Hagness, "Computational electrodynamics: the finite-difference time-domain method," 3rd edition, *Norwood, MA: Artech House*, 2005.

[2] A. Elsherbeni and V. Demir, "The finite difference time domain method for electromagnetics: with MATLAB simulations," *SciTech Publishing*, 2009.

[3] J. Maloney and M. P. Kesler, "Analysis of periodic structures, computational electrodynamics: the finite-difference time-domain method," 3rd ed., *Norwood, MA: Artech House*, 2005.

[4] J. A. Roden, S. D. Gedney, P. Kesler, J. G. Maloney, and P. H. Harms, "Time-domain analysis of periodic structures at oblique incidence: orthogonal and non-orthogonal FDTD implementations," *IEEE Transaction on Antennas and Propagation*, vol. 46, no. 4, pp. 420-427, 1998.

[5] Y. C. A. Kao and R. G. Atkins, "A finite-difference time-domain approach for frequency selective surfaces at oblique incidence," *IEEE Antennas and Propagation Society International Symposium*, vol. 2, pp. 21-26, 1996.

[6] P. Harms, R. Mittra, and W. Ko, "Implementation of the periodic boundary condition in the finite-difference time-domain algorithm for FSS structures," *IEEE Transaction on Antennas and Propagation*, vol. 42, no. 9, pp. 1317-1324, 1994.

[7] F. Yang, J. Chen, R. Qiang, and A. Z. Elsherbeni, "A simple and efficient FDTD/PBC algorithm for scattering analysis of periodic structures," *Radio Science*, vol. 42, RS4004, 2007.

[8] F. Yang, J. Chen, R. Qiang, and A. Z. Elsherbeni, "FDTD analysis of periodic structures at arbitrary incidence angles: a simple and efficient implementation of the periodic boundary conditions," *IEEE Antennas and Propagation Society International Symposium*, pp. 2715-2718, 2006.

[9] F. Yang, A. Z. Elsherbeni, and J. Chen, "A hybrid spectral-FDTD/ARMA method for periodic structure analysis," *IEEE Antennas and*

Propagation Society International Symposium, pp. 3720-3723, 2007.

[10] K. ElMahgoub, F. Yang, and A. Z. Elsherbeni, "Scattering analysis of periodic structures using finite-difference time-domain method," *Morgan and Claypool*, 2012.

[11] Roden and S. Gedney, "Convolution PML (CPML): an efficient FDTD implementation of the CFS-PML for arbitrary media," *Microwave and Optical Technology Letters*, vol. 27, no. 5, pp. 334-339, 2000.

[12] P. Sypek, A. Dziekonski, and M. Mrozowski, "How to render FDTD computations more effective using a graphics accelerator," *IEEE Transactions on Magnetics*, vol. 45, no. 3, pp. 1324-1327, 2009.

[13] N. Takada, T. Shimobaba, N. Masuda, and T. Ito, "High-speed FDTD simulation algorithm for GPU with compute unified device architecture," *IEEE International Symposium on Antennas & Propagation & USNC/URSI National Radio Science Meeting, 2009*, North Charleston, SC, United States, p. 4, 2009.

[14] V. Demir and A. Z. Elsherbeni, "Compute unified device architecture (CUDA) based finite-difference time-domain (FDTD) implementation," *Journal of the Applied Computational Electromagnetics Society (ACES)*, vol. 25, no. 4, pp. 303-314, April 2010.

[15] B. A. Munk, "Frequency selective surface," *New York: Wiley*, 2000.

[16] V. Demir, "A stacking scheme to improve the efficiency of finite-difference time-domain solutions on graphics processing units," *Journal of the Applied Computational Electromagnetics Society (ACES)*, vol. 25, no. 4, pp. 323-330, April 2010.

Veysel Demir is an Assistant Professor with the Department of Electrical Engineering at Northern Illinois University. His research interests include numerical analysis techniques as well as microwave and Radio Frequency (RF) circuit analysis and design. He is a member of IEEE, Sigma Xi, and Applied Computational Electromagnetics Society (ACES).

Modeling Resonant Frequency of Rectangular Microstrip Antenna Using CUDA-Based Artificial Neural Network Trained by Particle Swarm Optimization Algorithm

Feng Chen and Yu-bo Tian

School of Electronics and Information
Jiangsu University of Science and Technology, Zhenjiang 212003, Jiangsu, P. R. China
cfcfchenfeng@163.com, tianyubo@just.edu.cn

Abstract ─ Resonant frequency is a vital parameter in designing Microstrip Antenna (MSA). Artificial Neural Network (ANN) based on Particle Swarm Optimization (PSO) algorithm (PSO-ANN) has been used to model the resonant frequency of rectangular MSA. To deal with the problem of the long execution time when training PSO-ANN, its parallel implementation in the Graphic Processing Unit (GPU) environment is proposed in this paper. The presented approach uses the particle behavior parallelization of PSO to accelerate ANN training, and is applied to modeling the resonant frequency of rectangular MSA under Compute Unified Device Architecture (CUDA). Experimental results indicate that compared with CPU-based sequential PSO-ANN, more than 300 times of speedup ratio has achieved in GPU-based parallel PSO-ANN with the same optimization stability. Furthermore, the network error can be significantly reduced with the very limited runtime increment when substantially enlarging the number of particles on GPU side.

Index Terms ─ Artificial Neural Network (ANN), Compute Unified Device Architecture (CUDA), Microstrip Antenna (MSA), Particle Swarm Optimization (PSO), resonant frequency.

I. INTRODUCTION

Microstrip Antenna (MSA) is used in a broad range of applications in communication systems, and this is primarily due to its thin profile, small size, light weight, and low manufacturing cost [1,2]. As is known to all, MSA has narrow frequency band and works effectively only in the vicinity of its corresponding resonant frequency, which is a vital parameter in designing MSA. So a model to determine the resonant frequency is helpful in antenna design. Many scholars have proposed some traditional methods with different accuracy and computing power to calculate the resonant frequency of the most commonly used rectangular MSA [3-13].

In the past several years, Artificial Neural Network (ANN) model has been used in antenna design, including modeling the resonant frequency of rectangular MSA [14,15] due to its excellent abilities of learning and generalization, little memory requirement and fast real-time operation. The related data of the antenna can be got by measurement or simulation. After training these data, the ANN related to the antenna design problem can be achieved, and this quickly provides solutions to the problem. Particle Swarm Optimization (PSO) algorithm [16,17] has been gradually applied to ANN training (PSO-ANN) due to its simple concept, easy implementation, and strong abilities of convergence and global search. PSO-ANN has been used to model the resonant frequency of rectangular MSA and proved with better convergence precision and stronger predictive ability than common BP-based ANN (BP-ANN) [18-20]. However, PSO-ANN needs long computing time, especially for large scale problems, such as the problem of modeling the resonant frequency of rectangular MSA. Parallel optimization is an effective way to solve this problem.

Besides ANN's data parallelization and node parallelization [21], PSO's natural particle

behavior parallelization is in PSO-ANN. There are many parallel ways to accelerate PSO algorithm. Compared with computer cluster [22,23], multi-core CPU [24] or other professional parallel devices like FPGA [25,26], graphic processing unit (GPU) [27,28] has the most significant advantages in hardware cost. Since the NVIDIA company introduced the Compute Unified Device Architecture (CUDA) in 2007, CUDA has become the most popular GPU programming architecture due to its excellent programmability.

Ground on the existing research of GPU-based PSO algorithm, we design the CUDA-based parallel PSO-ANN scheme to fast model the resonant frequency of rectangular MSA in this paper. Experimental results show that when using the same number of particles on GPU side, the modeling runtime can be greatly reduced and more than 300 times of speedup ratio has obtained, while the modeling error is similar or same to the CPU-based program. When using substantially more number of particles on GPU side, the modeling error can be significantly reduced and better than the corresponding results in literatures.

The rest of this paper is organized as follows. Section II briefly discusses the calculation formula of the resonant frequency of rectangular MSA. Section III slightly introduces the implementation of PSO-ANN algorithm on CPU side. The CUDA-based parallel implementation of PSO-ANN is presented in Section IV. We use the GPU-based parallel PSO-ANN to rapidly model the resonant frequency of rectangular MSA, give the performance results, and provide some employment suggestions in Section V. Some concluding remarks of this work are finally reported in Section VI.

II. RESONANT FREQUENCY OF RECTANGULAR MSA

The model of rectangular MSA is shown in Fig. 1. Its length, width, dielectric substrate's thickness, and relative dielectric constant are W, L, h and ε_r, respectively. The resonant frequency of rectangular MSA can be calculated as formulas (1)~(3) [1,2]:

$$f_{mn} = \frac{c}{2\sqrt{\varepsilon_e}} \left[\left(\frac{m}{L_e} \right)^2 + \left(\frac{n}{W_e} \right)^2 \right]^{1/2}, \quad (1)$$

where ε_e is the effective relative permittivity. c is electromagnetic wave propagation velocity in vacuum. m and n are integers. L_e and W_e are effective length and width. When calculating the resonant frequency of rectangular MSA in main mode TM10, formula (1) can be written as:

$$f_{10} = \frac{c}{2L_e\sqrt{\varepsilon_e}}. \quad (2)$$

The effective length can be defined as follows:

$$L_e = L + 2\Delta L, \quad (3)$$

where ΔL is the boundary extension length, which is connected with dielectric substrate's thickness h.

Obviously, the resonant frequency of rectangular MSA depends on $h, \varepsilon_r, m, n, W$ and L.
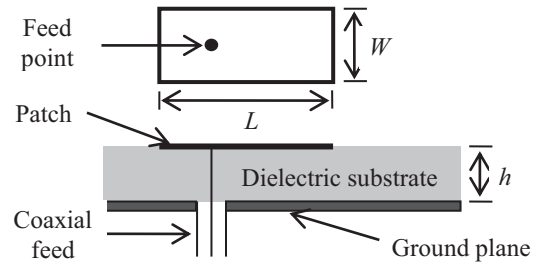
Fig. 1. Model of rectangular MSA.

III. PSO-BASED ANN

A. Standard PSO algorithm

There have been many versions of PSO algorithm. The version introducing inertia weight [16] is used and called "Standard PSO" in this paper. The optimization problem dimension is D and the number of particles is N. The positions of each particle represent a potential solution to the problem in the D-dimensional search space, and the velocities of each particle represent its movement. All particles have fitness values that are evaluated by the fitness function to be optimized. During each of the iteration, the positions and velocities of every particle are updated according to its Personal best positions (Pbest) and the Global best positions (Gbest). The velocities and positions updating in PSO can be formulated as follows:

$$V_{id}(t+1) = wV_{id}(t) + c_1r_1(Pbest_{id}(t) - X_{id}(t)) + c_2r_2(Gbest_d(t) - X_{id}(t)), \quad (4)$$

$$X_{id}(t+1) = X_{id}(t) + V_{id}(t+1). \quad (5)$$

In equation (4) and equation (5), $i=1,2,...,N$ and $d=1,2,...,D$. The learning factors c_1 and c_2 are nonnegative constants. r_1 and r_2 are random numbers uniformly distributed in [0,1]. $V_{id}(t) \in [-V_{max}, V_{max}]$, where V_{max} limits the maximum velocity of each dimension of the particle. $X_{id}(t) \in [-X_{max}, X_{max}]$, where X_{max} limits the maximum position of each dimension of the particle. Usually $V_{max}=kX_{max}$, where $0 \leqslant k \leqslant 1$. The inertia weight w is used to balance the ability between global exploration and local exploitation, and can be either a constant or a variable in [0,1].

B. ANN trained by PSO algorithm

PSO algorithm can be used to train ANN. ANN training includes optimization of ANN's structure and optimization of ANN's weights and thresholds (hereinafter referred to as weights). This article only concerns the optimization of ANN's weights under the condition of the given ANN's structure. ANN's weights must be encoded before training. There are two encoding strategies, namely vector encoding and matrix encoding. Vector encoding is chosen in this paper. For convenience, a feedforward ANN with 2 nodes in the input layer, 3 nodes in the hidden layer, and 1 nodes in the output layer (13-dimensional), is shown in Fig. 2.
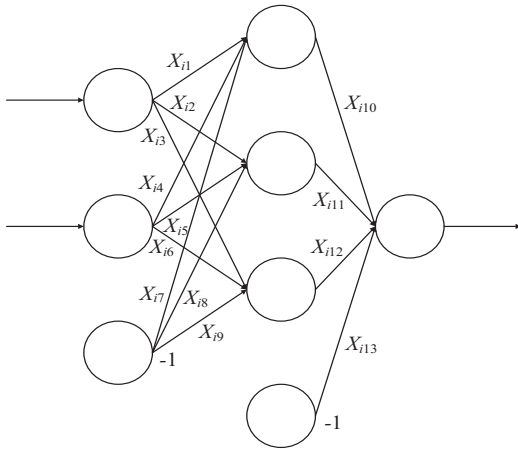

Fig. 2. Feedforward ANN model with 2-3-1 structure.

In PSO-ANN, each particle is encoded to a vector, representing a solution of ANN's weights [18]:

$$P_i = [X_{i1}\, X_{i2}\, X_{i3} \cdots X_{i11}\, X_{i12}\, X_{i13}]. \tag{6}$$

Each particle's fitness value is set as its corresponding Mean Squared Error (MSE) of ANN's output of training samples. All the particles revise their values by PSO algorithm. The final best solution Gbest is namely the well-trained ANN's weights. It is easy to see that PSO-ANN is essentially the special PSO algorithm whose fitness value is ANN's output error.

The steps of PSO-ANN algorithm used in this paper are as follows:
(a) Load training samples and testing samples. Data preprocesses. Set the maximum iteration number T_{max}.
(b) Initialize all particles' positions $X_{id}(t)$ and velocities $V_{id}(t)$ at random.
(c) Initialize all personal best positions $Pbest_{id}(t)$ and the global best positions $Gbest_d(t)$.
(d) Update all particles' velocities $V_{id}(t)$ and positions $X_{id}(t)$ according to equation (4) and equation (5).
(e) Evaluate all particles' fitness values F(X_i).
(f) Update all personal best positions $Pbest_{id}(t)$ and their corresponding fitness values F($Pbest_i$). Update the global best positions $Gbest_d(t)$ and their corresponding fitness value F($Gbest$).
(g) If the iteration number reaches T_{max}, go to step (h), else go to step (d).
(h) Evaluate total output error of training samples and testing samples.

IV. CUDA IMPLEMENTATION OF PARALLEL PSO-ANN

A. CUDA programming model

CUDA adopts the CPU+GPU heterogeneous cooperative computing platform. As the host, CPU takes responsibility for logic processing and serial computing. As the device or coprocessor, GPU takes responsibility for compute-intensive, highly parallel computing. CUDA uses similar C language as its basic programming language to achieve good programmability and portability. A CUDA kernel is a parallel function, which follows the SIMT (Single Instruction, Multiple Threads) execution model on GPU. CUDA program process typically includes the following 6 steps:
(1) Allocate and initialize CPU memory.
(2) Allocate GPU memory.
(3) Transfer data from CPU side to GPU side.
(4) Perform parallel computing on GPU side.

(5) Transfer results from GPU side back to CPU side.
(6) Process data obtained in step (5) on CPU side.

B. Design scheme and specific realization

Currently, the parallel implementation of ANN training mainly uses two parallelization strategies, namely data parallelization and node parallelization. However, for a common ANN, the number of neuron nodes or training samples is often only from ten to several ten. Therefore, these two strategies are suitable for parallel ways like computer cluster [21,29], but somewhat unsuitable for GPU because they have not enough parallel degree. Besides ANN's data parallelization and node parallelization, PSO's natural particle behavior parallelization is in PSO-ANN. For some complex problems, the number of particles can be from hundred to several hundred or more. Therefore, particle behavior parallelization is quite suitable for GPU architecture, which needs as many threads as possible to make full use of its powerful parallel computing ability.

In 2009, Veronese and Krohling firstly used CUDA to accelerate the PSO algorithm [27], which raised the research upsurge in GPU-based parallel PSO algorithm [28]. Particle behavior parallelization in PSO-ANN can be reflected in three aspects: (a), (b), and (c), as follows. In addition, CUDA-based PSO-ANN can use CUDA's unique parallelism, which can be reflected in aspect (d).

(a) The process of updating particles' velocities and positions is parallel.
(b) The process of evaluating particles' fitness values is parallel.
(c) The process of updating personal best positions and their corresponding fitness values is parallel.
(d) CUDA's parallel reduction algorithm can accelerate the process of finding the minimum fitness value when updating the global best positions.

According to the analyses above, the approach of GPU-based parallel PSO-ANN algorithm is designed in Fig. 3. The proposed approach corresponds one particle to one thread, and deals with a large number of GPU threads in parallel. This greatly saves the computing time and improves the computing accuracy.
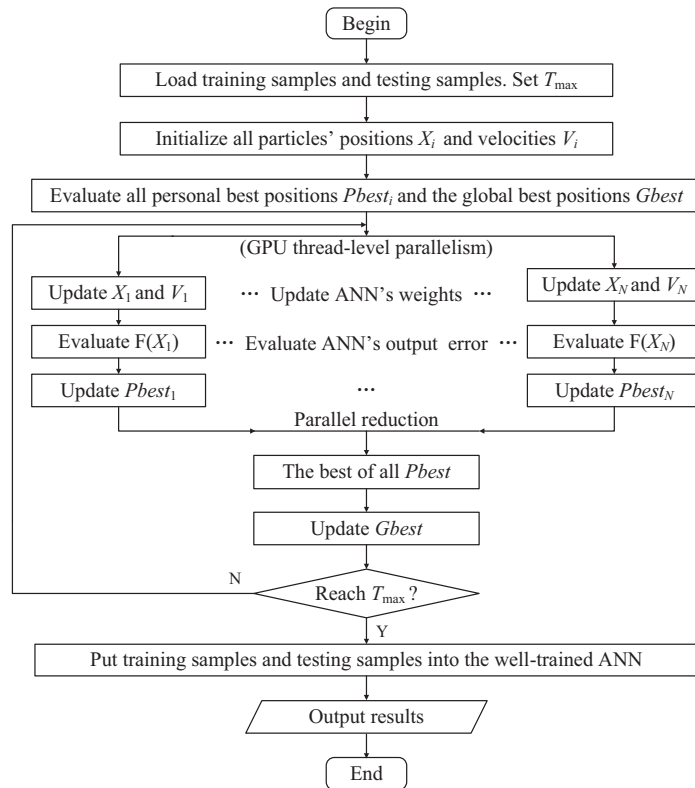

Fig. 3. CUDA-based parallel PSO-ANN algorithm flowchart.

The steps of GPU-based parallel PSO-ANN algorithm are as follows:
(1) Load the training samples and testing samples on CPU side. Data preprocesses.
(2) Call the malloc() function and cudaMalloc() function on CPU side. Allocate variable space on CPU side and GPU side.
(3) Initialize particles' positions and velocities on CPU side.
(4) Call the cudaMemcpy() function on CPU side, and transfer the data of particles from CPU side to GPU global memory. Call the cudaMemcpyToSymbol() function on CPU side, and transfer training samples from CPU side to GPU constant memory.
(5) Call the kernel() function on CPU side. Perform parallel computing tasks (ANN training) on GPU side.
(6) Call the cudaMemcpy() function on CPU side, and transfer the useful data (well-trained ANN) from GPU side back to CPU side.
(7) Evaluate the output results on CPU side by training samples, testing samples and well-trained ANN.
(8) Call the free() function and cudaFree() function on CPU side. Release variable space on CPU side and GPU side.

The step (5) is used to accelerate ANN training, and it is the core step of the whole algorithm. The pseudo-code of step (5) is as follows:

```
for (i=0; i<generationsNumber; i++)
{
<Update velocities and positions of each particle>
                                        // kernel 1
<Compute fitness of each particle>      // kernel 2
<Update Pbest of each particle>         // kernel 3
<Update Gbest of all particles>         // kernel 4
}
```

V. MODELING RESONANT FREQUENCY OF RECTANGULAR MSA USING CUDA-BASED PARALLEL ANN-PSO

In this section, we use CPU-based sequential PSO-ANN and the designed GPU-based parallel PSO-ANN, respectively, to model the resonant frequency of rectangular MSA and test their acceleration performance. The computing platform used in our experiments is shown in Table 1. The input sets of samples (W, L, h, ε_r) are the related parameters of rectangular MSA. The output set of samples (f_{ME}) is the corresponding measured resonant frequency. The well-trained ANN can establish the mapping between the related parameters of the rectangular MSA and its corresponding measured resonant frequency. The training samples and testing samples used in this paper are from previous works [12,30]. Column 1-6 of Table 2 gives the total 33 sets of data, in which 26 sets of data are used for ANN training and the remaining 7 sets of data marked with asterisks are used for ANN testing. Column 2-5 of Table 2 shows the related parameters of rectangular MSA. Column 6 ("Theoretical f_{ME}") of Table 2 shows the actual measured resonant frequency of rectangular MSA in mode TM10 ("theoretical values"). Tables 3 and 4 give the sum of the absolute error between experimental and theoretical values of the resonant frequency from traditional methods and CPU-based ANN models in different literatures. The f_{EDBD}, f_{DBD}, f_{PTS}, f_{PSO-BP} and f_{BiPSO} in Table 4 represent, respectively, the experimental resonant frequency calculated by using the ANN model trained by EDBD (Extended Delta-Bar-Delta), DBD (Delta-Bar-Delta), PTS (Parallel Tabu Search), PSO-BP (PSO and BP together), and BiPSO (Binary PSO). It's worth noting that the "theoretical values" mean the actual measured resonant frequency (Column 6 of Table 2), while the "experimental values" mean the experimental resonant frequency from traditional methods [3-13], CPU-based ANN models [14-15,18-20], or our GPU-based parallel PSO-ANN model.

Table 1: Computing platform

Name	Type
CPU	Intel Core i3-2100, 3.1 GHz
GPU	NVIDIA Tesla K20c, 706 MHz, 2496 CUDA Cores, Compute Capability 3.5
Operating System	Windows 7 SP1 32 bit Professional
Programming Environment	Microsoft Visual C++ 2010, CUDA 5.0

Table 2: Experimental values of the resonant frequency of rectangular MSA in mode TM10 from the GPU-based PSO-ANN model

No	W/cm	L/cm	h/cm	ε_r	Theoretical f_{ME}	Experimental f_{ANN}										
1	0.850	1.290	0.017	2.22	7740	7827.1	7775.0	7833.3	7756.6	7764.5	7764.0	7741.8	7763.0	7748.0	7764.9	7738.7
2*	0.790	1.185	0.017	2.22	8450	8042.6	8063.7	8255.9	8163.5	8144.4	8170.8	8162.9	8126.0	8117.5	8170.3	8149.8
3	2.000	2.500	0.079	2.22	3970	3962.7	3949.1	3991.3	3988.6	3958.7	3974.0	3973.5	3969.4	3973.6	3964.6	3968.8
4	1.063	1.183	0.079	2.25	7730	7652.3	7678.8	7720.3	7664.3	7737.2	7706.0	7727.8	7712.2	7719.5	7701.5	7716.3
5	0.910	1.000	0.127	10.20	4600	4645.1	4592.5	4602.4	4607.6	4603.4	4598.3	4601.1	4598.1	4599.7	4601.8	4600.8
6	1.720	1.860	0.157	2.33	5060	5138.7	4943.5	5051.2	5048.8	5091.8	5042.6	5047.5	5040.9	5053.1	5061.2	5068.5
7*	1.810	1.960	0.157	2.33	4805	4936.7	4663.9	4813.4	4767.8	4851.5	4774.3	4756.3	4758.5	4771.8	4812.6	4802.0
8	1.270	1.350	0.163	2.55	6560	6526.8	6568.4	6491.6	6524.5	6532.6	6527.1	6546.2	6551.0	6565.9	6537.1	6560.7
9	1.500	1.621	0.163	2.55	5600	5595.2	5588.1	5488.6	5611.1	5614.5	5629.5	5623.9	5629.6	5608.4	5626.7	5592.1
10*	1.337	1.412	0.200	2.55	6200	6162.4	6205.3	6173.5	6187.2	6176.5	6181.1	6201.6	6190.4	6203.1	6180.7	6211.5
11	1.120	1.200	0.242	2.55	7050	7053.1	7138.2	7061.9	7075.9	7039.5	7064.1	7044.8	7054.6	7049.2	7062.6	7052.6
12	1.403	1.485	0.252	2.55	5800	5765.3	5809.7	5830.9	5805.4	5780.2	5804.5	5809.0	5798.4	5797.6	5792.4	5809.7
13	1.530	1.630	0.300	2.50	5270	5262.9	5277.2	5364.6	5248.4	5256.7	5268.4	5259.9	5264.0	5262.7	5265.8	5261.1
14	0.905	1.018	0.300	2.50	7990	7935.1	7935.3	7933.2	7978.9	8024.8	8032.1	8016.1	8024.3	8011.9	8022.2	8002.5
15	1.170	1.280	0.300	2.50	6570	6616.4	6661.0	6631.4	6595.5	6568.7	6560.3	6573.5	6560.3	6569.2	6553.5	6569.4
16*	1.375	1.580	0.476	2.55	5100	5207.2	5155.0	5077.6	5112.1	5181.9	5177.8	5143.6	5227.8	5158.7	5083.9	5151.3
17	0.776	1.080	0.330	2.55	8000	7831.5	7880.8	7900.6	7948.2	7943.0	7959.1	7959.3	7965.7	7962.4	7961.5	7960.7
18	0.790	1.255	0.400	2.55	7134	7181.4	7183.7	7139.2	7183.0	7140.4	7130.7	7152.6	7144.4	7156.8	7145.4	7158.1
19	0.987	1.450	0.450	2.55	6070	6154.8	6066.4	6063.4	6108.5	6091.4	6108.2	6061.2	6062.3	6075.7	6085.4	6077.0
20*	1.000	1.520	0.476	2.55	5820	5903.8	5835.7	5833.0	5880.7	5870.0	5894.9	5842.6	5853.4	5860.2	5869.6	5862.6
21	0.814	1.440	0.476	2.55	6380	6481.9	6377.8	6412.7	6395.0	6409.4	6392.9	6399.3	6393.7	6391.3	6395.6	6395.8
22	0.790	1.620	0.550	2.55	5990	5976.1	5958.7	5980.6	5895.0	5954.4	5955.1	5957.0	5969.3	5937.9	5950.8	5941.5
23	1.200	1.970	0.626	2.55	4660	4561.9	4643.9	4629.7	4619.1	4649.0	4650.7	4666.5	4694.3	4679.0	4660.8	4660.5
24	0.783	2.300	0.854	2.55	4600	4571.8	4734.5	4665.5	4629.1	4631.7	4636.6	4633.1	4611.1	4647.5	4636.5	4646.9
25*	1.256	2.756	0.952	2.55	3580	3566.3	3623.1	3645.7	3508.0	3633.7	3538.3	3688.3	3583.9	3542.3	3558.2	3562.2
26	0.974	2.620	0.952	2.55	3980	3902.1	3990.6	3978.4	4021.5	3973.8	3962.6	3962.0	3958.3	3956.1	3970.1	3962.4
27	1.020	2.640	0.952	2.55	3900	3836.0	3920.4	3910.0	3947.0	3913.7	3889.6	3913.4	3895.8	3883.5	3898.3	3891.3
28	0.883	2.676	1.000	2.55	3980	3940.0	3990.9	3982.9	4021.0	3986.3	3984.2	3946.5	3973.4	3977.9	3985.9	3982.1
29	0.777	2.835	1.100	2.55	3900	3890.8	3856.1	3875.9	3857.0	3877.3	3884.8	3891.4	3902.5	3899.0	3886.8	3892.7
30	0.920	3.130	1.200	2.55	3470	3485.2	3433.9	3410.2	3455.6	3450.3	3463.3	3480.4	3476.4	3465.7	3461.2	3455.3
31*	1.030	3.380	1.281	2.55	3200	3240.4	3197.1	3158.1	3184.1	3166.2	3198.6	3213.9	3196.4	3203.9	3193.7	3193.0
32	1.265	3.500	1.281	2.55	2980	3071.5	3042.3	3019.7	2956.3	3021.5	3005.2	2986.9	2983.3	2985.0	2990.9	3009.0
33	1.080	3.400	1.281	2.55	3150	3203.5	3159.9	3119.5	3140.3	3139.3	3156.5	3157.5	3152.0	3153.7	3148.9	3151.3
	Sum of the absolute error					2196	1702	1361	1293	1108	992	897	885	839	794	765
	Number of particles					128	256	512	1024	2048	4096	8192	16384	32768	65536	131072

Data with * are the sets of testing samples. The unit of frequency in this table is MHz.

Table 3: Sum of the absolute error between experimental and theoretical values of the resonant frequency of rectangular MSA in mode TM10 from traditional methods

Traditional Method	Sum of the Absolute Error/MHz
[3]	13136
[4]	24097
[5]	11539
[6]	12322
[7]	30996
[8]	8468
[9]	22572
[10]	18148
[11]	30504
[12]	56698
[13]	1393

Table 4: Sum of the absolute error between experimental and theoretical values of the resonant frequency of rectangular MSA in mode TM10 from CPU-based ANN models

ANN Model	Sum of the Absolute Error/MHz
f_{EDBD} [14]	2392
f_{DBD} [14]	2427
f_{BP} [14]	2372
f_{PTS} [15]	2239
f_{PSO} [18]	1049
f_{PSO-BP} [19]	1777
f_{BiPSO} [20]	863

In our experiment, the structure of ANN is designed as 4-10-1 and its corresponding particle dimension is 61. The number of particles is equal to the number of threads and is generally more than particle dimension (61 in our experiment). A warp is a group of 32 neighboring threads executed physically in parallel on a Stream Multiprocessor (SM) in CUDA. Therefore, the number of particles is designed to the multiples of 32. The activation function in the hidden layer is chosen as Bi-polar sigmoid function (formula (7)). The activation function in the output layer is chosen as Uni-polar sigmoid function (formula (8)). The inertia weight w decreases linearly from 0.9 to 0.4 during the whole process. The learning factors c_1 and c_2 are set to 2.8 and 1.3 respectively. The maximum iteration number T_{max} is set to 1000.

$$f(u)=\frac{2}{1+\exp(-2\times u)}-1, \quad -\infty < u < +\infty, \qquad (7)$$

$$f(u)=\frac{1}{1+\exp(-u)}, \quad -\infty < u < +\infty. \qquad (8)$$

Speedup ratio S is the most commonly-used index to measure the acceleration performance. S is defined as the ratio of T_{CPU} (the running time of the CPU-based program) and T_{GPU} (the running time of the GPU-based program) under the condition of the same number of particles and the same number of iterations in the PSO-ANN algorithm:

$$S=\frac{T_{CPU}}{T_{GPU}}. \qquad (9)$$

To get the running time, clock() function is used on CPU side and cudaEventElapsedTime() function based on "Events" is used on GPU side. Considering the influence caused by randomness, the program is run 20 times repeatedly under the circumstance of the same number of particles whenever on CPU or GPU side, and the result is their average value. To ensure the computing precision, all decimals use double precision on both CPU side and GPU side.

The experimental results are shown in Table 5 and Column 7-17 of Table 2. It's worth noting that the meanings of the "sum of the absolute error" (in Table 3 and Table 4) and the "average sum of the absolute error" (in Table 5) are different. The "sum of the absolute error" means the sum of the absolute error of the average of the experimental values and the theoretical values. The "average sum of the absolute error" means the average of the sum of the absolute error of the experimental values and the theoretical values. We believe that compared to the "sum of the absolute error", the "average sum of the absolute error" can be easily got by calculation, objectively reflects the results in each experiment, and is greater than the "sum of the absolute error" under the same conditions. In other words, if the "average sum of the absolute error" in Table 5 is superior to the "sum of the absolute error" in Table 4, the "average sum of the absolute error" in Table 5 is certainly superior to the "average sum of the absolute error" corresponding in Table 4. In Column 7-17 of Table 2, each column gives particular experimental values from GPU-based algorithm, the "sum of the absolute error" of which is closest to the "average sum of the absolute error" in Table 5.

Table 5: Speedup ratio achieved by parallel PSO-ANN when modeling the resonant frequency of rectangular MSA

Number of Particles	Running Time/s		Average Sum of the Absolute Error/MHz		Speedup Ratio
	CPU	GPU	CPU	GPU	
32	1.309	1.680	3171.6	3259.4	0.8
64	2.495	1.672	2559.1	2534.0	1.5
128	4.839	1.672	2189.3	2200.4	2.9
256	9.659	1.680	1694.5	1697.4	5.7
512	19.141	1.686	1331.9	1352.5	11.4
1024	38.267	1.717	1215.0	1267.6	22.3
2048	77.445	1.920	1098.7	1103.3	40.3
4096	155.406	2.186	974.2	997.5	71.1
8192	309.941	2.636	863.9	895.2	117.6
16384	620.352	2.824	795.1	885.7	219.7
32768	1241.120	5.647	722.8	840.1	219.8
65536	2481.003	8.768	689.4	792.9	283.0
131072	4958.867	15.160	674.7	765.0	327.1

We make some analysis on Table 3, Table 4 and Table 5:

(a) Generally, ANN models have obvious advantages over traditional methods in calculation precision. GPU-based parallel PSO-ANN has obvious advantages over CPU-based sequential PSO-ANN in running speed.

(b) The more number of particles, the higher speedup ratio. Compared with CPU-based sequential PSO-ANN, 327 times of maximum speedup ratio has achieved in GPU-based parallel PSO-ANN. When the number of particles doubles, the speedup ratio roughly doubles if the number of particles is less than 16384 (The maximum number of resident threads on this GPU is 26624.), and increases at a relatively slow rate if the number of particles is more than 32768.

(c) Compared with CPU-based sequential PSO-ANN, GPU-based parallel PSO-ANN has the same optimization stability. When the number of particles increases, the error of CPU-based program and the error of GPU-based program both decreases. The error of CPU-based program and the error of GPU-based program are similar or same under the condition of the same number of particles.

(d) Substantially increasing the number of particles on GPU side is a special method, which adapts to the CUDA programming model. The runtime increases very limitedly when substantially increasing the number of particles on GPU side. The error of GPU-side parallel PSO-ANN is superior to the results of [14,15] when the number of particles is greater than or equal to 128, superior to the results of [19] when the number of particles is greater than or equal to 256, superior to the results of all the traditional methods including [13] when the number of particles is greater than or equal to 512, superior to the results of [18] when the number of particles is greater than or equal to 4096, and superior to the results of all the literatures including [20] when the number of particles is greater than or equal to 32768.

We provide the following suggestions as reference for GPU-based parallel PSO-ANN algorithm:

(1) For the standard PSO-ANN algorithm in this study, the network error can be significantly reduced with the very limited runtime increment when substantially increasing the number of particles on GPU side.

(2) Other types of improved PSO-ANN algorithm do not always adapt to the GPU parallel architecture. The algorithm performance can be further improved if the improved PSO-ANN algorithm is suitable to parallelize on GPU side.

VI. CONCLUSION

The CUDA-based parallel PSO-ANN scheme is designed to rapidly model the resonant frequency of rectangular MSA. The proposed

approach corresponds one particle to one thread, and deals with a large number of GPU threads in parallel to greatly save computing time and improve computing accuracy. The experiments show that the modeling runtime can be greatly reduced when parallelizing the PSO-ANN algorithm on GPU side. Furthermore, the network error can be significantly reduced with the very limited runtime increment when substantially enlarging the number of particles on GPU side. The proposed GPU-based parallel PSO-ANN in this paper can be extended to other similar microwave engineering designs easily.

ACKNOWLEDGMENT

REFERENCES

[1] K. L. Wong, "Compact and broadband microstrip antennas," *New York: John Wiley & Sons Inc.*, 2002.

[2] D. G. Fang, "Antenna theory and microstrip antennas," *Beijing: Science Press*, 2007 (in English).

[3] J. Q. Howell, "Microstrip antennas," *IEEE Transactions on Antennas and Propagation*, vol. 23, no. 1, pp. 90-93, 1975.

[4] E. O. Hammerstad, "Equations for microstrip circuits design," *Proc. 5th Eur. Microw. Conf.*, Hamburg, Germany, pp. 268-272, September 1975.

[5] K. R. Carver, "Practical analytical techniques for the microstrip antenna," *Proc. Workshop Printed Circuit Antenna Tech.*, New Mexico State Univ., Las Cruces, NM, 7.1-7.20, October 1979.

[6] I. J. Bahl and P. Bhartia, "Microstrip antennas," *MA: Artech House*, 1980.

[7] J. R. James, P. S. Hall, and C. Wood, "Microstripa antennas-theory and design," *London: Peregrinus*, 1981.

[8] D. L. Sengupta, "Approximate expression for the resonant frequency of a rectangular patch antenna," *Electronics Letters*, vol. 19, no. 20, pp. 834-835, 1983.

[9] R. Garg and S. A. Long, "Resonant frequency of electrically thick rectangular microstrip antennas," *Electronics Letters*, vol. 23, no. 21, pp. 1149-1151, 1987.

[10] W. C. Chew and Q. Liu, "Resonance frequency of a rectangular microstrip patch," *IEEE Transactions on Antennas Propagation*, vol. 36, no. 8, pp. 1045-1056, 1988.

[11] K. Guney, "A new edge extension expression for the resonant frequency of electrically thick rectangular microstrip antennas," *Int. J. Electron.*, vol. 75, pp. 767-770, 1988.

[12] M. Kara, "Closed-form expressions for the resonant frequency of rectangular microstrip antenna elements with thick substrates," *Microwave and Optical Technology Letters*, vol. 12, no. 3, pp. 131-136, 1996.

[13] K. Guney, "A new edge extension expression for the resonant frequency of rectangular microstrip antennas with thin and thick substrates," *J. Commun. Tech. Electron.*, vol. 49, no. 1, pp. 49-53, 2004.

[14] K. Guney, S. Sagiroglu, and M. Erler, "Generalized neural method to determine resonant frequencies of various microstrip antennas," *International Journal of RF and Microwave Computer-Aided Engineering*, vol. 12, no. 1, pp. 131-139, 2002.

[15] S. Sagiroglu and A. Kalinli, "Determining resonant frequencies of various microstrip antennas within a single neural model trained using parallel tabu search algorithm," *Electromagnetics*, vol. 25, no. 6, pp. 551-556, 2005.

[16] Y. Shi and R. Eberhart, "A modified particle swarm optimizer," *Proceedings of the IEEE International Conference on Evolutionary Computation*, pp. 69-73, 1998.

[17] R. Poli, J. Kennedy, and T. Blackwell, "Particle swarm optimization: an overview," *Swarm Intelligence*, vol. 1, no. 1, pp. 33-57, 2007.

[18] Y. B. Tian, Z. Q. Li, and J. H. Wang, "Model resonant frequency of rectangular microstrip antenna based on particle swarm neural network," *Journal of Microwaves*, vol. 25, no. 5, pp. 45-50, 2009 (in Chinese).

[19] Y. Dong and Y. B. Tian, "Modeling resonant frequency of microstrip antenna based on neural network trained by PSO-BP algorithm," *Journal of Communication University of China (Science and Technology)*, vol. 16, no. 2, pp. 58-63, 2009 (in Chinese).

[20] Y. B. Tian and Y. Dong, "Modeling resonant frequency of microstrip antenna based on neural network ensemble," *Chinese Journal of Radio Science*, vol. 24, no. 4, pp. 610-616, 2009 (in Chinese).

[21] M. Pethick, et al., "Parallelization of a backpropagation neural network on a cluster computer," *The Fifteenth IASTED International Conference on Parallel and Distributed Computing and Systems*, pp. 574-582, 2003.

[22] G. Singhal, A. Jain, and A. Patnaik, "Parallelization of particle swarm optimization using message passing interfaces (MPIs)," *IEEE*

World Congress on Nature & Biologically Inspired Computing, pp. 67-71, 2009.

[23] K. Deep, S. Sharma, and M. Pant, "Modified parallel particle swarm optimization for global optimization using message passing interface," *2010 IEEE Fifth International Conference on Bio-Inspired Computing: Theories and Applications*, pp. 1451-1458, 2010.

[24] D. Z. Wang, et al., "Parallel multi-population particle swarm optimization algorithm for the uncapacitated facility location problem using openMP," *IEEE Congress on Evolutionary Computation*, pp. 1214-1218, 2008.

[25] G. K. Venayagamoorthy and V. G. Gudise, "Swarm intelligence for digital circuits implementation on field programmable gate arrays platforms," *IEEE Conference on Evolvable Hardware*, pp. 83-86, 2004.

[26] Y. Maeda and N. Matsushita, "Simultaneous perturbation particle swarm optimization using FPGA," *IEEE International Joint Conference on Neural Networks*, pp. 2695-2700, 2007.

[27] L. Veronese and R. Krohling, "Swarm's flight: accelerating the particles using C-CUDA," *Proceedings of the IEEE Congress on Evolutionary Computation*, pp. 3264-3270, 2009.

[28] P. Kromer, J. Platos, and V. Snasel, "A brief survey of advances in particle swarm optimization on graphic processing units," *2013 IEEE World Congress on Nature and Biologically Inspired Computing*, pp. 182-188, 2013.

[29] K. Ganeshamoorthy and D. N. Ranasinghe, "On the performance of parallel neural network implementations on distributed memory architectures," *8th IEEE International Symposium on Cluster Computing and the Grid*, pp. 90-97, 2008.

[30] M. Kara, "The resonant frequency of rectangular microstrip antenna elements with various substrate thicknesses," *Microwave and Optical Technology Letters*, vol. 11, no. 2, pp. 55-59, 1996.

Feng Chen (1989-) graduate student. His main research is high performance computing and computational intelligence technologies and its applications in electronics and electromagnetism. Presently at the School of Electronics and Information, Jiangsu University of Science and Technology, Zhenjiang 212003, P. R. China.
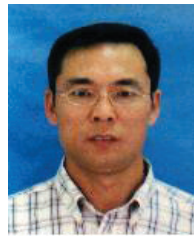
Yu-bo Tian (1971-), received his Ph. D. in 2004 from Nanjing University. Now, he is a Full Professor at Jiangsu University of Science and Technology. His main research concerns computational intelligence and swarm intelligence technologies and applications in electronics and electromagnetism.

Surface Impedance Absorbing Boundary for Terminating FDTD Simulations

Yunlong Mao [1,2], Atef Z. Elsherbeni [2], Si Li [1,2], and Tao Jiang [1]

[1] College of Information and Communication Engineering
Harbin Engineering University, Harbin, 150001 China
maoyunlong@hrbeu.edu.cn, jiangtao@hrbeu.edu.cn, lisi@hrbeu.edu.cn

[2] Department of Electrical Engineering and Computer Science
Colorado School of Mines, Golden, 80401, USA
aelsherb@mines.edu

Abstract — An Absorbing Boundary Condition (ABC) for FDTD simulations based on the concept of surface impedance boundary, which is referred to as Surface Impedance Absorbing Boundary Condition (SIABC), is proposed in this paper. It is extremely easy to implement relative to other absorbing boundaries and is found to be sufficient for many practical applications. The formulation of the SIABC is developed and implemented. The performance of SIABC is comparable with that of 10-layers CPML.

Inedx Terms — ABC, CPML, FDTD, SIABC.

I. INTRODUCTION

Since the moment it was introduced, absorbing boundary condition is widely used in the simulation of electromagnetic problems. Many absorbing boundaries are developed in the past years, like Engquist-Majda' ABC [1], Mur's ABC [2], PML [3], and CPML [4]. Engquist-Majda's ABC, along with Mur's ABC, are developed from wave equations. These ABCs are acceptable in 1D and 2D problems, but not usually very effective in 3D problems. Besides, a sufficiently far distance between the boundaries and the objects inside the computational domain is needed. Both PML and CPML, which are the most widely used nowadays, are developed by setting the impedance of ABCs' layers the same as that of free space. Thus, there won't be significant reflections back into the

problem space, while a small distance between the objects and the boundaries is used. However, even though PML and CPML have great performance in 1D, 2D, and 3D problems, these two ABCs are not easy to implement and extra storage requirements are needed.

In 1997, Senior et al [5] presented the connection between Rytov's surface impedance boundary conditions [6] and Engquist-Majda's absorbing boundary conditions in partial differential equations (PDE) form. However, since the method is developed from the very old ABC which is no longer used in most cases, the performance of this method is not so good especially in 3D problems, compared to PML or CPML. Besides, it can only be applied to curvilinear/double-curved surfaces. In spite of these disadvantages, this is the first time to the best of our knowledge that surface impedance boundary conditions are tried as ABC for FDTD simulations.

In most FDTD simulations, the outer absorbing boundary conditions are planar surfaces, where Leontovich's surface impedance boundary condition [7] is suitable. In 1992, Maloney [8] and John Beggs [9] both successfully implemented Leontovich's surface impedance boundary condition with FDTD method, but not as an absorbing boundary. Thus, it is possible to construct a new absorbing boundary condition by setting the surface impedance of Leontovich's surface to that of free space in order to terminate

the outer boundary of the FDTD computational domain.

In this paper, this new absorbing boundary condition, which is referred to as Surface Impedance Absorbing Boundary Condition (SIABC), is introduced. Formulas for SIABC in 1D, 2D and 3D are derived and implemented with FDTD method. To verify the accuracy of this SIABC, a few examples are given, and the results are compared to those based on CPML in 3D, and PML in 1D configurations.

II. FORMULATION

Leontovich's surface impedance boundary conditions can be represented as:

$$\vec{E} = Z_s(\omega)\left[\vec{n} \times \vec{H}\right], \qquad (1)$$

where $\vec{E}$ is the electric field, and $\vec{H}$ is the magnetic field parameter. $Z_s(\omega)$ refers to the surface impedance of the interface, while $\vec{n}$ is the normal vector.

Equation (1) describes the relationship of electric field and magnetic field on the interface of two regions. If the wave propagate from free space into another free space, then the impedance of the interface should be:

$$Z_s(\omega) = Z_0 = \sqrt{\frac{\mu_0}{\epsilon_0}}, \qquad (2)$$

where μ_0 and ϵ_0 are the free space permeability and permittivity, respectively.

A. 3D SIABC formulation

The setup of SIABC for a 3D problem space is illustrated in Fig. 1, where SIABC is applied to all 6 boundaries.

In a 3D problem, the inward normal vector $\vec{n}$ can be rewritten as:

$$\vec{n} = c_x\vec{e_x} + c_y\vec{e_y} + c_z\vec{e_z}, \qquad (3)$$

where $\vec{e_x}, \vec{e_y}, \vec{e_z}$ are unit vectors of different directions, and c_x, c_y, c_z are the coefficients.

Substituting equation (3) into equation (1), and replacing $\vec{E}$ and $\vec{H}$ with:

$$\begin{cases} \vec{E} = E_x\vec{e_x} + E_y\vec{e_y} + E_z\vec{e_z}, \\ \vec{H} = H_x\vec{e_x} + H_y\vec{e_y} + H_z\vec{e_z}, \end{cases}$$

one can obtain that:

$$\begin{cases} E_x = Z_0\left[c_y H_z - c_z H_y\right], \\ E_y = Z_0\left[c_z H_x - c_x H_z\right], \\ E_z = Z_0\left[c_x H_y - c_y H_x\right]. \end{cases} \qquad (4)$$

The value of $\vec{n}$ is decided by the value of the coefficients c_x, c_y, c_z. When $\vec{n}$ is normal to any of the boundaries identified in Fig. 1, one of c_x, c_y, c_z should be '1' or '-1' meanwhile the other 2 are both '0'. Table 1 lists the values of c_x, c_y, c_z for different boundaries.
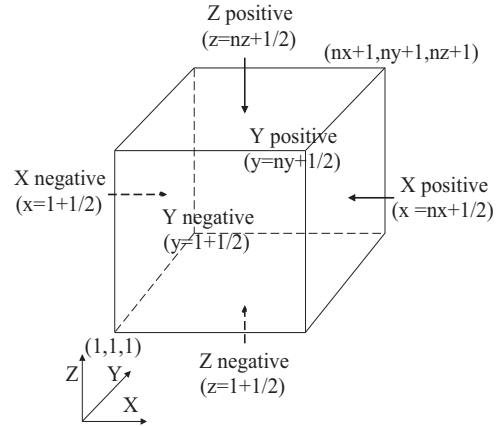

Fig. 1. Geometry of a 3D problem space with SIABC boundaries.

Table 1: Values of c_x, c_y, c_z for different boundaries

SIABC	c_x	c_y	c_z
$X_{negative}$	1	0	0
$X_{positive}$	-1	0	0
$Y_{negative}$	0	1	0
$Y_{positive}$	0	-1	0
$Z_{negative}$	0	0	1
$Z_{positive}$	0	0	-1

According to Maxwell's equations, in a source-free region,

$$\begin{cases} \dfrac{\partial H_x}{\partial t} = \dfrac{1}{\mu_x}\left(\dfrac{\partial E_y}{\partial z} - \dfrac{\partial E_z}{\partial y}\right), \\[2mm] \dfrac{\partial H_y}{\partial t} = \dfrac{1}{\mu_y}\left(\dfrac{\partial E_z}{\partial x} - \dfrac{\partial E_x}{\partial z}\right), \\[2mm] \dfrac{\partial H_z}{\partial t} = \dfrac{1}{\mu_z}\left(\dfrac{\partial E_x}{\partial y} - \dfrac{\partial E_y}{\partial z}\right). \end{cases} \qquad (5)$$

For the SIABC on the X negative boundary, according to Table 1, and as shown in Fig. 2, equation (4) becomes:

$$\begin{cases} E_y(1, j, k) = Z_0\left[-H_z(1, j, k)\right], \\ E_z(1, j, k) = Z_0\left[H_y(1, j, k)\right]. \end{cases} \qquad (6)$$

On this boundary, E_x is not needed as it is not tangential to the boundary. Then, we can substitute

equations (6) into equation (5), which yields:

$$
\begin{cases}
\dfrac{\partial H_x}{\partial t} = \dfrac{E_y(1,j,k+1) - E_y(1,j,k)}{\mu_x \triangle z} \\
\quad - \dfrac{E_z(1,j+1,k) - E_y(1,j,k)}{\mu_x \triangle y}, \quad (7a) \\
\dfrac{\partial H_y}{\partial t} = \dfrac{E_z(2,j,k) - Z_0 H_y(1,j,k)}{\mu_y \triangle x/2} \\
\quad - \dfrac{E_x(1,j,k+1) - E_x(1,j,k)}{\mu_y \triangle z}, \quad (7b) \\
\dfrac{\partial H_z}{\partial t} = \dfrac{E_x(1,j+1,k) - E_x(i,j,k)}{\mu_z \triangle y} \\
\quad - \dfrac{E_y(2,j,k) + Z_0 H_z(1,j,k)}{\mu_z \triangle x/2}. \quad (7c)
\end{cases}
$$

Unlike the normal FDTD method, the electric fields, E_y and E_z in the equations are half a cell away from the $x = 1$ plane, as shown in Fig. 2.
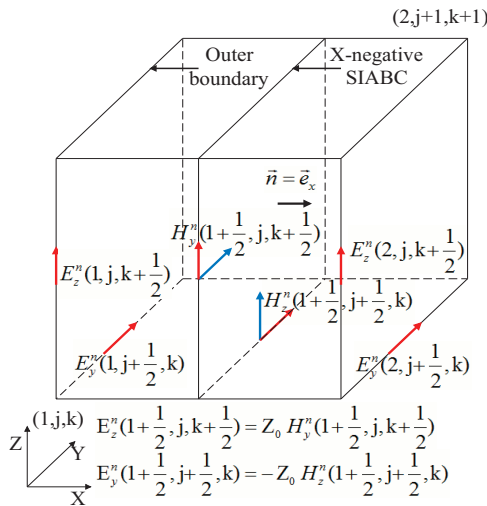
Fig. 2. SIABC for the X negative boundary.

One should notice that the indices, i, j, k are not exactly the same in the figures and formulas. Table 2 lists the relationship between these indices.

Table 2: Correspondences of indices in figures and updating equations

Fomulations	Figures
$E_x(i,j,k)$	$E_x(i+1/2, j, k)$
$E_y(i,j,k)$	$E_y(i, j+1/2, k)$
$E_z(i,j,k)$	$E_z(i, j, k+1/2)$
$H_x(i,j,k)$	$H_x(i, j+1/2, k+1/2)$
$H_y(i,j,k)$	$H_y(i+1/2, j, k+1/2)$
$H_z(i,j,k)$	$H_z(i+1/2, j+1/2, k)$

Since both H_y^n and H_z^n can be approximated using time difference with:

$$
\begin{cases}
H_y^n = \dfrac{1}{2}[H_y^{n+1/2} + H_y^{n-1/2}], \\
H_z^n = \dfrac{1}{2}[H_z^{n+1/2} + H_z^{n-1/2}].
\end{cases}
$$

Then equations (7b) and (7c) of this X negative plane become:

$$
\begin{cases}
H_y^{n+\frac{1}{2}}(1,j,k) = \dfrac{1 - \frac{dtZ_0}{\mu_y \triangle x}}{1 + \frac{dtZ_0}{\mu_y \triangle x}} H_y^{n-\frac{1}{2}}(1,j,k) \\
\quad + \dfrac{\frac{2dt}{\mu_y \triangle x}}{1 + \frac{dtZ_0}{\mu_y \triangle x}} E_z^n(2,j,k) - \dfrac{\frac{dt}{\mu_y \triangle z}}{1 + \frac{dtZ_0}{\mu_y \triangle x}} \\
\quad [E_x^n(1,j,k+1) - E_x^n(1,j,k)], \\
H_z^{n+\frac{1}{2}}(1,j,k) = \dfrac{1 - \frac{dtZ_0}{\mu_z \triangle x}}{1 + \frac{dtZ_0}{\mu_z \triangle x}} H_z^{n-\frac{1}{2}}(1,j,k) \\
\quad - \dfrac{\frac{2dt}{\mu_y \triangle x}}{1 + \frac{dtZ_0}{\mu_z \triangle x}} E_y^n(2,j,k) + \dfrac{\frac{dt}{\mu_z \triangle y}}{1 + \frac{dtZ_0}{\mu_z \triangle x}} \\
\quad [E_x^n(1,j+1,k) - E_x^n(1,j,k)].
\end{cases}
\tag{8}
$$

The above equations for calculating $H_y^{n+\frac{1}{2}}$ and $H_z^{n+\frac{1}{2}}$ are in the same form as those used in the normal source-free FDTD method as listed in [10], which are:

$$
\begin{cases}
H_y^{n+\frac{1}{2}}(i,j,k) = C_{hyh} H_y^{n-\frac{1}{2}}(i,j,k) \\
\quad + C_{hyez}(E_z^n(i+1,j,k) - E_z^n(i,j,k)) \\
\quad - C_{hyex}(E_x^n(i,j,k+1) - E_x^n(i,j,k)), \\
H_z^{n+\frac{1}{2}}(i,j,k) = C_{hzh} H_y^{n-\frac{1}{2}}(i,j,k) \\
\quad + C_{hzex}(E_x^n(i,j+1,k) - E_x^n(i,j,k)) \\
\quad - C_{hzey}(E_y^n(i+1,j,k) - E_y^n(i,j,k)).
\end{cases}
\tag{9}
$$

One should point out that for $i = 1$, the $E_z(1,j,k)$ and $E_y(1,j,k)$ remains 0 during the entire updating process. Thus, it is obvious that the only difference between SIABC and normal FDTD updating equations is the expression of the C coefficients for the tangential magnetic field components on the boundary.

The formulas of SIABC for the other five boundaries can be derived using the same procedure.

For the SIABC on the X positive boundary, the geometry of this case is shown in Fig. 3, and the corresponding updating equations for this case are given as:

$$
\begin{cases}
H_y^{n+\frac{1}{2}}(nx,j,k) = \dfrac{1 - \frac{dtZ_0}{\mu_y \triangle x}}{1 + \frac{dtZ_0}{\mu_y \triangle x}} H_y^{n-\frac{1}{2}}(nx,j,k) \\[2ex]
\quad - \dfrac{\frac{2dt}{\mu_y \triangle x}}{1 + \frac{dtZ_0}{\mu_y \triangle x}} E_z^n(nx,j,k) - \dfrac{\frac{dt}{\mu_y \triangle z}}{1 + \frac{dtZ_0}{\mu_y \triangle x}} \\[2ex]
\quad [E_x^n(nx,j,k+1) - E_x^n(nx,j,k)], \\[2ex]
H_z^{n+\frac{1}{2}}(nx,j,k) = \dfrac{1 - \frac{dtZ_0}{\mu_z \triangle x}}{1 + \frac{dtZ_0}{\mu_z \triangle x}} H_z^{n-\frac{1}{2}}(nx,j,k) \\[2ex]
\quad + \dfrac{\frac{2dt}{\mu_y \triangle x}}{1 + \frac{dtZ_0}{\mu_z \triangle x}} E_y^n(nx,j,k) + \dfrac{\frac{dt}{\mu_z \triangle y}}{1 + \frac{dtZ_0}{\mu_z \triangle x}} \\[2ex]
\quad [E_x^n(nx,j+1,k) - E_x^n(nx,j,k)].
\end{cases}
\tag{10}
$$
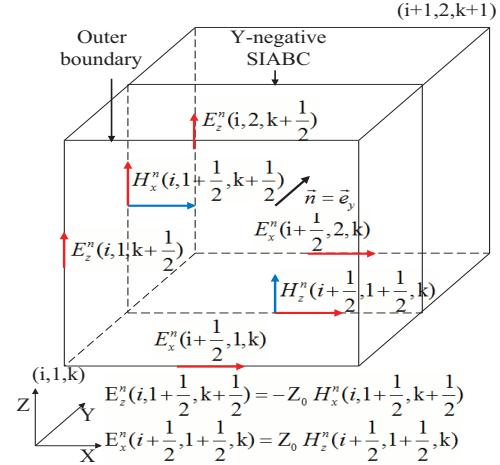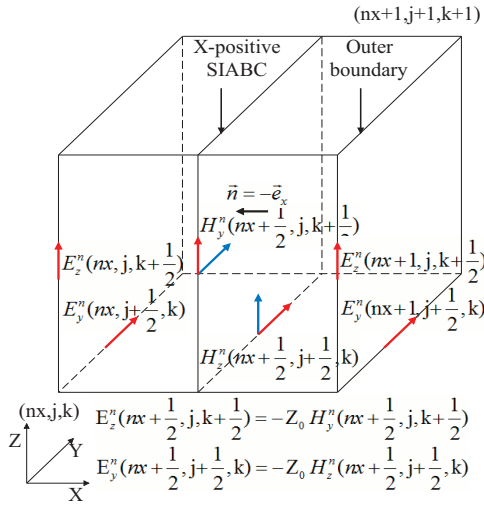
Fig. 3. SIABC for the X positive boundary.

For the SIABC on the Y negative boundary, the geometry of this case is shown in Fig. 4, and the updating equations for this case are given as:

$$
\begin{cases}
H_x^{n+\frac{1}{2}}(i,1,k) = \dfrac{1 - \frac{dtZ_0}{\mu_x \triangle y}}{1 + \frac{dtZ_0}{\mu_x \triangle y}} H_x^{n-\frac{1}{2}}(i,1,k) \\[2ex]
\quad - \dfrac{\frac{2dt}{\mu_x \triangle y}}{1 + \frac{dtZ_0}{\mu_y \triangle y}} E_z^n(i,2,k) + \dfrac{\frac{dt}{\mu_x \triangle z}}{1 + \frac{dtZ_0}{\mu_x \triangle y}} \\[2ex]
\quad [E_y^n(i,1,k+1) - E_y^n(i,1,k)], \\[2ex]
H_z^{n+\frac{1}{2}}(i,1,k) = \dfrac{1 - \frac{dtZ_0}{\mu_z \triangle y}}{1 + \frac{dtZ_0}{\mu_z \triangle y}} H_z^{n-\frac{1}{2}}(i,1,k) \\[2ex]
\quad + \dfrac{\frac{2dt}{\mu_z \triangle y}}{1 + \frac{dtZ_0}{\mu_z \triangle y}} E_x^n(i,2,k) + \dfrac{\frac{dt}{\mu_z \triangle x}}{1 + \frac{dtZ_0}{\mu_z \triangle y}} \\[2ex]
\quad [E_y^n(i+1,1,k) - E_y^n(i,1,k)].
\end{cases}
\tag{11}
$$

Fig. 4. SIABC for the Y negative boundary.

For the SIABC on the Y positive boundary, the geometry of this case is shown in Fig. 5, and the updating equations for this case are given as:

$$
\begin{cases}
H_x^{n+\frac{1}{2}}(i,ny,k) = \dfrac{1 - \frac{dtZ_0}{\mu_x \triangle y}}{1 + \frac{dtZ_0}{\mu_x \triangle y}} H_x^{n-\frac{1}{2}}(i,ny,k) \\[2ex]
\quad + \dfrac{\frac{2dt}{\mu_x \triangle y}}{1 + \frac{dtZ_0}{\mu_y \triangle y}} E_z^n(i,ny,k) + \dfrac{\frac{dt}{\mu_x \triangle z}}{1 + \frac{dtZ_0}{\mu_x \triangle y}} \\[2ex]
\quad [E_y^n(i,ny,k+1) - E_y^n(i,ny,k)], \\[2ex]
H_z^{n+\frac{1}{2}}(i,ny,k) = \dfrac{1 - \frac{dtZ_0}{\mu_z \triangle y}}{1 + \frac{dtZ_0}{\mu_z \triangle y}} H_z^{n-\frac{1}{2}}(i,ny,k) \\[2ex]
\quad - \dfrac{\frac{2dt}{\mu_z \triangle y}}{1 + \frac{dtZ_0}{\mu_z \triangle y}} E_x^n(i,ny,k) + \dfrac{\frac{dt}{\mu_z \triangle x}}{1 + \frac{dtZ_0}{\mu_z \triangle y}} \\[2ex]
\quad [E_y^n(i+1,ny,k) - E_y^n(i,ny,k)].
\end{cases}
\tag{12}
$$
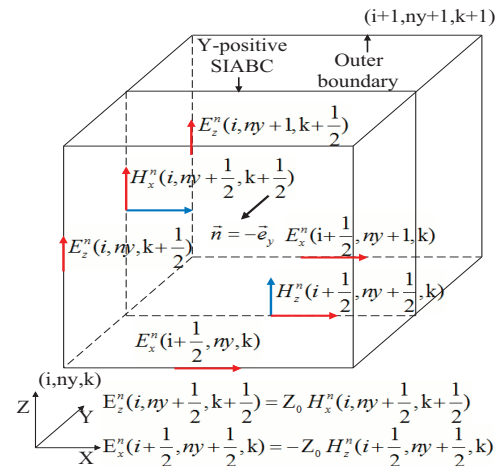
Fig. 5. SIABC for the Y positive boundary.

For the SIABC on the Z negative boundary, the geometry of this case is shown in Fig. 6, and the updating equations for this case are given as:

$$\begin{cases} H_x^{n+\frac{1}{2}}(i,j,1) = \dfrac{1-\frac{dtZ_0}{\mu_x \triangle z}}{1+\frac{dtZ_0}{\mu_x \triangle z}} H_x^{n-\frac{1}{2}}(i,j,1) \\[2mm] + \dfrac{\frac{2dt}{\mu_x \triangle z}}{1+\frac{dtZ_0}{\mu_y \triangle z}} E_y^n(i,j,2) + \dfrac{\frac{dt}{\mu_x \triangle y}}{1+\frac{dtZ_0}{\mu_x \triangle z}} \\[2mm] [E_z^n(i,j+1,1) - E_z^n(i,j,1)], \\[2mm] H_y^{n+\frac{1}{2}}(i,j,1) = \dfrac{1-\frac{dtZ_0}{\mu_y \triangle z}}{1+\frac{dtZ_0}{\mu_y \triangle z}} H_y^{n-\frac{1}{2}}(i,j,1) \\[2mm] - \dfrac{\frac{2dt}{\mu_y \triangle z}}{1+\frac{dtZ_0}{\mu_y \triangle z}} E_x^n(i,j,2) + \dfrac{\frac{dt}{\mu_y \triangle x}}{1+\frac{dtZ_0}{\mu_y \triangle z}} \\[2mm] [E_z^n(i+1,j,1) - E_z^n(i,j,1)]. \end{cases} \quad (13)$$
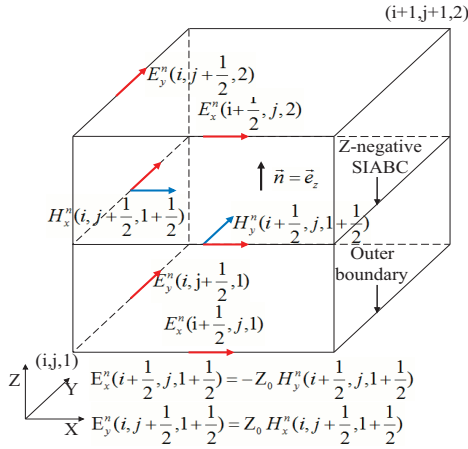
Fig. 6. SIABC for the Z negative boundary.

For the SIABC on the Z positive boundary, the geometry of this case is shown in Fig. 7, and the updating equations for this case are given as:

$$\begin{cases} H_x^{n+\frac{1}{2}}(i,j,nz) = \dfrac{1-\frac{dtZ_0}{\mu_x \triangle z}}{1+\frac{dtZ_0}{\mu_x \triangle z}} H_x^{n-\frac{1}{2}}(i,j,nz) \\[2mm] - \dfrac{\frac{2dt}{\mu_x \triangle z}}{1+\frac{dtZ_0}{\mu_y \triangle z}} E_y^n(i,j,nz) + \dfrac{\frac{dt}{\mu_x \triangle y}}{1+\frac{dtZ_0}{\mu_x \triangle z}} \\[2mm] [E_z^n(i,j+1,nz) - E_z^n(i,j,nz)], \\[2mm] H_y^{n+\frac{1}{2}}(i,j,nz) = \dfrac{1-\frac{dtZ_0}{\mu_y \triangle z}}{1+\frac{dtZ_0}{\mu_y \triangle z}} H_y^{n-\frac{1}{2}}(i,j,nz) \\[2mm] + \dfrac{\frac{2dt}{\mu_y \triangle z}}{1+\frac{dtZ_0}{\mu_y \triangle z}} E_x^n(i,j,nz) + \dfrac{\frac{dt}{\mu_y \triangle x}}{1+\frac{dtZ_0}{\mu_y \triangle z}} \\[2mm] [E_z^n(i+1,j,nz) - E_z^n(i,j,nz)]. \end{cases} \quad (14)$$
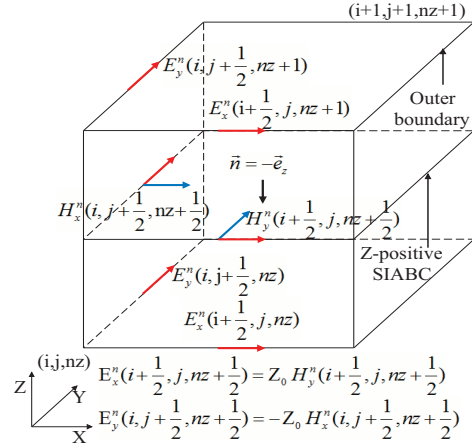

Fig. 7. SIABC for the Z positive boundary.

With these equations, one can now implement this SIABC in FDTD codes. It is also obvious from these equations that, compared to PML or CPML, the only thing needed to be done is to initialize the update coefficients for the tangential magnetic field components at the boundaries, no other changes are required in the FDTD codes when SIABC is used. That is really a great benefit specially for implementation on parallel or GPU hardware in order to accelerate the computations.

B. 2D SIABC formulation

The 2D problem is a simplification of the 3D problem. In a 2D problem, for example, a TM_z case, which is composed of E_z, H_x, H_y only, the formulas can be extracted from the 3D formulas easily. The geometry of a 2D problem is shown in Fig. 8 with designated SIABC boundaries.
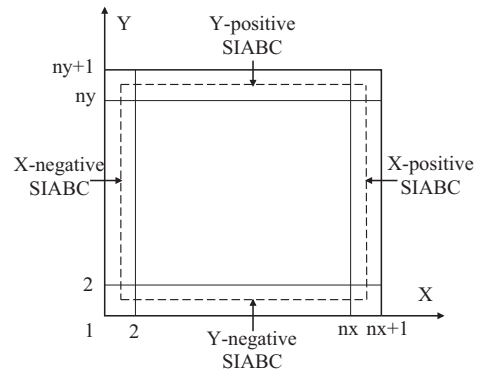

Fig. 8. Geometry of a 2D problem with SIABC boundaries.

For the SIABC on the X negative boundary,

the geometry of this case is illustrated in Fig. 9, and the updating equation is given as:

$$H_y^{n+1/2}(1,j) = \frac{\mu_y dx - Z_0 dt}{\mu_y dx + Z_0 dt} H_y^{n-1/2}(1,j) + \frac{2dt E_z^n(2,j)}{\mu_y dx + Z_0 dt}. \quad (15)$$
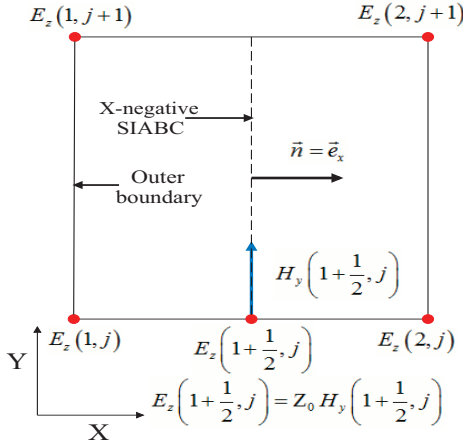

Fig. 9. SIABC for the X negative boundary.

For the SIABC on the X positive boundary, the geometry of this case is illustrated in Fig. 10, and the updating equation is given as:

$$H_y^{n+1/2}(nx,j) = \frac{\mu_y dx - Z_0 dt}{\mu_y dx + Z_0 dt} H_y^{n-1/2}(nx,j) - \frac{2dt E_z^n(nx,j)}{\mu_y dx + Z_0 dt}. \quad (16)$$
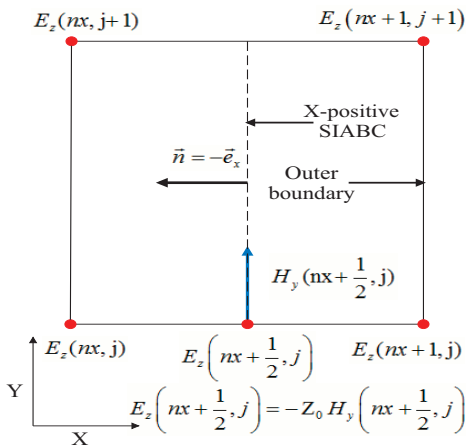
Fig. 10. SIABC for the X positive boundary.

For the SIABC on the Y negative boundary, the geometry of this case is illustrated in Fig. 11,

and the updating equation is given as:

$$H_x^{n+1/2}(i,1) = \frac{\mu_x dy - Z_0 dt}{\mu_x dy + Z_0 dt} H_x^{n-1/2}(i,1) - \frac{2dt E_z^n(i,2)}{\mu_x dy + Z_0 dt}. \quad (17)$$
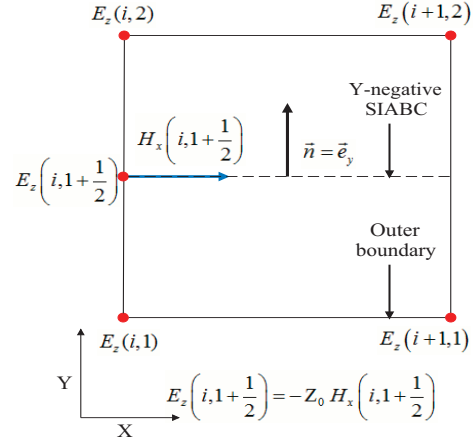
Fig. 11. SIABC for the Y negative boundary.

For the SIABC on the Y positive boundary, the geometry of this case is illustrated in Fig. 12, and the updating equation is given as:

$$H_x^{n+1/2}(i,ny) = \frac{\mu_x dy - Z_0 dt}{\mu_x dy + Z_0 dt} H_x^{n-1/2}(i,ny) + \frac{2dt E_z^n(i,ny)}{\mu_x dy + Z_0 dt}. \quad (18)$$
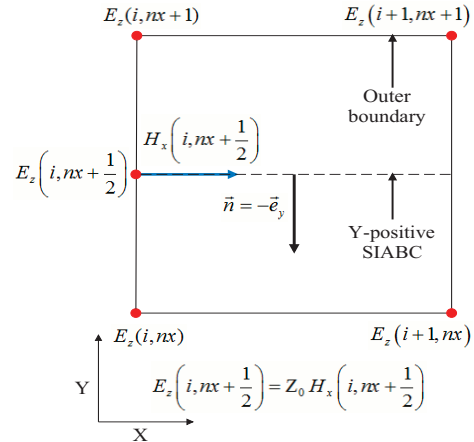

Fig. 12. SIABC for the Y positive boundary.

C. 1D SIABC formulation

The 1D problem is also a simplification of the 2D problem. In a one dimensional case there is no variation in the problem geometry and field

distributions in 2 of the coordinate dimensions. For instance, if there are only E_z and H_y, as shown in Fig. 13, and the wave propagates in the X direction, the corresponding FDTD updating equations can be derived as below:

For the SIABC on the X negative boundary,

$$H_y^{n+1/2}(1) = \frac{\mu_0 dx - Z_0 dt}{\mu_0 dx + Z_0 dt} H_y^{n-1/2}(1)$$
$$+ \frac{2dt}{\mu_0 dx + Z_0 dt} E_z^n(2). \quad (19)$$

For the SIABC on the X positive boundary,

$$H_y^{n+1/2}(nx) = \frac{\mu_0 dx - Z_0 dt}{\mu_0 dx + Z_0 dt} H_y^{n-1/2}(nx)$$
$$- \frac{2dt}{\mu_0 dx + Z_0 dt} E_z^n(nx). \quad (20)$$
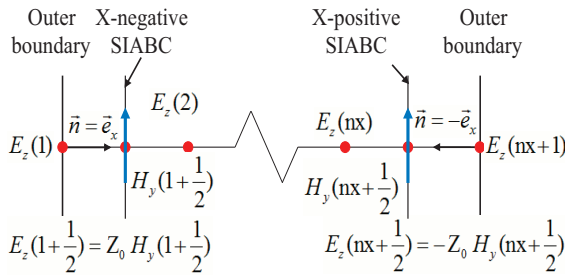
Fig. 13. Geometry of a 1D problem with SIABC boundaries.

III. VERIFICATION EXAMPLES AND RESULTS

In this section, a few examples are discussed. All examples except the first and the last are similar to those in [10] where the CPML parameters were selected for optimum CPML performance.

A. Dipole radiation near a sphere

In a 3D problem, a dipole antenna is located 20 cells away from a dielectric sphere of radius $= 10mm$, whose parameters are $\epsilon = 3, \mu = 1, \sigma = 0$. The cell size of this problem is $\triangle x = \triangle y = \triangle z = 1mm$. Components of the electric field are sampled 20 cells away from the sphere center, at 11 different points, designated $P1$ to $P11$, as shown in Fig. 14. The dipole antenna is activated with a Gaussian pulse. For the absorbing boundary condition with 10-layers of CPML, the air buffer between the objects (in this case, the dielectric sphere) inside the problem space and the outer boundaries is 15 cells. For the SIABC absorbing boundary condition,

the air buffer is varying from 30 cells to 50 cells, since the distance between the scattering objects and SIABC can affect the performance of SIABC greatly.

S(0,0,0), P1(0,10,0), P2(0,16,14), P3(0,30,20)
P4(0,44,14), P5(0,50,0), P6(20,30,0), P7(10,20,14)
P8(14,30,14), P9(10,40,14), P10(14,16,0), P11(14,44,0)
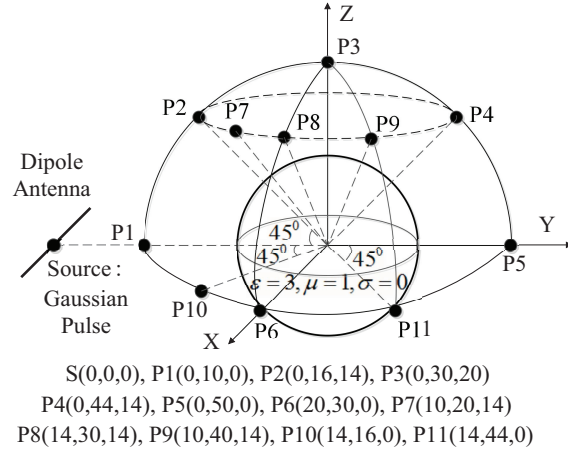
Fig. 14. Geometry of the 3D problem.

Table 3 lists the time needed for the simulations when applying SIABC and 10-layers CPML.

Table 3: Time needed for the simulations using Matlab with 1000 time steps

ABCs	Number of Air Buffer	Time (m)
CPML(10)	15	2.2737
SIABC	25	1.8138
SIABC	30	2.5159
SIABC	50	7.9297

Table 4 lists the maximum percentage difference of field values from SIABC compared to those from 10-layers CPML in time domain and frequency domain separately, with the number of air buffer between the scattering objects and SIABC changing. The percentage difference is calculated according to:

$$Differ = \frac{|E_{SIABC} - E_{CPML}|}{max(|E_{CPML}|)} \times 100\%, \quad (21)$$

where E_{SIABC} refers to the magnitude of sampled electric field when the ABC is SIABC, E_{CPML} refers to the magnitude of sampled electric field when the ABC is 10-layers CPML.

As listed in Table 4, point P4 has the largest maximum difference among all sample points. Figure 15 shows the sampled electric field at point P4 in time and frequency domains.

Table 4: Maximum percentage difference between SIABC and 10-layers CPML

Point	25 Cells		30 Cells		50 Cells	
	Time	Freq	Time	Freq	Time	Freq
P1	1.51	2.222	1.03	1.34	0.33	0.46
P2	1.80	2.74	1.07	1.58	0.45	0.57
P3	5.79	7.38	3.83	3.40	1.39	2.65
P4	19.05	11.78	13.15	6.94	4.28	2.96
P5	17.00	11.40	11.44	9.69	3.63	2.22
P6	6.08	6.24	3.70	5.00	2.11	3.08
P7	3.14	4.35	2.11	2.07	0.60	0.70
P8	6.98	6.25	4.60	3.30	1.04	1.25
P9	13.35	11.47	9.38	5.87	2.43	2.80
P10	3.79	5.51	2.98	2.83	1.41	1.47
P11	7.48	6.11	6.51	4.26	2.88	3.46

(a)

(b)
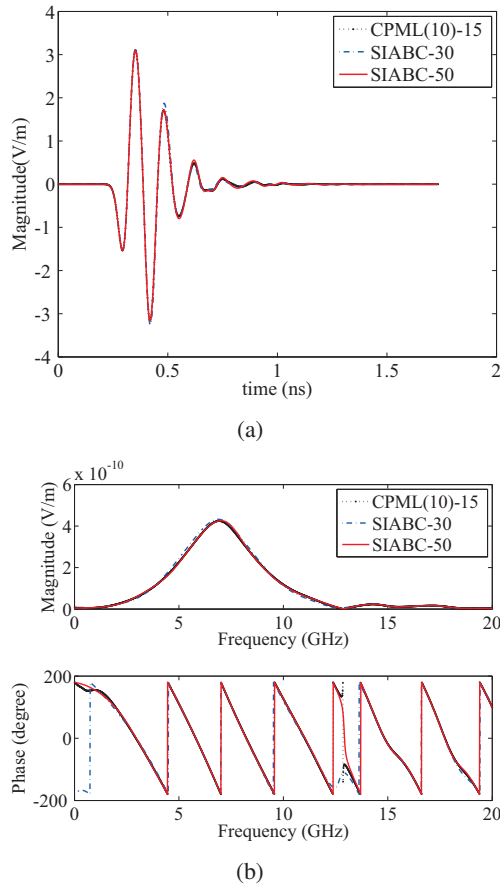
Fig. 15. Sampled E_x at P4 in (a) time domain; (b) frequency domain.

B. Microstrip low-pass filter

For this problem, the space is composed of cells with $\triangle x = 0.4064mm$, $\triangle y = 0.4233mm$, $\triangle z = 0.265mm$. An air gap of 5 cells is left between the filter and the outer boundary in the xn, xp, yn, yp, zn and zp direction. The substrate is $3 \times \triangle z$ thick and has a relative dielectric constant of 2.2. The microstrip filter is terminated by a voltage source with 50Ω internal resistance on one end and by a 50Ω on the other end. The voltage is excited by a Gaussian waveform. The FDTD problem space is illustrated in Fig. 16.
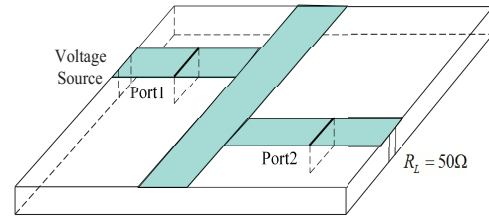

Fig. 16. A microstrip low pass filter geometry.

In the CPML case, the boundaries are terminated by 10 cells of CPML, and the number of cells between the CPML and the filter is 5. In the SIABC case, the air gap surrounding the filter is changing from 10 to 80.

Table 5 lists the maximum percentage difference based on the SIABC relative to those of the CPML values. It is obvious that the performance of SIABC with 30 cells air buffer is already quite acceptable compared to the performance of the CPML.

Table 5: Maximum percentage difference of S-parameters based on SIABC relative to those based on 10-layers CPML

Air Gap	S_{11} Difference	S_{21} Difference
20	7.4654 (5.02 GHz)	13.361 (8.38 GHz)
30	2.1921 (5.02 GHz)	2.2190 (8.30 GHz)
40	1.2828 (11.06 GHz)	1.1573 (8.32 GHz)
50	1.7183 (11.10 GHz)	0.5650 (8.32 GHz)
60	1.2654 (11.06 GHz)	0.7433 (8.32 GHz)
70	0.9164 (11.10 GHz)	0.7001 (8.32 GHz)
80	0.6800 (11.08 GHz)	0.8002 (8.32 GHz)

Figures 17 and 18 show the calculated S_{11} and S_{21} of the low pass filter when the absorbing boundary condition is set as CPML and SIABC.
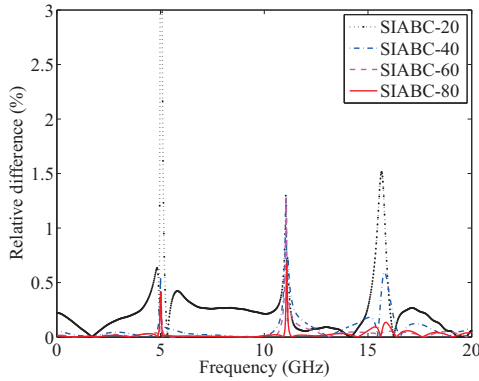
Fig. 17. Percentage difference of S_{11}.
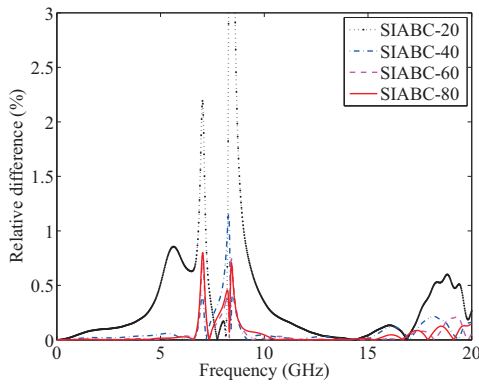
Fig. 18. Percentage difference of S_{21}.

C. Scattering from a dielectric sphere

Figure 19 shows an FDTD problem space including a dielectric sphere illuminated by an x polarized plane wave travelling in the positive z direction. The problem space is divided into cells with size $\triangle x = 0.75cm, \triangle y = 0.75cm$, and $\triangle z = 0.75cm$. The dielectric sphere has a radius of 10 cm, relative permittivity of 3, and relative permeability of 2. The waveform of the plane wave is Gaussian. The RCS is calculated from the FDTD simulations at 1 GHz.

Figures 20 and 21 display the normalized RCS when the absorbing boundary condition is 10-layers CPML and SIABC, respectively. The exact RCS of this dielectric sphere is also calculated as presented in [11] and is shown in the figure.

Here, the number of cells of air buffer is 10 for the CPML case, and for the SIABC case, it is ranging from 20 to 40. The maximum percentage error of RCS based on 10-layers CPML and SIABC relative to analytic solution is listed in Table 6.
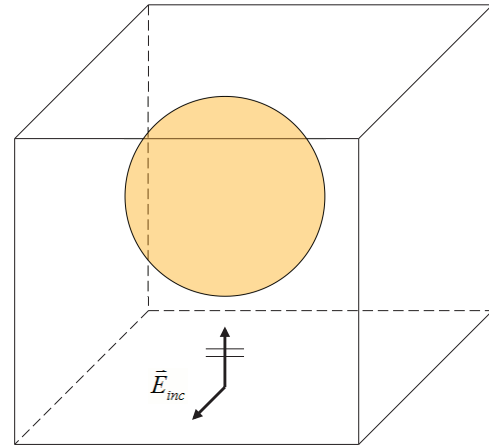

Fig. 19. A FDTD problem space including a dielectric sphere.
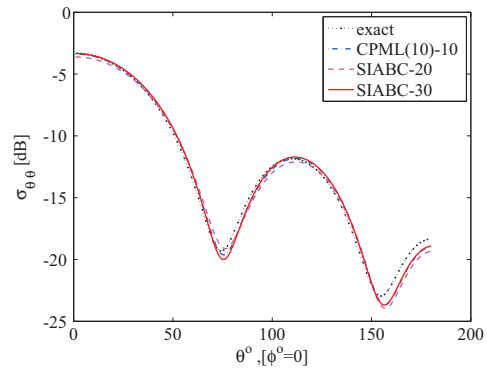
Fig. 20. RCS_θ at 1 GHz in the xz plane compared with the analytical solution.
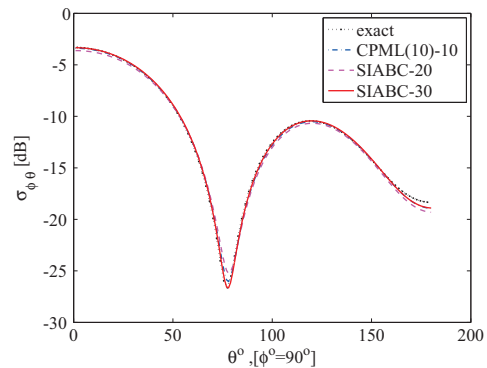
Fig. 21. RCS_ϕ at 1 GHz in the yz plane compared with the analytical solution.

One can draw from the figures and the table that when the air buffer between SIABC and the dielectric sphere is larger than 30 cells, the

performance of SIABC is in the same order as that of 10-layers CPML.

Table 6: Maximum percentage error of RCS based on 10-layers CPML and SIABC relative to analytic solution

ABCs	Air Buffer	RCS_θ	RCS_ϕ
CPML(10)	10	4.1483	2.5428
SIABC	20	5.5099	5.2008
SIABC	30	3.6534	2.1599
SIABC	40	3.5760	3.6353

D. Radiation from a patch antenna

In this example, a patch antenna is used to examine the performance of SIABC. A microstrip rectangular square patch antenna is constructed, as shown in Fig. 22. The problem space identified with grid size $\triangle x = 2mm, \triangle y = 2mm, \triangle z = 0.95mm$. A rectangular brick in the problem space representing the substrate of the antenna with dimensions of $60mm \times 40mm \times 1.9mm$ and dielectric constant of 2.2. A PEC plate as the ground of the antenna is placed right under the bottom side of the substrate covering its entire surface area. A PEC patch sits on the top surface of the substrate with $56mm$ width and $20mm$ length in the x and y directions, respectively. The patch is centred on the top surface of the substrate. The feeding point to the patch is in the middle point of the long edge of the patch. A voltage source with 50Ω internal resistance between the ground plane and the feeding point is used. This patch antenna operates at 3.45 GHz.
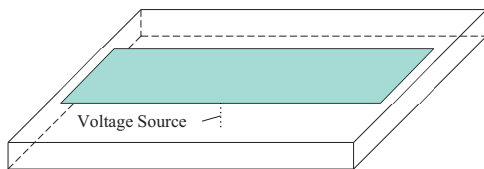
Fig. 22. A microstrip patch antenna geometry.

Table 7 lists the maximum percentage difference of SIABC results relative to those of the 10-layers CPML. The number of cells of the air buffer for the CPML case is 10, while for the SIABC case, it is ranging from 20 to 50.

Figures 23 and 24 compare the performance when using 10-layers CPML and SIABC.

Table 7: Maximum difference of directivity based on SIABC relative to those based on 10-layers CPML

| Air Buffer	Directivity Difference
20	2.5859
30	1.8525
40	1.7813
50	0.4508
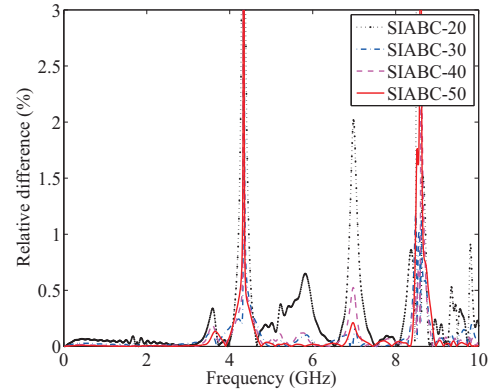
Fig. 23. Relative difference of S_{11}.
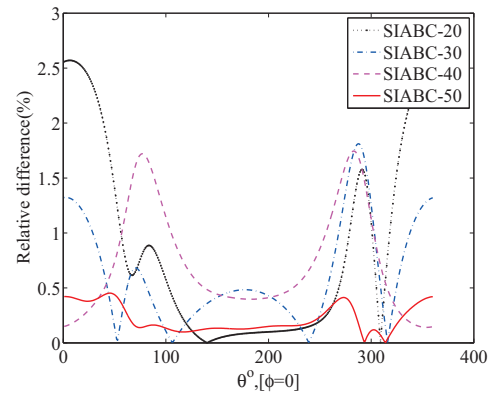
Fig. 24. Relative difference of directivity in xz plane.

E. Absorbing performance in a 1D problem

For a one dimensional problem, a Gaussian pulse is generated in the middle of a problem space of 1m length. Here, the cell size is $\triangle x = 1mm$. One side of the problem space is terminated by PML, and the other side by SIABC. Thus, the performance of PML and SIABC can be easily compared in time domain right after the first reflection from both sides. The geometry of this problem is shown in Fig. 25.
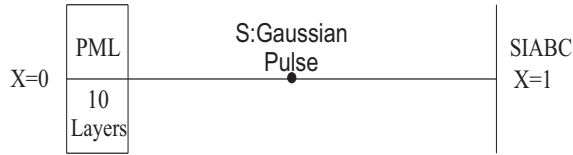
Fig. 25. Geometry of a 1D problem with PML (left) and SIABC (right) boundaries.

The result shown in Fig. 26 indicates that the reflected wave when using SIABC is 4 times smaller than that when using 10 layers of PML.
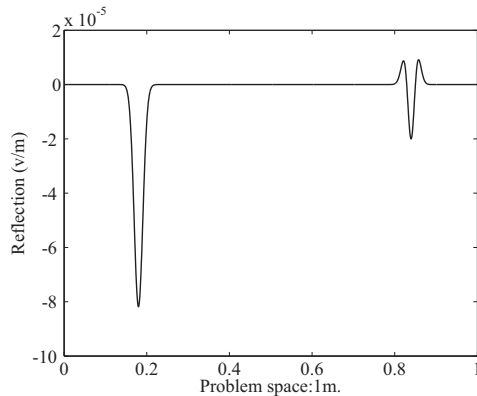

Fig. 26. Comparison of reflection from PML (left) and SIABC (right) boundaries.

IV. MEMORY USAGE

In this section, the memory usage of 10-layers CPML and SIABC is compared for a 3D computational domain. In order to simplify the analysis, the number of cells of the domain in x, y, and z directions are all the same. The relative memory increase due to the required air buffer cells when using SIABC relative to 10-layers CPML is computed as follows:

$$M_{increase} = \frac{M_{SIABC} - M_{CPML}}{M_{CPML}} \times 100\%. \quad (22)$$

Figure 27 illustrates the comparison of memory usage for domain sizes reaching one billion cells.

For practical size problems it is clear that the extra memory required is not prohibitive. Furthermore, it should be pointed out that the use of the non-uniform discretization for the free space between the objects and the outer boundary will drastically reduce the usage of this extra memory. Results based on this approach will be reported soon.
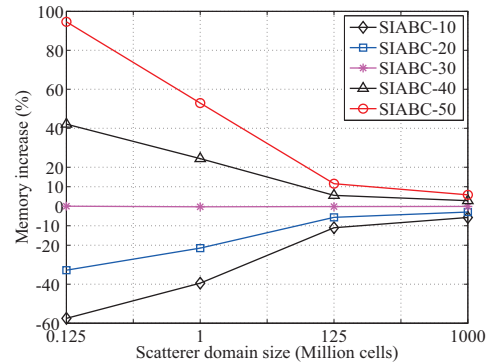

Fig. 27. Memory usage of SIABC relative to 10-layers CPML.

V. CONCLUSION

In this paper, a novel absorbing boundary condition, SIABC is introduced. Formulas of SIABC in 3D, 2D, and 1D are derived and implemented for FDTD method. From the formulations one can find out that this ABC is extremely easy to implement. The performance of SIABC is compared to that of 10-layers PML in 1D and 10-layers CPML in 3D. All the results show that when the distance between the objects inside the computational and the SIABC is in the order of 50 cells, SIABC can achieve a comparable or better results than those based on CPML results.

REFERENCE

[1] B. Engquist and A. Majda, "Absorbing boundary conditions for numerical simulation of waves," *Proceedings of the National Academy of Sciences*, vol. 74, no. 5, pp. 1765–1766, 1977.

[2] G. Mur, "Absorbing boundary conditions for the finite-difference approximation of the time-domain electromagnetic-field equations," *Electromagnetic Compatibility, IEEE Transactions on*, no. 4, pp. 377–382, 1981.

[3] J. P. Berenger, "A perfectly matched layer for the absorption of electromagnetic waves," *Journal of Computational Physics*, vol. 114, no. 2, pp. 185–200, 1994.

[4] J. A. Roden and S. D. Gedney, "Convolutional PML (CPML): an efficient fdtd implementation of the cfs-pml for arbitrary media," *Microwave and Optical Technology Letters*, vol. 27, no. 5, pp. 334–338, 2000.

[5] T. B. Senior, J. L. Volakis, and S. R. Legault, "Higher order impedance and absorbing boundary conditions," *Antennas and Propagation, IEEE Transactions on*, vol. 45, no. 1, pp. 107–114, 1997.

[6] S. Rytov, "Calcul du skin-effect par la méthode des perturbations," *J. Phys. USSR*, vol. 2, no. 3, pp. 233–242, 1940.

[7] M. Leontovich, "Approximate boundary conditions for the electromagnetic field on the surface of a good conductor," *Investigations on Radiowave Propagation*, vol. 2, pp. 5–12, 1948.

[8] J. G. Maloney and G. S. Smith, "The use of surface impedance concepts in the finite-difference time-domain method," *Antennas and Propagation, IEEE Transactions on*, vol. 40, no. 1, pp. 38–48, 1992.

[9] J. H. Beggs, R. J. Luebbers, K. S. Yee, and K. S. Kunz, "Finite-difference time-domain implementation of surface impedance boundary conditions," *Antennas and Propagation, IEEE Transactions on*, vol. 40, no. 1, pp. 49–56, 1992.

[10] A. Z. Elsherbeni and V. Demir, *The finite-difference time-domain method for electromagnetics with MATLAB simulations*. Raleigh, NC: SciTech Publishing Inc., 2009.

[11] V. Demir, A. Z. Elsherbeni, D. Worasawate, and E. Arvas, "A graphical user interface (GUI) for plane-wave scattering from a conducting, dielectric, or chiral sphere," *Antennas and Propagation Magazine, IEEE*, vol. 46, no. 5, pp. 94–99, 2004.

Biologically Inspired Optimization of Antenna Arrays

Paolo Rocca [1] and Randy L. Haupt [2]

[1] ELEDIA Research Center, Department of Information Engineering and Computer Science
University of Trento, Via Sommarive 5, Trento, Italy
paolo.rocca@disi.unitn.it

[2] Department of Electrical Engineering and Computer Science
Colorado School of Mines, Golden, CO 80401, USA
rhaupt@mines.edu

Abstract ─ Modeling biological evolution on a computer began in the 1960s with evolution strategies in Europe and genetic algorithms in the United States. Genetic algorithms were introduced to the antenna community in the early 1990s. Since that time, they have become ubiquitous in computational electromagnetics and standard options on commercial software packages. Other biological design methods based upon biological processes in nature have also been introduced. This article provides an introduction to genetic algorithms, particle swarm optimization, and ant colony optimization. Several examples of antenna array optimization are presented to illustrate the power of these algorithms.

Index Terms ─ Ant colony optimization, antenna arrays, genetic algorithms, numerical optimization, particle swarm optimization, phased arrays.

I. INTRODUCTION

Modeling biological evolution on a computer started in the 1960s when Rechenberg [1] introduced evolution strategies while Holland [2] introduced genetic algorithms. Evolutionary algorithms with real-valued solutions had a parent and a mutated version of a parent. Genetic algorithms with binary encoded solutions used populations of variables and crossover between variables to add variety. Goldberg [3] launched global optimization into the mainstream through applications of genetic algorithms to practical problems.

Antenna applications of genetic algorithms began in the early 1990s [4]. Since that time, thousands of papers and some books have been written about antenna optimization using a genetic algorithm [5], [6]. Later in the 1990s, other biologically inspired approaches to random optimization appeared. The antenna community quickly picked up on these algorithms and tackled optimization with a new flare. All of these algorithms are random searches with the ability of jumping out of local minima in an effort to find the global minimum. In spite of the claims that one random search algorithm is better than another, the No Free Lunch (NFL) theorem says that the computational cost of finding a solution for a class of mathematical problems is the same for any random search algorithm when averaged over all problems in the class. Thus, tweaking the parameters of one algorithm can cause it to outperform another algorithm for a handful of problems but not for all problems.

This paper presents three antenna array optimization applications that are solved using three different global search algorithms. We do not advocate one algorithm over the other because of the NFL theorem. These algorithms do not guarantee the "best" solution, but they usually find very good solutions that meet specifications.

II. GENETIC ALGORITM

The inspiration for the Genetic Algorithm or "GA" came from genetics and natural selection [7]. The GA starts with a list of randomly generated solutions. The list is called the population and each solution is an individual or

chromosome. The original GAs, had the solutions encoded into binary, but today both binary and continuous GAs are used [8]. Each solution is evaluated by the objective function output. Maximization problems have a fitness while minimization problems have a cost. Those chromosomes with a low fitness are discarded, while those with a high fitness are retained in the population (natural selection). The most fit chromosomes have the highest probability of mating or combining chromosomes in such a way as to create new chromosomes or offspring that replace the chromosomes discarded in natural selection. Finally, chromosomes in the new population are mutated (randomly changes made to the chromosome). The fitness of this generation is evaluated, then a new generation begins with natural selection. This process continues until a suitable solution is found.

In our first example of using biologically inspired algorithms to optimize antenna arrays, we use the binary GA to design a dynamically thinned array that suppresses sidelobe interference [9]. Each element can be either connected to (i.e., element is on) or disconnected from (i.e., element is off) the beam forming network by means of a switch (Fig. 1). The GA maximizes a quantity that is proportional to the Signal-to-Noise plus Interference Ratio (SINR) by determining the best configuration for the switches.

Consider a uniform array of 64 half-wavelength spaced elements. The interference configuration is supposed static with two interfering signals impinging on the antenna from $\phi_1 = 42°$ and $\phi_2 = 113°$, while the desired signal arrives from broadside ($\phi = 90°$). The power of each interfering signal is 30 dB above that of the desired signal, while the background noise contribution is negligible. The values of the fitness function, defined according to [10], and of the SINR are shown in Fig. 2 (a) for the best individual (i.e., solution) of the GA population for each generation throughout the optimization process. It is worth noting how the SINR increases generation after generation starting from very low values close to -5 dB up to almost 25 dB. This is achieved through the generation of deeper and deeper sidelobe nulls in the interference directions. In particular, Fig. 2 (b) shows the depth of the nulls in the directions of the two interferences for each generation. Although the fitness always stays the same or goes up, the null depths can go up, stay the same, or go down with each generation. One null may go down a lot while another null may go up, but on the average, the SINR goes up.

The array factor and the corresponding on-off configuration of the switches obtained by the best solution of the GA optimization at the end of the optimization are shown in Figs. 3 (a) and 3 (b), respectively. It is evident in Fig. 3 (a) that the GA is effective in suppressing the interferences by placing deep nulls in the sidelobe region in their directions of arrival.
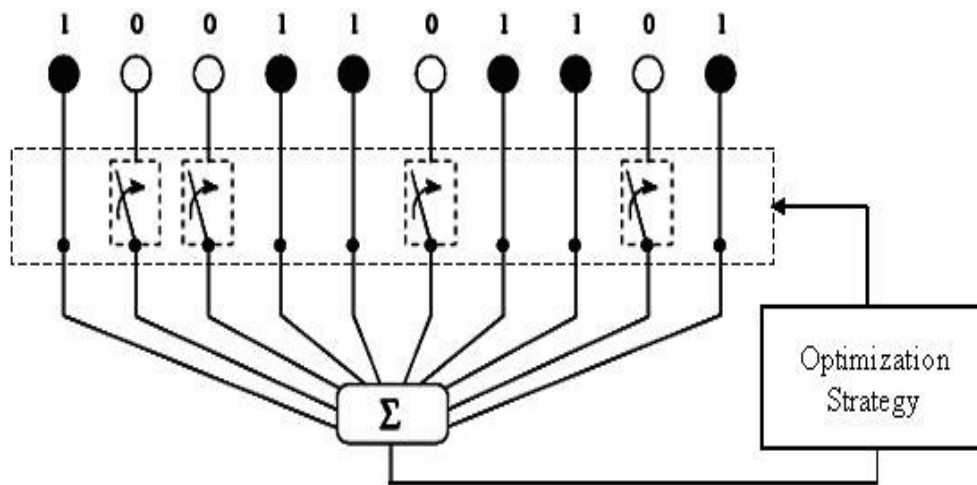

Fig. 1. Sketch of a dynamic thinned array.

(a)

(b)
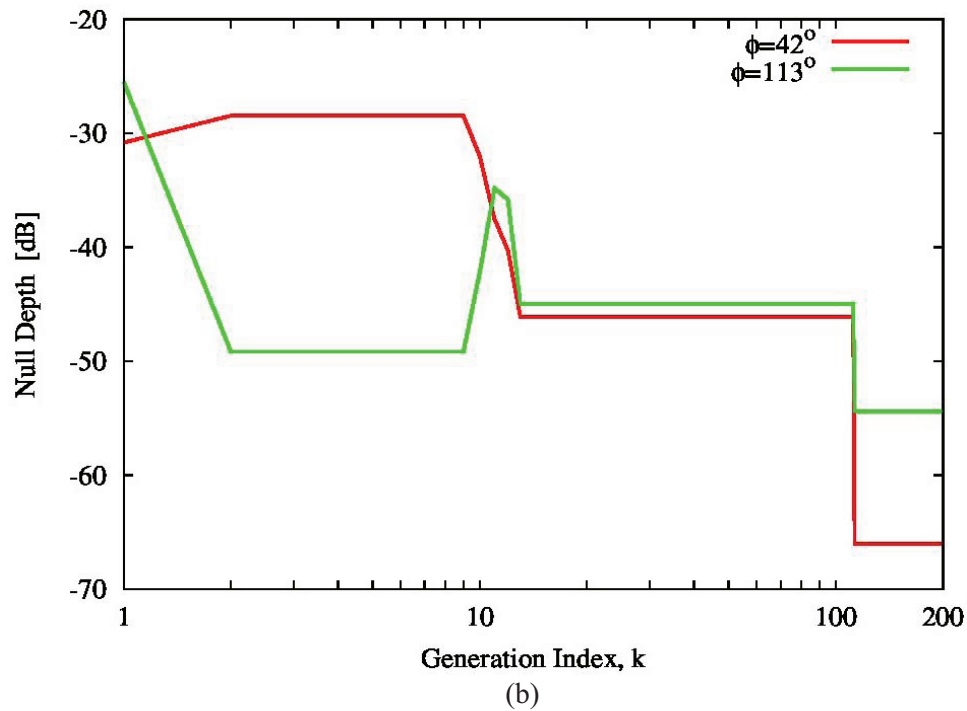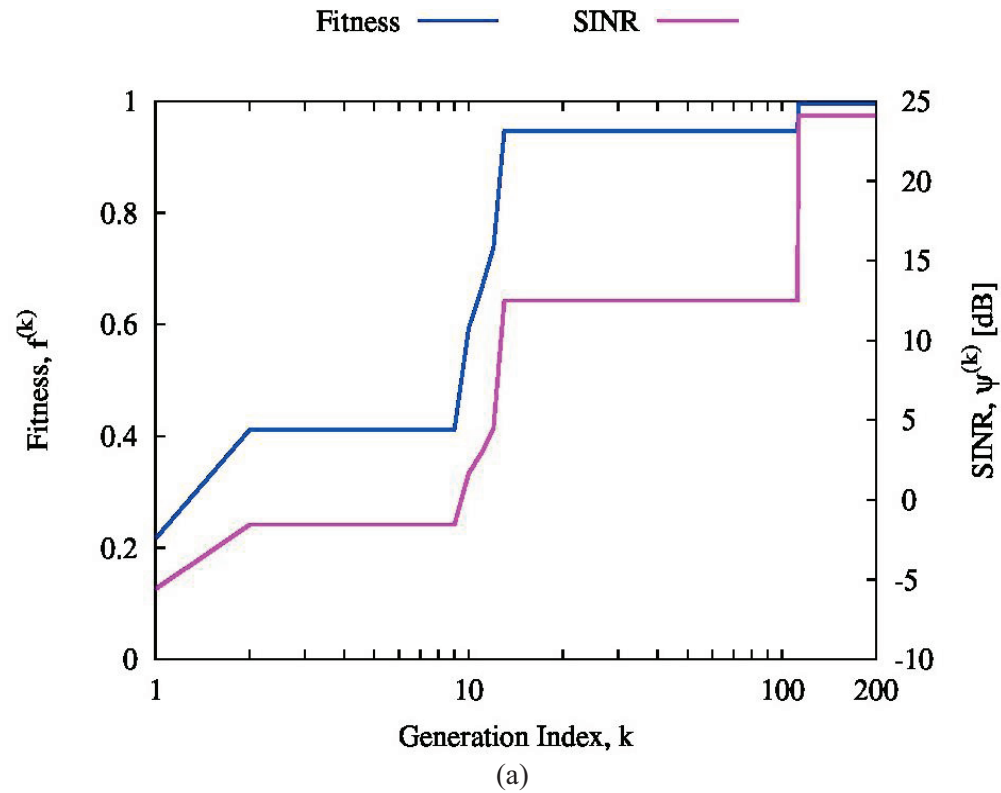
Fig. 2. Behavior: (a) of the fitness function and of the SINR for the best solution defined by means of the GA, and (b) of the null depths in the directions of the interferences versus the iteration index.

(a)

(b)
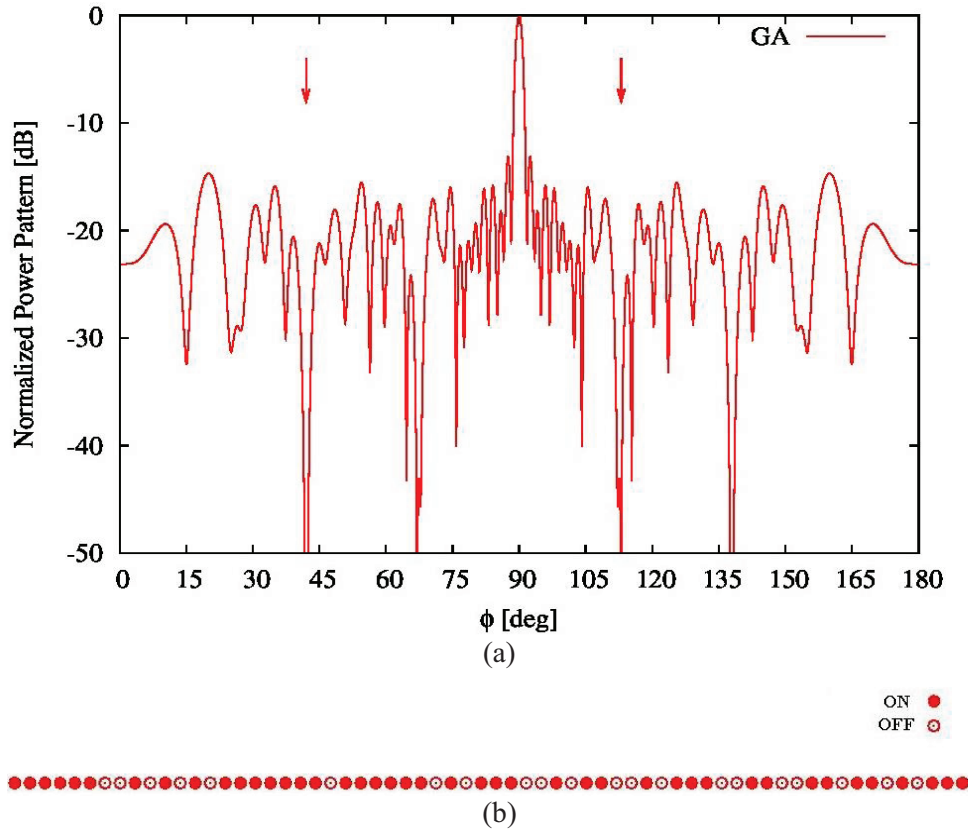
Fig. 3. Plot: (a) of the power pattern with arrows along the interference directions, and (b) of the on-off configuration of the switches for the best solution of the GA optimization at the final generation.

III. PARTICLE SWARM OPTIMIZATION

Particle Swarm Optimization (PSO) models the swarming or flocking animals and their motion [11][12]. PSO has a random population matrix like the GA, but the rows in the matrix are called particles instead of chromosomes. Particles are potential solutions that move in a particular direction on the cost surface with a certain velocity. Particles update their positions and velocities using formulas based on the knowledge about the best solution achieved by each particle in its movements (i.e., personal best) and by the complete swarm of particles (i.e., global best).

Our second example applies PSO to optimize the design of a Time-Modulated Linear Array (TMLA) [13], allowing the generation of multiple beam patterns on receive. As for the antenna architecture of a TMLA, it is very similar to that of the thinned array shown in Fig. 1. Unlike thinned arrays, in TMLAs the switches are periodically turned on and off by means of proper time switching sequences such that the average

harmonic patterns generated within the modulation period are characterized by user-defined properties [13].

The example TMLA has 16 elements with half-wavelength spacing. The goal is to simultaneously generate sum and difference patterns using the first (h=1) and central (h=0) harmonic radiation patterns. The two beam patterns must have the minimum Sidelobe Level (SLL) of the secondary lobes. Furthermore, the level of the higher harmonic terms (h>1), the so-called Sideband Level (SBL), generated by the periodic time-modulation of the switches should be as low as possible. Towards this aim, the cost function is defined according to the guidelines of [13].

The array patterns of the best solution are shown in Fig. 4. Figure 4 (a) shows the difference and sum patterns generated by means of the TMLAs at the central (h=0) and first (h=1) harmonic radiation when controlling the switches according to the on-off configuration of Fig. 4 (b). In Fig. 4 (b), the bars represent the instants when

the elements are on while the elements are disconnected from the feeding network in the remaining part of the modulation period.

Figure 5 (a) is a graph of the different components of the cost function, related to the SLL at both h=0 and h=1, and of the SBL, as well as the cumulative cost function values for the best solution of the PSO at each iteration. SLLs of -17 dB are achieved for both power patterns [Fig. 4

(a)] and the SBL of the higher harmonics is effectively suppressed for h>1 [Fig. 5 (b)]. The percentage of power, with respect to the total, associated to the pattern at the central and first nine harmonics is shown in Fig. 6. It is possible to observe that the largest amount of power is used for the sum and difference patterns at h=0 and h=1, while the power gets quickly to zero for higher harmonic modes.


(a)

(b)
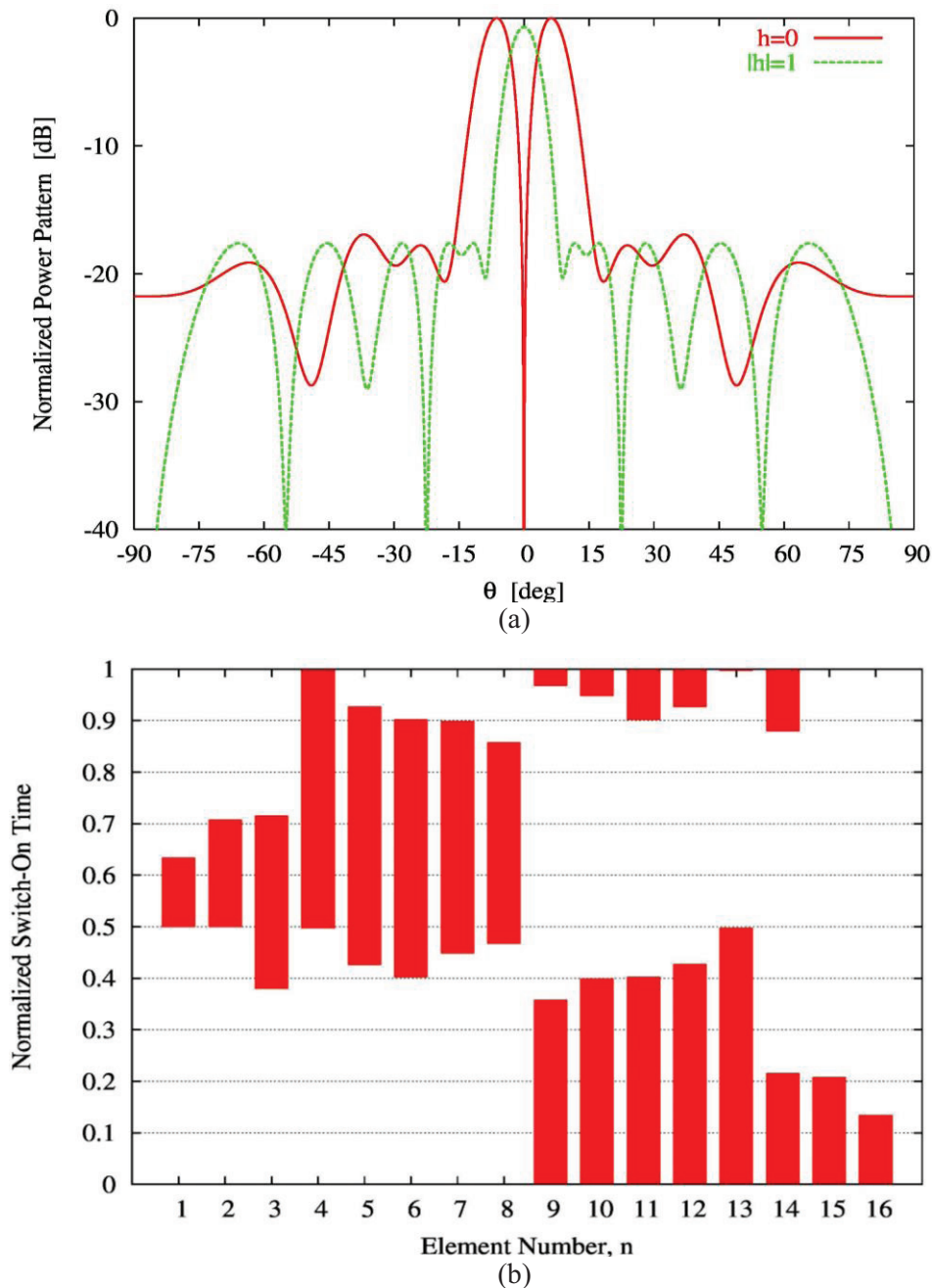
Fig. 4. Plot: (a) of the power patterns generated by the TMLA for h=0 and |h|=1, and (b) of on-off time-modulation sequence for the best solution of the PSO optimization at convergence.

(a)

(b)
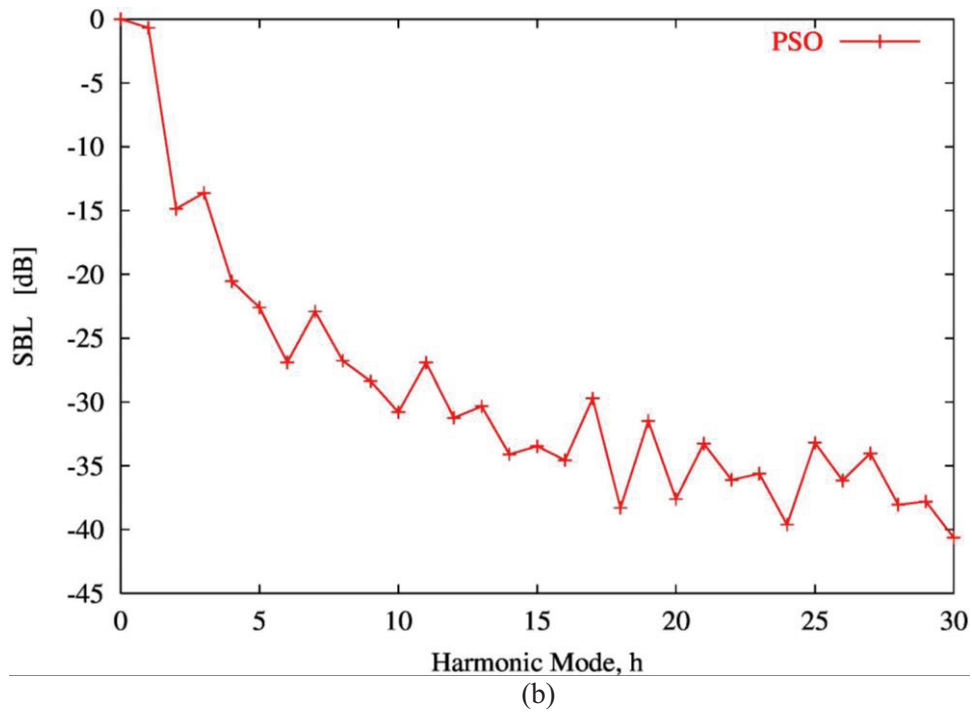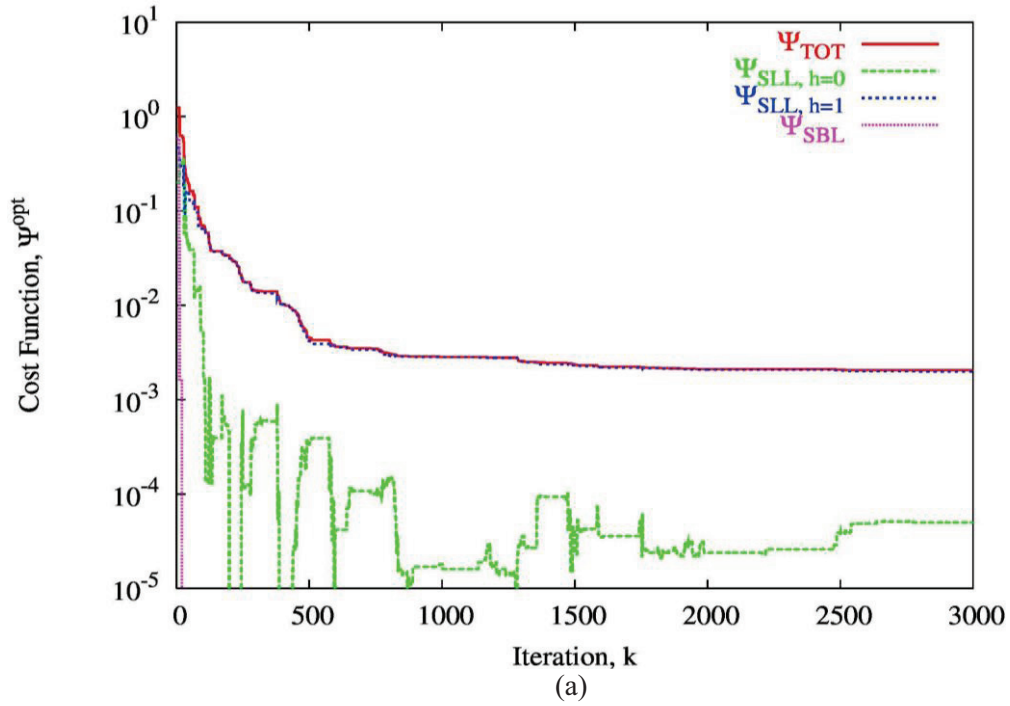
Fig. 5. Behavior: (a) of the cost function terms and of their sum for the best solution defined by means of the PSO versus the iteration index, and (b) of the SBL as a function of the harmonic index.
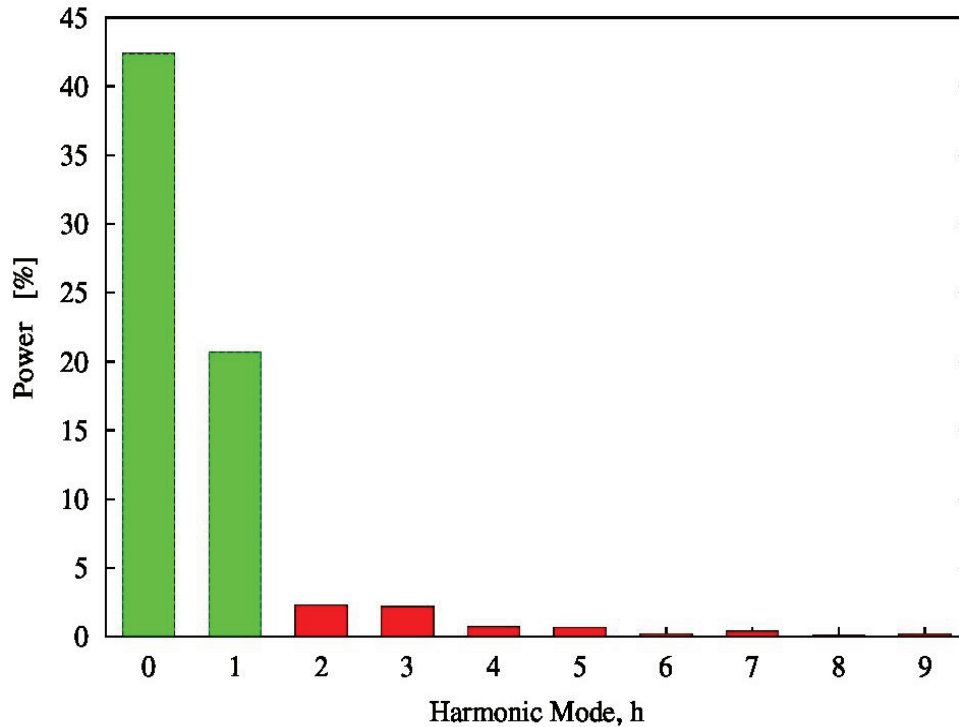
Fig. 6. Percentage of individual power associated to the harmonic radiations.

IV. ANT COLONY OPTIMIZATION

Ant Colony Optimization (ACO) is based on the behavior of ant colonies in obtaining food and carrying it back to the nest [14]. When ants search for food, they emit a pheromone (chemical) along their trail. Other ants follow the pheromone path to the food while laying down more pheromone. Shorter paths to the food result in stronger trails of pheromone, because the pheromone evaporates with time. Stronger pheromone paths are also the shortest paths, so they attract more ants an eventually, the shorter path dominates. When the food source is gone, the pheromones gradually evaporate, and ants no longer follow that path.

A traveling salesperson problem is perfect for ACO, because this problem closely resembles finding the shortest path to a food source. ACO results in premature convergence to a local optimal solution unless pheromone evaporation is implemented; a solution disappears after a period of time. As a result, the pheromone along the best path found so far by the algorithm is given some weight in calculating the new pheromone levels.

The design of a sub-arrayed antenna array generating an optimal sum pattern through a set of independent and optimal weighting coefficients and a compromise/sub-optimal difference pattern by aggregating the array elements into sub-arrays and defining suitable sub-array weights is addressed by means of the ACO. A sketch of the antenna configuration appears in Fig. 7, where only half array is shown due to symmetry.

Exploiting the theoretical guidelines of [15], it has been shown that the problem can be defined as an excitation matching problem, where the excitations of the compromise difference pattern can be obtained by approximating the values of a set of excitations generating an optimal difference power pattern. Moreover, the solution space can be represented in this case by means of a binary tree [Fig. 8 (a)], where each path identifies a possible sub-array configuration and the corresponding set of sub-array weights. Accordingly, the goal is to find the sub-optimal difference pattern closest to the optimal one. Besides the ad-hoc local optimization technique

originally proposed in [15], called Border Element Method (BEM), the ACO has been adopted [16] and has showed superior performance thanks to the fact that it can avoid local minima. In this case, the ants leave pheromone on the edges of the binary tree proportionally to the suitability of the solutions obtained at the previous iteration. As a representative example, Fig. 8 (b) shows the pheromone level, higher where the lines are ticker, left by the ants of the colony on the edges of the binary tree. At the next generations, the ants will choose with higher probability paths/solutions with more pheromone.

Our final example is a 40 element array with 4 sub-arrays in each half of the array. The reference/optimal excitations are chosen to generate a Zolotarev difference pattern with SLL=-30 dB. The best solutions obtained by means of the ACO is shown in Fig. 9, together with the one achieved through the BEM. As a first observation, it is possible to note that the compromise pattern synthesized with the ACO is closer to the reference one than the BEM pattern. This fact is confirmed by the values of the cost function of Fig. 10. The fitness of the BEM oscillates as it converges. After 100 iterations, the BEM seems to be stuck in a local minimum, while the average ACO run has found a much lower minimum.
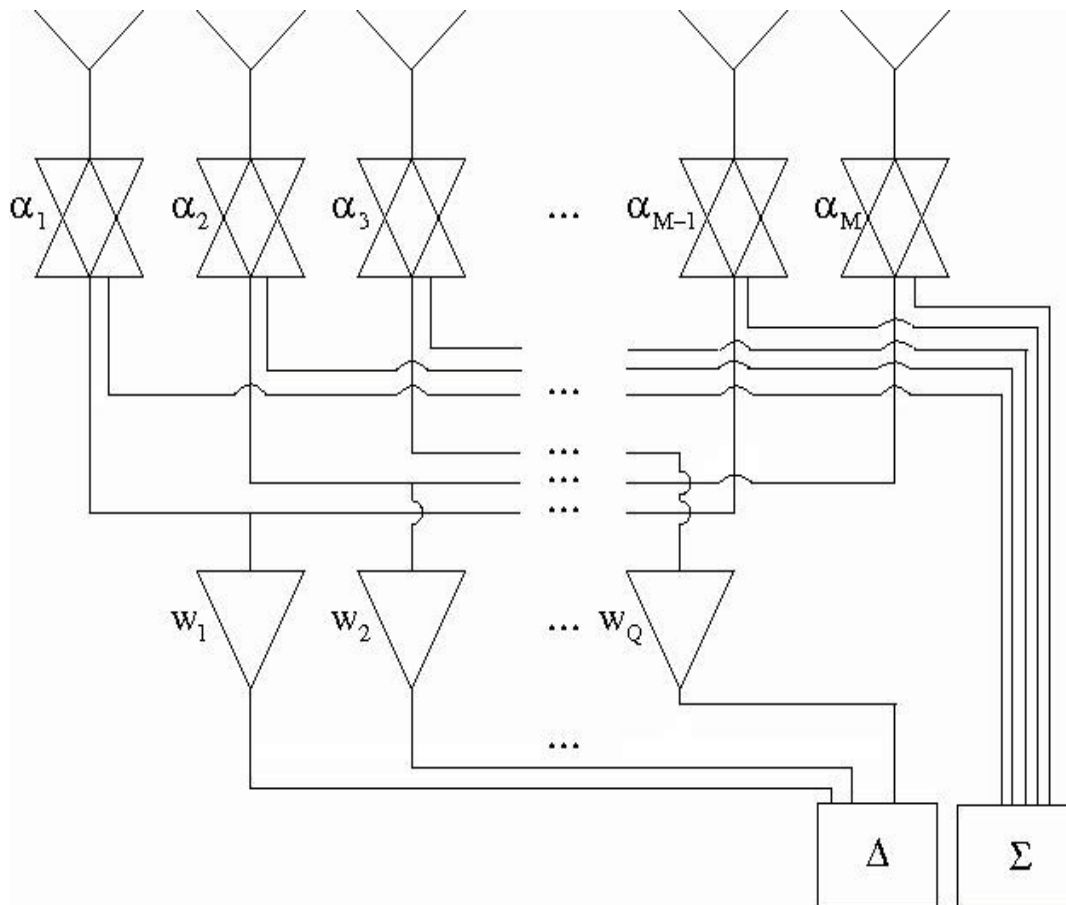

Fig. 7. Sketch of a compromise sub-arrayed array.

{1,1,1,2,3}

{1,1,2,3,3}

{1,2,2,3,3}

(a)

{1,1,1,2,3}

{1,1,2,3,3}

{1,2,2,3,3}

(b)
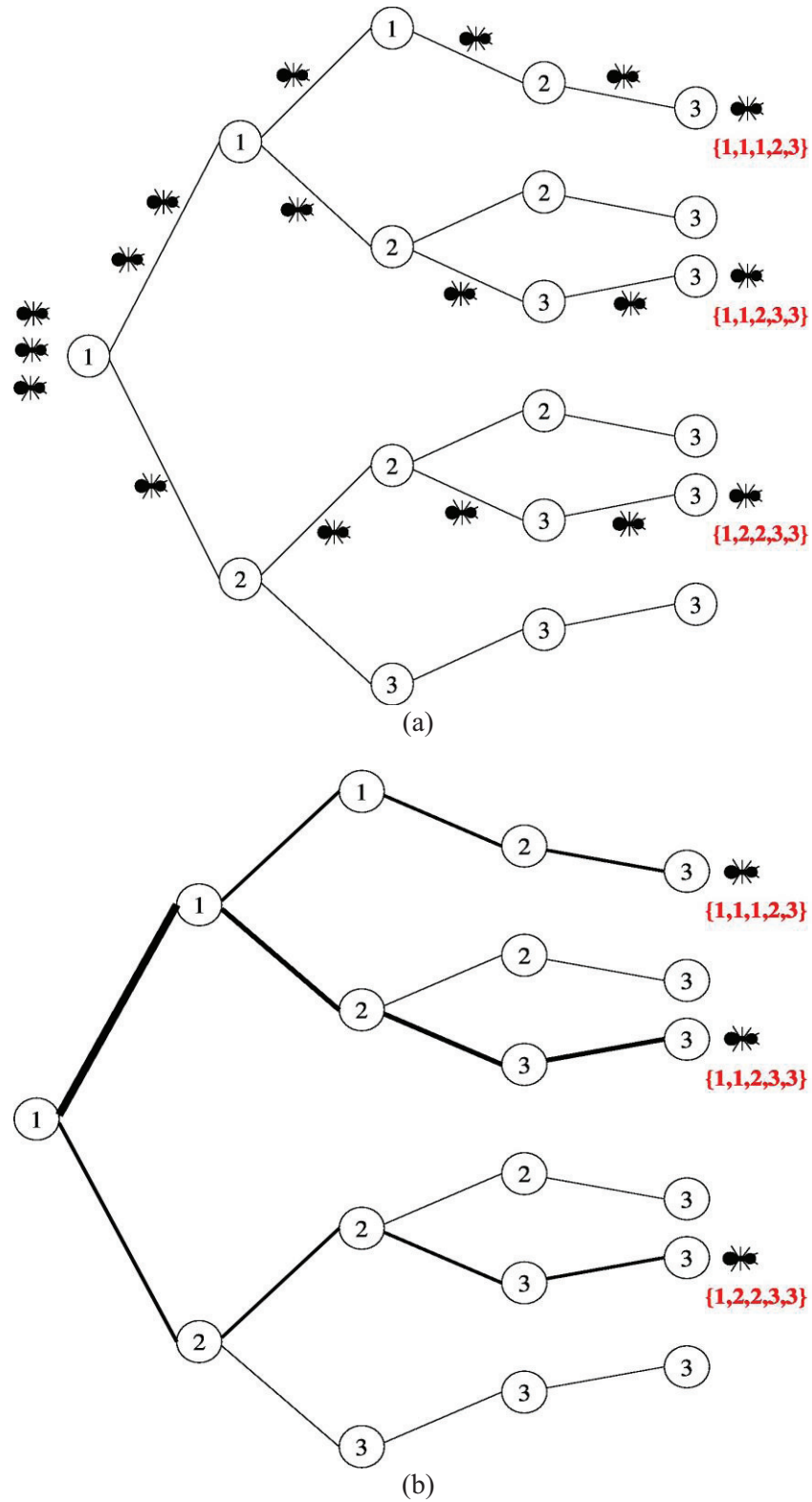
Fig. 8. Sketch: (a) of the solution tree where each ant defines a trial sub-array configuration whose sub-array weights are computed as in [15], and (b) of the solution tree with updated levels of pheromone left on the edges from the ants.
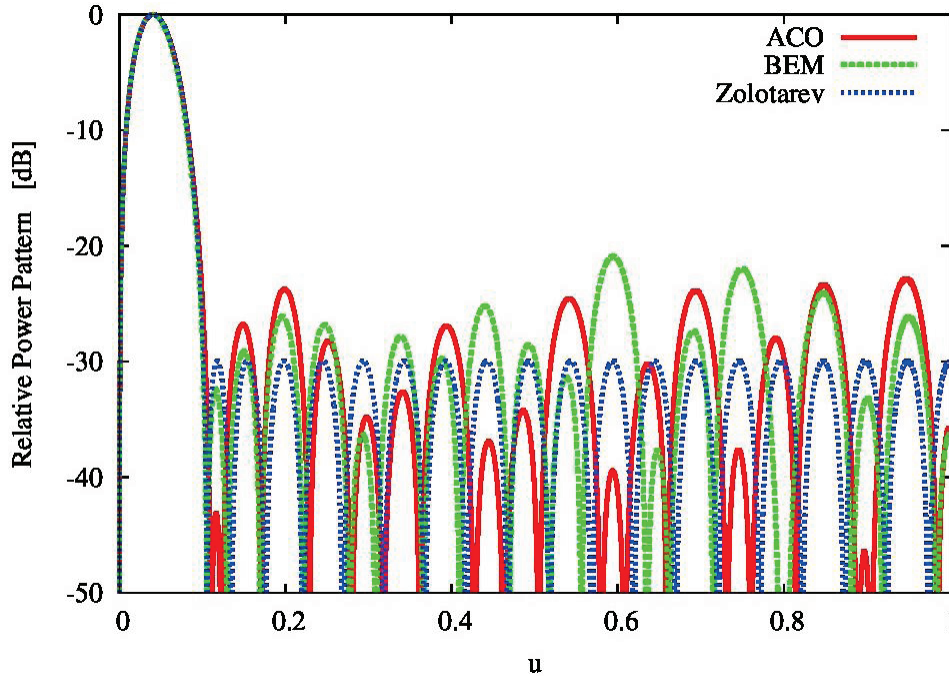
Fig. 9. Plot of the reference power pattern (Zolotarev) and of the compromise power patterns synthesized with the ACO and the BEM.
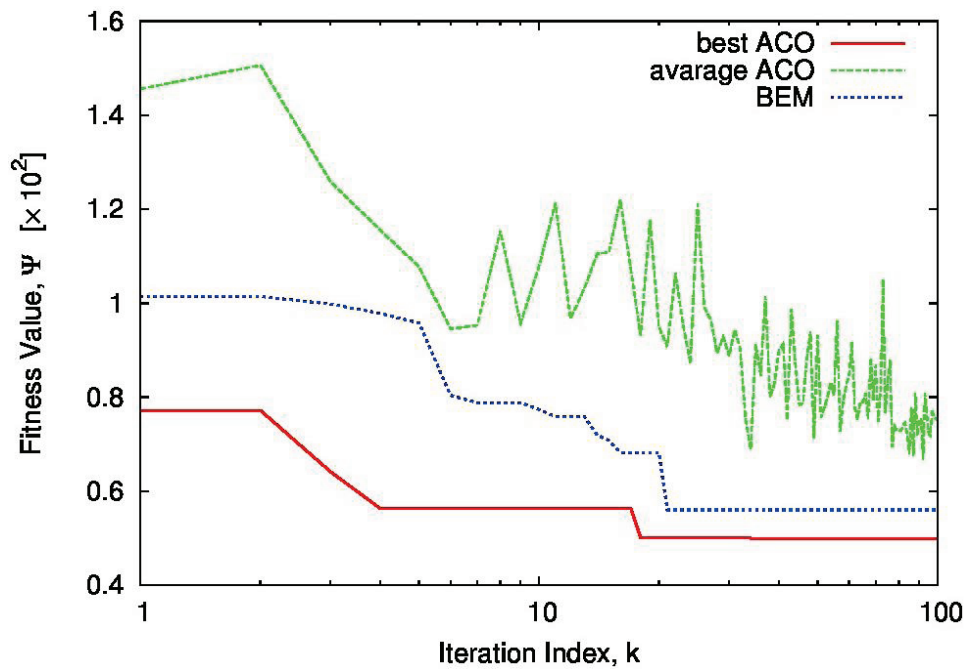

Fig. 10. Behavior of the cost function versus the iteration index for the best solution of the ACO and the average of the ACO colony and for the BEM.

VI. CONCLUSIONS

This paper presented three different biologically based numerical optimization strategies and applied each approach to an antenna array design problem. GA, PSO, and ACO are all random search algorithms that are guided by biological principles. Table 1 lists the major terms associated with each of these algorithms. They all

maintain a collection of possible solutions and use biologically based rules to search the objective function space for the best solution. The flowcharts for these algorithms are very similar as shown in Fig. 11. They are all very parallel in nature in that many individual evaluations can be done simultaneously. This parallelism was not a strong point of some other well-known global optimizations approaches, such as simulated annealing and evolutionary strategies.

Which algorithm should you use? The ACO is primarily designed for traveling salesman type problems (i.e., optimization problems where the solution space can be represented through a graph), so it is not as universally applicable to antenna design. Both GA and PSO have yielded excellent results in computational electromagnetics, although the PSO have been mainly used for the optimization of real-valued parameters over continuous spaces while the GA has binary, integer, and continuous versions [17]. We do not advocate one over the other, and the NFL theorem backs our decision.

Table 1: Terms for GA, PSO, and ACO

|	GA	PSO	ACO
Solution matrix	Population	Swarm	Colony
Individual solution (Phenotype Space) [1]	Individual	Particle	Ant
Individual solution (Genotype Space)	Chromosome	Position	Path
Best solutions	Parent	Current position	Current path
New solution	Offspring	Next position	Next path
Iteration	Generation	Generation	Generation
Objective function evaluation	Fitness/cost	Fitness/cost	Desirability/cost
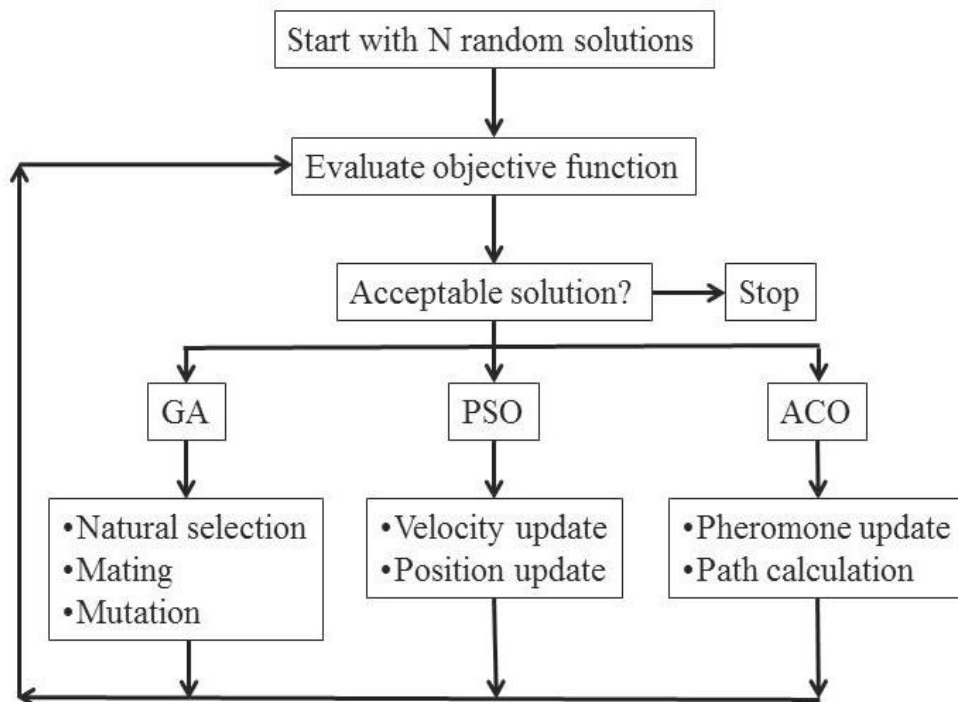
Fig. 11. Flowchart for biological optimization algorithms.

---

[1] The phenotype space is the space of the input parameter as they appear in the "real world," while the genotype space is the work space of the coded parameters.

REFERENCES

[1] H. Schwefel, "Evolution and optimum seeking," *New York: John Wiley*, 1995.

[2] J. H. Holland, "Adaptation in natural and artificial systems," *Ann Arbor: The University of Michigan Press*, 1975.

[3] D. E. Goldberg, "The design of innovation: lessons from and for competent genetic algorithms," *Kluwer Academic Publishers*, Boston, MA, 2002.

[4] R. L. Haupt, "An introduction to genetic algorithms for electromagnetics," *IEEE Antennas and Propagation Magazine*, vol. 37, issue 2, pp. 7-15, April 1995.

[5] R. L. Haupt and D. H. Werner, "Genetic algorithms in electromagnetics," *John Wiley and Sons, Inc.*, 2007.

[6] Y. Rahmat-Samii and E. Michielssen, "Electromagnetic optimization by genetic algorithms," *New York: Wiley*, 1999.

[7] J. H. Holland, "Genetic algorithms," *Scientific American*, vol. 267, pp. 66-72, 1992.

[8] R. L. Haupt and S. E. Haupt, "Practical genetic algorithms," 2nd edition, *New York: John Wiley & Sons*, 2004.

[9] P. Rocca, R. L. Haupt, and A. Massa, "Interference suppression in uniform linear arrays through a dynamic thinning strategy," *IEEE Transactions on Antennas and Propagation*, vol. 59, no. 12, pp. 4525-4533, 2011.

[10] L. Poli, P. Rocca, M. Salucci, and A. Massa, "Reconfigurable thinning for the adaptive control of linear arrays," *IEEE Transactions on Antennas and Propagation*, vol. 61, no. 10, pp. 5068-5077, 2013.

[11] J. Kennedy and R. C. Eberhart, "Particle swarm optimization," *Proceedings IEEE International Conference on Neural Networks, IV, Piscataway, NJ: IEEE Service Center*, pp. 1942-1948, 1995.

[12] J. Kennedy, R. C. Eberhart, and Y. Shi, "Swarm intelligence," *San Francisco: Morgan Kaufmann*, 2001.

[13] L. Poli, P. Rocca, G. Oliveri, and A. Massa, "Harmonic beamforming in time-modulated linear arrays," *IEEE Transactions on Antennas and Propagation*, vol. 59, no. 7, pp. 2538-2545, 2011.

[14] M. Dorigo, V. Maniezzo, and A. Colorni, "Ant system: optimization by a colony of cooperating agents," *IEEE Transactions on Systems, Man, and Cybernetics, Part B*, vol. 26, no. 1, pp. 29-41, 1996.

[15] L. Manica, P. Rocca, A. Martini, and A. Massa, "An innovative approach based on a tree-searching algorithm for the optimal matching of independently optimum sum and difference excitations," *IEEE Transactions on Antennas and Propagation*, vol. 56, no. 1, pp. 58-66, 2008.

[16] P. Rocca, L. Manica, and A. Massa, "An improved excitation matching method based on an ant colony optimization for suboptimal-free clustering in sum-difference compromise synthesis," *IEEE Transactions on Antennas and Propagation*, vol. 57, no. 8, pp. 2297-2306, 2009.

[17] R. L. Haupt, "A mixed integer genetic algorithm for electromagnetics applications," *IEEE Transactions on Antennas and Propagation*, vol. 55, no. 3, March 2007.

Paolo Rocca received the M.S. degree in Telecommunications Engineering from the University of Trento in 2005 (summa cum laude) and the Ph.D. degree in Information and Communication Technologies from the same University in 2008. He is currently an Assistant Professor with the Department of Information Engineering and Computer Science (University of Trento) and a Member of the ELEDIA Research Center. He is the author/co-author of over 200 peer reviewed papers on international journals and conferences. Rocca has been awarded from the IEEE Geoscience and Remote Sensing Society and the Italy Section with the best Ph.D. thesis award IEEE-GRS Central Italy Chapter. His main interests are in the framework of antenna array synthesis and design, electromagnetic inverse scattering, and optimization techniques for electromagnetics. He serves as an Associate Editor of the IEEE Antennas and Wireless Propagation Letters.

Randy L. Haupt received the B.S.E.E. from the USAF Academy (1978), the M.S. in Engineering Management from Western New England College (1982), the M.S.E.E. from Northeastern University (1983), and the Ph.D. in E.E. from The University of Michigan (1987). He is Professor and Department Head of the Electrical Engineering and Computer Science Department at the Colorado School of Mines and was an RF Staff Consultant at Ball Aerospace & Technologies, Corp., a Senior Scientist and Department Head at the Applied Research Laboratory of Penn State, Professor and Department Head of ECE at Utah State, Professor and Chair of EE at the University of Nevada Reno, and Professor of EE at the USAF Academy. He was a Project Engineer for the OTH-B Radar and a Research Antenna Engineer for Rome Air Development

Center early in his career. Haupt's research interests and expertise spans a wide range of topics in electromagnetics that include theoretical, numerical, and experimental projects. He is co-author of the books *Practical Genetic Algorithms*, 2nd ed., John Wiley & Sons, 2004, *Genetic Algorithms in Electromagnetics*, John Wiley & Sons, 2007, and *Introduction to Adaptive Antennas*, SciTech, 2010, as well as author of *Antenna Arrays a Computation Approach*, John Wiley & Sons, 2010. Haupt was the Federal Engineer of the Year in 1993 and is a Fellow of the IEEE and Applied Computational Electromagnetics Society (ACES). He is a Member of the IEEE Antenna Standards Committee and the IEEE Antennas and Propagation Society representative to the National Academy of Sciences Union of Radio Science. He serves as an Associate Editor for the "Ethically Speaking" column in the IEEE AP-S Magazine.

Robust Adaptive Array Beamforming Based on Modified Norm Constraint Algorithm

Wenxing Li, Xiaojun Mao, Wenhua Yu, Yingsong Li, and Chongyi Yue

College of Information and Communications Engineering
Harbin Engineering University, Harbin 150001, China
liwenxing@hrbeu.edu.cn, maoxiaojun@hrbeu.edu.cn, wenyu@2comu.com
liyingsong@ieee.org, chongyiyue@hrbeu.edu.cn

Abstract ─ In order to further improve the performance of the Norm Constrained Capon Beamforming (NCCB) algorithm, a Modified Norm Constraint Capon algorithm (MNCCB) is proposed and investigated in detail. The proposed MNCCB algorithm is realized by exerting an orthogonal projection on the array weight vector and restricting the norm constraint to enhance the array weight vector constraint when Array Steering Vector (ASV) mismatch is large. The simulation results show that the proposed MNCCB can provide stronger robustness against ASV mismatches and can achieve higher output Signal to Interference plus Noise Ratio (SINR), compared with existing adaptive beamforming algorithms.

Index Terms ─ Norm constraint, orthogonal projection, robust adaptive beamforming.

I. INTRODUCTION

Array signal processing has been widely used in radar, mobile communications, sonar and microphone array speech processing. Adaptive beamforming is one of the hottest topics in array signal processing. As for adaptive beamformer, it can adaptively adjust weight vector to achieve maximum gain at the direction of desired signal and suppress interferences by forming nulls at the directions of interferences [1-3]. To meet these applications, many beamformers have been proposed, such as Standard Capon Beamformer (SCB), Diagonal Loading SCB (DL-SCB) and NCCB [4-14]. However, the SCB is very sensitive to the ASV mismatch and may suppress the signal of interest, which might reduce the array output SINR [4-6]. As for the DL-SCB algorithm, although it can improve the robustness of the SCB, it is difficult to choose the optimal diagonal loading factor and it may increase the power noise [7]. Another effective beamformer is the Robust Capon Beamforming algorithm (RCB) [9], which can enhance the robustness of the DL-SCB. It is proved that RCB is equivalent and belongs to the class of diagonal loading. The RCB may lose its interference suppression capability when the mismatch is large. Recently, a popular beamformer named as NCCB is studied to achieve higher performance compared with the basic SCB algorithm for small ASV mismatch [11,13], while its performance is not good for large ASV mismatch.

In this paper, an MNCCB is proposed to further improve the performance of NCCB for large ASV mismatch by using the orthogonal projection and norm constraint techniques. The proposed MNCCB algorithm can ensure approximate orthogonality between the weight vector and noise subspace, which significantly improves the robustness performance with respect to ASV mismatch. The detailed theoretical analysis and analytical expression of the proposed MNCCB algorithm is provided in detail. The simulation results demonstrate that the proposed MNCCB algorithm has excellent performance against the ASV mismatches.

II. SIGNAL MODEL

We consider an N elements omnidirectional array, spaced with element distance of d, and M far field narrow band signals are incident on

this antenna array. A signal $s_k(t)$ is incident from angle θ_k, and the received data $\mathbf{X}$ can be expressed as follows:

$$\mathbf{X}(t) = \mathbf{A}\mathbf{S}(t) + \mathbf{N}(t), \qquad (1)$$

where $\mathbf{x}(t) = [x_1(t), x_2(t), \cdots, x_N(t)]^T$ is $N \times 1$ snap data vector. $\mathbf{S}(t) = [s_0(t), s_1(t), \cdots, s_{M-1}(t)]^T$ is a vector, which contains the complex signal envelops from M narrow-band signal sources. $\mathbf{N}(t) = [n_1(t), n_2(t), \cdots, n_N(t)]^T$ is a vector of zero-mean white Gaussian noise with variance of σ_n^2 and $\mathbf{A}$ is an array manifold matrix that can be written as $\mathbf{A} = [\mathbf{a}(\theta_0), \mathbf{a}(\theta_1), \cdots, \mathbf{a}(\theta_{M-1})]$. Here, $\mathbf{a}(\theta_1) = [1, e^{j\beta_k}, \cdots, e^{j(N-1)\beta_k}]^T$, $k = 1, 2, \cdots, M$, represents an ASV in the direction of θ_k, and β_k is the phase difference that can be expressed as:

$$\beta_k = \frac{2\pi}{\lambda} d \sin(\theta_k). \qquad (2)$$

Assume that the signal and noise are statistically independent, and the covariance of the received data can be written as:

$$\mathbf{R} = E\{\mathbf{X}(t)\mathbf{X}^H(t)\} = \mathbf{A}\mathbf{R}_s\mathbf{A}^H + \sigma_n^2\mathbf{I}, \qquad (3)$$

where0 $E\{\ \}$ is an expectation operator; $\mathbf{R}_s = E\{\mathbf{S}(t)\mathbf{S}^H(t)\}$ represents the autocorrelation matrix of the complex signal envelops. $\mathbf{I}$ is the unit matrix and $(\cdot)^H$ denotes the Hermitian transpose.

On the basis of the previous researches on the SCB, we assume that the ASV of the desired signal $\mathbf{a}(\theta_0)$ is known precisely. Then, the Capon beamformer can be expressed as:

$$\begin{cases} \min_{\mathbf{w}} \mathbf{w}^H \hat{\mathbf{R}}_{i+n} \mathbf{w} \\ s\,t \ \ \mathbf{w}^H \mathbf{a}(\theta_0) = 1 \end{cases}, \qquad (4)$$

where $\mathbf{w}$ is the beamformer weight vector. $\hat{\mathbf{R}}_{i+n}$ is the inference-plus-noise covariance matrix, which is commonly replaced by the sampled covariance matrix in the practical applications and it can be written as:

$$\hat{\mathbf{R}} = \frac{1}{K} \sum_{i=1}^{K} \mathbf{X}(i)\mathbf{X}^H(i), \qquad (5)$$

where K is the number of snapshots collected by the beamformer. The optimal solution of (4) is given by:

$$\mathbf{W}_{opt} = \frac{\mathbf{R}_{i+n}^{-1}\mathbf{a}(\theta_0)}{\mathbf{a}^H(\theta_0)\mathbf{R}_{i+n}^{-1}\mathbf{a}(\theta_0)}. \qquad (6)$$

The array output power is:

$$P_{out} = \mathbf{W}^H \mathbf{R}_{i+n}^{-1} \mathbf{W} = \frac{1}{\mathbf{a}^H(\theta_0)\mathbf{R}_{i+n}^{-1}\mathbf{a}(\theta_0)}. \qquad (7)$$

The array output SINR is expressed as:

$$\begin{aligned} SINR_{opt} &= \frac{\sigma_s^2 \left|\mathbf{W}_{opt}^H\mathbf{a}(\theta_0)\right|^2}{\mathbf{W}_{opt}^H\mathbf{R}_{i+n}\mathbf{W}_{opt}} \\ &= \frac{\sigma_s^2 \left|\mathbf{a}^H(\theta_0)\mathbf{R}_{i+n}^{-1}\mathbf{a}(\theta_0)\right|^2}{\mathbf{a}^H(\theta_0)\mathbf{R}_{i+n}^{-1}\mathbf{R}_{i+n}\mathbf{R}_{i+n}^{-1}\mathbf{a}(\theta_0)}, \\ &= \sigma_s^2 \mathbf{a}^H(\theta_0)\hat{\mathbf{R}}_{i+n}^{-1}\mathbf{a}(\theta_0) \end{aligned} \qquad (8)$$

where $\sigma_s^2 = E\left[\left|s_0(t)\right|^2\right]$ is the desired signal power. The SCB algorithm can obtain high output SINR when the ASV of the desired signal is known accurately. However, in practical applications, there often exist differences between the assumed signal arrival angle and true arrival angle. Therefore, the ASV may be imprecise, resulting in steering vector mismatches [12]. It is found that the SCB cannot provide good robustness against ASV errors between the presumed and actual ASVs. We assume that $\bar{\mathbf{a}}$ denotes the actual ASV of the desired signal. We can get:

$$\bar{\mathbf{a}} = \mathbf{a} + \Delta, \qquad (9)$$

where Δ is an unknown complex vector which describes the effect of steering vector distortion. In this case, the mismatch of the ASV may result in desired signal suppression and get poor output SINR. Thus, robust adaptive beamforming is necessary in practical applications.

In order to improve the robustness of the SCB, an effective NCCB algorithm is widely investigated, which is realized by using a norm constraint on the weight vector. Thus, the NCCB is formulated as follows:

$$\begin{cases} \min_{\mathbf{w}} \mathbf{w}^H \hat{\mathbf{R}}\mathbf{w} \\ s\,t \ \ \mathbf{w}^H \bar{\mathbf{a}}(\theta_0) = 1 \\ \quad \|\mathbf{w}\|^2 \leq \xi \end{cases}, \qquad (10)$$

where $\bar{\mathbf{a}}(\theta_0)$ is the presumed signal steering vector, $\|\cdot\|$ denotes the l_2 norm and ξ is the norm constraint parameter. From the analysis of [13], we can see that the NCCB can enhance the robustness of the SCB. However, the analysis and

simulation results show that its efficiency is not good enough when the ASV mismatch is large. Although, the performance of the NCCB can be controlled by ξ, the optimal method for obtaining ξ is difficult.

III. MODIFIED NORM CONSTRAINT ROBUST BEAMFORMING

In this section, we develop an MNCCB to improve the robustness performance, which is realized by adding an orthomodular constraint on the NCCB. Here, we first discuss the formulation of the MNCCB and then give the detailed theoretical analysis.

Define the projection matrix as $\hat{\mathbf{R}}^{-m}$, where m is positive integer. By projecting the matrix $\hat{\mathbf{R}}^{-m}$ to the weight vector, we can get $\hat{\mathbf{w}}=\hat{\mathbf{R}}^{-m}\mathbf{w}$. Thus, the MNCCB algorithm can be described as:

$$\begin{cases} \min_{\mathbf{w}} \mathbf{w}^H \hat{\mathbf{R}} \mathbf{w} \\ s\,t \quad \mathbf{w}^H \overline{\mathbf{a}}(\theta_0) = 1 \quad , \\ \quad \| \hat{\mathbf{R}}^{-m} \mathbf{w} \|^2 \leq \zeta \end{cases} \tag{11}$$

where ζ is a constraint parameter with a small value. It found that the optimization of (11) is a convex problem, which can be solved by using inter-point method [15]. In this paper, Lagrange multiplier method is employed to find the solution of (11).

Firstly, let S be the set that is defined by the constraints in (11):

$$S=\{\mathbf{w} \mid \mathbf{w}^H \overline{\mathbf{a}}(\theta_0) = 1, \| \hat{\mathbf{R}}^{-m} \mathbf{w} \|^2 \leq \zeta \}. \tag{12}$$

Define:

$$f_1(\mathbf{w},\lambda,\mu) = \mathbf{w}^H \hat{\mathbf{R}} \mathbf{w} + \lambda(\| \hat{\mathbf{R}}^{-m} \mathbf{w} \|^2 - \zeta) \\ + \mu(-\mathbf{w}^H \overline{\mathbf{a}} - \overline{\mathbf{a}} \mathbf{w} + 2), \tag{13}$$

where λ is the real-valued Lagrange multiplier and $\lambda \geq 0$ satisfying $\hat{\mathbf{R}}+\lambda\mathbf{I}>0$. By minimizing $f_1(\mathbf{w},\lambda,\mu)$ with respect to $\mathbf{w}$, we have:

$$f_1(\mathbf{w},\lambda,\mu) \leq \mathbf{w}^H \hat{\mathbf{R}} \mathbf{w} \quad \forall \mathbf{w} \in S. \tag{14}$$

From the discussion of the SCB algorithm shown in (6), $\mathbf{a}$ is replaced by $\overline{\mathbf{a}}$. Then, we get:

$$\hat{\mathbf{w}} = \frac{\hat{\mathbf{R}}^{-1}\overline{\mathbf{a}}}{\overline{\mathbf{a}}^H \hat{\mathbf{R}}^{-1} \overline{\mathbf{a}}}. \tag{15}$$

Consider the condition:

$$\zeta < \frac{\overline{\mathbf{a}}^H \hat{\mathbf{R}}^{-2} \overline{\mathbf{a}}}{[\overline{\mathbf{a}}^H \hat{\mathbf{R}}^{-1} \overline{\mathbf{a}}]^2}. \tag{16}$$

We can rewrite $f_1(\mathbf{w},\lambda,\mu)$ as follows:

$$\begin{aligned} f_1(\mathbf{w},\lambda,\mu) = &[\mathbf{w} - \mu(\hat{\mathbf{R}} + \lambda(\hat{\mathbf{R}}^{-m})^H \hat{\mathbf{R}}^{-m})^{-1}\overline{\mathbf{a}}]^H \\ &(\hat{\mathbf{R}} + \lambda(\hat{\mathbf{R}}^{-m})^H \hat{\mathbf{R}}^{-m}) \\ &[\mathbf{w} - \mu(\hat{\mathbf{R}} + \lambda(\hat{\mathbf{R}}^{-m})^H \hat{\mathbf{R}}^{-m})^{-1}\overline{\mathbf{a}}] \\ &- \mu^2 \overline{\mathbf{a}}^H (\hat{\mathbf{R}} + \lambda(\hat{\mathbf{R}}^{-m})^H \hat{\mathbf{R}}^{-m})^{-1}\overline{\mathbf{a}} \\ &- \lambda\zeta + 2\mu. \end{aligned} \tag{17}$$

Therefore, for the fixed parameters λ and μ, the unconstrained minimizer of $f_1(\mathbf{w},\lambda,\mu)$ is given by:

$$\hat{\mathbf{w}}_{\lambda,\mu} = \mu(\hat{\mathbf{R}} + \lambda(\hat{\mathbf{R}}^{-m})^H \hat{\mathbf{R}}^{-m})^{-1}\overline{\mathbf{a}}. \tag{18}$$

Substituting (18) to (17), we can rewrite (17) as:

$$\begin{aligned} f_2(\lambda,\mu) = &-\mu^2 \overline{\mathbf{a}}^H (\hat{\mathbf{R}} + \lambda(\hat{\mathbf{R}}^{-m})^H \hat{\mathbf{R}}^{-m})^{-1}\overline{\mathbf{a}} \\ &- \lambda\zeta + 2\mu \leq \mathbf{w}^H \hat{\mathbf{R}} \mathbf{w}. \end{aligned} \tag{19}$$

By considering the maximization of $f_2(\lambda,\mu)$ with respect to μ, we have:

$$\hat{\mu} = \frac{1}{\overline{\mathbf{a}}^H (\hat{\mathbf{R}} + \lambda(\hat{\mathbf{R}}^{-m})^H \hat{\mathbf{R}}^{-m})^{-1}\overline{\mathbf{a}}}. \tag{20}$$

and we can get:

$$\begin{aligned} f_3(\lambda) = f_2(\lambda,\hat{\mu}) = &-\lambda\zeta \\ &+ \frac{1}{\overline{\mathbf{a}}^H (\hat{\mathbf{R}} + \lambda(\hat{\mathbf{R}}^{-m})^H \hat{\mathbf{R}}^{-m})^{-1}\overline{\mathbf{a}}}. \end{aligned} \tag{21}$$

Thus, the maximization of $f_3(\lambda)$ with respect to λ can be expressed as:

$$\frac{\overline{\mathbf{a}}^H (\hat{\mathbf{R}} + \lambda(\hat{\mathbf{R}}^{-m})^H \hat{\mathbf{R}}^{-m})^{-2}\overline{\mathbf{a}}}{[\overline{\mathbf{a}}^H (\hat{\mathbf{R}} + \lambda(\hat{\mathbf{R}}^{-m})^H \hat{\mathbf{R}}^{-m})^{-1}\overline{\mathbf{a}}]^2} = \zeta. \tag{22}$$

Hence, the optimal Lagrange multiplier $\hat{\lambda}$ can be efficiently obtained by using a Newton's method.

By introducing $\hat{\mu}$ into $\hat{\mathbf{w}}_{\lambda,\mu}$, we get:

$$\hat{\mathbf{w}} = \frac{(\hat{\mathbf{R}} + \lambda(\hat{\mathbf{R}}^{-m})^H \hat{\mathbf{R}}^{-m})^{-1}\overline{\mathbf{a}}}{\overline{\mathbf{a}}^H (\hat{\mathbf{R}} + \lambda(\hat{\mathbf{R}}^{-m})^H \hat{\mathbf{R}}^{-m})^{-1}\overline{\mathbf{a}}}, \tag{23}$$

which satisfies:

$$\hat{\mathbf{w}}^H \overline{\mathbf{a}} = 1, \tag{24}$$

and

$$\| \hat{\mathbf{R}}^{-m} \hat{\mathbf{w}} \|^2 \leq \zeta. \tag{25}$$

In addition, it is observed that the proposed MNCCB is also an improved DL-SCB algorithm and the λ is the diagonal loading factor. The optimal diagonal loading can be precisely calculated by solving the constrained quadratic optimization problem.

Let us pay attention to the constraint $|\hat{\mathbf{R}}^{-m}\hat{\mathbf{w}}|^2 \leq \zeta$. According to Schmidt's orthogonal subspace theory, $\hat{\mathbf{R}}$ can be decomposed as [16]:

$$\hat{\mathbf{R}} = \begin{bmatrix} \mathbf{U}_s & \mathbf{U}_n \end{bmatrix} \begin{bmatrix} \mathbf{\Lambda_s} & \mathbf{0} \\ \mathbf{0} & \sigma_n^2\mathbf{I} \end{bmatrix} \begin{bmatrix} \mathbf{U}_s^H \\ \mathbf{U}_n^H \end{bmatrix}$$

$$= \mathbf{U}_s\mathbf{\Lambda}_s\mathbf{U}_s^H + \sigma_n^2\mathbf{U}_n\mathbf{U}_n^H, \qquad (26)$$

where $\mathbf{U}_s$ represents the desired signal-plus-interference subspace, which is formed by P interferences and one desired signal. $\mathbf{U}_n$ is the noise subspace. $\mathbf{\Lambda}_s = diag\{\lambda_1, \lambda_2, \ldots, \lambda_M\}$ is the big eigenvalues corresponding to signal and interferences. On the basis of the above discussion, we have:

$$\hat{\mathbf{R}}^{-m} = \frac{1}{\sigma_n^{2m}}\left\{ \mathbf{U}_s diag\left\{ (\frac{\sigma_n^2}{\lambda_i})^m \right\}\mathbf{U}_s^H + \mathbf{U}_n\mathbf{U}_n^H \right\}. \quad (27)$$

We can clearly see that $\frac{\sigma_n^2}{\lambda_i} < 1$. Thereby, $(\frac{\sigma_n^2}{\lambda_i})^m$ converges to zero when m is large. Taking above discussions into consideration, we can get $\lim_{m \to \infty} diag\left\{ (\frac{\sigma_n^2}{\lambda_i})^m \right\} = 0$, which means:

$$\lim_{m \to \infty} \sigma_n^{2m}\hat{\mathbf{R}}^{-m} = \mathbf{U}_n\mathbf{U}_n^H. \qquad (28)$$

In practical applications, m is usually a fixed and finite integer, and hence the equation (28) can be satisfied, which means that the noise subspace $\mathbf{U}_n\mathbf{U}_n^H$ can be obtained without decomposition of the covariance matrix $\hat{\mathbf{R}}$. Furthermore, it is indicted that the number of incident signals is not necessary for the estimation.

From equations (26) and (28), we can see that $\hat{\mathbf{R}}^{-m}$ is an orthogonal projection matrix. The constraint $|\hat{\mathbf{R}}^{-m}\hat{\mathbf{w}}|^2 \leq \zeta$ not only imposes norm constraint on the weight vector, but also ensures approximate orthogonality between the weight vector and noise subspace. Thus, the MNCCB algorithm can effectively improve the robustness of the SCB against large ASV mismatch.

The proposed MNCCB algorithm can be summarized as follows:

The MNCCB algorithm

Step 1) Compute the covariance matrix $\hat{\mathbf{R}}$;

Step 2) Compute the power of covariance matrix $\hat{\mathbf{R}}^{-m}$;

Step 3) Project $\hat{\mathbf{R}}^{-m}$ to the weight vector;

Step 4) Solve (22) to obtain $\hat{\lambda}$;

Step 5) Substitute $\hat{\lambda}$ to (23) to get $\hat{\mathbf{w}}$.

IV. NUMERICAL EXAMPLES

In this section, we will discuss the performance of the proposed MNCCB algorithm. A Uniform Line Array (ULA) with 10 omnidirectional antennas spaced half a wave length uniformly. The Direction-of-Arrival (DOA) of the desired signal is 0°. The DOAs of the two independent interferences are 30° and 50°, respectively, while the Interference to Noise Ratio (INR) is INR = 30 dB. The number of snapshots is $K = 100$. The other key parameters for the proposed MNCCB algorithm are $m = 2$ and $\zeta = 0.03$. The simulation results of the proposed MNCCB are obtained in comparison with SCB, RCB [9], ESB [8], NCCB [11], DL-SCB [7] and SQP [10]. $\varepsilon = 0.3N$ is used for the RCB, and the diagonal loading factor in [7] is twice as great as the noise power, and $\xi = 0.11$ is used for NCCB. In all experiments, 100 Monte Carlo runs are used to obtain each simulation point.

Example 1: *Exactly known signal steering vector*

In this example, we assume the presumed DOA of desired signal is also set as 0°. The normalized beampattern plots of the mentioned beamformers with the SNR = 0 dB are shown in Fig. 1 and the output SINR of these beamformers are shown in Fig. 2. It can be seen from the Fig. 1, that the SCB, NCCB and MNCCB perform well with the exactly known ASV. The peak response of these algorithms are well agreed with the actual direction of desired signal, while the nulls are located at the directions of interferences, which can help to suppress unwanted interferences. In addition, it is observed that the MNCCB algorithm has the lowest sidelobe level. From Fig. 2, we can see that the MNCCB algorithm has the highest output SINR because it exhibits deeper null than

other methods. Thus, we can conclude that our proposed MNCCB algorithm outperforms previously reported algorithms.
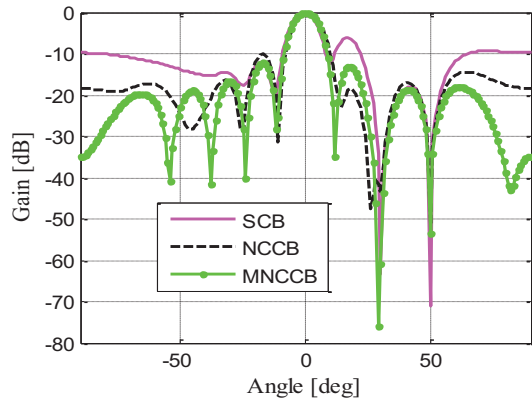

Fig. 1. Normalized beampatterns at zero pointing error.
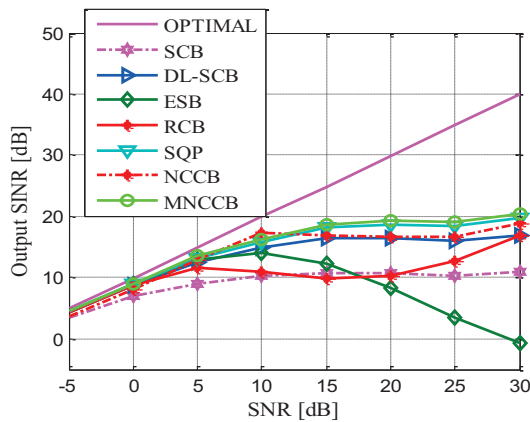
Fig. 2. Output SINR versus SNR at zero pointing error.

Example 2: *Signal look direction with 5° mismatch*

In the second experiment, the presumed DOA is 5° of the desired signal. The normalized beampattern plot of the proposed MNCCB beamformer with the input SNR=0 dB is shown in Fig. 3 in comparison with SCB and NCCB algorithms. It can be seen from Fig. 3, that the SCB with 5° ASV mismatch completely fails and its main lobe departs from the actual signal direction, which means that it cannot distinguish the desired signal and interferences, and hence will suppress the desired signal. Additionally, although the performance of the NCCB is better than SCB, its main lobe also departs from the actual signal direction. However, our proposed MNCCB

algorithm shows excellent performance in interference suppression, which gives deep nulls at the directions of inferences. Thus, the response peaks for the MNCCB estimation algorithm is located at the actual direction of desired signal without target signal cancellation.
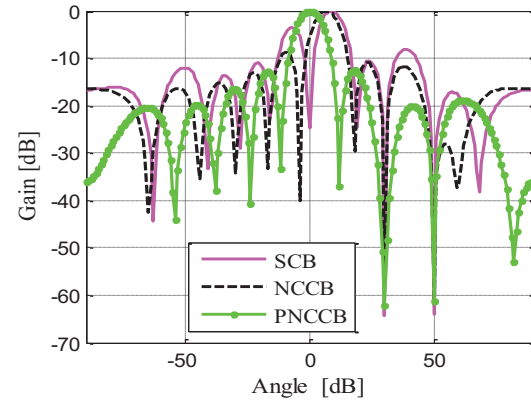

Fig. 3. Normalized beampatterns at 5° pointing error.

Figure 4 demonstrates the output SINR performance of the above mentioned beamformers versus the input SNR. We can see that the proposed MNCCB algorithm has better performance compared to other beamformers when the ASV mismatch is 5°. The SCB and DL-SCB algorithms suffer from severe degradation when SNR increases from 0 dB to 30 dB, while the performance of the NCCB significantly degraded at low SNR. In other words, the proposed MNCCB algorithm is superior to other beamformers.
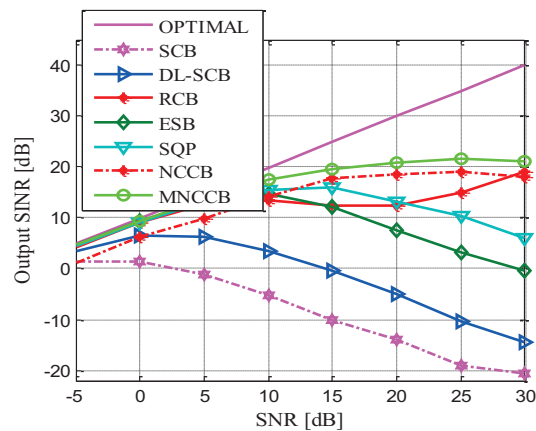

Fig. 4. Output SINR versus SNR at 5° pointing error.

Figure 5 exhibits the output SINR performance with respect to the number of training snapshots K at SNR=10 dB. It can be seen that the proposed MNCCB algorithm still has highest robustness against the ASV mismatch and better performance than other methods.
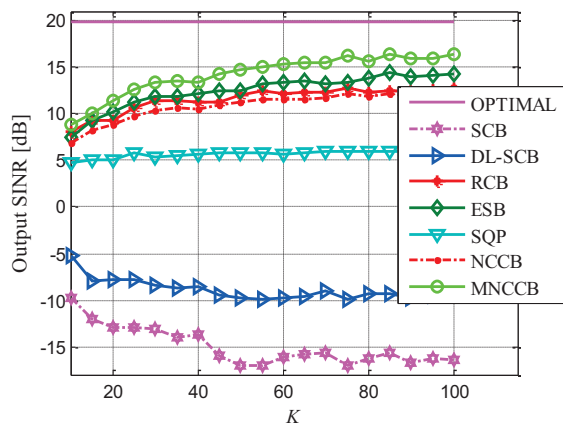

Fig. 5. Output SINR versus K at 5° pointing error.

Example 3: *Effect of the signal direction mismatch*

In this experiment, the steering direction error is preselected as [-8°-8°]. The performance of output SINR versus signal direction mismatch is given in Fig. 6. We can clearly see that the performance of the SCB, DL-SCB and RCB are severely deteriorated with an increase of the signal direction mismatch, while the output SINR of MNCCB is stable. It is worth noting that when the angle error is 8°, the output SINR of the NCCB and SQP are -7.5 dB and 2.2 dB, respectively, while the output SINR of the MNCCB is 7.9 dB, which exceeds the NCCB 15.4 dB.
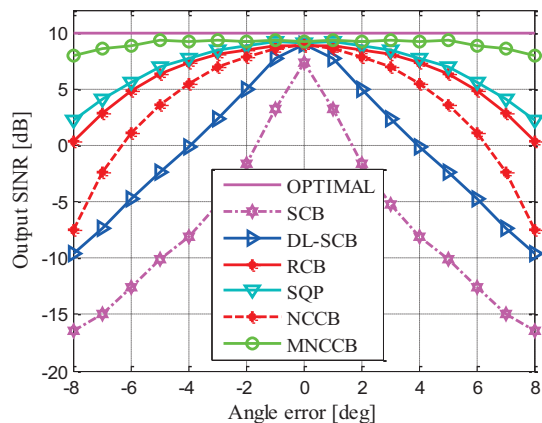

Fig. 6. Output SINR against pointing error.

Example 4: *Effects of the parameters m and ξ*

In this example, we will discuss the effects of the parameters m and ξ on the performance of the MNCCB algorithm with the presumed DOA is 5°. The output SINRs with different m and ξ are shown in Fig. 7. It can be seen that the MNCCB is not insensitive to parameter m and ξ. The output SINR curves are almost the same for different m and ξ. The proposed MNCCB beamformer can provide a good performance over a wide range of ξ making the proposed MNCCB operable and practical compared with previously proposed methods.
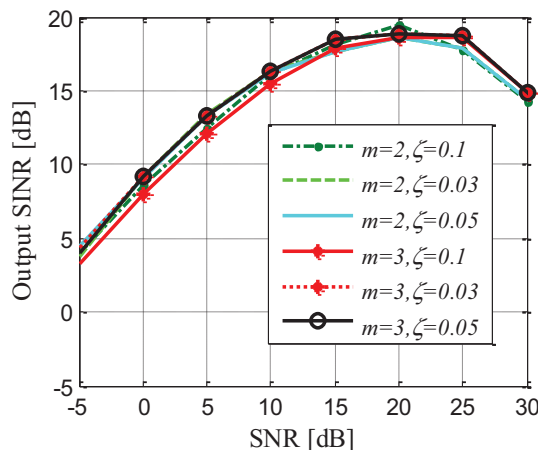

Fig. 7. Output SINR versus SNR.

V. CONCLUSION

In order to improve the degradation of adaptive beamformer with large ASV mismatch, a robust adaptive beamformer denoted as MNCCB was proposed and its performance was verified in detail. The proposed MNCCB was realized via the modification of the norm constraint, which was to add an orthogonal projection in the early reported NCCB to improve its robustness. As a result, the proposed MNCCB could give better performance than the NCCB and the diagonal loading algorithms. Theoretical analysis and numerical examples were presented to improve the performance of previous beamformers. Simulation results demonstrated that the proposed MNCCB can not only provide better interference suppression, but also achieve higher output SINR with steering vector mismatch in comparison with existing popular robust beamforming algorithms.

REFERENCES

[1] H. L. Van Trees, "Optimum array processing," *Wiley*, New York, 2002.

[2] P. S. Naidu, "Sensor array signal processing," *CRC Press*, Florida, 2001.

[3] H. Cox, R. M. Zeskind, and M. H. Owen, "Robust adaptive beamforming," *IEEE Trans. Acoust, Speech, Signal Process*., vol. ASSP-35, pp. 1365-1376, October 1987.

[4] I. S. Reed, J. D. Mallett, and L. E. Brennan, "Rapid convergence rate in adaptive arrays," *IEEE Trans. Aerosp. Electron. Syst*., vol. 10, pp. 853-863, November 1974.

[5] L. J. Griffiths and C. W. Jim, "An alternative approach to linearly constrained adaptive beamforming," *IEEE Trans. Antennas Propagat*., vol. 30, pp. 27-34, January 1982.

[6] A. B. Gershman, "Robust adaptive beamforming in sensor arrays," *Int. J. Electron. Commun*., vol. 53, pp. 305-314, December 1999.

[7] H. Cox, R. M. Zeskind, and M. H. Owen, "Robust adaptive beamforming," *IEEE Trans. Acoust, Speech, Signal Process*., vol. ASSP-35, pp. 1365-1376, October 1987.

[8] L. Chang and C. C. Yeh, "Performance of DMI and eigenspace-based beamformers," *IEEE Trans. Antennas Propagat*., vol. 40, no. 11, pp. 1336-1347, November 1992.

[9] J. Li, P. Stotica, and Z. Wang, "On robust capon beamforming and diagonal loading," *IEEE Trans. Signal Process*., vol. 51, no. 7, pp. 1702-1714, July 2003.

[10] A. Hassanien, S. A. Vorobyov, and K. M. Wong, "Robust adaptive beamforming using sequential programming: an iterative solution to the mismatch problem," *IEEE Signal Process. Letts*., vol. 15, pp. 733-736, 2008.

[11] J. Li, P. Stotica, and Z. Wang, "Doubly constrained robust capon beamformer," *IEEE Trans. Signal Process*., vol. 52, no. 9, pp. 2407-2423, September 2004.

[12] S. E. Nai, W. Ser, Z. L. Yu, and H. Chen, "Iterative robust minimum variance beamforming," *IEEE Trans. Signal Processing*, vol. 59, no. 4, pp. 1601-1611, April 2011.

[13] C. F. Liu and G. S. Liao, "Robust capon beamformer under norm constraint," *Signal Processing*, vol. 90, no. 6, pp. 1573-1581, November 2010.

[14] A. Beck and Y. C. Eldar, "Doubly constrained robust capon beamformer with ellipsoidal uncertainty sets," *IEEE Trans. Signal Processing*, vol. 55, no. 2, pp. 753-758, February 2007.

[15] CVX Research, "CVX: matlab software for disciplined convex programming," version 2.0 beta', *http://cvxr.com/cvx*, accessed August 2013.

[16] H. Liu, G. Liao, and Y. Xie, "Unified framework for two robust beamforming methods," *Electronics Letters*, vol. 42, no. 7, pp. 425-426, March 2006.

Study on Array Source Stirring Reverberation Chamber

Wenxing Li, Chongyi Yue, and Wenhua Yu

Department of Information and Communication Engineering
Harbin Engineering University, Harbin, 150001, China
liwenxing@hrbeu.edu.cn, yuechongyi@hrbeu.edu.cn, wenyu2comu@gmail.com

Abstract ─ Because the structure of transmitting antenna significantly affects the performance of source stirred reverberation chamber, a source stirring reverberation chamber excited by antenna array with a novel configuration is proposed and investigated in this paper. In contrast to traditional source stirring techniques, fewer array elements in reasonable arrangement are employed to use the test space efficiently and ensure the desired field characteristics, such as uniform statistics, isotropic and random polarization. Numerical experiments demonstrate that the statistical distribution of electrical field meets Standard IEC 61000-4-21 and has advantage over the traditional stirring systems.

Index Terms ─ Array antenna, Chi-square test, reverberation chamber, source stirring technique.

I. INTRODUCTION

Compared with traditional EMC test facilities, the Reverberation Chamber (RC) is a new kind of EMC test facility with advantages in construction cost and dynamic range. Better electric field intensity using the same input power and accurate results can be obtained in RC. More attentions have been attracted to RCs and the related research has become one of the hottest research topics today [1-4]. A RC usually consists of a shielding cavity, transmitting antenna, receiving antenna, field probe and stirring device(s), which has characteristics of statistical homogeneity, isotropy and random polarization [5]. Both radiation sensitivity and shielding performance tests can be conducted in the chamber.

The mechanical stirred RC is first reported [6] and widely used in both industrial and academic research. The stirring relies on rotation of metal plates in irregular shapes, which make the operation

and installation complicated and available space relatively small for EUT (equipment under test) [7,8]. In order to tackle this problem, the existing source-stirred RC [8] requires a mobile transmitting antenna on the ground. It does simplify the structure of reverberation chamber, but it is difficult or impossible to obtain the random changes of antenna positions and ensure the independence between different states of stirring. Meanwhile, the manual processing on the antenna may decrease accuracy and efficiency. To overcome this shortage, a source-stirred method is proposed by exciting multiple antennas at different times [9], which needs to employ several independent transmitting antennas. The electric field distribution will be changed when different antennas are excited. However, these independent transmitting antennas occupy a large cavity space and increase the construction cost.

To resolve this contradiction, a source stirring method via an array antenna is proposed [10]. Four array elements are mounted on each surface of a hexahedral structure and this structure is located on the ground. Different elements of array are motivated separately to stir the chamber. The source stirring method via an antenna array can obtain larger EUT space and guarantees independence of electric field distributions on different stirring steps. But this antenna array in a hexahedral pattern still occupies a large space in the chamber and reduces the area available for EUT.

Aiming at the issues above, a reverberation chamber stirred by a novel antenna array is developed in this paper, and the planar array is distributed near the chamber wall. This antenna array includes twelve array elements, three of which are excited simultaneously on each stirring step. This design reduces the volume occupied by

transmitting antenna array and has a simple structure with small quantity of array elements. In addition, this design is also satisfied with the requirements of the number of stirring steps and independence in different stirring states.

II. SOURCE-STIRRED TECHNIQUE ANALYSIS

The electric field density inside a source-stirred chamber is associated with both position and orientation of transmitting antenna. The inhomogeneous wave in a chamber satisfies the following equation:

$$\nabla E + \omega^2 \mu_0 \varepsilon_0 E = j\omega\mu_0 J. \tag{1}$$

The eigen solution of (1) is expressed as:

$$\begin{cases} E_x = \cos\dfrac{m\pi x}{L}\sin\dfrac{n\pi y}{W}\sin\dfrac{p\pi z}{H} \\[2mm] E_y = \sin\dfrac{m\pi x}{L}\cos\dfrac{n\pi y}{W}\sin\dfrac{p\pi z}{H} \\[2mm] E_z = \sin\dfrac{m\pi x}{L}\sin\dfrac{n\pi y}{W}\cos\dfrac{p\pi z}{H}, \end{cases} \tag{2}$$

where L, W and H represent the length, width and height of chamber, respectively; and m, n and p are mode numbers,

$$\left[\left(\frac{m\pi}{L}\right)^2 + \left(\frac{np}{W}\right)^2 + \left(\frac{p\pi}{H}\right)^2\right] = k_{mnp}^2. \tag{3}$$

The resonant frequency of source-stirred chamber can be expressed as:

$$\begin{aligned} f_{mnp} &= \frac{k_{mnp}}{2\pi\sqrt{\mu_0\varepsilon_0}} \\ &= \frac{c_0}{2}\sqrt{\left(\frac{m}{L}\right)^2 + \left(\frac{n}{W}\right)^2 + \left(\frac{p}{H}\right)^2}. \end{aligned} \tag{4}$$

If $A_{m'np}$, $A_{mn'p}$ and $A_{mnp'}$ are mode values, the electrical field components E_x, E_y and E_z inside the chamber can be expressed as:

$$\begin{aligned} E = \sum_{m,n,p} (c_{xmnp}A_{m'np}\hat{e}_x \\ + c_{ymnp}A_{mn'p}\hat{e}_y + c_{zmnp}A_{mnp'}\hat{e}_z), \end{aligned} \tag{5}$$

where c_{xmnp}, c_{ymnp} and c_{zmnp} can be obtained by [11]:

$$c_{xmnp} = \frac{c^2}{4\pi^2\left(f^2 - f_{mnp}^2\right)}\frac{8}{LWH}$$
$$\iiint j\omega\mu_0 J_x A_{m'np}\,dxdydz$$

$$c_{ymnp} = \frac{c^2}{4\pi^2\left(f^2 - f_{mnp}^2\right)}\frac{8}{LWH}$$
$$\iiint j\omega\mu_0 J_y A_{mn'p}\,dxdydz \tag{6}$$

$$c_{zmnp} = \frac{c^2}{4\pi^2\left(f^2 - f_{mnp}^2\right)}\frac{8}{LWH}$$
$$\iiint j\omega\mu_0 J_z A_{mnp'}\,dxdydz,$$

where J_x, J_y and J_z are components of the current density vector. From (5) and (6), both position and orientation of transmitting antenna will influence the field in the cavity. For an antenna array in the chamber, both position and orientation of array elements are different from each other. Motivating different elements at different times can change the field distributions in the chamber. When an antenna array has sufficient emission states, a field distribution of statistical uniformity can be formed during a stirring period.

III. ARRAY ANTENNA DESIGN

A. The lowest usable frequency

The Lowest Usable Frequency (LUF) of reverberation chamber refers to the lowest available frequency of EMC test in the chamber, which is an important indicator of RC. The dimensions of the chamber in this paper are selected to be L=4,000 mm, W=2,480 mm and H=3,000 m, which determine $f_0 = 62.5$ MHz (the lowest resonant frequency) and $f_{LUF} = 3f_0$. The variation of mode number and density with frequency can be expressed as [11]:

$$N(f) \approx \frac{8\pi}{3}LWH\left(\frac{f}{c_0}\right)^3 - \left(L+W+H\right)\frac{f}{c_0} + \frac{1}{2}, \tag{7}$$

$$\frac{\partial N}{\partial f} \approx 8\pi LWH\frac{f^2}{c_0^3} - \left(L+W+H\right)\frac{1}{c_0}. \tag{8}$$

The chamber will have a good performance at the mode quantity of 100 or mode density of 1.5 Mode/MHz. It is observed from Fig. 1 that the quantity of mode increases linearly with frequency. The number of mode in the chamber reaches 100 at the frequency of 230 MHz, and the mode density qualifies the requirement of 1.5 modes/MHz at the frequency of 235 MHz. The reverberation chamber can perform well at the frequency of 235 MHz and above. It is indicated from Fig. 2 that with increasing of frequency, the gap between two modes is getting smaller, which means the field uniformity is getting better as the frequency increases. The change of modal gap between two adjacent modes is shown in Fig. 2.


Fig. 2. Modal gap in the source-stirred chamber.

B. The design of array antenna

In order to get an insight into the coupling mechanism between antenna array and the chamber, and to reduce the impact caused by the structure of antenna on the field distribution, a half-wave dipole is chosen to be an array element in this paper. The maximum likelihood estimation method and the given confidence level are considered to decide the number of stirring steps, which is the same as the sampling size of electric field when the array antenna is designed. Electrical field in cavity obeys Rayleigh distribution, whose PDF can be deduced as:

$$f(E_i) = \frac{E_i}{\sigma^2} e^{-\frac{E_i^2}{2\sigma^2}}, \tag{9}$$

where i represents x, y or z. Using the maximum likelihood estimation can get the estimator as:

$$\hat{\sigma}^2 = \frac{1}{2n} \sum_{j=1}^{n} E_{ij} = \frac{\overline{E_i}^2}{2}. \tag{10}$$

If the sampling number n is sufficiently large, the estimator $\hat{\sigma}^2$ will be the normal distribution, and the variance is:

$$\text{var}\left[\hat{\sigma}^2\right] = \left\{ -nE\left[\frac{\partial^2 \ln f}{\partial \left(\sigma^2\right)^2} \right] \right\}^{-1} = \frac{\sigma^4}{n}, \tag{11}$$

where E is an expected value and f is the function in (9). After normalizing $\hat{\sigma}^2$, the normalized confidence interval is expressed as:

Fig. 1. Variation of mode number and mode density with frequency.

$$d(\text{dB}) = 10\log\frac{1+k/\sqrt{n}}{1-k/\sqrt{n}}, \qquad (12)$$

and the sample size can be derived as:

$$n = k^2\left(\frac{10^{d/10}+1}{10^{d/10}-1}\right)^2. \qquad (13)$$

We choose d, ideal confidence level, k and number of samples to be 1 dB, 90%, 1.65 and 207, respectively [12].

Based on the discussions above, 207 stirring steps can reach the ideal confidence level. Enough stirring steps can be obtained by exciting different combination of elements of the array at each time. 66, 220 or 495 stirring steps can be achieved when 2, 3 or 4 array elements are excited at each time. Obviously, 3 elements and 220 stirring steps is enough for sample size, which is calculated in (13). Therefore, as different elements are excited, 220 emission statuses are achieved by exciting different combinations. It is indicated in Fig. 3 how the elements are motivated in the array, where white and black points represent active elements and non-active elements, respectively.

(a)   (b)

(c)   (d)
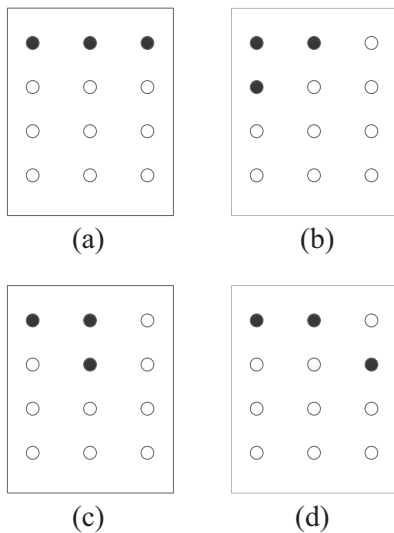
Fig. 3. Excitation configuration of array antennas.

The spacing between adjacent elements also has significant influence on the field distribution in the cavity. For the sake of good statistical distribution of electric field samples, the field independence of different stirring steps is an important factor to determine the configuration of array elements. According to the plane wave spectrum [13], the correlation function of field

intensity in a reverberation chamber is:

$$\rho(r_1, r_2) = \frac{\langle E(r_1)E^*(r_2)\rangle}{\sqrt{\langle|E(r_1)|^2\rangle\langle|E(r_2)|^2\rangle}}, \qquad (14)$$

where r_1 and r_2 are two position vectors, and a simplified formulation is given as:

$$\rho(r_1, r_2) = \frac{\sin(k|r_1 - r_2|)}{k|r_1 - r_2|}. \qquad (15)$$

We can see from (15) that the minimization distance of adjacent elements for the relevant function $\rho = 0$ is $\lambda/2$, which ensures the independence of different field samples. The orientation of elements is random but should be neither parallel to each other nor parallel to the chamber wall, which ensures wave to radiate and reflect in different paths to avoid strong mutual coupling. The schematic diagram of arrangement of elements is shown in Fig. 4, where the distance between adjacent elements is $\lambda/2$ and the orientation of elements is different from each other.
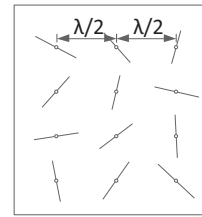
Fig. 4. Schematic diagram of array antenna.

In conclusion, the maximum wavelength is $\lambda = 1.58\text{m}$ in frequency band over 190 MHz to 250 MHz. The distance between the antenna array and the chamber wall is $\lambda \approx 0.4\text{m}$, and twelve elements of different orientations are distributed in a plane with distance of $\lambda/2$ from each other. The simulation model of this source-stirred reverberation chamber is shown in Fig. 5.
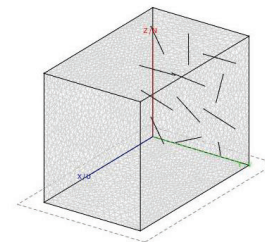

Fig. 5. Simulation model of source-stirred chamber.

C. The utilization of EUT area

The planar array antenna in this paper takes little space of cavity so that most of the space can be used to conduct EMC test, which effectively improves the space utilization of the cavity. It is shown in Table 1 the comparison of utilization ratio of cavity space between different reverberation chambers.

Table 1: The comparison of utilization ratio of cavity

Type of Chamber	Volume of Cavity (m^3)	Spatial Volume for EUT (m^3)	Utilization Ratio of Cavity
Mechanical stirred RC [14]	22.475	9.61	42.76%
Source-stirred RC [15]	130.416	30.525	23.41%
Source-stirred RC [16]	60	26.25	43.75%
Source-stirred RC in this paper	29.76	14.92	50.14%

The volume of the cavity refers to the inner spatial volume in the reverberation chamber, and the volume of space for EUT is calculated according to IEC61000-4-21. The ratio of spatial volume for EUT to the volume of the cavity is utilization ratio of cavity. It is indicated that the utilization ratio of cavity of chamber designed in this paper is bigger than that in mechanical stirred chamber and other source-stirred chambers, which means that the chamber designed in this paper can be used for bigger EUT test if the volume of all the chambers are the same.

IV. SIMULATION TESTS AND RESULTS

A. Establishment and controlling of simulation model

The simulation of source-stirred reverberation chamber has the following characteristics:

(1) The inner volume of cavity is large and mesh generation requires a large amount of computing resources.

(2) The position and orientation of transmitting antennas are continuously changing.

(3) The conductivity of cavity wall cannot be infinitely large.

(4) The cavity is totally enclosed with multiple resonance points and no electromagnetic energy radiates outside.

According to these characteristics, MoM based FEKO software is chosen as a kennel in this paper. MoM only needs to mesh the cavity wall, which can reduce the burden on computing resources and artificial errors caused by continuous model changing. In addition, this method can deal with good conductor and resonant cavity such as convergence and numerical dispersion, better than other numerical methods.

Then the array antenna is arranged in one side of the cavity and the other side is reserved for the EUT. Two observation points are chosen in the EUT area and electrical field data on these points are used to analyze the field distribution inside the cavity. The coordinates of eight vertices (A~D, A′~D′) of working volume and two observation points (P, Q) are shown in Table 2.

Table 2: Coordinates of vertices and observation points

Point	X	y	Z
A	0.8	0.4	0.4
B	0.8	2	0.4
C	3.6	0.4	0.4
D	3.6	2	0.4
A′	0.8	0.4	2.6
B′	0.8	2	2.6
C′	3.6	0.4	2.6
D′	3.6	2	2.6
P	2	1.2	1.4
Q	1.4	1.6	2

Matlab program is used to control the excitation of array antenna as well as save and process sampling data of electric field during the whole stirring procedure in this paper. Different field distributions are formed in the working volume for each excitation, as shown in Fig. 6. Three electric field components at eight vertices of working volume and observation point P and Q are recorded respectively at different stirring status. After a complete stirring period, the recorded data of

electric field is processed to obtain the statistical characteristic of field component samples to compare with theoretical results. The controlling of the excitation storage of data, both data process and analysis are realized through Matlab, and the flow chart of simulation procedure is shown in Fig. 7.
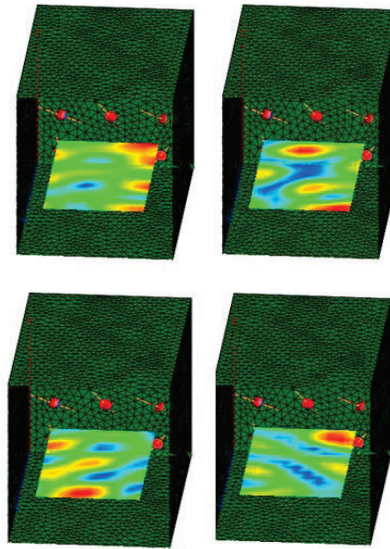

Fig. 6. Variation of electric field of different stirring steps.
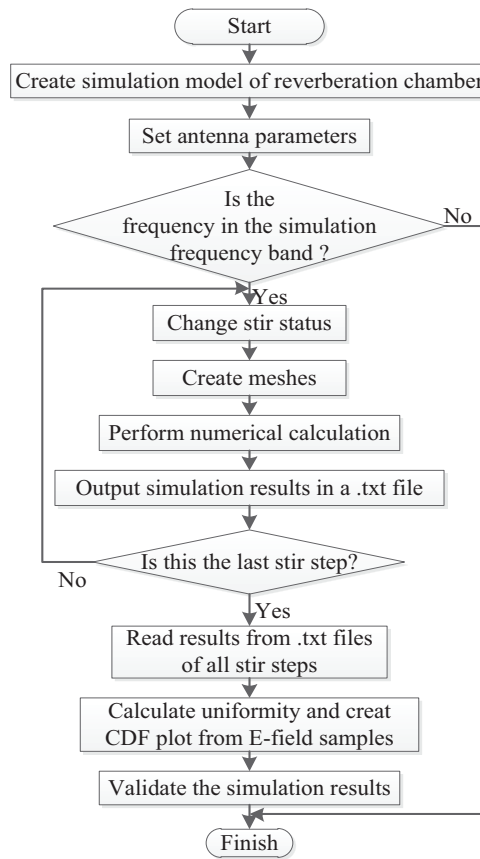
Fig. 7. Flow chart of one complete stirring procedure.

B. CPU runtime and memory requirements

The computational requirements needed for the simulation of source-stirred reverberation chamber increase as frequency rises, in terms of both the memory needed and the solution time. Therefore, it is useful to estimate the memory and CPU time to complete one simulation run. The memory M needed for storage of the matrix **Z** in MoM method can be calculated as:

$$M \approx 36N_T^2 + 16N_S^2 \quad \text{Byte,} \qquad (16)$$

where N_T and N_S represent the number of triangles and segments respectively. The CUP time for one stirring step can be also estimated as:

$$t \sim O_t\left(f^{4\sim6}\right) + O_s\left(f^4\right), \qquad (17)$$

which means the time needed for triangles and segments is on the order of $f^{4\sim6}$ and f^4 [11], respectively.

Memory requirements and CPU runtime for one stirring step obtained in source-stirred reverberation chamber simulations with FEKO are listed in Table 3.

Table 3: CUP runtime and memory requirements for one frequency and one stirring step

Frequency MHz	N_T	Memory MByte	CPU Runtime mm:ss
190	6833	806	08:27
202	7600	996	10:51
217	8633	1266	15:39
229	9563	1547	19:51
238	10633	1873	25:37
247	12030	2322	37:02

C. Simulation results

After one stirring cycle, the statistical distribution of field samples at the observation point P can be obtained. The comparison between the field component samples and theoretical results is shown in Fig. 8, and the simulation is carried out at 190 MHz with 220 stirring steps in one stirring cycle. It can be seen from Fig. 8 that the simulated and theoretical results are in a good agreement, implying that the field distribution of the stirring period in this source-stirred reverberation chamber obeys Rayleigh distribution [11]. The simulation result of x-component is closer to theoretical one, because the dimension of x-direction in the chamber is larger and the electric field distribution is close to uniform.
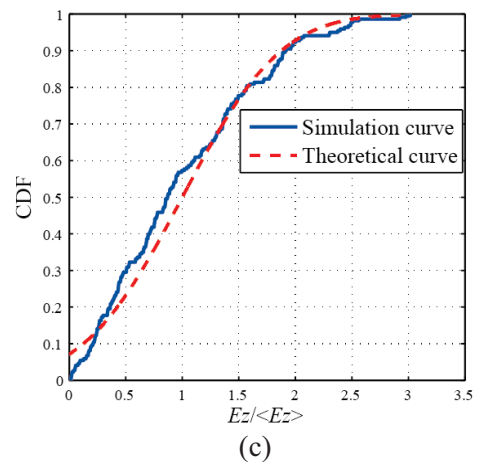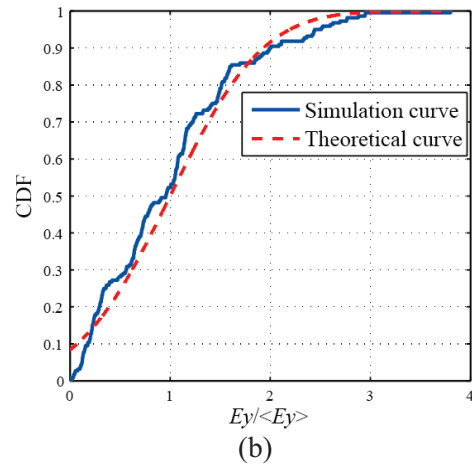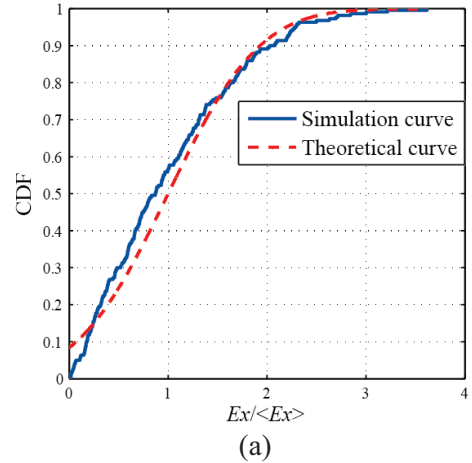

Fig. 8. Simulation and theoretical CDF curves of three electric field components.

In order to verify the fitting degree of theoretical and simulated CDF curves, the Chi-square goodness-of-fit is adopted. The difference

between the observed samples and expected distribution can be defined as:

$$\chi^2 = \sum_{i=1}^{n} \frac{(o_i - e_i)^2}{e_i},$$ (18)

where o_i is sampling quantity of the ith interval, and e_i is the expected quantity of samples in the ith interval if the hypothesized distribution is correct. When the sample size turns out to be infinite, the statistic χ^2 would obey n-p-3 Chi-square distribution of n-p-3 degrees of freedom, in which p is a parameter in the hypothesized distribution. The χ^2 can be calculated using (18). If $\chi^2 < \chi^2_{(n-p-3)1-\alpha}$, the hypothesized distribution is acceptable.

If the recorded field samples are divided into 10 intervals, the parameter will be 1 and the confidence level will be 0.5. The statistics $\chi^2_{E_x}$, $\chi^2_{E_y}$ and $\chi^2_{E_z}$ are 9.941, 11.015 and 10.983, respectively, which are smaller than the threshold value and demonstrates the samples of field component to be Raleigh distribution and the statistically uniform electric field environment in this chamber.

Field uniformity is also an important factor [1, 3] when evaluating the performance of reverberation chamber, and it can be achieved by collecting all the maximum electric field samples at vertices of cubic working volume. The ranges in three directions are x=0.8~3.6 m, y=0.4~2 m and z=0.4~2.6 m. The uniformity of three electric field components and total electric field is shown in Figs. 9 (a)-(d). The blue polyline represents the field uniformity of chamber stirred by a mobile dipole, and the red line represents uniformity of chamber stirred by array antenna. The model of single dipole source-stirring is established to compare the stirring effect between the traditional method and proposed one in this paper, and the dimensions, material of chamber, and the simulation frequency of these two models are the same. The only difference is that the single dipole is moving randomly on the surface.


(a)

(b)

(c)
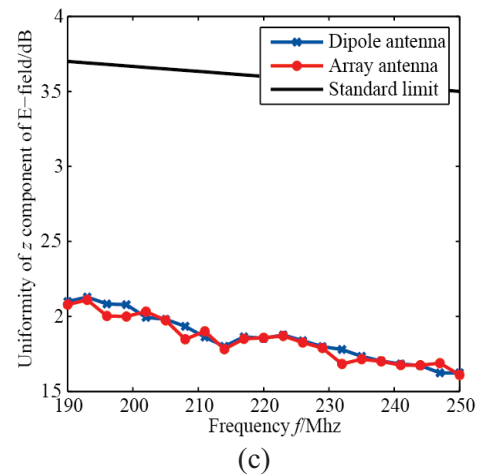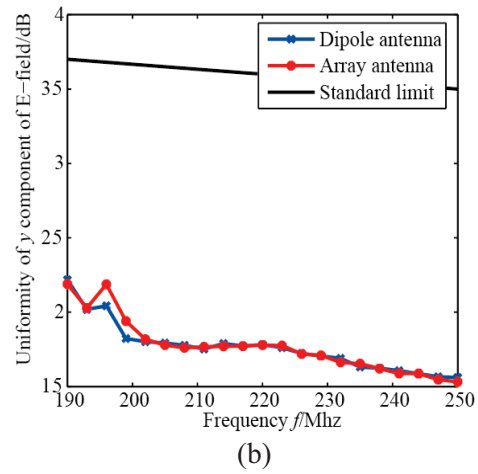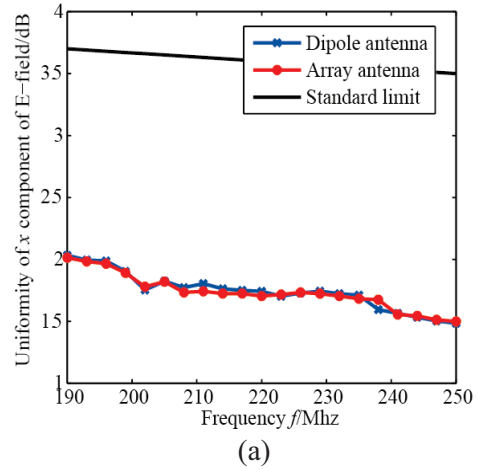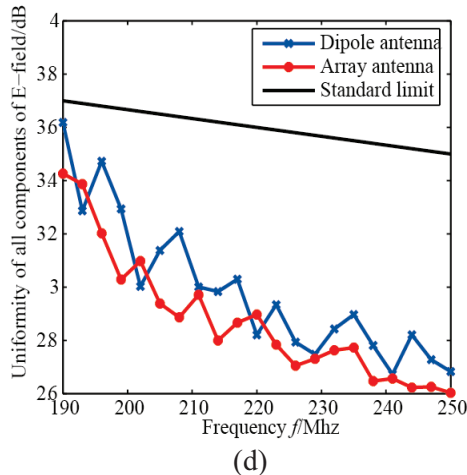
Fig. 9. Uniformity of electric field.

From Figs. 9 (a)-(c), uniformities of three field components are less than 2 dB, and the difference between two curves are not significant. But from Fig. 9 (d), the total field uniformity of array antenna stirring is not only better than that of single mobile dipole stirring, but also closer to the limits on field uniformity in the IEC Standard. Compared with the traditional way of single mobile antenna stirring, the source-stirred technique by array antenna can reduce the standard deviation of field uniformity, namely, a better electromagnetic environment of EMC test can be obtained.

V. CONCLUSION

A novel type of source-stirred chamber via a planar antenna array is designed in this paper. The composition of the array is uncomplicated and space efficient, which effectively increases the available space for EUT. Matlab is used to control the electromagnetic computational software to realize the stirring automation. The simulation results demonstrate that the simulation CDF distributions of the electric field in the working volume of the chamber is in a good agreement with the theoretical value, and is also validated by Chi-square good-of-fitness test. The electric field uniformity of this antenna array not only meets the IEC61000-4-21 Standard, but also proves that this new source stirring technique is better than traditional ones.

REFERENCES

[1] V. Rajamani, C. Bunting, and G. Freyer, "Why consider EMC testing in a reverberation chamber," *IEEE Int. Conf. on Electromagnetic Interference & Compatibility*, Bangalore, India, pp. 303-308, November 2008.

[2] L. De Vries-Venter and D. C. Baker, "EMC radiated immunity testing an overview of the reverberation chamber," *Proceedings of the 1998 South African Symposium on Communications and Signal Processing*, pp. 471-474, 1998.

[3] *IEC 61000-4-21*, "Electromagnetic compatibility (EMC): testing and measurement techniques-reverberation chamber test methods," edition 2.0, Geneva, January 2011.

[4] P. Corona, J. Ladbury, and G. Latmiral, "Reverberation-chamber research-then and now: a review of early work and comparison with current understanding," *IEEE Trans. on EMC*, vol. 44, no. 1, pp. 87-94, August 2002.

[5] D. A. Hill, "Electromagnetic theory of reverberation chambers," *National Institute of Standards and Technology, US Department of Commerce, CO, NIST*, 1998.

[6] P. Corona, J. Ladbury, and G. Latmiral, "Reverberation-chamber research-then and now: a review of early work and comparison with current understanding," *IEEE Trans. on EMC*, vol. 44, no. 1, pp. 87-94, August 2002.

[7] T. A. Loughry, "Frequency stirring: an alternate approach to mechanical mode-stirring for the conduct of electromagnetic susceptibility testing," *Phillips Laboratory, Kirtland Air Force Base, NM*, November 1991.

[8] Y. Huang and D. Edwards, "A novel reverberating chamber: the source-stirred chamber," *IEEE Eighth Int. Conf. on EMC*, Edinburgh, pp. 120-124, September 1992.

[9] Y. Shen, D. Shi, Y. Gao, H. Y. Liu, and S. L. Liu, "Improvement in field uniformity introduced by multiple-antenna in source-stirred reverberation chamber," *Chinese Jour. of Radio Science*, vol. 24 no. 1, pp. 682-686, September 2009.

[10] G. Cerri, C. Sanctis, V. Primiani, C. Monteverde, and P. Russo, "Array of antennas design for the source stirring technique," *IEEE 20th Int. Symp. On EMC*, Zurich, pp. 105-108, January 2009.

[11] C. Bruns, "Three-dimensional simulation and experimental verification of a reverberation chamber," *Universitat Fridericiana Karlsruhe (TH)*, Germany, 2005.

[12] W. Li, C. Yue, W. Yu, and Y. Mao, "Design and investigation of source-stirred reverberation chamber based on array antennas," *The 30th Int. Review of Progress in Applied Computational Electromagnetics*, CA, March 2013.

[13] D. Hill, "Spatial correlation function for fields in a reverberation chamber," *IEEE Trans. on EMC*, vol. 37, no. 1, pp. 138, February 1995.

[14] C. Bruns and R. Vahldieck, "A closer look at reverberation chambers-3D simulation and experimental vertification," *IEEE Transactions on Electromagnetic Compatibility*, vol. 47, issue 3, 2005.

[15] S. Liang, J. Xun, and J. Ding, "Investigation of antennas layout in the source stirred reverberation chamber," *Measurement & Control Technology*, vol. 30, issue 1, 2011.

[16] V. M. Primiani, P. Russo, and G. Cerri, "Experimental characterization of a reverberation chamber excited by the source stirring technique," *2012 International Symposium on Electromagnetic Compatibility (EMC EUROPE)*, pp. 1-6, 2012.

Wenxing Li received his B.S. and M.S. degrees from Harbin Engineering University (HEU), Harbin, China, in 1982 and 1985, respectively. He is currently a Full Professor of the College of Information and Communication Engineering at HEU, China. He is also the Head of Research Centre of EM Engineering & RF Technology. He visited the Department of Electrical Engineering, Pennsylvania State University, USA, from June to August 2010. And he visited Oriental Institute of Technology, Taiwan, from August to October 2010. He is also the organizer of the 30th Progress in Electromagnetics Research Symposium (PIERS), IEEE International Workshop on Electromagnetics (iWEM), TPC of 2012 Asia-Pacific Symposium on Electromagnetic Compatibility (APEMC 2012) and 2012 Global Symposium on Millimeter Waves (GSMM 2012). His recent research interests are mainly in computational electromagnetic, microwave engineering, modern antenna design and microwave and millimeter wave circuits.

Chongyi Yue received his B.S. and M.S. degrees from Harbin Engineering University, Harbin, Heilongjiang, China, in 2010 and 2012, respectively. He is currently working towards the doctor's degree in Information and Communication Engineering at Harbin Engineering University in China. His research interests include source stirring reverberation chamber, computational electromagnetics and design of antenna array.

Wenhua Yu joined the Department of Electrical Engineering of the Pennsylvania State University, and has been a group leader of electromagnetic communication lab since 1996. He received his Ph.D. in Electrical Engineering from the Southwest Jiaotong University in 1994. He worked at Beijing Institute of Technology as a Postdoctoral Research Associate from February 1995 to August 1996. He has published one book on CFDTD software and two FDTD books: Conformal Finite-Difference Time-Domain Maxwell's Equations Solver: Software and User's Guide (Artech House, 2003), Parallel Finite-Difference Time-Domain (CUC Press of China, 2005, in Chinese), and Parallel Finite-Difference Time-Domain Method (Artech House, 2006). He has published over 100 technical papers and four book chapters. He created the Computer and Communication Unlimited Company (http://www.2comu.com), and serves as its President. He is a Senior Member of the IEEE. He was included in Who's Who in America, Who's Who in Science and Engineering, and Who's Who in Education. He is also a Visiting Professor and Ph.D. Advisor of the Communication University of China. Yu's research interests include computational electromagnetic, numerical techniques, parallel computational techniques, and the theory and design of parallel computing systems.

Computational Electromagnetics for the Evaluation of EMC Issues in Multi-Component Energy Systems

M. R. Barzegaran and O. A. Mohammed

Energy Systems Research Laboratory, Department of Electrical and Computer Engineering
Florida International University, Miami, FL 33174, USA
mohammed@fiu.edu

Abstract ─ This paper reviews the physics based modeling based on the electromagnetic stray fields and interference in the electric power network. The low frequency as well as high frequency equivalent source modeling of the power components for the study of radiated and conducted electromagnetic compatibility were implemented. The 3-D finite element analysis with some modification were applied in the solution method, as well as meshing strategies for the simulation of large scale components. Moreover, the stray field of the components was utilized for improving the control of the machine-drive system using hardware in loop method. The optimization in the design of the components such as the power converter based on the EMC compliance was also applied. This was achieved by coupling MATLAB with 3-D finite element technique for applying the numerical optimization techniques. The results were verified experimentally.

Index Terms ─ EMC compliance, equivalent source modeling, large scale computational problems, low frequency and high frequency modeling.

I. INTRODUCTION

The compliance with Electromagnetic Compatibility (EMC) standards is an increasingly important aspect in the design of practical engineering systems. Consideration of EMC issues at the design stage is necessary to ensure the functional safety and reliability of complex modern products, which are increasingly reliant on electronic sub-systems to provide power, communications, control and monitoring functions that are needed to provide enhanced levels of functionality of systems. Typical examples include transportation vehicles (road, rail, sea and air), manufacturing plants, power generation and distribution, and communications. The opportunities for using numerical simulation techniques to predict and analyze the system EMC and related issues (e.g., human field exposure and installed antenna performance) are therefore of considerable interest in many industries.

A basic performance of modern electrical power systems is significantly related to the area of low frequency disturbances. Based on the above background, the importance of low frequency EMC study is considerably increasing. On the other hand, power electronic technologies are also used in evolving machine-drive equipment such as vessels and aircrafts. The magnetic signature is observable in the low frequency local magnetic field, but then several threats are present in military applications: detection and classification by and subsequent detonation of sea mines, detection and localization of submarines out of the air. Due to the improvement of the sensitivity of electromagnetic field sensors and smart signal processing techniques, signature reduction is vital. Thus, the first goal is to decrease the detection range by complying with the strict signature requirements.

The other signature study aspect of the radiated fields in low frequency is condition monitoring of the components. The faults in the winding of the machines as well as switch failures and many other problems can be detected without the need to dismantle the system. This is critically beneficial for the sensitive applications in which it may not be easily possible to get near to the components for online testing, and on the other

hand offline testing of the component is costly.

The previous works in the study of the radiated fields in power system can be categorized into EMC studies in power systems, electromagnetic computational modeling studies, electromagnetic signature studies, system monitoring studies and fault and failure diagnosis. The electromagnetic computational modeling is the concern of this paper.

The modeling process in the field of electromagnetic compatibility means the establishment of a connection between the source of interference or any other cause and its effect, which can be the response of the component as the part of the system. This relationship can be established in several ways depending on the type of problem, its complexity, and the degree of approximations with respect to an exact formulation. The possible methods involve:

- Using circuit theory for describing the conducted disturbance, such as voltage dips, over-voltages, voltage stoppages, harmonics, and common ground coupling [1], [2].

- Using an equivalent model (usually circuit) with either distributed or lumped parameters, such as in low-frequency electromagnetic field coupling expressed in terms of mutual inductances and stray capacitances, field-to-line coupling using the transmission line approximation, and cable crosstalk [3], [4].

- Formulating the problem in terms of formal solutions to Maxwell's equation and making analytical models based on that [5].

- Physics based modeling using numerical methods such as finite element method, finite differential method, method of moments and so forth [6]-[8].

Generally, the methods used in EMC modeling are not only to visualize electromagnetic phenomena, but also to predict and suppress the interferences.

In this paper, first the procedure of physics based modeling for EMC study is explained. Then, the equivalent source modeling versus 3-D full finite element modeling is discussed. Afterward, the EMC modeling of the power converter with the purpose of the optimization of power electronic components' performance is described.

Through these studies, the techniques for the physics based modeling for special purpose are discussed.

II. PHYSICS BASED MODELING FOR THE ANALYSIS OF MACHINE DRIVE

A. Multi-scale problems

In applications such as radiated emissions or immunity of a system, cables and any ground loop current and on-board antennas can be considered as a complex multi-port antenna that can be characterized using electromagnetic modeling techniques. For building an EMC model, however, it is necessary to consider a range of modeling techniques, as outlined in Table 1, operating at a number of different levels. The clearest need for combining models of different types is the integration of circuit behavior ("type A3" models) with the electromagnetic performance of the installation (a "type A1" model). However, difficulties in prediction of EMI still exist. As the number of components within a device increase, the complexity in modeling all the parasitic, especially the mutual coupling ones, would increase exponentially, resulting in a task that is unpractical even with today's most powerful computers. Therefore, in some cases a combination of the models type A2 and A3 may be useful for computationally expensive calculation. Moreover, the complexity of parameter extraction can be reduced by only modeling of the major EMI related components and circuits. Ideally, such a simplification would need some specialist knowledge of the device electrical behavior and basic EMI characteristics. For example, a distinction between the power handling and logic circuits in a motor drive will justify the concentration on salient EMI related circuitry and components, thus, leading to considerably reduced efforts in parameter extraction.

Due to the nature of the multi-scale problem, which is the multi-level numerical modeling, as well as the requirement of the numerical test environment which needs to be simple and quickly recreated, the separate modeling of each of the components and sub-components is needed. Therefore, it is beneficial to divide the problem

into three levels, as shown in Fig. 1.

The device level consists of each of the physical model of all components calculated from a 2D or 3D quasi-static electromagnetic finite element analysis. In the device level, the component models can be divided into several subsystems, based upon their power range, their location inside the components, their degree of importance from EMC and EMI issues, force outage rate, and the related fault diagnosis issues. The interface level consists of any resistive, capacitive, or inductive paths between enclosures of the components and the additional decoupling capacitor which are used to reduce the area of ground current loop and also to cut the current path and prevent it to enter the control units. The environmental level consists of the physical model of chamber filled with air and the enclosure model of each of the components placed in it.

Table 1: Classification of the numerical level necessary to predict the different performance measures in the virtual test environment

|	Model Dimension	Model Character	Objectives
A1	3D in time or Frequency Domain	Electromagnetic (surface or volumes meshing)	3D electromagnetic field distribution and related parameters
A2	2D or 3D quasi-static analysis in time harmonic domain	Quasistatic, electromagnetic (surface, volumes, or peripheral meshing)	Calculation of low to high frequency RLC elements of each of the components, frames, and frame to outer chamber
A4	0D in time or frequency domain	Lumped element circuit (discrete mathematical models)	Physics-based circuit model (circuit simulation environment)
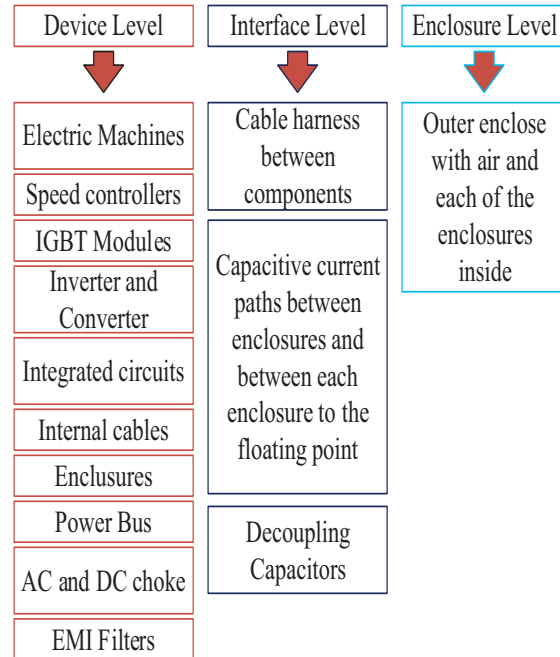
Fig. 1. Decomposition of modeling problem for creation of numerical test environment.

B. Numerical virtual prototyping

As previously explained, the modeling problem can be decomposed into three different levels; i.e., device level, interface level, and the environmental level. In each level, the sets of numerical analyses are required to enable the designer to predict the performance measure of the device under developed, either under fault or no-fault situations. Figure 2 illustrates the modeling procedure required at each level to provide the designer with a performance measure.

A schematic view of a complete motor drive system [8,9] is shown in Fig. 3. In this system, the motor component, the Insulated-Gate Bipolar Transistor (IGBT) switch module component, DC bus component, cable component, and the logic components establish the main parts of this system. Each of the components is enclosed in an enclosure, and all of the enclosures are placed inside a chamber that is electromagnetically isolated from outer environment.
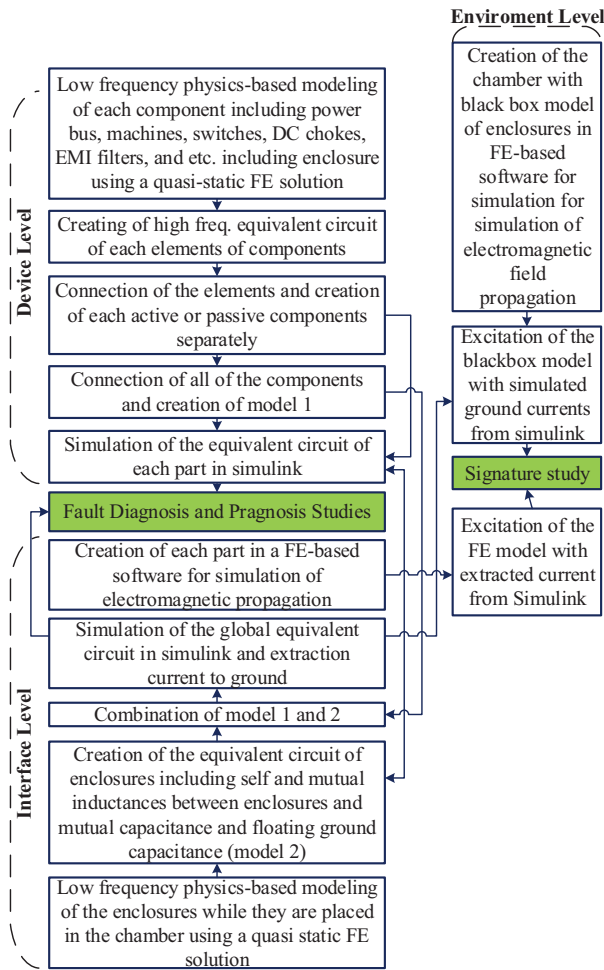
Fig. 2. Functional model of the numerical test environment.
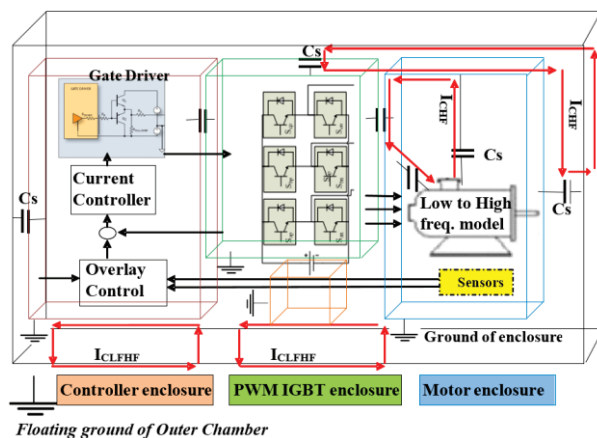
Fig. 3. A view of the numerical test environment for machine-drive design. C_s: stray capacitance, I_{CHF}: high frequency circulating current, I_{CLFHF}: low and high frequency circulating current.

For preparation of the numerical test environment for a motor-drive schema, the following procedure is implemented to evaluate the EMC and EMI in the environment that the motor-drive is located inside. In brief, the step by step implementation of the modeling procedure is summarized as:

1- A coupled field-circuit 3D finite element electromagnetic and electrostatic analysis is done to calculate low to high frequency model of each of the components. For the motor, this task is done both for differential mode and for common mode. This stage is done by using 3D finite element analysis for a given full and equivalent configuration including layout and ground schemes. At this stage, the estimation of the low to high frequency current paths inside the structure of each of the components is also done.

2- Estimation of the current multi-paths between the enclosures, and between each of enclosures to the outer chamber including physically grounded paths and high frequency capacitive paths. Here, the proximity effects, and skin effects are ignored and the static capacitances are calculated; however, the geometry and material effects are taken into account. In the cable component, the enclosure is assumed as the shield of the cable which is grounded.

3- Simulation of the whole motor-drive circuit including all the high-frequency parasitic parameters and extraction of the ground current to the floating ground point from all of the high frequency ground paths and the physically grounded paths in hybrid finite element/circuit modeling.

4- Implementation of the estimated current distributions path inside each of the components via line wires in a 3D finite element software and evaluation of radiated field to the surrounding environment while the simulated line and line to ground current form circuit is modeled as a current source to inject the current to the corresponding line wires that represent the current paths model. At this stage, the FE analysis is limited to the component and its enclosure.

5- Implementation of the estimated current distribution paths via line wires inside the outer chamber along with the enclosures

model, in a 3D finite element software, and evaluation of radiated field to the surrounding environment while the simulated ground currents form circuit model are assumed as current sources that inject the proper current to the their corresponding line wires that represent the current path models.

6- The uncertain and stochastic impact of noise currents propagated by fields can be analyzed through placing a current source noise inside the model.

Through this type of modeling, the complexity of the physics based modeling is split into three shown major sub-problems.

III. EQUIVALENT SOURCE MODELING

In this section, the electromagnetic signature study of electrical components is estimated by evaluating the fields at a distance from their sources. A numerical three-dimensional model is developed and utilized for this purpose. The estimation of these radiated fields from electrical components requires significant computational time, especially for cases involving multiple components such as generators, motors, power converters and cable-run (see Fig. 4).
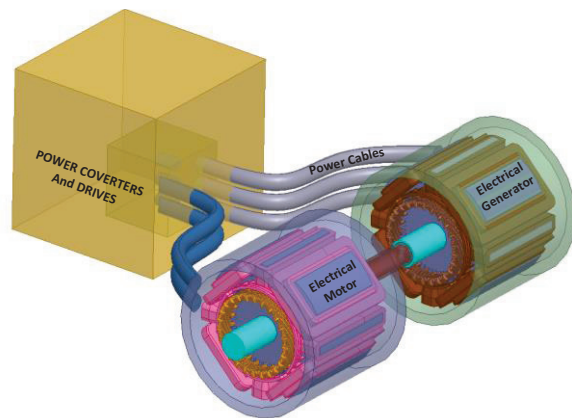
Fig. 4. Prototype of a multi-component system.

A. Electrical machines

It's proposed to develop equivalent source models using edge modeling technique in finite element analysis to overcome this limitation while maintaining accuracy. The proposed model consists of loops with various branch currents and node voltages as shown in Fig. 5 [8-10].
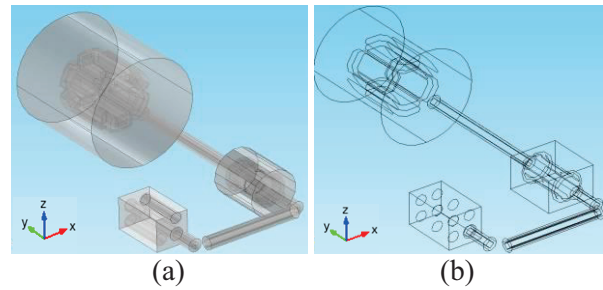

Fig. 5. Schematics of the power setup: (a) full FE model, and (b) equivalent model.

In order to model a multi component system in a large study environment, each of the components need to be modeled individually (see Fig. 5). The wire model of the system is designed and created based on the current directions. The path of the winding arrangement for the machine and the other components, including the position of the voltage terminals, should be identified. The models are shown in Figs. 5 (a) and (b). As shown in this figure, the wire model consists of numerous lines with specific currents flowing and voltages established at the nodes of these wires. The currents of the wire model are calculated based on equalizing the magnetic field densities. Using the Biot-Savart law, the radiated magnetic field density of a line at an R distance away from the line is as follows:

$$B_l = \frac{\mu_0}{4\pi} \int \frac{I_l dl \times \hat{a}_R}{R^2}, \qquad (1)$$

where the l is the length of the line and I_l is the carrying current of the line and $\hat{a}_R$ is the unit distance vector between dl and the observation point. Similarly, for a volume current, the radiated magnetic field density at a distance R is as follows:

$$B_v = \frac{\mu_0}{4\pi} \int \frac{Jdv \times \hat{a}_R}{R^2}. \qquad (2)$$

The idea of this model is to have the same field, while the model is a line and doesn't have cross-section. Hence, by equalizing the two above equations and considering J, R, ds and dl as the known parameters, then the I_l, the current amplitude of the line, can be calculated. The voltages of nodes are similarly calculated by equalizing the electric field due to the charge distribution of the line and the volume. More

details about the basics of the model are mentioned in [10].

The magnetic fluxes radiated from the actual and the wire models are derived from the simulation at 7 m away from the arrangement and shown in Figs. 6 (a) and (b), respectively. As can be seen, the magnitude of the radiated magnetic field of the optimized wire model is almost the same as the full 3D model. The proposed wire model performed the analysis accurately while the analysis time was significantly shorter in comparison with the full 3DFE model (about 50 times lower), while the full model had 8 million degrees of freedom versus one million degrees of freedom of the equivalent model.
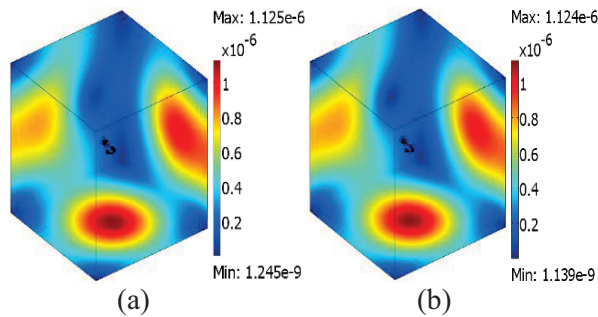
Fig. 6. Radiated magnetic flux density of: (a) 3D full model, and (b) wire model in Tesla (T).

The simulated model is verified experimentally based on the setup shown in Fig. 7. The setup consists of a synchronous generator: 13.8 kW, 3 phase, 230 V; induction motor: 3 phase, 5.5 kW, 230 V; 3 kW AC load, XLPE cable with armored PVC sheathed. The coil antenna and the real-time spectrum analyzer which is used in the measurement are specifically for low frequency analysis with high precision. The frequency range is between 20 Hz-500 kHz. The winding of the antenna is 36 turns of 7-41 litz wire shielded with 10-Ohms resistance and 340 µH inductance. The antenna and the setup are located based on the standards (MIL-461-STD). The spectrum analyzer, also covers 1 Hz - 3 GHz with ±0.5 dB absolute amplitude accuracy to 3 GHz. Note that there is a controller connected to the drive shown in Fig. 7 which is out of the system and the system is turned on manually.
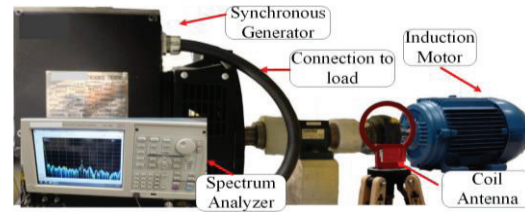

Fig. 7. The studied setup including machines, measurement equipment and control drive (for switching).

As the case study, all components including the synchronous generator, the induction motor and the electric load are turned on. The cables are passing currents; therefore, they also can be considered ON. All switches are turned on and the H-field is measured experimentally and also obtained from the simulation models. The machines are tested at their nominal voltages. The magnetic field intensity (H-field) of the measurement and simulation models is shown in Fig. 8. As shown in this figure, the full finite element model and the wire model have similar radiated H-field compared to the measurement. The small differences of the amplitudes are because of the effects of the bodies of the other components around the system.
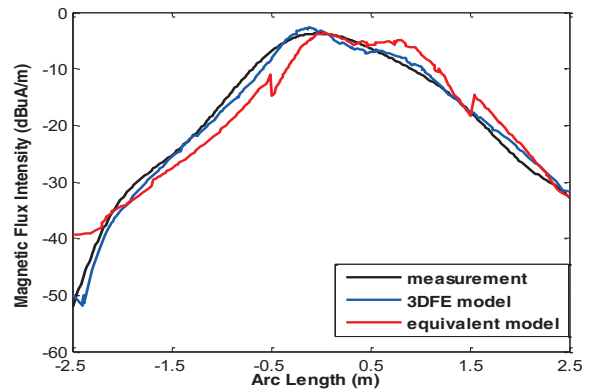

Fig. 8. The measured magnetic field intensity at 55 cm far from the setup on Y axis while all components were turned on at 60 Hz (dBµA/m).

The informative part of the figure for the monitoring purpose is the peak point at the critical frequencies, such as the power frequency and the consequent harmonics. Since the machines are

designed to be symmetric, the peak of the radiated H-field would be placed on a perpendicular line in the lateral side of the motor's casing at equal distance from the two sides of the shaft (see the dashed line in Fig. 9). This can be inferred by comparing Fig. 8 and Fig. 10. Hence, if the peak point of the Fig. 8, which is located at the junction of the dashed line and the solid line, moves back or forward along the solid line in Fig. 9, then this shift may be considered as a symptom of the asymmetry or unbalanced condition of the motor.

Fig. 9. The assumed line perpendicular to the lateral side of the motor. The maximum field is radiated at this point.

The frequency response of the experimental setup is also shown in Fig. 10 for both switch cases. Comparing Fig. 10 (b) with Fig. 10 (a), since there are two 4pole machines running in this case, the peak at the mechanical frequency which is 30 Hz, has higher amplitude at 55 cm away from the setup. For recognition of the operating machines, this can be considered as a helpful symptom. Note that, the peak of the H-field at 60 Hz in Fig. 10 (a) is the effect of the other components in the vicinity of the setup arrangement [11].
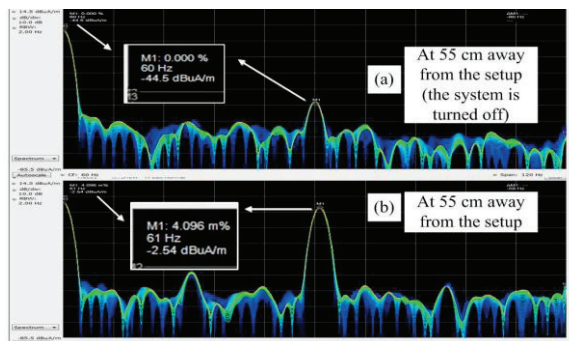

Fig. 10. The measured magnetic field intensity at distance away from the setup in lateral side of the motor while all components except IM were turned off (dBµA/m). The bandwidth of frequency is 120 Hz and the center frequency is 60 Hz.

B. Power converters

The same procedure of modeling is applied for the power converter with the exception that the power electronics converter has switches and the switching activities should be considered. The prototype of the inverter's FE model is shown in Fig. 11.
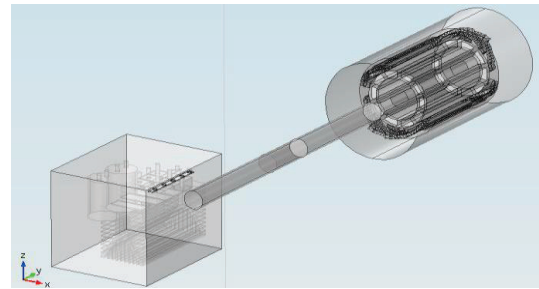

Fig. 11. The prototype of the inverter, induction motor and the connection cable.

To model the IGBT switches of the inverter for signature studies, the switches must be considered OFF for a moment of time and then it must be considered ON for the next time instant. This shift occurs based on the switching frequency of the converter. In order to do this in FE simulation, the plate between the load and the positive bus, shown in Fig. 12, is considered a conductive plate for the switch-ON case. Subsequently, this plate is considered a non-conductive plate for the switch-OFF case. This alteration of the conductivity of the plate occurs 5000 times in a second due to the switching frequency (5 kHz).
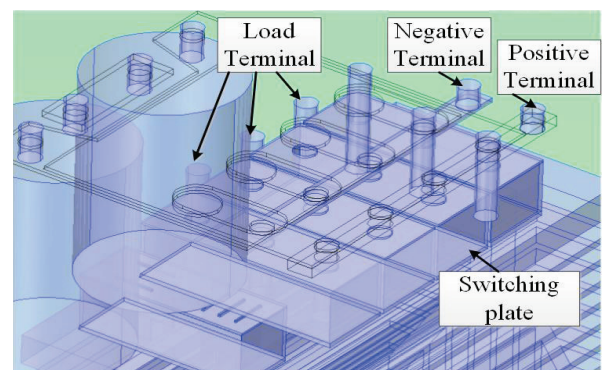

Fig. 12. Physical model of the inverter switches.

The simulation was computed in six hours with about one million elements including face,

line and node meshes in the model with six million degrees of freedom. The large number of elements is necessary because of the very small surfaces, edges and lines of the critical part of inverter and cable, as shown in Fig. 13. The details of FE modeling is reflected in [12]-[14]. The simulation was performed in a fast computer with 192 GB RAM and 16 core Intel Xeon 3.47 GHz CPU.
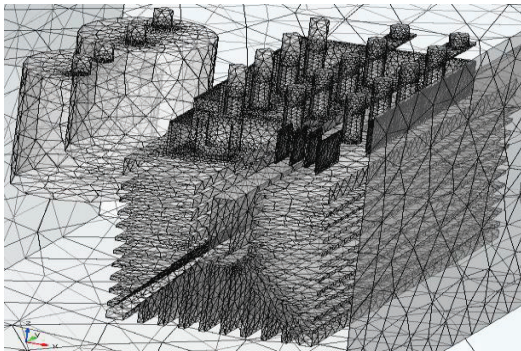

Fig. 13. Mesh pattern of the modeled inverter.

As the case study, the inverter is connected to an induction motor. The induction motor is the same as the previous test. The inverter is 5.5 kW, 320 V, 3 phase with space vector modulation as the switching algorithm. The simulation was computed in six hours with 950,000 elements and 5.7 million degrees of freedom (one million mesh elements). Since the case includes very small elements and also nonlinear materials, e.g., the core of the machine, the simulation of the inverter connected to the load or motor may take 8 hours or more for only one time instant. The experimental setup is shown in Fig. 14.
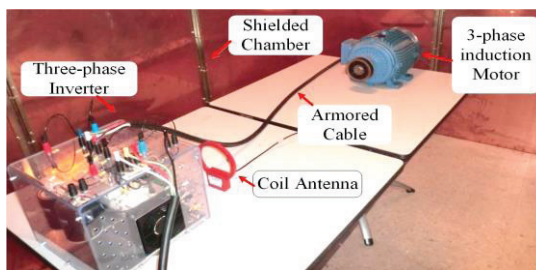

Fig. 14. The scheme of the measurement setup shown in Fig. 11.

Generally, linear or non-linear solvers are being used in the FE simulations. In this case, since there are several materials with nonlinear characteristics, the linear solver cannot be used. On the other hand, using nonlinear material rises the simulation time dramatically. Hence, a modified solver and an associated iterative technique was employed. Instead of having linear or curved commutation curve, the ramp of the curve in several zones was calculated (μ_{r1}, μ_{r2} …) and used instead of the commutation curve in this part as shown in Fig. 15. The benefit of this modification is that the magnetic flux density of a component changes in a very small period due to the steady state condition of the system. For example, the magnetic flux density of the stator core of the induction motor is about 1.5-2 T in power frequency analysis, 50-60 Hz. For higher frequencies, it goes down to under 1 T. Therefore in this case, a specific zone of the permeability can be chosen for this component. Similarly, the permeability of the other components of the system can be chosen based on the working frequency. Therefore, having the idle parts of the commutation curves of the elements would be avoided and the simulation time decreases. This algorithm can be applied in the material defining part of the FE simulation.

In addition to the modification in defining the material properties, some modification needs to be performed for the solver to have a flexible solution. Hence, as the iterative solver, the fast Generalized Minimal Residual Technique (GMRES), with the Krylov as the pre-conditioner was used. The fast GMRES is a variant of the GMRES method with flexible preconditioning that enables the use of a different pre-conditioner at each step of the Arnoldi process. The Krylov subspace is a linear subspace which enables multi-preconditioning [15]. In particular, a few steps of GMRES can be used as a pre-conditioner for fast GMRES. The flexibility of this solution method is beneficial for the problem with nonlinear material characteristics such as the motor's core. Therefore, the simulation time decreases from about 8-9 hours to about 20 minutes. More explanation is given in [16].
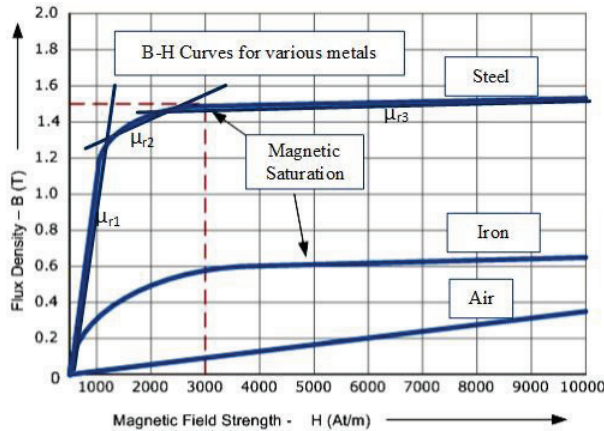
Fig. 15. Magnetization curves of some material used in the simulation.

Fig. 16. Stray magnetic field intensity of the setup case 2 at 5 kHz simulated in FE (µA/m).

In addition to the simulation, the experimental setup was implemented in a chamber which isolates the setup from the outside environment, shown in Fig. 14. The coil antenna was located at 10 cm away from the inverter to obtain the stray magnetic field. The fields were transferred to an EMI receiver, real-time spectrum analyzer, with a cable of 50-Ω impedance.

The magnetic field intensity (H-field) generated from the setup in simulation is shown in Fig. 16. The H-field at 5-kHz frequency is shown on a slice at 10 cm away from the setup, the same as experimental setup. As illustrated in this figure, the amplitude of the stray field around the inverter box is higher than other places. The reason is that the switching frequency of the inverter is 5 kHz, the same as the frequency depicted from the simulation figure. The simulation was performed at several other frequencies. Only the switching frequency of the inverter which is 5-kHz, is shown here. The setup was also implemented experimentally. The frequency response from DC to 20-kHz was obtained and shown in Fig. 17.

The unit of the simulation result is µA/m, while the unit of the experimental results is dBµA/m. The µA/m can be converted to dBµA/m by using Eq. (3). Using this equation, the peak of the stray magnetic field at 5-kHz at the given distance is -4.37 dBµA/m would be 0.61 µA/m experimentally, which is very close to the value in simulation, see Fig. 16;

$$\mu A/m = 10^{\frac{dB\mu A/m}{20}}. \tag{3}$$

Fig. 17. Measured frequency response of the stray magnetic field intensity of the setup from DC to 20 kHz (dBµA/m).

C. Power cables

The actual physical modeling of cables for signature studies requires all the details to be considered even in a large region. The XPLE cables similar to all electromagnetic sources propagate dipoles at a far distance. However, interacting several components such as electrical machines, power converters modify the shape and the amplitude of dipoles. Therefore, each model should be modeled and studied independently. However, there is a problem with the modeling of the relatively small layers of a multi-core XLPE cables. The study region could be about 20,000 times bigger. This causes deformation of the cable's model during meshing in numerical

modeling method. The present study is performed on the XLPE insulated and armored PVC sheathed cable (0.6/1 kV).

Figure 18 shows the typical model, as well as original and the deformed models of the studied cable in finite element analysis environment. In order to solve this issue, a specific modeling including multi dipoles with several line currents and node voltages are designed similar to the procedure explained in III.A. As shown in Fig. 19, the model is replaced by a collection of lines located in the position of the windings in actual machine. More details are mentioned in [17].


(a) (b) (c)
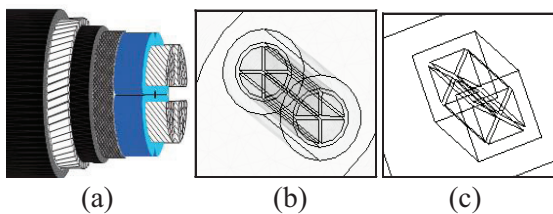
Fig. 18. Models of the proposed cable in finite element design: (a) typical model, (b) orignial FE model, and (c) deformed FE model.
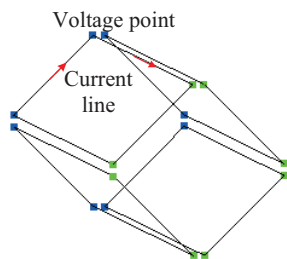

Fig. 19. Prototype of the multi-dipole models of the studied cable.

Many case studies are implemented related to cables, but for brevity only one of them is explained in the following.

The proposed model is analyzed in connection with a power component. A synchronous generator is coupled with a multi-core XLPE cable. In order to model the synchronous generator, the wire modeling is used which is basically similar to the proposed modeling of the cable, further details are explained in [18]. The actual and equivalent models of the cable connected to the machine are shown in Fig. 20.


(a) (b)
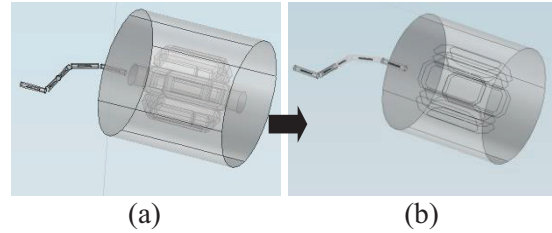
Fig. 20. Schematic of the synchronous machine connected to the cable: (a) the detailed model, and (b) the equivalent model.

The rated voltage is applied to the cable which is connected to the machine and the radiated field is measured at a far distance from the sources. Also, the current and voltage values of the equivalent model are calculated based on the individual actual models of the machine and cable. Figure 21 shows the propagated fields of both models along X axis in XY plane. The proposed line is also shown in the figure. The difference of amplitude between these two models is because of superposition of materials. Since the cables and machine are so close together, therefore, there is a superposition effect in magnetic field. The radiated magnetic field from cable is induced into the machine and creates an induced current which radiates an additional field from the machine. These phenomena cannot be simulated perfectly in the proposed multi-dipole modeling so there is a difference in the curves. More studies are in [17].
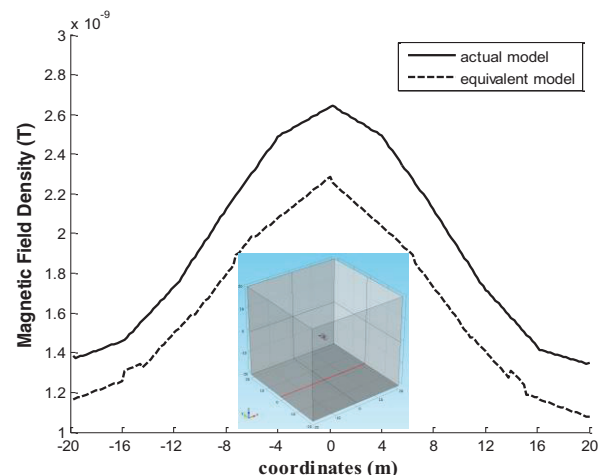

Fig. 21. Radiated magnetic field density along X axis in XY plane.

IV. HIGH-FREQUENCY EQUAIVALENT SOURCE MODELING

For EMC modeling the power components, especially power electronic components such as drives and converters, the high frequency modeling of them is needed which is implemented based on Fig. 22. The detail models of the power converters are reflected in [19].
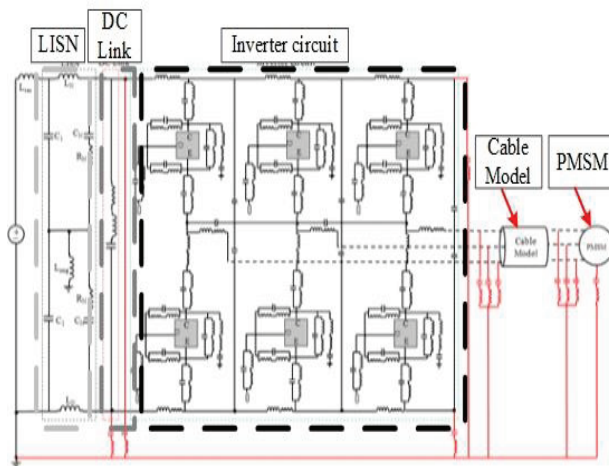

Fig. 22. Inverter circuit of AC motor drive, used in simulation with inclusion of parasitic components.

Figure 23 demonstrates the connection of a three-phase 42-V inverter, armored power cable and three-phase PMSM. The inverter adopts power IGBT as the switching device. In the inverter model, all the semiconductor devices are substituted with their corresponding physics-based models. To simulate such an inverter drive, the time-domain simulation approach is used. To construct the simulation model for motor-drive system, the three major components of the system (i.e., inverter, cable and PMSM) are replaced with their corresponding physics-based models.

The test setup used to measure the frequency spectrum in different point in the drive system is shown in Fig. 23 (b). The illustrated test setup consists of a DC power supply, LISN, inverter circuit, 2 m long armored power cable and a 250 Watt PMSM. To measure the common mode current, all these components are assembled on a metallic plate. Subsequently, the conducted current can be measured between these plates. In order to avoid time-consuming computing process and better evaluation, the frequency domain simulation approach is used.


(a)

(b)
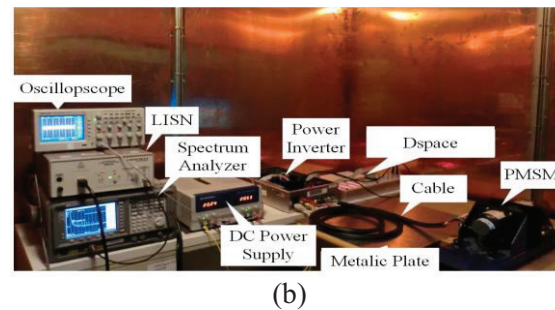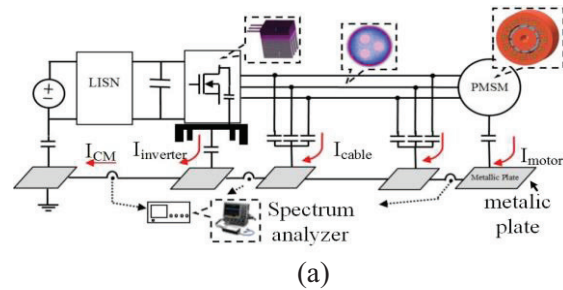
Fig. 23. Schematic view of a motor-drive system: (a) schematic of motor-drive system used for CM measurement, and (b) experimental setup.

Figure 24 shows the system structure in the FE model. This model was solved to estimate the values of the parasitic elements in the circuit model. Figure 25 shows comparisons of conducted EMI common mode between the measurements data and two modeling approaches in the frequency domain.
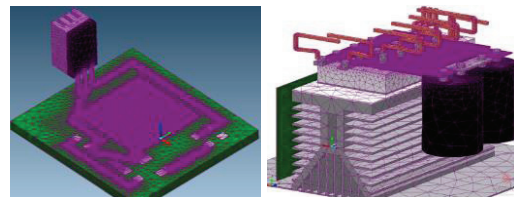

Fig. 24. The converter model in finite element and its corresponding mesh.
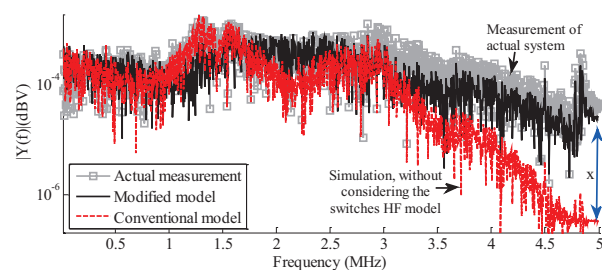
Fig. 25. Frequency spectrum of the common mode current.

To study the effectiveness of our models, the equivalent models for cable and PMSM were added to the inverter model and the simulation results are compared to the experimental results. To verify the accuracy of our numerical results, the common mode current of the setup in Fig. 24 was measured using the current probe with 100 MHz bandwidth. The current of Fig. 24 is measured at the ground port of the input DC power supply.

As an application of this modeling, three switching techniques (Hysteresis, Space Vector Modulation and Sinusoidal PWM) with a carrier frequency of 5 kHz applied to the inverter. A three-phase 5 kW RL load was connected to the inverter, which makes the inverter operate at nominal power. The calculated currents were then injected to the terminals in the 3D-FE based model. The 3D-FE solution was obtained using harmonic propagation analysis. The step time for this simulation was 5 µs. To validate the obtained numerical results, the experimental setup was implemented and the inverter's phase current spectrum is measured using a spectrum analyzer and a 100 MHz current probe. The measured and simulated frequency spectrums of the inverter's phase current for SVM as an example is shown in Fig. 26. Subsequently, the magnetic field spectrum of the components designed using the physics based modeling are shown in Fig. 27.
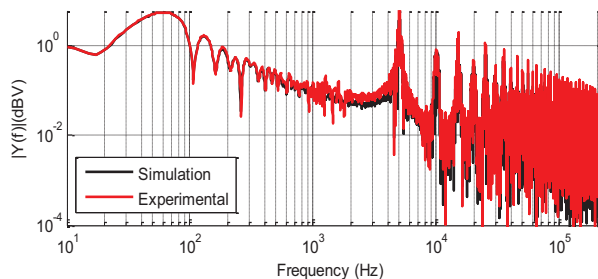

Fig. 26. Comparison of the frequency spectrum of the inverter's phase current between equivalent model and experiments.
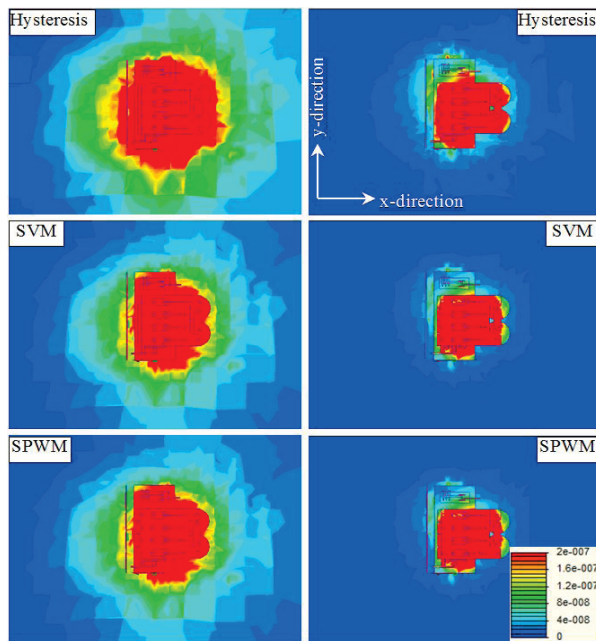

Fig. 27. Magnetic flux density at different switching patterns before (left) and during switching (right): (a) hysteresis, (b) SVM, and (c) SPWM.

It can be easily inferred from the figure that within this model, various parameters can be changed and studied in order to identify an EMI mitigation strategy during the design stage of these systems. In the proposed model, the EMI can be analyzed at any point or plane within the simulation volume, and can be solved for different switching patterns. The time dependence of the radiated EMI can also be evaluated using the model. We can see how the magnetic flux density behaves over time at specific locations and at various switching patterns and frequencies. Furthermore, the field image can be obtained for various scenarios specified by the designer and provide them with information that can be obtained quickly. This would allow for efficient and effective complete design work using computational electromagnetics.

V. OPTIMIZATION OF POWER ELECTRONIC CONVERTERS USING PHYSICS-BASED MODELS

In this study, the optimization of a physics-based representation of a frequency modulated switch mode converter is presented. The proposed physics based model can be used to evaluate the electromagnetic interference in the structure of the converter. In this method, the power converter magnetic components and their position on the circuit board are modeled numerically using Finite Element Analysis (FEA). Subsequently, the placement of the components and also the electrical and operating parameters of the converter are optimized in a way to limit the propagated electromagnetic field of the components. This is an essential fact in design of the power converters and the evaluation of their EMI interactions for EMC compliance.

Figure 28 depicts the flowchart of the parameter optimizing procedure using GA. Parameters for optimization are the converter's operating parameters and placement of the magnetic components with respect to each other. The genetic algorithm evolves the given population of individuals. The object function is consisting of the area of the circuit board and energy of the output voltage signal. In order to change the area which confines the two inductors, the filter inductor's position is considered as a reference and the resonant inductor placement is changing all around the reference point (filter inductor). Figure 29 illustrates the process of changing the placement of the two inductors as with respect to each other.

Fig. 29. Iteration accomplished by GA to minimize the objective function.

Table 2 shows the results from the optimization process. The magnetic component positions of this converter are shown in Fig. 30. It is clear that this power converter is showing a poor EMI performance at initial design stage (Fig. 29 (a)). FE analysis is performed observe the near-field effects for the given layout. Further, we performed repeated simulations to determine the best EMI performance versus geometry of the board and the frequency (Fig. 30 (b)).

Table 2: Optimization results

Parameters	L_r (µH)	f (kHz)	Area (mm²)
Initial design	120	50	3360
Optimized design	45	90	11000

Fig. 28. The optimization process diagram.

(a)

(b)
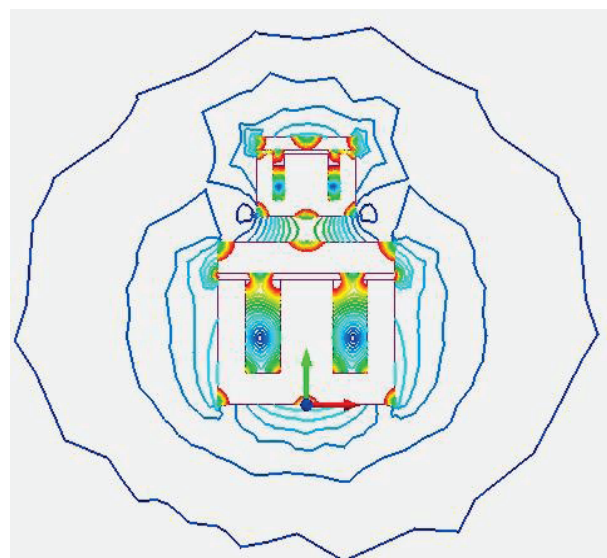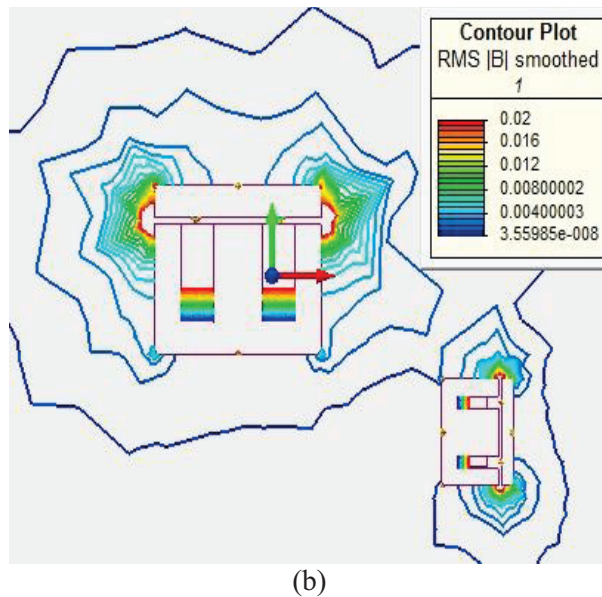
Fig. 30. Layout of the system: (a) before optimization, and (b) after optimization.

Figure 31 compares the input current spectrum, filter inductor's current spectrum and output voltage spectrum of the converter in the ideal case and physics-based mode (non-optimized case), respectively. It is noticed that in the optimized case, the pick of the frequency spectrum has been decreased, as compared to the non-optimized case. Figure 32 shows the circuit layout of the converter in the optimized case. In this case, the magnetic components are placed, somehow, that the magnetic field generated by each one has the less interference with the other. More details are reflected in [20].
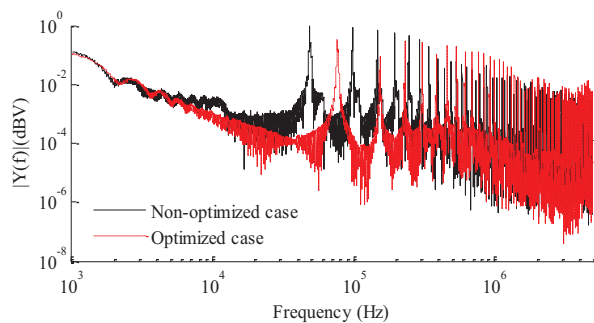

Fig. 31. Comparison of FFT spectrum between optimized and non-optimized quasi-resonant converter, resonant inductor's current.
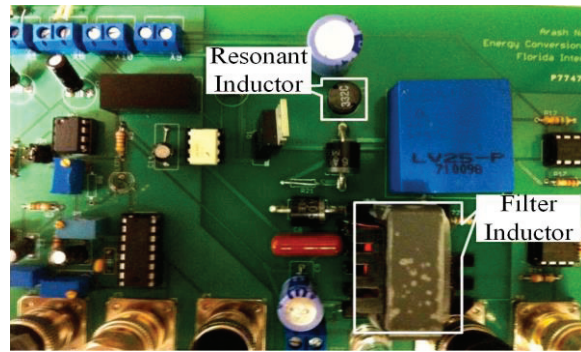

Fig. 32. ZCS quasi-resonant buck converter's circuit in the optimized layout.

VI. CONCLUSION

This paper reviewed the physics based modeling analysis for the purpose of EMC evaluation in multi components power system. It introduced the algorithm of physics based modulation for both low and high frequency analysis. The equivalent source modeling of the powertrain was implemented for EMC studies and the results showed that the equivalent model can make the same result of the full model with significantly less simulation time. The model has been used for condition monitoring of the components based on the EM signatures. Moreover, the optimization of the switching algorithm, as well as the proper placement of the magnetic components on the PCB was achieved all based on the radiated electromagnetic fields.

AKNOWLEDGEMWNTS

REFERENCES

[1] W. Zhang, M. T. Zhang, F. C. Lee, J. Roudet, and E. Clavel, "Conducted EMI analysis of a boost PFC circuit," *IEEE Appl. Power Electron. Conf.*, pp. 223-229, 1997.

[2] B. Revol, et al., "EMI study of a three phase inverter-fed motor drives," *IEEE Industry Applications Conference, 2004*, vol. 4. IEEE, 2004.

[3] Y. L. Zhong, et al., "HF circuit model of conducted EMI of ground net based on PEEC," *Zhongguo Dianji Gongcheng Xuebao*, vol. 25, no. 17, 2005.

[4] H. Zhu, et al., "Analysis of conducted EMI emissions from PWM inverter based on empirical models and comparative experiments," *IEEE*

Annual Power Electronics Specialists Conference, (PESC 99), 30th, vol. 2, 1999.

[5] X. Pei, et al., "Analytical estimation of common mode conducted EMI in PWM inverter," *IEEE Industry Applications Conference*, vol. 4, 2004.

[6] L. Sevgi, "EMC and BEM engineering education: physics-based modeling, hands-on training, and challenges," *IEEE Antennas and Propagation Magazine*, vol. 45, no. 2, pp. 114-119, 2003.

[7] D. S. Dixon, M. Obara, and N. Schade, "Finite-element analysis (FEA) as an EMC prediction tool," *IEEE Transactions on Electromagnetic Compatibility*, vol. 35, no. 2, pp. 241-248, 1993.

[8] A. Sarikhani, M. Barzegaran, and O. A. Mohammed, "Optimum equivalent models of multi-source systems for the study of electromagnetic signatures and radiated emissions from electric drives," *IEEE Transaction on Magnetics*, vol. 48, issue 2, pp. 1011-1014, 2012.

[9] M. R Barzegaran, A. Sarikhani, O. A. Mohammed, "An optimized equivalent source modeling for the evaluation of time harmonic radiated fields from electrical machines and drives," *Applied Computational Electromagnetics Society Journal*, vol. 28, no. 4, pp. 273-282, April 2013.

[10] M. R Barzegaran and O. A. Mohammed, "A generalized equivalent source model of AC electric machines for numerical electromagnetic field signature studies," *IEEE Transaction on Magnetics*, vol. 48, no. 11, November 2012.

[11] M. R Barzegaran and O. A. Mohammed, "3-D FE equivalent source modeling and analysis of electromagnetic signatures from electric power drive components and systems," *IEEE Transaction on Magnetics*, vol. 49, no. 5, pp. 1937-1940, May 2013.

[12] M. R. Barzegaran, A. Nejadpak, and O. A. Mohammed, "Evaluation of high frequency electromagnetic behavior of planar inductor designs for resonant circuits in switching power converters," *Applied Computational Electromagnetic Society (ACES) Journal*, vol. 26, no. 9, pp. 737-748, September 2011.

[13] G. Skibinski, R. J. Kerkman, and D. Schlegel, "EMI emissions of modern PWM AC drives," *IEEE Ind. Appl. Mag.*, vol. 5, no. 6, pp. 47-80, 1999.

[14] O. Martins, S. Guedon, and Y. Marechal, "A new methodology for early stage magnetic modeling and simulation of complex electronic systems," *IEEE Trans. Magn.*, vol. 48, no. 2, pp. 319-322, 2012.

[15] W. E. Arnoldi, "The principle of minimized iterations in the solution of the matrix eigenvalue problem," *Quarterly of Applied Mathematics*, V. 9, pp. 17-29, 1951.

[16] J. Stoer and R. Bulirsch, "Introduction to numerical analysis," 3rd edition, S*pringer*, New York, 2002.

[17] M. R Barzegaran and O. A. Mohammed, "Multi-dipole modeling of XLPE cable for electromagnetic field studies in large power systems," *International Journal for Comp. and Math. in Electrical Eng. (COMPEL)*, vol. 33, no. 1, 2014.

[18] M. R Barzegaran and O. A. Mohammed, "Near field evaluation of electromagnetic signatures from wound rotor synchronous generators using wire modeling in finite element domain," *28th ACES Conf.*, Columbus, OH, USA, April 2012.

[19] A. Nejadpak, "Development of physics-based models and design optimization of power electronic conversion systems," *FIU Electronic Theses and Dissertations*, paper 824, (2013).

[20] A. Nejadpak and O. A. Mohammed, "Physics-based optimization of EMI performance in frequency modulated switch mode power converters," *Electromagnetic Field Problems and Applications (ICEF)*, pp. 1-4, June 19-21, 2012.

Mohammadreza Barzegaran (S'10) obtained his B.Sc. and M.Sc. degrees in Power Engineering from the University of Mazandaran, Iran in 2007 and 2010, respectively. He defended his Ph.D. degree in the department of Electrical and Computer Engineering, Florida International University, Florida, USA. He is now Assistant Professor at Lamar University. His research interests include studying electromagnetic compatibility in power components, life assessment of electrical power components, fault detection in electrical machines, and also computer-aid simulation of power components. He has many published papers in journals and conferences.

Osama A. Mohammed (S'79, M'83 SM'84, F'94) is a Professor of Electrical and Computer Engineering and the Director of the Energy Systems Research Laboratory at Florida International University. He received his M.S. and Ph.D. degrees in Electrical Engineering from Virginia Polytechnic Institute and State University. He published numerous journal articles over the past 30 years in areas relating to power systems, electric machines and drives, computational electromagnetics and in design optimization of

electromagnetic devices, artificial intelligence applications to energy systems. He authored and co-authored more than 350 technical papers in the archival literature. He has conducted research work for government and research laboratories in shipboard power conversion systems and integrated motor drives. He has been successful in obtaining a number of research contracts and grants from industries and Federal government agencies for projects related to these areas. Mohammed also published several book chapters including Chapter 8 on Direct Current Machinery in the Standard Handbook for Electrical Engineers, 15th Edition, McGraw-Hill, 2007 and a book Chapter entitled "Optimal Design of Magnetostatic Devices: The Genetic Algorithm Approach and System Optimization Strategies," in the Book entitled: Electromagnetic Optimization by Genetic Algorithms, John Wiley & Sons, 1999.

Mohammed is a Fellow of IEEE and is the recipient of the IEEE PES 2010 Cyril Veinott Electromechanical Energy Conversion Award.

Mohammed is also a Fellow of the Applied Computational Electromagnetic Society. He is Editor of IEEE Transactions on Energy Conversion, IEEE Transactions on Magnetics, IEEE Transactions on Smart Grid and COMPEL. Mohammed was the past President of the Applied Computational Electromagnetic Society (ACES). He received many awards for excellence in research, teaching and service to the profession and has delivered numerous invited lectures at scientific organizations around the world.

Mohammed has been the General Chair of several international conferences including ACES-2013, ACES 2006, IEEE-CEFC 2006, IEEE-IEMDC 2009, IEEE-ISAP 1996 and COMPUMAG-1993. He has also Chaired technical programs for other major international conferences including IEEE-CEFC 2010, IEEE-CEFC-2000 and the 2004 IEEE Nanoscale Devices and System Integration. Mohammed also organized and taught many short courses on power systems, electromagnetics and intelligent systems in the U.S.A and abroad.

FDTD Implementations of Integrated Dependent Sources in Full-Wave Electromagnetic Simulations

Khaled ElMahgoub [1,2] and Atef Z. Elsherbeni [3]

[1] Trimble Navigation, Woburn, MA 01801, USA
kelmahgoub@ieee.org

[2] Auto-ID Labs
Massachusetts Institute of Technology, Cambridge, MA 02139, USA

[3] Electrical Engineering and Computer Science Department
Colorado School of Mines, Golden, CO 80401, USA
aelsherb@mines.edu

Abstract ─ The implementation of dependent sources such as: Current Controlled Current Source in full-wave electromagnetic simulation using the Finite-Difference Time-Domain method is introduced. This simple new approach is verified with several numerical examples. In one example, the CCCS is used to implement a circuit with Bipolar Junction Transistor. Good agreement is obtained when the results of the developed FDTD code are compared with those based on analytical solution.

Index Terms ─ Bipolar Junction Transistor (BJT), Current Controlled Current Source (CCCS), Current Controlled Voltage Source (CCVS), dependent sources, Finite-Difference Time-Domain (FDTD), Voltage Controlled Current Source (VCCS), Voltage Controlled Voltage Source (VCVS).

I. INTRODUCTION

The Finite-Difference Time-Domain (FDTD) method has gained great popularity as a tool for full wave electromagnetic simulations. Although it is based on a time-domain solution, it provides a wideband frequency-domain response using time to frequency transformation. It can easily handle composite geometries consisting of different types of materials. In addition, it can easily implement different algorithms for parallel computations. These features of the FDTD have made it one of the most attractive techniques in computational electromagnetics for many applications [1]-[2]. One of the strengths of the FDTD method is implementation of lumped linear and nonlinear circuit elements such as resistors, inductors, capacitors, diodes, transistors, etc. In addition, it can implement independent sources such as current and voltage sources which makes FDTD method widely used in simulating microwave circuits, such as amplifiers, active filters, etc. These circuits usually consist of nonlinear components as well as linear components. Most of the nonlinear elements such as transistors are modeled using dependent sources. A dependent source is a source that generates a voltage or current whose value depends on another voltage or current in the same circuit. There are in general four different types of dependent sources, namely: Voltage Controlled Current Source (VCCS), Current Controlled Current Source (CCCS), Voltage Controlled Voltage Source (VCVS) and Current Controlled Voltage Source (CCVS). Dependent sources appear in most of the equivalent circuit models for devices such as: Bipolar Junction Transistor (BJT) and Metal Oxide Field Effect Transistor (MOSFET), operational amplifiers, static substrate thermal coupling, etc.

To the best of the authors' knowledge, the full implementation of dependent sources using FDTD has not been adequately addressed before, except in [3]-[5], which doesn't cover all four kinds of

dependent sources. One should point out, that the direct implementation of nonlinear devices such as transistors in full wave simulation using FDTD, has been previously investigated by many research groups [6]-[17]. For example, the work done in [6], where Ebers-Moll model was used to implement BJT using Newton Raphson method; in [7] and [8], the BJT was implemented by applying Taylor expansion on the nonlinear transport equations of the BJT based on Gummel-Poon model; while in [10], FDTD formulation based on two port network formulation using its admittance matrix and then transformed to Z-domain and then to difference equation is used to model such devices. In [11], a coupled FDTD-SPICE is used to implement an amplifier, [12] describes a voltage-source-based formulation for the purpose of modeling microwave devices, [13] applies the extended FDTD method to implement nonlinear active microwave circuits. In [14] and [15], reduced nonlinear lumped network FDTD method for the global modeling of RF and microwave circuits is presented. While in [17], 2-D FDTD extended method is used to implement non-linear elements.

In this paper, simple implementation of all four kinds of dependent sources using FDTD is introduced with efficient use of both memory and computational time. This new approach can be used to analyze circuits containing VCCS, CCCS, VCVS and CCVS, or circuits with devices such as MOSFETs, BJTs, operational amplifier or any kind of devices that can be represented using dependent sources in their equivalent circuit model. The FDTD updating equations of the different dependent sources will be derived and used directly to simulate several resistive circuits with different dependent sources. In addition, these dependent sources will be used to represent non-linear devices such as BJT with its equivalent model as an application for the dependent sources implementation. The paper is organized as follows: in Section II, the dependent sources implementation approach is described and the FDTD equations are derived. In Section III, numerical examples to prove the validity of the new approach are presented, including a simple resistive circuits with different dependent sources, and BJT circuit. In Section IV, conclusions are provided.

II. FDTD IMPLEMENTATION

In this section, the new approach is described

and the FDTD updating equations are derived. In general, every dependent source is connected between two adjacent nodes and its value is controlled by the voltage or the current between two other nodes that are not necessary adjacent to each other. To drive the FDTD updating equations for different dependent sources, let's consider the four circuits shown in Figs. 1 (a), (b), (c) and (d). As shown in the figure, all nodes can be normally updated using lumped elements FDTD implementation as in [1], except for the dependent source which needs special handling. For all nodes containing dependent sources, the current density J_{iz} needs to be represented in terms of the controlling parameter voltage (V_0) or current (I_0) as shown in Fig. 1.


(a)

(b)

(c)

(d)

(e)
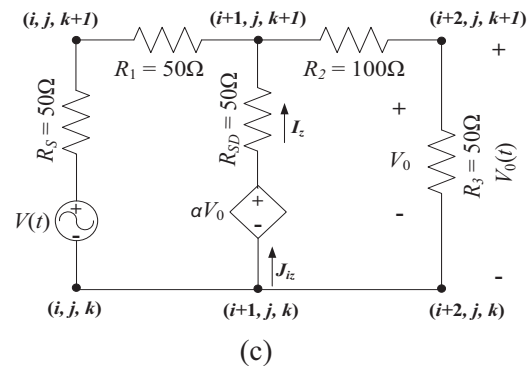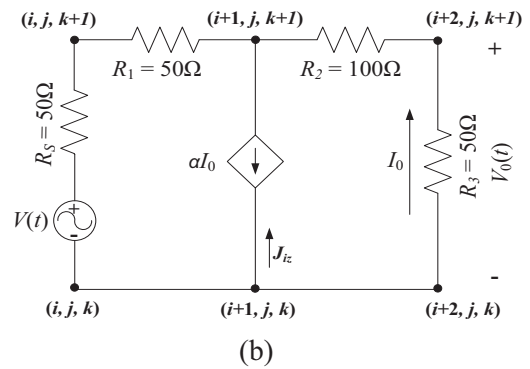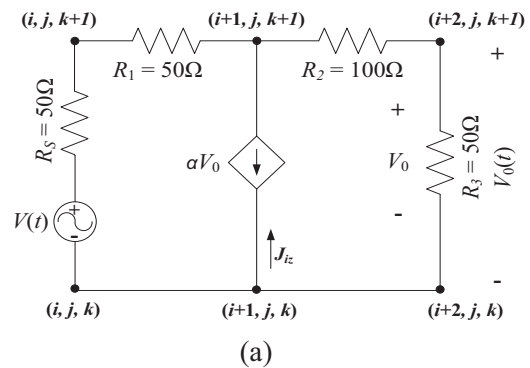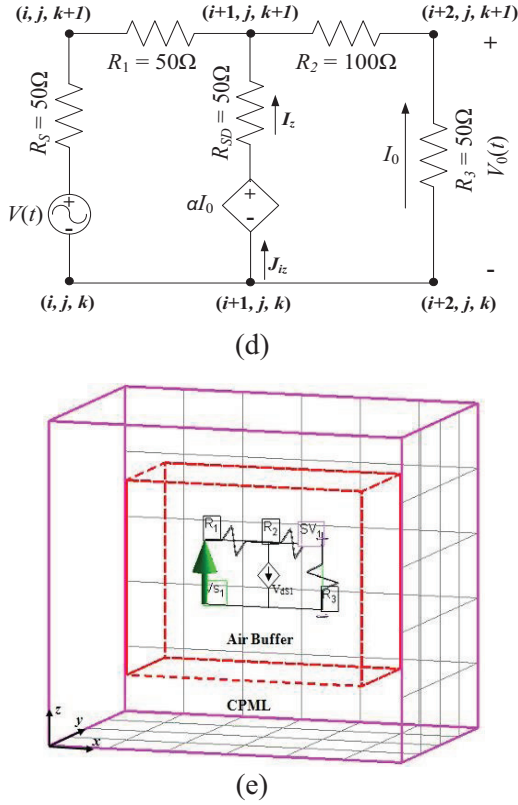
Fig. 1. Simple resistive circuits with different kinds of dependent sources: (a) VCCS, (b) CCCS, (c) VCVS, (d) CCVS, and (e) FDTD computational domain for circuit (a).

The controlling voltages and currents can be calculated using the same formulas used for the sampled current and voltages as presented in [1]. For example, for elements oriented along the z-direction and connected between two nodes with the k index ranges from s to e, we get for the sampled voltage:

$$V_{ZSampled} = -\int \vec{E} \cdot \vec{dl}, \qquad (1)$$

writing (1) in discrete form:

$$V_{ZSampled}^{n+\frac{1}{2}} = -\Delta z \times \sum_{k=ks}^{ke-1} E_Z^{n+\frac{1}{2}}(is, js, k)$$

$$= -\Delta z \times \sum_{k=ks}^{ke-1} \left[\frac{E_Z^{n+1}(is, js, k) + E_Z^n(is, js, k)}{2} \right], \qquad (2)$$

and for the sampled currents between the same two nodes, one has:

$$I_{ZSampled} = \oint \vec{H} \cdot \vec{dl}, \qquad (3)$$

writing (3) in discrete form:

$$I_{Zsampled}^{n+\frac{1}{2}} = \Delta x \times \sum_{i=is}^{ie} H_x^{n+\frac{1}{2}}(i, js-1, ke-1)$$

$$+ \Delta y \times \sum_{j=js}^{je} H_y^{n+\frac{1}{2}}(ie, j, ke-1)$$

$$- \Delta x \times \sum_{i=is}^{ie} H_x^{n+\frac{1}{2}}(i, je, ke-1)$$

$$- \Delta y \times \sum_{j=js}^{je} H_y^{n+\frac{1}{2}}(is-1, j, ke-1), \qquad (4)$$

where is, ie, js, je, ks and ke are the minimum and maximum cell indices in x, y, and z-direction, respectively. In this implementation the sampled voltage or current is used directly as the controlling value instead of calculating it separately as in [2].

A. VCCS updating equation

To update the electric field at node $(i+1, j, k)$ shown in Fig. 1 (a), the J_{iz} should be calculated as follows:

$$\frac{\partial E_z}{\partial t} = \frac{1}{\varepsilon_z} \left(\frac{\partial H_y}{\partial x} - \frac{\partial H_x}{\partial y} - \sigma_z^e E_z - J_{iz} \right), \qquad (5a)$$

where

$$J_{iz}^{n+\frac{1}{2}}(i+1, j, k) = \frac{I_{iz}^{n+\frac{1}{2}}(i+1, j, k)}{\Delta x \Delta y} = \frac{-\alpha V_0^{n+\frac{1}{2}}}{\Delta x \Delta y}, \qquad (5b)$$

where n represent the time index, ε is the permittivity of the medium, σ is the conductivity, α is the control factor, and V_0 is equal to $V_{ZSampled}$ between the two nodes $(i+2, j, k)$ and $(i+2, j, k+1)$ at time index $n+\frac{1}{2}$ which can be calculated using (2). The updating equation for E_z^{n+1} at node $(i+1, j, k)$ can then be written using the coefficient convention presented in [1] as follows:

$$E_z^{n+1}(i+1, j, k) = C_{eze}(i+1, j, k) E_z^n(i+1, j, k)$$

$$+ C_{ezhy}(i+1, j, k) \left[H_y^{n+\frac{1}{2}}(i+1, j, k) - H_y^{n+\frac{1}{2}}(i, j, k) \right]$$

$$+ C_{ezhx}(i+1, j, k) \left[H_x^{n+\frac{1}{2}}(i+1, j, k) - H_x^{n+\frac{1}{2}}(i+1, j-1, k) \right] \qquad (6)$$

$$+ C_{ezvccs}(i+1, j, k) V_{ZSampled}^{n+\frac{1}{2}},$$

where

$$C_{eze}(i+1,j,k) = \frac{A_0}{B_0}, C_{ezhy}(i+1,j,k) = \frac{2\Delta t}{B_0 \Delta x},$$

$$C_{ezhx}(i+1,j,k) = \frac{-2\Delta t}{B_0 \Delta y}, C_{ezvccs}(i+1,j,k) = \frac{2\Delta t\alpha}{B_0 \Delta x \Delta y},$$

$$A_0 = [2\varepsilon_z(i+1,j,k) - \Delta t\sigma_z^e(i+1,j,k)],$$
$$B_0 = [2\varepsilon_z(i+1,j,k) + \Delta t\sigma_z^e(i+1,j,k)]. \tag{7}$$

Using (6), the electric fields at step $n+1$ appear on both sides of the equation due to the use of equation (2). Special sequence for the update of E_z^{n+1} is followed to overcome this issue as explained in section E below.

B. CCCS updating equation

To update the electric field component E_z^{n+1} at node $(i+1,j,k)$ shown in Fig. 1 (b), the J_{iz} should be calculated as follows:

$$J_{iz}^{n+\frac{1}{2}}(i+1,j,k) = \frac{I_{iz}^{n+\frac{1}{2}}(i+1,j,k)}{\Delta x \Delta y} = \frac{-\alpha I_0^{n+\frac{1}{2}}}{\Delta x \Delta y}, \tag{8}$$

where α is the control factor and I_0 is equal to $I_{ZSampled}$ between the two nodes $(i+2,j,k)$ and $(i+2,j,k+1)$ at time index $n+\frac{1}{2}$ which can be calculated using (4). The updating equation at node $(i+1,j,k)$ can then be written using the coefficient convention presented in [1] as follows:

$$E_z^{n+1}(i+1,j,k) = C_{eze}(i+1,j,k)E_z^n(i+1,j,k)$$

$$+C_{ezhy}(i+1,j,k)\left[H_y^{n+\frac{1}{2}}(i+1,j,k) - H_y^{n+\frac{1}{2}}(i,j,k)\right]$$

$$+C_{ezhx}(i+1,j,k)\left[H_x^{n+\frac{1}{2}}(i+1,j,k) - H_x^{n+\frac{1}{2}}(i+1,j-1,k)\right] \tag{9}$$

$$+C_{ezccs}(i+1,j,k)I_{ZSampled}^{n+\frac{1}{2}},$$

with

$$C_{eze}(i+1,j,k) = \frac{A_0}{B_0}, C_{ezhy}(i+1,j,k) = \frac{2\Delta t}{B_0 \Delta x},$$

$$C_{ezhx}(i+1,j,k) = \frac{-2\Delta t}{B_0 \Delta y}, C_{ezvccs}(i+1,j,k) = \frac{2\Delta t\alpha}{B_0 \Delta x \Delta y},$$

where A_0 and B_0 are given by (7). Using (9), the updating equation of the electric field associated with a CCCS can be easily implemented in a FDTD code.

C. VCVS updating equation

The voltage source here is considered as a soft source (with internal resistance R_{SD}). To update the electric field component E_z^{n+1} at the node $(i+1,j,k)$ shown in Fig. 1 (c), the J_{iz} should be calculated as follows:

$$J_{iz}^{n+\frac{1}{2}}(i+1,j,k) =$$

$$\frac{\Delta z}{2\Delta x \Delta y R_{SD}} \times [E_z^{n+1}(i+1,j,k) + E_z^n(i+1,j,k)] \tag{10}$$

$$+\frac{1}{\Delta x \Delta y R_{SD}} \times \alpha V_0^{n+\frac{1}{2}},$$

where α is the control factor and V_0 is equal to $V_{ZSampled}$ between the two nodes $(i+2,j,k)$ and $(i+2,j,k+1)$ at the time index $n+\frac{1}{2}$ which can be calculated using (2). The updating equation at node $(i+1,j,k)$ can then be written using the coefficient convention presented in [1] as follows:

$$E_z^{n+1}(i+1,j,k) = C_{eze}(i+1,j,k)E_z^n(i+1,j,k)$$

$$+C_{ezhy}(i+1,j,k)\left[H_y^{n+\frac{1}{2}}(i+1,j,k) - H_y^{n+\frac{1}{2}}(i,j,k)\right]$$

$$+C_{ezhx}(i+1,j,k)\left[H_x^{n+\frac{1}{2}}(i+1,j,k) - H_x^{n+\frac{1}{2}}(i+1,j-1,k)\right] \tag{11}$$

$$+C_{ezvcvs}(i+1,j,k)V_{Sampled}^{n+\frac{1}{2}},$$

with

$$C_{eze}(i+1,j,k) = \frac{R_{SD}\Delta x \Delta y A_0 - \Delta t \Delta z}{R_{SD}\Delta x \Delta y B_0 + \Delta t \Delta z},$$

$$C_{ezhy}(i+1,j,k) = \frac{2R_{SD}\Delta y \Delta t}{R_{SD}\Delta x \Delta y B_0 + \Delta t \Delta z},$$

$$C_{ezhx}(i+1,j,k) = \frac{-2R_{SD}\Delta x \Delta t}{R_{SD}\Delta x \Delta y B_0 + \Delta t \Delta z},$$

$$C_{ezvcvs}(i+1,j,k) = \frac{-2\Delta t\alpha}{R_{SD}\Delta x \Delta y B_0 + \Delta t \Delta z},$$

where A_0 and B_0 are given by (7). Using (11), the updating equation of the electric field associated with a VCVS can be easily implemented in the FDTD method. For hard voltage sources one can simply set R_{SD} to zero.

D. CCVS updating equation

Similar to the VCVS, the electric field

component E_z^{n+1} at node $(i+1, j, k)$ shown in Fig. 1 (d), can be updated as follows:

$$J_{iz}^{n+\frac{1}{2}}(i+1,j,k) =$$

$$\frac{\Delta z}{2\Delta x \Delta y R_{SD}} \times [E_z^{n+1}(i+1,j,k) + E_z^n(i+1,j,k)] \quad (12)$$

$$+\frac{1}{\Delta x \Delta y R_{SD}} \times \alpha I_0^{n+\frac{1}{2}},$$

where α is the control factor and I_0 is equal to $I_{ZSampled}$ which can be calculated using (4).

$$E_z^{n+1}(i+1,j,k) = C_{eze}(i+1,j,k)E_z^n(i+1,j,k)$$

$$+C_{ezhy}(i+1,j,k)\left[H_y^{n+\frac{1}{2}}(i+1,j,k) - H_y^{n+\frac{1}{2}}(i,j,k)\right]$$

$$+C_{ezhx}(i+1,j,k)\left[H_x^{n+\frac{1}{2}}(i+1,j,k) - H_x^{n+\frac{1}{2}}(i+1,j-1,k)\right] \quad (13)$$

$$+C_{ezccvs}(i+1,j,k)I_{sampled}^{n+\frac{1}{2}},$$

with

$$C_{eze}(i+1,j,k) = \frac{R_{SD}\Delta x \Delta y A_0 - \Delta t \Delta z}{R_{SD}\Delta x \Delta y B_0 + \Delta t \Delta z},$$

$$C_{ezhy}(i+1,j,k) = \frac{2R_{SD}\Delta y \Delta t}{R_{SD}\Delta x \Delta y B_0 + \Delta t \Delta z},$$

$$C_{ezhx}(i+1,j,k) = \frac{-2R_{SD}\Delta x \Delta t}{R_{SD}\Delta x \Delta y B_0 + \Delta t \Delta z},$$

$$C_{ezccvs}(i+1,j,k) = \frac{-2\Delta t \alpha}{R_{SD}\Delta x \Delta y B_0 + \Delta t \Delta z},$$

while A_0 and B_0 are given by (7). Using (13), the updating equation of the electric field associated with a CCVS can be easily implemented in the FDTD method. For hard voltage sources one can simply set R_{SD} to zero.

E. Updating procedure

Similarly, the procedures can be used for electric field components in x- or y-directions if the dependent sources are along the x- or y-directions. It is necessary to point out that the current implementation allows for easy update for dependent source, close examination of equations (6) and (11) reveals that there is a future field component in the last term of the R.H.S. This term is not considered at the same step as the traditional FDTD updating sequence. The FDTD approaches for these two equations could be summarized as follows:

1. Update all magnetic field components at time instant $(n+\frac{1}{2})$ Δt using traditional updating equations [1].
2. Update all electric field components at time instant $(n+1)$ Δt, taking into account the independent sources and lumped elements using traditional updating equations [1], and dependent source using equations (6), (9), (11) and (13). However, for equations (6) and (11), the last term should not be considered at this step.
3. Compute the $V_{ZSampled}$ using (2) then complete the update of (6) and (11) to include the last term in these two equations.
4. Apply the boundary conditions.
5. Increment the time step, n to n+1. Repeat steps 1 to 4.

Step 2 and 3 in the updating sequence above are the key for a successful implementation of this simple and direct implementation of dependent sources in FDTD.

III. NUMERICAL RESULTS

In this section, numerical results generated using the new approach are presented. The FDTD code was developed in MATLAB [18] and run on a computer with an Intel Core i7 CPU Q720, 1.6 GHz with 6 GB RAM. These results demonstrate the validity of the new approach for analyzing circuits with different dependent sources in FDTD. The first set of examples is a simple resistive circuit containing VCCS, CCCS, VCVS or CCVS. The second example is a BJT circuit analyzed using the equivalent circuit model of the BJT. The results are compared with those obtained from analytical solutions.

A. Test case 1 (simple resistive circuits with different dependent sources)

For the circuits shown in Figs. 1 (a), (b), (c) and (d). The FDTD grid cell size is $\Delta x = \Delta y = \Delta z = 0.25$ mm, $\Delta t = 0.43$ psec with 3000 time steps, the circuit is simulated with $3 \times 1 \times 2$ cells in x, y and z-directions, respectively, as shown in Fig. 1 (e). Only 8 convolutional perfect matched layers (CPML) are used as the absorbing boundary of the computational domain as implemented in [1], with 5 cells air buffer in every direction. The voltage

source $V(t)$ is implemented using sinusoidal waveform with amplitude of 10 volts and frequency of 5 GHz, the α factor is equal to 0.01 for the circuit in Fig. 1 (a). As for the circuit shown in Fig. 1 (b), $V(t)$ is implemented using a unit step function with amplitude of 5 volts and α factor of 0.1. For the circuit shown in Fig. 1 (c), $V(t)$ is implemented using Gaussian pulse with amplitude of 10 volts and α factor of 0.2. For the circuit shown in Fig. 1 (d), $V(t)$ is implemented using a cosine modulate Gaussian pulse centered at 16 GHz with bandwidth of 8 GHz (in this paper the bandwidth of the modulated Gaussian pulse is defined as the frequency band where the magnitude in the frequency domain reaches 10% of its maximum), amplitude of 20 volts and α of 0.3. The main goal is to implement the circuits with their VCCS, CCCS, VCVS and CCVS using the new approach and calculate the value of the output voltage $V_0(t)$. The results are compared with analytical results in Figs. 2 (a), (b), (c) and (d). The analytical solution is based on mesh analysis method and it was found that for the values of α factors mentioned above: $V_0(t)$ for Fig. 1 (a) is equal to $V(t)/6$, $V_0(t)$ for Fig. 1 (b) it is equal to $0.2083 \times V(t)$, $V_0(t)$ for Fig. 1 (c) is equal to $0.0943 \times V(t)$ and $V_0(t)$ for Fig. 1 (d) is equal to $0.0908 \times V(t)$. Figure 2 demonstrates good agreement between analytical solutions and the results based on the new approach. The computational time is 0.75 minute and the memory usage is 320 KB.


(a)

(b)

(c)

(d)
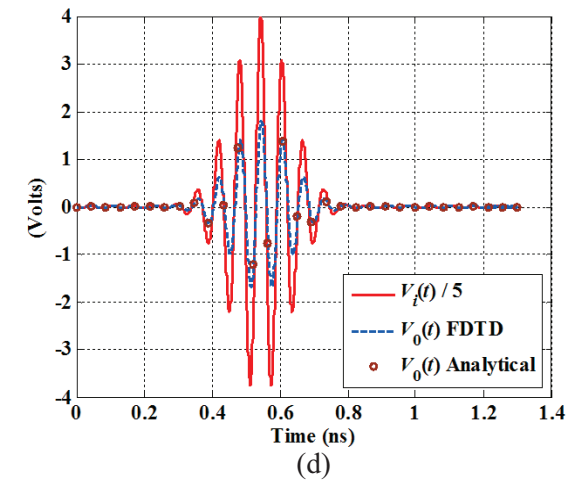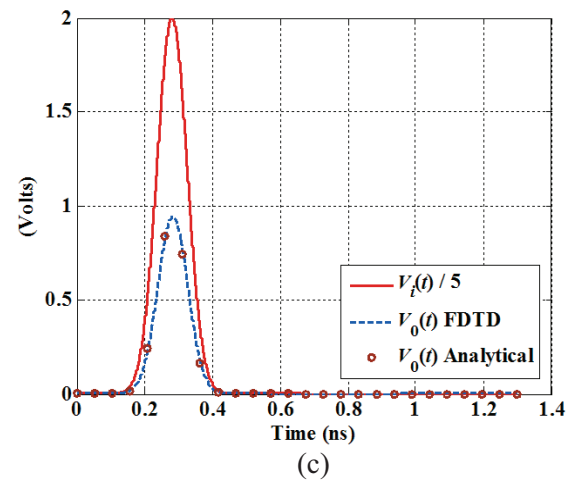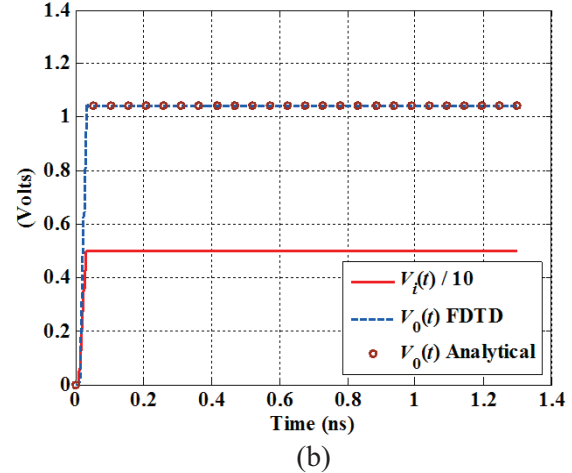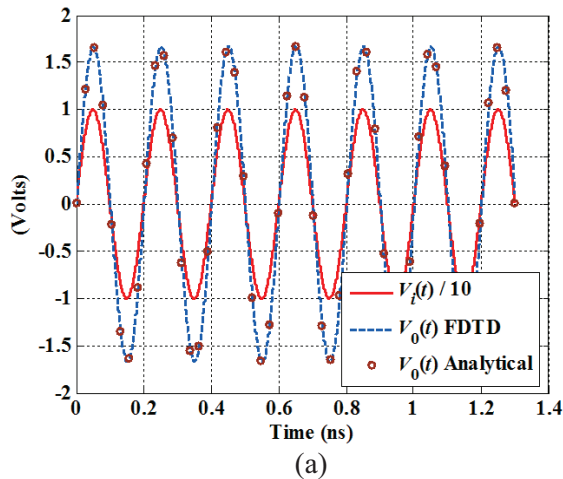
Fig. 2. Time-domain response for test case 1: (a) VCCS, (b) CCCS, (c) VCVS, and (d) CCVS.

B. Test case 2 (BJT circuit)

In this example, the BJT circuit shown in Fig. 3 (a) is analyzed. It consists of a PNP BJT, two resistor R_C (collector resistor) and R_E (emitter resistor), two infinite capacitors to separate the direct current (DC) biasing from the alternating current (AC), and an input AC voltage source $v_i(t)$. The BJT is implemented in the FDTD using the equivalent circuit model shown in Fig. 3 (b). The values of the equivalent circuit parameters after DC analysis of the circuit according to [19] were found to be $r_e = 27\ \Omega$ and $\alpha = 0.99$. The $v_i(t)$ is simulated by sinusoidal waveform with frequency of 100 MHz and amplitude of 0.1 V, the FDTD grid cell size is $\Delta x = \Delta y = \Delta z = 0.25$ mm, $\Delta t = 0.43$ psec with 50,000 time steps, $3 \times 1 \times 3$ cells in x, y and z-directions, respectively, 8 CPML layers are used with 5 cells air buffer in every direction. The main goal here is to implement the circuit using the CCCS model shown in Fig. 3 (b) with the new approach and calculate the value of the voltage $v_0(t)$. The results are compared with results generated using analytical solution in Fig. 4 (a). The analytical solution is based on mesh analysis method and it was found that for the values mentioned above, $v_0(t)$ is equal to $64.1732 \times v_i(t)$ (BJT circuit with a gain of 64.1732). Figure 4 (a) demonstrates good agreement between analytical solutions and the results of the new approach, which proves the validity of the approach. The error between FDTD and analytical solution is calculated

as follows: $\left| \dfrac{V_{FDTD} - V_{Analytical}}{\max\left(V_{Analytical}\right)} \right| \times 100\%$ and plotted in

Fig. 4 (b) (the max error is ~3.5%). Furthermore, the same BJT is used to terminate a strip transmission line (TL) as in [15]. Figure 3 (c) shows the BJT circuit with the strip transmission line and ground plane. In this case, $v_i(t)$ is implemented using cosine modulate Gaussian pulse centered at 150 MHz with bandwidth of 250 MHz, and amplitude of 1 V and all other FDTD parameters are kept the same, the transmission line is implemented using $260 \times 1 \times 1$ FDTD cells in x, y and z-directions, respectively (6.5 cm long).

From the analytical solution of the BJT circuit, it was found that the voltage gain A_v is 64.1732 as shown above. The time domain results are shown in Fig. 4 (c), the results are compared with the no TL case to show the time delay introduced by the presence of the transmission line. The

computational time using the proposed algorithm is 7.9 minutes, while for the algorithm in [6], it is 8.2 minutes for 50,000 time steps, both were implemented with MATLAB and run using the same computer. In addition to the lower computational time, the proposed algorithm is easier to implement and it could be used for any type of dependent sources application.

(a)   (b)

(c)
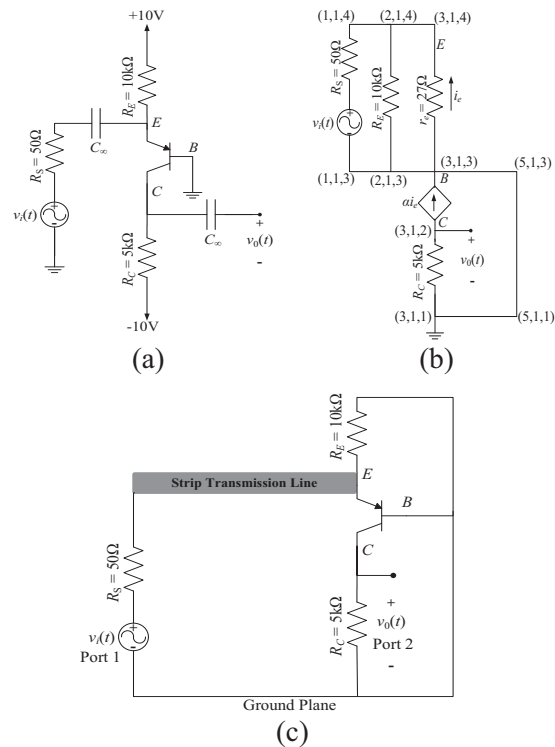
Fig. 3. Test case 2: (a) circuit diagram, (b) the AC analysis equivalent circuit model for BJT using the CCCS T-model with FDTD cell numbers, and (c) AC circuit with integrated transmission line.


(a)

(b)

(c)
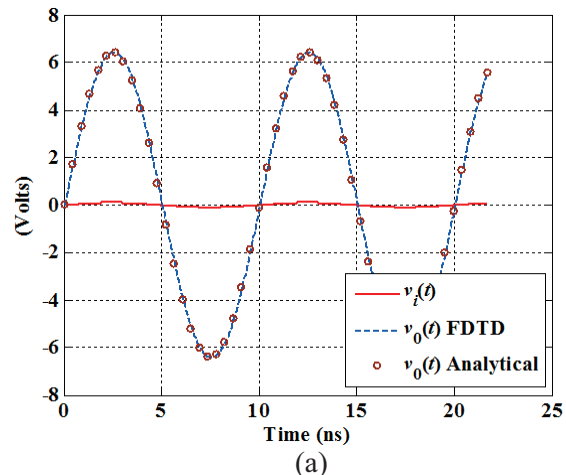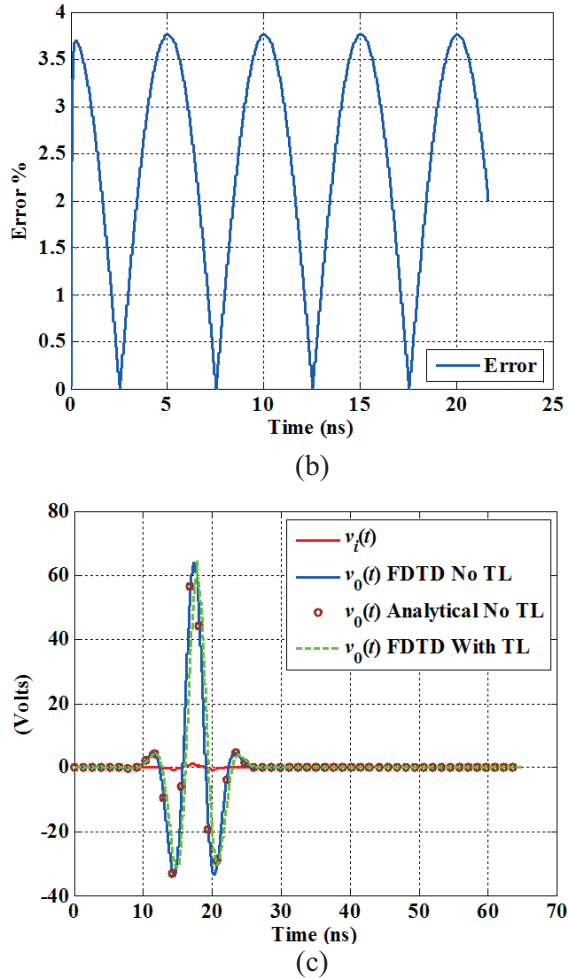
Fig. 4. Time-domain response for test case 2 $v_0(t)$: (a) without TL, (b) shows the relative error for the case without TL, and (c) time-domain response with TL.

IV. CONCLUSION

This paper introduces a new FDTD approach to analyze different types of dependent sources. The approach is simple to implement and efficient in terms of both computational time and memory usage. The approach can be used as a tool to analyze microwave circuits that include dependent sources. In addition, it can be used to implement different non-linear devices using their equivalent circuit models that contain depended sources. The numerical results based on the new approach show very good agreement with results from the analytical solutions, which proves the validity of this approach.

REFERENCES

[1] A. Z. Elsherbeni and V. Demir, "The finite difference time-domain method for electromagnetics: with MATLAB simulations," *SciTech Publishing*, Raleigh, NC, January 2009.

[2] K. ElMahgoub, F. Yang, and A. Z. Elsherbeni, "Scattering analysis of periodic structures using finite-difference time-domain method," *Morgan & Claypool Publishing*, May 2012.

[3] K. ElMahgoub and A. Z. Elsherbeni, "Implementing voltage controlled current source in electromagnetic full-wave simulation using the FDTD method," *International Microwave Symposium Digest (MTT), 2012 IEEE MTT-S*, June 2012.

[4] K. ElMahgoub and A. Z. Elsherbeni, "Implementing current controlled current source in electromagnetic full-wave simulation using the FDTD method," *IEEE International Conference Wireless Information Technology and Systems (ICWITS)*, November 2012.

[5] K. ElMahgoub and A. Z. Elsherbeni, "FDTD implementation of current controlled voltage source," *Middle East Conference on Antennas and Propagation (MECAP)*, December 2012.

[6] M. Piket-May, A. Taflove, and J. Baron, "FD-TD modeling of digital signal propagation in 3-D circuits with passive and active loads," *IEEE Transactions Microwave Theory and Techniques*, vol. 42, no. 8, pp. 1514-1532, August 1994.

[7] F. Kung and H. T. Chuah, "Modeling of bipolar junction transistor in FDTD simulation of printed circuit board," *Progress In Electromagnetics Research, PIER 36*, 179-192, 2002.

[8] F. Kung and H. T. Chuah, "A study on the stability of bipolar-junction-transistor formulation in finite-difference time-domain framework," *IEEE Transactions on Microwave Theory and Techniques*, vol. 53, no. 4, pp. 1189-1196, April 2005.

[9] V. S. Reddy and R. Garg, "An improved extended FDTD formulation for active microwave circuits," *IEEE Transactions on Microwave Theory and Techniques*, vol. 47, no. 9, pp. 1603-1608, September 1999.

[10] O. González, J. A. Pereda, A. Herrera, and A. Vegas, "An extension of the lumped-network FDTD method to linear two-port lumped circuits," *IEEE Transactions on Microwave Theory and Techniques*, vol. 54, no. 7, pp. 3045-3051, July 2006.

[11] C. N. Kuo, V. A. Thomas, S. T. Chew, B. Houshmand, and T. Itoh, "Small signal analysis of active circuits using FDTD algorithm," *IEEE Microwave and Guided Wave Letters*, vol. 5, no. 7,

pp. 216-218, 1995.

[12] C. N. Kuo, R. B. Wu, B. Houshmand, and T. Itoh, "Modeling of microwave active devices using the FDTD analysis based on the voltage-source approach," *IEEE Microwave and Guided Wave Letters*, vol. 6, no. 5, pp. 199-201, May 1996.

[13] C. N. Kuo, B. Houshmand, and T. Itoh, "Full-wave analysis of packaged microwave circuits with active and nonlinear devices: an FDTD approach," *IEEE Transactions on Microwave Theory and Techniques*, vol. 45, no. 5, pp. 819-826, May 1997.

[14] O. El Mrabet and M. Essaaidi, "An efficient algorithm for the global modeling of RF and microwave circuits using a reduced nonlinear lumped network (RNL^{2}N)-FDTD approach," *IEEE Microwave and Wireless Components Letters*, vol. 14, no. 2, pp. 86-88, February 2004.

[15] O. El Mrabet, M. Essaaidi, and M. Drissi, "Global modeling of microwave three terminal active devices using the FDTD method," *IEICE Electronics Express*, vol. 2, no. 2, pp. 43-48, January 2005.

[16] J. Mix, J. Dixon, Z. Popovic, and M. Piket-May, "Incorporating non-linear lumped elements in FDTD: the equivalent source method," *International Journal of Numerical Modeling: Electronic Networks, Devices and Fields*, vol. 12, pp. 157-170, May 1999.

[17] W. Sui, D. A. Christensen, and C. H. Durney, "Extending the two-dimensional FDTD method to hybrid electromagnetic systems with active and passive lumped elements," *IEEE Transactions on Microwave Theory and Techniques*, vol. 40, pp. 724-730, April 1992.

[18] "MATLAB distributed by Mathworks," *www.mathworks.com*.

[19] A. S. Sedra and K. C. Smith, "Microelectronic circuits," fourth edition, *Oxford University Press*, 1997.

Khaled ElMahgoub received his B.Sc. and M.Sc. degrees in Electronics and Electrical Communications Engineering from Cairo University, Egypt, in 2001 and 2006, respectively. He received his Ph.D. degree in Electrical Engineering from the University of Mississippi, USA in 2010. From 2001-2006, he was a Teaching and Research Assistant at Cairo University. From 2007-2010, he was a Teaching and Research Assistant at the University of Mississippi. ElMahgoub is a Research Affiliate with the Auto-ID Labs at MIT. Currently, he is working as Senior Engineer at Trimble Navigation, Cambridge, MA, USA. Possessing over eight years of experience in the industry, he is a Senior Member of the team working in testing and developing RFID technology. Throughout his academic years, he coauthored over 35 technical journals and conference papers. He is a Senior Member of IEEE, Member of ACES and Phi Kappa Phi Honor Society. ElMahgoub is listed in Who's Who in Science and Engineering. He is the recipient of ACES Early Career Award, University of Mississippi scholarship for Ph.D. degree and University of Mississippi graduate school summer assistantship. His current research interests include RFID systems, channel coding, FDTD, antenna design, and numerical techniques for electromagnetics.

Atef Z. Elsherbeni received his Ph.D. degree in Electrical Engineering from Manitoba University, Winnipeg, Manitoba, Canada, in 1987. He joined the University of Mississippi in August 1987 as an Assistant Professor of Electrical Engineering. He advanced to the Associate Professor rank on July 1991, and to the Professor rank in July 1997. At the University of Mississippi, he was also the Director of the School of Engineering CAD Lab from August 2002 to August 2013, the Director of the Center for Applied Electromagnetic Systems Research (CAESR) from July 2011 to August 2013, and the Associate Dean of Engineering for Research and Graduate Programs from 2009 to 2013. He was appointed as Adjunct Professor, with the Department of Electrical Engineering and Computer Science of the L.C. Smith College of Engineering and Computer Science at Syracuse University in January 2004. He spent a sabbatical term in 1996 with the Electrical Engineering Department, University of California at Los Angeles (UCLA), and was a Visiting Professor at Magdeburg University, in Germany during the summer of 2005 and at Tampere University of Technology in Finland during the summer of 2007. He was a Finland Distinguished Professor from 2009 to 2011. Elsherbeni became the Dobelman Distinguished Chair and Professor of Electrical Engineering at the Colorado School of Mines in August 2013. He is a Fellow Member of the Institute of Electrical and Electronics Engineers (IEEE) and a Fellow Member of the Applied Computational Electromagnetic Society (ACES) and the Editor-in-Chief for ACES Journal.

SLF/ELF Electromagnetic Field of a Horizontal Dipole in the Presence of an Anisotropic Earth-Ionosphere Cavity

G. Z. Li, T. T. Gu, and K. Li

Department of Information Science and Electronic Engineering
Zhejiang University, Hangzhou, Zhejiang 310027, China
21231013@zju.edu.cn, 11331025@zju.edu.cn, daiwei@zju.edu.cn, kaili@zju.edu.cn

Abstract ─ In this paper, the region of interest is a cavity between a spherical and electrically homogeneous earth and an anisotropic homogeneous ionosphere. Both the dipole (Vertical Electric Dipole (VED), Vertical Magnetic Dipole (VMD), or Horizontal Electric Dipole (HED)) and the observation point are assumed to be located on or near the spherical surface of the earth. The approximate formulas are obtained for the electromagnetic field of a vertical magnetic dipole and that of a vertical electric dipole in the presence of an anisotropic earth-ionosphere cavity, respectively. Based on the results obtained, the approximate formulas are derived readily for the electromagnetic field of a horizontal electric dipole in the presence of an anisotropic earth-ionosphere cavity by using a reciprocity theorem. Analysis and computations in SLF/ELF ranges are carried out specifically.

Index Terms ─ Anisotropic earth-ionosphere cavity, reciprocity theorem, SLF/ELF electromagnetic field.

I. INTRODUCTION

The subject on the VLF/ULF/SLF/ELF electromagnetic waves (VLF: 3 kHz - 30 kHz; ULF: 300 Hz - 3 kHz; SLF: 300 Hz - 30 Hz; ELF: 30 Hz - 3 Hz) in the earth-ionosphere waveguide or cavity were intensively investigated for over 60 years because of its myriad applications in submarine communication and navigation, geophysical prospecting and diagnostics, and earthquake electromagnetic detection [1-7].

Since the 1950s, driven by the defense requirement, the VLF radio wave propagation theory was investigated by many researchers, especially including several pioneers, such as Budden [3], Wait [4,8-10], and Galejs [14-17]. In early works by Wait and Galejs, detailed analysis was carried out on the VLF radio wave propagation in an earth-ionosphere waveguide. Naturally, the VLF radio wave propagation theory can be extended in the study on SLF/ELF radio wave propagation. Since the 1960s, the SLF/ELF wave propagation were studied widely [11-26]. In particular, it was noted that the outstanding contributions on the SLF/ELF wave propagation and application were made by Galejs, and the detailed findings were well summarized in the classic book [5]. With the extension of the pioneering works by Budden, Wait, and Galejs, some important developments on the SLF/ELF wave propagation were accomplished [18-26]. It was also pointed that some excellent works on the SLF/ELF wave propagation were also carried out in China, and those works were summarized in recent book [28].

In SLF/ELF ranges, when considering the effect by geomagnetic field, it is necessary that the ionosphere should be idealized as anisotropic plasma. Unfortunately, the complete analytical solution on SLF/ELF electromagnetic field of a horizontal electric dipole source in the presence of an anisotropic earth-ionosphere waveguide or cavity are still in dark by now. In what follows, we will attempt to outline the complete approximate solution for the SLF/ELF electromagnetic field of a horizontal electric dipole in the presence of an anisotropic earth-ionosphere cavity. The region of interest is a cavity between a spherical and electrically homogeneous earth and an anisotropic homogeneous ionosphere, and both the dipole source and the observation point are assumed on

or near the earth's surface. First, the approximate formulas are obtained for the electromagnetic field of a vertical magnetic dipole in an anisotropic earth-ionosphere cavity. Based on the obtained results of vertical magnetic dipole and the available results of vertical electric dipole, the approximate formulas are derived readily for the electromagnetic field of a horizontal electric dipole in the presence of an anisotropic earth-ionosphere cavity by using a reciprocity theorem. Finally, computations and analysis in SLF/ELF ranges are carried out specifically.

II. EM FIELD IN AN ANISOTROPIC EARTH-IONOSPHERE CAVITY

The geometry under consideration is shown in Fig. 1. The cavity is occupied by the air characterized by the permeability μ_0, uniform permittivity ε_0, and conductivity $\sigma_0 = 0$. The spherical earth is characterized by μ_0, uniform permittivity ε_g, and conductivity σ_g. Assuming that the earth's magnetic field $\boldsymbol{B}_0$, which has the angle θ_0 with $z-$direction, is in the $x-z$ plane, the ionosphere can be characterized by a tensor permittivity $\overset{=}{\varepsilon}$ [3]. It is:

$$\overset{=}{\varepsilon} = \varepsilon_0 \left([\mathbf{I}] + [\mathbf{M}] \right), \tag{1}$$

where ε_0 is the free-space permittivity, $[\mathbf{I}]$ is 3×3 unit matrix, the susceptibility $[\mathbf{M}]$ is expressed in the following form:

$$[\mathbf{M}] = -\frac{X}{U(U^2 - l_x^2 y^2)}$$

$$\times \begin{bmatrix} U^2 - l_x^2 y^2 & il_z Uy & -l_x l_z y^2 \\ -il_z Uy & U^2 & il_x Uy \\ -l_x l_z y^2 & -il_x Uy & U^2 - l_z^2 y^2 \end{bmatrix}, \tag{2}$$

where $U = 1 + i(\varsigma/\omega)$ and ς is the effective electron collision frequency of the ionosphere, $y = (\omega_H)/(\omega)$, $X = (\omega_0^2)/(\omega^2)$, ω_H and ω_0 are the gyrofrequency of the electrons and the angular plasma frequency of the ionosphere, respectively; $l_x = \sin \theta_0$ and $l_z = \cos \theta_0$ are the directional cosines of the Earth's magnetic field in the x and z directions, respectively.
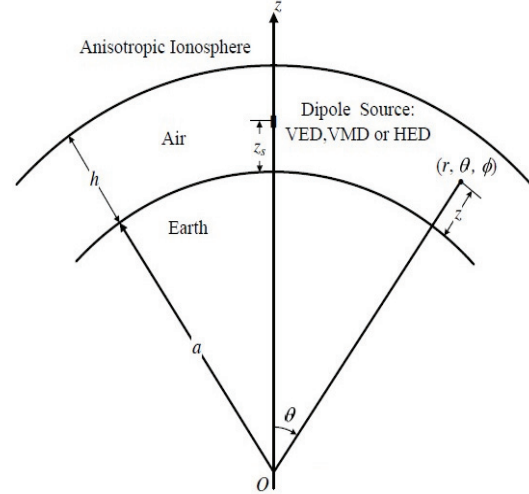

Fig. 1. Geometry of a dipole source in the presence of an anisotropic earth-ionosphere cavity.

In general, a SLF/ELF radiation source is usually employed a horizontal linear antenna. So that it is necessary to investigate SLF/ELF electromagnetic field of a horizontal electric dipole in the presence of an anisotropic earth-ionosphere cavity. In available reference [27], the electromagnetic field of a vertical electric dipole in the presence of an anisotropic earth-ionosphere cavity is addressed specifically. If the corresponding electromagnetic field of a vertical magnetic dipole, the analytical solution on the electromagnetic field of a horizontal electric dipole in the presence of an anisotropic earth-ionosphere cavity can be obtained readily. Next, we will attempt to derive the approximated formulas for the electromagnetic field of a vertical magnetic dipole in the presence of an anisotropic earth-ionosphere cavity.

A. Field of vertical magnetic dipole

Assume that a vertical magnetic dipole is represented by its moment $\hat{z}Ida\delta(x)\delta(y)\delta(z-b)$, where da is the area of the loop, $b = a + z_s$, and $z_s > 0$ denotes the height of the magnetic dipole above the earth's surface. Considering anisotropic properties of the ionosphere, the field components radiated by a vertical electric dipole in the presence of an anisotropic earth-ionosphere cavity can be expressed in the terms of the potential

functions U and V, which is addressed in the book by Pan [27]. In this paper, we assume that the characteristics of SLF/ELF wave propagation are determined by the propagation path from the dipole source to the field point, namely, the propagation characteristics are not affected by other propagation paths. Then, we have $\partial/\partial\phi = 0$. Additionally, the surface impedances of the earth and the ionosphere are changed very slowly to the propagation distances. For mathematical convenience, the surface impedances of the earth and the ionosphere are regarded as constants. Thus, we write:

$$E_r = \left(\frac{\partial^2}{\partial r^2} + k^2\right)(Ur), \tag{3a}$$

$$E_\theta = \frac{1}{r}\frac{\partial^2}{\partial\theta\partial r}(Ur), \tag{3b}$$

$$E_\phi = -\frac{i\omega\mu}{r}\frac{\partial}{\partial\theta}(Vr), \tag{3c}$$

$$H_r = \left(\frac{\partial^2}{\partial r^2} + k^2\right)(Vr), \tag{3d}$$

$$H_\theta = \frac{1}{r}\frac{\partial^2}{\partial\theta\partial r}(Vr), \tag{3e}$$

$$H_\phi = \frac{i\omega\varepsilon}{r}\frac{\partial}{\partial\theta}(Ur). \tag{3f}$$

It is noted that the potential functions U and V satisfy the following wave equation:

$$\left(\nabla^2 + k^2\right)\begin{bmatrix} U \\ V \end{bmatrix} = 0. \tag{4}$$

With similar procedure for the electromagnetic field of a vertical electric dipole as addressed in the book by Pan [27], by using the boundary conditions at $r = a$ and $r = a + h$, the potential functions U and V are expressed in the following forms:

$$Ur = \sum_n \Lambda_n F_n^{(M)}(z) P_v(\cos(\pi - \theta)), \tag{5a}$$

$$\bar{V}r = \sum_n \Lambda_n G_n^{(M)}(z) P_v(\cos(\pi - \theta)), \tag{5b}$$

where $\bar{V} = V\eta$, η is wave impedance in free space, Λ_n is the excitation factor, and $P_v(\cos(\pi - \theta))$ is the potential function U is used to express the electromagnetic field components when the dipole source is a vertical electric dipole (TM mode), and

the potential function V is used when the dipole source is a vertical magnetic dipole (TE mode).

For the electromagnetic field radiated by a vertical magnetic dipole, the "height-gain" function $G_n^{(M)}(z)$ of the potential function $\bar{V}$ should be normalized, namely, $G_n^{(M)}(z = 0) = 1$. Then, we have:

$$G_n^{(M)}(z) = \frac{1}{1 + R_{hn}}\left\{\exp\left[-ik\int_0^z (C_n^2 + \frac{2z}{a}S_n^2)^{1/2}\,dz\right] + R_{hn}\exp\left[ik\int_0^z (C_n^2 + \frac{2z}{a}S_n^2)^{1/2}\,dz\right]\right\}. \tag{6}$$

The normalized "height-gain" functions $F_n^{(M)}(z)$ of the potential function U is expressed in the form of:

$$F_n^{(M)}(z) = \frac{1/M_n}{1 + R_{hn}}\left\{\exp\left[-ik\int_0^z (C_n^2 + \frac{2z}{a}S_n^2)^{\frac{1}{2}}\,dz\right] + R_{gn}\exp\left[ik\int_0^z (C_n^2 + \frac{2z}{a}S_n^2)^{\frac{1}{2}}\,dz\right]\right\}. \tag{7}$$

In the above two formulas, C_n are the roots of the following mode equation:

$$\left[\left(1 + R_h e^{2ikH}\right) - C'\Delta_{22}\left(1 - R_h e^{2ikH}\right)\right]$$
$$\left[C'\left(1 - R_g e^{2ikH}\right) + \Delta_{11}\left(1 + R_g e^{2ikH}\right)\right]$$
$$+ C'\Delta_{21}\Delta_{12}\left(1 + R_g e^{2ikH}\right)\left(1 - R_h e^{2ikH}\right) = 0, \tag{8}$$

where

$$R_g = \frac{C - \Delta_g}{C + \Delta_g}, \tag{9}$$

$$R_h = \frac{C - 1/\Delta_g}{C + 1/\Delta_g}, \tag{10}$$

$$H = \int_0^h \left(C^2 + \frac{2z}{a}S^2\right)^{\frac{1}{2}}\,dz, \tag{11}$$

$$C' = \left(C^2 + \frac{2h}{a}S^2\right)^{\frac{1}{2}}, \tag{12}$$

and Δ_g is the normalized surface impedance of the earth. At lower frequencies, the normalized surface impedance Δ_g at the earth's surface is approximated as:

$$\Delta_g = \frac{k}{k_g}\sqrt{1 - \left(\frac{k}{k_g}\right)^2}, \tag{13}$$

where Δ_g is the wave number of the earth. The normalized surface impedance matrix of the ionosphere $[\Delta]$ is written in the form:

$$[\Delta] = \begin{bmatrix} \Delta_{11} & \Delta_{12} \\ \Delta_{21} & \Delta_{22} \end{bmatrix}. \tag{14}$$

It is noted that the normalized surface impedance matrix of ionosphere $[\Delta]$ can be determined and computed by using the proposed method in the classic book by Budden [3]. The parameters C and S are defined by:

$$\frac{v(v+1)}{k^2 a^2} = S^2; \quad C^2 = 1 - S^2. \tag{15}$$

And M_n in (7) is the coupling factor to show the coupling relationship between TE wave and TM wave. It is written in the form:

$$M_n = \frac{\Delta_{12} C_n' (1 - R_{hn} e^{2ikH_n})}{C_n' (1 - R_{gn} e^{2ikH_n}) + \Delta_{11} (1 + R_{gn} e^{2ikH_n})}. \tag{16}$$

It is noted that the excitation factor for the electromagnetic field of a vertical magnetic dipole is different to that for the electromagnetic field of vertical electric dipole. It is necessary to examine the "orthogonality" between waves of different orders. The inner product of the two waves with different orders is defined by:

$$A_{mn} = \int_0^h \left[G_n^{(M)}(z) G_m^{(M)}(z) + \rho_1 F_n^{(M)}(z) F_m^{(M)}(z) \right] dz, \tag{17}$$

where $\rho_1 = \Delta_{21}/\Delta_{12}$. Since $G_n^{(M)}$, $G_m^{(M)}$, $F_n^{(M)}$ and $F_m^{(M)}$ satisfy the following differential equation:

$$Z''(r) + k^2 \left[1 - \frac{v(v+1)}{k^2 r^2} \right] Z(r) = 0, \tag{18}$$

we get:

$$\frac{d}{dz} \left(F_n^{(M)} F_m'^{(M)} - F_m^{(M)} F_n'^{(M)} \right)$$
$$= F_n^{(M)} F_m''^{(M)} - F_m^{(M)} F_n''^{(M)}$$
$$= k^2 \left[\frac{\mu(\mu+1)}{k^2 r^2} - \frac{v(v+1)}{k^2 r^2} \right] F_n^{(M)} F_m^{(M)}$$
$$\approx k^2 \left(S_m^2 - S_n^2 \right) F_n^{(M)} F_m^{(M)}, \tag{19}$$

where

$$S_m^2 = \frac{\mu(\mu+1)}{k^2 a^2}; \quad S_n^2 = \frac{v(v+1)}{k^2 a^2}. \tag{20}$$

Considering the boundary conditions, we have:

$$\int_0^h F_n^{(M)} F_m^{(M)} dz = \frac{1}{k^2 (S_m^2 - S_n^2)}$$
$$\left[F_n^{(M)}(z) F_m'^{(M)}(z) - F_m^{(M)}(z) F_n'^{(M)}(z) \right]_0^h$$
$$= -\frac{1}{k^2 (S_m^2 - S_n^2)} \frac{ik\Delta_{12}}{\Delta_{22}}$$
$$\left[F_n^{(M)}(h) G_m^{(M)}(h) - F_m^{(M)}(h) G_n^{(M)}(h) \right]. \tag{21}$$

Similarly, we write:

$$\int_0^h G_n^{(M)} G_m^{(M)} dz = -\frac{1}{k^2 (S_m^2 - S_n^2)} \frac{ik\Delta_{21}}{\Delta_{22}}$$
$$\left[G_n^{(M)}(h) F_m^{(M)}(h) - G_m^{(M)}(h) F_n^{(M)}(h) \right]. \tag{22}$$

It is seen that, when $\Delta_{12} = \Delta_{21} = 0$, both TE and TM waves are not coupled each other. When $n \ne m$, we have:

$$A_{mn} = \int_0^h \left(G_n^{(M)} G_m^{(M)} + \rho_1 F_n^{(M)} F_m^{(M)} \right) = 0. \tag{23}$$

Then, the factor A_{nn} is expressed in the following form:

$$A_{nn} = \int_0^h \left(G_n^{(M)} G_n^{(M)} + \rho_1 F_n^{(M)} F_n^{(M)} \right) dz$$
$$= \frac{1}{2k^2 S_n} \left\{ \left[G_n^{(M)}(h) \frac{dG_n'(h)}{dS_n} - G_n'(h) \frac{dG_n^{(M)}(h)}{dS_n} \right] \right.$$
$$\left. + \rho_1 \left[F_n^{(M)}(h) \frac{dF_n'(h)}{dS_n} - F_n'(h) \frac{dF_n^{(M)}(h)}{dS_n} \right] \right\}. \tag{24}$$

With substitutions (6) and (7) into (23), we have:

$$A_{nn} = \frac{1}{2k^2 S_n (1 + R_h)^2}$$
$$\left\{ -4k^2 C_n' \left(\frac{\rho_1}{M_n^2} R_g + R_h \right) \frac{\partial H}{\partial S_n} \right.$$
$$+ \left[\left(\frac{\rho_1}{M_n^2} R_g^2 + R_h^2 \right) \exp(2ikH) \right.$$
$$\left. - \left(\frac{\rho_1}{M_n^2} + 1 \right) \exp(-2ikH) \right] ik \frac{\partial C_n'}{\partial S_n}$$
$$\left. + 2ikC_n' \left(\frac{\rho_1}{M_n^2} \frac{\partial R_g}{\partial S_n} + \frac{\partial R_h}{\partial S_n} \right) \right\}. \tag{25}$$

Then, the field component E_ϕ can be expressed in the form:

$$E_\phi = -\frac{i\omega\mu}{r\eta} \sum \Lambda_n G_n^{(M)}(z) \frac{\partial}{\partial\theta} P_v(\cos(\pi - \theta)). \tag{26}$$

In the next step, the main task is to determine the excitation factor Λ_n. It is noted that the excitation source (vertical magnetic dipole) can be regarded as a small loop antenna which is placed at the height of z_s. When the observation point is infinitely close to the excitation source, the effects by the earth and the ionosphere can be neglected. Thus, we write:

$$\lim_{\theta \to 0} 2\pi r_s E_\varphi (r,\theta) = iu_0 \omega H(r,0) da$$

$$\to \frac{i\mu_0 \omega Ida}{\theta} \delta(r - r_s). \quad (27)$$

Multiplying the function $G_n^{(M)}(z)$ on both sides of (27) and integrating from 0 to h for z, with (26), it follows that:

$$\lim_{\theta \to 0} \frac{i\omega\mu_0 Ida}{2\pi r_s \theta} G_n^{(M)}(z_s)$$

$$= \lim_{\theta \to 0} -\frac{i\omega\mu_0}{r_s \eta} \Lambda_n A_{nn} \frac{\partial}{\partial \theta} P_v(\cos(\pi - \theta)). \quad (28)$$

Considering,

$$\lim_{\theta \to 0} \frac{\partial P_v(\cos(\pi - \theta))}{\partial \theta} = \frac{2\sin v\pi}{\pi\theta}, \quad (29)$$

we have:

$$\Lambda_n = -\frac{\eta Ida G_n^{(M)}(z_s)}{4 A_{nn} \sin v\pi}. \quad (30)$$

In SLF/ELF ranges, the normalized surface impedance Δ_g is small, so that the excitation factor of a vertical magnetic dipole Λ_n is very small. In other words, for the electromagnetic field in SLF/ELF ranges radiated by a vertical magnetic dipole in the presence of an earth-ionosphere cavity, the excitation efficiency is very low.

From (3a)-(3f), (5a)-(5b), and (30), the six field components E_r, E_θ, E_ϕ, H_r, H_θ and H_ϕ of the electromagnetic field radiated by a vertical magnetic dipole at $(a + z_s, 0, 0)$ in the presence of an anisotropic earth-ionosphere cavity, are expressed in the following forms:

$$E_r(r,\theta,\varphi) = \frac{\eta Ida}{4r^2} \sum_n \frac{G_n^{(M)}(z_s) F_n^{(M)}}{A_{nn}}$$

$$\frac{\partial^2 P_v(\cos(\pi - \theta))}{\sin v\pi \partial^2 \theta}, \quad (31)$$

$$E_\theta(r,\theta,\varphi) = \frac{-\eta Ida}{4r} \sum_n \frac{G_n(vz_s)}{A_{nn}} \frac{\partial F_n^{(M)}(z)}{\partial z}$$

$$\frac{\partial P_v(\cos(\pi - \theta))}{\sin v\pi \partial \theta}, \quad (32)$$

$$E_\varphi(r,\theta,\varphi) = \frac{i\omega\mu Ida}{4r} \sum_n \frac{G_n^{(M)}(z_s) G_n^{(M)}(z)}{A_{nn}}$$

$$\frac{\partial P_v(\cos(\pi - \theta))}{\sin v\pi \partial \theta}, \quad (33)$$

$$H_r(r,\theta,\varphi) = \frac{Ida}{4r^2} \sum_n \frac{G_n^{(M)}(z_s) G_n^{(M)}(z)}{A_{nn}}$$

$$\frac{\partial^2 P_v(\cos(\pi - \theta))}{\sin v\pi \partial^2 \theta}, \quad (34)$$

$$H_\theta(r,\theta,\varphi) = \frac{-Ida}{4r} \sum_n \frac{G_n^{(M)}(z_s)}{A_{nn}} \frac{\partial G_n^{(M)}(z)}{\partial z}$$

$$\frac{\partial P_v(\cos(\pi - \theta))}{\sin v\pi \partial \theta}, \quad (35)$$

$$H_\varphi(r,\theta,\varphi) = \frac{-i\omega\varepsilon\eta Ida}{4r} \sum_n \frac{G_n^{(M)}(z_s) F_n^{(M)}(z)}{A_{nn}}$$

$$\frac{\partial P_v(\cos(\pi - \theta))}{\sin v\pi \partial \theta}, \quad (36)$$

where $r = z + a$.

B. Field of vertical electric dipole

If the excitation source is replaced by a vertical electric dipole, which is represented by the current density $\hat{z} Idl \delta(x)\delta(y)\delta(z - b)$, the formulas for the components E_r, E_θ, E_ϕ, H_r, H_θ and H_ϕ of the electromagnetic field radiated by a vertical electric dipole at $(a+z,0,0)$ in the presence of an anisotropic earth-ionosphere cavity, were derived specifically in the monograph by Pan [27]. We write:

$$E_r(r,\theta,\varphi) = \frac{iIda}{4\omega\varepsilon r^2} \sum_m \frac{F_m^{(E)}(z_s) F_m^{(E)}(z)}{A_{mm}}$$

$$\frac{\partial^2 P_\mu(\cos(\pi - \theta))}{\sin \mu\pi \partial^2 \theta}, \quad (37)$$

$$E_\theta(r,\theta,\varphi) = \frac{-iIdl}{4\omega\varepsilon r} \sum_m \frac{F_m^{(E)}(z_s)}{A_{nn}} \frac{\partial F_m^{(E)}(z)}{\partial z}$$

$$\frac{\partial P_\mu(\cos(\pi - \theta))}{\sin \mu\pi \partial \theta}, \quad (38)$$

$$E_\varphi(r,\theta,\varphi) = \frac{-\mu I dl}{4r\eta\varepsilon} \sum_m \frac{F_m^{(E)}(z_s) G_m^{(E)}(z)}{A_{mm}}$$
$$\frac{\partial P_\mu(\cos(\pi-\theta))}{\sin\mu\pi\partial\theta}, \qquad (39)$$

$$H_r(r,\theta,\varphi) = \frac{iIdl}{4\eta\omega\varepsilon r^2} \sum_n \frac{F_m^{(E)}(z_s) G_m^{(E)}(z)}{A_{mm}}$$
$$\frac{\partial^2 P_\mu(\cos(\pi-\theta))}{\sin\mu\pi\partial^2\theta}, \qquad (40)$$

$$H_\theta(r,\theta,\varphi) = \frac{-iIdl}{4\eta\omega\varepsilon r} \sum_m \frac{F_m^{(E)}(z_s)}{A_{mm}} \frac{\partial G_m^{(E)}(z)}{\partial z}$$
$$\frac{\partial P_\mu(\cos(\pi-\theta))}{\sin\mu\pi\partial\theta}, \qquad (41)$$

$$H_\varphi(r,\theta,\varphi) = \frac{Idl}{4r} \sum_n \frac{F_m^{(E)}(z_s) F_m^{(E)}(z)}{A_{mm}}$$
$$\frac{\partial P_\mu(\cos(\pi-\theta))}{\sin\mu\pi\partial\theta}, \qquad (42)$$

where

$$A_{mm} = \frac{1}{2k^2 S_n (1+R_g)^2}$$
$$\left\{ -4ikC_n'\left(R_g + \rho^2 M_m^2 R_h\right)\frac{\partial H}{\partial S_m} \right.$$
$$+\left[\left(1+\rho_2 M_m^2\right)\exp(-2ikH_m)\right.$$
$$\left. -\left(R_g^2 + \rho_2 M_n^2 R_h^2\right)\exp(2ikH)\right]\frac{\partial C_m'}{\partial S_m}$$
$$\left. -2C_n'\left(\frac{\partial R_g}{\partial S_m} + \rho_2 M_n^2 \frac{\partial R_h}{\partial S_m}\right)\right\}, \qquad (43)$$

$$\rho = \Delta_{12}/\Delta_{21}. \qquad (44)$$

It is noted that the "height-gain" function $F_m^{(E)}(z)$ of the potential function U is normalized as $F_m^{(E)}(z=0)=1$. Then, we write:

$$F_m^{(E)}(z) = \frac{1}{1+R_{gm}} \left\{ \exp\left[-ik\int_0^z (C_m^2 + \frac{2z}{a} S_m^2)^{\frac{1}{2}} dz\right] \right.$$
$$\left. +R_{gm} \exp\left[ik\int_0^z (C_m^2 + \frac{2z}{a} S_m^2)^{\frac{1}{2}} dz\right]\right\}. \qquad (45)$$

Correspondingly, the normalized "height-gain" function $G_m^{(E)}(z)$ of the potential function $\overline{V}$ is written as follows:

$$G_m^{(E)}(z) = \frac{M_m}{1+R_{gm}} \left\{ \exp\left[-ik\int_0^z (C_m^2 + \frac{2z}{a} S_m^2)^{\frac{1}{2}} dz\right] \right.$$
$$\left. +R_{hm} \exp\left[ik\int_0^z (C_m^2 + \frac{2z}{a} S_m^2)^{\frac{1}{2}} dz\right]\right\}. \qquad (46)$$

C. Field of a horizontal electric dipole

The electromagnetic field of a horizontal electric dipole can be obtained from the electromagnetic fields of vertical electric and magnetic dipoles by the reciprocity theorem [4-5]. Following similar manner addressed in Sec. 4.2.4 in the monograph by Galejs [5], the vertical field components E_r^{he} and H_r^{he} at $(a+z,0,0)$, where the subscript he designates the horizontal electric dipole, can be derived readily. We write:

$$E_r^{he}(r,\theta,\varphi) = -\frac{iIds^{he}}{4\omega\varepsilon_0 r}\cos\varphi \sum_m \frac{F_m^{(E)}(z)}{A_{mm}}$$
$$\frac{\partial F_m^{(E)}(z_s)}{\partial z} \frac{\partial P_\mu(\cos(\pi-\theta))}{\sin\mu\pi\partial\theta}, \qquad (47)$$

$$H_r^{he}(r,\theta,\varphi) = -\frac{Ids^{he}}{4r}\sin\varphi \sum_n \frac{G_n^{(M)}(z_s) G_n^{(M)}(z)}{A_{nn}}$$
$$\frac{\partial P_\nu(\cos(\pi-\theta))}{\sin\nu\pi\partial\theta}. \qquad (48)$$

From Maxwell's equations, the other field components E_θ^{he}, E_ϕ^{he}, H_θ^{he} and H_ϕ^{he} can be expressed in the terms of E_r^{he} and H_r^{he}, we have

$$\left(k^2 + \frac{\partial^2}{\partial r^2}\right)\left(r\sin\theta H_\theta^{he}\right) = -i\omega\varepsilon_0 \frac{\partial E_r^{he}}{\partial\varphi} + \sin\theta \frac{\partial^2 H_r^{he}}{\partial r\partial\theta}, (49)$$

$$\left(k^2 + \frac{\partial^2}{\partial r^2}\right)\left(r\sin\theta E_\theta^{he}\right) = \frac{\partial^2 E_r^{he}}{\partial r\partial\varphi} - i\omega\mu_0 \sin\theta \frac{\partial H_r^{he}}{\partial r\partial\theta}, (50)$$

$$\left(k^2 + \frac{\partial^2}{\partial r^2}\right)\left(r\sin\theta H_\varphi^{he}\right) = i\omega\varepsilon_0 \sin\theta \frac{\partial E_r^{he}}{\partial\theta} + \frac{\partial^2 H_r^{he}}{\partial r\partial\varphi}, (51)$$

$$\left(k^2 + \frac{\partial^2}{\partial r^2}\right)\left(r\sin\theta E_\theta^{he}\right) = \sin\theta \frac{\partial^2 E_r^{he}}{\partial r\partial\theta} + i\omega\mu_0 \frac{\partial H_r^{he}}{\partial\theta}. (52)$$

It is seen that the height functions of all modes of the electromagnetic field components in the earth-ionosphere cavity should be satisfied to the equation (18).

With substitutions (47) and (48) into (49)-(52), and considering the relation $\nu(\nu+1)/r \approx k^2 a$, the analytical formulas of the remaining four components are obtained readily. We write:

$$H_\theta^{he}(r,\theta,\phi) = \frac{Ids^{he}}{4k^2a^2}\sin\phi\left[\frac{1}{\sin\theta}\sum_m\frac{F_m^{(E)}(z)}{A_{mn}S_m^2}\right.$$

$$\frac{\partial F_m^{(E)}(z_s)}{\partial z}\frac{\partial P_\mu(\cos(\pi-\theta))}{\sin\mu\pi\partial\theta}$$

$$-\sum_n\frac{1}{A_{nn}S_n^2}\frac{\partial G_n^{(M)}(z)}{\partial z}G_n^{(M)}(z_s)$$

$$\left.\frac{\partial^2 P_\nu(\cos(\pi-\theta))}{\sin\nu\pi\partial^2\theta}\right], \qquad (53)$$

$$H_\phi^{he}(r,\theta,\phi) = \frac{Ids^{he}}{4k^2a^2}\cos\phi\left[\sum_m\frac{F_m^{(E)}(z)}{A_{mn}S_m^2}\right.$$

$$\frac{\partial F_m^{(E)}(z_s)}{\partial z}\frac{\partial^2 P_\mu(\cos(\pi-\theta))}{\sin\mu\pi\partial^2\theta}$$

$$-\frac{1}{\sin\theta}\sum_n\frac{1}{A_{nn}S_n^2}\frac{\partial G_n^{(M)}(z)}{\partial z}G_n^{(M)}(z_s)$$

$$\left.\frac{\partial P_\nu(\cos(\pi-\theta))}{\sin\nu\pi\partial\theta}\right], \qquad (54)$$

$$E_\phi^{he}(r,\theta,\phi) = \frac{iIdS}{4k^2a^2}\sin\phi$$

$$\left[\frac{1}{\omega\varepsilon_0\sin\theta}\sum_m\frac{1}{A_{mm}S_m^2}\frac{\partial F_m^{(E)}(z)}{\partial z}\right.$$

$$\omega\mu_0\sum_n\frac{1}{A_{nn}S_n^2}G_n^{(M)}(z)G_n^{(M)}(z_s)$$

$$\left.\frac{\partial^2 P_\nu(\cos\pi-\theta)}{\sin\nu\pi\partial^2\theta}\right], \qquad (55)$$

$$E_\theta^{he}(r,\theta,\phi) = -\frac{iIds^{he}}{4k^2a^2}\cos\phi$$

$$\left[\frac{1}{\omega\varepsilon_0}\sum_m\frac{1}{A_{mn}S_m^2}\frac{\partial F_m^{(E)}(z)}{\partial z}\right.$$

$$\frac{\partial F_m^{(E)}(z_s)}{\partial z}\frac{\partial^2 P_\mu(\cos(\pi-\theta))}{\sin\mu\pi\partial^2\theta}$$

$$+\frac{\omega\mu_0}{\sin\theta}\sum_n\frac{G_n^{(M)}(z)G_n^{(M)}(z_s)}{A_{mn}S_n^2}$$

$$\left.\frac{\partial P_\nu(\cos(\pi-\theta))}{\sin\nu\pi\partial\theta}\right]. \qquad (56)$$

III. FIELD OF A HORIZONTAL ELECTRIC DIPOLE

From above derivations and analysis, it is seen that the approximated formulas are derived for the electromagnetic field of a horizontal electric dipole in the presence of an anisotropic earth-ionosphere cavity. In VLF ranges, the electromagnetic fields of a dipole source (vertical electric dipole, vertical magnetic dipole, and horizontal electric dipole) can be computed readily by using (47), (48), and (53)-(56). Obviously, the computations can also be carried out for the electromagnetic field in SLF/ELF ranges of a dipole source (VED, VMD, or HED) in the presence of anisotropic earth-ionosphere cavity.

In practical applications, the horizontal antenna is usually placed on or near the earth's surface, and considering the height of the antenna is very small comparing to the wavelength of the electromagnetic wave in SLF/ELF ranges, the horizontal dipole source and the observation point can be regarded to be placed on the surface of the earth; namely, $z_s \sim 0$ and $z \sim 0$. Then, we have:

$$F_m^{(E)}(0)=1, \qquad G_m^{(E)}(0)=M_m(1+R_{hm})/(1+R_{gm}),$$

$$G_n^{(M)}(0)=1, \qquad F_n^{(M)}(0)=(1+R_{gn})/M_n(1+R_{hn}),$$

$$\left.\frac{\partial F_m^{(E)}(z)}{k\partial z}\right|_{z=0}=-i\Delta_g, \qquad \left.\frac{\partial G_n^{(M)}(z)}{k\partial z}\right|_{z=0}=\frac{-i}{\Delta_g}.$$

At large distance between the dipole source and the observation point, namely, $k\rho \gg 1$, and the observation is not close to an antipole, the Legendre function of the first kind is approximated by:

$$\frac{P_\nu(\cos(\pi-\theta))}{\sin\nu\pi}$$

$$\approx -\sqrt{\frac{2}{\pi kaS_n\sin\theta}}\exp(ikaS_n\theta+\frac{i\pi}{4}). \qquad (57)$$

Thus, we have:

$$\frac{\partial P_\nu(\cos(\pi-\theta))}{\sin\nu\pi\partial\theta} \approx -i\sqrt{\frac{2kaS_n}{\pi\sin\theta}}$$

$$\exp\left[i\left(\nu+\frac{1}{2}\right)\theta+\frac{i\pi}{4}\right], \qquad (58)$$

$$\frac{\partial^2 P_\nu(\cos(\pi-\theta))}{\sin\nu\pi\partial^2\theta} \approx \sqrt{\frac{2}{\pi\sin\theta}}(kaS_n)^{3/2}$$

$$\exp\left[i\left(\nu+\frac{1}{2}\right)\theta+\frac{i\pi}{4}\right]. \qquad (59)$$

When the observation point is close to an antipole of the dipole source, the approximate formulas of the functions $\frac{\partial P_\nu(\cos(\pi-\theta))}{\partial\theta}$ and $\frac{\partial^2 P_\nu(\cos(\pi-\theta))}{\partial^2\theta}$ are written in the following forms:

$$\frac{\partial P_\nu(\cos(\pi-\theta))}{\partial \theta} \approx \frac{\delta}{2}\left[\left(\nu+\frac{1}{2}\right)^2-\frac{1}{4}\right]-\frac{\delta^3}{16}\left(\nu+\frac{1}{2}\right)^2$$

$$\left[\left(\nu+\frac{1}{2}\right)^2-\frac{7}{6}\right], \tag{60}$$

$$\frac{\partial^2 P_\nu(\cos(\pi-\theta))}{\partial \theta^2} \approx \frac{-1}{2}\left[\left(\nu+\frac{1}{2}\right)^2-\frac{1}{4}\right]$$

$$+\frac{3\delta^2}{16}\left(\nu+\frac{1}{2}\right)^2\left[\left(\nu+\frac{1}{2}\right)^2-\frac{7}{6}\right], \tag{61}$$

where $\delta=\pi-\theta$.

At short distance between the dipole source and the observation point, namely, $k\rho \ll 1$, we have:

$$\frac{\partial P_\nu(\cos(\pi-\theta))}{\sin\nu\pi\partial\theta} \approx i\left(\nu+\frac{1}{2}\right)H_1^{(1)}\left[\left(\nu+\frac{1}{2}\right)\theta\right], \tag{62}$$

$$\frac{\partial^2 P_\nu(\cos(\pi-\theta))}{\sin\nu\pi\partial^2\theta} \approx \frac{i(\nu+\frac{1}{2})H_1^{(1)}[(\nu+\frac{1}{2})\theta]}{\theta}. \tag{63}$$

By using above approximate formulas, the computations can be simplified greatly. In the following computations, the electron density of the lower ionosphere is described by a two-parameter exponential profile [29,30],

$$N_e(z)=1.43\times10^7 e^{-0.15h}e^{(\beta-0.15)(z-h)}cm^{-3}, \tag{64}$$

where the two parameters h in kilometers and β in km^{-1} control the altitude of the profile and the sharpness of the ionospheric transition, respectively. Then, by using the proposed method in the book by Budden [3], the normalized surface impedance matrix of the anisotropic ionosphere $[\Delta]$ can be computed readily.

With a=6378 km, $\phi=\pi/4$, $\sigma_g=10^{-4}$ S/M, h=85 km, and β=0.3 km^{-1}, the magnitudes of E_θ and H_ϕ at f=100 Hz are computed and shown in Figs. 2 and 3, respectively. In above computations, numerical results are obtained for both isotropic and anisotropic case by using the proposed method, respectively. Comparing to the available results for isotropic case, it is seen that the numerical results for isotropic case by using the proposed method in this paper are in good agreement with the corresponding results by using spherical harmonic series solution addressed in Chapter 2 in the book [28]. From Figs. 2 and 3, it is seen that when the propagation distance ρ is close to 20000 km, the magnitudes of the field

components are enlarged. This is caused by the multi-path effects.
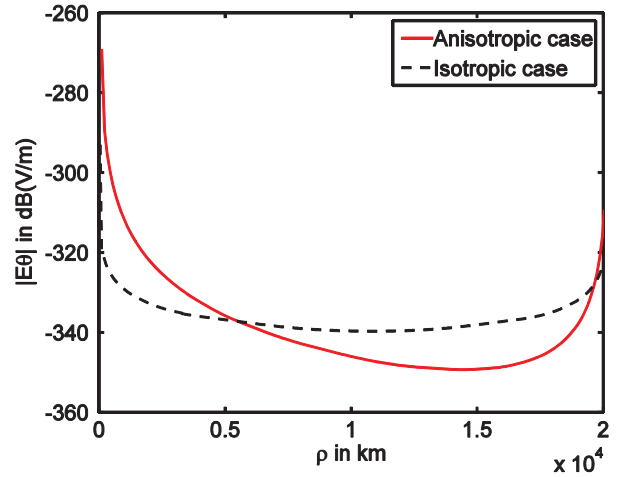

Fig. 2. The electric field $|E_\theta|$ in V/m at f=100 Hz with a=6378 km, $\phi=\pi/4$, $\sigma_g=10^{-5}$ S/m, h=85 km, and β=0.3 km^{-1}.
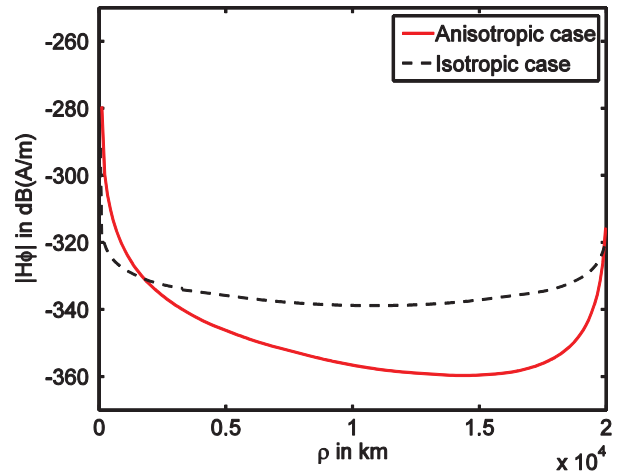

Fig. 3. The magnetic field $|H_\phi|$ in A/m at f=100 Hz with a=6378 km, $\phi=\pi/4$, $\sigma_g=10^{-5}$ S/m, h=85 km, and β=0.3 km^{-1}.

When the observation point is close to the antipole of the dipolesource, the multipath effects should be considered. The electric field components E_r, E_θ, and E_ϕ, and the magnetic field components H_θ and H_ϕ versus the distance ρ from the antipole at f=100 Hz are computed and shown in Figs. 4 and 5, respectively. The

electromagnetic wave, which propagates along the large circular path should not be neglected. The total field included the electromagnetic wave propagating along both the short and large circular paths. Obviously, it is seen that when the observation point is close to the antipole, the interference between the electromagnetic waves along different propagation paths occurs.
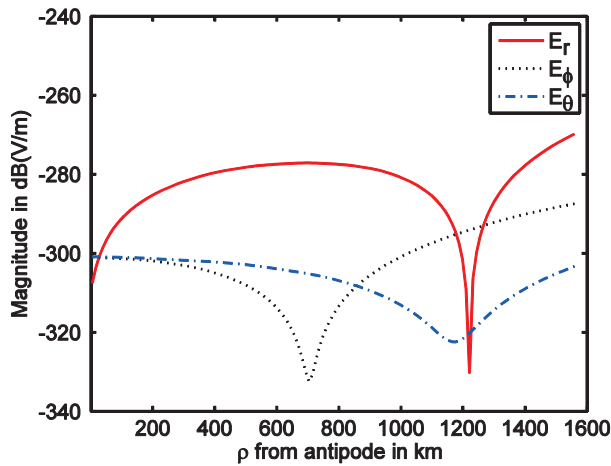

Fig. 4. Magnitudes of the components E_r, E_θ, E_ϕ at f=100 Hz with a=6378 km, $\phi = \pi/4$, $\sigma_g = 10^{-5}$ S/m, h=85 km, and β =0.3 km^{-1}.
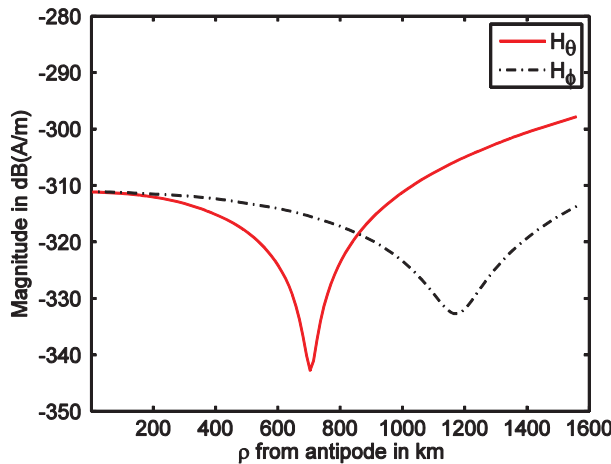

Fig. 5. Magnitudes of the components H_θ and H_ϕ at f=100 Hz with a=6378 km, $\phi = \pi/4$, $\sigma_g = 10^{-5}$ S/m, h=85 km, and β =0.3 km^{-1}.

REFERENCES

[1] H. Bremmer, "Terrestrial radio waves," *New York: Elsevier*, 1949.

[2] C. J. Bouwkamp and H. B. G. Casimir, "On multipole expansions in the theory of electromagnetic radiation," *Physica*, vol. 20, pp. 539-554, 1954.

[3] K. G. Budden, "Radio waves in the ionosphere," *Cambridge: Cambridge University Press*, 1961.

[4] J. R. Wait, "Electromagnetic waves in stratified media," *New York: Pergamon Press*, 1970.

[5] J. Galejs, "Terrestrial propagation of long electromagnetic waves," *New York: Pergamon Press*, 1972.

[6] L. B. Felsen and N. Marcuvitz, "Radiation and scattering of waves, englewood cliffs," *New York: Prentice-Hall*, 1973.

[7] A. P. Nickolaenko and M. Hayakawa, "Resonances in the earth-ionosphere cavity," *Kluwer Acad. Pub.*, 2002.

[8] J. R. Wait, "The mode theory of VLF ionospheric propagation for finite ground conductivity," *Proceedings of the IRE*, vol. 45, no. 6, pp. 760-767, 1957.

[9] J. R. Wait, "Terrestrial propagation of very-low-frequency radio waves, a theoretical investigation," *J. Res. Nat. Bureau Stand.*, vol. 64D, pp. 153-204, 1960.

[10] J. R. Wait and K. P. Spies, "Influence of finite ground conductivity on the propagation of VLF radio waves," *Radio Sc.*, vol. 3, pp. 787-791, 1965.

[11] W. O. Schumann, "On the radiation free self-oscillations of conducting sphere which is surrounded by an air layer and an ionospheric shell," (In German), *Zeitschrift und Naturfirschung*, 72: 149-154, 1952.

[12] W. O. Schumann, "On the damping of electromagnetic self-oscillations of the system earth-air-ionosphere," (In German), *Zeitschrift und Naturfirschung*, 72: 250-252, 1952.

[13] J. Galejs and R. Row, "Propagation of ELF waves below an inhomogeneous anisotropic ionosphere," *IEEE Trans. Antennas Propagat.*, vol. 12, no. 1, pp. 74-83, 1964.

[14] J. Galejs, "Terrestrial extremely-low-frequency propagation, natural electromagnetic phenomena below 30 kc/s," Bleil DF (ed.), New York, NY, USA: Plenum Press, 205-258, 1964.

[15] J. Galejs, "ELF and VLF fields of a horizontal electric dipole," *IEEE Trans. Antennas Propagat.*, vol. 16, no. 6, pp. 689-700, 1968.

[16] J. Galejs, "ELF and VLF propagation for models of a perturbed ionosphere," *Radio Sci.*, vol. 5, no. 7, pp. 1041-1044, 1970.

[17] J. Galejs, "Stable solutions of ionospheric fields in the propagation of ELF and VLF waves," *Radio Sci.*, vol. 7, no. 6, pp. 549-561, 1972.

[18] P. R. Bannister, E. A. Wolkoff, J. R. Katan, and F. J. Williams, "Far-field, extremely-low-frequency propagation measurements," *Radio Sci.*, vol. 8, no. 7, pp. 623-631, 1973.

[19] V. K. Tripathi, C. L. Chang, and K. Papadopoulos, "Excitation of the earth-ionosphere waveguide by an ELF source in the ionosphere," *Radio Sci.*, vol. 17, no. 5, pp. 1321-1326, 1982.

[20] P. R. Bannister, "ELF propagation update," *IEEE J. Oceanic Eng.*, vol. 9, no. 3, pp. 179-188, 1984.

[21] K. J. Carroll and A. J. Ferraro, "Computer simulation of ELF injection in the earth-ionosphere waveguide," *Radio Sci.*, vol. 25, no. 6, pp. 1363-1367, 1990.

[22] A. C. Fraser-Smith and P. R. Bannister, "Reception of ELF signals at antipodal distance," *Radio Sci.*, vol. 33, no. 1, pp. 83-88, 1998.

[23] D. E. Barrick, "Exact ULF/ELF dipole field strengths in the earth-ionosphere cavity over the schumann resonance region: idealized boundaries," *Radio Sci.*, vol. 34, no. 1, pp. 209-227, 1999.

[24] S. A. Cummer, "Modeling electromagnetic propagation in the earth-ionosphere waveguide," *IEEE Trans. Antennas Propagat.*, vol. 48, no. 9, pp. 468-474, 2000.

[25] S. T. Rybachek and M. J. Ponomariev, "Efficiency of the earth-ionosphere waveguide excitation by ELF sources located in an anisotropic ionosphere," *Int. J. Geomagn. Aeron.*, vol. 7, GI1005, doi:10.1029/2005GI000123, 2007.

[26] V. V. Kirillov and A. E. Pronin, "Normal waves of the anisotropic earth-ionosphere waveguide in the VLF-ULF range," *Int. J. Geomagn. Aeron.*, vol. 7, GI2006, doi:10.1029/2005GI000126G, 2007.

[27] W. Y. Pan, "LF/VLF/ELF wave propagation," (In Chinese), *UESTC Press*, Chengdu, China, 2004.

[28] W. Y. Pan and K. Li, "Propagation of SLF/ELF electromagnetic waves," *Springer-Verlag jointly with ZJU Press*, 2014.

[29] K. Rawer, D. Bilitza, and S. Ramakrishnan, "Goals and status of the international reference ionosphere," *Rev. Geophys.*, vol. 16, pp. 177-181, 1978.

[30] S. A. Cummer, U. S. Inan, and T. F. Bell, "Ionospheric d region remote sensing using VLF radio atmospherics," *Radio Sci.*, vol. 33, pp. 1781-1792, November-December 1998.

Guo Heng Li was born in Puyang, Henan, China, in May of 1985. He received his B.Eng. degree in Electronic Information Engineering from Hangzhou Dianzi University, Hangzhou, China, in 2009, and his M.Eng. degree in Electromagnetic Theory from Zhejiang University, Hangzhou, China, in 2012, respectively. His current research interests include SLF/ELF wave propagation and application.

Ting Ting Gu was born in Leshan, Sichuan, China, on June 18, 1988. She received her B.Sc. and M.Sc. degrees in Electromagnetic Field and Microwave Technology from Zhejiang University of Media and Communications, and Hangzhou Dianzi University, Hangzhou, China, in 2010 and 2013, respectively. She is currently working towards her Ph.D. degree in Radio Wave Propagation Theory with the Department of Information Science and Electronic Engineering, Zhejiang University, Hangzhou, China. Her current research interests include radio wave propagation theory and its applications.

Kai Li was born in Xiao County, Anhui, China, on February 10, 1968. He received his B.S. degree in Physics from Fuyang Normal University, Anhui, China, in 1990, his M.S. degree in Radio Physics from Xidian University, Xi'an, Shaanxi, China, in 1994, and his Ph.D. degree in Astrophysics from Shanxi Astronomical Observatory, the Chinese Academy of Sciences, Shaanxi, China, in 1998, respectively. From August 1990 to December 2000, he was on the Faculty of China Research Institute Radiowave Propagation (CRIRP). From January 2001 to December 2002, he was a Postdoctoral Fellow at the Information and Communications University (ICU), Daejeon, Rep. of Korea. From January 2003 to January 2005, he was a Research Fellow with the School of Electrical and Electric Engineering, Nanyang Technological University (NTU), Singapore. Since January 2005, he has been a Professor with the Department of Information Science and Electronic Engineering, Zhejiang University, Hangzhou, China. His current research interests include classic electromagnetic theory and radio wave propagation. Li is a senior member of the Chinese Institute of Electronics (CIE) and a member of the Chinese Institute of Space Science (CISS).

Study on Fabry-Pérot Antennas Using Dipole Exciters

Yong Zhang [1], Wenhua Yu [1], and Wenxing Li [2]

[1] 2Comu, INC., VA 22030, USA
robeyzhang@gmail.com, wenyu@2comu.com

[2] Harbin Engineering University, Harbin, Heilongjiang 150001, China
liwenxing@hrbeu.edu.cn

Abstract ─ Fabry-Pérot (F-P) cavity antennas with Artificial Magnetic Conductor (AMC) ground planes and Frequency Selective Surface (FSS) superstrates have been investigated in this paper. The method of periodic imaging is used to analyze the cavity antennas, and we can calculate the working frequency and quality factor. One or two dipole antennas are utilized to excite the cavity antennas. The results demonstrate that the gain will be enhanced with the increase of the cavity size, and two exciters in the cavity will improve radiation efficiency obviously.

Index Terms ─ AMC, F-P cavity antennas, FSS superstrate.

I. INTRODUCTION

F-P cavity antennas have attracted a lot of interests for requirements of high-directivity, low-cost and simple-feeding radiation problems [1-4]. The antenna usually consists of a partial reflection surface that is a superstrate, a ground plane and one or several exciters. Therefore, complexity of a traditional feeding network can be significantly reduced.

In order to get a high directivity, the height of a cavity formed by the superstrate and metal ground plane is about one-half wavelength. AMC, which can generate a reflected wave with a zero phase, is utilized to replace the metal ground plane. The height of cavity will be reduced by half while retaining the peak performance of the antenna [5].

Patch FSS superstrate investigated in this paper is used as not quite a band-stop filter, which is just a partially reflecting surface. Substrates with a high electric permittivity are also used for superstrate, while high loss and not high enough reflection coefficients will reduce the directivity.

Excitation in a cavity antenna plays an important role because it's a cavity and the boundary conditions are changed. It is difficult to generate the desired cavity mode with a high directivity and low return loss. Dipole, patch or slot antennas have been used as the exciters for such cavity antennas.

In the following sections, square patch cells are used for AMC ground planes and FSS superstrates. A method of periodic imaging is utilized to analyze the cavity. One and two dipole antennas are used as the exciters for different size cavity antennas.

II. F-P ANTENNA DESIGN

We begin with the design process by choosing the AMC ground plane and superstrate. The simulations have been carried out by GEMS [6], which is an efficient 3-D parallel electromagnetic simulator for modeling complex EM systems. For an AMC unit, a square patch is printed on a metal-backed substrate, whose height and relative permittivity are 1.6 mm and 2.55, respectively. The dimensions of the element unit are $2.6 \times 2.6 \times 1.6$ mm^3, and the patch size is 2.5×2.5 mm^2. The reflection phase of AMC is shown in Fig. 1, and the zero reflection phase occurs at 11.4 GHz. We set the height of cavity to be 7 mm that corresponds to about one quarter of wavelength at 11.4 GHz.
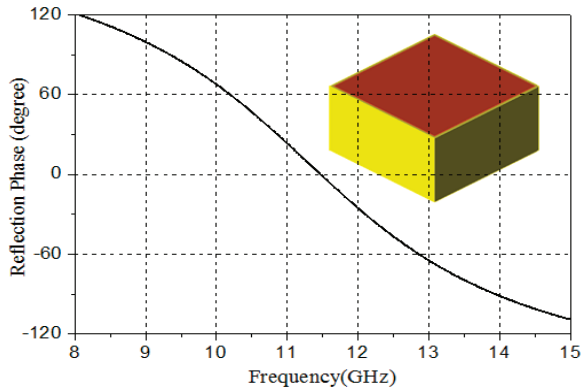
Fig. 1. Reflection phase of the patch AMC.

We use an FSS layer as the superstrate, while the dielectric layer is the same as those used in AMC. The square patches are printed on one side of the dielectric layer. The dimensions of element unit and the patch are $7.8 \times 7.8 \times 1.6$ mm^3 and 7×7 mm^2, respectively. The reflection coefficients of superstrate are plotted in Fig. 2. The reflection magnitude is about 0.9 and the phase is -157 degrees at 11.4 GHz.


(a) Magnitude

(b) Phase
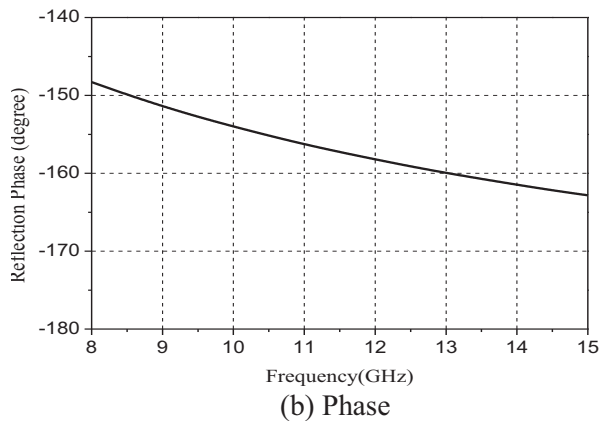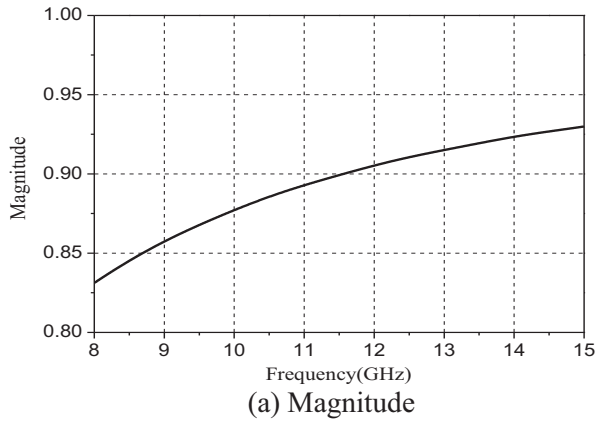
Fig. 2. Reflection characteristics of the patch FSS.

We use the method of periodic imaging to get the characteristics of the cavity [2-3]. This method is effective to analyze the working frequency and get the field distribution inside the cavity. As shown in Fig. 3, one unit cell of the cavity consists of one FSS unit cell and nine AMC unit cells. The unit cell is truncated by using the Periodic Boundary Conditions (PBCs); therefore, we only need to simulate a single cell to get the solution. The metal ground is replaced by an imaging of the AMC and superstrate. The plane wave is incident along the -z-axis direction, and the reflection and transmission coefficients are calculated as shown in Fig. 4. The cavity works at around 11.7 GHz, and the Quality Factor (Q) of the cavity is 58.5. The field distribution in one cutting plane in the cavity is presented in Fig. 5.
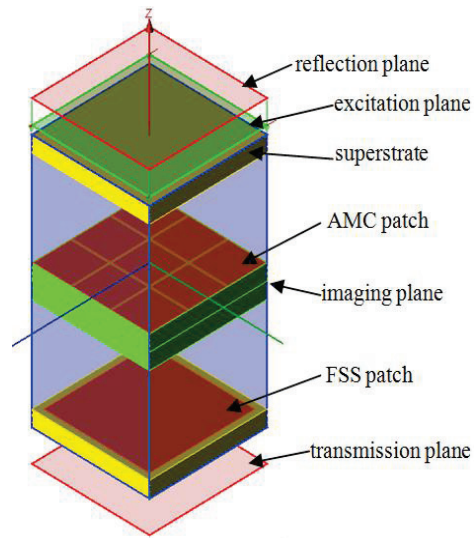

Fig. 3. Configuration of periodic imaging.
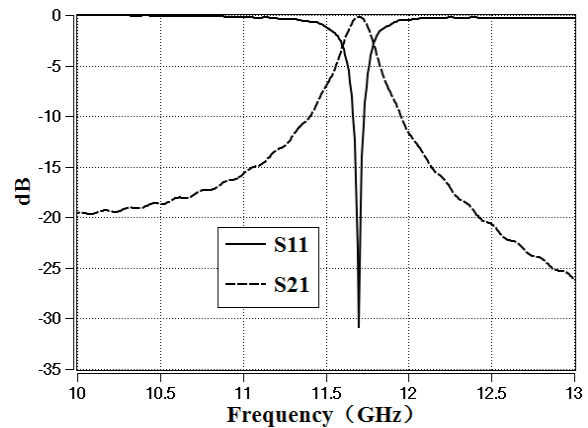
Fig. 4. S-parameters of the F-P cavity.
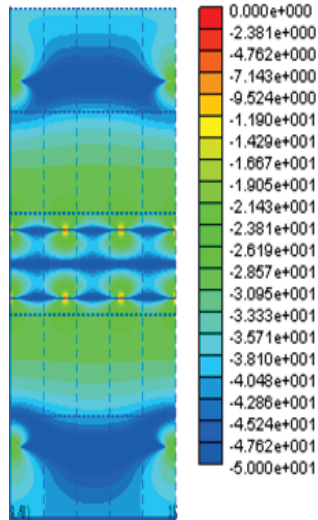
Fig. 5. Field distribution of one cutting plane inside the cavity.

The resonant frequency is a little different from the AMC design since the reflection phase of FSS is not -180 degrees. By increasing the height of the cavity, the frequency can be modified as well for the AMC case. Therefore, the periodic imaging method is very important for the F-P antennas design, and it can be used to modify the parameters of cavities. In this case, we will still choose the height of 7 mm.

Next, two antenna cavities with different sizes but same height are constructed, shown in Table 1.

Table 1: Cavities geometry information

Cavity	AMC Cells	FSS Cells	Size (mm)
1	14x14	4x4	36.4x36.4
2	39x39	13x13	101.4x101.4

III. RESULTS AND DISCUSSION

In Fig. 6, a dipole antenna with L=6 mm is located at the center of the cavity. For the cavity configuration 1, the S_{11} and gain can be plotted in Fig. 7. The maximum gain is 13.3 dB at 12.35 GHz, and the S_{11} is -12dB. The working frequency shift for the cavity is small, while periodic imaging method is just used to simulate an infinite case.
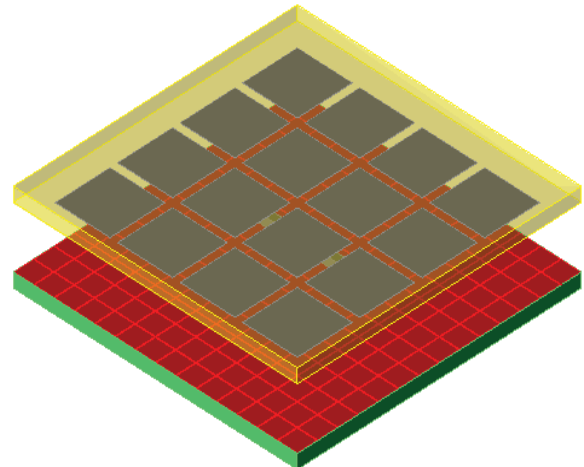

(a) 3D view
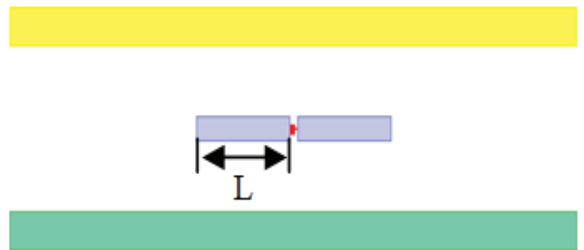
(b) Side view

Fig. 6. Configuration of the F-P antenna.
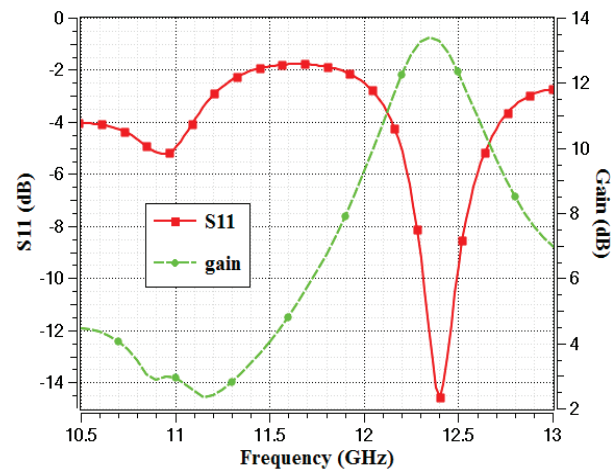
Fig. 7. Performance of cavity 1 with one dipole.

The results for the cavity 2 with one dipole excitation at the center of the cavity are shown in

Fig. 8. The antenna works at 11.75 GHz, the gain is around 19 dB and the S_{11} is -13 dB. We observe from Fig. 8, that the antenna gain will be improved with the increase of the cavity size. At the same time, the working frequency will approach to the resonant frequency in Fig. 4.
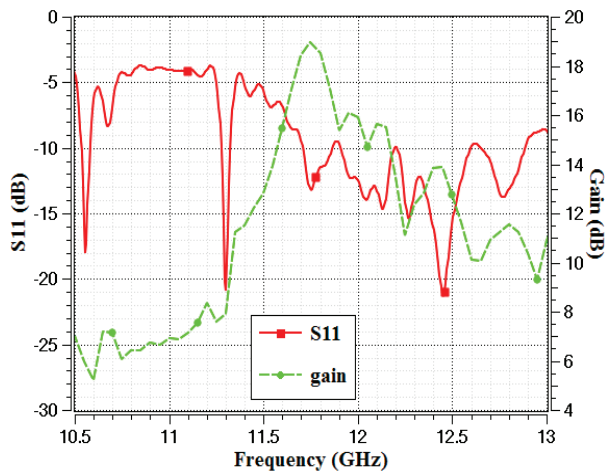

Fig. 8. Performance of cavity 2 with one dipole.

Next, we consider two dipole antennas in the case of the cavity 2 shown in Fig. 9. They are arranged symmetrically along the *x*-axis, and centrally along the *y*- and *z*-axis inside the cavity. The simulation results are presented in Fig. 10. The antenna works at 11.75 GHz, the antenna gain is around 21 dB and the S_{11} is -15 dB. The 2-D and 3-D radiation patterns are presented in Fig. 11.
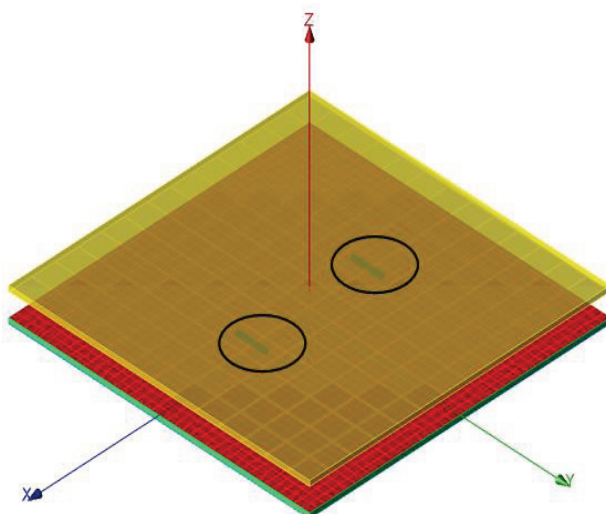

Fig. 9. Configuration of the F-P antenna with two dipoles.
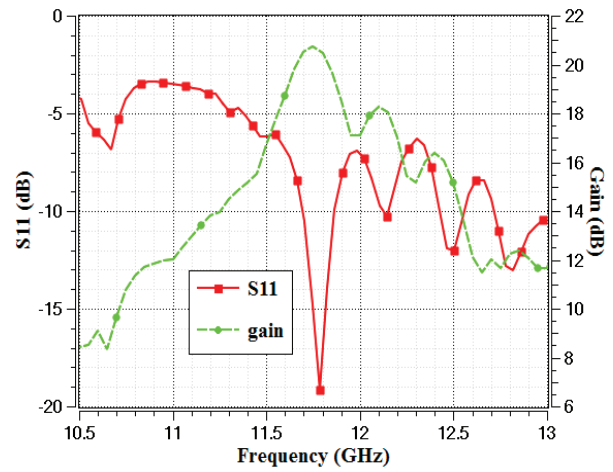
Fig. 10. Performance of cavity 2 with two dipoles.
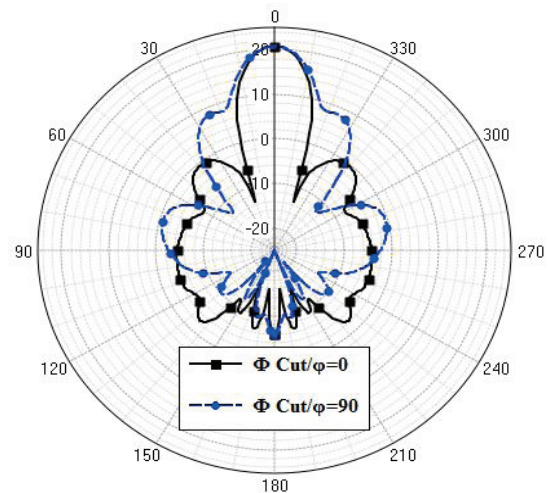

(a) 2D patterns
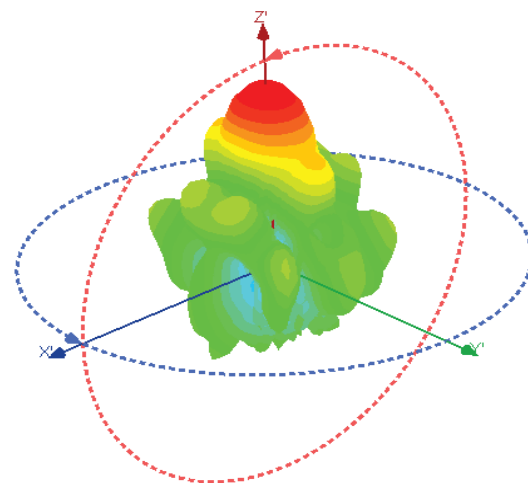
(b) 3D patterns

Fig. 11. Radiation patterns of cavity 2 with two dipoles.

The theory of effective aperture field for array antennas can be used as a reference for the performance of the F-P antennas. As shown in Fig. 7, the cavity 1 with one dipole has good radiation efficiency. The effective aperture of the cavity 2 is almost eight times larger than the cavity 1. For one dipole exciter, the directivity of cavity 2 antenna increases about 5.5 dB than the cavity 1. Two dipole exciters increase the directivity about 7.5 dB. Therefore, for large size F-P antennas, more exciters, even small arrays are necessary for high directivity.

IV. CONCLUSION

In this paper, AMC ground planes and an FSS superstrate are used to construct the F-P cavities. The method of periodic imaging is used to analyze the working frequency and quality factor of the cavity. The dipole antennas are utilized to excite the cavity. The simulation results demonstrate that the F-P antennas have good radiation efficiency with simple excitations. The future work will focus on characteristics analysis of larger F-P antennas, including beam scanning, beam forming, and array excitation.

REFERENCES

[1] A. P. Feresidis and J. C. Vardaxoglou, "High gain planar antenna using optimized partially reflective surfaces," *IET Proceeding Microwave, Antennas and Propagation*, vol. 48, no. 6, pp. 345-350, 2001.

[2] J. Y. Young, Y. Junho, R. Mittra, et al., "Application of electromagnetic bandgap (EBG) superstrates with controllable defects for a class of patch antennas as spatial angular filters," *IEEE Trans. Antennas Propag.*, vol. 53, no. 1, pp. 224-235, 2005.

[3] A. Pirhadi, M. Hakkak, F. Keshmiri, et al., "Design of compact dual band high directive electromagnetic bandgap (EBG) resonator antenna using artificial magnetic conductor," *IEEE Trans. Antennas Propag.*, vol. 55, no. 6, pp. 1682-1690, 2007.

[4] A. Foroozesh and L. Shafai, "Effects of artificial magnetic conductors in the design of low-profile high-gain planar antennas with high-permittivity dielectric superstrate," *IEEE Antennas and Wireless Propagation Letters*, vol. 8, pp. 10-13, 2009.

[5] D. F. Sievenpiper, "High impedance electromagnetic surfaces," *Ph.D. thesis, University of California at Los Angeles*, 1999.

[6] "GEMS," *www.2comu.com*.

Yong Zhang received his M. Sc. and Ph. D. degrees in Radio Physics from the University of Electronic Science and Technology of China (UESTC), Chengdu, China, in 2006 and 2011, respectively. He was a Visiting Scholar in the Electromagnetic Communication Laboratory, at Pennsylvania State University in 2008. His research interests include the reconfigurable antenna technique, AMC applications and high directivity antenna design.

Wenhua Yu received his Ph.D. degree in Electrical Engineering from the Southwest Jiaotong University in 1994. He worked at Beijing Institute of Technology as a Postdoctoral Research Associate from February 1995 to August 1996. He has published over 100 technical papers and several books. He is CEO of Computer and Communication Unlimited Company. He is a Senior Member of the IEEE. He is currently a Professor with the College of Information and Communication Engineering, Harbin Engineering University, China. He is also a Visiting Professor and Ph.D. Advisor with the Communication University of China. Yu's research interests include computational electromagnetic, parallel computational techniques, and the theory and design of parallel computing systems.

Wenxing Li received his B.S. and M.S. degrees from Harbin Engineering University, Harbin, Heilongjiang, China, in 1982 and 1985, respectively. He is currently a Full Professor with the College of Information and Communication Engineering, Harbin Engineering University, China. He is also the Head of Research Centre of EM Engineering & RF Technology since 2010. He is also the organizer of the 30th Progress in Electromagnetics Research Symposium (PIERS), IEEE International Workshop on Electromagnetics (iWEM), the TPC of 2012 Asia-Pacific Symposium on Electromagnetic Compatibility (APEMC 2012) and 2012 Global Symposium on Millimeter Waves (GSMM 2012). His recent research interests are mainly on computational electromagnetic, microwave engineering, modern antenna design and microwave and millimeter wave circuits.

Exact Transient Field of a Horizontal Electric Dipole with Double Exponential Excitation on the Boundary Two Dielectrics

B. J. Xia, T. T. Gu, W. Dai, and K. Li

Department of Information Science and Electronic Engineering
Zhejiang University, Hangzhou, Zhejiang 310027, China
21231013@zju.edu.cn, 11331025@zju.edu.cn, daiwei@zju.edu.cn, kaili@zju.edu.cn

Abstract ─ In this paper, the exact formulas are derived for the time-domain electromagnetic field radiated by a horizontal electric dipole with double exponential excitation along the boundary between two different dielectrics. The transient field components consist of two lateral pulses with the amplitude attenuation factor ρ^{-2}. In particular, the two lateral pulses travel along the boundary in Regions 1 and 2 with different velocities.

Index Terms ─ Double exponential excitation, exact formulas, horizontal electric dipole.

I. INTRODUCTION

The frequency-domain electromagnetic field radiated by horizontal and vertical electric dipoles on or near the plane boundary between two dielectrics like air and earth or sea water and rock, had been investigated widely for its useful applications in subsurface and closed-to-the-surface communication, radar, and geophysical prospecting and diagnostics [1-11]. This problem is well summarized in the monograph by King, Owens, and Wu [11]. In addition, the time-domain properties and applications of the transient field radiated by a dipole source on the plane boundary between two dielectrics have also been treated by many investigators [12-22]. In pioneering work by Van der Pol [12], the detailed analysis was carried out on the transient field of a vertical electric dipole with a delta-function excitation on the

boundary between two half-spaces by invoking the Hertz potential. The important work on the exact formulas for the transient field components generated by a vertical electric dipole with delta-function excitation on the boundary between two dielectrics, was addressed by Wu and King [18]. Lately, the exact solution on the lateral electromagnetic pulses due to horizontal and vertical dipoles with delta-function excitation and Gaussian pulse excitation on the boundary between two dielectrics, was subsequently obtained in [19][20]. In the past decade, with the extensions of the work by Wu and King [18], some progresses were made on the exact and approximated solutions for the transient field of a dipole source with delta and Gaussian excitations on the boundary of two different media [21-24].

It is well known that both the lighting electromagnetic pulse source and the nuclear electromagnetic pulse source are a typical double exponential excitation source. It is seen that the double exponential excitation source is more popular comparing with the source with delta-function excitation, and that with Gaussian excitation. Evidently, it is important to treat the exact solution on the transient field of a dipole source excited by double exponential currents. In what follows, we will attempt to obtain the exact formulas for the transient field components radiated by a horizontal electric dipole with double exponential excitation on the planar boundary

between two dielectrics.

II. EXACT FIELD COMPONENTS OF HORIZONTAL ELECTRIC DIPOLE WITH DOUBLE EXPONENTIAL EXCITATION ON THE BOUNDARY BETWEEN TWO DELECTRICS
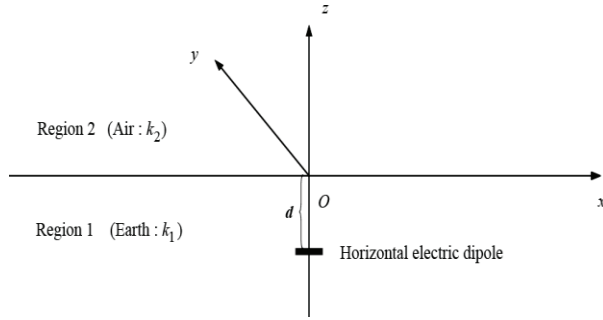

Fig. 1. Geometry of a horizontal electric dipole on the boundary between two dielectrics.

When a horizontal electric dipole is excited by double exponential currents, the problem of the exact solution on the transient field components will be in general more complicated. The relevant geometry and Cartesian coordinate system are shown in Fig. 1, where a horizontal electric dipole in the $\hat{x}$ direction is located at $(0,0,-d)$. The lower half-space $z \leq 0$ (Region 1) is with the earth characterized by the permeability μ_0 and relative permittivity ε filled by with the air, and the upper half-space $z \geq 0$ (Region 2) is with the air characterized by the permeability μ_0 and uniform permittivity ε_0. The wave numbers of the two regions are $k_1 = \sqrt{\varepsilon}\,\omega/c$ and $k_2 = \omega/c$, respectively. When both the dipole and the observation point approach the boundary from above $(d \to 0^+)$ and $(z \to 0^+)$, with the time dependence of $e^{-i\omega t}$, the exact transient field of a horizontal electric dipole with a delta-function excitation on the boundary between two dielectrics can be obtained by using Fourier's transform technique [24]. From Chapter 8 in the book [24], the exact formulas for the transient field components with delta-function excitation can be

written readily in the following forms:

$$
\left[E_{2\rho}(\rho,t)\right]_\delta = \frac{1}{2\pi\varepsilon_0 c\rho^2}\cdot\left[\delta\left(t-\frac{\rho}{c}\right)+\frac{1}{\sqrt{\varepsilon}}\delta\left(t-\frac{\sqrt{\varepsilon}\rho}{c}\right)\right]
$$
$$
-\frac{1}{2\pi\varepsilon_0\rho^3(\varepsilon+1)}
$$
$$
\times\begin{cases} 0 & ,\dfrac{ct}{\rho}<1 \\[2ex] 1-\dfrac{\varepsilon^2}{(\varepsilon-1)(\varepsilon+1)^{\frac{3}{2}}}\left(\dfrac{c^2t^2}{\rho^2}+\dfrac{2\varepsilon}{\varepsilon+1}\right)\left(\dfrac{c^2t^2}{\rho^2}-\dfrac{\varepsilon}{\varepsilon+1}\right)^{\frac{5}{2}} & ,1<\dfrac{ct}{\rho}<\sqrt{\varepsilon} \\[2ex] 2 & ,\dfrac{ct}{\rho}>\sqrt{\varepsilon} \end{cases}, \tag{1}
$$

$$
\left[E_{2\phi}(\rho,t)\right]_\delta = \frac{1}{2\pi\varepsilon_0 c(\varepsilon-1)\rho^2}\left[\delta\left(t-\frac{\rho}{c}\right)-\sqrt{\varepsilon}\delta\left(t-\frac{\sqrt{\varepsilon}\rho}{c}\right)\right]
$$
$$
+\frac{1}{2\pi\varepsilon_0(\varepsilon-1)\rho^2}
$$
$$
\times\begin{cases} 0 & ,\dfrac{ct}{\rho}<1 \\[2ex] 2-\dfrac{1}{\varepsilon+1}+\dfrac{\varepsilon^2}{(\varepsilon+1)^{5/2}}\left(\dfrac{c^2t^2}{\rho^2}-\dfrac{\varepsilon}{\varepsilon+1}\right)^{-3/2} & ,1<\dfrac{ct}{\rho}<\sqrt{\varepsilon} \\[2ex] \dfrac{\varepsilon-1}{\varepsilon+1} & ,\dfrac{ct}{\rho}>\sqrt{\varepsilon} \end{cases}, \tag{2}
$$

$$
\left[B_{2z}(\rho,t)\right]_\delta = \frac{\mu_0}{2\pi\rho^2(\varepsilon-1)}\left[\delta\left(t-\frac{\rho}{c}\right)-\varepsilon\delta\left(t-\frac{\sqrt{\varepsilon}\rho}{c}\right)\right]
$$
$$
-\frac{\mu_0}{2\pi\rho^3(\varepsilon-1)}\begin{cases} 0 & ,\dfrac{ct}{\rho}<1 \\[2ex] \dfrac{3ct}{\rho} & ,1<\dfrac{ct}{\rho}<\sqrt{\varepsilon} \\[2ex] 0 & ,\dfrac{ct}{\rho}>\sqrt{\varepsilon} \end{cases}. \tag{3}
$$

In above formulas, the double exponential pulse is defined by:

$$
i(t) = a\left[e^{-\alpha t}-e^{-\beta t}\right]U(t), \tag{4}
$$

where $U(t)$ is unit step function. Thus, the exact formulas of the transient field components of a horizontal electric dipole excited by double exponential currents can be represented as follows:

$$
E_{2\rho}(\rho,t) = \int_{-\infty}^{\infty}\left[E_{2\rho}(\rho,0;t-\zeta)\right]_\delta\cdot a\left(e^{-\alpha\zeta}-e^{-\beta\zeta}\right)U(\zeta)d\zeta, \tag{5}
$$

$$
E_{2\phi}(\rho,t) = \int_{-\infty}^{\infty}\left[E_{2\phi}\left(\rho,\frac{\pi}{2};t-\zeta\right)\right]_\delta\cdot a\left(e^{-\alpha\zeta}-e^{-\beta\zeta}\right)U(\zeta)d\zeta, \tag{6}
$$

$$
B_{2z}(\rho,t) = \int_{-\infty}^{\infty}\left[B_{2z}\left(\rho,\frac{\pi}{2};t-\zeta\right)\right]_\delta\cdot a\left(e^{-\alpha\zeta}-e^{-\beta\zeta}\right)U(\zeta)d\zeta. \tag{7}
$$

Obviously, the formulas of the transient field can be expressed in terms of several integrals,

$$\frac{1}{a}E_{2\rho}(\rho,t) = \frac{1}{2\pi\varepsilon_0 c\rho^2}\left(I_1 + \varepsilon^{-\frac{1}{2}}I_2\right)$$

$$+ \frac{1}{2\pi\varepsilon_0(\varepsilon+1)\rho^3}\left[I_3 - \frac{1}{\varepsilon-1}\frac{\varepsilon^2}{(\varepsilon+1)^{\frac{3}{2}}}I_7 + 2I_5\right] \quad,$$

(8)

$$\frac{1}{a}E_{2\phi}(\rho,t) = \frac{1}{2\pi\varepsilon_0 c(\varepsilon-1)\rho^2}\left(I_1 - \varepsilon^{\frac{1}{2}}I_2\right) + \frac{1}{2\pi\varepsilon_0(\varepsilon-1)\rho^3}$$

$$\times\left[\left(2 - \frac{1}{\varepsilon+1}\right)\cdot I_3 + \frac{\varepsilon^2}{(\varepsilon+1)^{2/5}}\cdot I_8 + \frac{\varepsilon-1}{\varepsilon+1}\cdot I_5\right] \quad,$$

(9)

$$\frac{1}{a}B_{2z}(\rho,t) = \frac{\mu_0}{2\pi\rho^2}\frac{1}{\varepsilon-1}(I_1 - \varepsilon I_2) - \frac{3\mu_0 c}{2\pi\rho^3(\varepsilon-1)}\cdot I_9. \quad (10)$$

The integrals I_1, I_2, I_3, and I_5 can be found in Chapter 15 in the book by King, Owens, and Wu [11], and Chapter 8 in the book by Li [24]. In this paper, we will not rewrite the exact solutions of the above four integrals. In the next step, the main task is evaluating the integrals I_7, I_8, and I_9. We write:

$$I_7 = \int_{-\infty}^{\infty}\left[\frac{c^2(t-\zeta)^2}{\rho^2} + \frac{2\varepsilon}{\varepsilon+1}\right]\left[\frac{c^2(t-\zeta)^2}{\rho^2} - \frac{\varepsilon}{\varepsilon+1}\right]^{-5/2}$$

$$\times\left[U\left(t - \frac{\sqrt{\varepsilon}\rho}{c}\right) - U\left(t - \frac{\rho}{c}\right)\right]\left(e^{-\alpha\zeta} - e^{-\beta\zeta}\right)U(\zeta)d\zeta \quad,$$

(11)

$$I_8 = \int_{-\infty}^{\infty}\left[\frac{c^2(t-\zeta)^2}{\rho^2} - \frac{\varepsilon}{\varepsilon+1}\right]^{-3/2}$$

$$\times\left[U\left(t - \frac{\sqrt{\varepsilon}\rho}{c}\right) - U(t-\rho')\right]\left(e^{-\alpha\zeta} - e^{-\beta\zeta}\right)U(\zeta)d\zeta \quad,$$

(12)

$$I_9 = \int_{-\infty}^{\infty}\frac{c(t-\zeta)}{\rho}\left[U\left(t - \frac{\sqrt{\varepsilon}\rho}{c}\right) - U(t-\rho')\right]\left(e^{-\alpha\zeta} - e^{-\beta\zeta}\right)U(\zeta)d\zeta. \quad (13)$$

With $x = (t-\zeta)/\rho'$, $dx = -d\zeta/\rho'$, and $a^2 = \varepsilon/\varepsilon+1$, the results become:

$$I_7 = \begin{cases} \rho'\int_1^{\sqrt{\varepsilon}}\frac{x^2+2a^2}{(x^2-a^2)^{5/2}}\left[e^{-\alpha(t-\rho'x)} - e^{-\beta(t-\rho'x)}\right]dx & ,\sqrt{\varepsilon}\rho' \le t \\ \rho'\int_1^{t/\rho'}\frac{x^2+2a^2}{(x^2-a^2)^{5/2}}\left[e^{-\alpha(t-\rho'x)} - e^{-\beta(t-\rho'x)}\right]dx & ,\rho' \le t \le \sqrt{\varepsilon}\rho' \\ 0 & ,t < \rho' \end{cases}$$

(14)

$$I_8 = \begin{cases} \rho'\int_1^{\sqrt{\varepsilon}}(x^2-a^2)^{-3/2}\left[e^{-\alpha(t-\rho'x)} - e^{-\beta(t-\rho'x)}\right]dx & ,\sqrt{\varepsilon}\rho' \le t \\ \rho'\int_1^{t/\rho'}(x^2-a^2)^{-3/2}\left[e^{-\alpha(t-\rho'x)} - e^{-\beta(t-\rho'x)}\right]dx & ,\rho' \le t < \sqrt{\varepsilon}\rho' \\ 0 & ,t < \rho' \end{cases}$$

(15)

$$I_9 = \begin{cases} \rho'\int_1^{\sqrt{\varepsilon}}x\left[e^{-\alpha(t-\rho'x)} - e^{-\beta(t-\rho'x)}\right]dx & ,\sqrt{\varepsilon}\rho' \le t \\ \rho'\int_1^{t/\rho'}x\left[e^{-\alpha(t-\rho'x)} - e^{-\beta(t-\rho'x)}\right]dx & ,\rho' \le t < \sqrt{\varepsilon}\rho' \\ 0 & ,t < \rho' \end{cases}$$

(16)

The integrals in (14)-(16) can be evaluated readily by using numerical method. Then, the transient field components with double exponential pulse excitation can be derived readily. We write:

$$\frac{1}{a}E_{2\rho}(\rho,t) = \frac{1}{2\pi\varepsilon_0 c\rho^2}\left\{\left[e^{-\alpha(t-\rho')} - e^{-\beta(t-\rho')}\right]U(t-\rho')\right.$$

$$+ \varepsilon^{-1/2}\left[e^{-\alpha(t-\sqrt{\varepsilon}\rho')} - e^{-\beta(t-\sqrt{\varepsilon}\rho')}\right]U\left(t - \sqrt{\varepsilon}\rho'\right)\right\}$$

$$+ \frac{1}{2\pi\varepsilon_0(\varepsilon+1)\rho^3}\cdot\left\{-\frac{1}{\alpha}\left[e^{-\alpha(t-\rho')} - e^{-\alpha(t-\sqrt{\varepsilon}\rho')}\right]\right.$$

$$+ \frac{1}{\beta}\left[e^{-\beta(t-\rho')} - e^{-\beta(t-\sqrt{\varepsilon}\rho')}\right]\right\}U\left(t - \sqrt{\varepsilon}\rho'\right) + \frac{1}{2\pi\varepsilon_0(\varepsilon+1)\rho^3}$$

$$\times\left\{-\frac{1}{\alpha}\left[e^{-\alpha(t-\rho')} - 1\right] + \frac{1}{\beta}\left[e^{-\beta(t-\rho')} - 1\right]\right\}$$

$$\times\left[U(t-\rho') - U\left(t - \sqrt{\varepsilon}\rho'\right)\right] - \frac{1}{2\pi\varepsilon_0(\varepsilon+1)^{5/2}\rho^3}\frac{\varepsilon^2}{(\varepsilon-1)}$$

$$\times\left\{\rho'\int_1^{\sqrt{\varepsilon}}\frac{x^2+2a^2}{(x^2-a^2)^{5/2}}\cdot\left[e^{-\alpha(t-\rho'x)} - e^{-\beta(t-\rho'x)}\right]dxU\left(t - \sqrt{\varepsilon}\rho'\right)\right.$$

$$+ \rho'\int_1^{t/\rho'}\frac{x^2+2a^2}{(x^2-a^2)^{5/2}}\cdot\left[e^{-\alpha(t-\rho'x)} - e^{-\beta(t-\rho'x)}\right]dx$$

$$\times\left[U(t-\rho') - U\left(t - \sqrt{\varepsilon}\rho'\right)\right]\right\} + \frac{1}{\pi\varepsilon_0(\varepsilon+1)\rho^3}$$

$$\times\left\{-\frac{1}{\alpha}\left[e^{-\alpha(t-\sqrt{\varepsilon}\rho')} - 1\right] + \frac{1}{\beta}\left[e^{-\beta(t-\sqrt{\varepsilon}\rho')} - 1\right]\right\}U\left(t - \sqrt{\varepsilon}\rho'\right),$$

(17)

$$\frac{1}{a}E_{2\phi}(\rho,t)=\frac{1}{2\pi\varepsilon_0(\varepsilon-1)\rho^2}\left\{\left[e^{-\alpha(t-\rho')}-e^{-\beta(t-\rho')}\right]U(t-\rho')\right.$$

$$-\varepsilon^{1/2}\left[e^{-\alpha(t-\sqrt{\varepsilon}\rho')}-e^{-\beta(t-\sqrt{\varepsilon}\rho')}\right]U\left(t-\sqrt{\varepsilon}\rho'\right)\right\}$$

$$+\frac{1}{2\pi\varepsilon_0(\varepsilon-1)\rho^3}\left(2-\frac{1}{\varepsilon+1}\right)\cdot\left\{-\frac{1}{\alpha}\left[e^{-\alpha(t-\rho')}-e^{-\alpha(t-\sqrt{\varepsilon}\rho')}\right]\right.$$

$$\left.+\frac{1}{\beta}\left[e^{-\beta(t-\rho')}-e^{-\beta(t-\sqrt{\varepsilon}\rho')}\right]\right\}U\left(t-\sqrt{\varepsilon}\rho'\right)$$

$$+\frac{1}{2\pi\varepsilon_0(\varepsilon-1)\rho^3}\left(2-\frac{1}{\varepsilon+1}\right)\cdot\left\{-\frac{1}{\alpha}\left[e^{-\alpha(t-\rho')}-1\right]\right.$$

$$\left.+\frac{1}{\beta}\left[e^{-\beta(t-\rho')}-1\right]\right\}\left[U\left(t-\rho'\right)-U\left(t-\sqrt{\varepsilon}\rho'\right)\right]$$

$$-\frac{1}{2\pi\varepsilon_0(\varepsilon+1)^{5/2}\rho^3}\frac{\varepsilon^2}{(\varepsilon-1)}$$

$$\times\left\{\rho'\int_1^{\sqrt{\varepsilon}}\left(x^2-a^2\right)^{-3/2}\cdot\left[e^{-\alpha(t-\rho'x)}-e^{-\beta(t-\rho'x)}\right]dxU\left(t-\sqrt{\varepsilon}\rho'\right)\right.$$

$$+\rho'\int_1^{t/\rho'}\left(x^2-a^2\right)^{-3/2}\cdot\left[e^{-\alpha(t-\rho'x)}-e^{-\beta(t-\rho'x)}\right]dx$$

$$\left.\times\left[U\left(t-\rho'\right)-U\left(t-\sqrt{\varepsilon}\rho'\right)\right]\right\}+\frac{1}{2\pi\varepsilon_0(\varepsilon+1)\rho^3}$$

$$\times\left\{-\frac{1}{a}\left[e^{-\alpha(t-\sqrt{\varepsilon}\rho')}-1\right]+\frac{1}{\beta}\left[e^{-\beta(t-\sqrt{\varepsilon}\rho')}-1\right]\right\}U\left(t-\sqrt{\varepsilon}\rho'\right),$$

(18)

$$\frac{1}{a}B_{2z}(\rho,t)=\frac{\mu_0}{2\pi\rho^2}\left\{\left[e^{-\alpha(t-\rho')}-e^{-\beta(t-\rho')}\right]U\left(t-\rho'\right)\right.$$

$$\left.-\varepsilon\left[e^{-\alpha(t-\sqrt{\varepsilon}\rho')}-e^{-\beta(t-\sqrt{\varepsilon}\rho')}\right]U\left(t-\sqrt{\varepsilon}\rho'\right)\right\}$$

$$-\frac{3\mu_0 c}{2\pi\rho^3(\varepsilon-1)}\left\{\rho'\int_1^{\sqrt{\varepsilon}}x\left[e^{-\alpha(t-\rho'x)}-e^{-\beta(t-\rho'x)}\right]dxU\left(t-\sqrt{\varepsilon}\rho'\right)\right.$$

$$+\rho'\int_1^{t/\rho'}x\left[e^{-\alpha(t-\rho'x)}-e^{-\beta(t-\rho'x)}\right]dx$$

$$\left.\times\left[U\left(t-\rho'\right)-U\left(t-\sqrt{\varepsilon}\rho'\right)\right]\right\}.$$

(19)

By now, the analytical formulas for the three components $E_{2\rho}(\rho,t)$, $E_{2\phi}(\rho,t)$, and $B_{2z}(\rho,t)$ have been derived readily.

III. COMPUTATIONS AND CONCLUSIONS

From the above derivations and analysis, it is seen that the final exact formulas for the three components $E_{2\rho}(\rho,t)$, $E_{2\phi}(\rho,t)$, and $B_{2z}(\rho,t)$, radiated by a horizontal electric dipole with the double exponential pulse excitation can be expressed in terms of several fundamental functions.

After examining the equations (17)-(19), it is found that the three time-domain components $E_{2\rho}(\rho,t)$, $E_{2\phi}(\rho,t)$, and $B_{2z}(\rho,t)$ consist of two lateral electromagnetic pulses with the amplitude factor ρ^{-2}. In particular, the first pulse arrives at ρ/c, which travels along the boundary in Region 2 (air) with the velocity c; while the second pulse arrives at $\rho\sqrt{\varepsilon}/c$, which travels along the boundary in Region 1 (earth) with the velocity $c/\sqrt{\varepsilon}$.

In the following computations, the parameters of the double exponential pulse are taken as $a=30$ kA, $\alpha=2\times10^4$ sec^{-1}, and $\beta=2\times10^5$ sec^{-1}. Assuming that the relative permittivity of the earth is $\varepsilon=8$, both the electric field components $E_{2\rho}(\rho,t)$ and $E_{2\phi}(\rho,t)$ which are generated by a horizontal electric dipole with double exponential pulse excitation on the plane boundary between the air and the earth, are computed and shown in Figs. 2 and 3, respectively.
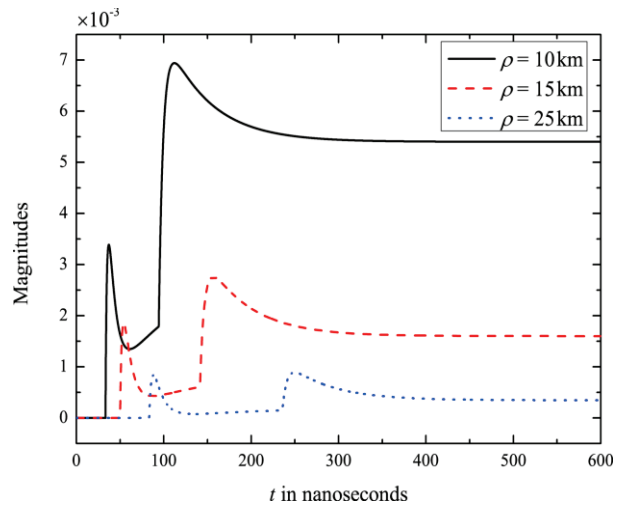

Fig. 2. Exact electric field $E_{2\rho}(\rho,t)$ on the boundary in air of a horizontal electric with the relative permittivity of the earth $\varepsilon=8$.
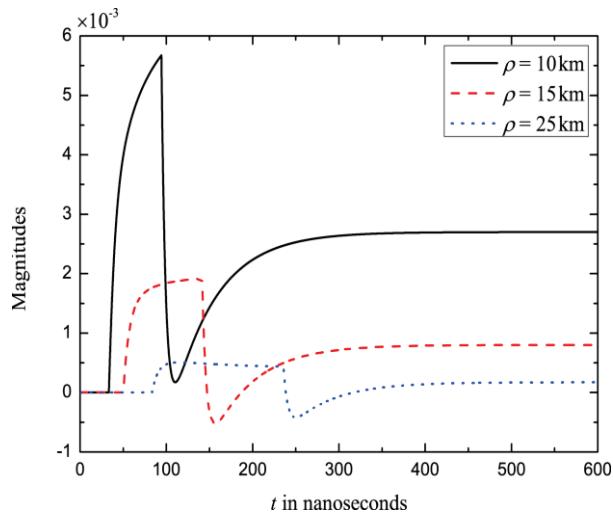
Fig. 3. Exact electric field $E_{2\phi}(\rho,t)$ on the boundary in air of a horizontal electric dipole with the relative permittivity of the earth $\varepsilon = 8$.

In these computations, the propagation distances are taken as $\rho = 10$ km, 15 km, and 25 km, respectively. Assuming that the propagation distance is $\rho = 15$ km, both the electric components $E_{2\rho}(\rho,t)$ and $E_{2\phi}(\rho,t)$ are computed and plotted in Figs. 4 and 5, respectively.
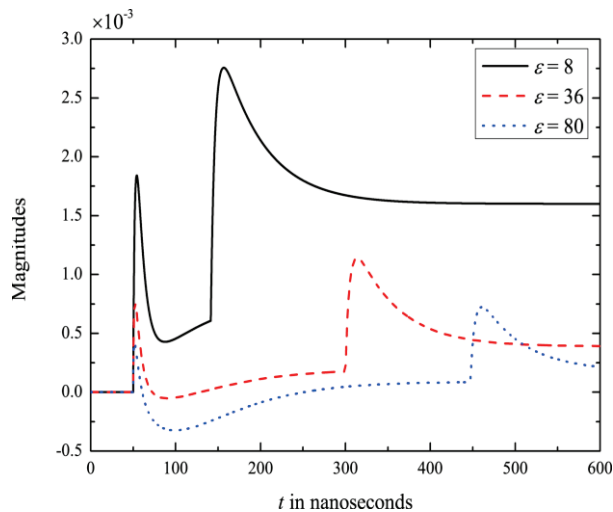

Fig. 4. Exact electric field $E_{2\rho}(\rho,t)$ on the boundary in air of a horizontal electric dipole at the propagation distance $\rho = 15$ km.
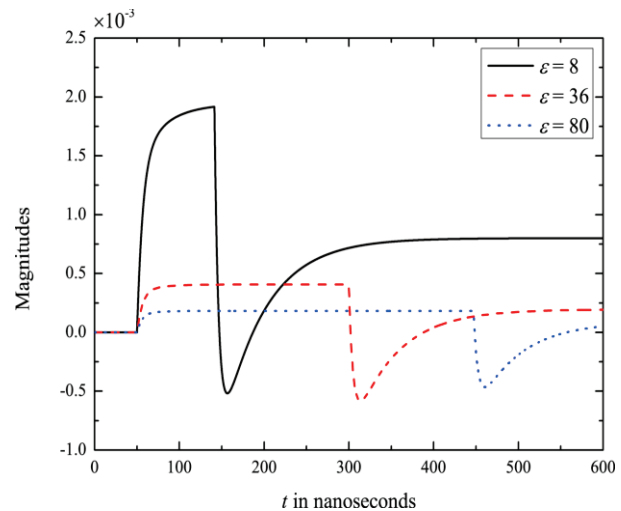

Fig. 5. Exact electric field $E_{2\phi}(\rho,t)$ on the boundary in air of a horizontal electric dipole at the propagation distance $\rho = 15$ km.

Actually, the amplitude of the second pulse for the component $E_{2\rho}(\rho,t)$ is smaller than that of the first pulse. It is noted that the term including the integral I_7 in $E_{2\rho}(\rho,t)$ has a large negative value near the first pulse, it is followed that the amplitude of the second pulse is larger than that of the first one. For the component $E_{2\phi}(\rho,t)$, there doesn't exists the term of the integral I_7. As a result, the amplitude of the first pulse is larger than that of the second pulse.

Similar to the case of the delta-function excitation, and that of the Gaussian excitation addressed in Chapter 8 in the book [24], the remaining three components $E_{2z}(\rho,t)$, $B_{2\rho}(\rho,t)$, and $B_{2\varphi}(\rho,t)$, cannot be expressed in terms of elementary functions and finite integrals.

ACKNOWLEDGMENT

REFERENCES

[1] A. Sommerfeld, "Propagation of waves in wireless telegraphy," *Ann. Phys.*, vol. 28, pp. 665-736, 1909.

[2] A. Sommerfeld, "Propagation of waves in wireless telegraphy," *Ann. Phys.*, vol. 81, pp. 1135-1153, 1926.

[3] J. R. Wait, "The electromagnetic fields of a horizontal dipole in the presence of a conducting half-space," *Can. J. Phys.*, vol. 39, pp. 1017-1027, 1961.

[4] R. W. P. King, "New formulas for the electromagnetic field of a vertical electric dipole in a dielectric or conducting half-space near its horizontal interface," *J. Appl. Phys.*, vol. 53, pp. 8476-8482, 1982; erratum, vol. 56, p. 3366, 1984.

[5] T. T. Wu and R. W. P. King, "Lateral waves: new formulas for $E_{1\phi}$ and E_{1z}," *Radio Sci.*, vol. 17, pp. 532-538, 1982; correction, vol. 19, p. 1422, 1984.

[6] T. T. Wu and R. W. P. King, "Lateral waves: a new formula and interference pattern," *Radio Sci.*, vol. 17, pp. 521-531, 1982.

[7] R. W. P. King and T. T. Wu, "Lateral waves: new formulas for the magnetic field," *J. Appl. Phys.*, vol. 54, pp. 507-514, 1983; erratum, vol. 56, p. 3365, 1984.

[8] R. W. P. King and M. F. Brown, "Lateral electromagnetic waves along plane boundaries: a summarizing approach," *Proc. IEEE*, vol. 72, pp. 595-611, 1984.

[9] R. W. P. King, "Electromagnetic surface waves: new formulas and applications," *IEEE Trans. Antennas Propagat.*, vol. AP-33, no. 11, pp. 1204-1212, 1985.

[10] D. Margetis and T. T. Wu, "Exactly calculable field components of electric dipoles in planar boundary," *J. Math. Phys.*, vol. 42, pp. 713-745, 2001.

[11] R. W. P. King, M. Owens, and T. T. Wu, "Lateral electromagnetic waves, theory and applications to communications, geophysical exploration, and remoting sensing," *Springer-Verlag*, 1992.

[12] B. Van der Pol, "On discontinuous electromagnetic waves and occurrence of a surface wave," *IRE Trans. Antennas and Propag.*, vol. AP-4, pp. 288-293, 1956.

[13] J. R. Wait, "The transient behavior of the electromagnetic ground wave on a spherical earth," *IRE Trans. Antennas and Propag.*, vol. AP-5, pp. 198-202, 1957.

[14] J. R. Wait, "Wave propagation theory," *Pergamon*, New York, 1981.

[15] H. J. Frankena, "Transient phenomena associated with sommerfield's horizontal dipole problem," *Applied Scientific Research, Section B*, vol. 8, pp. 357-368, 1960.

[16] A. T. De Hoop and H. J. Frankena, "Radiation of pulses generated by a vertical electric dipole above a plane, non-conducting earth," *Applied Scientific Research, Section B*, vol. 8, pp. 369-377, 1960.

[17] A. Ezzeddine, J. A. Kong, and L. Tsang, "Time response of a vertical electric dipole over a two-layer medium by the double deformation technique," *J. Appl. Phys.*, vol. 53, no. 2, pp. 813-822, 1981.

[18] T. T. Wu and R. W. P. King, "Lateral electromagnetic pulses generated by a vertical electric dipole on the boundary between two dielectrics," *J. Appl. Phys.*, vol. 62, pp. 4345-4355, 1987.

[19] R. W. P. King, "Lateral electromagnetic pulses generated by a vertical electric dipole on a plane boundary between dielectrics," *J. Electrom. Waves Appl.*, vol. 2, pp. 225-243, 1988.

[20] R. W. P. King, "Lateral electromagnetic pulses generated on a plane boundary between dielectrics by vertical and horizontal dipole source with gaussian pluse excitation," *J. Electrom. Waves Appl.*, vol. 2, pp. 589-597, 1989.

[21] K. Li, Y. Lu, and W. Y. Pan, "Exact formulas for the lateral electromagnetic pulses generated by a horizontal electric dipole on the boundary of two dielectrics," *Progress In Electromagnetics Research, PIER 55*, pp. 249-283, Jin Au Kong, Ed., *EMW Publishing*, Cambridge, Boston, 2005.

[22] K. Li, Y. Lu, and M. Li, "Approximate formulas for lateral electromagnetic pulses from a horizontal electric dipole on the surface of one-dimensionally anisotropic medium," *IEEE Trans. Antennas and Propag.*, vol. 53, no. 3, pp. 933-937, 2005.

[23] K. Li, Y. Lu, and W. Y. Pan, "Exact transient field of a horizontal electric dipole excited by a gaussian pulse on the boundary two dielectrics," *IEEE Antennas and Wireless Propagation Letters*, vol. 4, pp. 337-340, 2005.

[24] K. Li, "Electromagnetic fields in stratified media," *Springer-Verlag jointly with ZJU Press*, 2009.
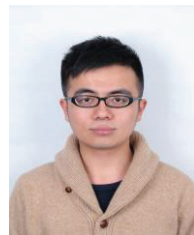
Bing Jun Xia was born in Wenzhou, Zhejiang, China, in September, 1988. He received his B.S. degree in Information and Computing Science from Northeast University, Shenyang, China, in 2011. He is currently working toward his M.S. degree in Electrical Engineering in the Department of Information and Electronic Engineering, Zhejiang University, Hangzhou, China. His current research interests include radio wave propagation theory and applications.

Ting Ting Gu was born in Leshan, Sichuan, China on June 18, 1988. She received her B.S. degree and M.S. degree in Electromagnetic Field and Microwave Technology from Zhejiang University of Media and Communications, and Hangzhou Dianzi University, Hangzhou, China, in 2010 and 2013, respectively. She is currently working towards her Ph.D. degree in radio wave propagation theory at the Department of Information Science and Electronic Engineering, Zhejiang University, Hangzhou, China. Her current research interests include radio wave propagation theory and applications.

Wei Dai was born in Yingtan, Jiangxi, China in August 1987. She received her BS degree in Electronic Science and Technology from Zhejiang University, Hangzhou, China in 2013. She is currently working at IT Service Department at Zhejiang Rural Credit Cooperatives.

Kai Li was born in Xiao County, Anhui, China, on February 10, 1968. He received his BS degree in physics from Fuyang Normal University, Anhui, China, in 1990, MS degree in radio physics from Xidian University, Xi'an, Shaanxi, China, in 1994, and PhD degree in astrophysics from Shaanxi Astronomical Observatory, the Chinese Academy of Sciences, Shaanxi, China, in 1998, respectively. From August 1990 to December 2000, he was on the faculty of China Research Institute Radiowave Propagation (CRIRP). From January 2001 to December 2002, he was a postdoctoral fellow at Information and Communications University (ICU), Daejeon, Rep. of Korea. From January 2003 to January 2005, he was a research fellow with the School of Electrical and Electric Engineering, Nanyang Technological University (NTU), Singapore. Since January 2005, he has been a professor with the Department of Information Science and Electronic Engineering, Zhejiang University, Hangzhou, China. His current research interests include classic electromagnetic theory and radio wave propagation. Dr. Li is a senior member of the Chinese Institute of Electronics (CIE) and a member of the Chinese Institute of Space Science (CISS).

Approximation Through Common and Differential Modes for Twist Wire Pair Crosstalk Model

Yaxiu Sun, Qinghui Jiang, Wenhua Yu, Qingkun Zhuo, and Qian Li

College of Information and Telecommunication
Harbin Engineering University, Harbin 150001, China
sunyaxiu@hrbeu.edu.cn, clj1-1@163.com, wenyu@2comu.com, zhuoqingkun@hrbeu.edu.cn,
liqian@hrbeu.edu.cn

Abstract ─ In this paper, an advanced approximation method is presented, which separates the twist wire pairs into common and differential modes using the multi-conductor transmission line model. The simulation storage and time cost has been significantly reduced and its accuracy is better than traditional approximation methods. Analyses of dealing with the impedance and admittance and the separation procedure of common and differential modes are presented. In addition, the load dealing methods for terminal and source has also been specified in this paper. Numerical experiments validate the accuracy and listed the storage efficiency and time cost reduction of the proposed method.

Index Terms ─ Common mode, crosstalk, different mode, twist wire pair.

I. INTRODUCTION

In the recent years, Twist Wire Pair (TWP) has been well developed and has become a most widely used physical layer for a number of technologies in communication systems, such as controller-area-network buses and gigabit Ethernet cables. Crosstalk comes on them when these wires are used to transport signals, which affects the bandwidth and the transmission rate. A special structure of TWP is used to reduce crosstalk, which introduces non-uniformity into model and makes prediction more difficult [1-4].

In order to predict crosstalk, a wiring structure is proposed based on the simplified circuit modeling and interpretation of crosstalk [5-8]. The twisted pair is modeled as a cascade of normal transmission-line loops consisting of two-wire sections with abrupt interchanges of wire positions between 2 different transmission line parts [5, 7]. This model is typically accurate for frequencies such that the total line length is no more than 1/10 of a wavelength [5]. According to this technique, one can easily add multiple TWPs into the normal Multi-Transmission Line Networks (MTLN). There are some advanced predicting techniques based on this model [9-14], such as the response of plane wave [9] and the effect of randomness of twist pitch lengths [10], but it needs more space and time cost to solve the transmission line parameters due to its model complexity and the parameters variation with distance, so some approximation is needed.

While introducing TWP or other cables into the transmission line model, one difficulty is the larger matrix size and the parameters stored in the MTLN model. In addition, the large-size matrices will also cause an extra simulation time.

Several approximation techniques have been proposed, such as the equivalent cable bundle method [15-19], which approximates the cable bundle size by calculating the common mode voltage and current along wires in the same group whose response is more critical than the differential-mode. Its accuracy depends on the ratio of the loading impedances on the terminal and the source sides to the characteristic impedance. For a model with TWP, this categorization may cause the two wires in TWP into two different groups. What is more, it will add the difficulties into the categorization since the characteristic impedance may vary with position.

An approximation model for TWP bundle was proposed using the finite-difference time-domain

method [20]. The abrupt section calculating was avoided for the approximation, so the procedure of solving the chain parameter matrix effect was much simplified, but this method does not have distinct reduction in the storage demand or the time cost.

In this paper, an advanced approximation method based on variation of the common and differential modes will be presented. Also, we will discuss the way of dealing the loading impedance in the advanced model and the usage of the simplified model in MTLN. The method will be proved to be accurate than the equivalent cable bundle method and will save much more space in storage and time.

II. TWISTED WIRE PAIR CROSSTALK MODEL CASCADED THEORY OF PAUL AND MCKNIGHT

A. Twisted wire pair crosstalk model cascaded theory of Paul and McKnight

Since TWP has a periodic structure, it can be cascaded. In the cascaded theory, the twisted wire pairs consist of loops of the half twists and each Half Twist (HT) is divided into a transmission line section and an abrupt transition section, as shown in Fig. 1. Wires 2 and 3 in Fig. 1 are twisted, while wire 1 is a single line. Δl is the length of the transmission line section, and the length of the abrupt transition section is assumed to be zero. This zero length will drive this section, acting an exchange of the voltages and currents on wires 2 and 3. In the transmission line section, the chain parameter matrix in Φ_s can be written as the following format:

$$, \qquad (1)$$
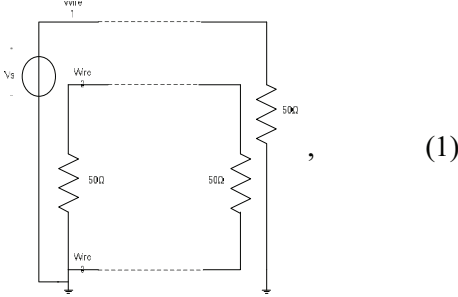
$$\mathbf{\Phi}_s = \begin{bmatrix} \cos(\beta\Delta l)\cdot\mathbf{I}_{3\times3} & -j\sin(\beta\Delta l)\mathbf{Z}_c \\ -j\sin(\beta\Delta l)\mathbf{Y}_c & \cos(\beta\Delta l)\cdot\mathbf{I}_{3\times3} \end{bmatrix}. \quad (2)$$

In the equations above, $V_1 \sim V_3$ and $I_1 \sim I_3$ are the voltages and currents on wires 1~3. $I_{3\times3}$ is a 3×3 identity matrix. Δl is the total length of the

transmission line section in the half twist. β is the wave coefficient. Z_c and Y_c are the transmission line characteristic impedance matrix and characteristic admittance matrix, respectively [8].

For the abrupt transition section, the voltages and currents on the wires exchanging with each other, the transition matrix can be written as follows [5,8]:

$$\begin{bmatrix} V_1(x_2) \\ V_2(x_2) \\ V_3(x_2) \\ I_1(x_2) \\ I_2(x_2) \\ I_3(x_2) \end{bmatrix} = P \begin{bmatrix} V_1(x_1) \\ V_2(x_1) \\ V_3(x_1) \\ I_1(x_1) \\ I_2(x_1) \\ I_3(x_1) \end{bmatrix}, \qquad (3)$$

$$P = \begin{bmatrix} P_a & O_{3\times3} \\ O_{3\times3} & P_a \end{bmatrix}, \qquad (4)$$

where the $O_{3\times3}$ represents a 3×3 identity matrix of zeros, and P_a is equal to:

$$P_a = \begin{bmatrix} 1 & 0 & 0 \\ 0 & 0 & 1 \\ 0 & 1 & 0 \end{bmatrix}. \qquad (5)$$

Combining the equations (1)-(5), the total chain matrix of a full twist loop, which consists of two half twists, is multiplication of the matrices:

$$\begin{bmatrix} V_1(x_4) \\ V_2(x_4) \\ V_3(x_4) \\ I_1(x_4) \\ I_2(x_4) \\ I_3(x_4) \end{bmatrix} = \mathbf{P\Phi}_s\mathbf{P\Phi}_s \begin{bmatrix} V_1(x_0) \\ V_2(x_0) \\ V_3(x_0) \\ I_1(x_0) \\ I_2(x_0) \\ I_3(x_0) \end{bmatrix}. \qquad (6)$$
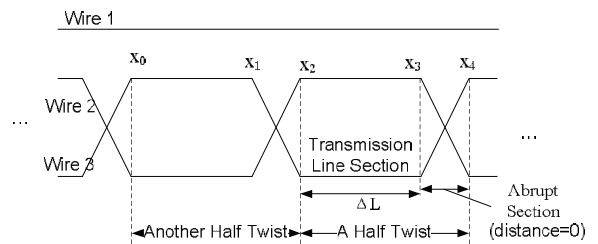

Fig. 1. Abrupt model of the TWP in the Paul and McKnight model.

B. The approximation impedance and the admittance matrix of a full twist

Original model of the cascade theory separates a full twisted loop into 4 sections, which consists of 2 transmission line sections and 2 abrupt transition sections. The description of a full twisted loop is shown in Fig. 2. Notice that the ground effect has been brought into the model, this effect can be reflected through the changes of the characteristic impedance matrices and admittance matrices [5]. The sections from the point x_1 to x_4 can be regarded as an independent part. In this part, the transmission line chain parameter matrix can be defined as:

$$\begin{bmatrix} V_1(x_4) \\ V_2(x_4) \\ V_3(x_4) \\ I_1(x_4) \\ I_2(x_4) \\ I_3(x_4) \end{bmatrix} = \mathbf{\Phi}_{sP} \begin{bmatrix} V_1(x_1) \\ V_2(x_1) \\ V_3(x_1) \\ I_1(x_1) \\ I_2(x_1) \\ I_3(x_1) \end{bmatrix}, \quad (7)$$

$$\mathbf{\Phi}_{sP} = \mathbf{P}\mathbf{\Phi}_s\mathbf{P}$$
$$= \begin{bmatrix} \cos(\beta\Delta l)\cdot E_{3\times3} & -j\sin(\beta\Delta l)Z_{cP} \\ -j\sin(\beta\Delta l)Y_{cP} & \cos(\beta\Delta l)\cdot E_{3\times3} \end{bmatrix}. \quad (8)$$

This part has an independent characteristic impedance matrix Z_{cP} and an independent characteristic admittance matrix Y_{cP}. The matrixes Z_{cP} and Y_{cP} in equation (8) are expressed as:

$$\mathbf{Z}_{cP} = \mathbf{P}_a\mathbf{Z}_c\mathbf{P}_a = \begin{bmatrix} z_{11} & z_{13} & z_{12} \\ z_{31} & z_{33} & z_{32} \\ z_{21} & z_{23} & z_{22} \end{bmatrix}$$
$$\mathbf{Y}_{cP} = \mathbf{P}_a\mathbf{Y}_c\mathbf{P}_a = \begin{bmatrix} y_{11} & y_{13} & y_{12} \\ y_{31} & y_{33} & y_{32} \\ y_{21} & y_{23} & y_{22} \end{bmatrix}. \quad (9)$$

Substituting the equations (8) and (9) into (6), the matrix of a full twisted loop can be derived easily:

$$\mathbf{P}\mathbf{\Phi}_s\mathbf{P}\mathbf{\Phi}_s = \mathbf{\Phi}_{sP}\mathbf{\Phi}_s = \begin{bmatrix} \mathbf{\Phi}_1 & \mathbf{\Phi}_Z \\ \mathbf{\Phi}_Y & \mathbf{\Phi}_1 \end{bmatrix}$$

$$\mathbf{\Phi}_1 = \cos^2(\beta\Delta l)\mathbf{I}_{3\times3} - \sin^2(\beta\Delta l)\cdot\mathbf{Z}_c\mathbf{Y}_{cP} \quad (10)$$
$$\mathbf{\Phi}_Z = -j\sin(\beta\Delta l)\cos(\beta\Delta l)(\mathbf{Z}_c + \mathbf{Z}_{cP})$$
$$\mathbf{\Phi}_Y = -j\sin(\beta\Delta l)\cos(\beta\Delta l)(\mathbf{Y}_c + \mathbf{Y}_{cP}).$$

Considering the case: $\sin(\beta\Delta l) \ll \cos(\beta\Delta l)$, the matrices Z_cY_{cP} and Y_cZ_{cP} after $\sin^2(\beta\Delta l)$ in (10) can be replaced by an identification matrix $E_{3\times3}$, then the equation (10) can be simplified into:

$$P\Phi_sP\Phi_s = \Phi_{sP}\Phi_s$$
$$\approx \begin{bmatrix} \cos(2\beta\Delta l)E_{3\times3} & -j\sin(2\beta\Delta l)(\dfrac{Z_c+Z_{cP}}{2}) \\ -j\sin(2\beta\Delta l)(\dfrac{Y_c+Y_{cP}}{2}) & \cos(2\beta\Delta l)E_{3\times3} \end{bmatrix}. \quad (11)$$

This can be true for several full twisted loops, if their total distance ($n\beta\Delta l$) satisfies the condition $\sin(n\beta\Delta l) \ll \cos(n\beta\Delta l)$.

The condition $\sin(\beta\Delta l) \ll \cos(\beta\Delta l)$ requires that the $(\beta\Delta l)$ is fewer than $\pi/12$, then the frequency should match $f<c/(24\Delta l)$, c is the speed of light of the material. For a TWP whose Δl is equal to 0.02 m, so the frequency should be no more than 625 MHz, it can match the condition $\sin(\beta\Delta l) \ll \cos(\beta\Delta l)$ for the frequencies discussed in [5] (which is no more than 10^7 Hz); also, its accuracy will become a little worse when the frequency grows.

Equation (11) can be rewritten through the approximation way, the approximation impedance and admittance is:

$$Z_{eq} = (Z_c + Z_{cP})/2$$
$$Y_{eq} = (Y_c + Y_{cP})/2. \quad (12)$$

It is worthwhile to mention this pair of simplified approximation impedance and admittance does not match the normal equation of the impedance and admittance $ZY=YZ=E_{3\times3}$.
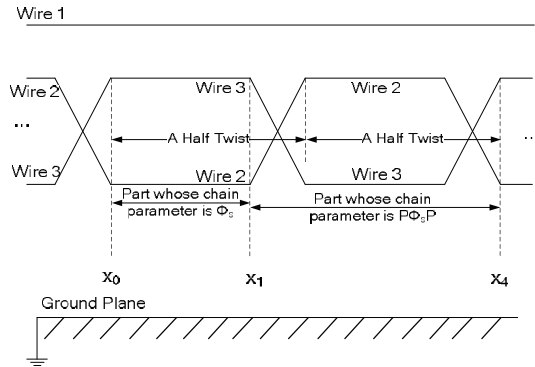
Fig. 2. Description of a full twist.

C. The effectiveness of the approximated matrices

To show the validation of this approximation method, we simulated a TWP model and compared the result with equivalent cable bundle method. The TWP model is presented in Fig. 5, the radius r=0.406 mm, the height of TWP is h=2mm, the height of wire 1 is h_g=4 mm; these heights are measured form the ground. The distance Δh is 0.432 mm, that is one half of the distance between the centers of wires 2 and 3. The load impedance on the terminal side and source side is showed in Fig. 6.

Figures 3 and 4 show the simulation results of the cascade theory matrix and the simplified matrix for length $2\Delta l$ and matrix for a total length of $8\Delta l$. Figure 3 is the current on wire 1 at the near end (the current point which is nearest to the source), and Fig. 4 is the current at the far end (the current point which is nearest to the load).
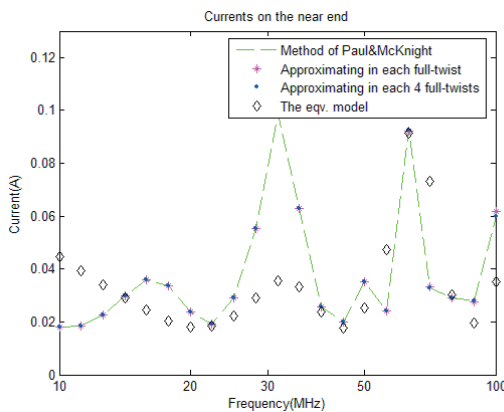

Fig. 3. Current variation with frequency on the source part on wire 1.
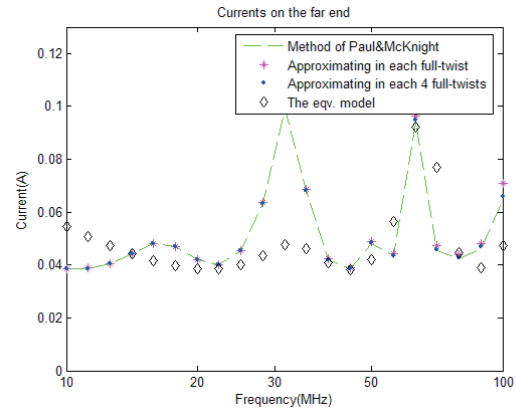
Fig. 4. Current variation with frequency on the load part on wire 1.
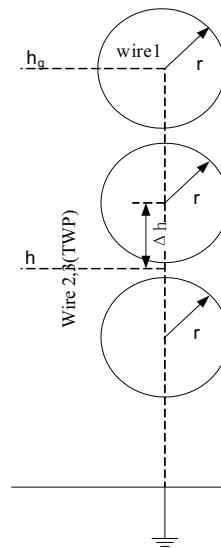
Fig. 5. Considered problem of one TWP and one signal line over earth.
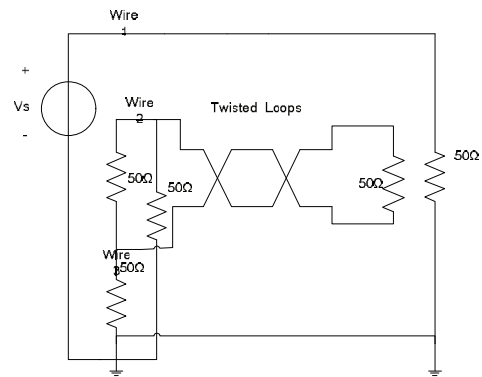

Fig. 6. The source side and the terminal side of the model.

In both Figs. 3 and 4, the result of using the method by Paul and McKnight was shown by the dashed line, and the result of the approximated by one full twist whose distance is $2\Delta l$ and whose chain parameter matrix is eq. (11), is shown by the dots. The octangle shows a simple model of each 4 full-twists whose distance is $8\Delta l$, and the factor in the cosine and sine factor $(2\beta\Delta l)$ in chain parameter matrix will be replaced by $8\beta\Delta l$. The diamond shows the result by using the equivalent cable bundle method.

Comparing the result of the current on wire 1 calculated by the different ways, we could find that their results vary little; it proves that the approximation method is valid when the distance satisfies the rule $\sin(n\beta\Delta l)<<\cos(n\beta\Delta l)$.

III. THE COMMON MODE AND THE DIFFERENTIAL MODE OF THE APPROXIMATION CHAIN PARAMETER MATRIX

A. The approximation impedance and admittance matrices

The transforming of the voltages and currents on wire 2 and wire 3 to common mode and differential mode are usually expressed as equations below:

$$\begin{bmatrix} I_c \\ I_d \end{bmatrix} = \begin{bmatrix} 1 & 1 \\ 1 & -1 \end{bmatrix} \begin{bmatrix} I_a \\ I_b \end{bmatrix}, \quad (13)$$

and

$$\begin{bmatrix} V_c \\ V_d \end{bmatrix} = \begin{bmatrix} 1/2 & 1/2 \\ 1/2 & -1/2 \end{bmatrix} \begin{bmatrix} V_a \\ V_b \end{bmatrix}. \quad (14)$$

Here we use another way of transforming, which is:

$$\begin{bmatrix} I_c \\ I_d \end{bmatrix} = \begin{bmatrix} 1/\sqrt{2} & 1/\sqrt{2} \\ 1/\sqrt{2} & -1/\sqrt{2} \end{bmatrix} \begin{bmatrix} I_a \\ I_b \end{bmatrix}, \quad (15)$$

and

$$\begin{bmatrix} V_c \\ V_d \end{bmatrix} = \begin{bmatrix} 1/\sqrt{2} & 1/\sqrt{2} \\ 1/\sqrt{2} & -1/\sqrt{2} \end{bmatrix} \begin{bmatrix} V_a \\ V_b \end{bmatrix}. \quad (16)$$

This is because the transforming matrix T,

$$\mathbf{T} = \begin{bmatrix} 1/\sqrt{2} & 1/\sqrt{2} \\ 1/\sqrt{2} & -1/\sqrt{2} \end{bmatrix}, \quad (17)$$

can match the condition $\mathbf{T}=\mathbf{T}^{-1}$; for a three-wire TWP system like Fig. 1 we get:

$$\mathbf{T} = \begin{bmatrix} 1 & 0 & 0 \\ 0 & 1/\sqrt{2} & 1/\sqrt{2} \\ 0 & 1/\sqrt{2} & -1/\sqrt{2} \end{bmatrix}. \quad (18)$$

For the MTLN theory, transforming the characteristic impedance matrix and admittance matrix into the common and differential mode can be expressed as:

$$\begin{aligned} \mathbf{Z}_{cd} &= \mathbf{TZT}^{-1} \\ \mathbf{Y}_{cd} &= \mathbf{TYT}^{-1}. \end{aligned} \quad (19)$$

For the approximation impendence and admittance based on the $\sin(\beta\Delta l) << \cos(\beta\Delta l)$ condition, which is shown in (12), these matrices will be transformed by (19), the result of the impendence transforming is:

$$\mathbf{Z}_{cd} = \begin{bmatrix} z_{11} & \dfrac{z_{13}+z_{12}}{2} & 0 \\ \dfrac{z_{21}+z_{31}}{2} & \dfrac{z_{33}+z_{22}+2z_{23}}{2} & 0 \\ 0 & 0 & \dfrac{z_{33}+z_{22}-2z_{23}}{2} \end{bmatrix}, \quad (20)$$

and the admittance $\mathbf{Y}_{cd}$ has a similar form.

For the approximation equation (11) (whose original equation is (10)), expressing the chain parameter matrix in (11) in a common and differential mode, and considering $\mathbf{TIT}^{-1}=\mathbf{I}$, for a full twist shown in Fig. 2 we get:

$$\begin{bmatrix} V_1(x_4) \\ V_c(x_4) \\ V_d(x_4) \\ I_1(x_4) \\ I_c(x_4) \\ I_d(x_4) \end{bmatrix} = \mathbf{\Phi}_{cd} \begin{bmatrix} V_1(x_0) \\ V_c(x_0) \\ V_d(x_0) \\ I_1(x_0) \\ I_c(x_0) \\ I_d(x_0) \end{bmatrix}, \quad (21)$$

where the chain parameter matrix is:

$$\mathbf{\Phi}_{cd} = \begin{bmatrix} \cos(2\beta\Delta l)\mathbf{I}_{3\times3} & -j\sin(2\beta\Delta l)\mathbf{Z}_{cd} \\ -j\sin(2\beta\Delta l)\mathbf{Y}_{cd} & \cos(2\beta\Delta l)\mathbf{I}_{3\times3} \end{bmatrix}. \quad (22)$$

There are 4 zero elements in above matrix (20), and these zero elements indicate that the voltages and currents of differential mode are irrelevant with the voltages and currents on other wires (wire 1) and the common mode, the voltage and current of the differential mode can be expressed as:

$$V_d(x_4) = \cos(\beta\Delta l)V_d(x_0)$$
$$- j\sin(\beta\Delta l)\frac{Z_{33} + Z_{23} - Z_{23}}{2}I_d(x_0)$$
$$I_d(x_4) = -j\sin(\beta\Delta l)\frac{Y_{33} + Y_{23} - Y_{23}}{2}I_d(x_0) \quad (23)$$
$$+ \cos(\beta\Delta l)I_d(x_0).$$

So the differential mode can be calculated independently, the differential part of the approximation chain parameter matrix for length Δl (from x0 to x4) is:

$$\mathbf{\Phi}_{sD} = \begin{bmatrix} \cos(\beta\Delta l) & -j\sin(\beta\Delta l)\frac{z_{c33} + z_{c22} - 2z_{c23}}{2} \\ -j\sin(\beta\Delta l)\frac{y_{c33} + y_{c22} - 2y_{c23}}{2} & \cos(\beta\Delta l) \end{bmatrix}. \quad (24)$$

Also, since the voltages and currents on other wires (wire 1) and the common mode are irrelevant with that on the differential mode, which is calculated already, the approximation matrix of the common mode and wire 1 has no elements relevant with the differential mode. The matrix is proposed in (25):

$$\mathbf{\Phi}_{sC} = \begin{bmatrix} \cos(\beta\Delta l)\mathbf{I}_{2\times2} & \sin(\beta\Delta l)\mathbf{Z}_{common2\times2} \\ \sin(\beta\Delta l)\mathbf{Y}_{common2\times2} & \cos(\beta\Delta l)\mathbf{I}_{2\times2} \end{bmatrix}. \quad (25)$$

Both $Z_{common2\times2}$ and $Y_{common2\times2}$ in (20) are 2×2 matrices with the equal elements of rows 1 and 2 and columns 1 and 2 in (22).

Above all, the total number of elements is 20 (see (24) and (25)), which are much fewer than the original number, 36.

B. The dealing of the load impedance

Since the voltages and currents have been changed into the common and differential modes, some transformations of the load and source impedance (or admittance) into the common and differential modes are required.

The definition of the load impedance is usually described as:

$$V(load) = \mathbf{Z}_l I(load). \quad (26)$$

In the equation above, Z_l represents the load impedance. While changing this equation into the common and differential modes by the way shown in part III in (14)-(16), one can get:

$$V_{cd}(load) = \begin{bmatrix} 1 & 0 & 0 \\ 0 & \frac{1}{\sqrt{2}} & \frac{1}{\sqrt{2}} \\ 0 & \frac{1}{\sqrt{2}} & -\frac{1}{\sqrt{2}} \end{bmatrix} V(load), \quad (27)$$

$$I(load) = \begin{bmatrix} 1 & 0 & 0 \\ 0 & \frac{1}{\sqrt{2}} & \frac{1}{\sqrt{2}} \\ 0 & \frac{1}{\sqrt{2}} & -\frac{1}{\sqrt{2}} \end{bmatrix} I_{cd}(load). \quad (28)$$

Substituting (27) and (28) into (26), the load impedance in the common and differential modes will be:

$$\mathbf{Z}_{l\_cd} = \mathbf{T}^{-1}\mathbf{Z}_l\mathbf{T}. \quad (29)$$

The load impedance can be transformed by the common and differential approach. We can also transform the source impedance in a same way. The voltage source V_s is added at wire 1, so the voltage source matrix is:

$$V_s = \begin{bmatrix} v_s \\ 0 \\ 0 \end{bmatrix}, \quad (30)$$

and this $\mathbf{V}_s$ multiplies the transformation matrix, $\mathbf{T}$ will be $\mathbf{TV}_s = \mathbf{V}_s$.

So in the new model TWP was changed into a common mode line and a differential mode line that has fewer total elements in their matrices.

IV. THE EFFECTIVENESS OF THE COMMON & DIFFERENTIAL MODE MODEL

A. Numerical experiment of one TWP and one single wire

Now, we simulate the TWP model in Fig. 5 again in the common and differential mode approach. In this approach, the mode transform will happen on wire 2 and wire 3. Through this

way, the total number of the non-zero elements in the impedance (or admittance) matrix will be reduced from 9 to 5, this simplification will save the 4 spaces. The octangle in Fig. 7 shows the current at the near end (the current point which is nearest to the source) on wire 1 using the common and differential mode approach, and Fig. 8 shows the current at the far end (the current point which is nearest to the load). The dashed and dot lines represent the results using the Paul and McKnight method and the method shown in Section II B, respectively. We also calculated the current result by using the equivalent cable method for TWP [16, 17], which is shown by the diamond dot.
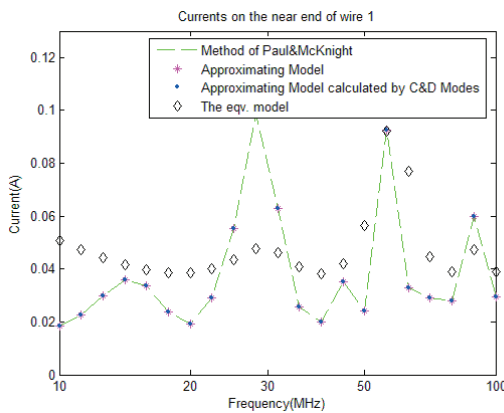

Fig. 7. Results of the near end current on wire 1 by different methods.
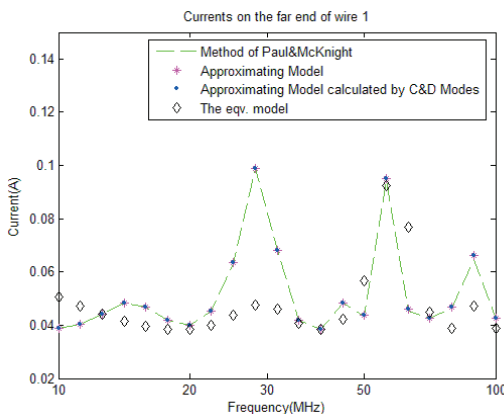
Fig. 8. Results of the far end current on wire 1 by different methods.

Figures 7 and 8 show that the variation in the original Paul and McKnight TWP model and the proposed approximated model is very little, the total Root-Mean-Square (RMS) form 10 MHz to 100 MHz is 3.1922×10^{-5} at the near end and the one at the far end is 3.8725×10^{-4}, and the RMSs of the equivalent cable method are 1.6046×10^{-2} and 2.1333×10^{-2}. So it is obvious that the present method is more accurate. The time cost of the non-approximated Paul & McKnight method and the time cost of/the approximating model are 0.47s and 0.31s. The time cost of the approximating by common and differential mode and the equivalent model [16, 17] are 0.16s. The 2 models have both shortened the solving process through their own way, so the time cost has been reduced.

B. Numerical experiment of two TWPs and one single wire

We have also calculated the situation of 2 TWPs. The equivalent bundle method's result has not been listed, this is because the model will approximate the TWPs by the value of the load and source impedance, and it was different from the model proposed. The model is shown in Fig. 9, and the lengths in Fig. 8 are selected to be h=2 mm, Δh=0.432 mm, d=3 mm, r=0.406 mm, h_g=4 mm and d_2=2 mm. In the common and differential mode we transform each wire pair twisted into their own common and differential modes. The results of the near end current and far end currents on the single wire are shown in Figs. 10 and 11. In this method, the mode transform will happen on each couple of the TWPs. There is 1 single wire and 2 common mode wires, and 2 differential mode wires in the total model. The differential modes are irrelevant with other wires, so non-zero elements number in the impedance or admittance matrixes of the reduced model will be 11 and the original number is 25. The total RMSs without mode transform are 1.1213×10^{-5} at the near end and 2.3106×10^{-5} at the far end. The ones with the transform are 7.0357×10^{-5} at the near end and 6.7700×10^{-5} at the far end. The RMSs grow a little because some errors occur in the calculation of the Z and Y in the mode transform, but it is still accurate for this method. When extending this method into N TWPs and M single wires, we could transform a $(2N+M)^2$ non-zero elements' matrix into an $(N+M)^2+N$ elements' one. The total reducing number is N(2N+2M-1), and it will save much space for storing the matrix that will affect on the result little by using the approximation method.
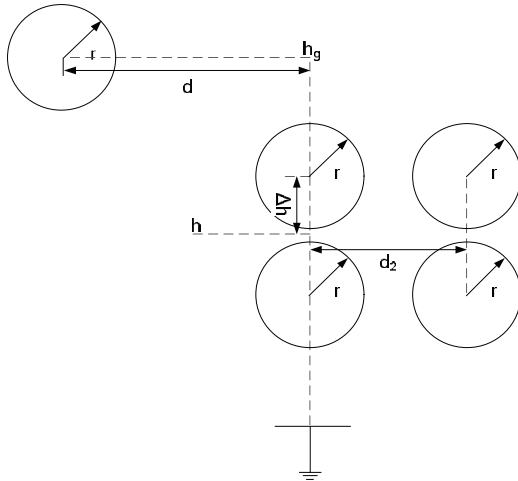
Fig. 9. Simulation model of 2 TWPs and one single wire.
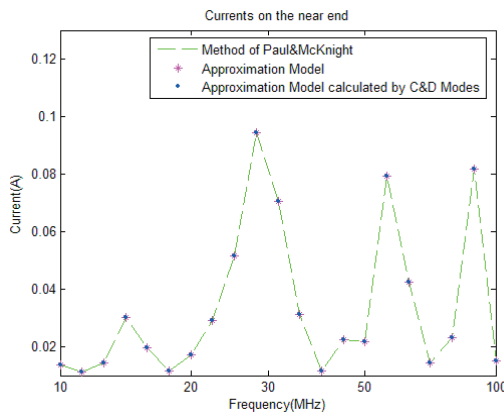
Fig. 10. Near end current results of the 2 TWPs and 1 single wire model.
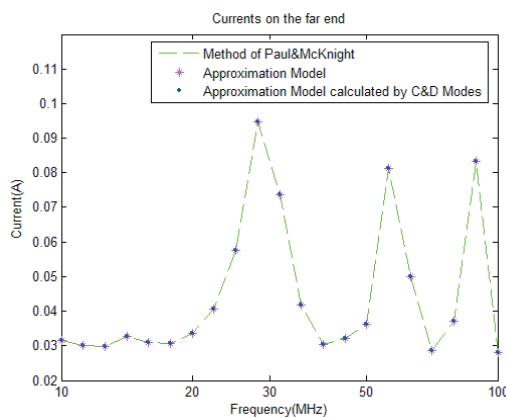
Fig. 11. Far end current results of the 2 TWPs and 1 single wire model.

V. CONCLUSION

In this paper, we proposed the approximation model of a twist wire pair into the common and differential mode, the derivation of the transforming has been provided. Due to the RMS result shown by the simulation, the approximation model varies little from the original model and it succeeded in the reduction in the total number of non-zero elements, and the method proposed has much reduction in storage and time cost.

ACKNOWLEDGMENT

REFERENCES

[1] S. Shenfeld, "Magnetic fields of twisted-wire pairs," *IEEE Trans. Electromagn. Compat.*, vol. EMC-11, no. 4, pp. 164-169, November 1969.

[2] M. B. Jolly and C. R. Paul, "Basic EMC technology advancement for C3 systems-crosstalk in twisted-wire circuits," *Rome Air Development Center*, Griffiss AFB, Rome, NY, USA, Tech. Rep. RADC-TR-82-286, vol. IV-C, November 1982.

[3] G. R. Piper and A. Prata, "Magnetic flux density produced by finite-length twisted-wire pairs," *IEEE Trans. Electromagn. Compat.*, vol. 38, no. 1, pp. 84-92, February 1996.

[4] C. Jullien, P. Besnier, M. Dunand, and I. Junqua, "Advanced modeling of crosstalk between an unshielded twisted pair cable and an unshielded wire above a ground plane," *IEEE Trans. Electromagn. Compat.*, vol. 55, no. 1, pp. 183-194, February 2013.

[5] C. R. Paul and J. A. McKnight, "Prediction of crosstalk involving twisted pairs of wires-part I: a transmission line model for twisted wire pairs," *IEEE Trans. Electromagn. Compat.*, vol. EMC-21, no. 2, pp. 92-105, May 1979.

[6] C. R. Paul and J. A. McKnight, "Prediction of crosstalk involving twisted pairs of wires-part II: a simplified, low-frequency prediction model," *IEEE Trans. Electromagn. Compat.*, vol. EMC-21, no. 2, pp. 105-114, May 1979.

[7] C. R. Paul and J. A. McKnight, "Applications of multiconductor transmission line theory to the predictions of cable coupling, vol. V: prediction of

crosstalk involving twisted wire pairs," *Rome Air Development Center*, Griffiss AFB, Rome, NY, USA, Tech. Rep. RADC-TR-76-101, February 1978.

[8] A. Shoory, M. Rubinstein, A. Rubinstein, C. Romero, N. Mora, and F. Rachidi, "Application of the cascaded transmission line theory of paul and mcknight to the evaluation of NEXT and FEXT in twisted wire pair bundles," *IEEE Trans. Electromagn. Compat.*, vol. 55, no. 4, pp. 648-656, February 2013.

[9] R. B. Armenta and C. D. Sarris, "Modeling the terminal response of a bundle of twisted-wire pairs excited by a plane wave," *IEEE Trans. Electromagn. Compat.*, vol. 49, no. 4, pp. 901-913, November 2007.

[10] G. Spadacini and S. A. Pignari, "A simplified statistical model for crosstalk in balanced twisted pairs," *ACES Conference 2007 Innovation in the Macromodeling of High Speed Interconnects*, 2007.

[11] S. A. Pignari and G. Spadacini, "Plane-wave coupling to a twisted-wire pair above ground," *IEEE Trans. Electromagn. Compat.*, vol. 53, no. 2, pp. 508-523, May 2011.

[12] G. Spadacini and S. A. Pignari, "Numerical assessment of radiated susceptibility of twisted-wire pairs with random nonuniform twisting," *IEEE Trans. Electromagn. Compat.*, vol. 55, no. 9, pp. 956-964, October 2013.

[13] G. Spadacini, F. Grassi, F. Marliani, and S. A. Pignari, "Transmission-line model for field-to-wire coupling in bundles of twisted-wire pairs above ground," *IEEE Trans. on EMC*, pp. 1-9, 2014.

[14] L. Tang, Z. Ye, L. Chen, Z. Xiang, and C. Liao, "The study on crosstalk of single wire and twisted-wire pair," *ISAP-2013 Int. Symp*, vol. 02, pp. 1008-1011, October 2013.

[15] G. Andrieu, L. Kone, F. Bocquet, B. Demoulin, and J. P. Parmantier, "Multiconductor reduction technique for modeling common-mode currents on cable bundles at high frequency for automotive applications," *IEEE Trans. Electromagn. Compat.*, vol. 50, no. 1, pp. 175-184, February 2008.

[16] G. Andrieu and A. Reineix, "On the application of the 'equivalent cable bundle method' to cable bundles in presence of complex ground structures," *IEEE Trans. Electromagn. Compat.*, vol. 55, no. 4, pp. 798-801, August 2013.

[17] G. Andrieu, A. Reineix, X. Bunlon, J. P. Parmantier, L. Kone, and B. Demoulin, "Extension of the 'equivalent cable bundle method' for modeling electromagnetic emissions of complex cable bundles," *IEEE Trans. Electromagn. Compat.*, vol. 51, no. 1, pp. 108-118, February 2009.

[18] L. Liu, Z. Li, M. Cao, and C. Gu, "Generalized equivalent cable bundle method for modeling crosstalk of complex cable bundles with multiple excitations," *Electromagn. Compat. (APEMC), 2012 Asia-Pacific Symp.*, pp. 269-272, May 2012.

[19] Z. Li, L. Liu, J. Yan, A. Xu, Z. Niu, and C. Gu "An efficient simplification scheme for modeling crosstalk of complex cable bundles above an orthogonal ground plane," *IEEE Trans. Electromagn. Compat.*, vol. 55, no. 5, pp. 975-978, October 2013.

[20] J. C. Ju, H. Y. Lee, D. C. Park, and N. S. Chung, "A simple model for a bundle of twisted-pair wires," *EMC. 2001 IEEE Int. Symp.*, vol. 1, 649-652, August 2001.

Hybrid Differential Evolution Particle Filter for Nonlinear Filtering

Chaozhu Zhang and Lin Li

College of Information and Communication Engineering
Harbin Engineering University, Harbin, Heilongjiang 150001, China
zhangchaozhu@hrbeu.edu.cn, lilin0214@yeah.net

Abstract ─ In this paper we propose a novel method for solving the nonlinear problem of the radar target tracking. The algorithm consists of a Particle Filter (PF) which employs the Unscented Kalman Filter (UKF) to generate the importance proposal distribution, and adopts the Hybrid Differential Evolution (HDE) algorithm based on Simulated Annealing (SA) algorithm as the resampling scheme. Firstly, the Importance Distribution (ID) which contains the newest measurements is constructed by the UKF. In addition, the UKF generates proposal distributions that match the true posterior more closely. Secondly, to solve the particle degeneracy and impoverishment phenomenon, the sampling particles are resampled by the HDE algorithm. The mutation and crossover steps of the Differential Evolution (DE) algorithm are executed to generate the trial vectors. Then the selection step is replaced by the Metropolis criterion of the SA algorithm. The proposed algorithm combines the advantages of the SA algorithm with the DE algorithm. It not only has superior estimation performance, but also the convergence speed is fast. Simulation results demonstrate that the proposed algorithm outperforms the standard PF, the Auxiliary Particle Filter (APF), the Regularized Particle Filter (RPF) and the Particle Filter based on Differential Evolution (PFDE).

Index Terms ─ Hybrid differential evolution, nonlinear filtering, particle filter, radar tracking, simulated annealing algorithm.

I. INTRODUCTION

As we know, most of the radar tracking filtering algorithms are linear filtering, such as Kalman filter. However, these linear filters are optimal only under the condition that the system is linear or the noise is Gaussian. Actually, the system model and the measurement equation of the target are nonlinear, and the noise is non-Gaussian. In that situation, if we still use linear filter to track targets, the tracking performance will be reduced, or even worse, the targets will be lost. Therefore, it is necessary to employ the nonlinear filtering to solve the nonlinear problem of the radar tracking.

Nonlinear filtering is a very active topic in signal processing and control theory. There is a vast literature on this subject; see [1-5] for excellent references among others. Although the equations of the optimal nonlinear filter have been developed since the middle of the 1960s, the involved integrals are still intractable. Hence, many suboptimal nonlinear filters have been proposed.

The simplest way to solve the problem of non-Gaussian, nonlinear filtering is the Extended Kalman Filter (EKF) [6]. It linearizes the state transition and the measurement equations through Taylor series expansions. However, the series approximations in the EKF algorithm could cause large errors of the nonlinear functions and probability distributions. So, this filter would result in divergency. The convergence of the EKF is studied in [7]. Later on, the UKF is proposed by Julier and Uhlmann, which uses several so-called sigma points to recursively calculate the mean and covariance used in the Kalman Filter [8]. The UKF could obtain more accurate results than the EKF, but it couldn't adapt to general non-Gaussian distributions. Essentially, the EKF and the UKF have the same principle; both of them use the Gaussian distribution to approximate the true posterior distribution.

A different approach to the nonlinear filtering problem is the Bayesian approximation, which is detailedly described in [9]. This kind of filter is based on the principle of constructing the posterior probability density of the state by the prior knowledge and the observation; and, the key point is to obtain a good approximation of the posterior density.

Another popular method for nonlinear filtering is Monte Carlo methods, also known as Particle Filter (PF). Up to now, the PF is the most successful nonlinear filter, which goes back to the 1950s, but it hadn't been used in practical applications until 1993 when Gorden proposed the Sequential Importance Resampling (SIR) algorithm [10]. The PF utilizes some random particles with associated weights to approximate the true posterior density function. The PF has been used successfully in many domains; however, its performance depends heavily on the choice of the importance distribution function and the resampling algorithms. To improve the performance of the PF, choosing a good proposal distribution or modifying the resampling scheme are often adopted. For example, Pitt and Shephard [11] introduced the Auxiliary Particle Filter (APF), which uses an auxiliary variable to select the particles. In [12], the Regularized Particle Filter (RPF) is put forward, which resamples from a continuous approximation of the posterior density to reduce the particle impoverishment problem. In [13], the EKF Gaussian approximation is used as the importance distribution for a PF. In [14], the EKF proposal is replaced by UKF proposal, and the Unscented Particle Filter (UPF) is proposed. We will propose a new method in this paper which uses the HDE based on SA algorithm as resampling schemes for the PF, which regards the resampling process as an optimization problem. We refer to it as Hybrid Differential Evolution Particle Filter (HDEPF). In the HDEPF, the importance distribution is generated by the UKF.

The remainder of this paper is organized as follows. At first, the problem statement and the principle of the basic PF are introduced in Section II. In Section III, we proposed the HDE algorithm and HDEPF. Then in Section IV, we discussed some experimental results. At last, conclusions and pointers for future research are presented in Section V.

II. PROBLEM STATEMENT AND THE BASIC PARTICLE FILTER

Many nonlinear filtering problems can be written in the form of the Dynamic State Space (DSS) model as follows:

$$x_k = f(x_{k-1}, u_{k-1}), \tag{1}$$

$$z_k = h(x_k, v_k), \tag{2}$$

where x_k and z_k are the state variable and observation at time k, respectively. k is the time index. $f(\cdot)$ and $h(\cdot)$ are some known functions, system noise u_{k-1} and observation noise v_k are random variables at time of given distributions. u_{k-1} and v_k are independent of past and current states. v_k is independent of system noise u_{k-1}. The objective of filtering is to recursively estimate the posterior density $p(x_k | z_{1:k})$ of the state x_k based on all available measurements $z_{1:k} = \{z_1, z_2 \cdots, z_k\}$. A recursive update of the posterior density as new observations arrive is given by the recursive Bayesian filter defined by:

$$p(x_k | z_{1:k-1}) = \int p(x_k | x_{k-1}) p(x_{k-1} | z_{1:k-1}) dx, \tag{3}$$

$$p(x_k | z_{1:k}) = \frac{p(z_k | x_k) p(x_k | z_{1:k-1})}{p(z_k | z_{1:k-1})}, \tag{4}$$

where the conditional density $p(z_k | z_{1:k-1})$ can be calculated by:

$$p(z_k | z_{1:k-1}) = \int p(z_k | x_k) p(x_k | z_{1:k-1}) dx_k. \tag{5}$$

It can be seen that the integrals are intractable. So, the PF uses Monte Carlo methods to translate the integrals problems into the cumulative process of limited particles probability transition. The PF uses the transition density $p(x_k | x_{k-1})$ as the importance distribution function $q(x_k^i | x_{k-1}^i, z_k)$ to generate particles. Then the posterior density $p(x_k | z_{1:k})$ at time k can be described as:

$$p(x_{0:k} | z_{1:k}) \propto p(z_k | x_k) p(x_k | x_{k-1}) p(x_{0:k-1} | z_{1:k-1}). \tag{6}$$

Accordingly, the weights of the particles are called importance weight. We define the unnormalized weights as:

$$\begin{aligned} w_k^i &= \frac{p(x_{0:k}^i | z_{1:k})}{q(x_{0:k}^i | z_{1:k})} \\ &= w_{k-1}^i \frac{p(z_k | x_k^i) p(x_k^i | x_{k-1}^i)}{q(x_k^i | x_{k-1}^i, z_k)}. \end{aligned} \tag{7}$$

Then we normalize the weights and begin the resampling process. The aim of resampling is to eliminate samples with low importance weights and copy samples with high importance weights. After the resampling process, the weights can be defined by $w_k^i = 1/N$. The popular resampling algorithm is the multinomial resampling.

Last the posterior density $p(x_k \mid z_{1:k})$ can be calculated by:

$$p(x_k \mid z_{1:k}) \approx \sum_{i=1}^{N} w_k^i \delta(x_k - x_k^i), \qquad (8)$$

where $\delta(\cdot)$ is the Dirac delta function, x_k^i is the i th particle with the normalized weight w_k^i. N is the particle number.

III. HYBRID DIFFERENTIAL EVOLUTION PARTICLE FILTER

A. Hybrid differential evolution algorithm

DE algorithm, proposed by Price and Storn [15], is a population-based stochastic algorithm for global optimization, which has earned a reputation as a very effective global optimizer. DE algorithm has the following advantages over the traditional genetic algorithm: more efficient memory utilization, lower computational complexity, and it is much more easy to use. However, DE algorithm has insurmountable shortcomings. It has slower convergence rate in latter periods, even failing to local extremes [16]. Then Hybrid Differential Evolution Algorithm based on SA algorithm is proposed by [17]. The new algorithm utilizes the search capability of the SA algorithm to enhance the convergence capability of the DE in latter periods and improve the robustness of the DE algorithm. The HDE algorithm uses the Metropolis criterion of the SA algorithm to replace the section step of the DE algorithm. So it relies on the initial population generation, mutation, recombination and the new selection to probe search space through iterative progress until the terminate criteria are met.

Detailed steps are presented accordingly in the subsequent sections.

Step 1: Creating initial population

The first step of HDE is to create the initial population samples (the number of generations is $g = 0$) in n dimension space as follows:

$$x_{ij}(0) = x_{ij}^L + rand_{ij}(0,1)(x_{ij}^U - x_{ij}^L), \qquad (9)$$

where $i = 1, 2, \ldots NP; j = 1, 2, \ldots n$, NP is the population size. x_{ij}^U and x_{ij}^L denote the upper and lower limit of the j th variable in the population, respectively. $rand_{ij}(0,1)$ represents a uniformly distributed random value within $[0,1]$.

Step 2: Mutation operation

The function of mutation in HDE is to maintain the diversity of population. A typical HDE mutation samples formulation is:

$$h_{ij}(g) = x_{ij}(g) + F \cdot (x_{r1j}(g) - x_{r2j}(g)), \quad (10)$$

where g represents the g th generation, $h_{ij}(g)$ are the mutated vector samples. $r1 \neq r2 \neq i$, and $r1$, $r2$ are randomly selected integers within NP, $r1, r2 \in \{1, 2, \ldots, NP\}$. F is scaling factor.

Step 3: Crossover operation

The basic crossover process is a discrete recombination, which employs a crossover constant $CR \in [0,1]$ to determine whether the new generated individual samples need to be recombined. The expression of the crossover process is given in (11):

$$v_{ij}(g) = \begin{cases} h_{ij}(g) & rand(0,1) \leq CR \\ x_{ij}(g) & rand(0,1) > CR \end{cases}, \qquad (11)$$

where $v_{ij}(g)$ are the trial vector samples.

Step 4: New selection operation

The HDE algorithm adopts the Metropolis criterion of the SA algorithm to select the trial vector samples.

Step 5: Cool-down operation

In this step, the cool-down operation of the SA algorithm is executed. We define $T = T \cdot \rho$, $\rho \in (0,1)$ as an annealing parameter.

When the new population is propagated, Step 2 to Step 5 is repeated until the pre-specified temperature $T0$ is reached.

B. Hybrid differential evolution particle filter

In the presented algorithm, the particles from using a UKF for importance distribution are regarded as the initial population of the HDE algorithm, and the corresponding weights are treated as the fitness functions of the target vectors, respectively. The HDE resampling scheme

recombines the particles by using an iterative process of mutation, crossover and the simulated annealing operator. Then a new set of diverse particles are propagated.

The new filter proposed in this paper is called HDEPF, and the steps follows.

In the first step, we can obtain Gaussian importance distribution with the mean $\tilde{x}_k^i$ and the variance $\tilde{P}_k^i$ by using UKF filter for all particles $x_k^i (i = 1, 2, \ldots N)$, where N is the particle number. Then the sampling particles can be gained by sampling the importance distribution, $\hat{x}_k^i \sim N(\tilde{x}_k^i, \tilde{P}_k^i)$, and their weights w_k^i can be calculated and normalized by equation (7).

In the second step, the sampling particles $\hat{x}_k^i$ are regarded as the initial population of the HDE algorithm, and the corresponding weights w_k^i are regarded as the fitness functions $f(x_{ij})$. Then a mutation step and a crossover step are executed. Finally, the trial vector samples $v_{ij}(g)$ can be obtain by equation (12), and the corresponding fitness function is calculated as

$$f(v_{ij}(g)) = \frac{p(z_k \mid v_{ij}(g)) p(v_{ij}(g) \mid x_{k-1}^i)}{q(v_{ij}(g) \mid x_{k-1}^i, z_k)} \text{ and is}$$

normalized as $f(v_{ij}(g)) = f(v_{ij}(g)) / \sum_i^{NP} v_{ij}(g)$, where NP is population size and $NP = N$.

In the third step, the new selection operator is proceeding. We construct the following parameter about fitness function values, $\Delta f = f(v_{ij}(g)) - f(x_{ij}(g))$, then we decide the trial vector samples by the Metropolis criterion.

In the fourth step, the cool-down operation of the HDE algorithm is executed.

In the fifth step, the process is repeated until the optimum is found or a pre-specified temperature T is reached.

And at last, we obtain the optimal particles $\{\dot{x}_k^i, \dot{w}_k^j : i = 1, 2 \ldots N\}$ and estimate the system state $x_k = \sum_{i=1}^N \dot{x}_k^i \dot{w}_k^j$.

IV. EXPERIMENT RESULTS AND DISCUSSIONS

To compare the performance of the proposed filters to those of the PF, the RPF, the PFDE and the APF, where the PFDE combines particle filter with differential evolution [19]. We choose the same model as Merwe, et al. used in his experiments [14]. This model is very representative due to its strong nonlinearity. And it has been used before in many publications [18-21]:

$$x_{k+1} = 1 + \sin(w\pi k) + \phi_1 x_k + v_k, \qquad (12)$$

$$z_k = \begin{cases} \phi_2 x_k^2 + n_k & k \le 30 \\ \phi_3 x_k - 2 + n_k & k > 30 \end{cases}, \qquad (13)$$

where v_k is a Gamma(3,2) random variable modeling the process noise, $w = 4e-2$, $\phi_1 = \phi_3 = 0.5$, and $\phi_2 = 0.2$ are scalar parameters. The observation noise n_k is drawn from a Gaussian distribution $N(0, 0.00001)$. Different filters are used to estimate the state sequence x_k for $k = 1, 2, \ldots T$, the total observation time is $T = 50$. The UKF parameters were set to $\alpha = 1$, $\beta = 0$ and $\kappa = 2$ [14]. In the proposed filters, $F = 0.9$, $Cr = 0.6$ and the maximum number of generations is $G = 20$, the annealing initial temperature $T0 = 100$, and the annealing parameter $\rho = 0.9$ [17,19]. All of the particle filters used $N = 10$ particles and systematic resampling. The experiment was repeated $M = 200$ Monte Carlo simulations to demonstrate the performance of the proposed algorithm.

To measure the performance of the algorithms, we introduce the Root Mean Squared Error ($RMSE$) and its mean $\overline{RMSE}$, RMSE for M simulations with observation time $RMSE'$ are shown as follows:

$$RMSE = \sqrt{\frac{1}{T} \sum_{k=1}^T (x_k - \hat{x}_k)^2}, \qquad (14)$$

$$\overline{RMSE} = \sqrt{\frac{1}{M} \sum_{m=1}^M \left[\frac{1}{T} \sum_{k=1}^T (x_k^m - \hat{x}_k^m)^2 \right]}, \qquad (15)$$

$$RMSE' = \sqrt{\frac{1}{M} \sum_{m=1}^M (x_k^m - \hat{x}_k^m)^2}, \qquad (16)$$

where x_k^m is the true value of target state and $\hat{x}_k^m$ is defined as the estimation of target state.

A. Simulation results of the estimation

Figure 1 compares the estimates of the different filters generated from a single run of the

state estimates. From Fig. 1, we can see that the tracking trajectory of the HDEPF is much closer to the true trajectory than other filters.
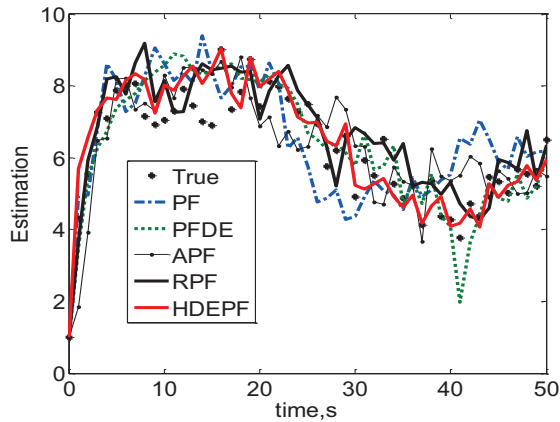

Fig. 1. Plot of estimates generated by the different filters for a simulation.

For clearly, the estimation RMSE with observation time and the estimation RMSE with simulation number of different filters are shown in Figs. 2 and 3, respectively. We can see that both two kinds of the RMSE curves of the proposed method are lower than other algorithms. Moreover, it can be found that the RMSE of HDEPF is higher than other methods before 2s or so in Fig. 2. That is because the UKF and HDE algorithms both need initialized process, but this time is shorter, as a whole, the result of the experiment proves that the new algorithm has good optimization effect. Meanwhile, Fig. 3 also illustrates this point.
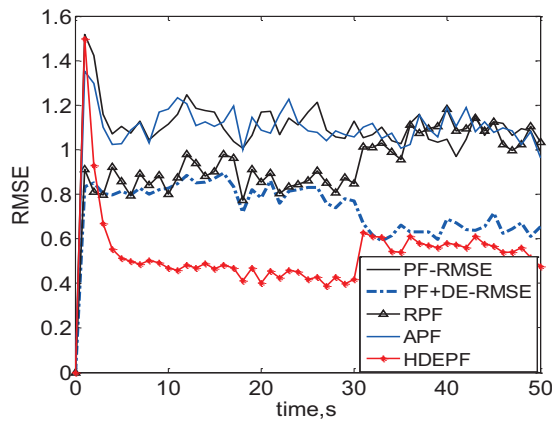

Fig. 2. RMSE' of PF, APF, RPF, PFDE and HDEPF with observation time for 200 MC simulations, where N=10.
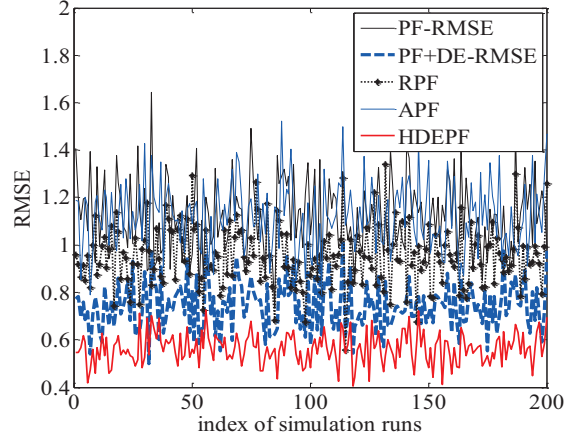

Fig. 3. RMSE of PF, APF, RPF, PFDE and HDEPF with simulation number, where N=10, T=50.

Table 1 displays and summarizes the performance of the five filters, where the means and variances of the state estimates are shown. It can be clearly seen that the Mean RMSE of the HDEPF is lower than others, as well as, the Variance RMSE is obviously low. From Figs. 1, 2, 3 and Table 1, we can realize that the estimation accuracy of the proposed algorithm (HDEPF) is much higher than other filters.

Table 1: Mean and variance of RMSE of PF, APF, RPF, PFDE and HDEPF for 200 MC simulations with N=10

Algorithm	Mean (RMSE)	Variance (RMSE)
PF	1.1132	0.0178
PFDE	0.7422	0.0103
APF	1.1049	0.0247
RPF	0.9543	0.0213
HDEPF	0.5574	0.0047

It is shown in Fig. 2 that the proposed algorithm has better estimation accuracy when $k \leq 30$. According to equation (13), we can find that the observation function is a quadratic function in the first 30 seconds, and it becomes a linear function after 20 seconds. Before 30 seconds, the nonlinear degree of system is greater than later time. From Table 2 we can see that the RMSE of the proposed algorithm has decreased by around 50% over the PF when $k \leq 30$. This shows that the proposed algorithm has better performance for nonlinear filtering than the PF algorithm.

Table 2: RMSE mean of PF and HDEPF for 200 MC of different observation time periods

Algorithm	0<k<30	30<k<50
PF	1.1232	0.7131
HDEPF	0.5654	0.3895
The percentage of improvements	49.66%	45.38%

B. Analysis of the runtime of the algorithms

Table 3 compares the run time for a simulation of different algorithms, where $N=10$ except the bracket, there $N=100$. It can be seen that the proposed algorithm has much more run time than others, except RPF and PFDE; because the proposed algorithm not only has the UKF filter but also combines the HDE, it wastes much time. The HDE uses the search capability of the SA algorithm, which improves its convergence speed. So the proposed algorithm has less run time than the PFDE algorithm.

Table 3: Comparison of the run time

Algorithm	Run Time
PF	0.031027 (0.137454/N=100)
PFDE	0.339256
APF	0.072424
RPF	0.372693
HDEPF	0.112712

Then we increase the particle number of the PF, here $N=100$, and kept the other particle numbers. It can be calculated that the RMSE mean of the PF with $N=100$ is 0.87414. From Table 1, we can see that the estimation accuracy of the PF with $N=100$ is also not as good as the proposed algorithm. However, Table 3 shows that the run time of the PF with $N=100$ is as much as the proposed algorithm. This represent that the estimation performance of the proposed algorithm is higher than the PF algorithm with the same run time. In addition, the proposed algorithm uses only 10 particles to reach the precision of the PF with $N=100$, it shows that the proposed algorithm has better efficiency. In the future, it will be interesting to investigate how to choose the parameters of the new algorithm.

V. CONCLUSION

In this paper, a new particle filter algorithm was developed for nonlinear filtering. Firstly, we use the experience of the UPF algorithm for reference to generate the importance proposal distribution though the UKF. Since the generated distribution matches the true posterior more closely. Secondly, the Hybrid Differential Evolution (HDE) based on SA is employed as the resampling scheme and is the major new contribution of this paper. The proposed resampling algorithm can effectively reduce the particle degeneracy and impoverishment problem, and improves the state estimation accuracy. In addition, the convergence performance of the HDE is better than the DE by utilized search capability of the SA [17]. Therefore, the proposed algorithm yields a better performance than the particle filter which based on the DE. Moreover, it has less run time. The numerical simulations were conducted to attest that the proposed algorithm has better estimation performance and higher particle utilization than the previous method. Future works will concentrate on the nonlinear no Gaussian radar target tracking using the proposed algorithm.

REFERENCES

[1] H. Tanizaki, "Nonlinear filter: estimation and applications (2nd ed.)," *Springer Verlag*, New York, 1996.

[2] M. West and J. Harriaon, "Bayesian forecasting and dynamic models (2nd ed.)," *Springer Verlag*, New York, 1997.

[3] J. Liang and X. Y. Peng, "Particle estimation algorithm using correlation of observation for nonlinear system state," *Electronics Letters*, vol. 44, no. 8, pp. 553-555, April 2008.

[4] J. Liang and X. Y. Peng, "Improved particle filter for nonlinear system state," *Electronics Letters*, vol. 44, no. 21, pp. 1275-1277, October 2008.

[5] A. Doucet, N. de Freitas, and N. Gordon (Eds.), "Sequential monte carlo methods in practice," *Springer Verlag*, New York, 2001.

[6] B. D. Anderson and J. B. Moore, "Optimal filtering," *Prentice-Hall*, New Jersey, 1979.

[7] K. Reif, "Stochastic stability of the discrete-time extended Kalman filter," *IEEE Trans. Automatic Contro.*, vol. 44, no. 4, pp. 714-728, 1999.

[8] S. J. Julier and J. K. Uhlmann, "A general method for approximating nonlinear transformations of

probability distributions," *Dept. of Engineering Science, University of Oxford*, 1996.

[9] Z. Chen, "Bayesian filtering: from kalman filters and beyond," *Communication Research Laboratory, McMaster University*, 2003.

[10] N. Gordon, D. Salmond, and A. Smith, "Novel approach to nonlinear/non-gaussian bayesian state estimation," *IEEE Proc. F.*, vol. 140, no. 2, pp. 107-113, 1993.

[11] M. Pitt and N. Shephard, "Filtering via simulation: auxiliary particle filter," *Journal of the American Statistical Association*, vol. 94, no. 446, pp. 590-559, 1999.

[12] C. Musso, N. Oudjane, and F. Legland, "Improving regularised particle filter," *In Sequential Monte Carlo Methods in Practice, Springer-Verlag*, pp. 247-271, 2001.

[13] J. F. G. De Freitas, M. Niranjan, A. H. Gee, and A. Doucet, "Sequential monte carlo methods to train neural network models," *Neural Comput.*, vol. 12, no. 4, pp. 955-993, 2000.

[14] R. Merwe, A. Doucet, N. Freitas, and E. Wan, "The unscented particle filter," *Technical Report CUED/F-INFENG/TR 380, Cambridge University Engineering Department*, pp. 1-40, 2000.

[15] R. Storn and K. Price, "Differential evolution-a simple and efficient heuristic for global optimization over continuous space," *Journal of Global Optimization*, vol. 11, pp. 341-359, 1997.

[16] S. Rahnamayan and H. R. Tizhoosh, "Opposition-based differential evolution," *IEEE Trans. On Evolutionary Computation*, vol. 12, pp. 64-78, 2008.

[17] H. ZhongBo and X. ShengWu, "Study of hybrid differential evolution based on simulated annealing," *Computer Engineering and Design*, vol. 28, no. 9, pp. 1989-1992, May 2007.

[18] Y. Wang, F. Sun, and Y. Zhang, "Central difference particle filter applied to transfer alignment for SINS on missiles," *IEEE Trans. Aerosp. Electron. Syst.*, vol. 48, no. 1, pp. 375-387, 2012.

[19] H. Li, J. Wang, and H. Su, "Improved particle filter based on differential evolution," *Electron. Lett.*, vol. 47, no. 19, pp. 1078-1079, 2011.

[20] J. Y. Zuo and Y. N. Jia, "Adaptive iterated particle filter," *Electron. Lett.*, vol. 49, no. 12, pp. 742-744, June 2013.

[21] C. Qi, "An efficient two-stage sampling method in particle filter," *IEEE Trans. Aerosp. Electron. Syst.*, vol. 48, no. 3, pp. 2666-2672, July 2012.

Chaozhu Zhang was born in 1970. He received his B.S. degree in Electronics and Information Engineering from Harbin Institute of Technology in 1993, his M.S. degree in Communications and Information Systems and his Ph.D. degree in Signal and Information Processing from Harbin Engineering University in 2002 and 2006, respectively. He is a Professor for Harbin Engineering University, China. He is a member of IEEE, academician of Chinese Aerospace Society and Heilongjiang Biomedical Engineering Society. His researches include signal processing applications in radar and communications and image processing.

Lin Li was born in 1987. She received her B.S. degree in Electronics and Information Engineering from Anhui Agricultural University in 2009. Now she is a Ph.D. candidate in Harbin Engineering University, China. Her research interests include radar signal processing, nonlinear filtering and target tracking.